THE EFFECT OF HIGH PORE WATER PRESSURES ON THE MECHANICAL BEHAVIOUR OF SEDIMENTS

A thesis submitted to the
University of London

by

Angus Evan Skinner, BSc(Eng) London

for the degree of

Doctor of Philosophy in the Faculty of Engineering

Imperial College

December 1974

ABSTRACT

The Principle of Effective Stress is fundamental to the application of Soil Mechanics theory to practical engineering problems. The research undertaken probes the validity of this principle in relation to the mechanical behaviour of granular soils. The line of questioning starts with the mechanism of interparticle contact under pure normal loading, and goes on to investigate the behaviour when the interparticle contacts are subjected to shear loading as well, and a theoretical model for the friction of minerals is put forward.

Using this model and observations on the mechanics of the particles it has been possible to compare the shear strength response of a granular soil with predictions based on various theoretical equations for effective stress that have been advanced in the past.

The model for interparticle behaviour is also used to investigate the stresses which effectively control the compression of a granular soil under isotropic and anisotropic conditions. The resulting relationships between stress and strain are used to compare theoretical predictions of settlements of Rockfill and field observations.

The physical bases of stress-strain theories are also reviewed in terms of interparticle behaviour, and a conceptual model for the behaviour of a granular soil is proposed.

ACKNOWLEDGEMENTS

The research work presented in this thesis was carried out in the Civil Engineering Department of the Imperial College of Science and Technology under the supervision of Professor A W Bishop.

It was made possible by successive awards from the Department of Scientific and Industrial Research and the Civil Engineering Research Association.

The author would like to express his gratitude to Professor A W Bishop for his continuous keen interest in the progress of the work. The author would also like to acknowledge the many useful discussions held with Professor N R Morgenstern and the late Mr S W Smotrych.

The research work could not have started or progressed but for the services rendered by the following persons:

1. The staff of the Civil Engineering Workshop under Mr N D Scott, in particular Mr F Winser who constructed the high pressure cells.

2. The Soil Mechanics technical staff under Mr D Evans, all of whom gave constant encouragement and support.

3. Miss J Gurr for the photographic reproduction.

4. Mrs D J Ratcliffe for her painstaking care in assisting with and preparing the typescript and her endless patience.

Finally the author would like to put on record the cheerful and dedicated support of his wife, Janet, for which he can not thank her enough.

CONTENTS

		Page Nos
ABSTRACT		i
ACKNOWLEDGEMENTS		ii
CHAPTER 1:	REVIEW AND OUTLINE OF WORK UNDERTAKEN	1.1-1.13
1.1	Introduction	1.1
1.2	Brief history of the concept of effective stress for fully saturated soils	1.3
1.3	Friction between mineral surfaces ..	1.5
1.4	Strength as influenced by the mechanism of deformation	1.9
1.5	Interparticle contact deformation ..	1.10
CHAPTER 2:	APPARATUS AND TESTING TECHNIQUES	2.1-2.15
2.1	Introduction	2.1
2.2	Setting up procedure and details of apparatus	2.2
	(7 plates and 12 figures)	
CHAPTER 3:	THE FRICTION OF MINERAL SURFACES UNDER LOW AND HIGH AMBIENT PRESSURE CONDITIONS - WITH SPECIAL REFERENCE TO QUARTZ	3.1-3.28
3.1	The contact between mineral surfaces	3.1
3.2	The strength of the asperities subjected to normal load without shear	3.1
3.3	The behaviour of asperities subjected to normal and shear loads	3.10
3.4	Theory of the friction between mineral surfaces	3.12
3.5	Prediction of the coefficient of friction for quartz on quartz	3.17

Page Nos

3.6 Experimental determination of the friction of quartz on quartz 3.17

3.7 Comparison of the theoretical prediction of friction coefficient with the experimental results 3.25

(29 figures)

CHAPTER 4: THE INFLUENCE OF INTERPARTICLE FRICTION ON THE SHEARING STRENGTH OF A NON-COHESIVE MATERIAL 4.1-4.32

4.1 Introduction 4.1

4.2 Theoretical relationships between shear strength and interparticle friction 4.2

4.3 Particle mechanics during shear .. 4.4

4.4 Surface friction of glass 4.5

4.5 Analysis of the mechanics of spheres and rollers subjected to various frictional tractions 4.11

4.6 Tests to establish the occurrence of particle rotation during shear .. 4.23

4.7 Comparison of theoretical relationships and experimental results 4.25

(46 figures)

CHAPTER 5: SHEAR CHARACTERISTICS OF PARTICULATE MATERIALS AND THE STRESSES THAT ARE EFFECTIVE IN CONTROLLING THEM 5.1-5.32

5.1 Introduction 5.1

5.2 Effective stress as applied to a single solid body 5.2

5.3 Effective stress as applied to two discrete solid bodies in contact .. 5.4

5.4 Mineral block in contact with a random assembly of mineral particles 5.9

5.5 Effective stress for a mass of mineral particles subjected to shear 5.14

(15 figures)

		Page Nos
CHAPTER 6:	STRESSES CONTROLLING VOLUME CHANGES	6.1-6.50
6.1	Volume changes due to isotropic stress changes	6.1
6.2	Measurement of volume changes when pore fluid pressures are changed	6.8
6.3	An investigation into the physical nature of the deformation process of isotropic compression	6.18
6.4	Settlement of granular fills	6.36
6.5	Creep of rockfill	6.46
6.6	Summary	6.50
(35 figures)		
CHAPTER 7:	FACTORS INFLUENCING THE STRESS-STRAIN BEHAVIOUR OF GRANULAR MATERIALS	7.1-7.25
7.1	Introduction	7.1
7.2	Particle fracture due to surface contact stresses	7.2
7.3	Particle fracture due to internal stresses	7.4
7.4	Factors influencing the stress-dilatancy theory	7.10
7.5	Stress-dilatancy correlations for variable stress ratio paths	7.12
7.6	Stress-dilatancy correlations for constant R paths	7.18
7.7	Stress-dilatancy correlations for elastic paths (including fretting friction)	7.22
7.8	Summary of the conditions during which the stress-dilatancy theory can be used as a soil model	7.22
7.9	Factors influencing the Cambridge soil models - namely Granta Gravel and Cam Clay models	7.23
(18 figures)		
(1 plate)		

		Page Nos
CHAPTER 8:	BEHAVIOUR OF GRANULAR SOIL	8.1-8.11
8.1	A conceptual model for granular non-cohesive soil	8.1
8.2	Early stress-strain behaviour predictions from anisotropic consolidation tests	8.7
8.3	Stress-strain behaviour during shear stages when slip and/or crushing mechanisms predominate	8.10
8.4	Summary	8.11
	(15 figures)	
BIBLIOGRAPHY		9 pages
		B.1-B.9

CHAPTER 1

REVIEW AND OUTLINE OF WORK UNDERTAKEN

1.1 Introduction:

Sediments are aggregates of mineral particles, and an individual grain only contacts a few of its immediate neighbours. Through these contacts are transmitted forces which are a consequence of the stresses applied to the sediment. The behaviour of the material involved in these particle to particle contacts will determine the deformation characteristics of the particles, and as the deformation of the sediment as a whole is purely the sum total of the individual deformations it is obvious that the interparticle contact characteristics must dominate the strength and deformation characteristics of the sediment as a whole.

Having made this statement one would expect to find in the literature on soil behaviour a substantial section devoted to interparticle contact behaviour, but this is not the case. Certainly the subject is not simple. For example, direct observations are difficult as optical microscopes may not have sufficient resolution to distinguish individual grains, let alone the contacts between grains. Even more sophisticated instruments such as the stereo scanning electron microscope, with magnifying power of up to 40,000 times, cannot resolve this problem. So for these materials various 'soil structure models' have been proposed (for example, the 'card house model') and have in some cases been used to explain possible

deformation mechanisms for particular soils. (The card house model has been used to explain the sensitivity of marine clays, (Rosenquist, 1959).)

Other difficulties with clay soils arise because particles are influenced by electrical attractive and repulsive forces, which will also influence the strength and volume change characteristics. These forces are variable - for example, they can be modified by changing the pore fluid. Sridharan and Venkatappa Rao (1973) conducted consolidation tests with various pore fluids, and showed that the equilibrium voids ratio for a particular consolidation pressure was indeed dependent on the dielectric constant of the pore fluid, but they had to interpret their results using assumed models for the deformation behaviour of the soils they tested, because the results showed that increasing the dielectric constant of the pore fluid reduced the equilibrium void ratio for kaolin whereas the opposite was true for montmorillonite.

The compressibility model of the soil structure advanced by Sridharan and Venkatappa Rao (loc cit) depended on the relative importance of the shearing resistance of grain to grain contacts as compared with the influence of long range electrical repulsive forces which increases with increase in dielectric constant. So if a law relating compression and applied stress is to be determined it is still necessary to determine the areas of real contact between particles.

It is easier to consider the behaviour of a material composed of particles which are very little influenced by long-range

electrical forces, and the experimental work conducted for this project is concerned with these materials, and the objective is to investigate the physical basis of various hypotheses which have been advanced which enable mathematical equations to be written defining the stresses which are effective in controlling strength or deformation.

1.2 Brief History of the Concept of Effective Stresses for fully saturated Soils:

The use of the concept of effective stress controlling deformation and strength was used by Terzaghi in the early 1920's, and the first statement in the form:

$$\sigma' = \sigma - u$$

where σ' is the effective stress, σ is the total stress and u the pore fluid pressure, was also made by Terzaghi, although an exact date for the statement of the concept is difficult to define. A very clear exposition of the development of the understanding leading towards the effective stress concept is given by Skempton in *From theory to practice in soil mechanics* under the heading 'Significance of Terzaghi's concept of effective stress'.

A period of assimilation followed, during which the effective stress concept was built into Soil Mechanics practice.

Then in 1953 Bishop proposed a modification for the equation governing compression of soil, taking into consideration the compressibility of the solid material C_s and of the skeleton

C. The resulting equation expressed as a change in effective stress $\Delta\sigma'$ was:

$$\Delta\sigma' = \Delta\sigma - \Delta u \left(1 - \frac{C_s}{C}\right)$$

This equation and Terzaghi's equation-were compared by Skempton in 1960, who stated that the effective stress controlling volume changes is given with sufficient accuracy by Bishop's equation, and that Terzaghi's equation was a very good approximation.

In this paper Skempton also proposed a new equation for the effective stress governing shear strength, and his equation was:

$$\sigma' = \sigma - \left(1 - \frac{a \tan \psi}{\tan \phi'}\right).u$$

where σ' is the effective stress

σ is the total stress

a is the contact area ratio

ψ is the angle of intrinsic friction of the solid material of the soil grains

ϕ' is the effective angle of shearing resistance

u is the pore water pressure

The derivation of this equation utilizes two assumptions, first that the deformation of the soil structure involves pure sliding of the particles in contact, and second that this deformation mechanism does not change for changes in external pressure or pore water pressure.

In this paper Skempton gives the background to discussions

on effective stress and compares the predictions of three effective stress equations, namely:

1. The intergranular stress equation for effective stress $\sigma' = \sigma - (1 - a)u$.
2. Terzaghi's equation $\sigma' = \sigma - u$.
3. Skempton's equation $\sigma' = \sigma - (1 - \frac{a \tan \psi}{\tan \phi'})u$.

The data presented by Skempton tended to support his equation. This brief review again reinforces the need to look more fully into the physical nature of interparticle contacts, their frictional characteristics and the mechanics of the particles during deformation.

1.3 Friction between Mineral Surfaces:

Friction, lubrication and wear (now called the science of Tribology) has become a subject in which there has been an enormous increase in research effort; even so, most of the effort has been devoted to the frictional behaviour of metal surfaces. Nevertheless, some of this work can be used to explain the frictional behaviour of non-metals.

Minerals are strong crystalline solids which are brittle in their behaviour, and until recently it was thought that plastic flow was not involved in contact and frictional phenomena. But the material is confined at interparticle contacts so brittle fracture will be inhibited and failure could be by plastic flow, if the stresses are large enough. In fact Marsh (1964) showed that glass flowed plastically

during indentation experiments. But when he calculated flow stresses, using flat rigid die theory for penetrating an elastic plastic material, values well below stresses at which brittle fracture occurs were obtained. However, using an alternative mode of deformation, a radial flow of material away from the indenter which the work of Samuels and Mulhearn (1957) and Mulhearn (1959) indicated as valid, Marsh advanced a new theory which provided a more realistic solution for materials like glass, and other materials with a high ratio of flow stress to modulus of elasticity.

Using this theory it is possible to calculate the stress conditions at contacting asperities. Starting from these stresses and using a plastic junction growth behaviour during the application of shear stresses it is possible to derive a relationship for the friction between the mineral grains, and so obtain values for the interparticle contact areas at slip.

This analysis would hold for first loading conditions, but for interparticle contacts which have sustained larger loads than those current, an elastic analysis should be used. Here a difficulty arises because the stress distribution at the interparticle contacts would be unknown and would depend on the shape of the contacts, as modified by the initial stressing if plastic deformation had been involved. In this respect the determination of contact area ratios becomes intractable. It is, however, important to note that the contact area ratio would be smaller than for the plastic junction growth analysis.

Another feature of the behaviour of elastically loaded contacts is important. This is partial slip at a loaded contact and an explanation of this phenomenon follows from the analyses of Mindlin (1949) and Hamilton and Goodman (1966), and the experimental work of Johnson (1955, 1961), which indicates that slip occurs over a peripheral band at a contact even if the tangential load applied is insufficient to produce gross slip, the width of the slip band being a function of the magnitude of the tangential force in relation to the normal force and explains the mechanism of fretting.

Hamilton and Goodman's work shows that quite small tangential tractions produce tensile stresses in the junction surface larger than those produced by the normal load itself, and these stresses play an important part in generating fracture during sliding of brittle soils.

Returning to the plastic junction growth approach; clearly, if this mechanism is valid, there must be adhesion of the material at the junction interface. There is now evidence that strong adhesion can occur between non-metals. A good example is freshly cleaved mica. Bailey and Courtney-Pratt (1955) showed that two such surfaces placed in contact have an interfacial strength almost as great as the original material.

Also King and Tabor (1954) showed that other non-metals adhere when placed in contact under pressure. For example, two pieces of rock salt pressed together at room temperature

welded together to form a very strong bond. Bowden and Hanwell (1966) showed that frictional tests on diamond surfaces, if clean, produce strong adhesion, and lead to fragmentation under the large tangential stresses induced, the friction coefficient rising to values of the order of unity.

A theory of friction based on brittle fracture was put forward by Byerlee (1967). His analysis showed that the coefficient of friction should lie between 0.1 and 0.15 for brittle materials, but many experimenters have reported values much larger. For example, Horne and Deere (1962) obtained values as high as 0.77 for feldspar and 0.66 for quartz, both values being for saturated conditions; lower values were obtained for dry surfaces.

It is known that the strength of massive structured minerals is reduced in the presence of polar liquids like water, which would mean that the coefficients of friction deduced from Byerlee's theory should be lower when tested submerged but, as can be seen, the reverse is observed. In addition his theory is contradicted by the results of Bowden and Hanwell (1966), who obtained friction coefficients ranging from 0.7 to 0.9 for clean crystal surfaces of minerals.

Thus it seems highly probable from this evidence that a theory of friction based on adhesion between crystal surfaces would be a more realistic description of the behaviour of interparticle contacts between mineral particles.

1.4 Strength as Influenced by the Mechanism of Deformation:

When soils are stressed the fabric or structure changes. This was clearly demonstrated by Skempton (1964) when he put forward the idea that part of the strength drop observed in the post-peak strain softening behaviour of overconsolidated clays was due to the development of preferred orientation of the clay particles. Beautiful micrographs of preferred orientations have since been published by Tchalenko (1967), Roscoe (1967) and many others as well.

Developed anisotropy in granular materials has also been shown by Arthur (1972). The development of stress-induced anisotropy was used by Horne (1965, 1969) to explain the ability of a triaxial sample of granular material to withstand a continuously increasing stress ratio.

Clearly then if structure (and its mode of deformation) reflects the strength of the soil, any investigation into stresses effective in controlling strength, using changes instress, must be done for a particular structure or fabric of the soil being studied, at a particular stage of its deformation. This means that those investigations involving stress changes must be made during the deformation process on a single specimen. In addition it must also be assumed that the stress changes do not invoke any change in the mode of deformation.

It is perhaps simpler to study the influence of boundary stress changes on specimens which are constrained in their

mode of deformation, such as two blocks of mineral sliding on each other. Then if stress changes can be made which do not change the frictional response, these stress changes can be discounted as effective stresses. But if similar stress changes are made to a mass of particles not constrained in the same way and their strength response changes, we shall be forced to consider them as contributing towards the effective stresses.

So the question of whether the effective stresses are functions of deformation mechanisms has to be answered.

Time is a parameter which will have to be excluded from the present investigation, because it is known that a soil structure changes with time under sustained stress, therefore structural changes due to creep could produce strength changes independent of any changes in strength due to changes in stresses. For this reason experimental work will be performed on materials substantially free from time-dependent behaviour.

1.5 Interparticle Contact Deformation and its Influence on Stress-Strain Relationships:

It is clear that several different models for interparticle behaviour could be followed, and for each a particular type of stress-strain behaviour would follow.

In soil mechanics problems stress-strain relationships, which could be described as either elastic or plastic, are used.

Usually the soil is assumed to behave perfectly isotropically, and, in the elastic case, to be linear in its behaviour. Elastic behaviour, in the context used in this work, will be taken to mean a material which, when subjected to a closed stress cycle, dissipates no energy. So a material having a non-linear strain behaviour can still behave elastically. Plastic behaviour means that energy is dissipated when the soil is subjected to a closed stress cycle.

Solutions to many soil mechanics problems have been obtained by replacing the soil with a model material which obeys a Coulomb failure criterion but exhibits plastic behaviour. Drucker and Prager (1952) showed that solutions with these assumptions implied a volume expansion accompanying the shearing of the soil. Although this expansion is observed with many soils the expansion is terminating. To satisfy this condition Drucker, Gibson and Henkel (1955) suggested that soil could be represented as a work-hardening material, which could reach a perfectly plastic state. This implied that a yield surface in addition to the Coulomb yield surface existed for soils.

A development of this approach led to the development of the 'Cam-Clay' soil model as outlined in "Critical State Soil Mechanics" by Schofield and Wroth (1968). The first concepts of this work were presented by Roscoe, Schofield and Wroth in 1958, and it has been expanded and developed by many researchers at Cambridge University, notably Calladine

(1963) and Burland (1965). The model is primarily intended for 'wet' soils, that is, those that contract when sheared under drained conditions. The soil is taken as isotropic, work hardens and Drucker's stability postulate is obeyed, which then enables the strain increment direction to be obtained. The material obeys a particular hardening law, which states that isotropic and anisotropic consolidation paths ($\frac{q}{p}$, = constant) form a set of parallel straight lines on a plot of e versus ln p', with the swelling lines forming a similar set with a smaller slope. The soil also obeys a particular yield function.

The shortcomings of these assumptions can be evaluated when studying real soil behaviour, and the theories have been shown to be deficient in some respects. These shortcomings will be studied in the light of interparticle contact behaviour.

Lastly, the stress-dilatancy concept of soil behaviour should be considered. This theory by Rowe (1962) and supported by Horne (1965, 1969) assumes that sliding occurs between individual particles or particle groups in such a way that the ratio of the rate of dissipation of energy in internal friction to rate of supply of energy in the direction of the major principal stress ~~energy dissipated~~ is a minimum. This approach gives a relationship for the instantaneous strain rate ratio as a function of the instantaneous stress state. Barden and Khayatt (1966) suggested that if the normality condition based on Drucker's stability postulate could be accepted, an equation for the current yield locus (which is also the plastic potential) can be derived.

This theory is based on interparticle contact behaviour, but of one kind only, that is, purely slip, and so the importance of mechanisms other than gross frictional slip must be studied.

CHAPTER 2

APPARATUS AND TESTING TECHNIQUES

2.1 Introduction:

The experimental work undertaken for this research project required the design, construction and development of apparatus not common to normal soil mechanics practice.

The main object of the research was, as indicated by the title, concerned with the effect of high pore water pressures on the mechanical behaviour of soils, and to compare the results with the predictions of the theory of 'effective stress' controlling both shear strength and compressibility. For the experimental work concerned with strength, it was necessary to measure, very accurately, the shear strength of weak samples tested in a high pressure environment. The mechanical system which enabled this to be done successfully was the idea of Professor A W Bishop, the detail design, commissioning and development being done by the author.

To prove the basic ideas, apparatus based on tried components was built - this is shown in the photograph Plate 2.1, and diagrammatically in Figure 2.1. This cell is designed to work with pressures up to 1000 psi. As can be seen, this cell consists of two identical cell tops with rotating bushes (Bishop, *et al.* 1965). The rotating bushes are used to minimize ram friction, and the rams are linked with yokes and tie-bars.

The whole assembly is counterbalanced with weights acting through balance beams. Thus, when the cell fluid is pressurized, the hydraulic pressure exerts an equal thrust on both rams and this thrust is absorbed in the tie-bars linking the two yokes. When the pedestal carrying the sample is moved upwards against the top ram, the axial load is applied through a proving ring which only registers the load on the sample. Therefore, in tests performed with varying cell pressures, the varying hydraulic thrust on the upper ram is automatically balanced by that on the lower. A calibration test on this apparatus gave a maximum axial load change of 0.06 lb for a change in cell pressure of 1000 psi.

The cell pressure is supplied from a self-compensating mercury control system (Bishop and Henkel, 1962) with one adjustable mercury column giving pressures from 0-75 psi and four fixed columns which extend the range to 150, 285, 568 and 1027 psi respectively. The layout is illustrated in Figure 2.2.

The top and bottom cylinders for the columns 3, 4, 5 and 6 are made from stainless steel cylinders, the lower cylinders of columns 3, 4 and 5 being placed on floors below the Soil Mechanics laboratory, which is on the fifth level of the Civil Engineering building.

2.2 Setting-up Procedure and Details of Apparatus:

Granular material:

All tests were performed on saturated material and the samples

were sedimented under water - the method is described fully in Bishop and Henkel (1962). The initial suction is very conveniently provided using mercury column 6 (see Figure 2.2) and the method is as follows. The pressure in the line A1 is adjusted (prior to setting up the sample) to balance the pressure due to mercury column 6, so as to achieve atmospheric pressure at the mid-height of the sample. The sample is erected inside a rubber membrane supported by a split former, the valves 15, 16, 13 and 14 are opened (valve 12 remains closed) and excess water is allowed to drain from the sample, and the membrane sealed to the sample top cap. The reading indicated by the volume gauge then forms the reference from which volume changes of the sample are noted. A small suction can now be applied to the sample, by reducing the pressure in line A1. After consolidation of the sample under the influence of the suction the sample former is removed, the sample dimensions are measured and the cell erected and filled. The test can now be performed using the standard procedure.

In one series of tests, used to study the validity of the effective stress equation, it was necessary to measure the effect on the shear strength of the sample of changing the pore water pressure u, without changing the value of $\sigma_3 - u$. This becomes very simple with the control system shown in Figure 2.2; the procedure adopted is as follows.

The chosen limits of cell pressures are pre-set; the upper by means of mercury columns 3, 4 and 5 and the pressure in

line A3, and the lower by adjusting the pressure in line A2. Also, the pressure in line A1 is set to equal the chosen value of $(\sigma_3 - u)$, and then the length of the self-compensating column 6 is set, with valves 13, 14, 15 and 16 open, and valves 12 and 17 closed, to give no flow through the volume gauge when the water pressure at mid-height of the sample is at atmospheric pressure. The sample is then formed and measured as described above and the cell erected and filled with water.

The sample is consolidated by a series of increments in the cell pressure, using line A2, until the cell pressure is equal to the pressure in line A1. It follows that the sample is now at the chosen value of $(\sigma_3 - u)$. Valve 14 is closed and valve 12 opened; the system now constrains the pore pressure to follow exactly any variation in cell pressure.

The test is performed drained. For the first stage the cell pressure is maintained with the self-compensating system supplying the pressure through line A2, then, at a chosen value of strain, valve 8 is closed, and with valves 1 and 2 open the cell pressure is increased smoothly, with the screw control, until the pressure reaches the upper value pre-set using line A3 and columns 3, 4 and 5. This pressure is now connected to the cell by opening valve 3, and the next strain stage is performed at this upper value of cell pressure. In this way a multi-stage compression test can be performed keeping $(\sigma_3 - u)$ constant while both σ_3 and u

are varied systematically.

Other tests performed in this apparatus were consolidated drained and undrained shear tests, a K_o consolidated undrained shear test and a consolidated drained test with the later portion of the shear stage performed under slowly decreasing cell pressure such that the stress path approached failure at a higher stress value than could be obtained in a standard consolidated drained test. The techniques for these tests, with the exception of the last mentioned were standard, and are described fully in Bishop and Henkel (1962). For the last mentioned test the procedure is the same as that used for a standard consolidated drained test up to the point in the shear stage when σ_3 is lowered; this is done by connecting the cell to the screw control and then closing the pressure supply line from the self-compensating control. The cell pressure is then controlled manually with the screw control while shearing, to achieve the desired stress path.

Both the volume gauge and null-indicator used in these tests are capable of sustaining pressures up to 1000 psi, the construction of the volume gauge is shown in Figure 2.3 and the perspex cylinder was machined from a solid bar and carefully annealed before use. The null-indicator is of the standard construction (see Bishop and Henkel, 1962), the only difference being in the thickness of the perspex block used; $1\frac{1}{2}$" thick instead of the normal $1\frac{1}{4}$". Here again the perspex block was annealed before use to relieve the stresses built in by the machining operations.

This apparatus was very successful so a high pressure version capable of sustaining 10,000 psi pressures was designed and built. The triaxial cell concept followed the prototype in using opposed hydraulically balanced rams running in rotating bushes, but, in this case, long cylindrical bushes were used to provide a long leakage path for the high pressure cell fluid. The main features of the cell are shown in Figure 2.4, with some details in Figures 2.5 and 2.6.

In the prototype apparatus the rotating bush was an integral part of the driven wheel of a worm and wheel drive gear, but in the high pressure apparatus the driven wheel of the worm and wheel drive gear was machined into the rim of a cup. This cup was carried by a tapered roller bearing used to transfer the thrust of the bush to the clamping rings. The bush was forced against the inside of the cup by the cell pressure. Rotation imparted to the bush was thus transmitted by a frictional link between it and the driven 'cup wheel'.

This system had the advantage of simplicity and it enabled the running surfaces of the ram, bush and the running bore in the cell heads to be ground and lapped without difficulty.

The running clearances chosen had to allow for the distortion of the cell head when pressurized. Because of the difficulties of determining the changes in bore diameter analytically, a model of the head was made, strain gauged and tested. These tests showed that to keep the bore diameter changes to

acceptable values, and so allow small clearances and hence low leakage rates through the bushes, very thick end plates would be required. To avoid this requirement the heads were re-designed so that the major thrust on the heads passed directly acrossto the clamping rings via the cell wall or pedestal base. This method relieved the cell heads of most of the bending stresses and so enabled very close tolerances to be used in the final design.

The final diameters of the rams and bores of the bushes were measured on a universal measuring machine which measures directly to 0.0001". The measurements made were 0.9999" over the whole length of both rams, and for one bush the bore diameter was 1.0003" at the ends, tapering to 1.0002" at the centre, and the second bush had an internal diameter of 1.0002" over its whole length. So the minimum radial clearance was 0.0001(5)" and the maximum was 0.0002".

The clearances on the outer diameter of the bushes were slightly larger. The outside diameters of the bushes were 1.5004" and 1.5003", and the inside diameters of their housing bores were 1.5009" to 1.5008" for one head and 1.5008" for the second, giving a minimum clearance of 0.0002" and a maximum of 0.0002(5)".

The surface finishes were measured with a Talysurf profile-ometer and were as follows:

ram 1	average	CLA	(centre	line	average)	1 micro	inch/inch
ram 2	"	"				2 "	" "

bush 1	average CLA	(centre line average)	4 micro inch/inch inside
			2 micro inch/inch outside
bush 2	average CLA	(centre line average)	5 micro inch/inch inside
			4 micro inch/inch outside

With these dimensions and finishes the difference in thrust for a change in confining pressure of 10,000 psi was less than 0.06 lb. (This corresponds to less than 1 division on the dial gauge of a 150 lb proving ring fitted with a dial gauge graduated in 0.0001" divisions.)

Although the cell design proved very satisfactory for accurate load measurements, the leakage rate of oil was fairly large at $\frac{3}{4}$ litre/hour when confining a pressure of 10,000 psi. With this leakage rate it was necessary to have a pressure generator which could provide this quantity of fluid at these high pressures and still maintain the pressure accurately.

The system used achieved this by means of a closed loop servo-controlled system, and the layout is shown in Figure 2.7.

The high pressures were generated by a swash plate piston pump, driven through a servo-controlled Kopp variator. Oil was fed to the main pump, through an oil cooler and filter which retained particles above 5 microns, under a small pressure, by a small primary gear pump. This was done to

avoid cavitation problems at the suction valves. The pump itself was kept at a fairly constant temperature by water from the mains supply flowing through copper tubing wrapped around its body. The high pressure oil from the pump was passed through a non-return valve, then through another cooler to a series of hydraulic resistors.

Details of these resistors are shown in Figure 2.8. By selecting an appropriate pumping speed and a fixed number of resistors a predetermined pressure could be built up. Required changes in pressure could be obtained either by varying the pump speed or, in steps, by increasing or decreasing the number of resistors in series.

The pump, being a piston pump, produced a pressure pulse during each stroke, this pressure pulse was damped out using a long length of high pressure rubber hose which was manufactured with a spirally wound wire reinforcement. This method of damping was very successful because no flutter of the cell pressure gauge could be seen even when pumping against it alone, that is when all the lines except that supplying the pressure gauge were shut off.

The selected pressure was monitored by sensing the position of the weights of a Budenburg dead weight pressure gauge tester (NPL certified accuracy 0.05% of pressure monitored) with an inductive displacement transducer. The signal generated was fed to a limit switching device which in turn controlled the servo drives. The layout of the control

circuits is shown in Figure 2.9. This control system is an 'on-off' system which was found to be adequate for the relatively short-term tests undertaken in this research project, but it would have been better, although much more expensive, to have used a proportional control system. Nevertheless the system enabled the weights of the dead weight tester to be held in position within the limits of ± 0.02" without difficulty or without introducing undue hunting. Although to achieve this it was necessary to introduce a secondary fine control in the form of a small direct acting hydraulic ram. This effectively eliminated 'hunting' of the main control system which occurred without this secondary system because the response of the main system was comparatively slow.

One problem involving instability of the pressure system was traced to the spring loaded safety valve shown in Figure 2.7. The instability was caused by a small intermittent leakage when working close to its preset 'blow off' pressure. This source of error was eliminated by introducing another type of safety device which consisted of a thin brass shim, permanently sealed, backed by a hardened steel die. This shim was designed to burst at a predetermined pressure which could be changed by selecting shims of different thickness.

For one series of tests the difference between the cell pressure and pore water pressure had to be maintained at a constant value while the cell pressure was varied. This

was achieved by building a system equivalent to the constant pressure self-compensating mercury control system (Bishop and Henkel, 1962) and submerging it in the high pressure cell fluid (see Figure 2.10). This system also incorporated a volume gauge built into the stationary reservoir of the mercury column. This volume gauge was very simple in that it consisted of a stainless steel float resting on the mercury. Attached to the float was the core of an inductive displacement transducer. This arrangement enabled the position of the float to be sensed. The capacity of the volume gauge was 20 cc, and the overall discrimination of the system was 1×10^{-4} cc, but the system could not be calibrated to this accuracy as its repeatability was only within $\pm$ 0.01 cc. Calibration data for the gauge is shown in Figure 2.11.

The adjustment of the spring length in the bottom pot of this system, to achieve constant $(\sigma_3 - u)$, was very tedious as it involved stripping down the bottom pot after every check test. The check consisted of balancing the system with the same pressure for a no-flow condition through the volume gauge at both ends of the travel of the gauge. The spring length was adjusted to ensure that this was satisfied.

The system was then checked at high pressure by first interconnecting both Budenburg gauges (see Figure 2.7) at the same pressure and balancing them by adding lead shot to a container resting on the weights of no 2. Then, with the cell erected, the cell pressure was applied and monitored by Budenburg

gauge (1) while the other was connected to the bottom pot of the $(\sigma_3 - u)$ = constant system and re-balanced with lead shot. The weight of lead shot added enabled the value of $(\sigma_3 - u)$ to be determined. This check confirmed the value of $(\sigma_3 - u)$ determined initially, which was 52.6 psi.

To prevent damage to the volume gauge a flow sensitive safety valve was incorporated in the sample drainage line. This consisted of a small piston which allows water to flow past it slowly. If, however, the flow rate increased suddenly the piston would be carried with the stream and seal the outlet orifice. Flow could be restarted if the pressure across the small piston was equalized, when the piston would fall away from the outlet and allow free flow to take place.

Tests with values of $(\sigma_3 - u) > 52.6$ psi had to be performed with manual control of the back pressure, and this was done with the manually controlled hydraulic ram. It was found to be very easy to control the back pressure manually if the pressure was constant, by maintaining the weights on the dead weight pressure gauge tester at a constant elevation. It was however very difficult to maintain $(\sigma_3 - u)$ constant when varying the cell pressure, as this difference could only be obtained by subtraction of the pressure gauge readings. A differential dead weight system was designed using opposed matched pistons similar to those in the standard deadweight pressure gauge testers, which should have eliminated this difficulty, but the manufacturers were not able to supply

the pistons before the end of the test programme.

A general view of the commissioned apparatus is shown in Plate 2.2 and a close-up view of the high pressure cell in Plate 2.3.

The accurate measuring devices and precise controls used were developed around the transducers supplied by Boulton Paul Aircraft Limited - Electronics Department.

The miniature inductive displacement transducers supplied by this firm had a fairly large clearance between the core and coils which enabled easy setting up, and it also ensured that a friction free displacement could be obtained. These transducers proved to be eminently suitable for use when immersed in high pressure oil, as they suffered no changes in output or calibration when the pressure was changed. The former was checked by resting the cores inside the transducers then changing the confining pressure while monitoring this output, and the latter by installing the transducer inside the cell and checking against a dial gauge mounted externally. (The dial gauge used was itself calibrated against a micrometer reading to 1/10,000".)

The instrument used for powering and reading the transducers was also supplied by Boulton Paul Aircraft Ltd, and was designated as their type C61 Transducer meter. It is based on a null balance measuring technique and uses a carrier source of 5V at 1 Kc/s, stabilized against changes in amplitude

and frequency. This source energizes both the transducer and the nulling system, and this feature automatically compensates for any small variations in supply. The nulling voltage is derived using a tapped-transformer technique ensuring great accuracy and stability. The overall accuracy of the instrument is better than $\pm$ 0.01%, and has a resolution of 1 part in 100,000. Two of these instruments were used in the research programme. They are seen in Plate 2.2 and Plate 2.4, which also show the switching control for the measuring transducers and the limit switching unit used for driving the servo controls.

One further piece of apparatus that was developed was for measuring the coefficient of friction between mineral surfaces while surrounded by a high ambient pressure. The details are clearly shown in Plate 2.5. The whole apparatus is assembled within the high pressure triaxial apparatus with the base slipped over the pedestal. The heart of this apparatus is the load measuring element which was designed to be comparatively stiff and yet to be sensitive. Here again a miniature inductive displacement transducer was used and a stiff boss proving ring was designed to accept it. The resulting transducer was capable of sustaining a load of 22 Kgf, and was able to discriminate loads less than 1 gramme, and by amplifying the transducer signal discrimination of 1/10 gramme is possible, but signal noise makes this procedure rather unreliable.

The same apparatus was used for measuring friction between

particles, and this test arrangement is shown in Plates 2.6 and 2.7.

In concluding this section it must be pointed out that one of the major problems encountered in the development and commissioning of this equipment was a very practical one, and was due to the difficulty of obtaining the materials for the high pressure cell, which was made from castings of EN 57 stainless steel. Two sets of castings had to be made, because the first set were found to have hair line fractures which were thought to be due to cooling the billets too fast; the second set of castings were cooled more slowly and were fault free. The time from ordering these castings to accepting them was just under one year.

The time taken to design, construct, commission and test the equipment prior to the experimental programme was two and a half years.

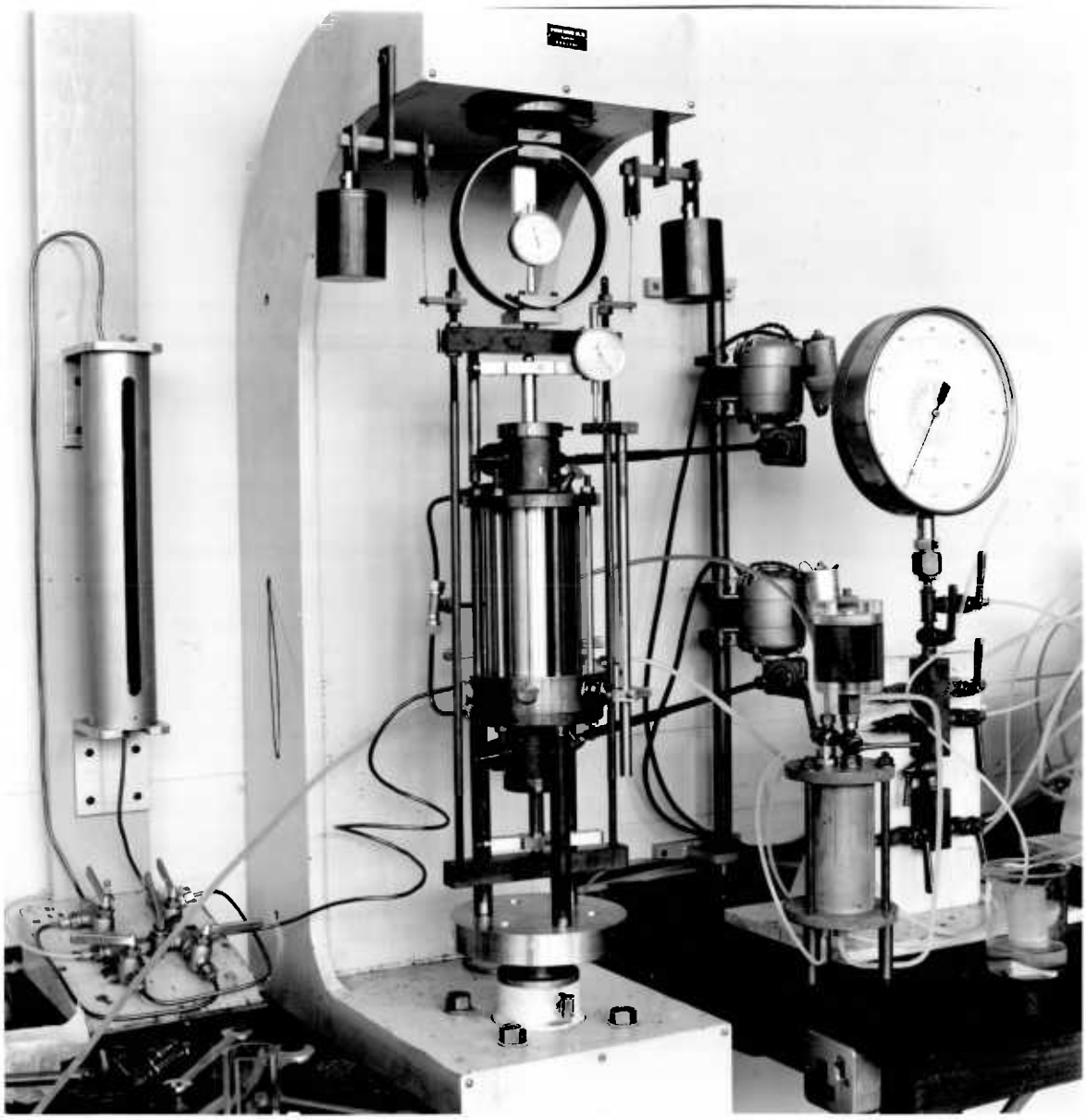


Plate 2.1 1000 p.s.i. Triaxial Apparatus

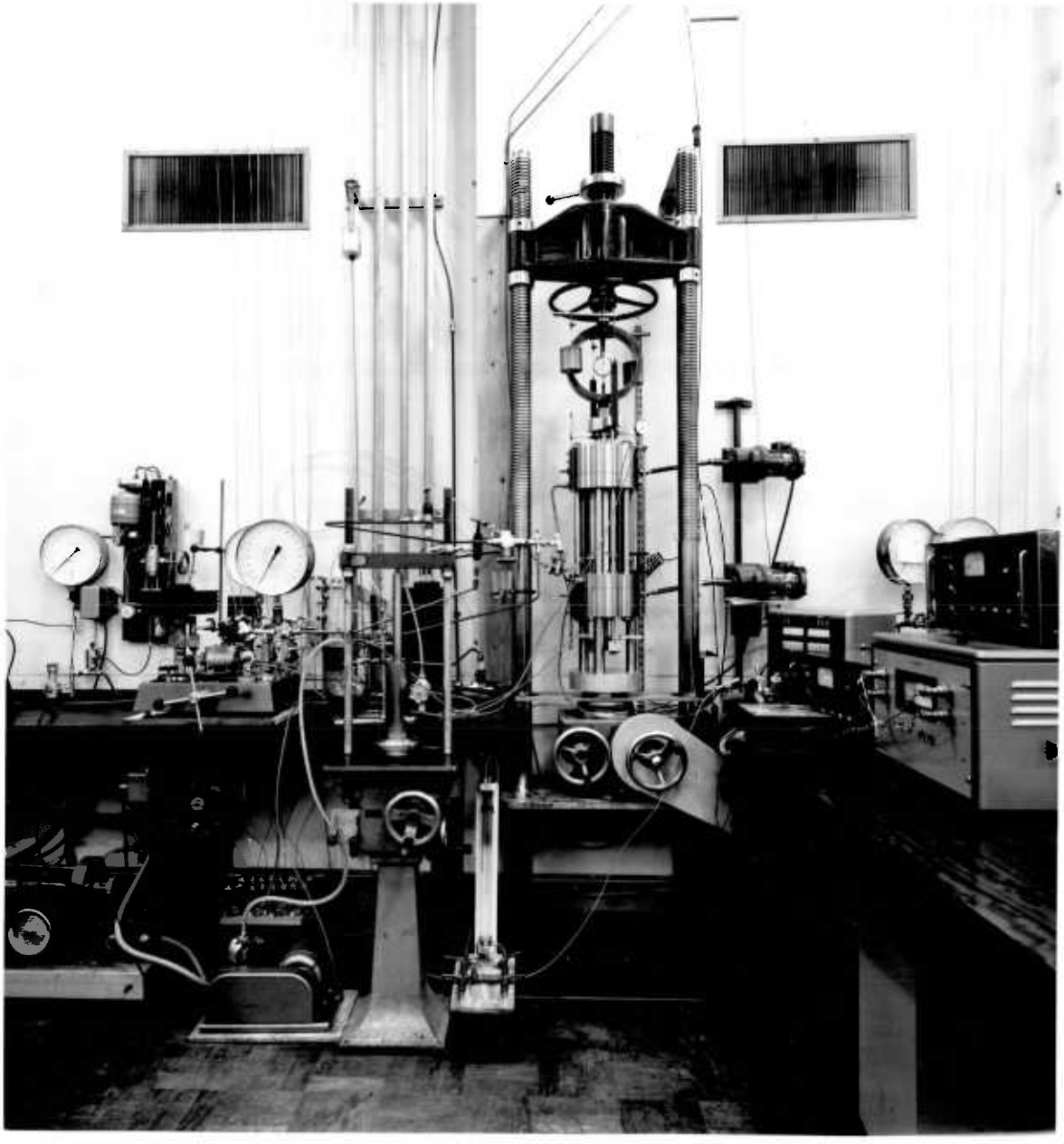


Plate 2.2 10,000 p.s.i. Triaxial Apparatus

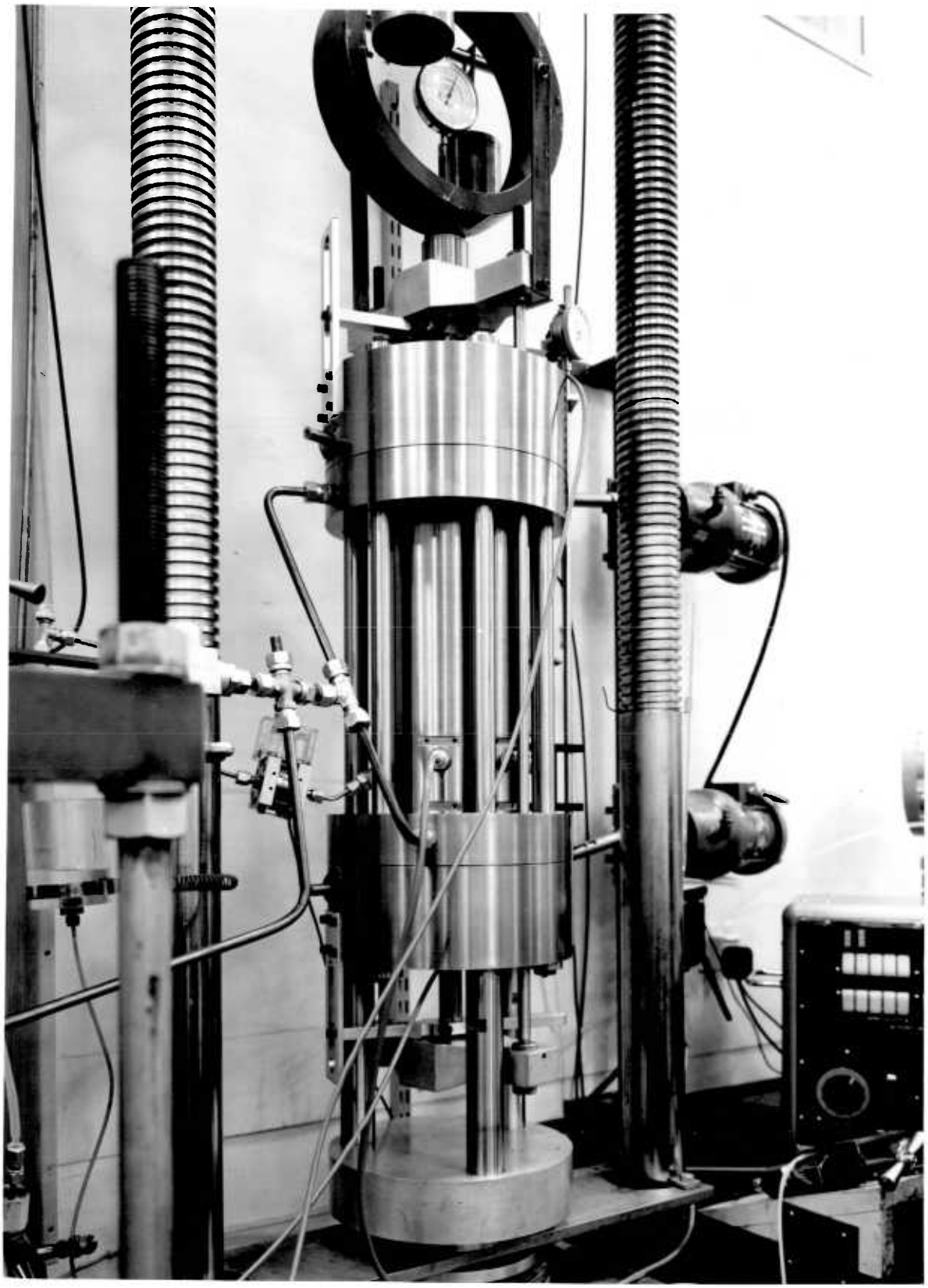


Plate 2.3 10,000 p.s.i. Triaxial Cell (close up)

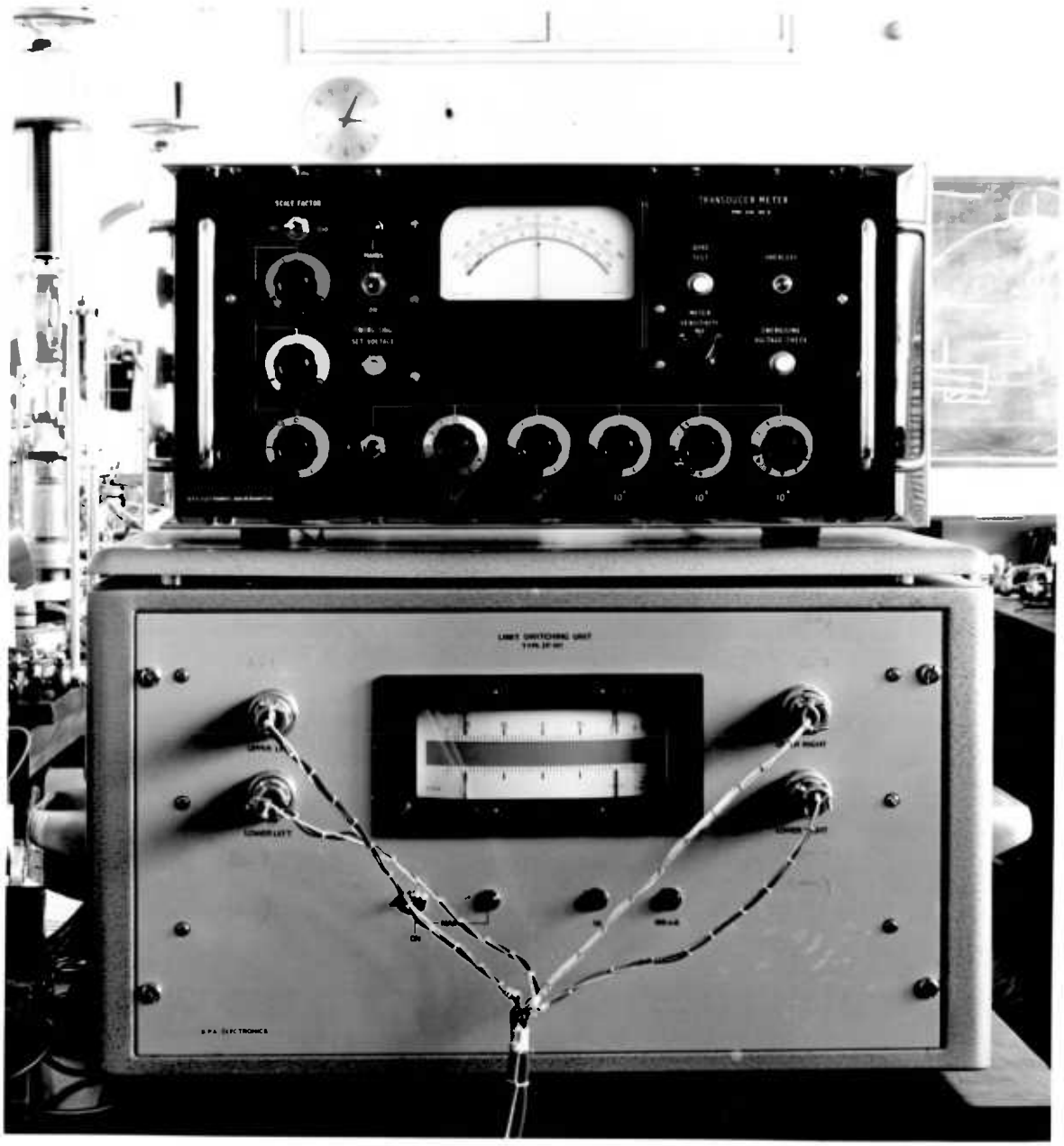


Plate 2.4 C 61 Transducer Meter
and Pantam Limit Switching Device



Plate 2.5 Friction Apparatus
as set up on Pedestal of 10,000 p.s.i. cell

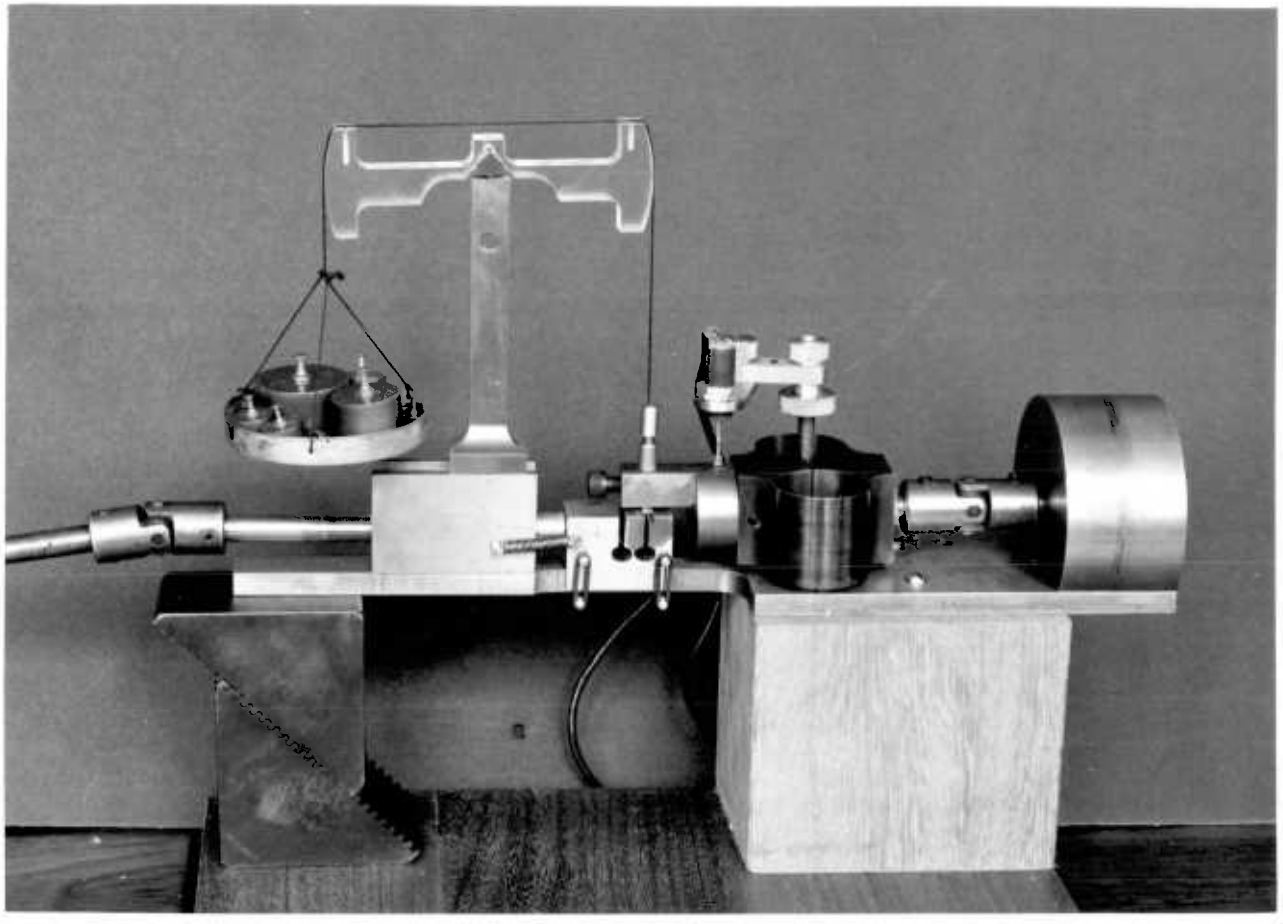


Plate 2.6 Friction Apparatus for Particles

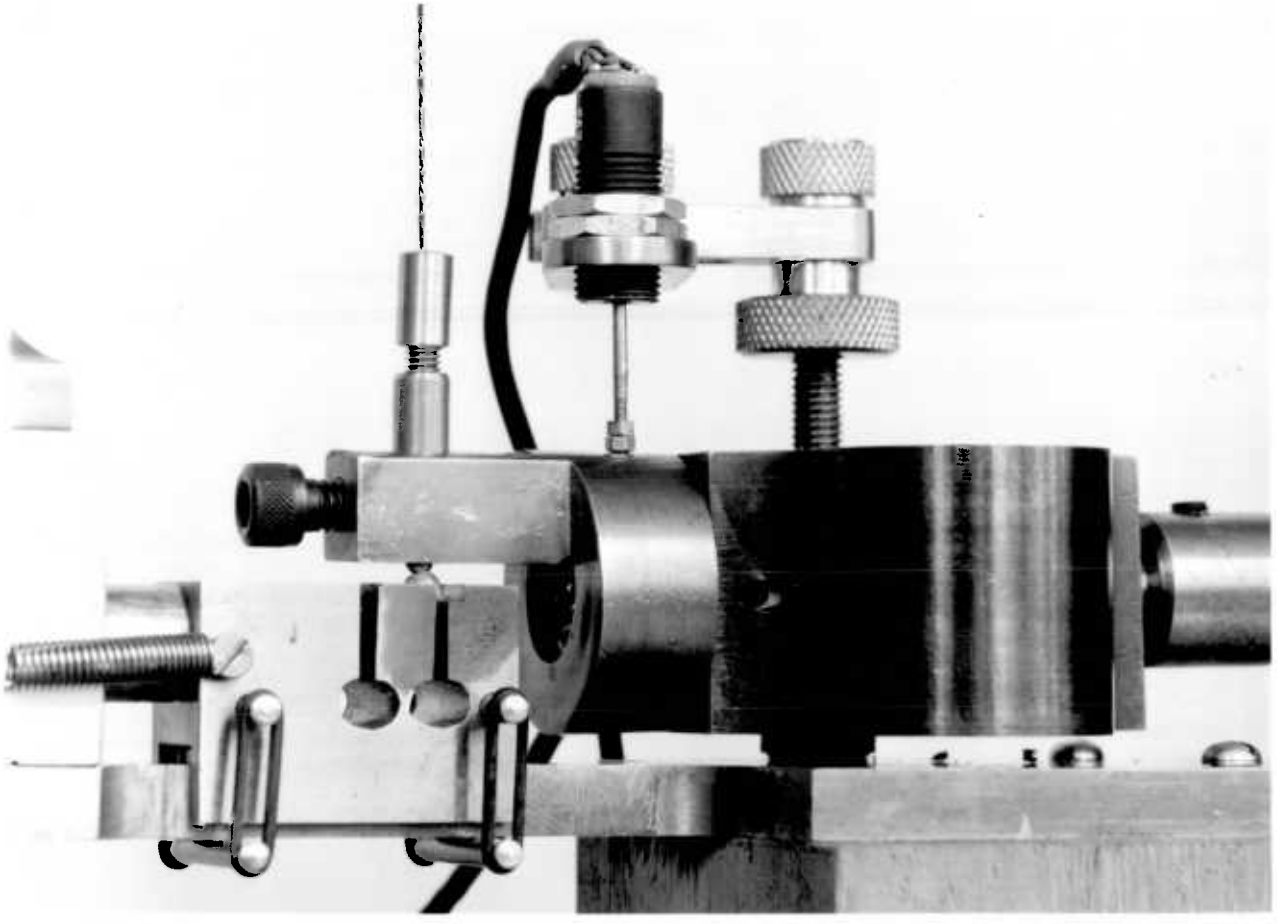
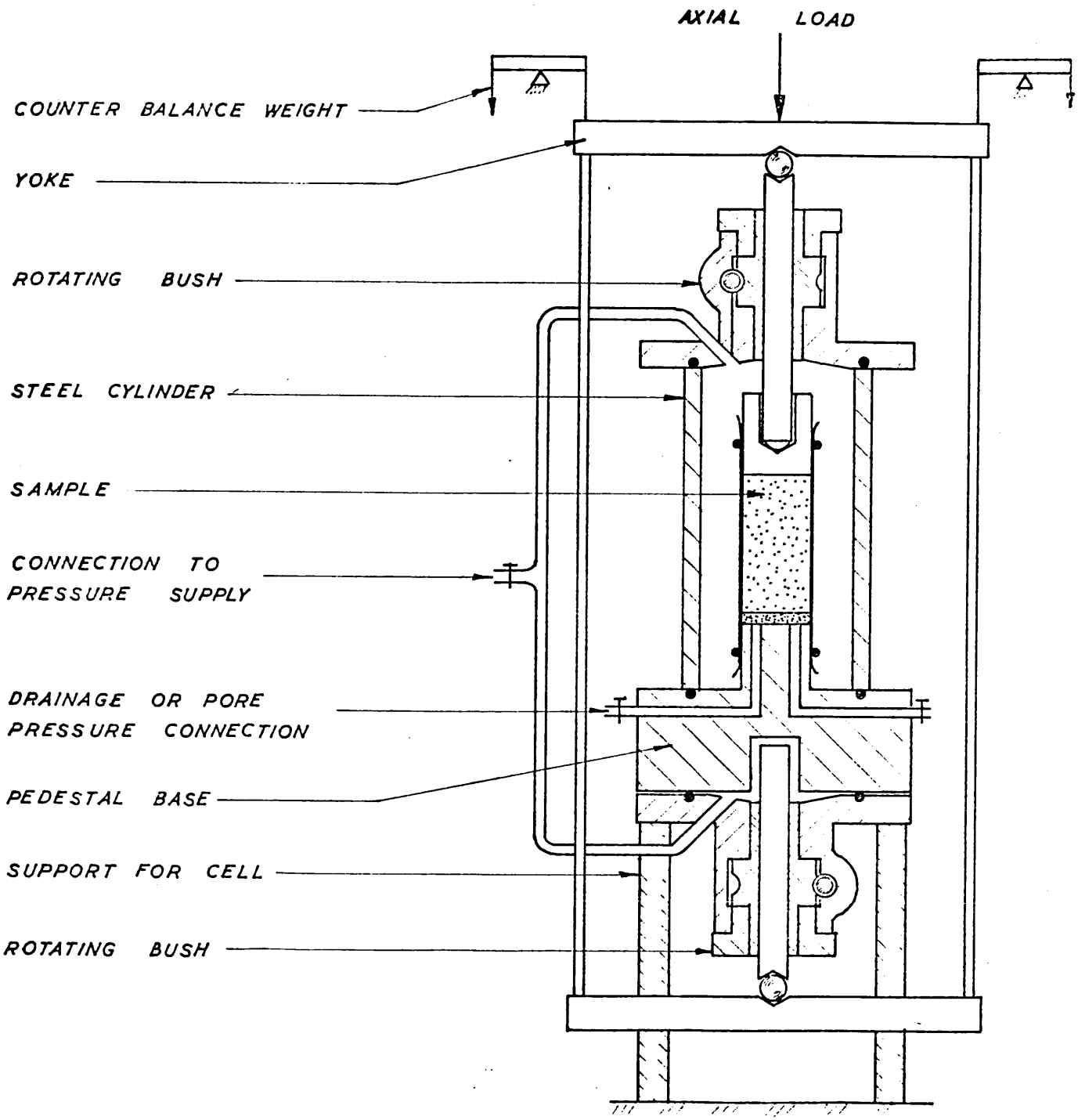


Plate 2.7 Friction Apparatus for Particles

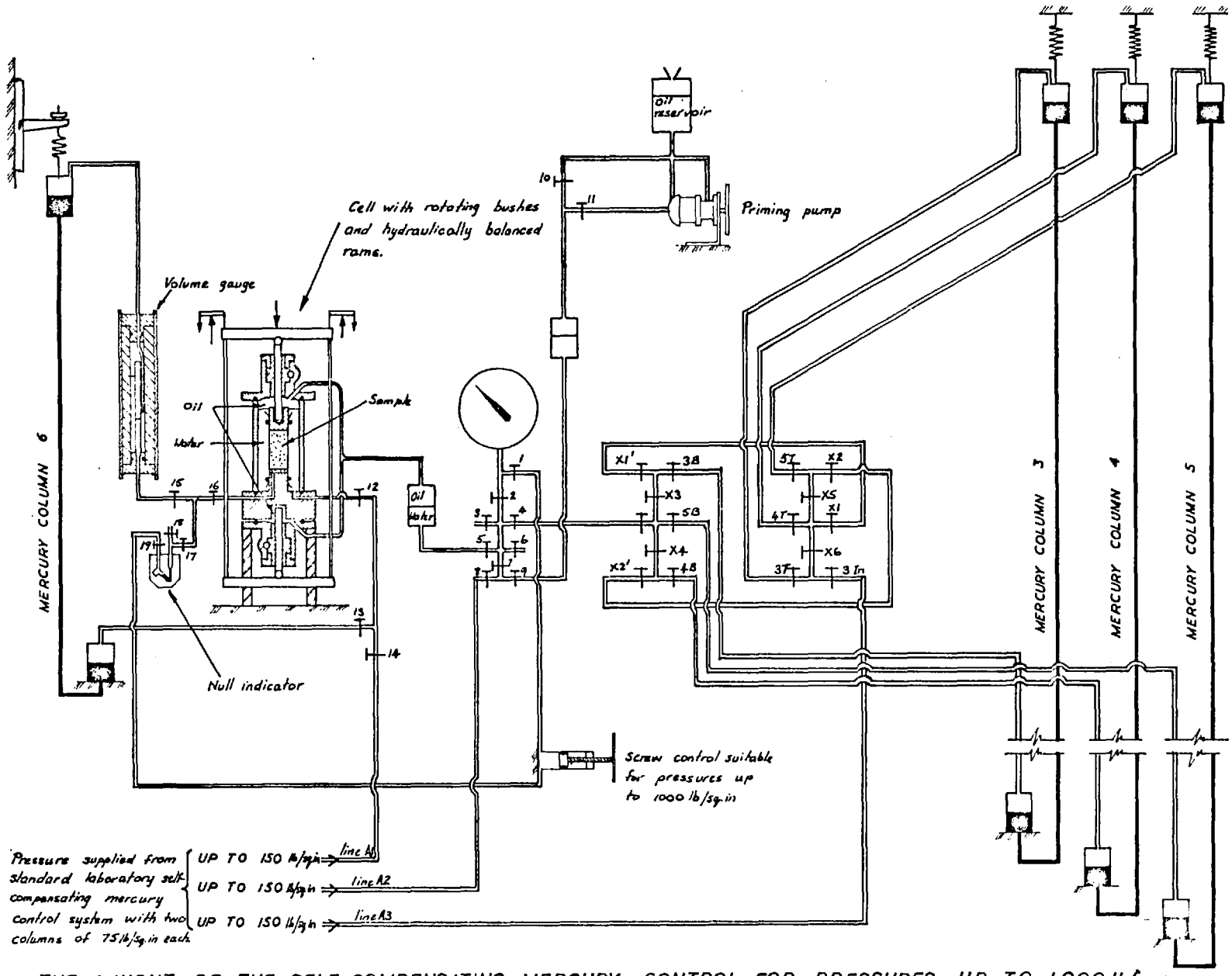


TRIAXIAL CELL WITH HYDRAULICALLY BALANCED RAMS

(DIAGRAMMATIC)

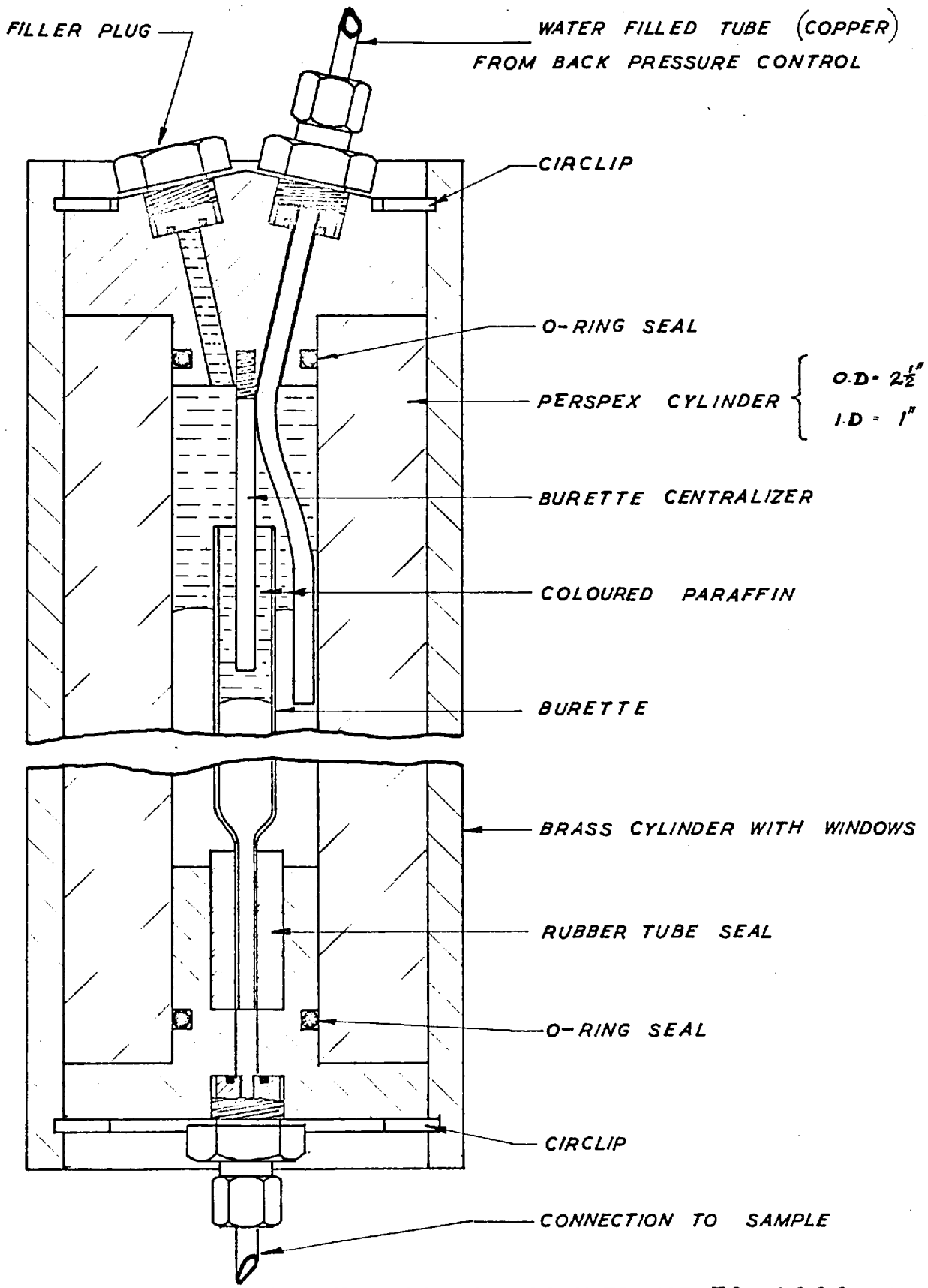
SUITABLE FOR SAMPLE CONFINING PRESSURES UP TO 1,000 lb/sq. in.

FIG 2·1.



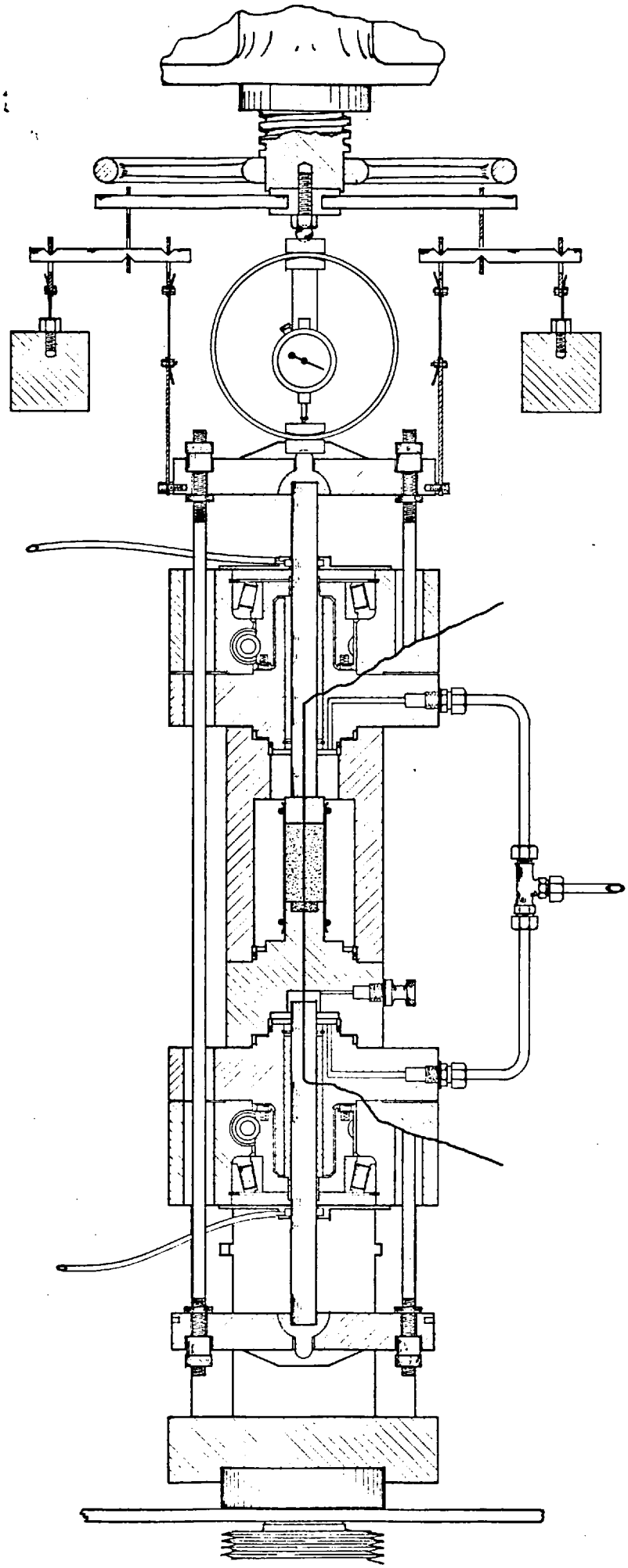
THE LAYOUT OF THE SELF-COMPENSATING MERCURY CONTROL FOR PRESSURES UP TO 1000 lb/sq.in

FIG 2·2



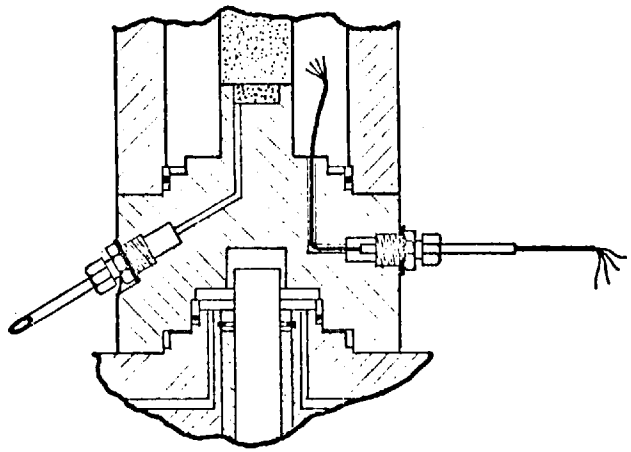
VOLUME GAUGE SUITABLE FOR PRESSURES UP TO 1,000 lb/sq.in.

FIG 2·3



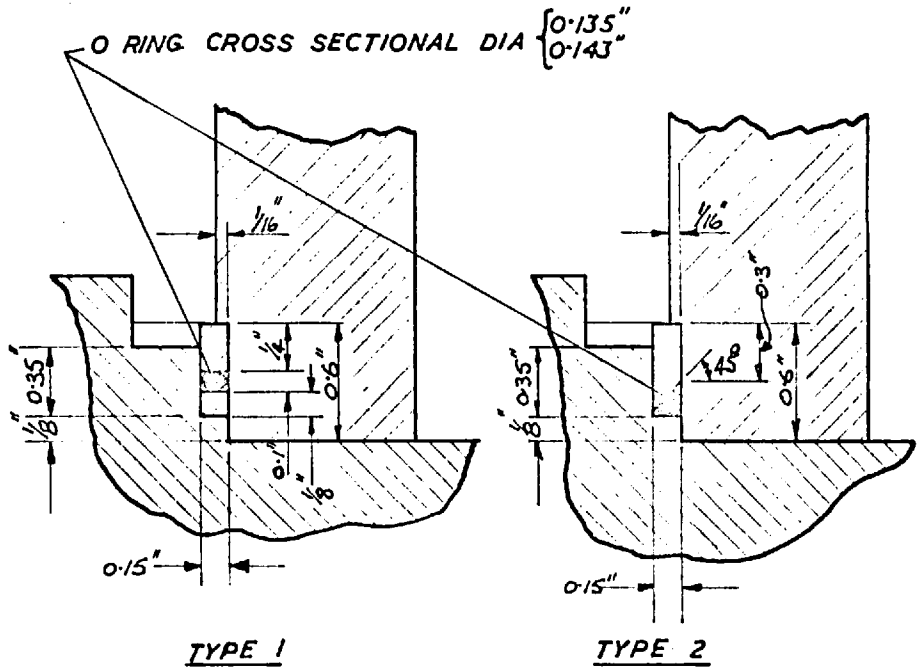
TRIAXIAL CELL WITH HYDRAULICALLY BALANCED RAMS

SUITABLE FOR SAMPLE CONFINING PRESSURES UP TO 10,000 lb/sq.in.



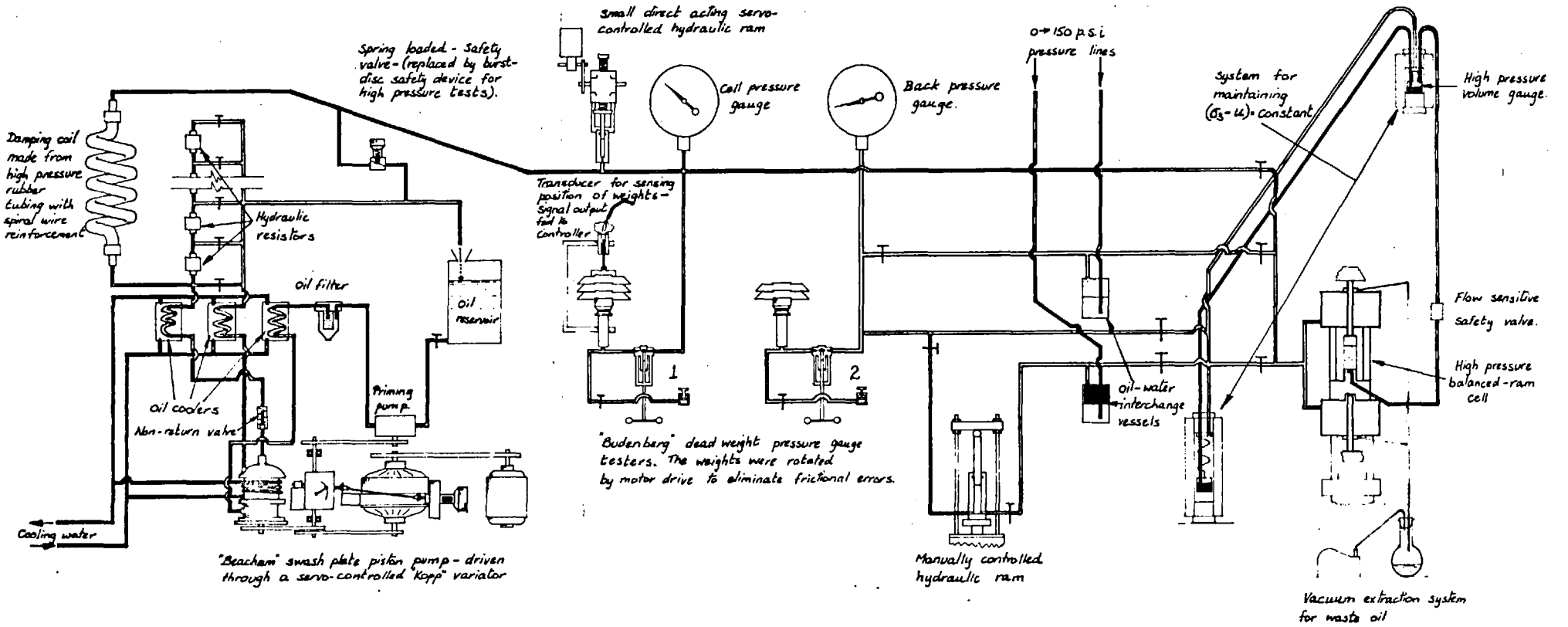
SERVICES TO PEDESTAL BASE

Fig 2·5.



SEALS USING THE UNSUPPORTED AREA PRINCIPLE

Fig 2·6.



DIAGRAMMATIC LAYOUT OF TRIAXIAL APPARATUS USED FOR TESTS WITH CELL PRESSURES UP TO 10,000 lb/sq. in.

Fig 2·7.

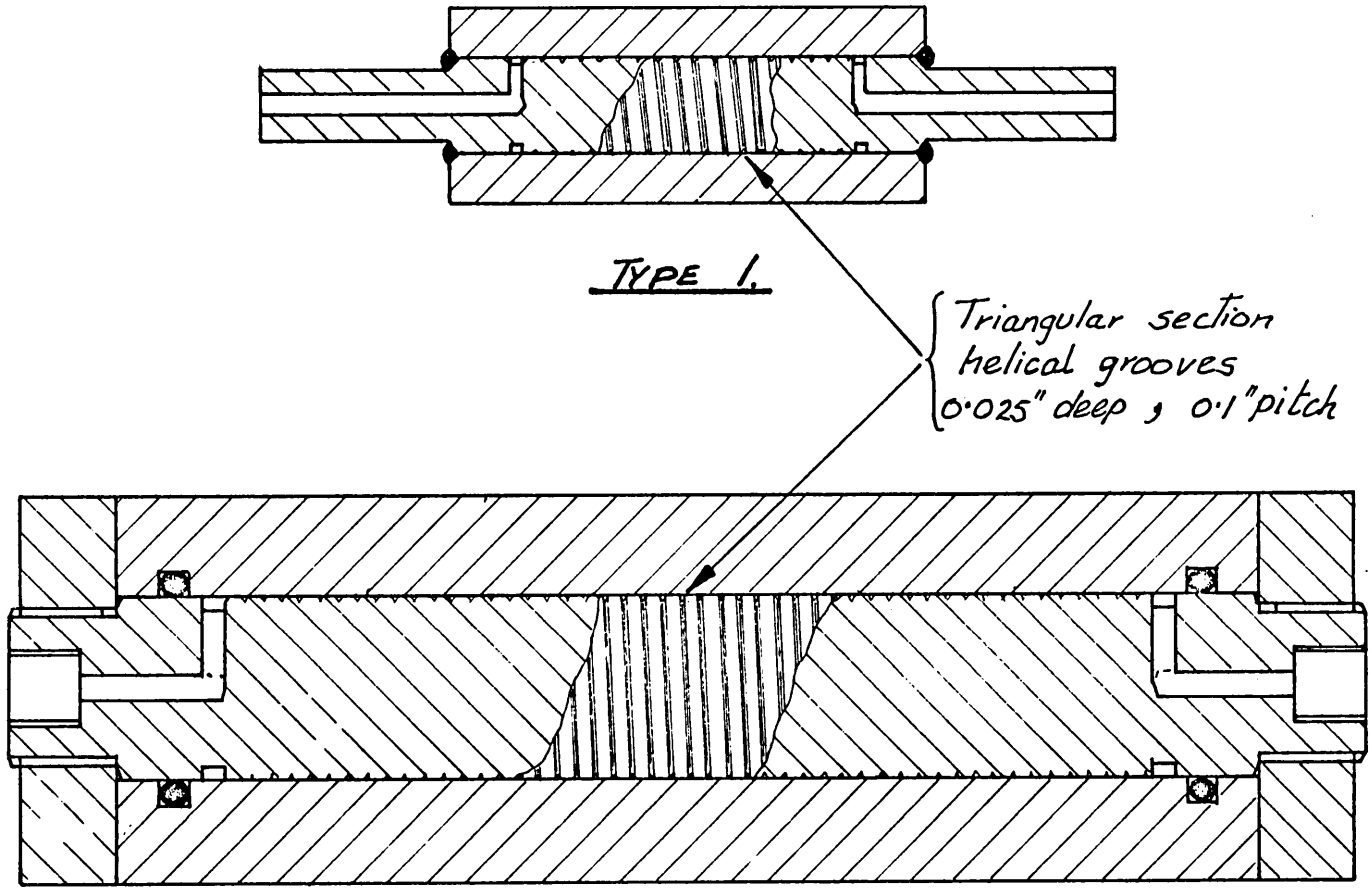
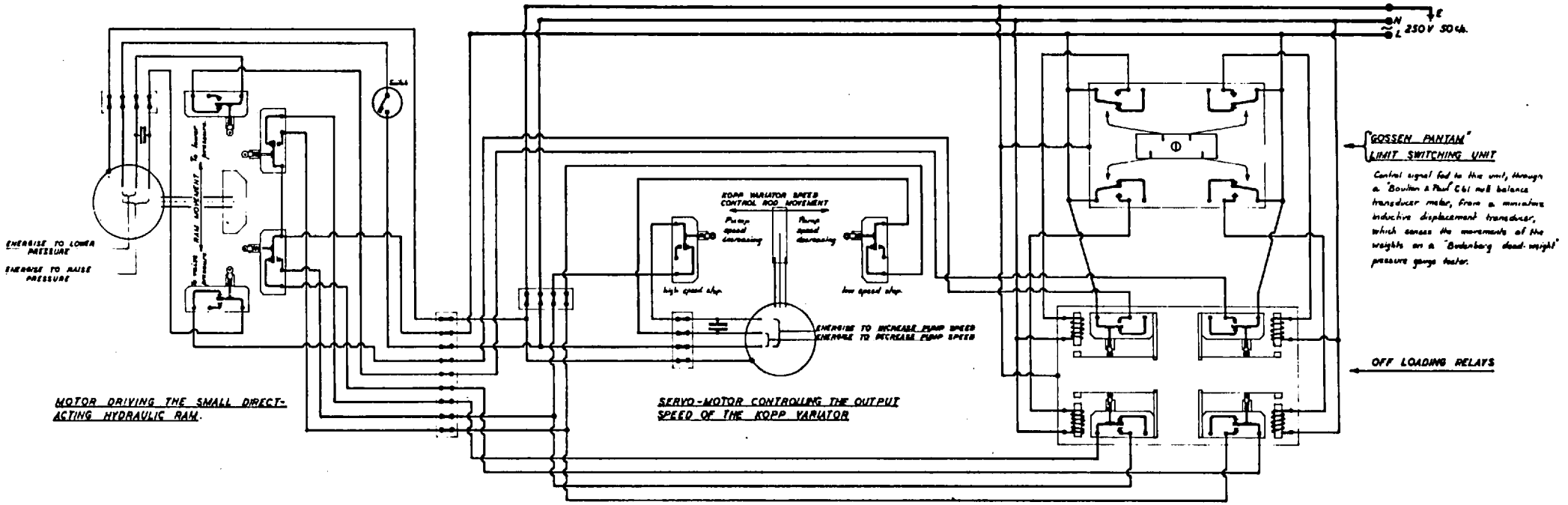


FIG. 2.8.

HYDRAULIC RESISTORS

Scale. FULL SIZE.

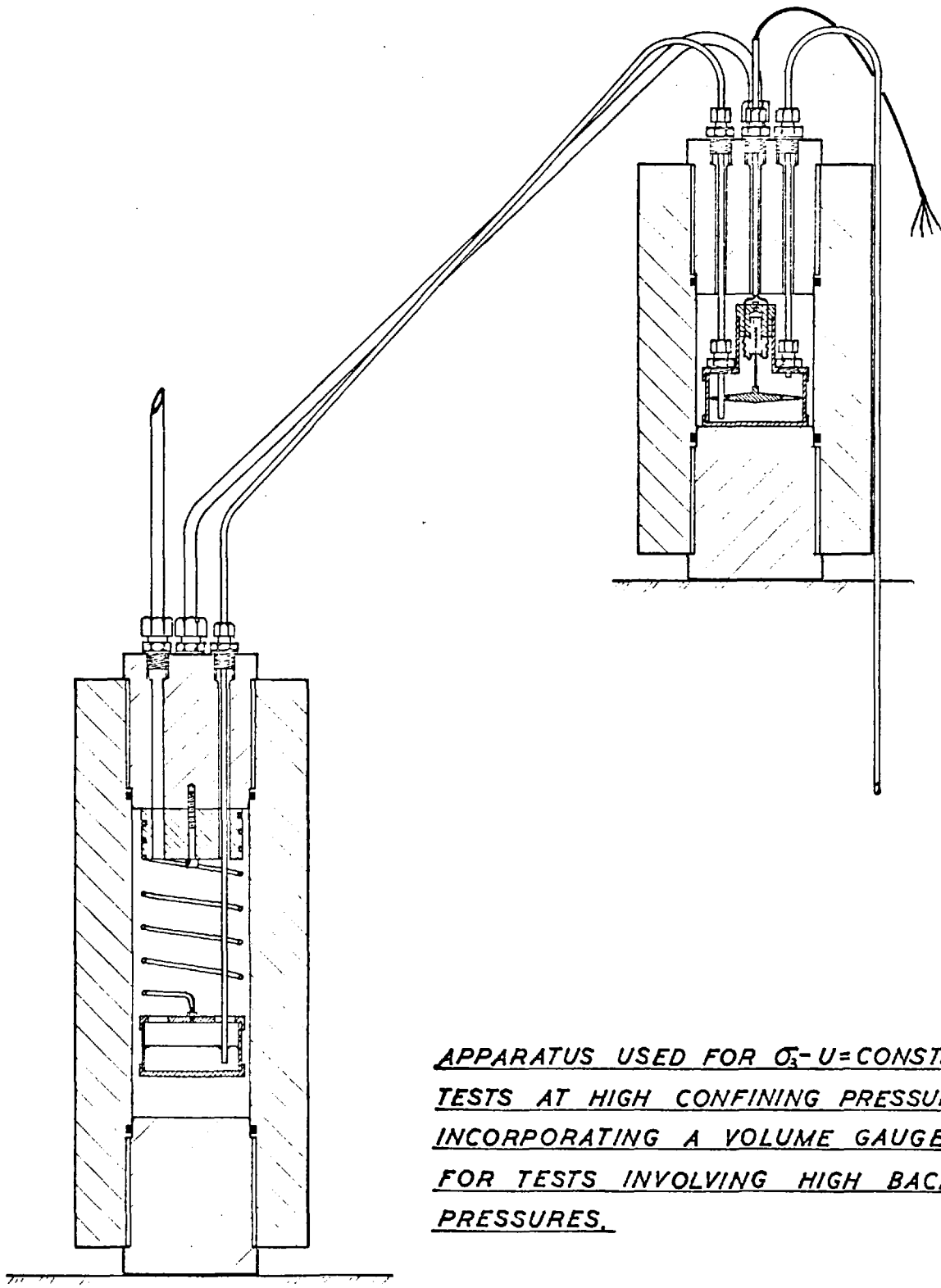


MOTOR DRIVING THE SMALL DIRECT-ACTING HYDRAULIC RAM.

SERVO-MOTOR CONTROLLING THE OUTPUT SPEED OF THE KOPP VARIATOR

ELECTRICAL CONTROL CIRCUIT FOR THE HYDRAULIC HIGH PRESSURE GENERATOR

Fig 2·9

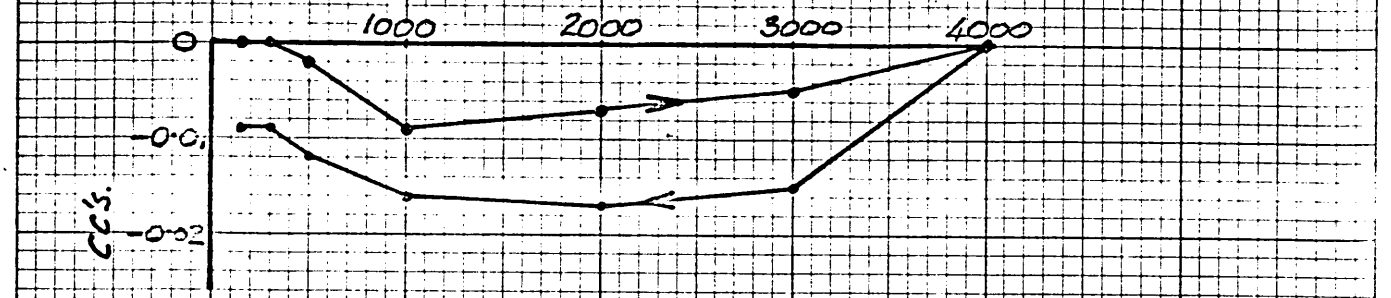


APPARATUS USED FOR $\sigma_3 - U = \text{CONSTANT}$ TESTS AT HIGH CONFINING PRESSURES, INCORPORATING A VOLUME GAUGE FOR TESTS INVOLVING HIGH BACK-PRESSURES.

FIG 2·10

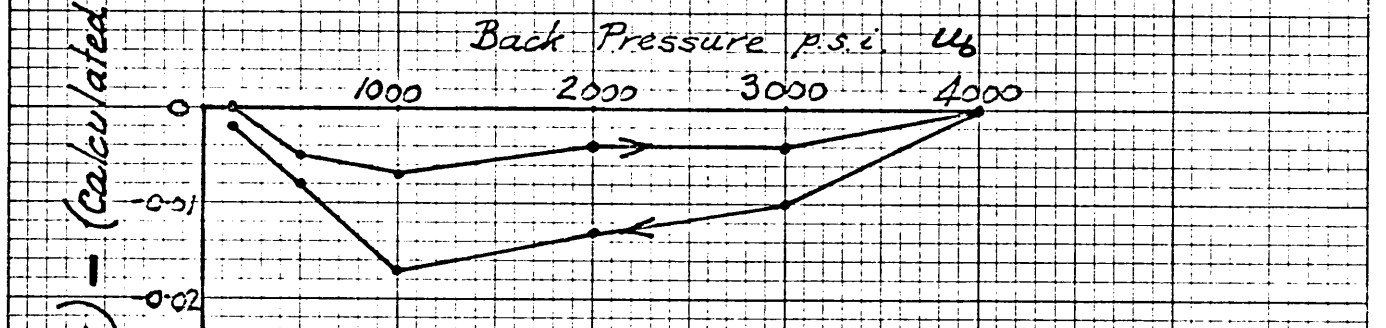
1. Volume gauge only.

$$\Delta V \text{ calc.} = -(86.34 + v_{150}) \frac{3.34}{10^6} (u_b - 150) \text{ cc.}$$



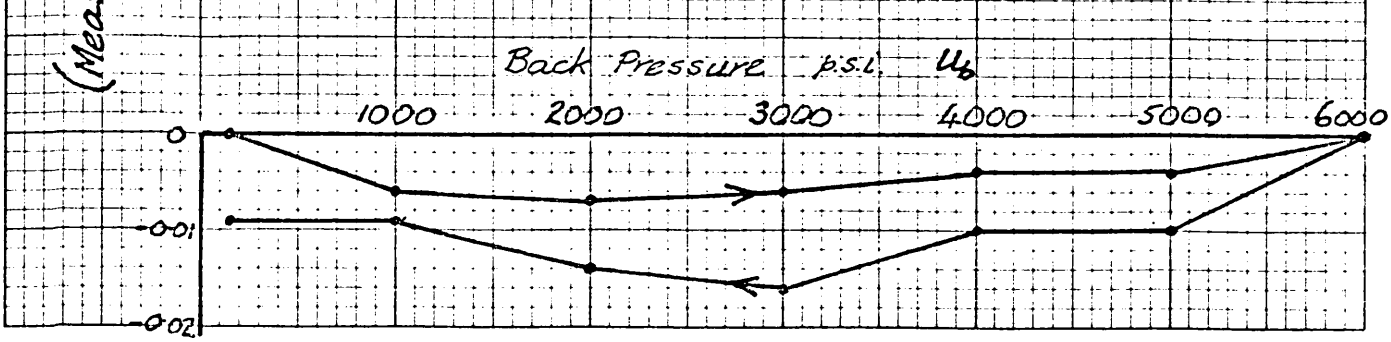
2. Volume gauge + cell base + pressure transducer.

$$\Delta V \text{ calc.} = -(97.705 + v_{150}) \frac{3.34}{10^6} (u_b - 150) \text{ cc.}$$



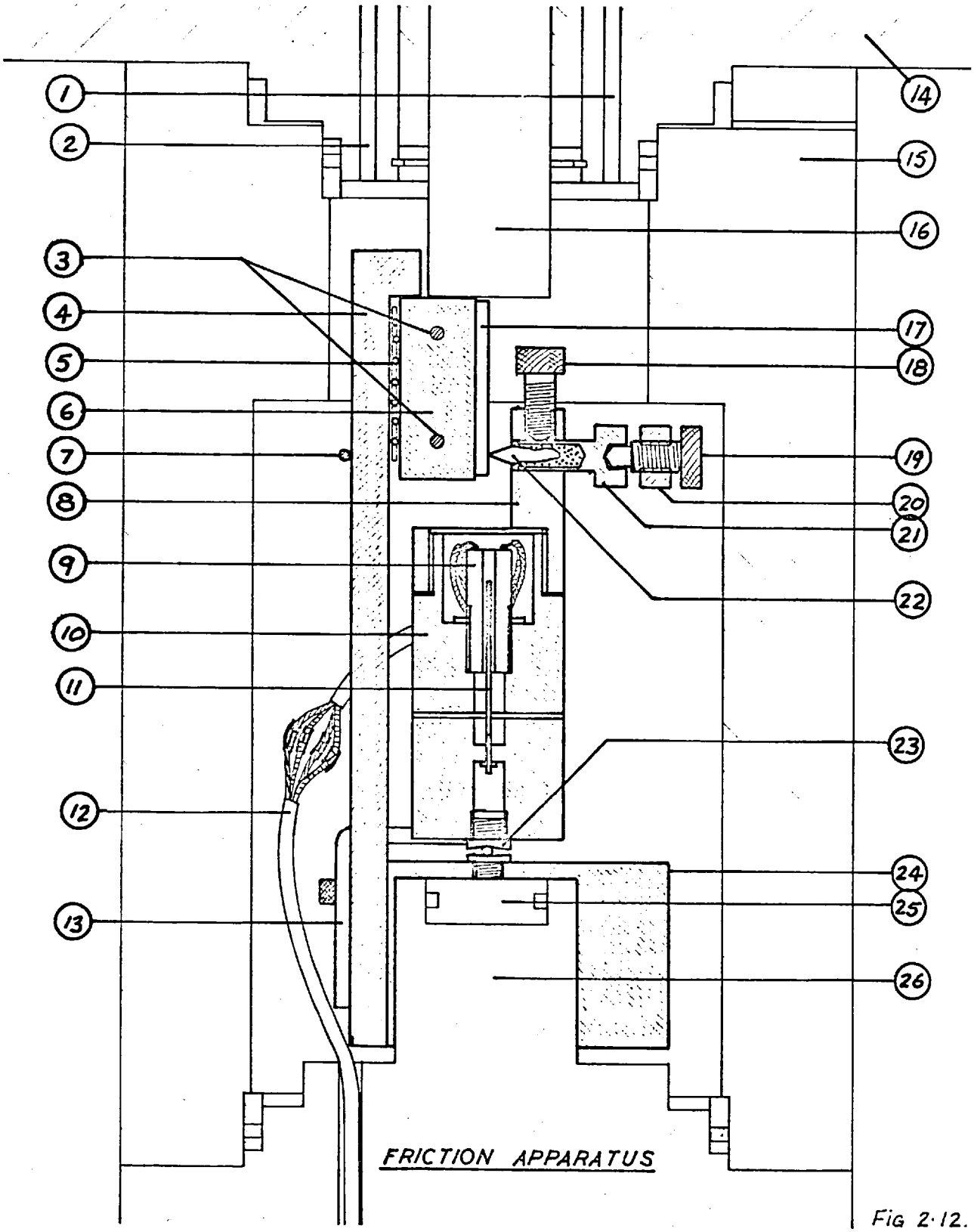
3. Volume gauge + cell base + pressure transducer + interconnecting valve assembly.

$$\Delta V \text{calc} = -(152.060 + v_{150}) \frac{3.34}{10^6} . (u_b - 150) \text{ cc}$$



(Measured volume changes) − (Calculated volume changes) cc's.

Volume Gauge - Pressure Characteristics. FIG 2·11.



FRICTION APPARATUS

Fig 2·12.

CHAPTER 3

THE FRICTION OF MINERAL SURFACES UNDER LOW AND HIGH AMBIENT PRESSURE CONDITIONS - WITH SPECIAL REFERENCE TO QUARTZ

3.1 The Contact between Mineral Surfaces:

The surfaces of minerals, as encountered in sands and silts, are likely to be complex in shape and their surface texture very variable. If, however, we look at the contact between two mineral grains, the forces will be transmitted from one to the other through contact areas formed by the deformation of the surface asperities on the grains (Bowden and Tabor, 1954). The shapes of these asperities tend to be approximately conical or pyramidal, as indicated in Fig 3.1 to Fig 3.4 which show the surface profile of quartz specimens prepared for the friction tests reported later in this chapter.

3.2 The Strength of the Asperities subjected to Normal Load without Shear:

When the mineral grains are forced together, the surface asperities in contact will deform, their tips being squeezed flat, and the mean normal pressure P_m at each contact will be related in some way to the yield stress Y of the deformed material at the tips. Therefore, before any progress can be made in discussing frictional behaviour, the strength of

the asperities must be determined. To facilitate the discussion the strength of quartz, for which data are available, will be taken as a typical example of a mineral.

The strength of quartz specimens cut from quartz crystals has been experimentally determined by a number of people, and most of the available data are summarized in the paper by Christie, Heard and La Mori (1964). Fig 3.5 shows a mean strength envelope assuming that quartz failure is governed by an equation of the form:

$$\tau_i = k + \sigma_n \tan \psi \qquad (3.1)$$ (Skempton, 1960)

where τ_i is the intrinsic shear strength of the material,

k is the intrinsic cohesion,

ψ is the angle of intrinsic friction.

The particular values of k and ψ are chosen bearing in mind the comments in the paper by Christie, Heard and La Mori (1964).

Bowden and Tabor (1954, Part 1, page 19) have shown that, when metal surfaces rest on one another, the peaks of their asperities readily deform plastically, the mean pressure being given by:

$$P_m = C.Y \qquad (3.2)$$

Y is some 'representative' measure of the elastic limit of the deformed material at the tip of the asperities. The factor C depends on the shape and size of the surface irregularities, but for conical and pyramidal asperities of a wide range of angles and for hemispherical asperities, C has a value of about 3. Thus the mean pressure of the surface

irregularities is approximately equal to 3Y. For work-hardened metal the value of Y is independent of the amount of deformation that has occurred, and even with annealed metals, the asperities are work-hardened by surface abrasion and again Y tends to a constant value.

Using data on work-hardened copper from Bowden and Tabor (1954, Part 1), we can draw the Mohr stress diagram corresponding to the mean stress conditions existing at a typical asperity contact in this material (see Fig 3.6). The diagram shows that a large mean confining pressure, σ_p, is induced at the junctions. In the case of work-hardened copper surfaces $\sigma_p = 1.84\ Y$; that is, almost $\frac{2}{3}$ of the mean pressure across the junction interface is hydrostatic.

However, the material composing mineral grains generally does not have a Mohr stress envelope of the form:

$$\tau_i = k \qquad (3.3)$$

but can be approximated to a form as shown in equation (3.1), which indicates that the 'yield' stress increases with increasing confining pressure, and in general, minerals tend to be highly elastic. Therefore larger elastic strains can be accommodated around the asperities, which would tend to lower the apparent confining pressure σ_p at the asperity tip. The effect of this on equation (3.2) is that the value of C is reduced. Even more significant is the mode of deformation of the material around the asperity. This was investigated

by Samuels and Mulhearn (1957) and Mulhearn (1959), who showed that for hardness test indentations, material is often displaced radially outwards from the indentations rather than towards the surface, as in the rigid die theory. Mulhearn assumes that the major deformation process is one of uniform radial compression, with the surfaces of equal displacement and equal strain being hemispheres. Marsh (1964) used this mechanism in formulating a new theory for the indentation hardness test, giving the equation:

$$\frac{P}{Y} = C + K\ B\ \ln\ Z \qquad (3.4)$$

where C and K are constants, $B = \frac{3}{(3 - \lambda)}$ and $Z = (\frac{3}{\lambda + 3\mu - \lambda\mu})$ where $\lambda = 6(1 - 2\nu).\frac{Y}{E}$ and $\mu = (1 + \nu).\frac{Y}{E}$, E is Young's modulus and ν is Poisson's ratio and Y is the flow stress of the material.

To test the validity of the above expression Marsh tested many highly elastic materials. The results of these tests are shown in Fig 3.7a and Fig 3.7b, which are based on the data from Marsh (1964). The line predicted from Marsh's spherical cavity theory is a 'best fit' line using values for C = 0.28 and for K = 0.60.

Since it is reasonable to assume that the material behaviour during the indentation test is similar to the behaviour of two asperities in contact, under load, the above theory can be used to explain the mechanics of contact between highly elastic materials. Before this is done for quartz the

indentation behaviour will be checked against the above equation.

The indentation hardness of quartz has been reported on by many workers, but undoubtedly the most comprehensive series of tests is reported by Brace (1963), who showed that the hardness increased with decreasing load. Although there is a great deal of controversy about the dependence of hardness on load (see Mott, 1956) and about the effect of elastic recovery on the value of the hardness, measured from the recovered indentation, it is usually accepted that for a Knoop indenter, as used by Brace, the long diagonal has a smaller recovery; the elastic recovery occurring mainly across the smaller diagonal. Therefore, it is more than likely that the variation measured by Brace is a real behaviour of the material. Brace's results are shown in Fig 3.8. It is the writer's opinion that this data can be looked at as if it were analogous to the tensile strength of imperfect quartz fibres - ie. as the size increases there is a greater possibility that there will be a larger number of faults in the material with a corresponding decrease in strength. In the same way, when the indentation load increases, the volume of material deformed increases, consequently increasing the possibility of including discontinuities which would lower the hardness.

To see if Marsh's theory can be used to explain what is happening in indentation tests on quartz, the value of Y, the flow stress, has to be known. For the materials tested by Marsh, the flow stresses of each material, in the fully

work-hardened condition, were measured by compressing small fully work-hardened cylinders, and the hardness of the specimens was subsequently measured. Marsh's results are shown in Fig 3.7a and Fig 3.7b. But it has been shown that the strength of quartz depends on confining pressure, see Fig 3.5. Therefore it follows that the yield stress Y is also a function of confining pressure. Fig 3.9 shows the strength envelope for quartz, as shown in Fig 3.5 but extrapolated, with the Mohr stress circles for some of Brace's hardness tests superimposed. Assuming that the maximum allowable stress for each particular hardness value measured is represented by the circle touching the strength envelope it is possible to determine the 'yield' strength for each test. This will be taken as the diameter of the appropriate stress circle. This yield stress can then be compared with the yield stress predicted from Marsh's analysis.

In order to determine the flow stress Y from Marsh's theory the value of Young's modulus E must be known. Here again E varies with crystallographic orientation (Brace and Walsh, 1962) and with pressure.

For quartz the elastic constants are known for atmospheric pressure conditions, but very little data exist on the effects of confining pressures on these parameters. Most of the available data concern the effect of confining pressures on compressibility, and this is shown in Fig 3.10 and Fig 3.11, from which it can be seen that the bulk modulus for the average stress conditions during an indentation

hardness test using a 1000 gm load would be approximately 0.48×10^6 kg/sq cm. In the case of a 2 gm load the mean stress is approximately 200,000 kg/sq cm and from the shock compression data we can see that the quartz at this pressure has probably undergone a polymorphic transition, which increases the compressibility, and the material behaves, according to Wackerle, rather like a fluid in this pressure region. In consequence the hardness behaviour for this pressure region could well be very different from the 'normal' behaviour. The 5 gm load indentation circle, shown dotted on Fig 3.9 has for a mean stress a value of 146,000 kg/sq cm, which approximately coincides with the transition pressure of 144 Kilobars quoted by Wackerle. However, Brace's hardness data show a marked change in behaviour below loads of 50 gm, which would indicate a lower value of mean stress for the transition; that is supposing the transition coincides with the change in indentation behaviour. However, in the indentation test the actual stresses are not uniform, and the maximum stress could well reach the transition pressure for lower loads, which would predicate a change in behaviour in the hardness test. In the discussion that follows only the hardness values for loads greater than 50 gm will be considered. For the 50 gm load the bulk modulus is approximately 0.53×10^6 kg/sq cm. From the above it is seen that there is an increase in the bulk modulus with increasing pressure, a 10% increase for the mean stress conditions corresponding to the indentation tests using 50 gm as compared with that for the mean stress conditions for the tests using a 1000 gm load. Consequently it is possible that there will be a similar

variation in the value of Young's modulus E. Another difficulty is that quartz exhibits a variation of E with crystallographic orientation, so average values will be used in the analysis. The value for Young's modulus for zero confining pressure will be taken as 0.76×10^6 kg/sq cm.

If we assume no variation of Poisson's ratio with pressure, the values of E for various pressures can be determined. These values for the mean pressure conditions of the indentation tests using 1000 gm and 50 gm loads are 1.00×10^6 kg/sq cm and 1.10×10^6 kg/sq cm respectively.

It is now possible to substitute the values of $\frac{P}{E}$ into Marsh's equation for the expansion of a cavity.

Indentation hardness test with 1000 gm load (Brace, 1963):

P = 67,000 kg/sq cm. Use $E = 1.00 \times 10^6$ kg/sq cm

$\frac{P}{E} = 0.067$ (for $\nu = 0.15$)

From Fig 3.7b $\frac{Y}{E} = 0.038$.

Therefore for Marsh's equation Y should be 38,000 kg/sq cm. This value is to be compared with the yield stress for the mean stress conditions for this test shown in Fig 3.9, which gives Y = 44,000 kg/sq cm.

Indentation hardness test with 50 gm load (Brace, 1963):

P = 101,000 kg/sq cm. Use $E = 1.10 \times 10^6$ kg/sq cm

$\frac{P}{E} = 0.090$

From Fig 3.7b $\frac{Y}{E} = 0.058$ (for $\nu = 0.15$).

Therefore for Marsh's equation Y should be 63,800 kg/sq cm. This value is to be compared with the yield stress for the mean stress conditions for this test shown in Fig 3.9, which gives Y = 58,000 kg/sq cm.

The above comparison shows that with the assumptions made, the cavity expansion theory fits the experimental data better than the rigid die theory. The values of $\frac{P}{Y}$ are 1.52 and 1.74 for the 1000 gm and 50 gm loads respectively, instead of 2.97, which would be the value if the rigid die theory was valid for this material.

From the above discussion it is clear that apart from the case where material transformation influences the behaviour, the contact between mineral grains can be considered to be controlled by the bulk strength of the material as defined by equation (3.1). This bulk strength includes the effects of the flaws present in the material. If the material was flawless it is possible that the strength envelope could be rather like that shown for work-hardened copper in Fig 3.6. Fig 3.9 shows that the tensile yield strength for drawn quartz fibres is much the same as the compressive yield stress, obtained by extrapolation for the indentation test using a 2 gm load. These tests are most likely to include material free from flaws, whereas the other indentation tests include some flaws within the stressed material.

It is thus possible to describe the behaviour of the contact between grains of quartz using Marsh's equation, when no shear

tractions are applied.

Since the material strength envelope is known, it is possible to determine the relationship between P, Y and $\bar{\sigma}_3$ ($\bar{\sigma}_3$ being the operative confining pressure at the grain contacts, made up by the sum of the ambient hydrostatic pressure and the self-induced confining pressure). The relationship between the ratio $\frac{P}{Y}$ and $\bar{\sigma}_3$ is shown in Fig 3.12 for quartz. The indentation test data from Brace (1963) for loads between 1000 and 50 gm indicate that the range of values of $\frac{P}{Y}$ should lie between 1.53 and 1.73. In a real soil the values of interparticle load are likely to lie closer to the smaller loads used by Brace, and it would be likely that the values of $\frac{P}{Y}$ encountered would be in the range 1.73 to 2 - that is, the variation should be quite small.

However, there is the problem of the transition behaviour for the smaller loads. One point which must be mentioned here is that the previous discussion considered the deformation behaviour of quartz indented by a diamond, which is a much harder material. When two quartz asperities come into contact the constraint is likely to be less, and would probably allow the smaller loads to be carried within the 'normal' behaviour range, so it would be reasonable to use Marsh's model for grain to grain contacts for much smaller loads than considered above.

3.3 The Behaviour of Asperities subjected to Normal and Shear Loads:

It is convenient at this point to refer to two papers. The

first is by F P Bowden and A E Hanwell and the second by F P Bowden and C A Brookes, both papers being in the Proceedings of the Royal Society, 1966, Vol 295. Conclusions reached in these papers were that friction of clean crystal surfaces for smooth and rounded sliders is due primarily to adhesion between the surfaces, and that the frictional behaviour of a hard conical slider can be considered in two regimes; in the first, with light loads on blunt sliders (when magnesium oxide was used) the load is borne largely by elastic stresses and plastic flow, the friction being mainly due to adhesion, provided the load is insufficient to cause deep penetration. In the second regime, penetration of the crystal occurs; thus the geometry of the slider and the associated ease of penetration controls the friction. However, it is shown that in the high friction regime the type and degree of bulk deformation, which is the major mechanism for relieving the frictional force, is determined by the value of μ, the coefficient of friction, and it does not matter whether this high value of μ is achieved by penetration of the slider or adhesion at the sliding contact. The deformation mechanism is slip parallel to crystal planes.

In the paper by Christie, Heard and La Mori (1964), the authors put forward a similar hypothesis to explain the crystallographic nature of the faults developed in their test samples. It was that the cracks were initiated by yielding and slight plastic flow on certain crystal planes, and then propagated rapidly in these planes by a brittle fracture mechanism.

3.4 Theory of the Friction between Mineral Surfaces:

It is apparent from the previous discussion that when mineral grains come together under load, their asperities in contact will deform plastically to support the applied load, and the friction between the two surfaces should follow a plastic adhesion type of theory.

In the theory outlined below the following assumptions will be made:

a) The normal and shear stresses, produced by the applied loading, are interdependent (McFarlane and Tabor, 1950).

b) The mean contact stress produced by the applied load, under conditions of no shear loading with zero ambient pressure, will be taken to be equivalent to the Vickers hardness, H_v, measured with the same load. In addition it will be assumed that the mean pressure in a hardness test at a pressure other than atmospheric is increased by the ambient pressure σ_3 in such a way that the mean confining pressure in the indentation is equal to the sum of the ambient pressure and the self-induced hydrostatic pressure for zero ambient pressure.

c) The mean confining pressure $\bar{\sigma}_3$ at the junctions between contacting asperities is equal to the sum of the ambient and self-induced hydrostatic pressures.

d) No work-hardening takes place during shear.

e) The shear strength of the contact region material increases linearly with the mean normal pressure - see equation (3.1) (Skempton, 1960).

Assumption a), as used by McFarlane and Tabor (1950), accepts that plastic flow occurs, and that a representative 'flow stress' can be ascribed to the material.

But for quartz it has been shown that the yield stress increases with increasing normal load, so that to use assumption a) some representative 'flow stress' has to be chosen. Therefore another assumption will be made, and that is:

f) When gross slip is about to occur the yield stress is given by:

$$Y = \frac{2\tau_s}{\cos \psi} \tag{3.5}$$

where τ_s is the shear stress at the junction at slip (see Fig 3.15) and that the junction would have behaved in the same way if this 'flow stress' had been operative throughout the yielding process.

Analysis:

From assumption a):

Using the same type of expression as McFarlane and Tabor (1950)

$$\sigma_n^2 + \alpha^2\tau^2 = P_o^2 \tag{3.6}$$

where $\sigma_n = \frac{L}{a} + \sigma_3$ and $\tau = \frac{F}{a}$ (see Fig 3.13).

When $\tau = 0$ it follows from b) and c)

$$\sigma_n = H_v + \sigma_3 \frac{(1 + \sin \psi)}{(1 - \sin \psi)} = P_o \tag{3.7}$$

But the operative yield stress to be used is $Y = \frac{2\tau_s}{\cos \psi}$ (assumption f).

So equation 3.6 can be re-written:

$$\sigma_n^2 + \alpha^2\tau^2 = \gamma^2\left(\frac{2\tau_s}{\cos \psi}\right)^2 \qquad (3.8)$$

where γ is a constant.

Therefore when $\tau = 0$ we have:

$$\sigma_n = \gamma\frac{(2\tau_s)}{(\cos \psi)} = H_v + \sigma_3\frac{(1 + \sin \psi)}{(1 - \sin \psi)} \qquad (3.9)$$

Now consider the other limiting condition, when the junction has grown, due to the shear traction increasing to such an extent that σ_n becomes very small. Then τ would tend to its maximum allowable value, i.e. $\tau \to \frac{Y}{2}$. But $\frac{Y}{2} = \frac{\tau_s}{\cos \psi}$ from (3.5).

Neglecting σ_n in equation 3.8 we have $\alpha^2\tau^2 \simeq \gamma^2 \left(\frac{2\tau_s}{\cos \psi}\right)^2$

Therefore $\alpha \simeq 2\gamma$ (3.10)

Hence equation (3.8) can be re-written:

$$\sigma_n^2 + \alpha^2\tau^2 = \alpha^2\left(\frac{\tau_s}{\cos \psi}\right)^2 \qquad (3.11)$$

This relationship is shown in Fig 3.15.

The limiting condition is slip when $\mu = \frac{\tau}{\sigma_n}$; but at slip $\tau = \tau_s$.

Therefore $\mu = \frac{\tau_s}{\sigma_n}$ (3.12)

or $$\mu = \frac{1}{\alpha \tan \psi} \tag{3.13}$$

From equations (3.9) and (3.10):

$$\alpha = \frac{\cos \psi \left\{ H_v + \sigma_3 \frac{(1 + \sin \psi)}{(1 - \sin \psi)} \right\}}{\tau_s} \tag{3.14}$$

But we also know that at slip:

$$\tau_s = k + \sigma_n \tan \psi \tag{3.15}$$

And from (3.12):

$$\sigma_n = \frac{\tau_s}{\mu} \tag{3.16}$$

Substituting (3.16) in (3.15) we obtain:

$$\tau_s = \frac{k\mu}{(\mu - \tan \psi)} \tag{3.17}$$

Therefore from (3.14) and (3.17):

$$\alpha = \frac{\cos \psi (\mu - \tan \psi) \left\{ H_v + \sigma_3 \frac{(1 + \sin \psi)}{(1 - \sin \psi)} \right\}}{k\mu} \tag{3.18}$$

Therefore from (3.18) and (3.13) the coefficient of friction is given by:

$$\mu = \tan \psi + \frac{k}{\sin \psi \left\{ H_v + \sigma_3 \frac{(1 + \sin \psi)}{(1 - \sin \psi)} \right\}} \tag{3.19}$$

Equation (3.19) shows that if a material had no intrinsic cohesion the value of μ, the coefficient of friction, would be given by $\mu = \tan \psi$. On the other hand if the material behaved as a true plastic material with constant yield stress (i.e. $\psi = 0$), the coefficient of friction, μ, would reach infinite proportions, i.e. seizure would result from the

application of a shear traction.

The above discussion relates to the friction of clean crystal surfaces. The effects of a contaminant film, which is weaker than the bulk material, can be argued in much the same way as that used by Bowden and Tabor (1964, p 74).

If we have the strength of the contaminant film = $\beta\tau_s$, where β is a coefficient between 0 and 1, then at slip $\tau = \beta\tau_s$.
So:

$$\mu_c = \frac{\beta\tau_s}{\sigma_n} \tag{3.20}$$

Substituting (3.20) into (3.11) gives:

$$\mu_c = \frac{\beta \cos\psi}{\alpha\sqrt{(1 - \beta^2\cos^2\psi)}} \tag{3.21}$$

At this point we have to make the assumption that the contaminant film does not affect the gross behaviour of the underlying material, so that the stress path followed is the same up to the point at which the film shears. This implies that α is unchanged by the introduction of the film.

Thus:
$$\mu_c = \frac{\beta\tau_s}{\left\{H_v + \sigma_3\frac{(1 + \sin\psi)}{3(1 - \sin\psi)}\right\}\sqrt{(1 - \beta^2\cos^2\psi)}} \tag{3.22}$$

We also know that at slip the shear stress = $\beta\tau_s$.

But:
$$\beta\tau_s = \beta(k + \sigma_n \tan\psi) \tag{3.23}$$

or:
$$\tau_s = \frac{\mu_c k}{(\mu_c - \beta \tan\psi)} \tag{3.24}$$

Substituting (3.24) in (3.22), the coefficient of friction for the contaminated surfaces is given by:

$$\mu_c = \beta \tan \psi + \frac{\beta k}{\left\{H_v + \sigma_3 \frac{(1 + \sin \psi)}{3(1 - \sin \psi)}\right\} \sqrt{(1 - \beta^2 \cos^2 \psi)}} \qquad (3.25)$$

3.5 Prediction of the Coefficient of Friction for Quartz on Quartz:

The friction between two quartz surfaces will depend on whether they are clean or contaminated. If the latter, it seems unlikely that a value of μ_c can be predicted because the value of β would have to be known. However, in the case of clean surfaces the known intrinsic parameters can be substituted into equation 3.19. Then we obtain:

$$\mu = 0.292 + \frac{34,310}{H_v + 1.777\ \sigma_3} \qquad (3.26)$$

(for K = 9600 kg/sq cm and $\psi = 16\frac{1}{4}^\circ$). Note that both H_v and σ_3 must be in kg/sq cm units.

Using Brace's indentation hardness data the value of the coefficient of friction can be predicted for a load on a single asperity, and also for various ambient pressures. These values are shown graphically in Fig 3.16 for both $\sigma_3 = 0$ and $\sigma_3 = 632.8$ kg/sq cm (9000 psi) ambient pressures.

3.6 Experimental Determination of the Friction of Quartz on Quartz:

For a full description of the friction apparatus see Chapter 2.

The tests described were performed with the apparatus shown in Plate 2.5 described in Chapter 2. The friction apparatus was mounted on the pedestal of the 'balanced ram high pressure cell'. The friction force on the slider was sensed by an inductive displacement transducer, mounted in the load ring, which was fed from the carrier source in a 'Boulton Paul Aircraft Limited' transducer meter, type C61. The response of the load cell transducer was fed back through the nulling system of the C61, and the remaining unbalanced voltage fed to a 'Leeds and Northrup Speedomax, type H' strip chart recorder, which had a full-scale deflection for 10 mV input signal.

Using this method of sensing, great accuracy in the measurement of the frictional force is possible. For example in the high sensitivity range, full-scale deflection on the strip chart recorder is obtained for a change in load of 72.3 gm; which means that each division on the chart corresponds to a change in load of 0.723 gm. On medium sensitivity the chart division corresponds to a load change of 7.23 gm (i.e. full-scale deflection for 723 gm) and on low sensitivity each chart division corresponds to 72.3 gm (i.e. full-scale deflection for 7230 gm).

In these tests on quartz specimens, where there is a small natural variation in the coefficient of friction from point to point of the surface, it was not possible to obtain a complete trace on the high sensitivity scale, because the

variations in the frictional force were too rapid for the response of the recorder, which is quite slow - nominally 5 seconds for full-scale travel - and in many cases even when the medium sensitivity scale was used, the trace ran off the chart because the frictional force was greater than could be indicated. However, with the type of measuring system used, it was possible to bring the trace back on to the paper by nulling a part of the out of balance voltage, using the nulling system on the C61 transducer meter, it being only necessary to note on the trace the change in nulling voltage indicated by the five decade switches.

The magnitude of the trace shift is 10.1 chart divisions to the left for a change of decade reading of -00100, and a shift to the right of 10.1 chart divisions for a change of decade reading of +00100 for the medium sensitivity range.

In the friction tests reported the traces are given for the slider advancing, this producing a deflection of the trace to the right; then reversing over the same friction track, giving a deflection of the trace to the left. To produce results which would be taken as if the tests were performed on identical tracks, the slider was moved backwards and forwards over the same track many hundreds of times before any results were taken. The frictional force required to move the slider in any one direction is one half of the force required to move the trace from right to left or vice versa.

A typical result is shown on the trace in Fig 3.17, which was a test performed on specimen 1 with slider 1, with the quartz surfaces dry in the normal atmospheric conditions; the load on the contact was 977 gm and the trace was recorded with the C61 meter set on medium sensitivity. The speed of the slider over the specimen block was 0.0025 inches per minute.

Fig 3.18 to Fig 3.22 inclusive show recorder traces of a series of tests performed on the same specimen 1 with the same slider 1, moving over the same friction track, which had been pre-formed as explained above. Fig 3.18 shows that the friction of the air dry surfaces was low, the maximum coefficient of friction being 0.19. By submerging the surfaces in distilled water (Fig 3.19) the coefficient of friction was increased to a value of 0.864 maximum and severe stick-slip was obtained. This test was repeated and a recorder trace with the tangential load scale reduced by a factor of 10 was obtained (see Fig 3.21a) and a coefficient of friction of 0.84 was obtained.

To reduce the tangential load scale it is only necessary to switch the sensitivity control on the C61 transducer meter from medium to low sensitivity. This reduces the out of balance signal transmitted to the strip chart recorder by a factor of 10. This was done in order to produce a trace which was defined completely within the width of the paper chart of the recorder. The ambient water pressure around

the contact was then increased to 9000 psi, and the friction tests repeated. The trace obtained with the medium sensitivity setting is shown in Fig 3.20 and that for the low sensitivity setting in Fig 3.21b. The behaviour under these conditions is seen to be much the same as for the 0 psi ambient pressure conditions. The coefficients of friction in the high ambient pressure tests were 0.887 and 0.84 respectively.

The difference in the maximum measured values of the coefficient of friction for an increase in the ambient pressure from 0 to 9000 psi when the medium sensitivity setting of the C61 transducer meter was used can be read off the charts in Fig 3.19 and Fig 3.20, and expressed as a percentage, is 3.1% increase in the coefficient of friction for an increase of 9000 psi in the ambient water pressure. This is a very small difference, bearing in mind the severe stick-slip motion being monitored. No difference in the coefficient of friction for the tests using low sensitivity was obtained. This is not unreasonable as a 3% change in coefficient of friction would have only changed the trace separation distance by 0.75 chart divisions, and the width of the trace itself is 0.3 chart divisions.

The traces obtained for the surfaces submerged show that the stick-slip mechanism depends on two parameters at least; first the variable coefficient of friction of the submerged surface, and secondly the stiffness of the mechanical system employed. The stiffness of the system for the forward trace

can be considered as due to the stiffness of the tangential load transducer itself; whereas, for the reverse track, additional flexibility is introduced into the system by the return springs, used to pull the specimen back. The combination of these two factors is clearly seen in Fig 3.21a and Fig 3.21b. It is therefore possible to reduce the amplitude of the stick-slip motion in the reverse direction by increasing the stiffness of the return springs. However, the stick-slip behaviour would still be present because it is not possible to increase the stiffness of the mechanical system to a value more than that of the tangential load transducer itself.

The only way to reduce the amplitude of the stick-slip motion would be to obtain sliding surfaces which had a more uniform coefficient of friction when submerged. To see if this is possible it is necessary to find out why the surface friction increases when the surfaces are saturated. When the surfaces are exposed to the laboratory atmosphere they become contaminated, a layer being formed on the quartz surfaces, and the shear strength of the contaminating film is less than that of the quartz itself. Hence the friction is low. But because the slider is traversed many hundreds of times before immersion in the distilled water, we can expect the contaminating film to be quite thin, probably only a few molecules thick. Now when the surfaces are immersed, those constituents in the contaminating film which are soluble in water dissolve. Also the quartz itself is very weakly soluble and so we

can expect that the surface film will be disrupted. The test results show an increase in friction when submerged, and so support this hypothesis. Only the more insoluble and more strongly adhering parts of the contaminating film are left. The result is a surface which will have non-uniform frictional properties, and this is again evident from the results. However, if this hypothesis is correct, we can expect that because the surfaces are immersed in distilled water, once the surface contamination is removed, the clean surfaces will tend to stay clean, as the mobility of the contaminating molecules in water should be low; and furthermore, the longer the surfaces are immersed the more uniform the frictional properties of the surface will become as the surface layers are dissolved off.

To test this hypothesis the quartz specimen 1 and slider 1 were kept immersed in distilled water for approximately 9 hours after the tests previously reported, shown in Fig 3.18 to Fig 3.21, and then the friction test was repeated. The result is shown in Fig 3.22a and Fig 3.22b, and it can be seen that the frictional properties of the surface are much more uniform than for the previous tests. (Compare the tests shown in Fig 3.21a and Fig 3.21b with that shown in Fig 3.22b.) There is still a small variation in the surface friction (this is shown up on the reverse traces) because of the lower stiffness of the mechanical system. The coefficients of friction for the tests shown in Fig 3.22a (medium sensitivity) and Fig 3.22b (low sensitivity) are 0.85 and 0.84 respectively.

These tests indicated that the stick-slip mechanism was avoidable, and consequently more representative tests for 'clean' quartz surfaces could be obtained by immersing the surfaces in distilled water for a sufficient time, to remove as much of the surface contaminating film as possible. Also, if the slider was moved backwards and forwards over the same track, while submerged, any residual contamination from the track itself could be worn away.

With this in mind a second series of tests was performed on another quartz specimen 2 with another slider 2, the results being presented in Fig 3.23 to Fig 3.28 inclusive. The behaviour again follows the hypothesis outlined previously, the stick-slip motion being eliminated after 24 hours of immersion (see Fig 3.25a and Fig 3.25b). To verify if the maximum amount of the surface contamination had been removed, the surfaces were kept immersed for a further 17 hours (*i.e.* 41 hours in all) and the tests repeated. This result is shown in Fig 3.27, the maximum coefficient of friction being 0.83(9) - this can be compared with the test shown in Fig 3.26, which is the corresponding trace for 24 hours immersion when the maximum coefficient of friction was found to be 0.83(5). Therefore we can say that after 41 hours of immersion virtually all the removable contamination had been removed. The test shown in Fig 3.28 is a repeat of that shown in Fig 3.27, with the ambient water pressure at the contacts increased to 9000 psi, the maximum coefficient of friction being 0.83(4). We can therefore conclude that

for the quartz specimens used, immersion in distilled water enables the friction of 'clean' quartz to be measured, and that increasing the ambient pressure by 9000 psi has a very small influence on the frictional behaviour.

3.7 Comparison of the Theoretical Prediction of Friction Coefficient with the Experimental Results:

From the theory outlined earlier in this chapter, it was shown that the coefficient of friction could be written, for clean crystal surfaces, as:

$$\mu = \tan \psi + \frac{k}{\sin \psi \left\{ H_v + \sigma_3 \frac{(1 + \sin \psi)}{(1 - \sin \psi)} \right\}} \qquad (3.19)$$

and for clean quartz surfaces in particular:

$$\mu = 0.292 + \frac{34,310}{H_v + 1.777\ \sigma_3}$$

To check if the theory outlined previously fitted the test results for the clean surface produced on specimen 2 with slider 2 it is necessary to find the correct value of H_v for the test. The results by Brace (1963) show a variation of hardness with load, therefore it is necessary to find approximately the number of asperities carrying the load of 732 gm applied to the slider. Referring to Fig 3.2, 3.3 and 3.29 it is seen that the flat tip of slider 2 could rest on anything between 1 and 10 asperities. If the assumption is made that these major asperities take the majority of the load it would seem reasonable to use a mean value of

H_v for loads between 70 gm and 700 gm. It was, however, very difficult to perform indentation tests below 300 gm because of the difficulty of measuring the very small size of the indentations produced. The mean values obtained for 300 gm and 500 gm loads were very close and are given below:

Load 500 gm H_v = 65,500 kg/sq cm
(for a mean of 10 tests, the maximum and minimum values being 71,500 kg/sq cm and 60,000 kg/sq cm respectively)

Load 300 gm H_v = 64,900 kg/sq cm
(for a mean of 10 tests, the maximum and minimum values being 76,300 kg/sq cm and 54,300 kg/sq cm respectively)

These hardness values show that there is a considerable variation in the hardness from point to point on the surface, which would reflect in varying coefficients of friction in the test. The variation is probably due to varying orientations of crystals making up the specimen, which was not a single crystal, and to impurities in the crystal structure which according to Brace (1963) lower the hardness.

Because of these difficulties it is apparent that verification of the theory can only be approximate. However, to test if the correct order of magnitude is forecast by the theory, the value of H_v = 65,200 kg/sq cm will be used.

Theoretical μ for $\sigma_3 = 0$ is given by:

$$\mu = 0.292 + \frac{34,310}{65,200 + 0} = 0.818$$

And for $\sigma_3 = 632.8$ kg/sq cm:

$$\mu = 0.292 + \frac{34,310}{65,200 + 1.777 \times 632.8} = 0.809$$

Maximum measured values (see Fig 3.27 and Fig 3.28):
for $\sigma_3 = 0$, $\mu = 0.839$; for $\sigma_3 = 632.8$ kg/sq cm, $\mu = 0.834$.

The predicted and experimental values are fairly well in agreement. It must however be pointed out that because of the limitations in the accuracy of the measuring system the third decimal place in the measured coefficients is in doubt.

One further check is available, using the data in the paper by Bowden and Hanwell (1966), for quartz sliding on quartz, under high vacuum conditions, and when special techniques were used to ensure clean crystal surfaces. In the test reported the normal load was 70 gm and the coefficient of friction $\mu = 0.71$. If Brace's (1963) data are used the hardness at 70 gm is $H_v = 98,000$ kg/sq cm. Substituting this value into equation 19 gives:

$$\mu = 0.292 + \frac{34,310}{98,000 + 0} = 0.64$$

Again the agreement is not unreasonable.

These results tend to confirm that an adhesion mechanism can be used to explain the frictional behaviour between quartz surfaces, and there seems no reason to doubt that the same

mechanism will obtain for other minerals as well. Furthermore it is seen that for the ambient pressure range used (i.e. 0 to 9000 psi) the coefficient of friction for clean crystal surfaces can be considered to be nearly constant.

The friction of mineral surfaces which are not clean will depend on the shear strength of the contaminating layer, and consequently the coefficient of friction will vary from that of clean surfaces. Thus if any correlations are to be made regarding the behaviour of a mass of mineral particles, with the interparticle friction, it will be necessary to determine the coefficients of friction for the mineral surfaces as occurring in the tests on the particulate mass.

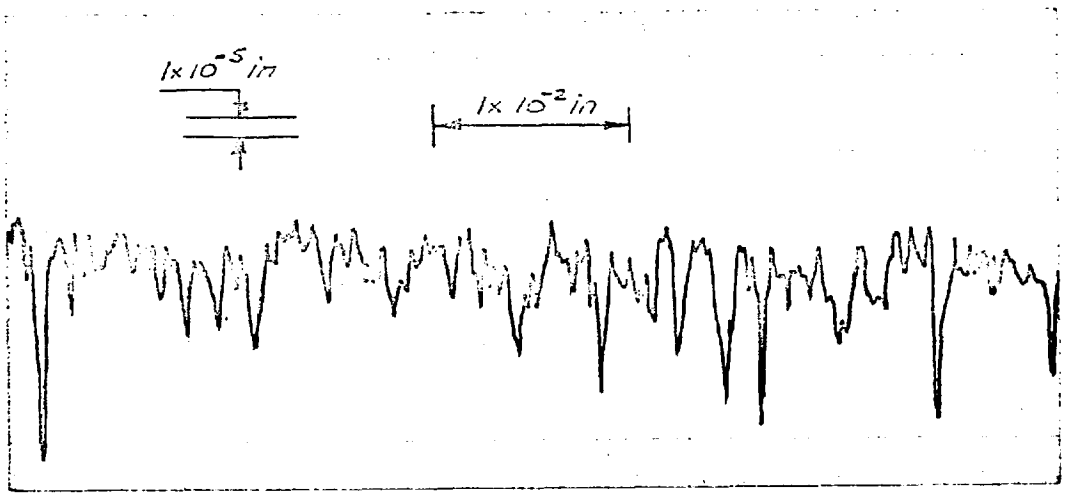


FIG.3.1. Talysurf profilometer record of the surface of specimen 2, along the length of the specimen off the line of the wear track.

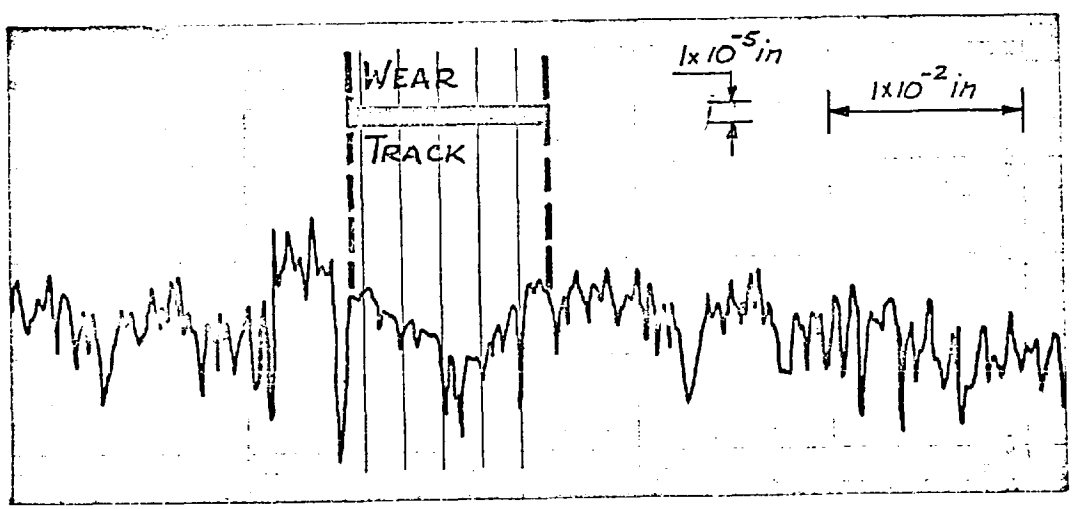


FIG.3.2. Talysurf profilometer record of the surface of specimen 2, across the specimen

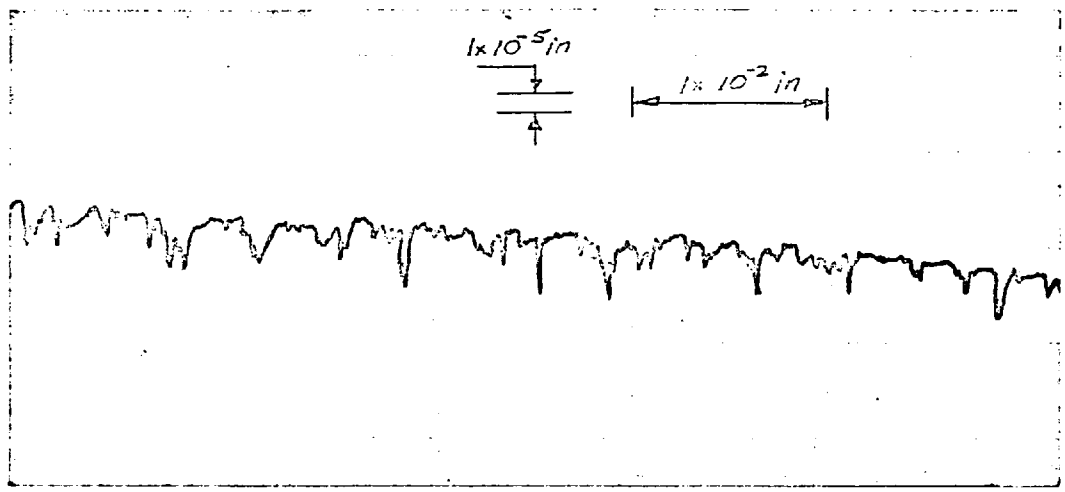


FIG.3. 3. Talysurf profilometer record of the surface of specimen 2,along the length of the specimen on the centre-line of the friction wear track.

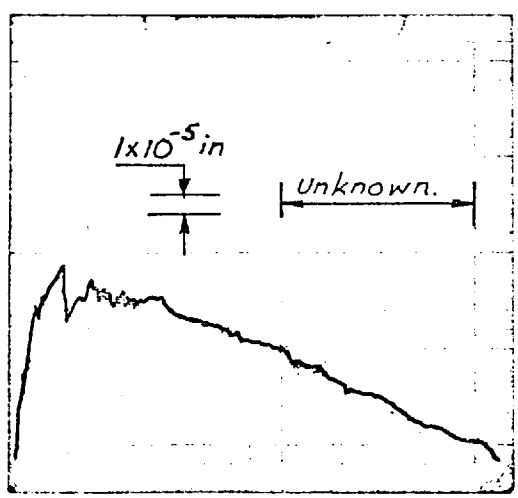


FIG.3.4. Talysurf profilometer record of the surface of slider 2, showing the smoothness of the worn tip.

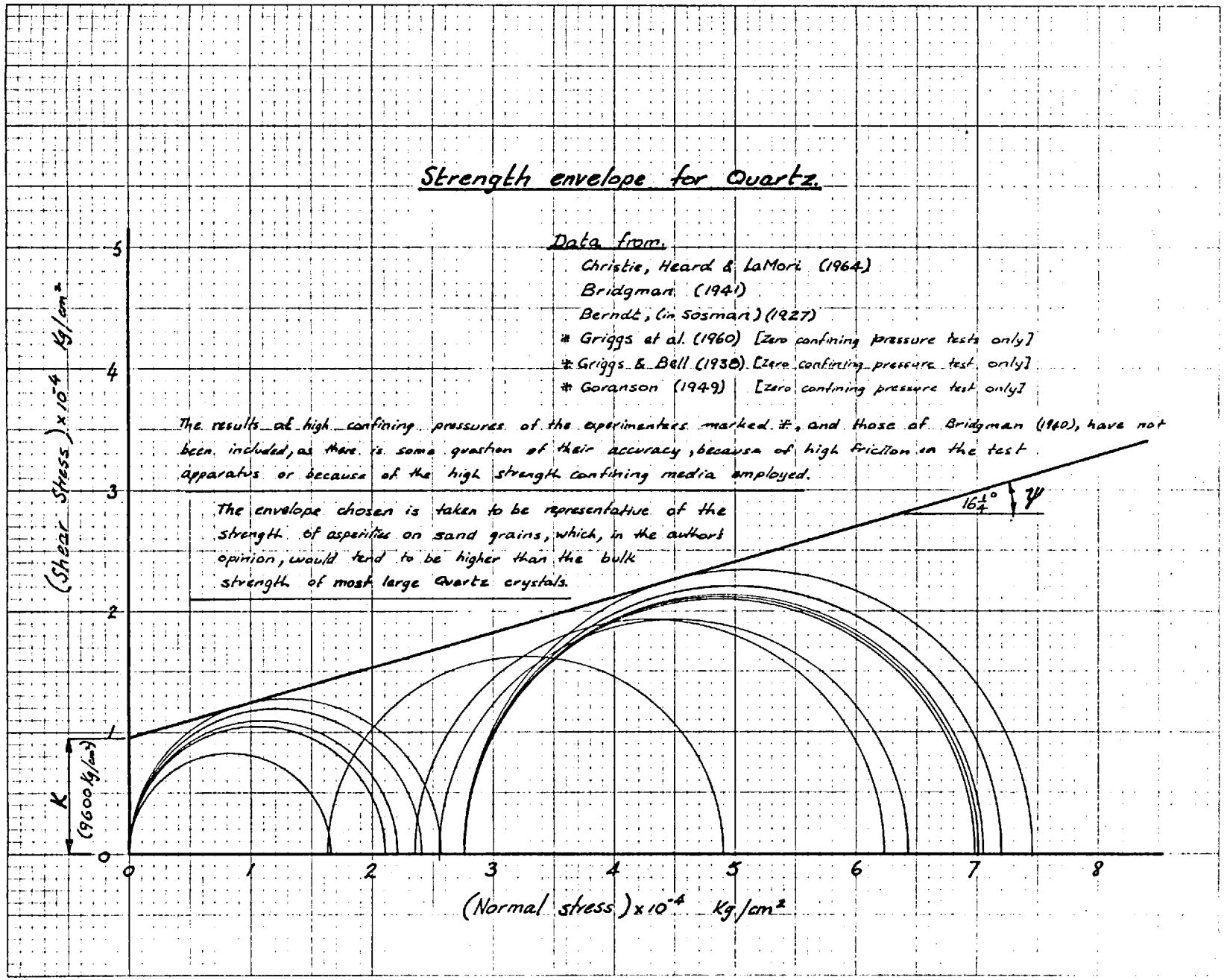

Strength envelope for Quartz.
Data from.
Christie, Heard & LaMori (1964)
Bridgman (1941)
Berndt, (in Sosman) (1927)
* Griggs et al. (1960) [Zero confining pressure tests only]
* Griggs & Bell (1938) [Zero confining pressure test only]
* Goranson (1949) [Zero confining pressure test only]
The results of high confining pressures of the experimenters marked *, and those of Bridgman (1960), have not been included, as there is some question of their accuracy, because of high friction in the test apparatus or because of the high strength confining media employed.
The envelope chosen is taken to be representative of the strength of asperities on sand grains, which, in the authors opinion, would tend to be higher than the bulk strength of most large Quartz crystals.
16½°
ψ
K
(9600 kg/cm²)
(Shear stress) x 10⁻⁴ kg/cm²
(Normal stress) x 10⁻⁴ kg/cm²
0
1
2
3
4
5
6
7
8

FIG 3.5

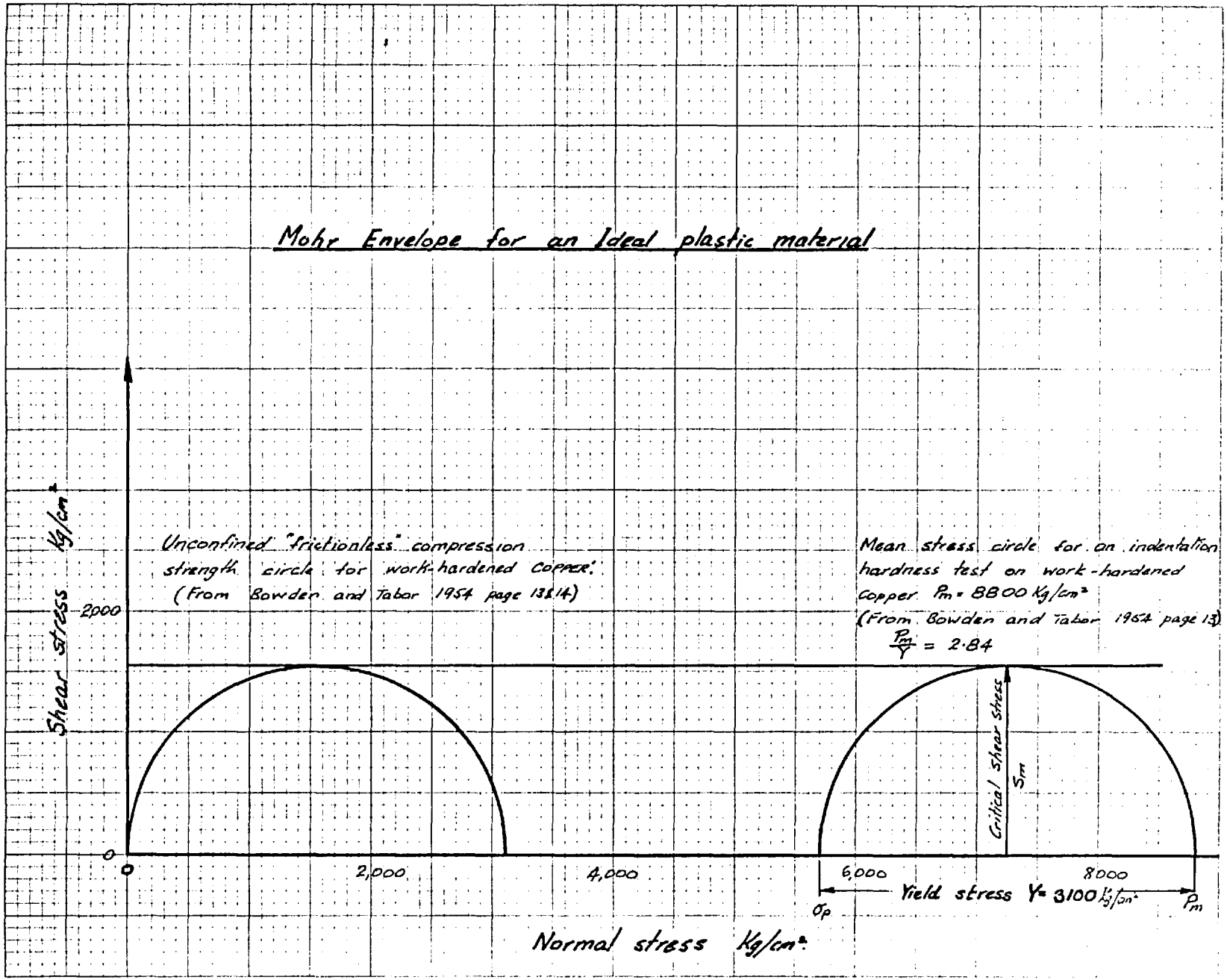
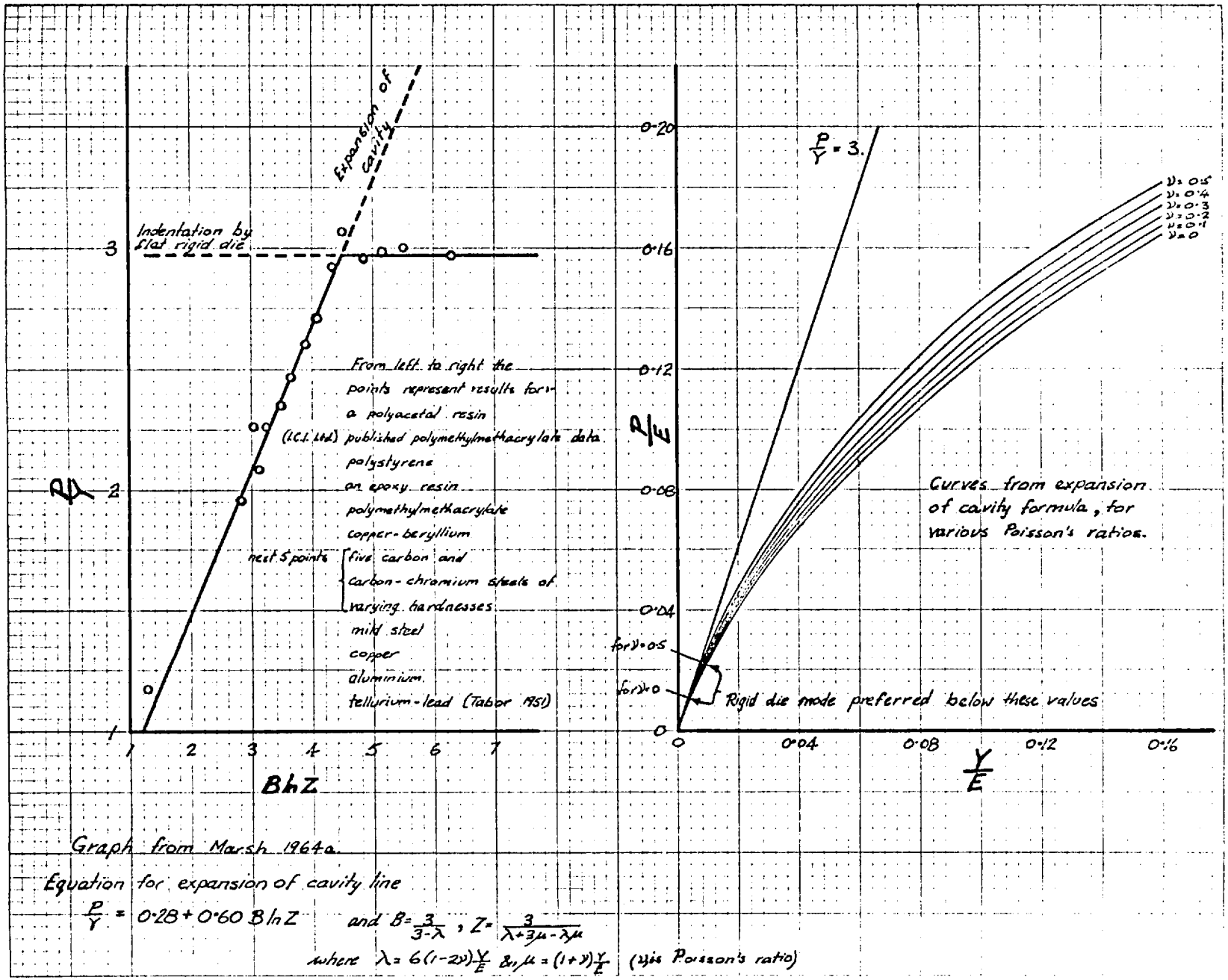

Mohr Envelope for an Ideal plastic material
Shear stress Kg/cm²
2000
0
Unconfined "frictionless" compression strength circle for work-hardened copper. (From Bowden and Tabor 1954 page 13&14)
Mean stress circle for an indentation hardness test on work-hardened copper Pm = 8800 Kg/cm² (From Bowden and Tabor 1954 page 13)
Pm/Y = 2·84
Critical shear stress
Sm
2,000
4,000
6,000
8000
Yield stress Y = 3100 Kg/cm²
σp
Pm
Normal stress Kg/cm²

Fig 3.6



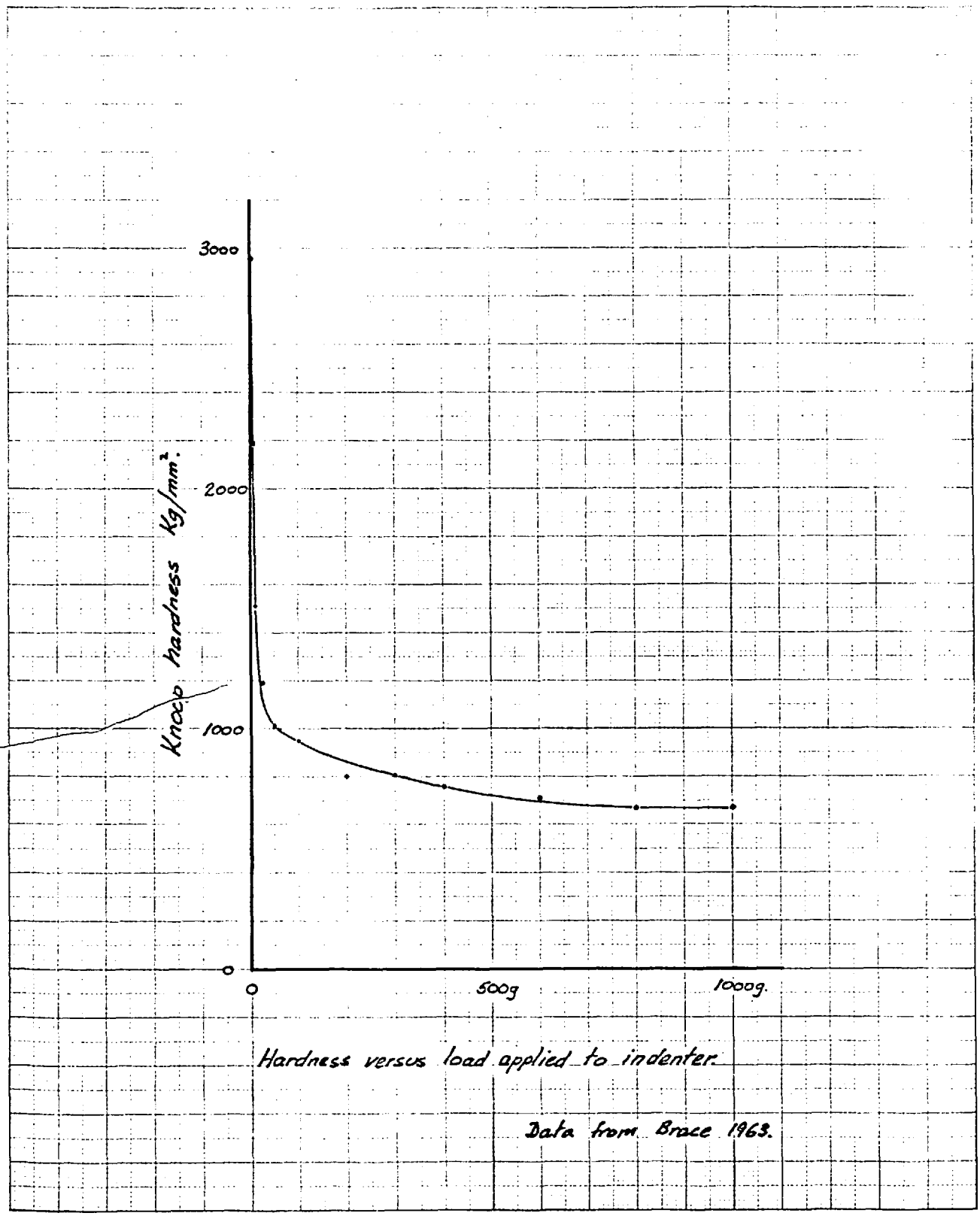
Graph from Marsh 1964a.

Equation for expansion of cavity line

$$\frac{P}{Y} = 0{\cdot}28 + 0{\cdot}60\, B \ln Z \quad \text{and} \quad B = \frac{3}{3-\lambda}, \; Z = \frac{3}{\lambda + 3\mu - \lambda\mu}$$

where $\lambda = 6(1-2\nu)\frac{Y}{E}$ & $\mu = (1+\nu)\frac{Y}{E}$ (ν is Poisson's ratio)

FIG 3·7a & b.



Hardness versus load applied to indenter.

Data from Brace 1963.

FIG 3·8

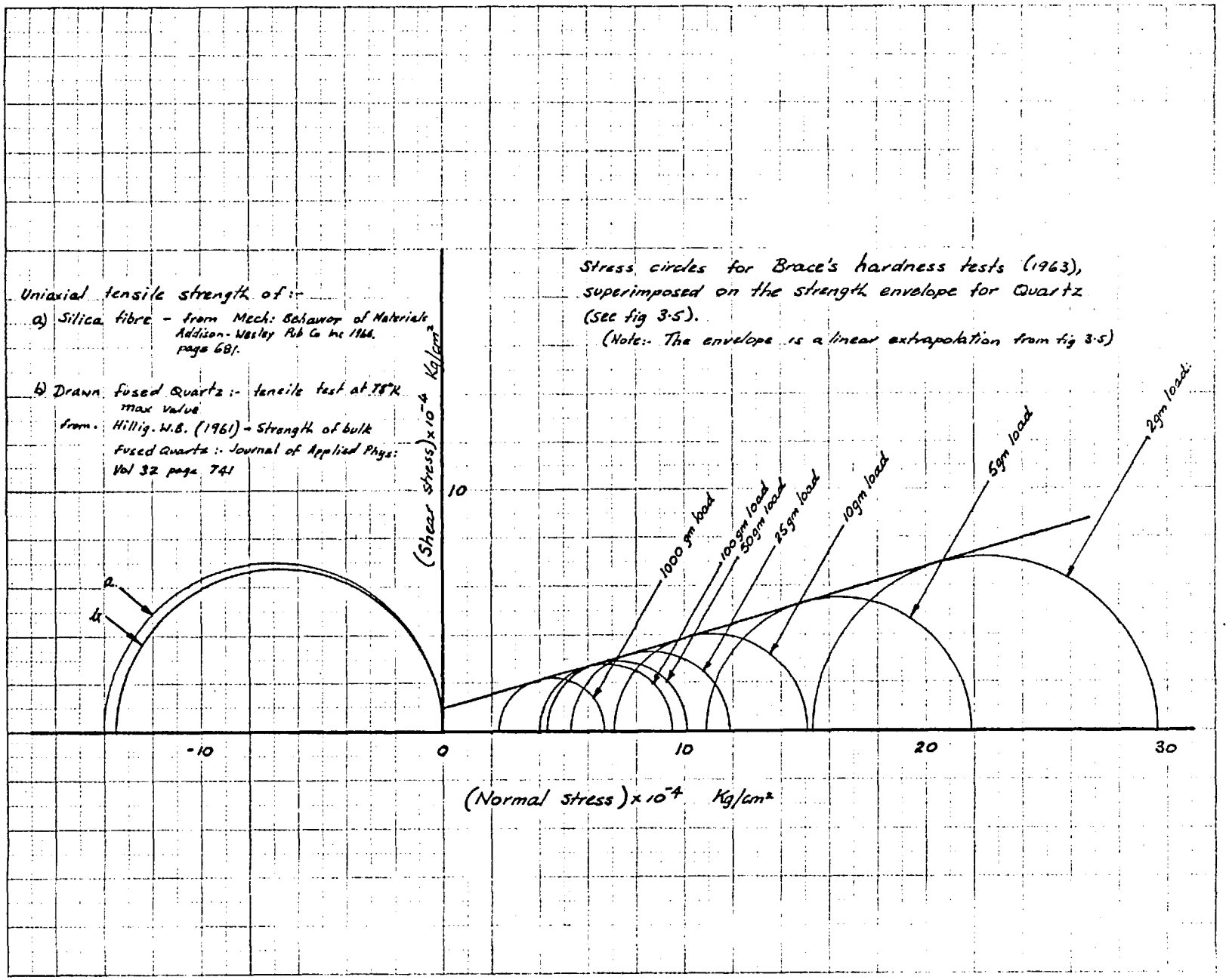

Uniaxial tensile strength of :-
a) Silica fibre - from Mech: Behaviour of Materials Addison-Wesley Pub Co Inc 1966. page 681.
b) Drawn fused Quartz :- tensile test at 78°K max value
from. Hillig. W.B. (1961) - Strength of bulk fused quartz :- Journal of Applied Phys: Vol 32 page 741
Stress circles for Brace's hardness tests (1963), superimposed on the strength envelope for Quartz (see fig 3.5).
(Note:- The envelope is a linear extrapolation from fig 3.5)
(Shear stress) x 10⁻⁴ Kg/cm²
(Normal stress) x 10⁻⁴ Kg/cm²
1000 gm load
100 gm load
50 gm load
25 gm load
10 gm load
5 gm load
2 gm load
a
b
-10
0
10
20
30
10

FIG 3·9

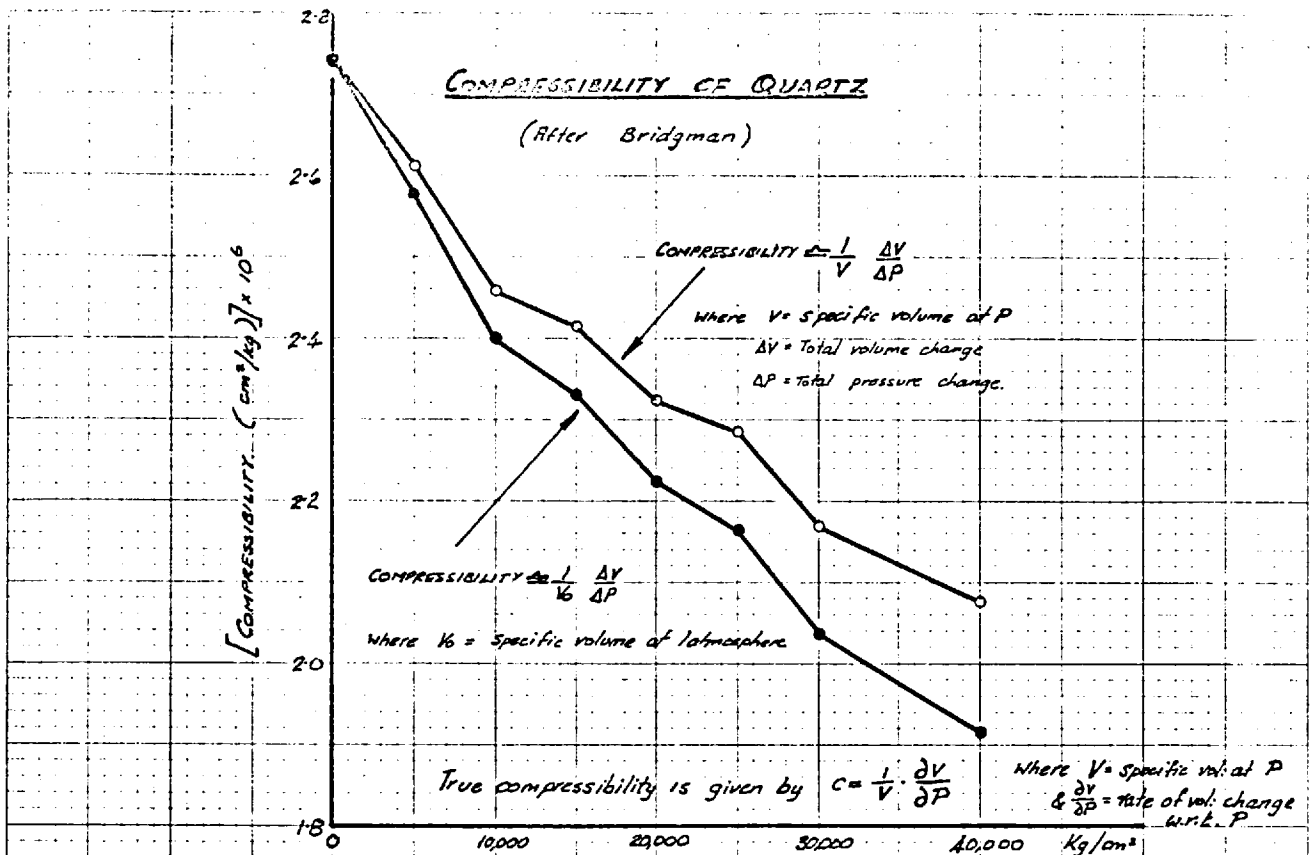


FIG 3·10

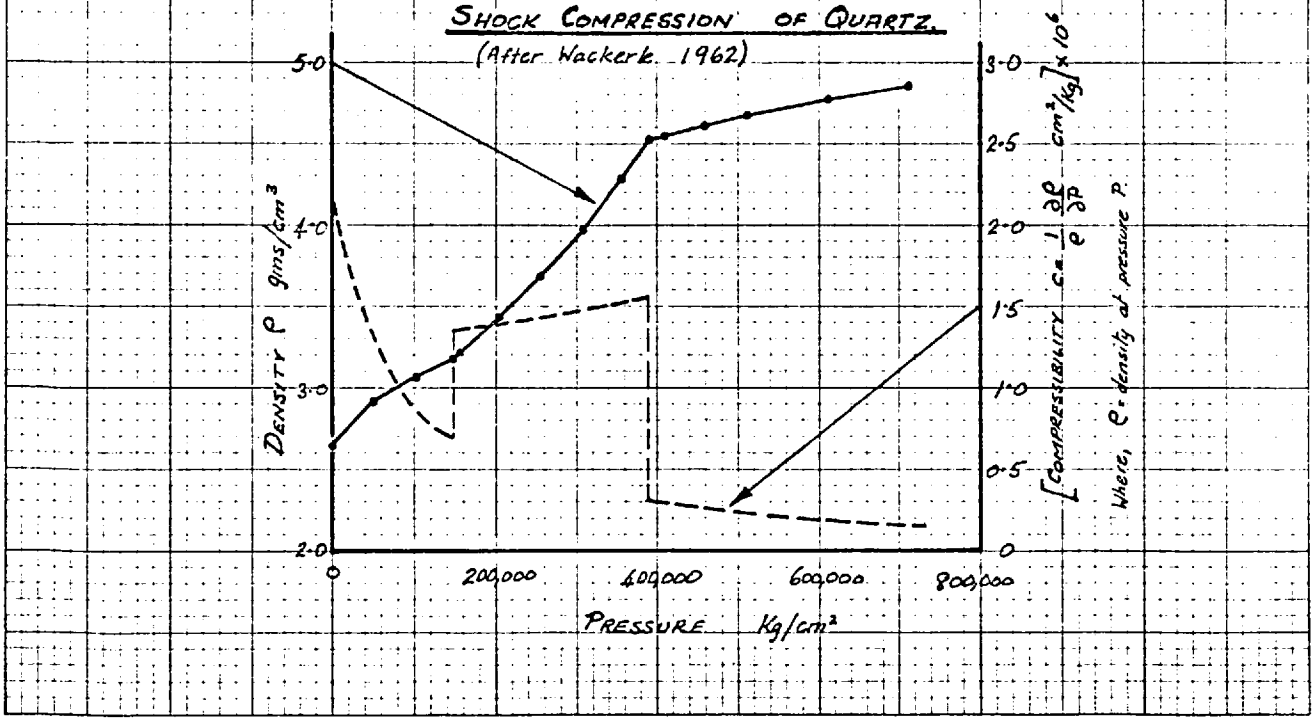


FIG 3·11

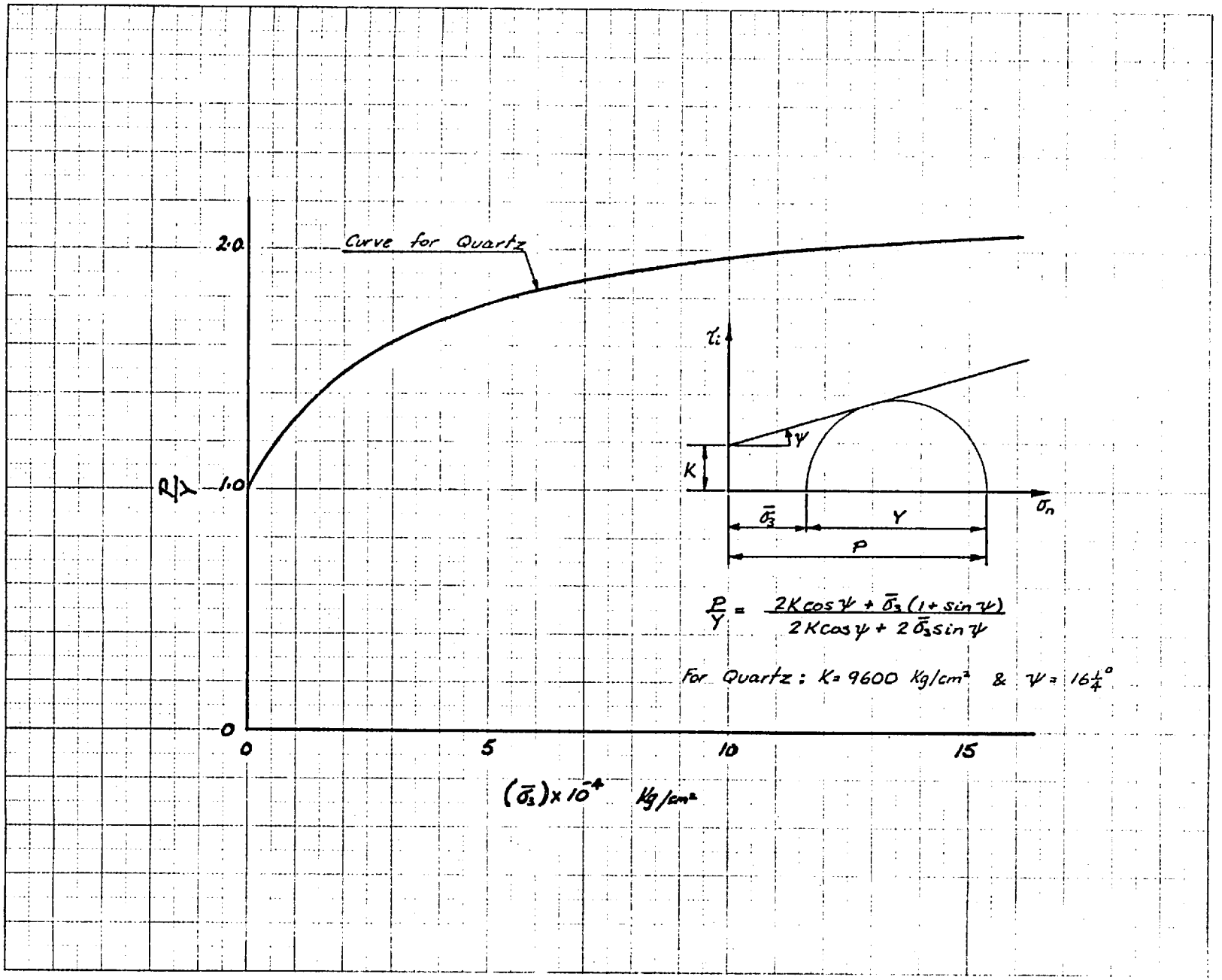

2.0
1.0
0
P/Y
Curve for Quartz
0
5
10
15
$(\bar{\sigma}_3) \times 10^{-4}$ kg/cm²
τ_i
σ_n
K
ψ
$\bar{\sigma}_3$
Y
P
$\frac{P}{Y} = \frac{2K\cos\psi + \bar{\sigma}_3(1+\sin\psi)}{2K\cos\psi + 2\bar{\sigma}_3\sin\psi}$
For Quartz : K = 9600 kg/cm² & ψ = 16¼°

FIG 3.12

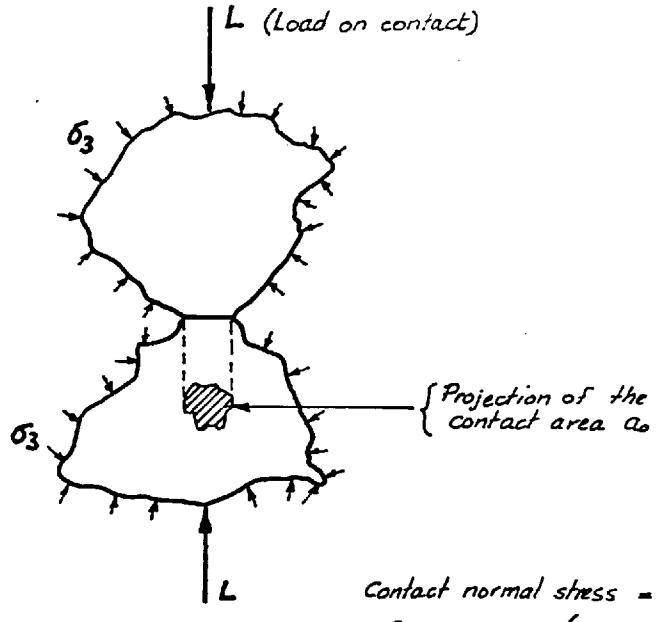


Fig. 3.13a. Typical contact between mineral grains when no shear tractions are applied.

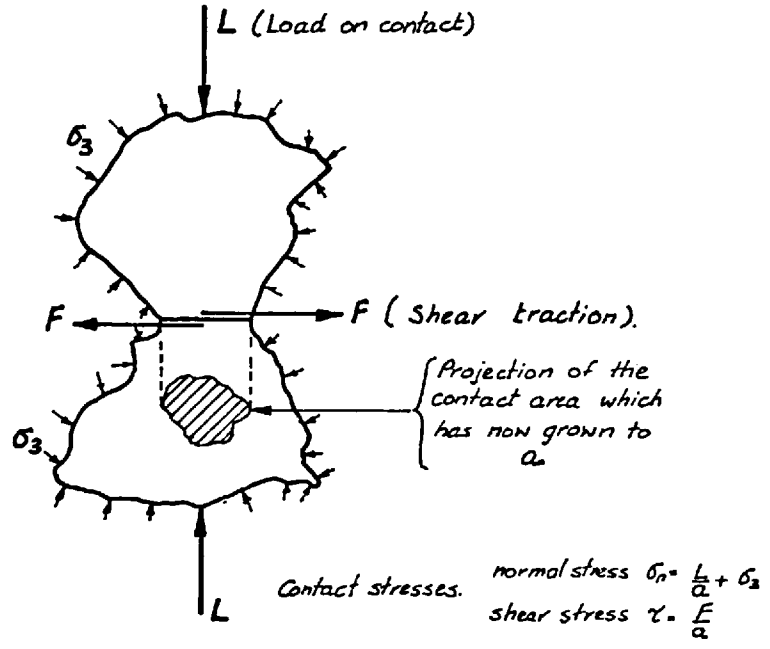
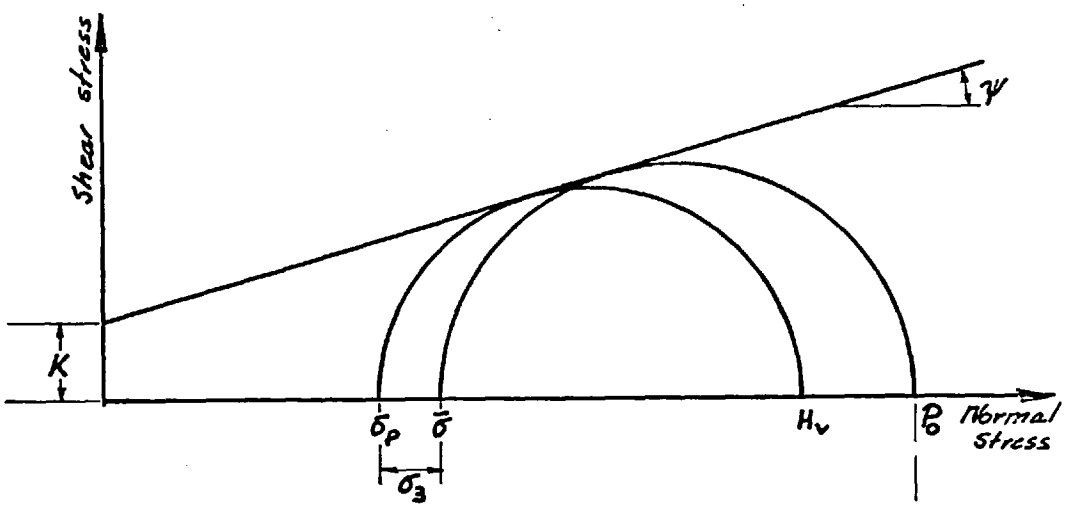
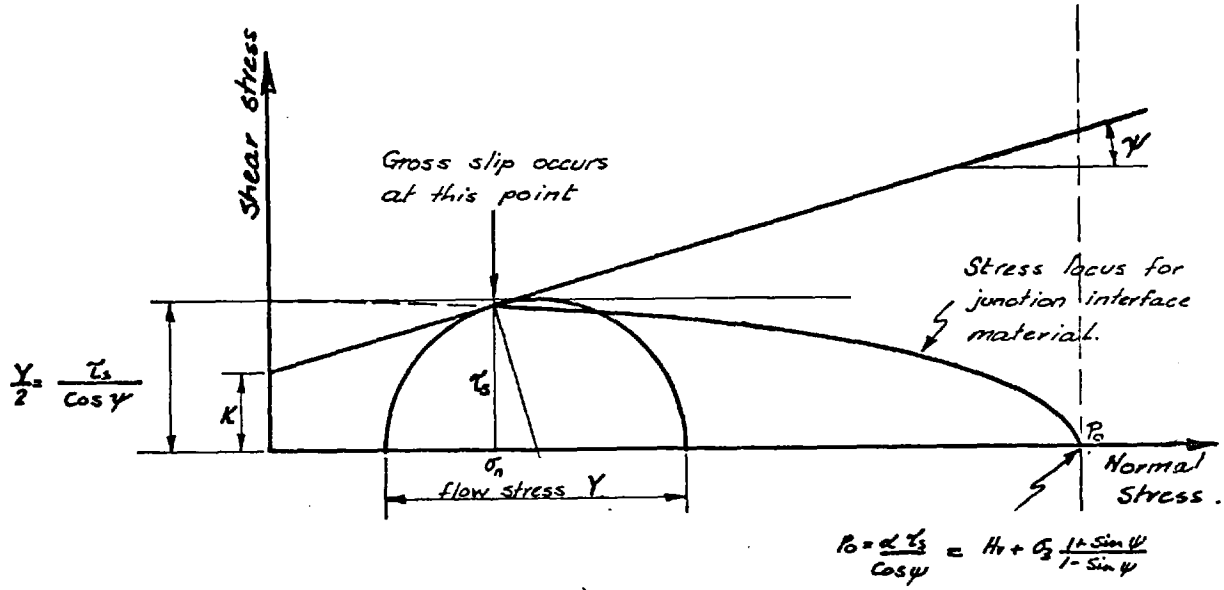


Fig. 3.13b. Contact as shown above, but in this case with shear tractions applied.



Initial stress conditions at contact with no shear traction.

FIG 3·14.



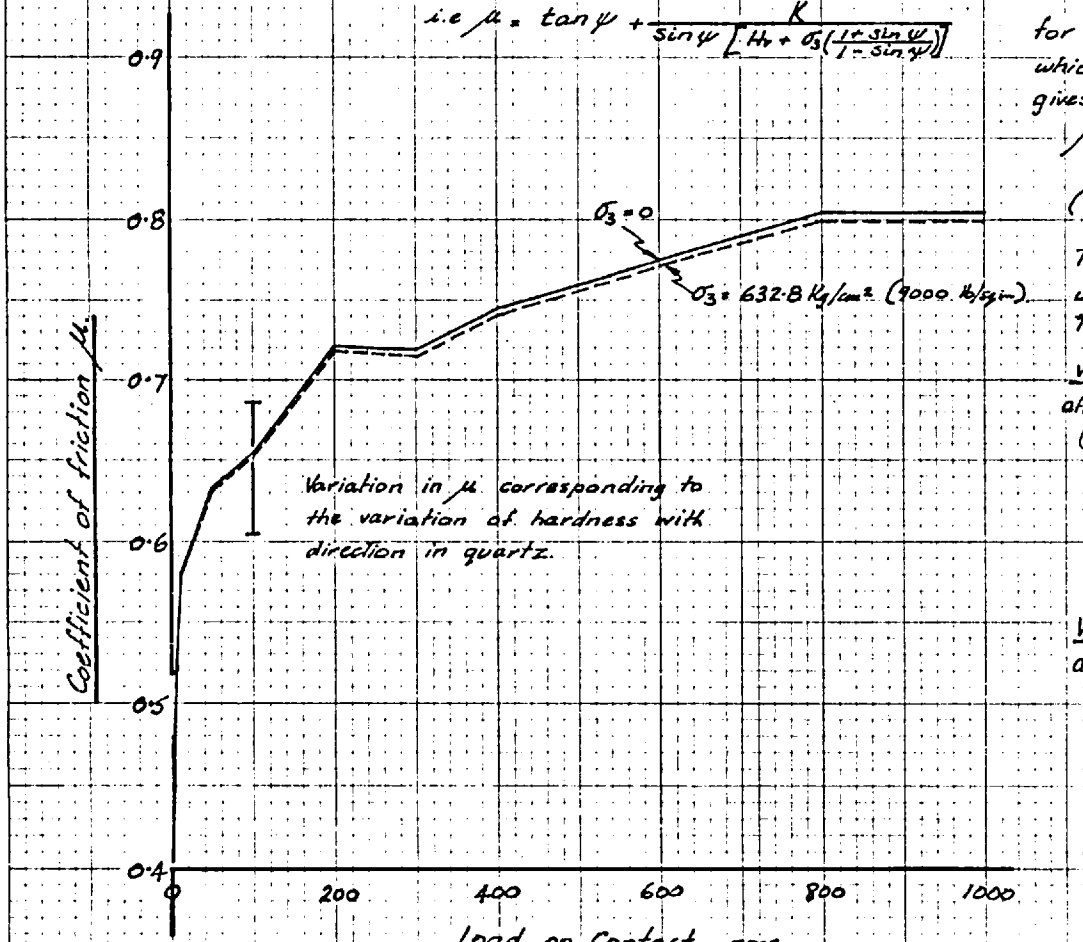
Stress locus for junction interface material.

FIG 3·15

Coefficient of friction for clean Quartz surfaces versus contact load.

Using equation (19) for μ

i.e $\mu = \tan\psi + \frac{K}{\sin\psi\left[H_v + \sigma_3\left(\frac{1+\sin\psi}{1-\sin\psi}\right)\right]}$



for Quartz $K = 9600$ Kg/cm² and $\psi = 16\frac{1}{4}°$ which when substituted into the eqn: for μ. gives:-

$$\mu = 0{\cdot}292 + \frac{34{,}310}{H_v + 1{\cdot}777\sigma_3}$$

(H_v & σ_3 in Kg/cm² units)

The graphs opposite were obtained using Brace's (1963) hardness data. The values used are quoted below:

Variation of hardness of Quartz with load

after Brace (1963)	1000 gm	67,000 Kg/cm²
	800	67,000
	600	71,000
	400	76,000
	300	80,600
	200	88,000
	100	95000
	50	101,000
	25	119,000
	10	151,000
	5	219,000
	2	296,000

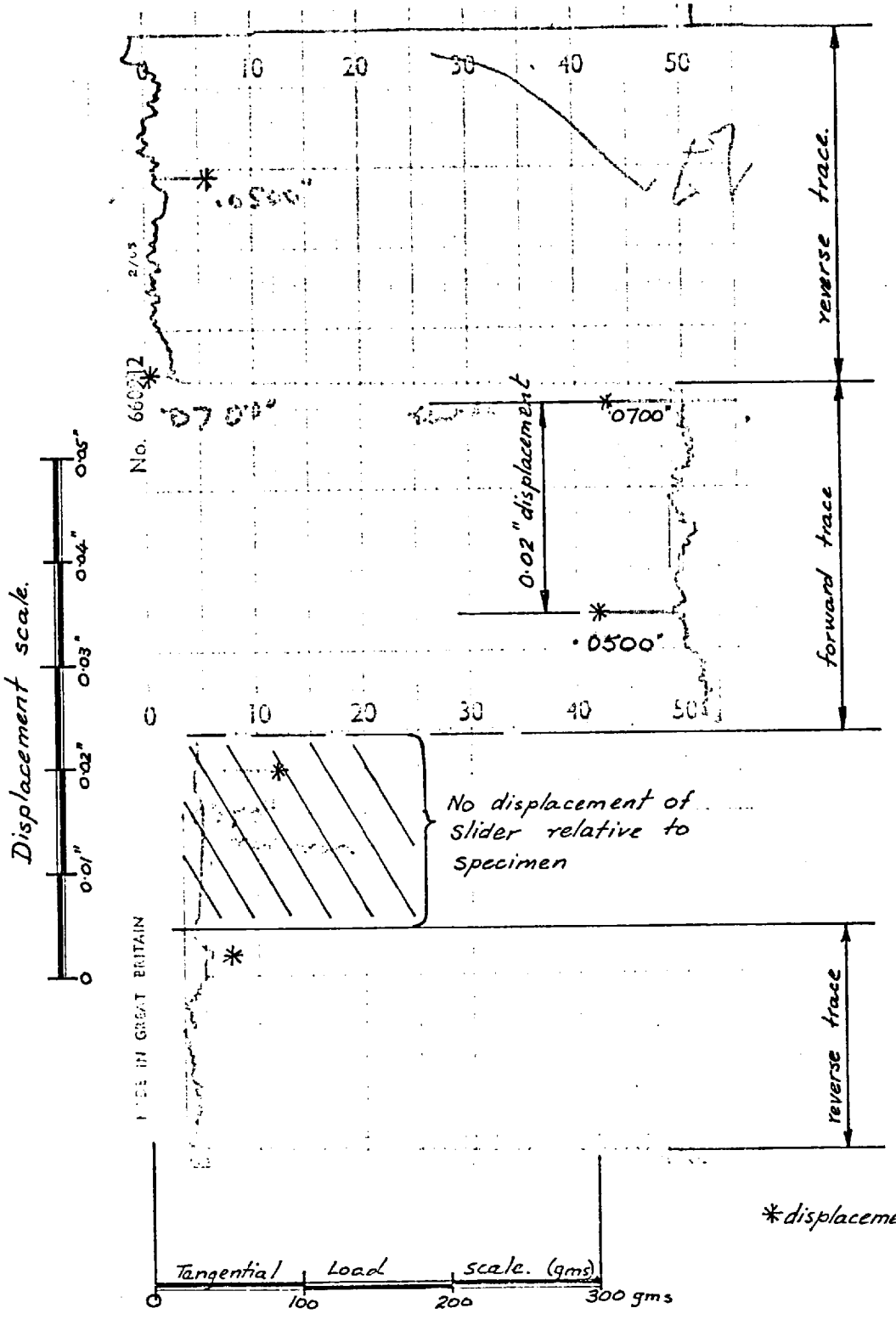
Variation of hardness with direction in Quartz

After Brace (1963) – Load 100 gm

direction	Hardness
r_0	100,000 Kg/cm²
r_{90}	87,000
Z_0	95,000
Z_{90}	89,000
m_0	95,000
m_{90}	110,000

where r_{90} means the $\{10\bar{1}1\}$ face with the long diagonal of the Knoop indenter perpendicular to the c-axis. Z is the $\{1\bar{1}01\}$ face and m is the $\{10\bar{1}0\}$ face.

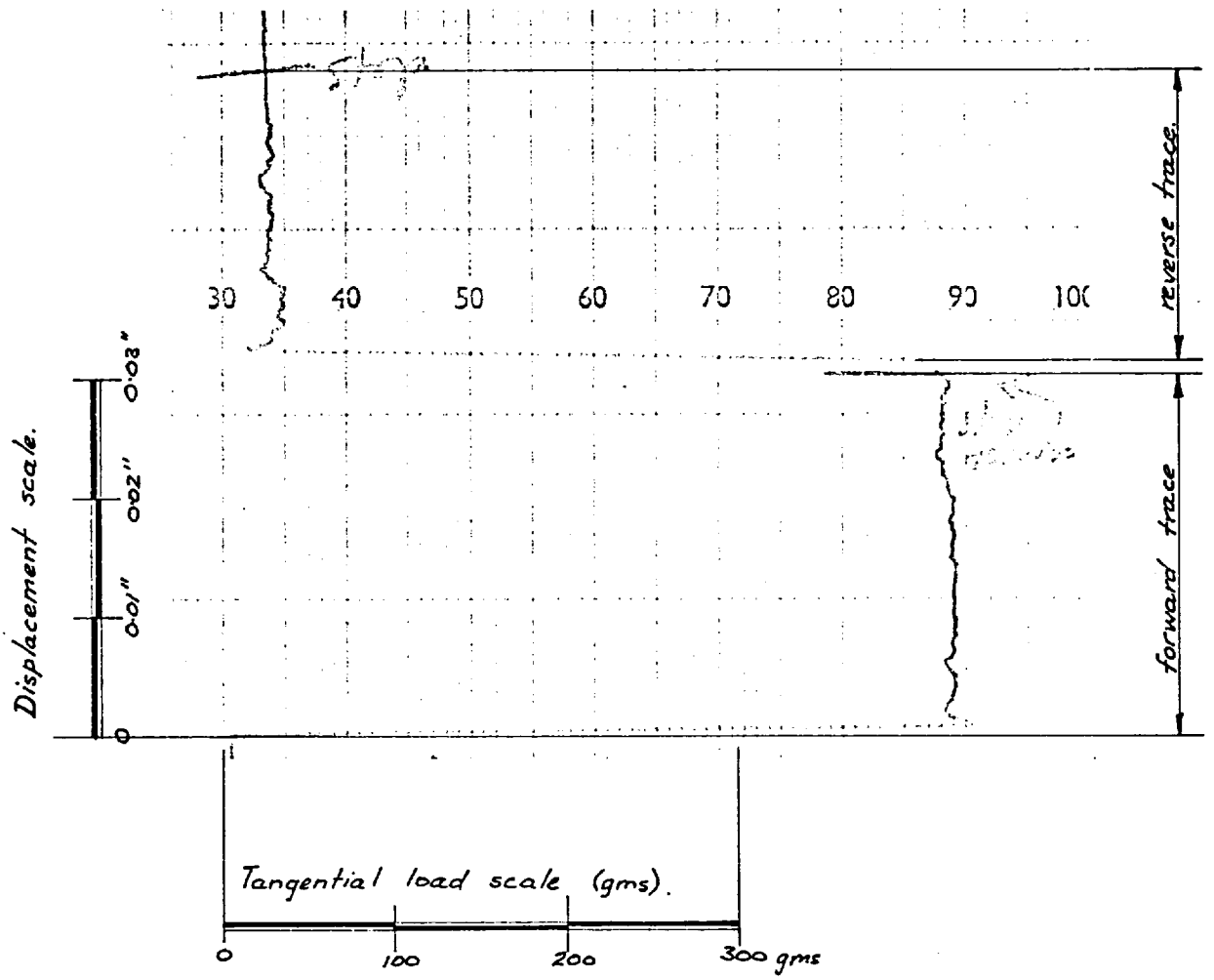
Fig 3.16



Recorder trace of test on milky-quartz specimen 1 with slider 1. Load on contact 977gms. Test dry.

Coefficient of friction μ · { 0·19 max: 0·15 min: 0·17 mean.

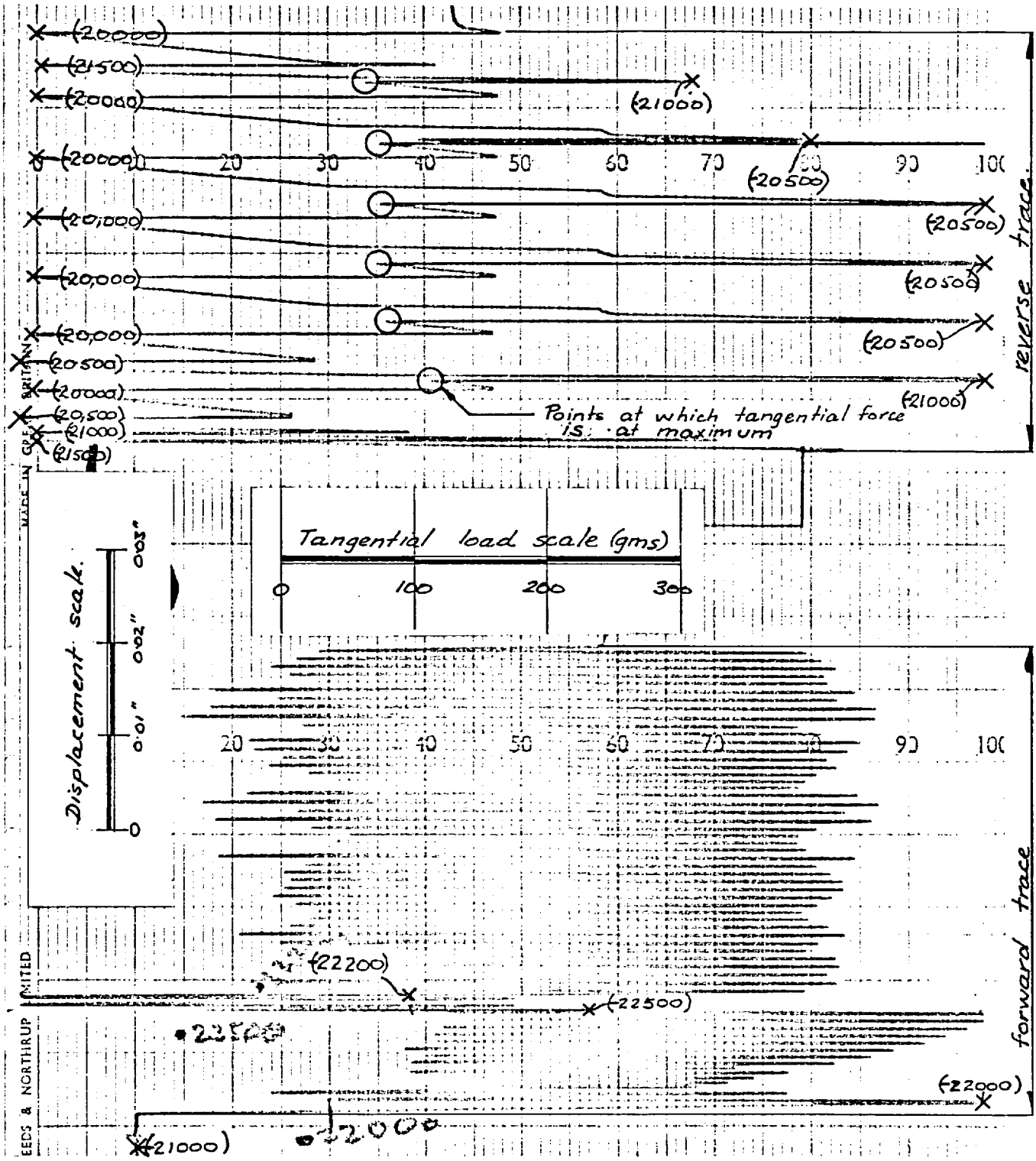
Fig 3·17



Recorder trace of a test on milky-quartz specimen 1 with slider 1. Surfaces dry.
Load on contact = 1110 gms

Coefficient of friction μ = { 0·19(1) max; 0·17(1) min; 0·17(8) mean.

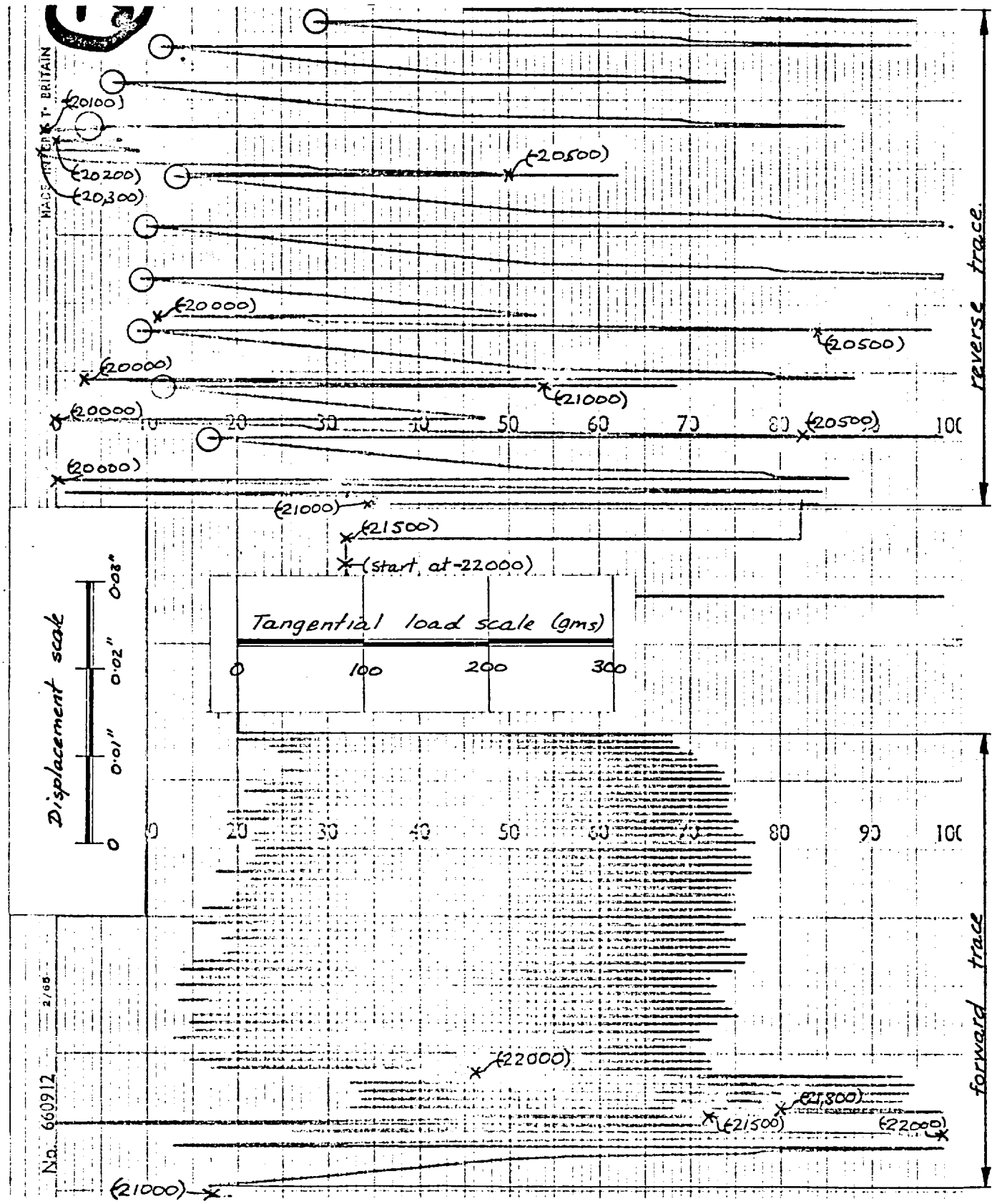
FIG 3·18



Recorder trace of a test on milky-quartz specimen 1 with slider 1. Surfaces submerged in distilled water.
Load on contact = 1110 gms. Ambient pressure = 0.
Coefficient of friction $\mu = 0.86(4)$ max.

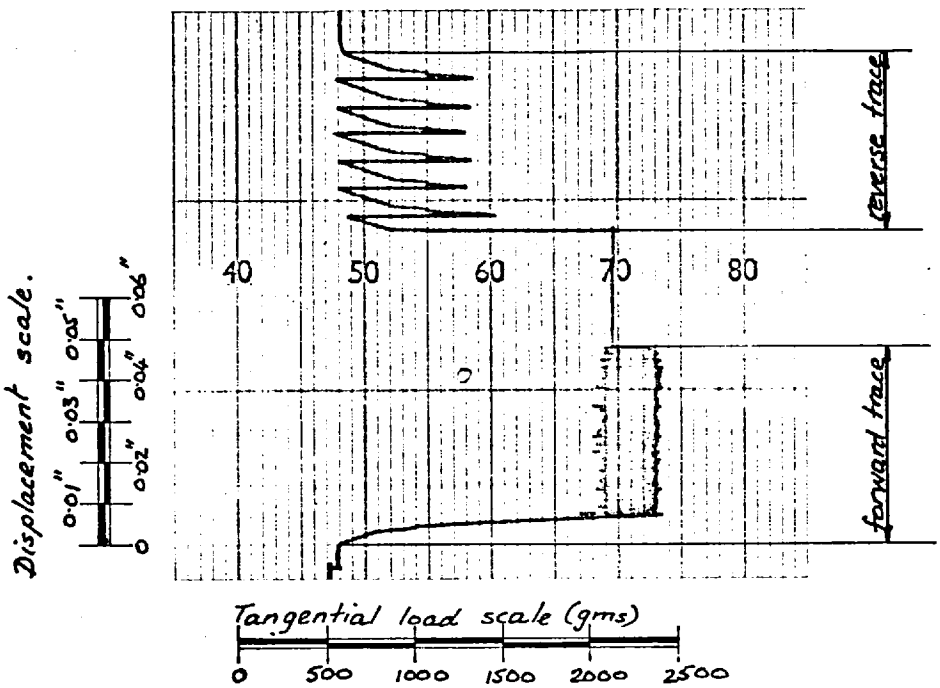
Note:- Points on the trace marked ×(20000) are points at which a part of the signal from the tangential load transducer was nulled, using the nulling decades of the C61. transducer meter (see text.).

FIG. 3·19



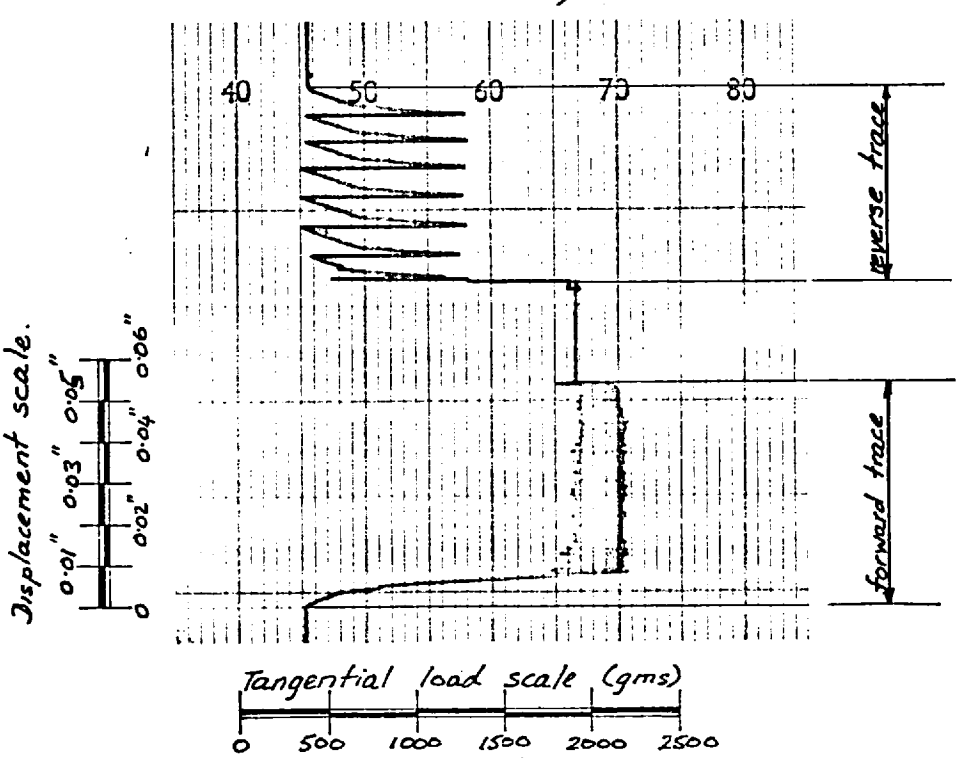
Recorder trace of a test on milky-quartz specimen 1 with slider 1. Surfaces submerged in distilled water
Load on contact = 1110 gms. Ambient pressure = 9,000 lb/sq. in.
Coefficient of friction μ = 0·88(7) max.

FIG 3·20



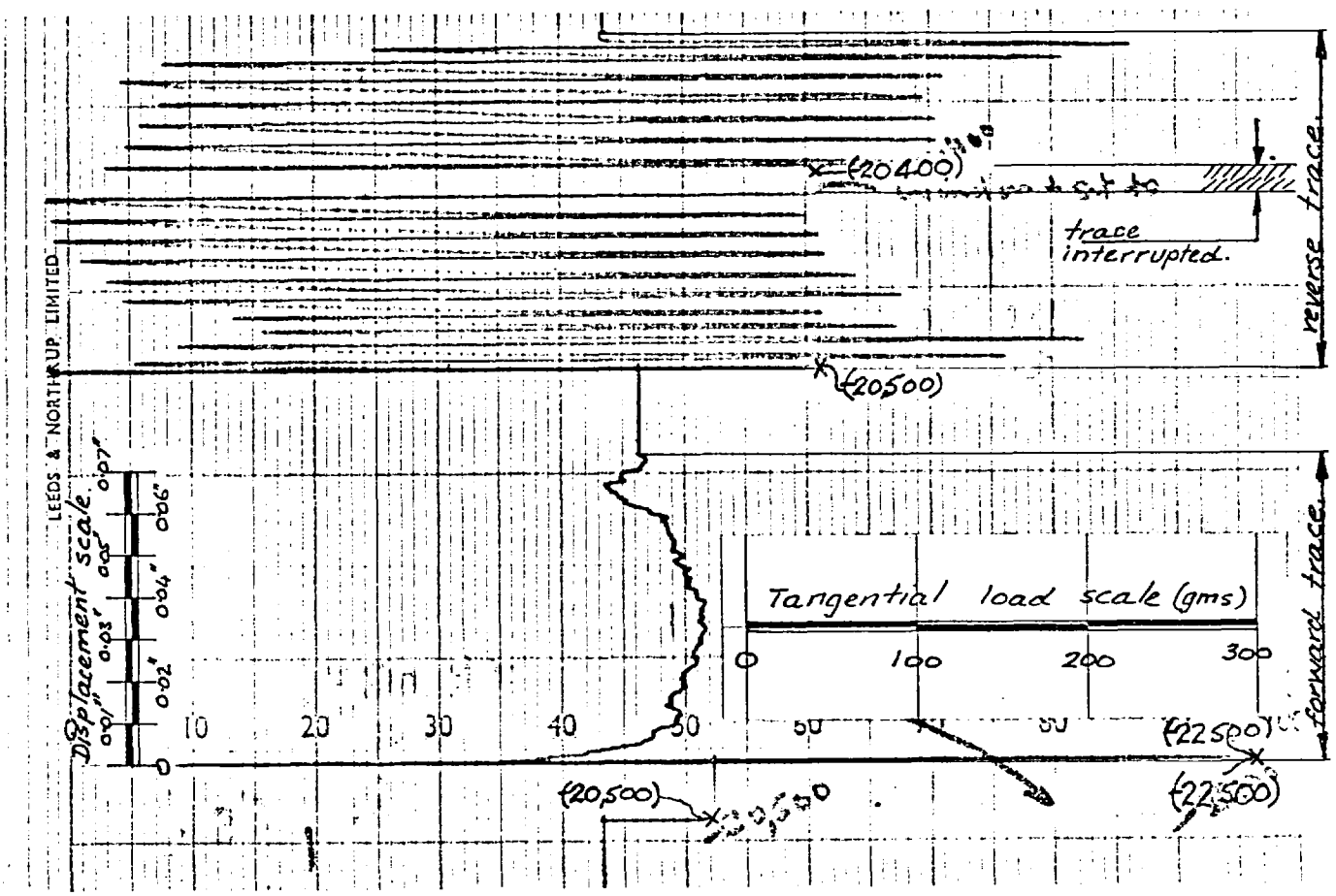
Recorder trace of a test on milky-quartz specimen 1 with Slider 1. Surfaces submerged in distilled water.
Load on contact = 1110 gms. Ambient pressure = 0.
Coefficient of friction $\mu = 0.84$ max.

FIG 3·21a



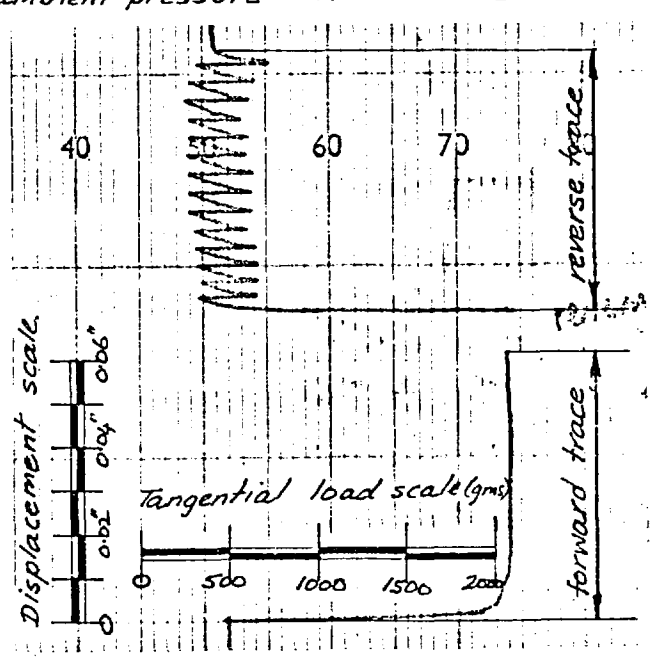
Recorder trace of a test on milky-quartz specimen 1 with Slider 1. Surfaces submerged in distilled water.
Load on contact = 1110 gms. Ambient pressure = 9000 lb/sq in
Coefficient of friction $\mu = 0.84$ max.

FIG 3·21b.



Recorder trace of a test on milky-quartz specimen 1 with slider 1. Surfaces submerged in distilled water for approx 9 hours. Load on contact = 1110 gms. ambient pressure = 0. FIG 3·22a.

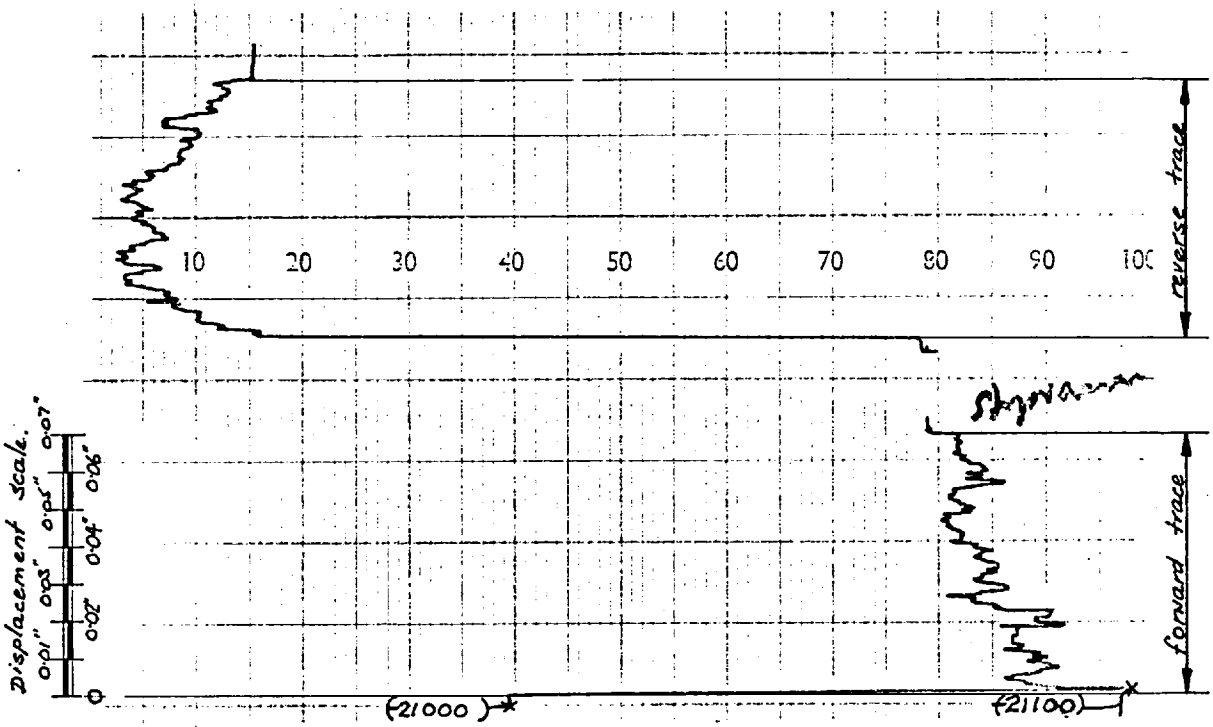
Coefficient of friction $\mu = 0.84(8)$ max.

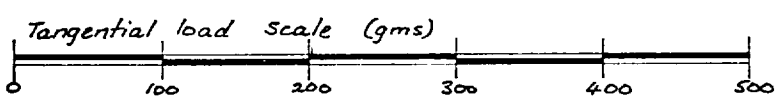


Recorder trace of test shown on trace above (FIG 14a), with load scale reduced by a factor of 10.

Coefficient of friction $\mu = 0.84$ max.

FIG 3·22b.

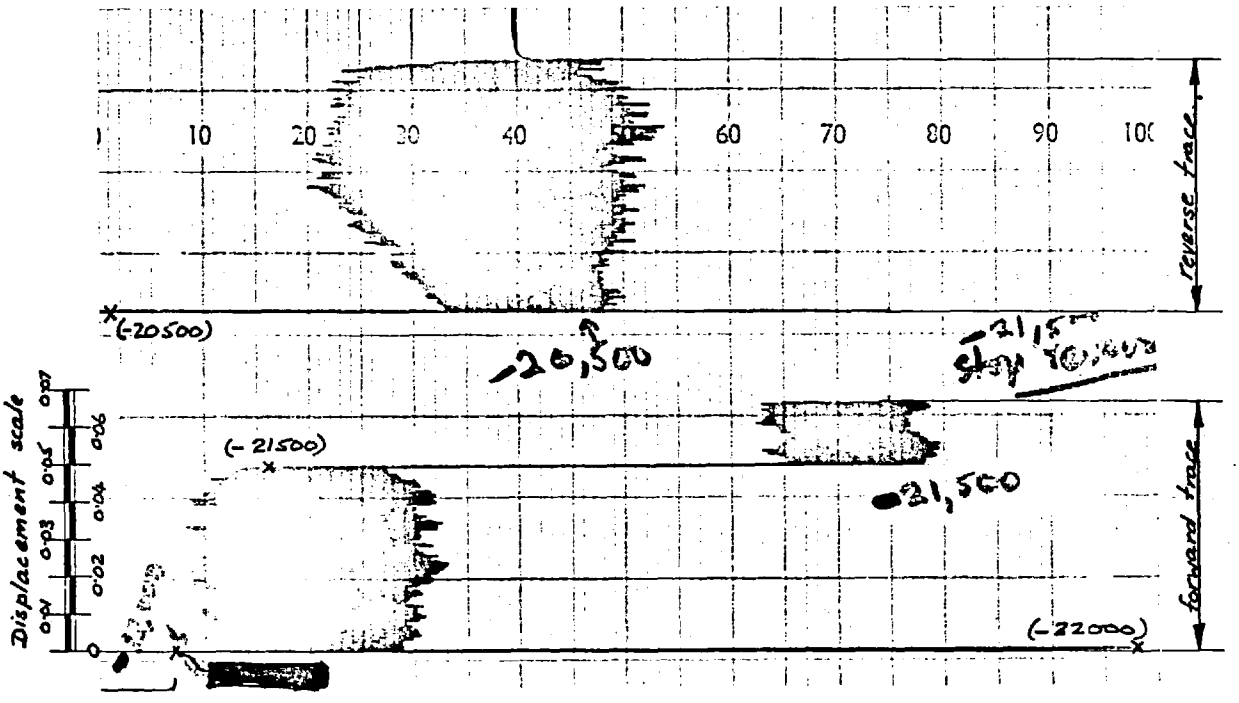


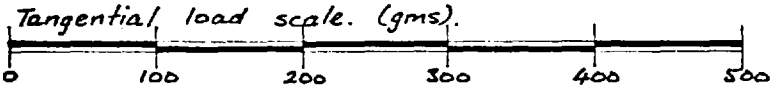


Recorder trace for milky-quartz specimen 2 with slider 2. Surfaces air dry.
Load on contact = 732 gms.

Coefficient of friction = { 0·44(0) max; 0·33(3) min; 0·38(0) mean }

Fig 3·23.

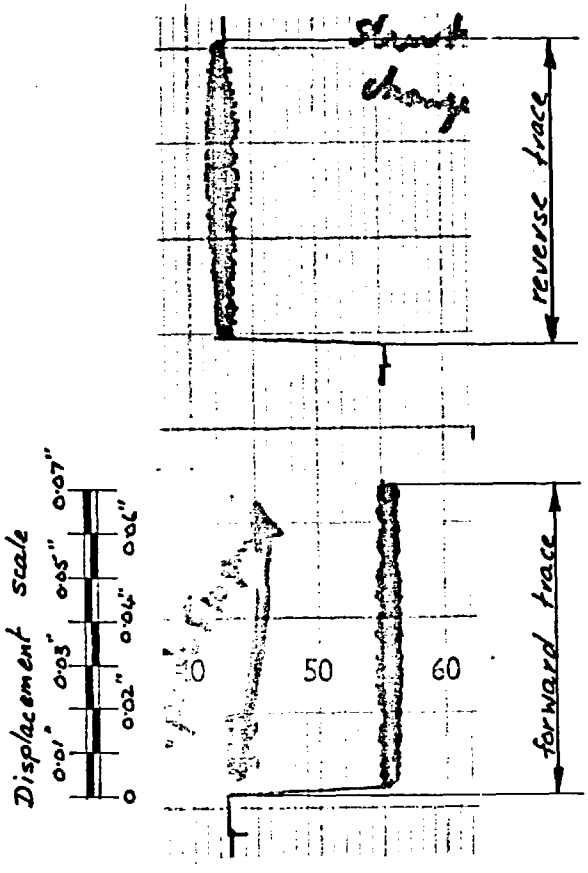




Recorder trace for milky-quartz specimen 2 with slider 2. Surfaces submerged in distilled water Load on contact = 732 gms, ambient pressure = 0.

Coefficient of friction = 0·81(2) max

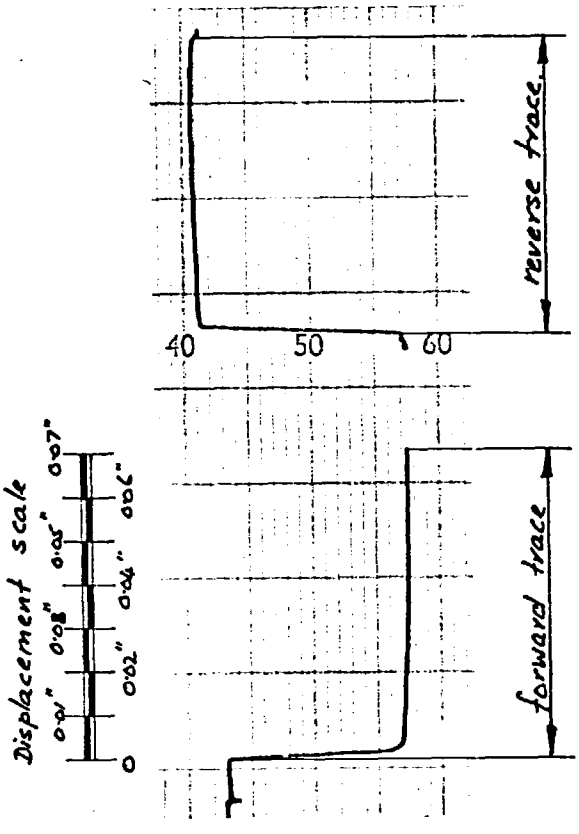
FIG 3·24.



Recorder trace for a test on milky-quartz Specimen 2 with slider 2. Surfaces submerged in distilled water.
Load on contact = 732 gms
Ambient pressure = 0

Coefficient of friction = 0·76 max

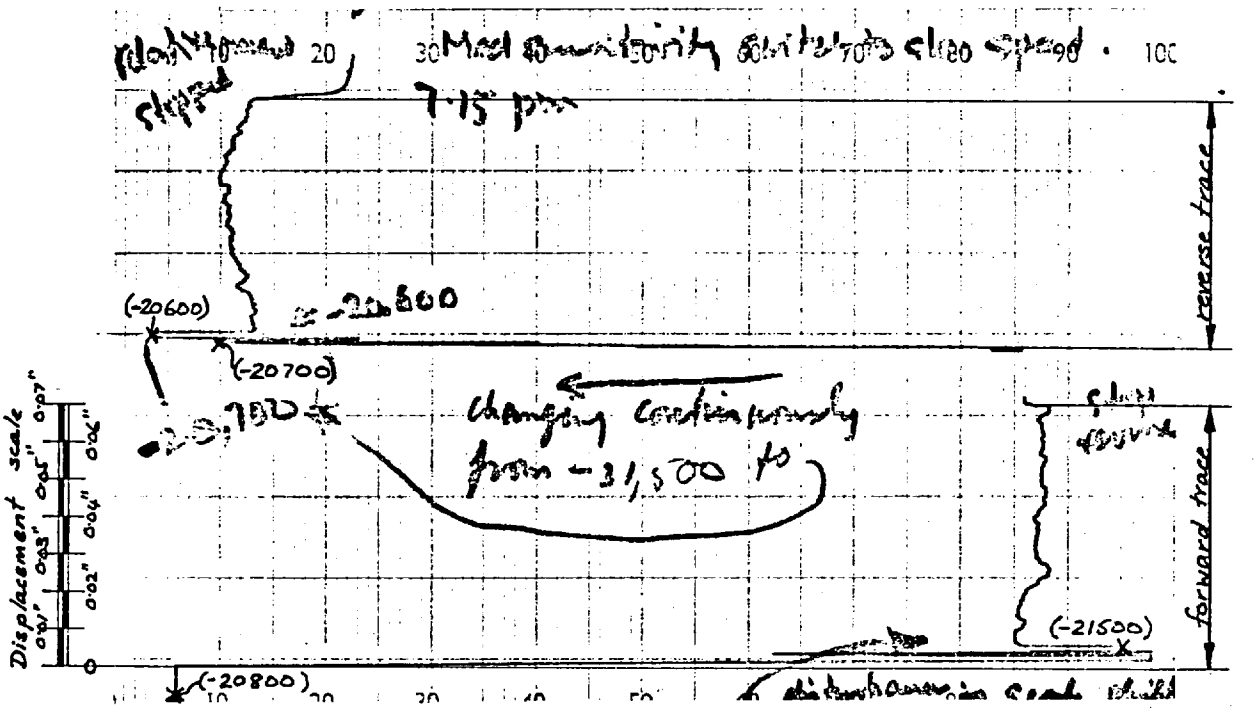
FIG. 3·25a

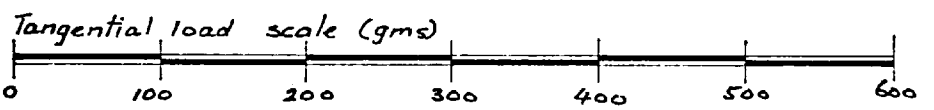


Recorder trace for a test on milky-quartz Specimen 2 with slider 2. surfaces submerged in distilled water for 24 hours
Load on contact = 732 gms
Ambient pressure = 0.

Coefficient of friction = 0·83 max.

FIG 3·25b.

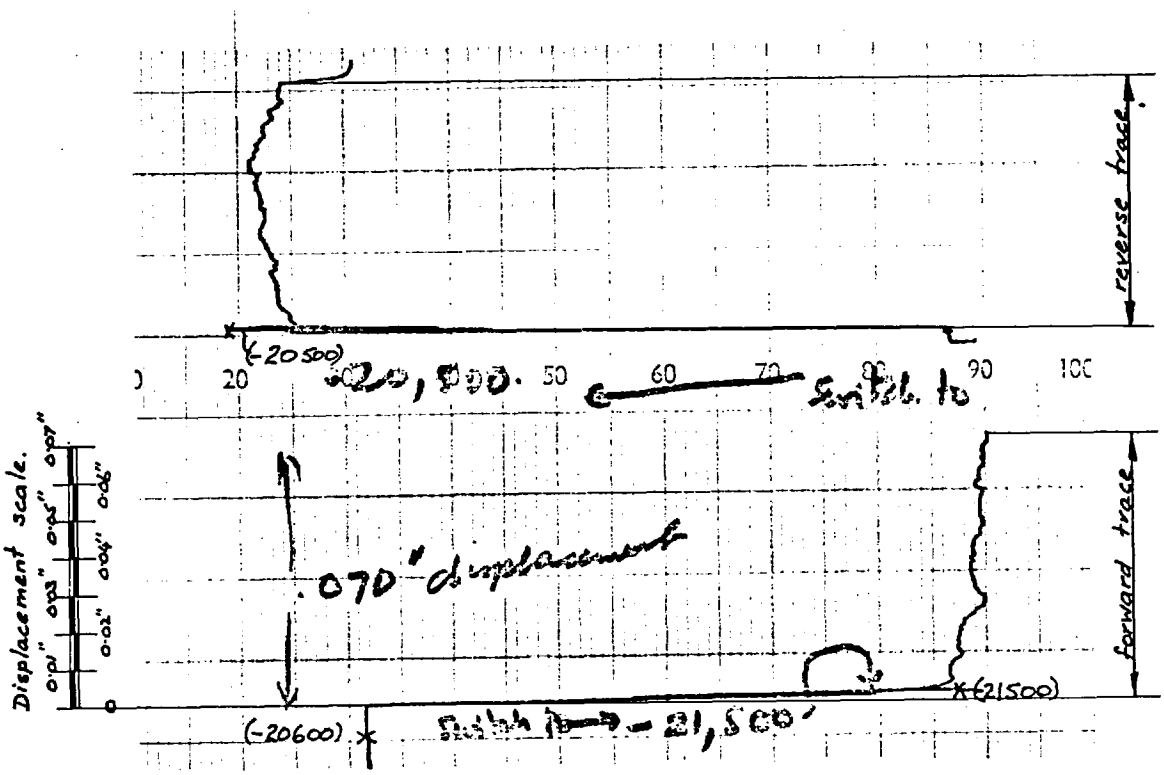




Recorder trace for a test on milky-quartz specimen 2 with slider 2. Surfaces submerged in distilled water for 24 hours — This test was performed immediately after the test shown in fig 3·25b, in this case the tangential load scale was expanded by a factor of 10.
Load on contact = 732 gms.
Ambient pressure = 0.

Coefficient of friction = 0·83(5) max.

FIG. 3·26



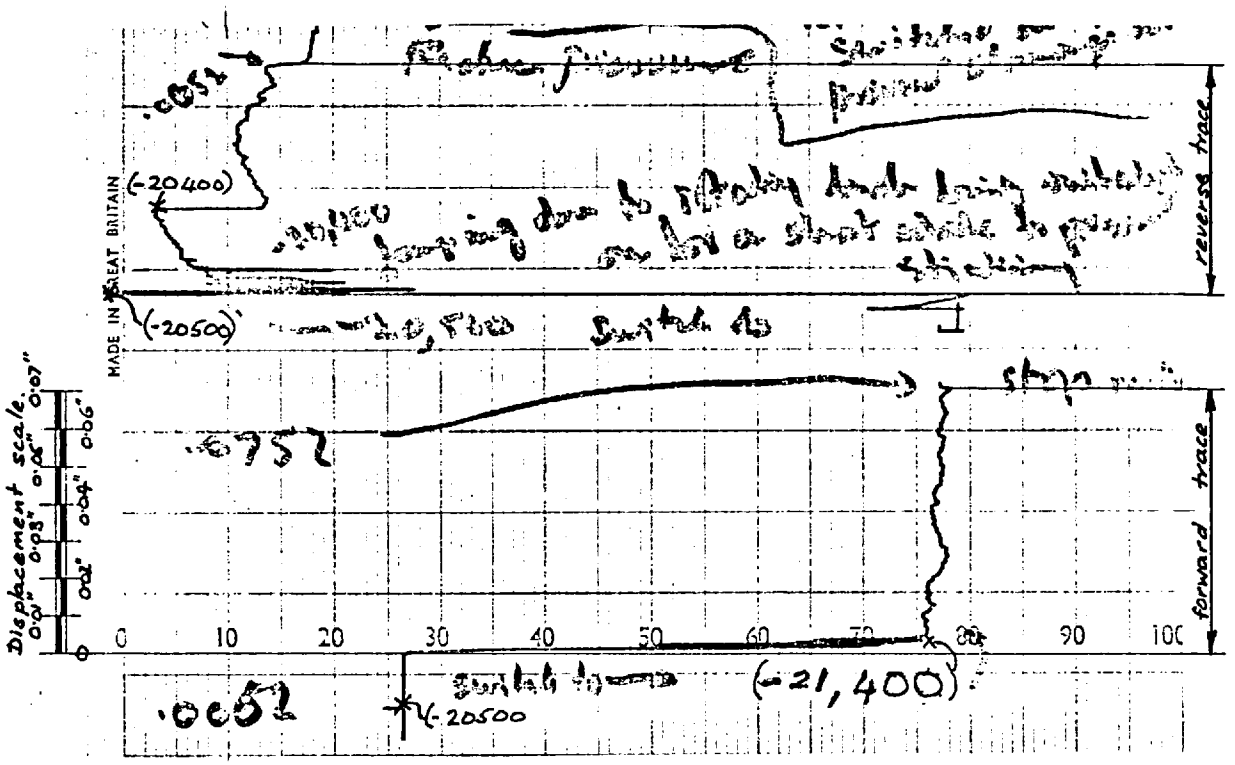
Recorder trace for a test on milky-quartz specimen 2. with slider 2. Surfaces submerged in distilled water for 41 hours.

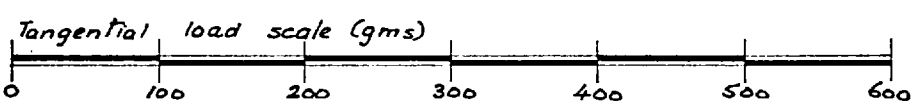
Load on contact = 732 gms.

Ambient pressure = 0.

Coefficient of friction = 0·83(9) max.

FIG. 3·27.

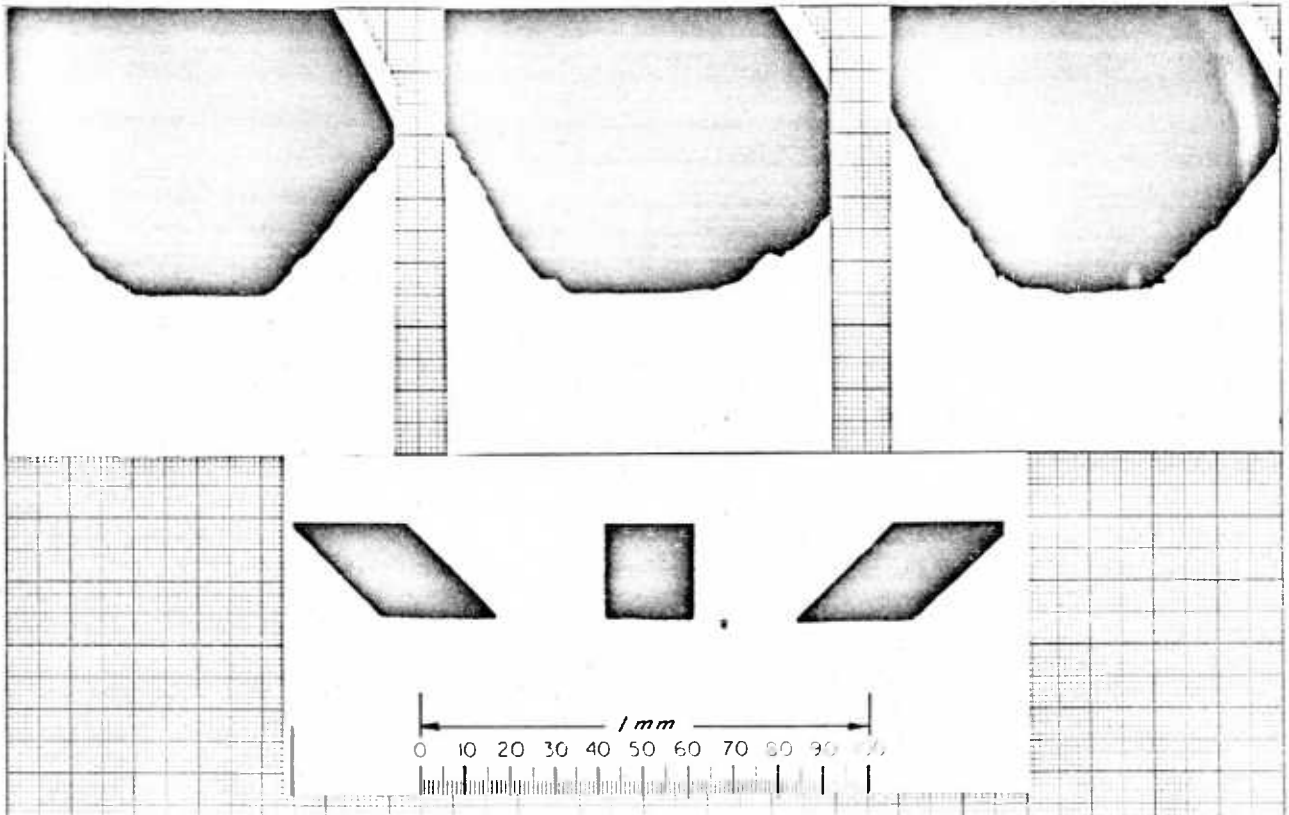




Recorder trace for a test on milky-quartz specimen 2. With slider 2. Surfaces submerged in distilled water for 41 hours.
Load on contact = 732 gms.
Ambient pressure = 9000 lb/sq. in.

Coefficient of friction = 0·83(4) max.

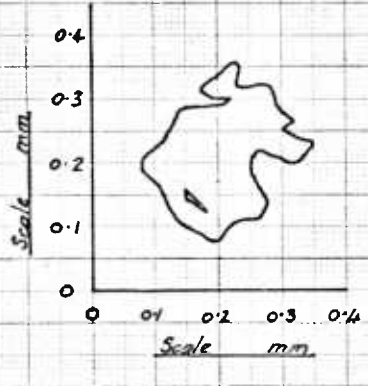
FIG. 3·28.



Scale of photographs.

Photographic silhouettes of tip of slider 2.

(taken at intervals of 120° rotation).



Area of flat end of tip is approx:

$0{\cdot}36 \times 10^{-3}$ sq cm.

Plan of flat end of tip of slider 2.

FIG 3·29

CHAPTER 4

THE INFLUENCE OF INTERPARTICLE FRICTION ON THE SHEARING STRENGTH OF A NON-COHESIVE MATERIAL

4.1 Introduction:

In the last chapter the friction of mineral surfaces under various conditions was considered. But, before the results can be applied to the shear strength of non-cohesive particulate materials, it is necessary to study the influence of interparticle friction on the shearing behaviour of the aggregate material. This point was clearly stated by Terzaghi in 1920, who, in a paper on 'Old earth pressure theories and new test results', published the following statement:

The fundamental assumptions of the traditional earth pressure theories cannot, in fact, stand even superficial examination. The fundamental error was introduced by Coulomb, who purposely ignored the fact that sand consists of individual grains, and who dealt with the sand as if it were a homogeneous mass with certain mechanical properties. Coulomb's idea proved very useful as a working hypothesis for the solution of one special problem of the earth pressure theory, but it developed into an obstacle against further progress as soon as its hypothetical character came to be forgotten by Coulomb's successors.

The way out of the difficulty lies in dropping the old fundamental principles and starting again from the elementary fact that sand consists of individual grains. This method of

dealing with the problem was first tried by Couplet, in 1627, forty-seven years before Coulomb published his theory, but Couplet failed. In 1916 and 1917 Professor Skibinsky of Limberg published a series of articles on the pressure exerted by a mass of spheres. Investigations of this kind are apt to be based on certain assumptions concerning the arrangement of the spheres, and the investigations result therefore in rather complicated formulae of limited value. In 1917 the author, who had no knowledge of Professor Skibinsky's publications, started to investigate along the same lines. But in the attempt to check theoretical results by observations he became convinced that earth pressure is an experimental rather than an analytical problem, and that we ought first of all to learn the physical facts of earth behaviour.

4.2 Theoretical Relationships between Shear Strength and Interparticle Friction:

In the development of strength theories many have followed the example of Coulomb, and have considered the behaviour of soils as if they behaved as continuous media; and consequently no relationship between the interparticle friction and the shearing strength of the material is considered. However, a few investigators have considered this problem, and some of their results are outlined below:

Caquot (1934):

Caquot showed theoretically that for plane strain conditions, with the assumption that only sliding takes place between the soil grains, the relationship between the effective angle of internal friction, ϕ'_{cv}, of a granular material and the

coefficient of friction acting between the grains, when shearing at constant volume, is:

$$\tan \phi'_{cv} = \mu \times \frac{\pi}{2}$$

Bishop (1954):

Bishop, using energy considerations, and assuming no rotation of the granular elements, i.e. angular strain being caused by sliding along surfaces of particles, obtained the following relationship:

a) Triaxial compression where $\sigma'_2 = \sigma'_3 < \sigma'_1$

$$\text{Sin } \phi'_{cv} = \frac{15\mu}{(10 + 3\mu)}$$

b) Plane strain, taking $\sigma'_2 = \frac{\sigma'_1 + \sigma'_3}{2}$

$$\text{Sin } \phi'_{cv} = \frac{3\mu}{2}$$

Rowe (1962):

Rowe produced a stress-dilatancy relation for static equilibrium of an assembly of particles in contact; the basis of which is that sliding occurs only on certain favourably-oriented and situated surfaces, the orientation being such as to minimize the rate of dissipation of energy in sliding friction between particles with respect to energy supplied. This produced a relation for triaxial stress conditions where $\sigma'_2 = \sigma'_3 < \sigma'_1$ of:

$$\frac{\sigma'_1}{\sigma'_3(1 + \frac{d\bar{V}}{V\bar{\varepsilon}})} = \tan^2(45^\circ + \frac{1}{2}\phi_\mu) \qquad \text{(from Rowe 1962)}$$

where $\tan \phi_\mu = \mu$, the coefficient of friction between the particles.

And for shearing at constant volume this would imply that

$$\frac{\sigma_1'}{\sigma_3'} = \tan^2 (45^\circ + \tfrac{1}{2}\phi_\mu)$$

This result is not supported by experimental results, and so Rowe introduces a variable parameter ϕ_f (such that $\phi_\mu < \phi_f < \phi_{cv}$) and ϕ_f becomes equal to ϕ_{cv} when the material is shearing at constant volume.

4.3 Particle Mechanics during Shear:

All the above results are obtained with the assumption that relative movement between soil grains is accomplished by sliding, no rotation of the grains being allowed.

However, many other investigators have suggested that the mechanism of deformation in a shearing sand mass involves both sliding and rotation; and as far back as 1925 Terzaghi, in Erdbaumechanik, describes 'The mechanism of resistance to sliding' in this way: *As the shearing stress applied to a mass of sand increases, the particles rotate without changing partners; the displacement is resisted largely by friction at the points of contact between grains. At constant shearing stress the rate of increase of displacement decreases and finally ceases. Sliding occurs suddenly, particles on one*

side of the surface sliding, advancing with reference to the other side, and thus changing partners. Resistance depends largely upon the degree of interlocking, so the coefficient of friction along surfaces of sliding in sand increases considerably with decreasing porosity of the sand.

Similarly Taylor (1948) in his book Fundamentals of Soil Mechanics, page 345, under the heading 'Factors contributing to Shearing Strength in Soils' also suggests that the shearing strength in sand may be said to consist of two parts: the internal frictional resistance between grains, which is a combination of rolling and sliding friction, and a second factor for which the most common name is interlocking.

The writer considered that because of the uncertainty of the movements of the particles, it was necessary to try to establish whether rotation of the grains takes place during shearing of a mass of particles, and what effect the coefficient of interparticle friction has on the mechanism of failure.

To do this, advantage was taken of the change of interparticle friction, which is observed with glass ballotini, when submerged under water as compared with the values obtained when tested surrounded by air.

4.4 Surface Friction of Glass:

The values obtained for the coefficient of friction are as

follows:

Series 1:

A single 1 mm glass ball sliding on a smooth slide glass. The test was carried out using the friction apparatus described in Chapter 2, Figure 2.12 and Plates 2.6 and 2.7.

The apparatus was modified, so that it could be mounted horizontally on the test bench, and the anvil (6) to which the slide glass was attached, was driven forwards by a push rod, moved by a screw rotating in a threaded guide, the retraction of the anvil being accomplished, as before, with strong return springs. The single glass ball was mounted on the end of the quill (21), and the adhesive used was 'Lakeside'. This adhesive is used generally for mounting thin sections of rock.

The surface traction between the two surfaces was monitored by means of the high sensitivity proving ring (10), whose output was fed through a Boulton and Paul C61 transducer meter to a Leeds and Northrup strip chart recorder.

Typical traces for wet and dry contacts are given in Figure 4.1. These correspond to the tabulated results numbered 3, 4, 5 for the dry contacts, and 10, 11, 12 for the wet contacts.

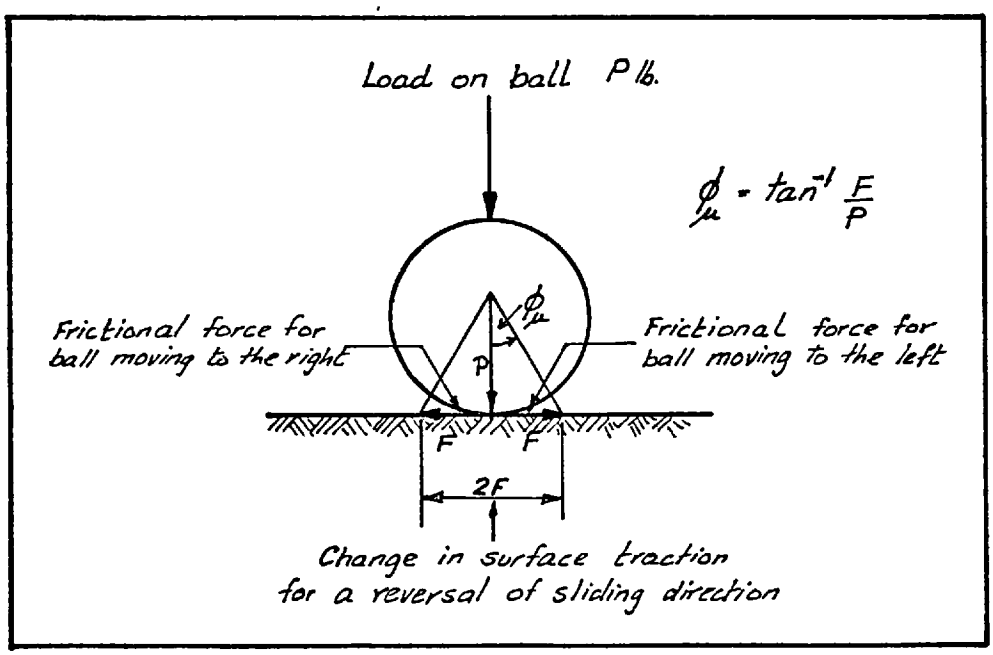
The recorder trace is deflected to the right when the anvil is pushed forwards, and when pulled back, the recorder trace is deflected to the left. The overall deflection from right to left thus corresponds to a complete reversal of the friction

force; consequently the angle of friction ϕ_μ is given by:

$$\tan \phi_\mu = \frac{1}{2} \frac{\text{(surface traction change)}}{\text{load on the contact}}$$

The deflections of the traces for test 11 and 12 were too large to be accommodated on the width of the chart, therefore a part of the transducer output was 'backed off'. This effectively shifts the trace back on to the chart. This shift of the trace, corresponding to a change in decade reading of +00100 units, is 10.1 chart divisions to the right, and a shift of 10.1 chart divisions to the left for a change in decade reading of -00100 units.

Series 1 - Results:



Surface traction load: in all calibrations 1 chart division = 0.014 lb.

Results of tests to determine the angle of friction between a 1 mm glass ball and a smooth glass slide under wet and dry conditions

Test No	Condn	Sliding speed in / min	Load P lb on Contact	2F lb	F/P	ϕ_μ
1	dry	0.062	0.382	0.135 (max)	0.178	10.1°
2	wet	0.062	0.382	0.688 (max)	0.900	42.0°
3	dry	0.062	0.378	0.068 (max)	0.090	5.1°
				0.061 (min)	0.081	4.6°
				0.064 (mean)	0.085	4.9°
4	dry	0.062	0.951	0.189 (max)	0.099	5.7°
				0.178 (min)	0.093	5.3°
				0.183 (mean)	0.096	5.5°
5	dry	0.062	1.951	0.412 (max)	0.106	6.0°
				0.405 (min)	0.104	5.9°
				0.408 (mean)	0.105	6.0°
6	dry	0.062	0.378	0.069 (max)	0.091	5.2°
				0.068 (min)	0.089	5.1°
				0.068 (mean)	0.089	5.1°
7	wet	0.012	0.378	0.689 (max)	0.910	42.3°
				0.606 (min)	0.801	38.7°
				0.648 (mean)	0.857	40.6°
8	wet	0.062	0.378	0.659 (max)	0.872	42.0°
				0.606 (min)	0.801	38.7°
				0.641 (mean)	0.849	40.3°
9	dry	0.062	0.378	0.071 (max)	0.093	5.3°
				0.059 (min)	0.078	4.5°
				0.065 (mean)	0.086	4.9°
10	wet	0.062	0.378	0.633 (max)	0.839	40.0°
				0.569 (min)	0.766	37.5°
				0.620 (mean)	0.820	39.4°
11	wet	0.062	0.951	1.584 (max)	0.832	39.8°
				1.530 (min)	0.804	38.8°
				1.560 (mean)	0.820	39.4°
12	wet	0.062	1.951	3.010 (max)	0.772	37.7°
				2.780 (min)	0.712	35.2°
				2.900 (mean)	0.742	36.6°

Series 2:

A further two sets of tests were performed, aimed at finding the coefficient of friction between glass ballotini directly. This was done for both 1 mm and 3 mm sized ballotini. For each size glass balls were mounted in pairs on the anvil, so that the line joining their centres was at right-angles to the direction of travel of the anvil, and a ball of the same size mounted on a quill of the friction apparatus. Loads were applied by dead weights on the head of the quill, whose vertical displacement was monitored by an inductive displacement transducer, mounted over the contact, powered by a second Boulton and Paul C61 transducer meter. This arrangement enabled the writer to measure the surface traction when the 'quill ball' was at the apogee of its travel. (The vertical movement of the quill could be discriminated to the order of 2×10^{-6} in.) The average values of surface traction change for three or four traverses were taken as a representative value and these results are given below.

Series 2 - Results:

In the results the following symbols are used (see next page).

For the geometry chosen:

At the apogee of the quill ball $P_c = W/\sqrt{3} = 0.5773W$.

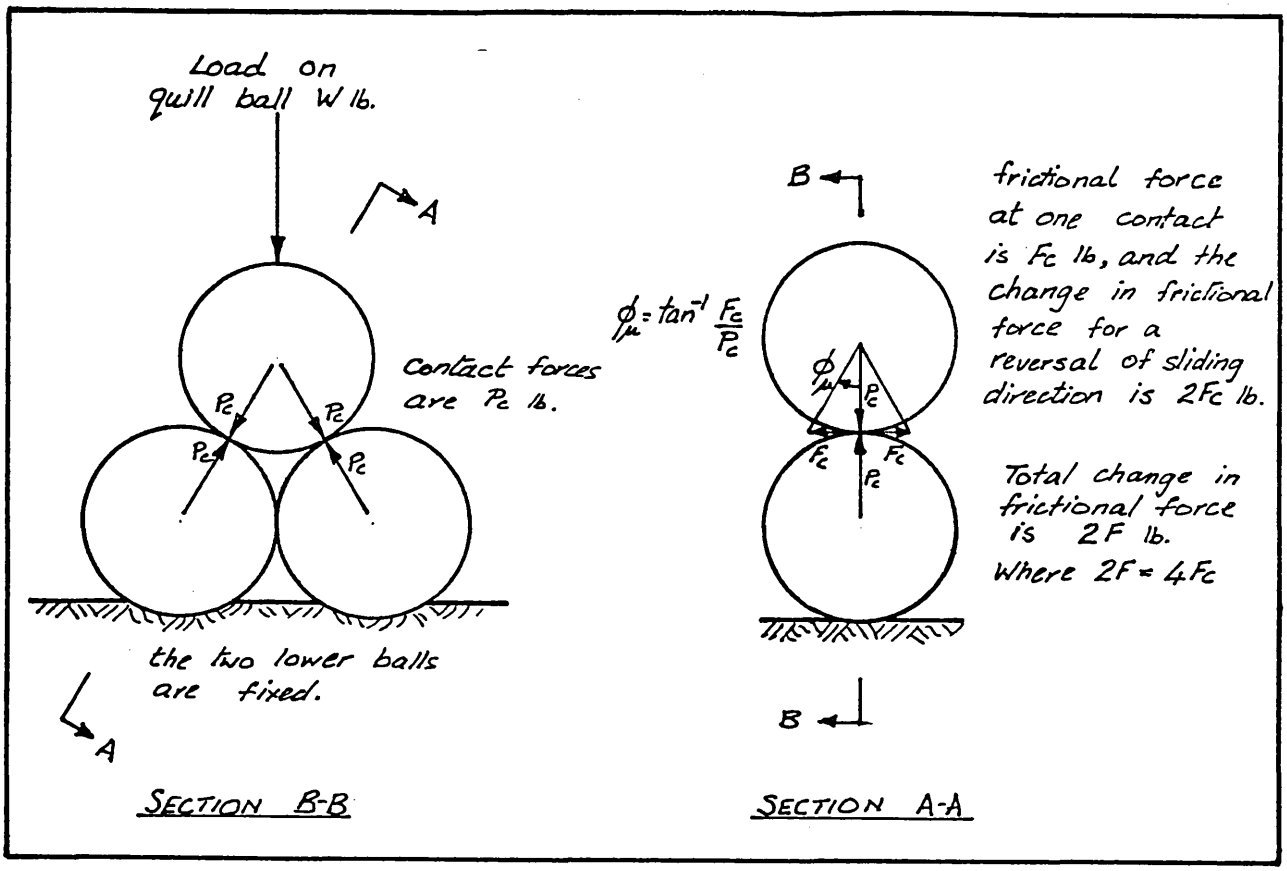
The surface traction change 2F measured in the test was the sum of the surface traction at both contacts, i.e.

$$2F = 2 \times 2F_c = 4F_c$$

$$\text{since } \phi_\mu = \tan^{-1} \frac{F_c}{P_c}$$

$$\phi_\mu = \tan^{-1} \frac{1}{4} \frac{\text{(measured surface traction change)}}{0.5773W}$$

Speed of sliding at contacts = 0.012 in/min.



Results of tests to determine the angle of friction between glass ballotini sliding on glass ballotini under wet and dry conditions

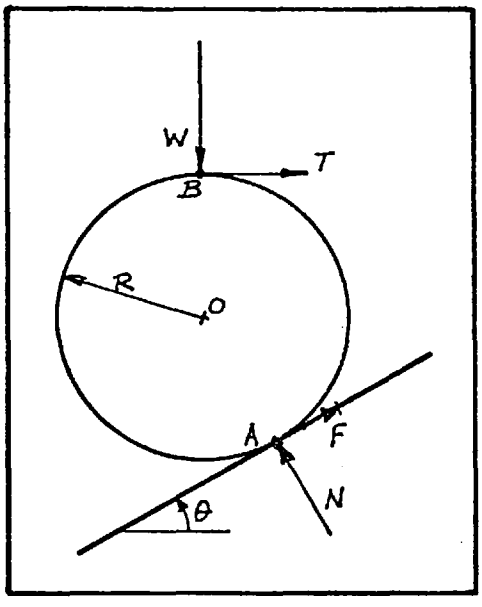
Test No	Condition	Ballotini size	Wlb	2F lb	0.866 F/W	
1	dry	3 mm	0.404	0.069	0.074	4.2°
	wet			0.631	0.677	34.1°
2	dry	3 mm	0.404	0.075	0.080	4.6°
	wet			0.603	0.646	32.9°
3	dry	1 mm	0.087	0.014	0.070	4.0°
	wet			0.124	0.618	31.7°

4.5 Analysis of the Mechanics of Spheres and Rollers subjected to various frictional Tractions:

In this section the mechanics of simple geometrical arrangements of rollers or spheres are analysed, with particular reference to the frictional conditions required to initiate slip at favourably-orientated contacts, or to those conditions which promote rotation of particular rollers or spheres without slip at contact points.

Case 1:

Ball or roller on a frictional inclined plane, under the influence of a load W and a horizontal frictional traction T at its apex.



Equilibrium normal to the plane:

$$N = W \cos\theta + T \sin\theta \qquad (4.1)$$

Equilibrium parallel to the plane:

$$F + T \cos\theta = W \sin\theta$$

$$\text{or } F = W \sin\theta - T \cos\theta \qquad (4.2)$$

Taking moments about point A:

$$W R \sin\theta = T R (1 + \cos\theta)$$

$$\text{or } W = T\frac{(1 + \cos\theta)}{\sin\theta} \qquad (4.3)$$

Limiting equilibrium is reached when either:

a) $F = \mu_1 N$ where μ_1 is the friction coefficient between the plane and the roller,

b) $T = \mu_2 W$ where μ_2 is the friction coefficient between the body providing the load W and the ball or roller.

From a) and equations (4.1), (4.2) and (4.3) we obtain:

$$\theta_a = 2 \tan^{-1}\mu_1 \qquad (4.4)$$

where θ_a is the critical value of θ for condition a).

And from b) and equation (4.3) we have:

$$\theta_b = 2 \tan^{-1}\mu_2 \qquad (4.5)$$

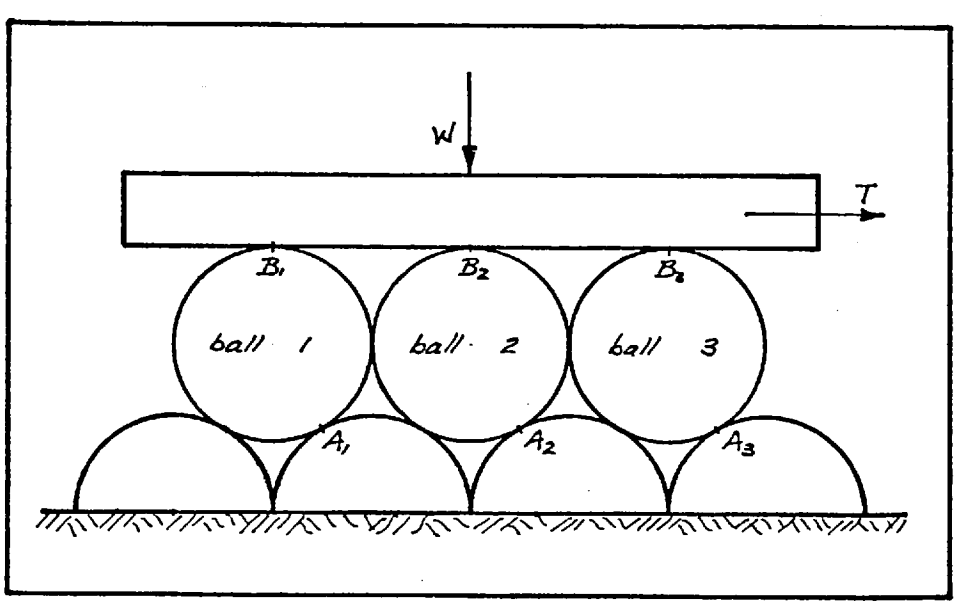
where θ_b is the critical value of θ for condition b).

If $\mu_2 > \mu_1$ the ball or roller will slip on the plane, the point A on the ball or roller moving down the plane, unless the angle θ is smaller than $\theta_a = 2 \tan^{-1}\mu_1$, when the ball or roller will start to roll up the incline raising the weight W.

If $\mu_1 > \mu_2$ then sliding will take place at point B until the angle θ becomes smaller than $\theta_b = 2 \tan^{-1}\mu_2$, when the ball or roller will start to roll up the incline raising the weight W.

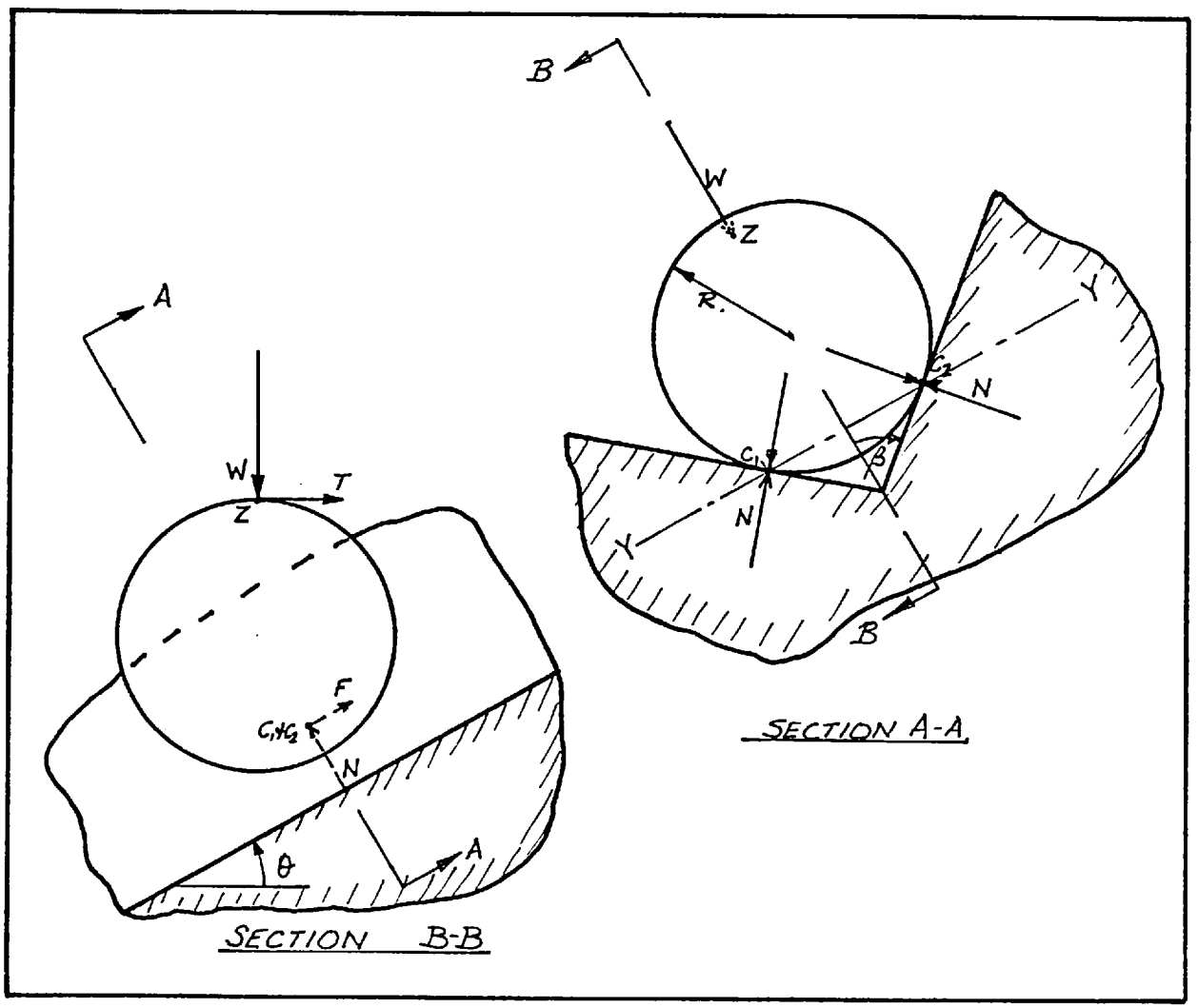
If $\mu_1 = \mu_2$ sliding will take place at either point A or B until the angle θ becomes smaller than $2 \tan^{-1}\mu$, when the ball or roller will start to roll up the incline raising the weight W.

If, for example, the case illustrated in the figure shown below is considered with balls or rollers 1, 2 and 3 free, and the half balls or rollers fixed to the bottom plane, and taking equal values of μ at B_1, B_2, B_3, A_1, A_2 and A_3, the plate would only travel horizontally if $\mu \leqslant \tan \frac{30^o}{2}$, i.e. $\mu \leqslant 0.268$. If $\mu > 0.268$, then the balls or rollers would roll and lift the plate.



Case 2:

A ball in a frictional groove, under the influence of a load W and a horizontal frictional Traction T at its apex.



Consider the equilibrium of the forces resolved in the plane of section B-B:

At right-angles to the slope:

$$2N \sin \beta = W \cos \theta + T \sin \theta$$

$$\text{or } N = \frac{W \cos \theta + T \sin \theta}{2 \sin \beta} \qquad (4.6)$$

Parallel to the slope:

$$2F + T \cos \theta = W \sin \theta$$

$$\text{or } F = \frac{W \sin \theta - T \cos \theta}{2} \tag{4.7}$$

Taking moments about the line YY:

$$W.R \sin \beta \sin \theta = T.R(1 + \sin \beta \cos \theta)$$

$$\text{or } W = \frac{T(1 + \sin \beta \cos \theta)}{\sin \beta \sin \theta} \tag{4.8}$$

Limiting equilibrium is reached when either:

a) $F = \mu_1 N$ where μ_1 is the friction coefficient between the groove and ball, or

b) $T = \mu_2 W$ where μ_2 is the friction coefficient between the body providing the load W and the ball.

From a) and equations (4.6), (4.7) and (4.8) we obtain:

$$\mu_1 = \frac{\sin \theta_a \sin \beta}{\cos \theta_a + \sin \beta} \tag{4.9}$$

where θ_a is the critical value of θ for condition a).

For $\pi/2 > \theta_a > 0$:

$$\theta_a = 2 \tan^{-1}\left\{- A + \sqrt{(A^2 + \frac{1 + \sin \beta}{1 - \sin \beta})}\right\} \tag{4.10}$$

where $A = \dfrac{\sin \beta}{\mu_1(1 - \sin \beta)}$

Now from b) and equation (4.8) we obtain:

$$\mu_2 = \frac{\sin \theta_b \sin \beta}{1 + \cos \theta_b \sin \beta} \tag{4.11}$$

where θ_b is the critical value of θ for condition b).

or $$\theta_b = 2 \tan^{-1} \left\{ B - \sqrt{\left(B^2 - \frac{1 + \sin \beta}{1 - \sin \beta}\right)} \right\} \qquad (4.12)$$

where $B = \dfrac{\sin \beta}{\mu_2 (1 - \sin \beta)}$

If slip is to occur simultaneously at the apex and at the contacts with the groove, for particular values of θ and β, μ_1 and μ_2 are given by equations (4.9) and (4.11), and by considering the differences between the denominators of these equations, it can be seen that for $\pi/2 > \theta > 0$, and $\pi/2 \geq \beta > 0$, $(\cos \theta + \sin \beta) \leq (1 + \cos \theta \sin \beta)$, i.e. $\mu_1 > \mu_2$ for $\pi/2 > \beta > 0$ and $\pi/2 > \theta > 0$

Therefore for equal values of μ, slip will always occur first at the contact points on the sides of the groove, the points C_1 and C_2 on the ball sliding down the plane, except for case 1, when the groove reduces to a plane, and slip takes place simultaneously on the plane and at the apex of the ball.

The limiting values of μ_1 and μ_2 are plotted against values of θ_a and θ_b respectively on the graph figure 4.2 for values of the groove half angle $\beta = 90^\circ$, $\beta = 60^\circ$ and $\beta = 30^\circ$, and tables of limiting values of μ_1 and μ_2 are given below:

θ_a	limiting values of μ_1						
	$\beta=90^\circ$	$\beta=75^\circ$	$\beta=60^\circ$	$\beta=45^\circ$	$\beta=30^\circ$	$\beta=15^\circ$	$\beta=0^\circ$
0	0	0	0	0	0	0	0
10	.087	.086	.081	.073	.058	.036	0
20	.176	.173	.164	.147	.119	.074	0
30	.268	.264	.250	.225	.183	.115	0
40	.364	.359	.341	.309	.254	.162	0
50	.466	.460	.440	.401	.335	.220	0
60	.577	.571	.549	.507	.433	.295	0
70	.700	.694	.674	.633	.558	.405	0
80	.839	.848	.821	.790	.731	.590	0
90	1	1	1	1	1	1	1

θ_b	limiting values of μ_2						
	$\beta=90^\circ$	$\beta=75^\circ$	$\beta=60^\circ$	$\beta=45^\circ$	$\beta=30^\circ$	$\beta=15^\circ$	$\beta=0^\circ$
0	0	0	0	0	0	0	0
10	.087	.086	.081	.072	.058	.036	0
20	.176	.173	.163	.145	.116	.071	0
30	.268	.262	.247	.219	.174	.106	0
40	.364	.357	.335	.295	.232	.139	0
50	.466	.456	.426	.372	.290	.170	0
60	.577	.564	.523	.452	.346	.198	0
70	.700	.682	.628	.535	.401	.223	0
80	.839	.815	.741	.620	.453	.244	0
90	1	.966	.866	.707	.500	.258	0

Since slip occurs at the sides of the groove first, for equal values of μ (see previous argument), it is possible to evaluate the magnitude of the limiting ratio of surface traction to applied load = $\frac{T}{W}$ in terms of θ, β and μ.

When slip occurs $F = \mu N$, and using equations (4.6) and (4.7):

$$\frac{T}{W} = \frac{\sin\theta \sin\beta - \mu \cos\theta}{\cos\theta \sin\beta + \mu \sin\theta} \qquad (4.13)$$

and the maximum value that μ can reach before rolling starts is μ_1 where

$$\mu_1 = \frac{\sin\theta_a \sin\beta}{\cos\theta_a + \sin\beta} \qquad (4.9)$$

Denoting the maximum ratio of $\frac{T}{W}$ by $\frac{\hat{T}}{W}$ we have:

$$\frac{\hat{T}}{W} = \frac{\sin\beta \sin\theta_a}{1 + \cos\theta_a \sin\beta} = \mu_1 \frac{(\cos\theta_a + \sin\beta)}{1 + \cos\theta_a \sin\beta} \qquad (4.14)$$

Now because $\cos\theta_a + \sin\beta \leqslant 1 + \cos\theta_a \sin\beta$ for $0 \leqslant \theta_a \leqslant 90^\circ$ and $0 \leqslant \beta \leqslant 90^\circ$ we have $\frac{\hat{T}}{W} \leqslant \mu_1$.

From this it is apparent that if a plate is put over an array

of free balls, which are themselves supported on another similar fixed array, and the plate loaded with a weight W, pulled with a horizontal force T (which causes the plate to just move in the direction of T, when the balls are about to roll and lift the weight W (i.e. dilate)), the ratio of $\frac{\hat{T}}{W}$ does not depend solely on the coefficient of friction μ, but on the geometry of the array as well.

To illustrate this the following geometrical arrangements of spheres are analysed for maximum μ_1 and $\frac{\hat{T}}{W}$ for the conditions of incipient dilation.

a) Uniform spheres in rhombic packing:

a_1) Traction in direction (1):

$\theta = 19.4^\circ \quad \beta = 60^\circ$

$\mu_1 = 0.159 \quad (\phi_\mu = 9.03^\circ)$

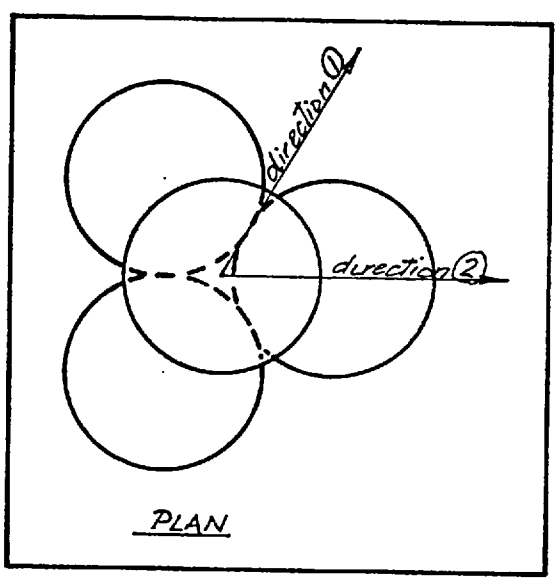
$\frac{\hat{T}}{W} = 0.996\mu_1$

a_2) Traction in direction (2):

$\theta = 35.3^\circ \quad \beta = 90^\circ$

$\mu_1 = 0.318 \quad (\phi_\mu = 17.65^\circ)$

$\frac{\hat{T}}{W} = \mu_1$



b) Uniform spheres in face-centred centre packing:

b_1) Traction in direction (1):

$\theta = 45^\circ \quad \beta = 90^\circ$

$\mu_1 = 0.414 \quad (\phi_\mu = 22.5^\circ)$

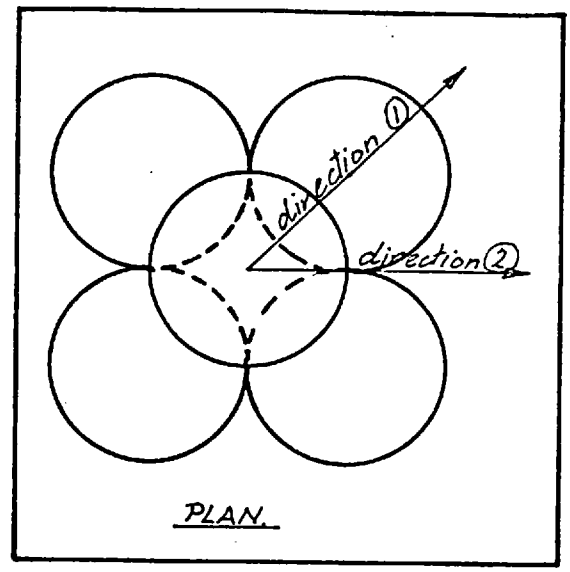
$\frac{\hat{T}}{W} = \mu_1$

b_2) Traction in direction (2):

$\theta = 35^\circ \quad \beta = 60^\circ$

$\mu_1 = 0.293 \quad (\phi_\mu = 16.33^\circ)$

$\frac{\hat{T}}{W} = 0.986\mu_1$



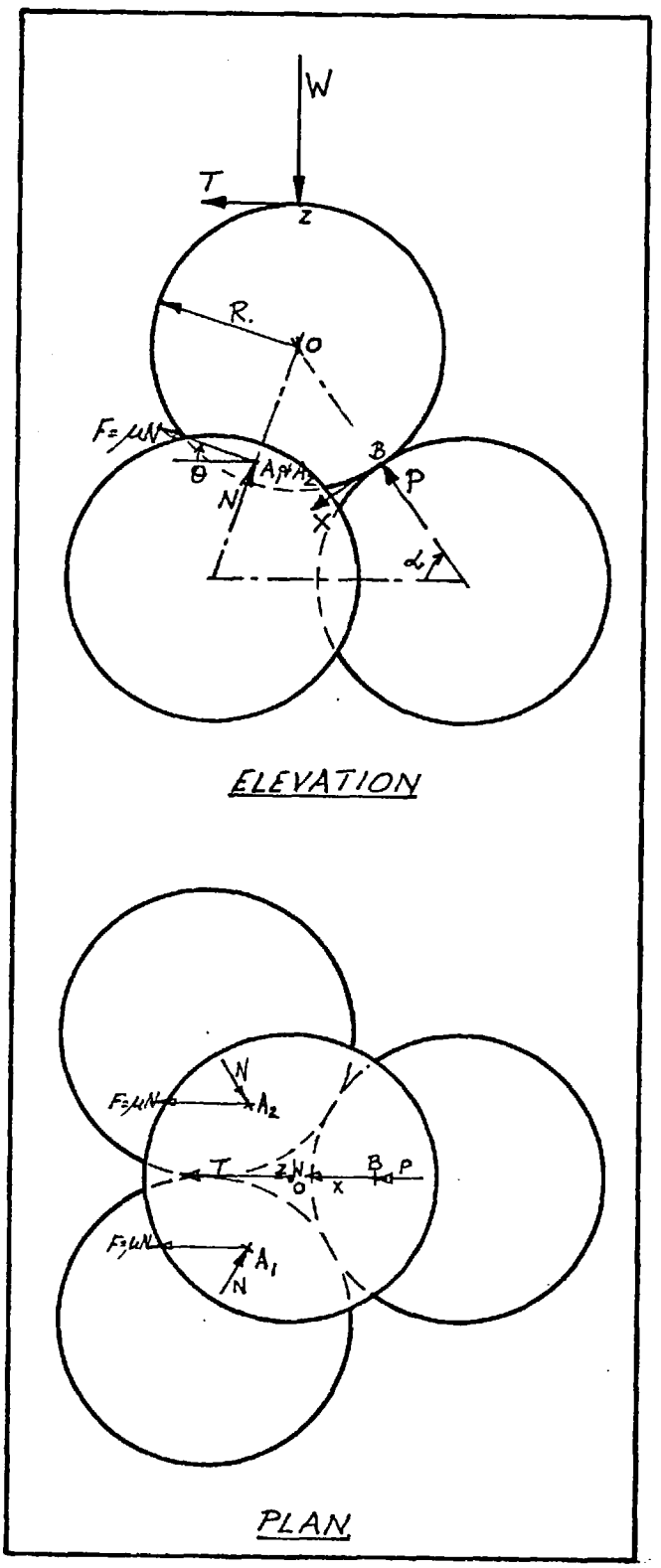
The previous analysis investigated the limiting conditions which could be applied to an array of free balls which are on the point of dilating on a similar fixed array, the balls having a coefficient of friction which is itself only just sufficient to prevent the free balls slipping down the faces or the valleys formed by the supporting balls.

If the coefficient of friction is greater than the critical value the layer of free balls would dilate. If, on the other hand, the friction coefficient is less than the critical value for the particular geometry of the array, then the value of $\frac{T}{W}$ cannot be determined by the previous analysis because each of the free balls would gain additional support from either one or two more balls in the fixed array. To illustrate this point consider the four balls shown in the figure below, the three lower balls being fixed in both position and orientation, the only free ball being the fourth 'upper' ball.

Then for equal values of μ if we put $F = \mu N$ and apply arbitrary forces P and X at B, it is seen that if sliding occurs at the

contact points A_1 and A_2 so that the ball centre 0 tends to rotate, then slip must also occur at point B. Therefore:

$$X = \mu P \qquad (4.15)$$



Taking moments about a horizontal axis through O:

$$T.R = 2\mu N.R \sin\beta + R\mu P$$

$$\text{or } T = 2\mu N \sin\beta + \mu P \qquad (4.16$$

Parallel to slope θ:

$$2\mu N + T\cos\theta - W\sin\theta + P\cos(\alpha - \theta) + \mu P\sin(\alpha - \theta) = 0 \qquad (4.17$$

Perpendicular to slope θ:

$$2N\sin\beta + P\sin(\alpha - \theta) - \mu P\cos(\alpha - \theta) - T\sin\theta - W\cos\theta = 0 \qquad (4.18$$

There are three unknowns T, N and P. We want to eliminate N and P in order to find T in terms of W. From (4.17):

$$N + P\frac{(\cos(\alpha - \theta) + \mu\sin(\alpha - \theta))}{2\mu} = \frac{W\sin\theta - T\cos\theta}{2\mu} \qquad (4.19$$

From (4.18):

$$N + P\frac{(\sin(\alpha - \theta) - \mu\cos(\alpha - \theta))}{2\sin\beta} = \frac{W\cos\theta + T\sin\theta}{2\sin\beta} \qquad (4.20$$

Subtracting (4.20) from (4.19) we obtain:

$$P\frac{(\sin\beta(\cos(\alpha - \theta) + \mu\sin(\alpha - \theta)) - \mu(\sin(\alpha - \theta) - \mu\cos(\alpha - \theta))}{2\mu\sin\beta}$$

$$= \frac{\sin\beta(W\sin\theta - T\cos\theta) - \mu(W\cos\theta + T\sin\theta)}{2\mu\sin\beta}$$

Hence:

$$P = \frac{\sin\beta(W\sin\theta - T\cos\theta) - \mu(W\cos\theta + T\sin\theta)}{\cos(\alpha - \theta)(\sin\beta + \mu^2) + \sin(\alpha - \theta)(\mu\sin\beta - \mu)} \qquad (4.21$$

Re-writing (4.16):

$$N + P\frac{1}{2\sin\beta} = \frac{T}{2\mu\sin\beta} \qquad (4.22$$

From (4.20) and (4.22):

$$P = \frac{(W \cos\theta + T \sin\theta) - T/\mu}{\sin(\alpha - \theta) - \mu \cos(\alpha - \theta) - 1} \tag{4.23}$$

Therefore from (4.21) and (4.23):

$$\frac{\cos\theta + \frac{T}{W}(\sin\theta - \frac{1}{\mu})}{\sin(\alpha - \theta) - \mu \cos(\alpha - \theta) - 1} =$$

$$\frac{(\sin\theta \sin\beta - \mu \cos\theta) - \frac{T}{W}(\cos\theta \sin\beta + \mu \sin\theta)}{\cos(\alpha - \theta)(\sin\beta + \mu^2) + \sin(\alpha - \theta)(\mu \sin\beta - \mu)}$$

Hence:

$$\frac{T}{W} = \frac{-\cos\theta . A + B . C}{(\sin\theta - \frac{1}{\mu}) . A + D . C} \tag{4.24}$$

where $A = \cos(\alpha - \theta)(\sin\beta + \mu^2) + \sin(\alpha - \theta)(\mu(\sin\beta - 1))$

$B = \sin\theta \sin\beta - \mu \cos\theta$

$C = \sin(\alpha - \theta) - \mu \cos(\alpha - \theta) - 1$

$D = \cos\theta \sin\beta + \mu \sin\theta$

If the ball does not slip at A_1 and A_2 but rolls, $P = 0$. Then the value of T is given by $\hat{T}$ where:

$$\frac{\hat{T}}{W} = \frac{\sin\beta \sin\theta}{1 + \sin\beta \cos\theta} \quad \text{(see previous analysis)}$$

Therefore this analysis holds for the range of μ values such that $0 \leqslant \frac{T}{W} \leqslant \frac{\hat{T}}{W}$ if in this range $\frac{T}{W} < \mu$. If, on the other hand, the analysis indicates that $\frac{T}{W} > \mu$, then the analysis is inadmissible, and in fact the top ball would remain fixed in position, and the body, through which the surface traction is applied, would slide across the top ball.

As an example the analysis has been applied to uniform spheres in rhombic packing with only the top ball free. The results obtained for $\frac{T}{W}$ by substitution into equation (4.24) of the values of θ, β and α for a rhombic pack are tabulated below. $\theta = 19^{\circ}\ 28'\ 16.4"$, $\beta = 60^{\circ}$ and $\alpha = 54^{\circ}\ 44'\ 8.15"$.

μ	T/W	
	From equation (4.24)	Limiting value
0.01	0.011	0.01
0.02	0.022	0.02
0.04	0.044	0.04
0.06	0.065	0.06
0.08	0.085	0.08
0.10	0.105	0.10
0.12	0.124	0.12
0.14	0.142	0.14
0.15	0.151	0.15
0.159	0.158	0.158

From the table it is seen that for all values of μ up to the critical value that will cause the top ball to roll, the top ball remains fixed and the frictional body providing the surface traction T slides across the top of the array.

4.6 Tests to establish the Occurrence of Particle Rotation during Shear:

The previous analysis suggests that if a test was conducted with glass ballotini in a shear box apparatus, with the bottom half of the box replaced with a flat plate of glass,

the sample would indicate very little dilation when the glass particles are dry, because ϕ_μ lies between 1° and 10°. However, some vertical displacement can be expected, because first the experimental arrangement of the glass ballotini is random, which may permit rolling together with sliding of the plate, as some values of θ could be low enough to cause rolling; second, the ballotini are not perfectly spherical and consequently some re-arrangement of the pack may occur under load, which could cause small vertical movements of the loading platten. However, when the glass is saturated (in which case ϕ_μ rises to values between 26.5° and 42.5°) most particles should lock and the rolling mechanism should predominate. If an initially dense packing is used, rolling must be accompanied by dilation of the mass of glass particles.

Two typical test results are shown in Figure 4.4 and Figure 4.5. In the first test 1 mm glass ballotini were used with a vertical normal load of 97.3 lb. No provision was made to keep the top part of the shear box clear of the glass plate, except that after the normal load was applied to the glass ballotini screws were inserted into threaded holes in the brass box, and by screwing against the glass plate a small clearance was obtained between the brass box and the glass plate; the screws were then removed before the shear load was applied. This load was applied in the usual way, the reaction being taken by a proving ring. One further small modification was made to the apparatus, and that was to the plunger loading the proving ring. This was modified so that

the line of thrust was level with the surface of the plate glass.

In the second test the usual proving ring was replaced with a high sensitivity proving ring, the deflection of which was monitored electronically, the electrical signal being fed through to a strip chart recorder. This chart is presented in Figure 4.5 and plotted on it are the vertical displacements of the normal load hanger. In this test a further refinement was made, this was to separate the top of the box from the plate glass, by a small amount, with small needle roller bearings, so that at no time were the plate and box allowed to come into contact. In this case 3 mm glass ballotini were used with a normal load of 20 lb.

In both cases the predicted behaviour occurs. It follows that a particle rolling mechanism occurs, and furthermore indicates that the values of interparticle friction cannot be obtained with this test method if dilation occurs. The interparticle friction must be measured directly between representative particles.

4.7 Comparison of Theoretical Relationships and Experimental Results:

It has now been established that rotation is a possible mechanism for the particles in the particular case where the mass of particles is sheared using a plate as the lower half of a

shear box. There seems no reason to doubt the existence of the same mechanism, combined with sliding, occurring in a mass of particles subjected to normal and shearing stresses on the boundaries of the mass.

If the trend established in the special tests were to be extended to the more general case of shearing within the granular mass, we should expect materials with differing values of friction coefficient, but similar in all other respects, to show more rolling of the particles the higher the friction coefficient. This effect would therefore change the energy input required to shear the granular mass compared with the energy required if only sliding were taking place.

As an example, let us consider the equation put forward by Caquot in 1934. For shearing at constant volume (no rotation allowed) with a normal load of W:

$$\tan \phi'_{cv} = \frac{\pi\mu}{2}$$

$$\text{or } \phi'_{cv} = \tan^{-1} \frac{\pi\mu}{2}$$

Energy input per unit horizontal displacement = $W\frac{(\pi\mu)}{2}$.

For glass particles we have shown that μ changes from about .07 when dry to about .62 when wet. This would correspond to a change of ϕ' from 6.27° to 44.25° for the two conditions, which should result in nearly a ninefold increase in strength.

Since we are now able to measure the intergranular friction

we can now test the above equation. To do this a series of tests was conducted on $\frac{1}{8}$" diameter steel ball bearings (dry), 3 mm diameter lead shot (dry), 3 mm diameter glass ballotini (dry and wet) and 1 mm diameter glass ballotini (dry and wet) in the shear box apparatus. The load displacement curves obtained, using the electronic monitoring system as used in the special tests described previously, are presented in Figure 4.13 to Figure 4.42. Plotted on these charts are the values of vertical displacement of the load hanger, which were visually monitored using a dial gauge during each test. In these tests the two halves of the shear box were separated by small needle roller bearings to eliminate friction between the two halves of the shear box.

The interparticle friction for each material was also measured for a series of differing vertical loads, and these values are given in Figure 4.6 to Figure 4.9. These friction tests were performed with the friction apparatus described previously, photographs of which are shown in Chapter 2.

Friction tests were also performed for glass ballotini sliding on the plate glass used in the special tests, and are shown in Figure 4.10. In these tests the particles were not stuck to the anvil or quill, but were clamped in a special vice made to hold the balls secure with their centres at right-angles to the direction of movement, and a chuck for holding the quill ball was used (see Chapter 2). The effect of differing surface conditions is also shown in Figure 4.11

and Figure 4.12.

From the shear tests on the various materials the values of ϕ'_{max} for each test have been plotted to a base of initial porosity in Figure 4.43a. This shows that the values of ϕ'_{max} for a particular value of initial porosity seem to be almost independent of material and interparticle friction. (The values of ϕ'_{max} were obtained using the conventional interpretation of the shear box test.) There is considerable scatter of the results which may be the result of using relatively large particles in a small shear apparatus. The scatter is very much less for the smaller 1 mm diameter glass ballotini, these results being plotted by themselves in Figure 4.44. The correspondence between the ϕ'_{max} values for a particular porosity for these tests is quite remarkable, and tends to confirm the observation made previously about particle size and scatter.

From these results we can conclude that for low stresses, such as were used in these tests, when particle fracture is not a feature of the shear process, the shear strength of a mass of spherical particles is not a unique function of the interparticle friction.

It is also suggested that a rolling mechanism accompanies sliding within the mass of particles, and that rolling increases as the value of the interparticle friction increases. Furthermore, there seems to be a direct correlation between particle rolling and the violent variations

in shear load observed with the higher friction particles, and therefore the material is more prone to rolling. This statement is supported by the result of the special test when the lower half of the shear box was replaced with a glass plate (see Figure 4.5). For this test it was shown that rolling was accompanied by dilation of the mass of particles, and it is seen that the dilation stage is also accompanied by the characteristically violent variations of the shear load observed with the standard tests on the higher friction materials. For the low friction materials, lead shot and dry glass ballotini, the shearing process is much smoother. The effect of suddenly increasing the interparticle friction is shown in the shear test using 1 mm glass ballotini (see Figure 4.37). There is a distinct change in behaviour, although there appears to be only slightly more variation in the shear strength than is observed with dry ballotini (see Figure 4.35). This test also underlines the statements above because even though the interparticle friction is increased by up to twelve times, the shearing strength is hardly affected at all. Therefore a change in the mechanism of the particles is demanded to satisfy this observed behaviour. Referring to Figure 4.2, it is seen that for the particular case analysed, for increasing values of μ_1 or μ_2, there is an increase in the permissible angles θ_a or θ_b, for which rolling is a possible mechanism. Therefore for higher values of μ_1 or μ_2 more particles are free to roll. It is suggested that this mechanism also applies to the mass of particles in the shear tests, and this is advanced as a possible explanation of the observed behaviour.

The results of these shear box tests can also be used to compare the theoretically established values of ϕ'_{cv} as a function of interparticle friction angle ϕ_μ which were summarized in Section 4.2. The coefficients of friction for the materials tested are given in the table below, and the range of values of ϕ'_{cv} are calculated from the load displacement curves for those portions when no dilation or consolidation was taking place. This data is summarized in Figure 4.46, which shows complete disagreement between the experimental results and the theoretical predictions.

Material	Test Condition	Contact Load (gm)	Coeff of Friction
1 mm dia glass ballotini	dry	5.7	0.03 - 0.05
		11.5	0.05 - 0.07
		23.1	0.07 - 0.09
		52.0	0.06 - 0.08
	flooded	5.7	0.50 - 0.58
		11.5	0.64 - 0.72
		23.1	0.76 - 0.79
		52.0	0.78 - 0.80
3 mm dia glass ballotini	dry	5.7	0.03 - 0.06
		11.5	0.03 - 0.07
		23.1	0.05 - 0.07
		52.0	0.07 - 0.12
		109.7	0.07 - 0.08
	flooded	5.7	0.79 - 0.89
		11.5	0.83 - 0.93
		23.1	0.87 - 0.89
		52.0	0.85 - 0.86
		109.7	0.80 - 0.82
$\frac{1}{8}$" dia steel balls	dry	5.7	0.29 - 0.48
		11.5	0.46 - 0.62
		23.1	0.52 - 0.66
		52.0	0.63 - 0.66
		109.7	0.60 - 0.62
3 mm dia lead shot	dry	5.7	0.07 - 0.08
		11.5	0.06 - 0.08
		23.1	0.08 - 0.09
		52.0	0.10 - 0.11
		109.7	0.10 - 0.12

(continued)

Material	Test Condition	Contact Load (gm)	Coeff of Friction
3 mm dia glass ball sliding on plate glass	dry	10.0	0.02 - 0.07
		20.0	0.02 - 0.08
		40.0	0.06 - 0.11
		90.0	0.11 - 0.13
		190.0	0.11 - 0.14
	flooded	10.0	0.61 - 0.90
		20.0	0.85 - 0.88
		40.0	0.85 - 0.88
		90.0	0.89 - 0.91
		190.0	0.80 - 0.90

The experimental results are for plane strain conditions, so the theoretical plane strain analyses of Caquot (1934) and Bishop (1954) can be compared with the experimental results. However, Taylor and Leps (1939) and others have shown that the shear strength of a granular material in triaxial compression tests differs marginally from that measured in the shear box apparatus. Hence it would seem probable that the conclusions derived from these results would apply in principle to triaxial tests as well.

If the analysis in Section 4.5 (which led to Figure 4.2) is borne in mind when looking at Figure 4.46, it would appear that because of the increasing likelihood of rolling as a mechanism for the higher values of ϕ_μ (i.e. μ values) for the likely θ values which will be in the low range, the energy input should be lower than that predicted for the pure slip theories. Therefore the ϕ_{cv} values for the tests on steel ball bearings and flooded glass ballotini could be expected to fall below the theoretical curves.

On the other hand the ϕ_{cv} values for lead shot and dry glass

ballotini could have been expected to lie close to the values predicted by the pure slip theories, because rolling is a less likely mechanism for these low ϕ_μ materials. The fact that the ϕ_{cv} values for these materials are not dissimilar to the values for high ϕ_μ materials leaves unanswered questions about the constraints imposed on the particles and their mechanics. For example, it is possible that even though the test is in essence a plane strain test, the low friction between the particles may allow weaving movements of the particles in the σ_2 direction, which would lead to more energy being dissipated. However, this is speculation, and a definitive analysis (for both high and low ϕ_μ materials) will have to await the results of further research into particle mechanics.

Note: The shear box tests are plotted to a base of horizontal displacement of the lower carriage. If a base of relative displacement is required, the correction to be applied depends only on the deflection of the proving ring, and is given by correcting the base scale by 0.010" for a load change of 15.5 lb.

Figure 4.45 shows a test on the two halves of the shear box, to establish that the friction was negligible when the roller bearings were used. However, as it turned out, this refinement was probably unnecessary, as the sample dilated in every case under these low stresses. Consequently the top half of the box probably remained in contact with the roller bearings for only the initial stages of these tests.

Recorder traces for 1mm glass ball sliding on a glass slide.

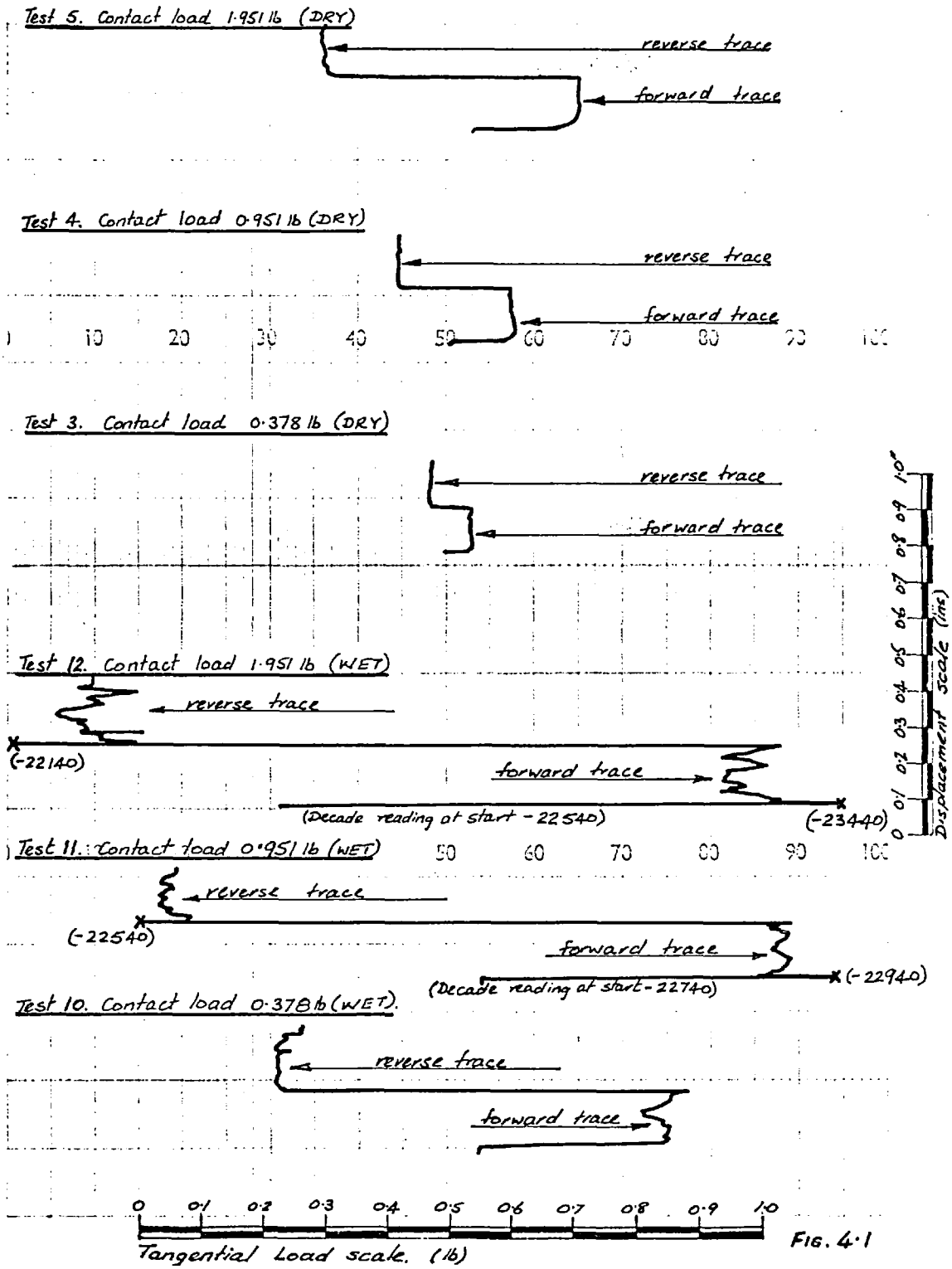


FIG. 4·1

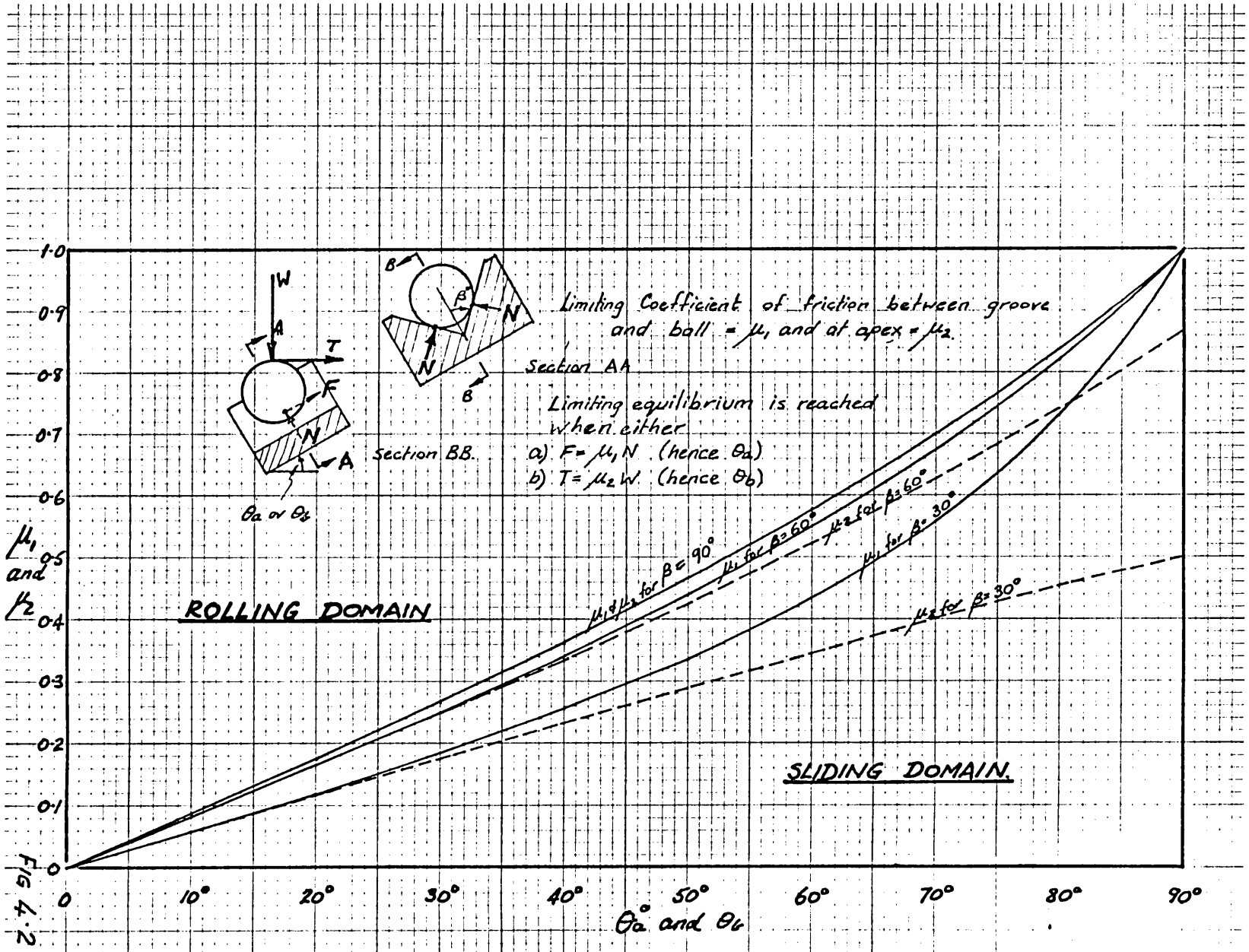

W
A
T
F
N
A
Section BB.
θa or θb
B
β
N
N
B
Section AA
Limiting Coefficient of friction between groove and ball = μ1 and at apex = μ2.
Limiting equilibrium is reached when either
a) F = μ1 N (hence θa)
b) T = μ2 W (hence θb)
ROLLING DOMAIN
SLIDING DOMAIN.
μ1 and μ2 for β = 90°
μ1 for β = 60°
μ2 for β = 60°
μ1 for β = 30°
μ2 for β = 30°
μ1 and μ2
θa° and θb
1·0
0·9
0·8
0·7
0·6
0·5
0·4
0·3
0·2
0·1
0
0
10°
20°
30°
40°
50°
60°
70°
80°
90°

Fig 4.2

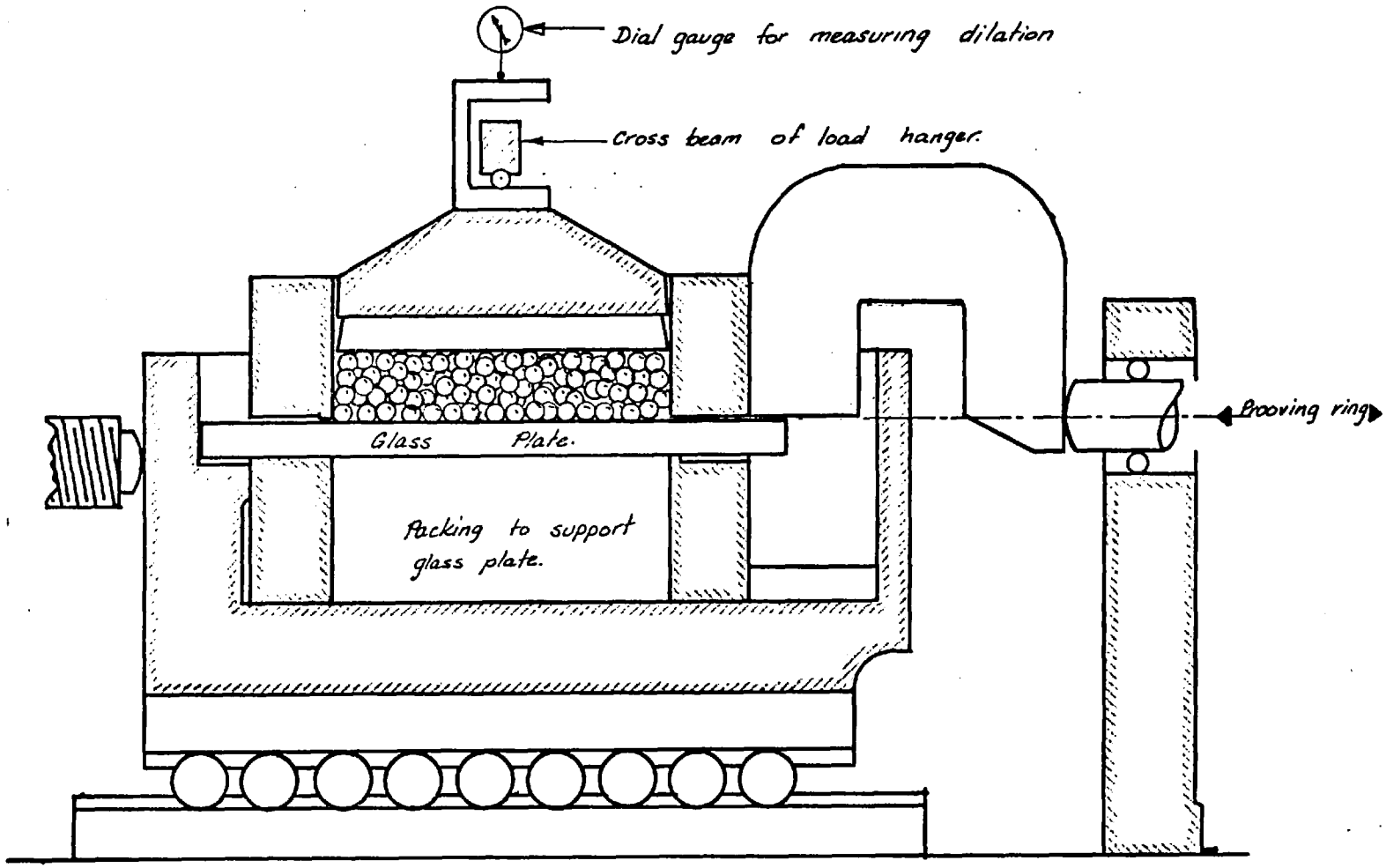


FIG 4·3.

Shear box as modified for special tests with glass ballotini and glass plate.

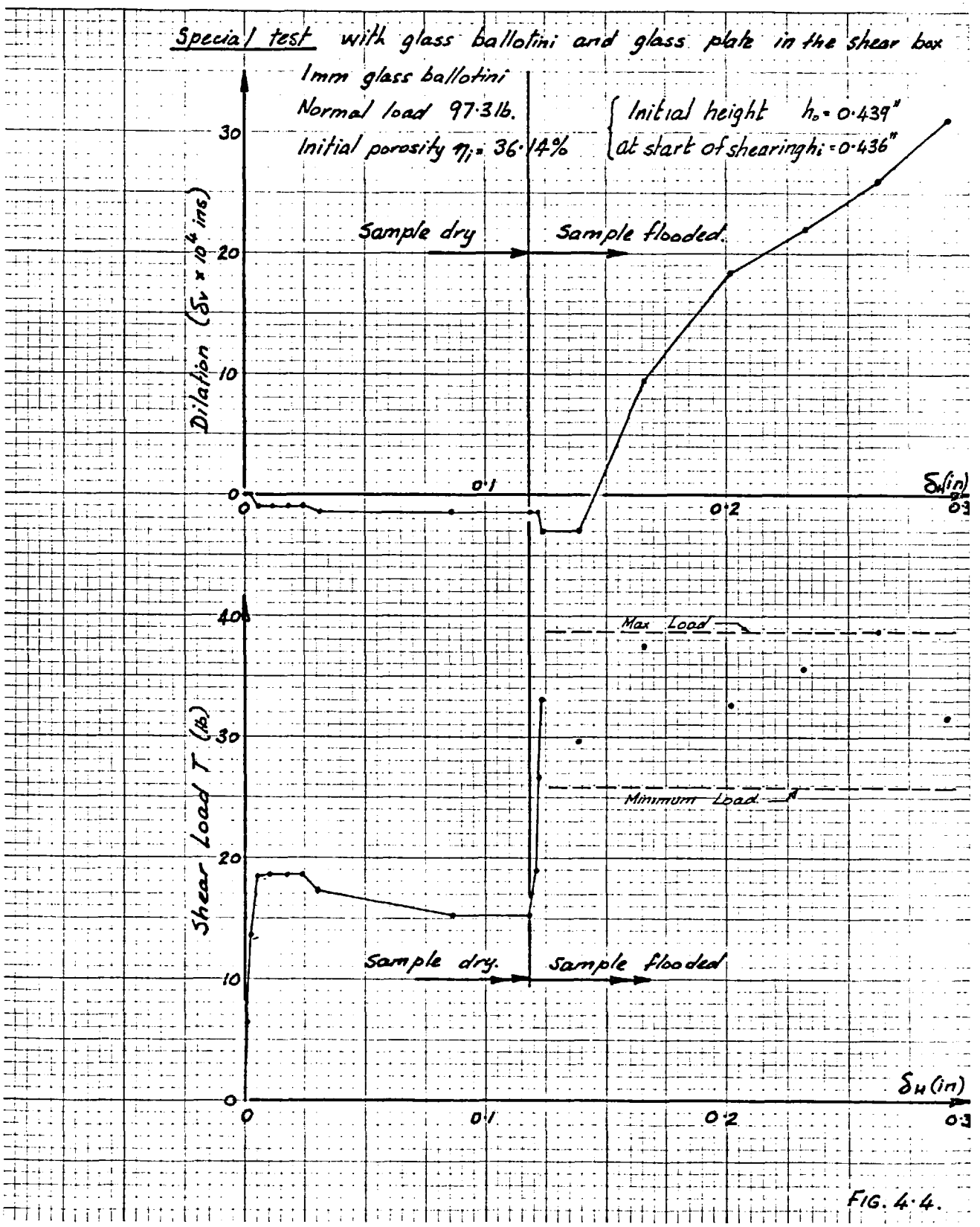

Special test with glass ballotini and glass plate in the shear box
1mm glass ballotini
Normal load 97·3 lb.
Initial porosity η_i = 36·14%
Initial height h_o = 0·439"
at start of shearing h_i = 0·436"
Sample dry
Sample flooded
Dilation ($\delta_v \times 10^4$ ins)
30
20
10
0
0·1
0·2
0·3
δ_H (in)
Max Load
Minimum Load
Shear Load T (lb)
40
30
20
10
0
Sample dry.
Sample flooded
δ_H (in)

FIG. 4·4.

Special test with glass ballotini and glass plate in the shear box.

3mm glass ballotini

Normal load 201b

Initial porosity η_i = 37.48%

Initial height h_0 = 0·503"

at start of shearing h_i = 0·502"

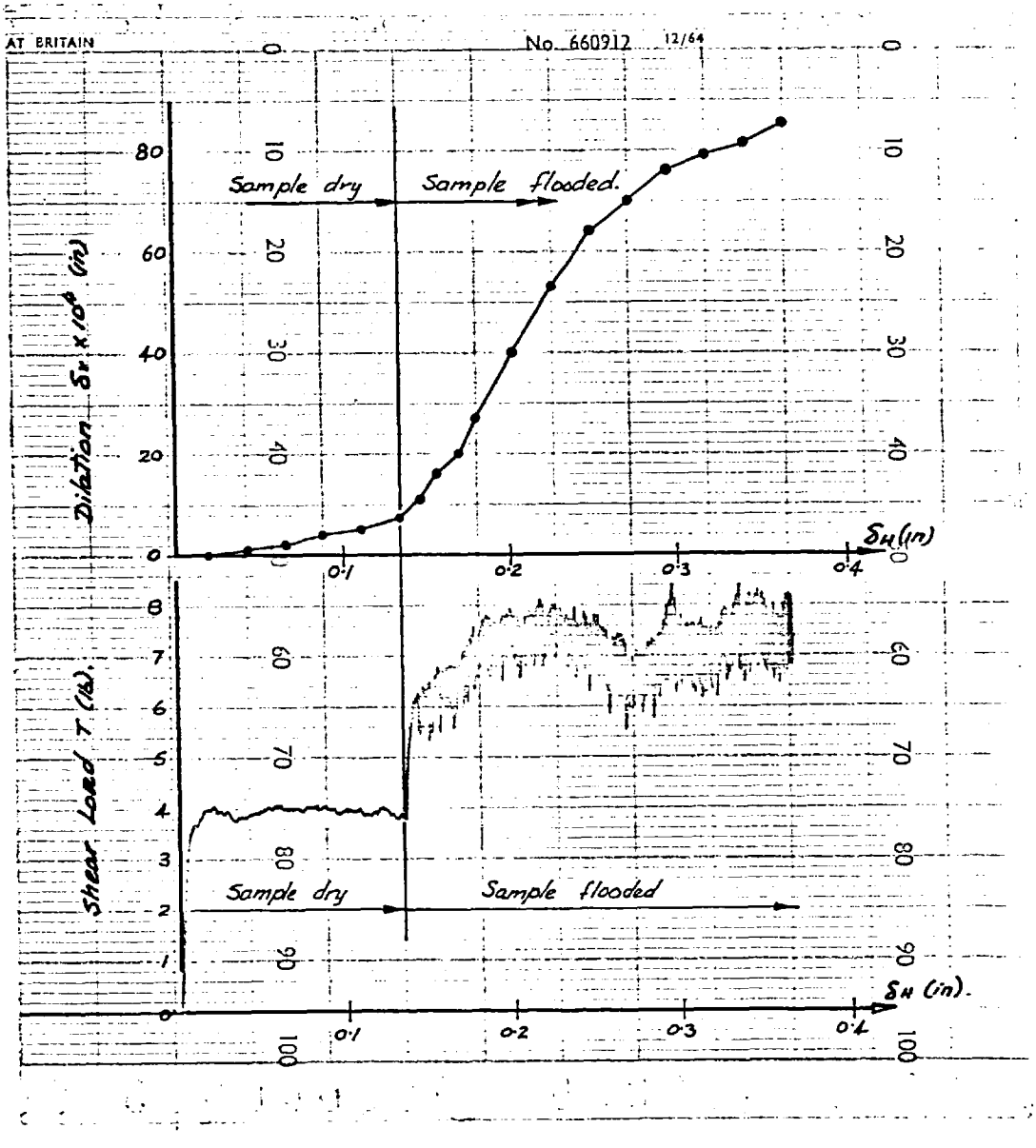
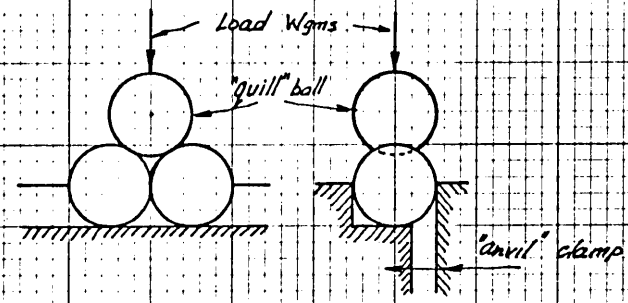


FIG 4·5.

Results of tests to determine the coefficient of friction between ¼" dia steel ball bearings



Coefficient of friction, μ.

1.0
0.8
0.6
0.4
0.2
0

0
50
100
150
200

Load W gms on "quill" ball.

Key
- range of values for tests on balls exposed to the laboratory atmosphere for 3 days prior to test.
- range of values for tests on "clean" balls, as used in the shear box tests.

FIG 4.6

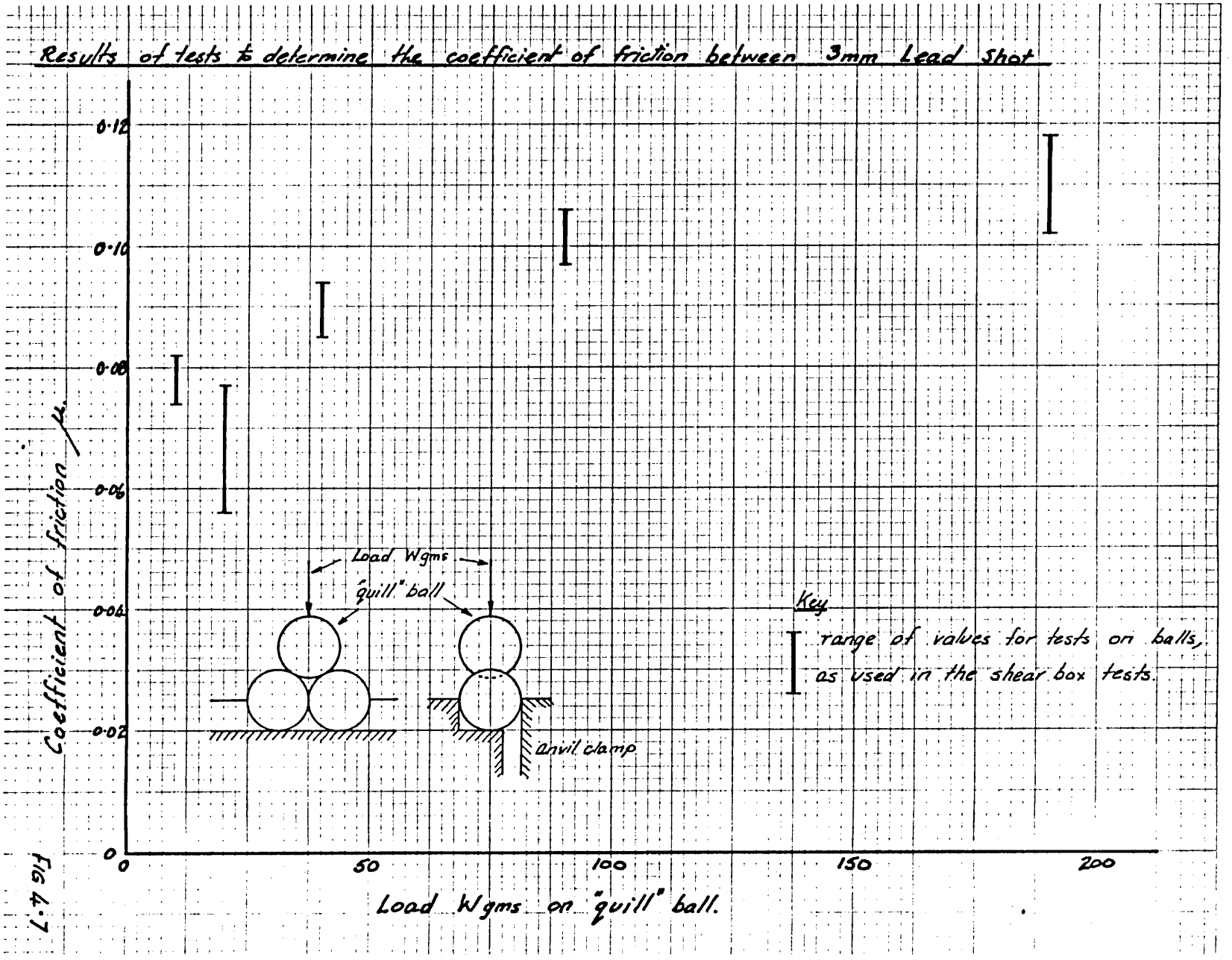
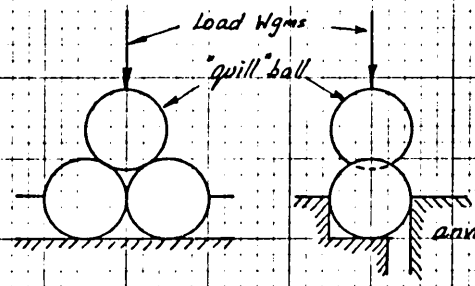

Results of tests to determine the coefficient of friction between 3mm Lead shot
0·12
0·10
0·08
0·06
0·04
0·02
0
Coefficient of friction μ.
0
50
100
150
200
Load Wgms on "quill" ball.
Load Wgms
"quill" ball
anvil clamp
Key
range of values for tests on balls, as used in the shear box tests.

Fig 4.7

Results of tests to determine the coefficient of friction between 3mm Glass ballotini.



Key

I range of values for tests on clean balls, as used in the shear box tests on dry balls.

II range of values for tests on clean balls, as used in the shear box tests on wet balls.

Coefficient of friction μ

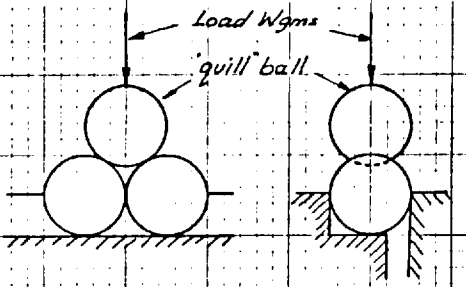
1·0
0·8
0·6
0·4
0·2
0

0
50
100
150
200

Load Wgms on "quill" ball

Fig 4·8

Results of tests to determine the coefficient of friction between 1mm Glass ballotini



Key.

I range of values for tests on clean balls, as used in the shear box tests on dry balls.

II range of values for tests on clean balls as used in the shear box tests on wet balls.

Coefficient of friction μ

1·0
0·8
0·6
0·4
0·2
0

0
50
100

Load Wgms on "quill" ball

Fig 6·7 Diy

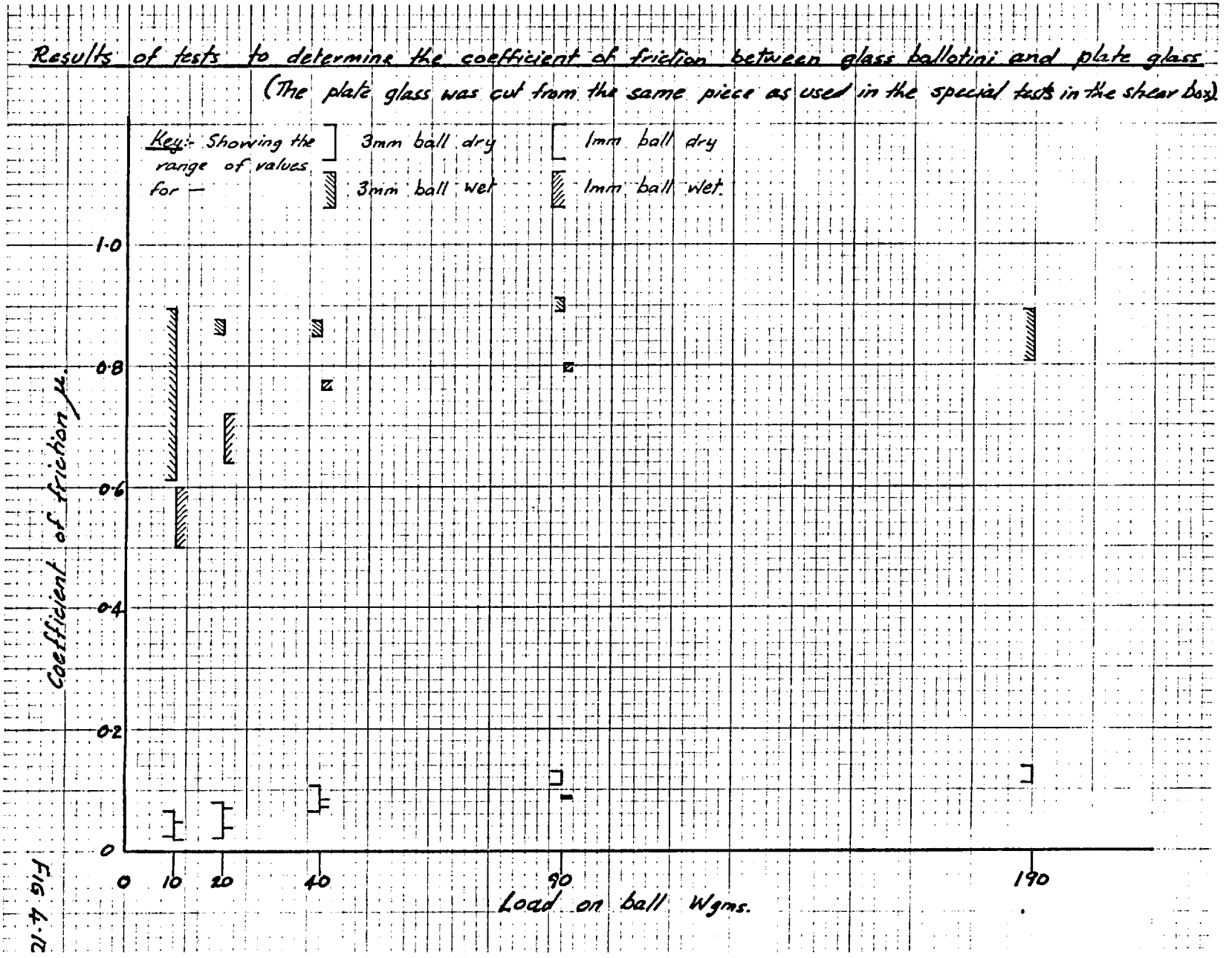

Results of tests to determine the coefficient of friction between glass ballotini and plate glass
(The plate glass was cut from the same piece as used in the special tests in the shear box)
Key:- Showing the range of values for —
3mm ball dry
3mm ball wet
1mm ball dry
1mm ball wet
Coefficient of friction μ.
1·0
0·8
0·6
0·4
0·2
0
0
10
20
40
90
190
Load on ball Wgms.

Fig 4·12

Result of test to show the effect of differing surface conditions on the value of the Coefficient of friction between glass ballotini.

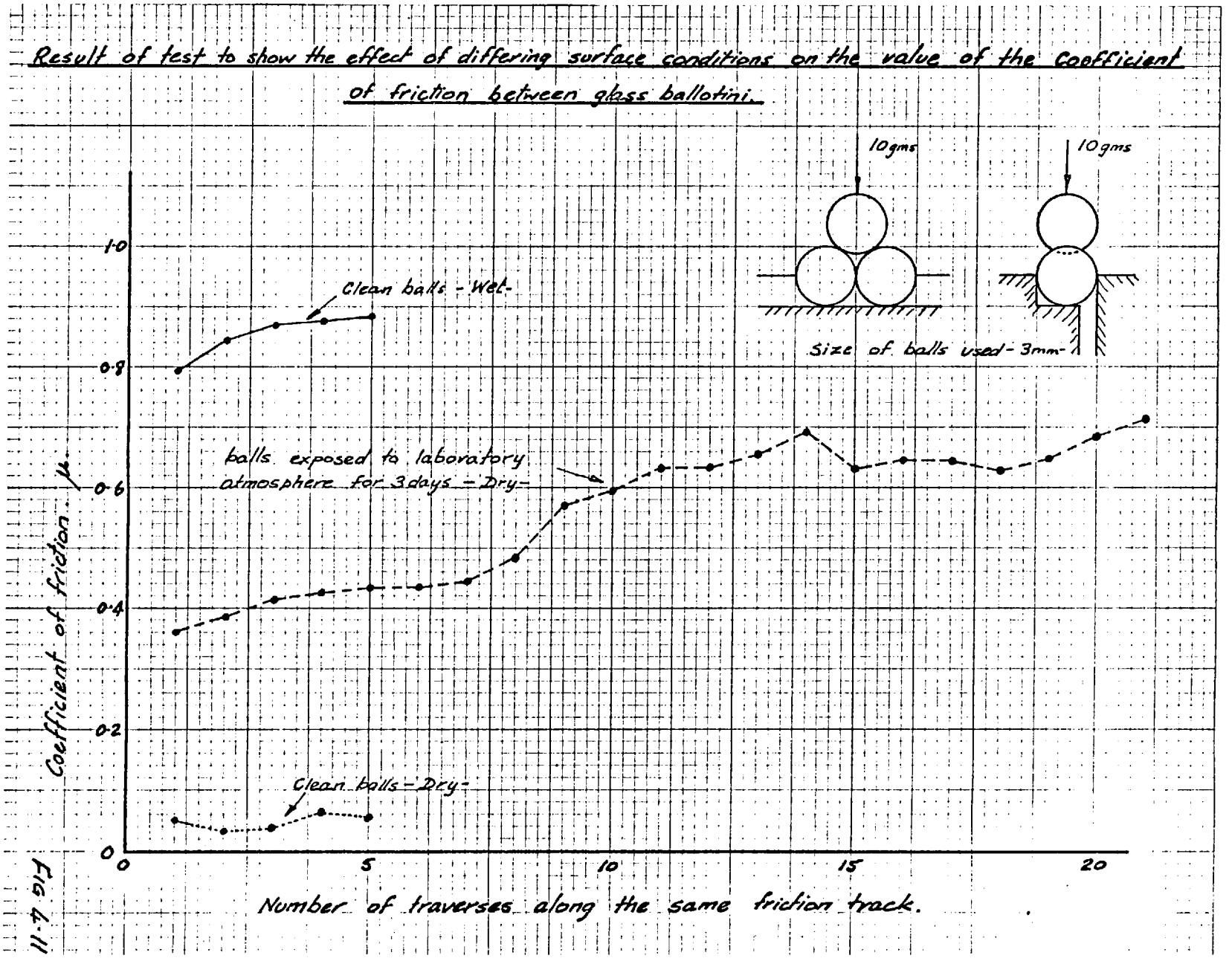


Fig 4-7 Sly

Result of test to show the effect of differing surface conditions on the value of the coefficient of friction between glass ballotini.

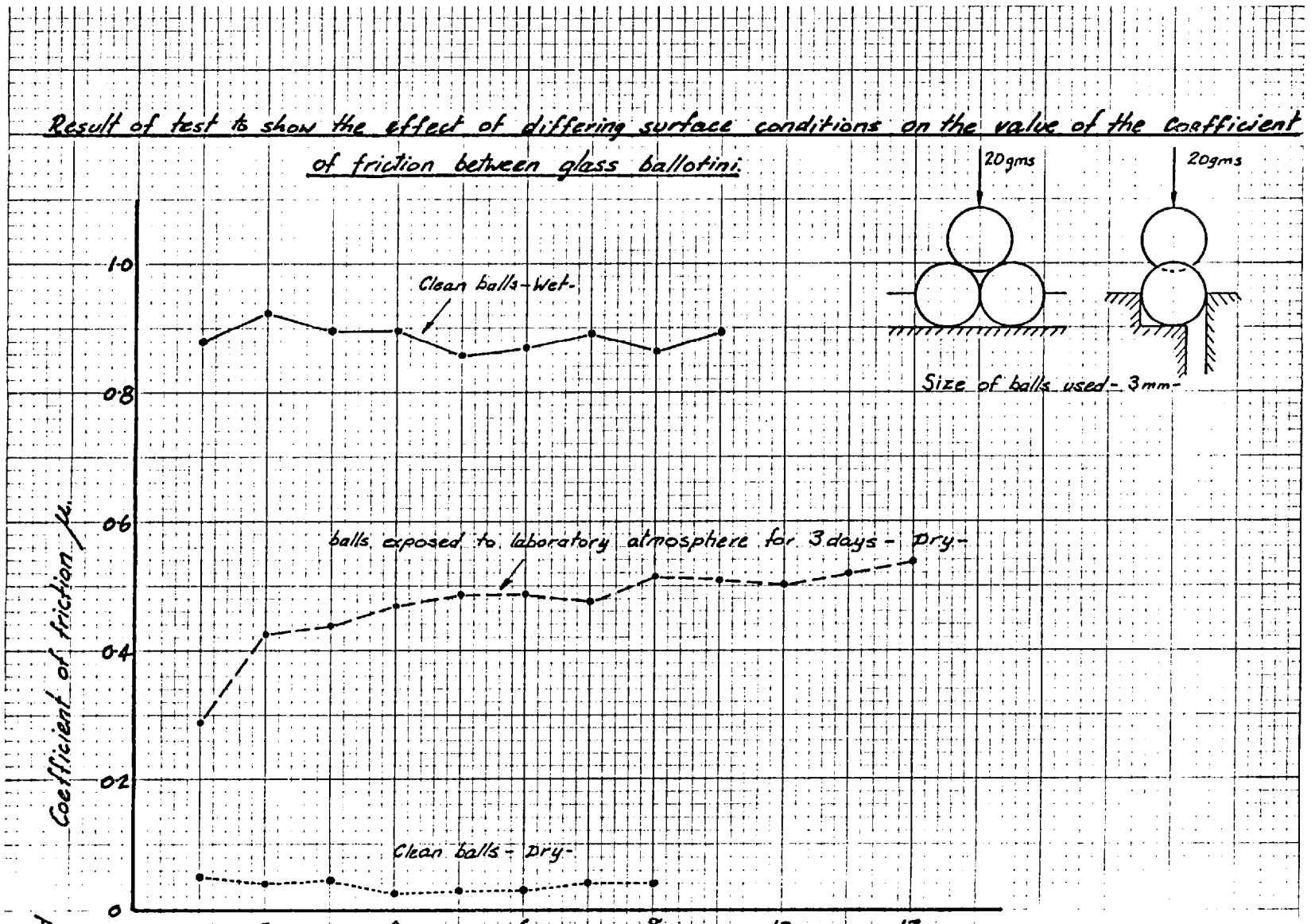


Fig 4.12.

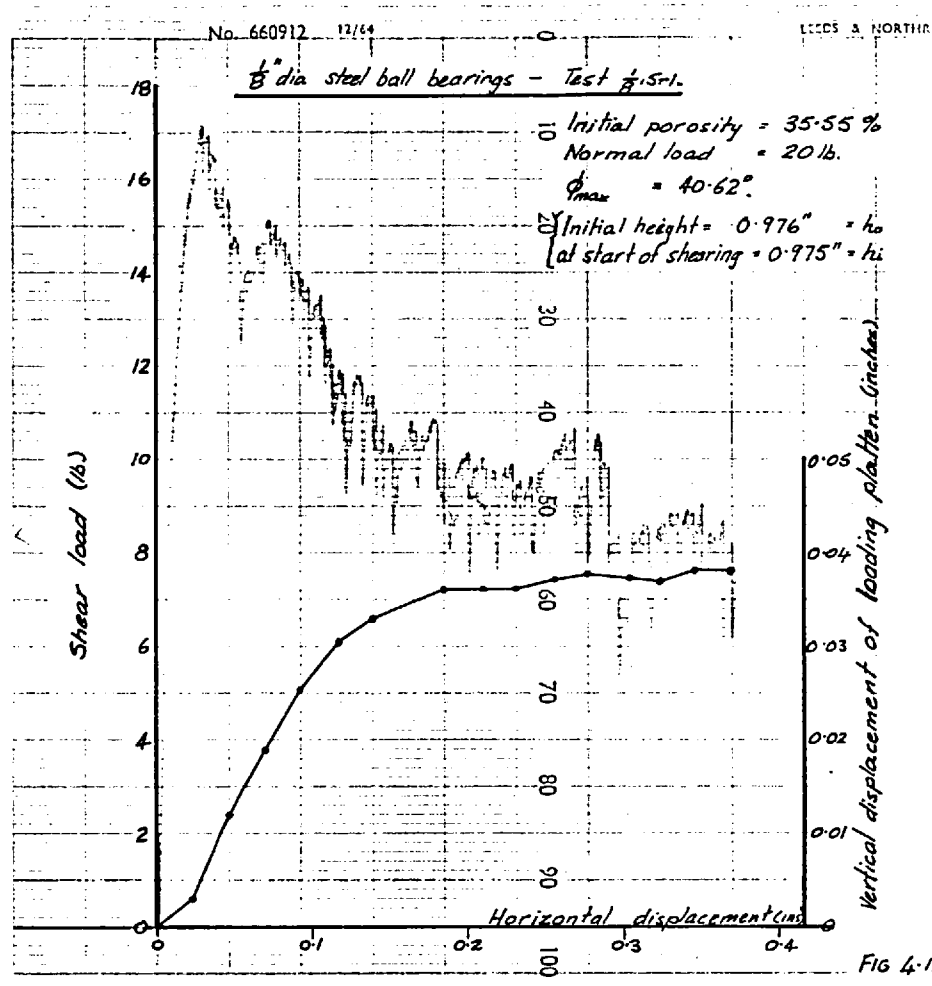


FIG 4·13.

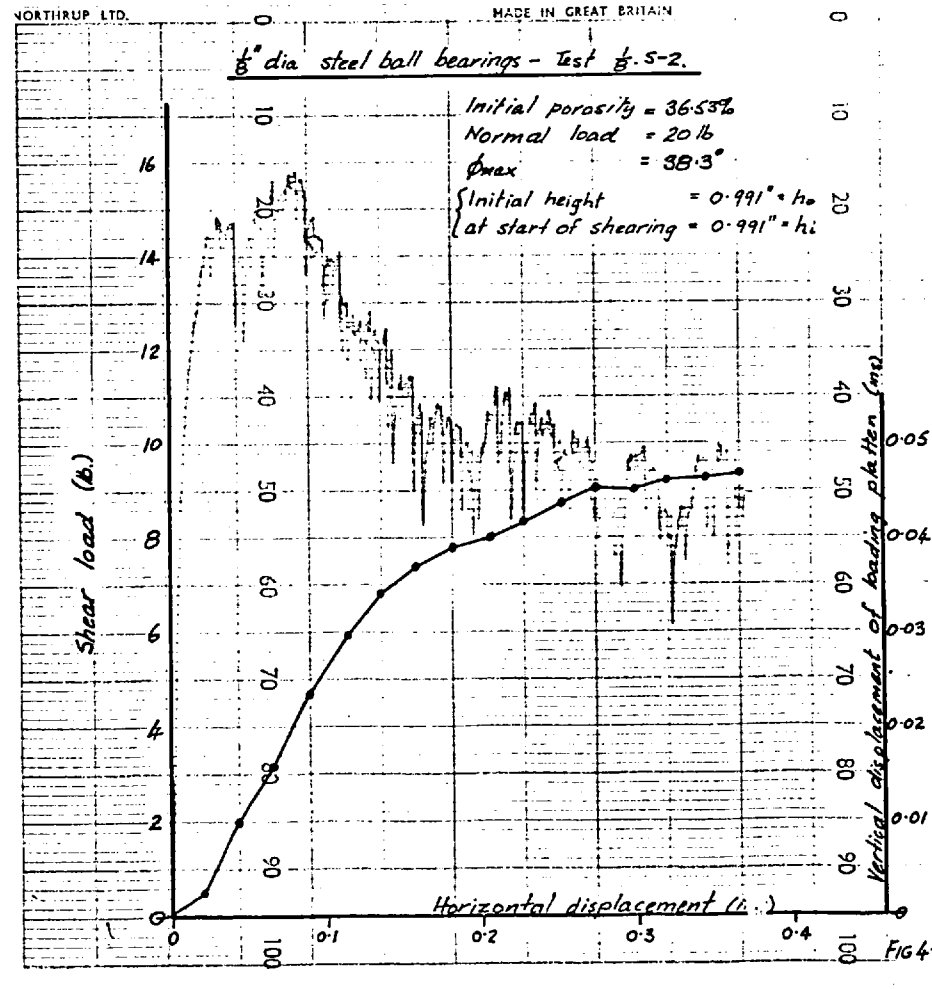


FIG 4·14.

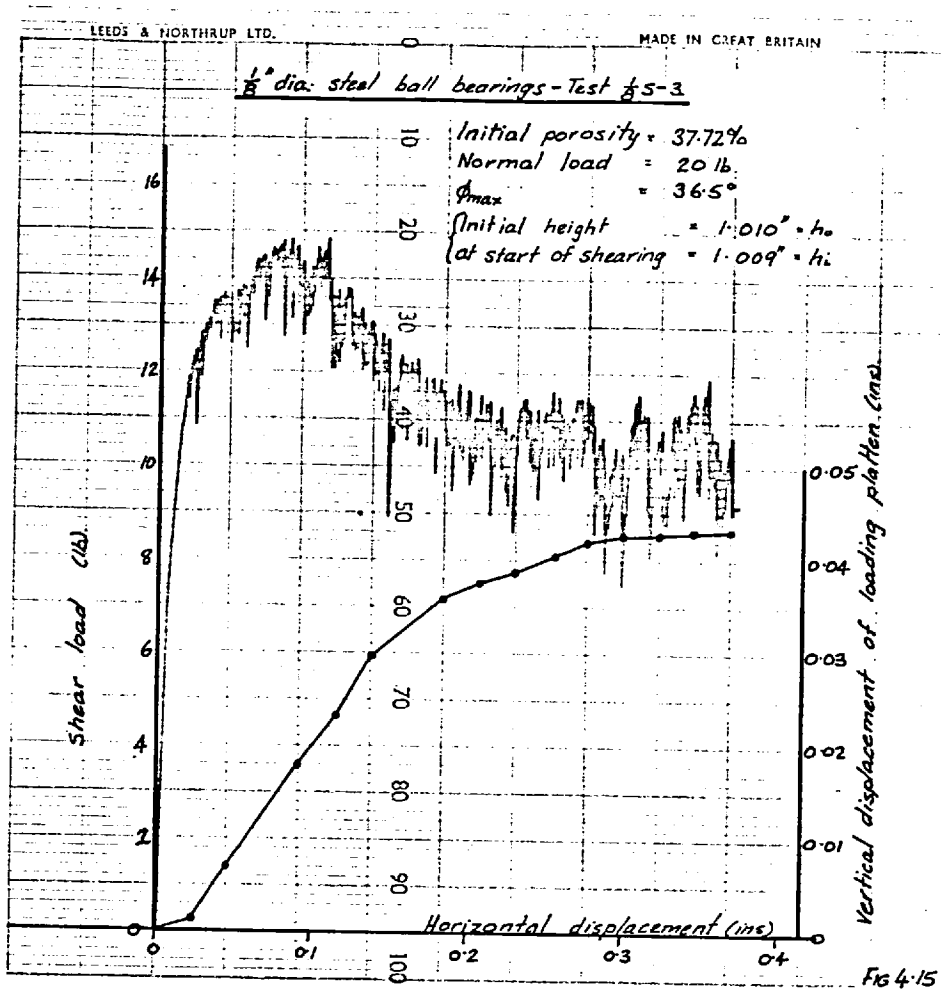


FIG 4.15

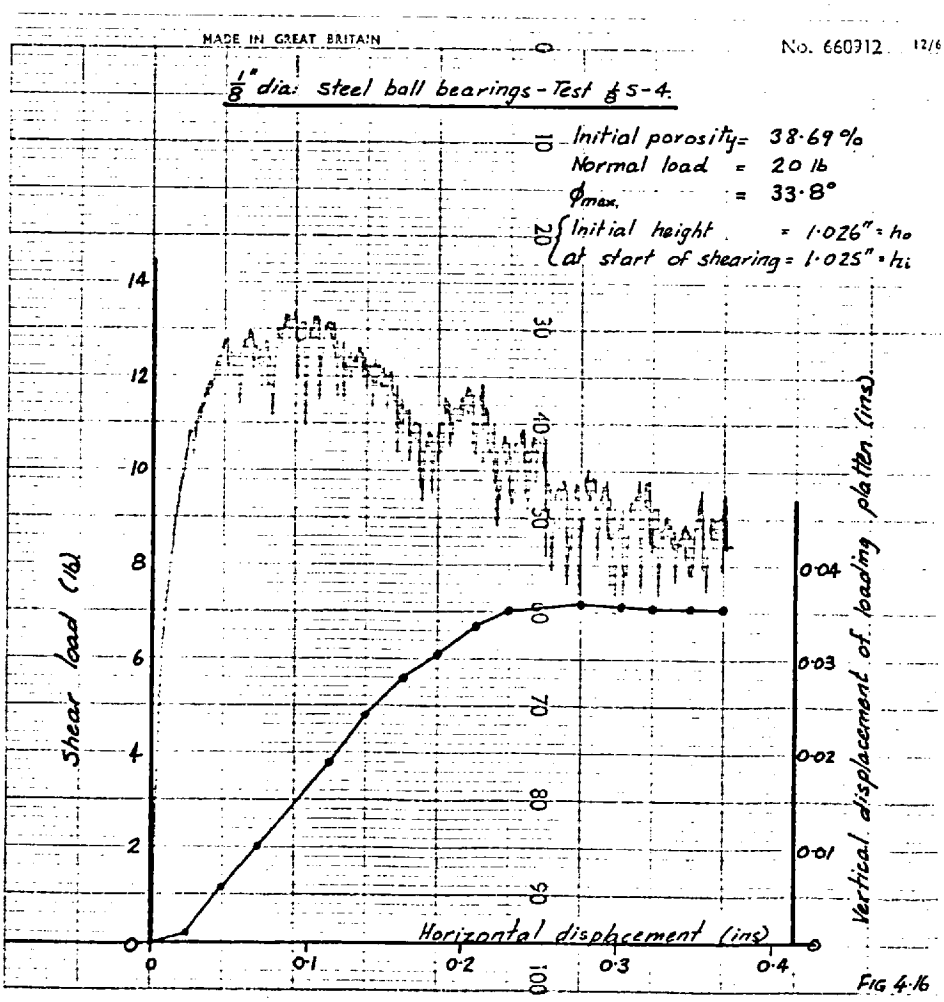


FIG 4.16

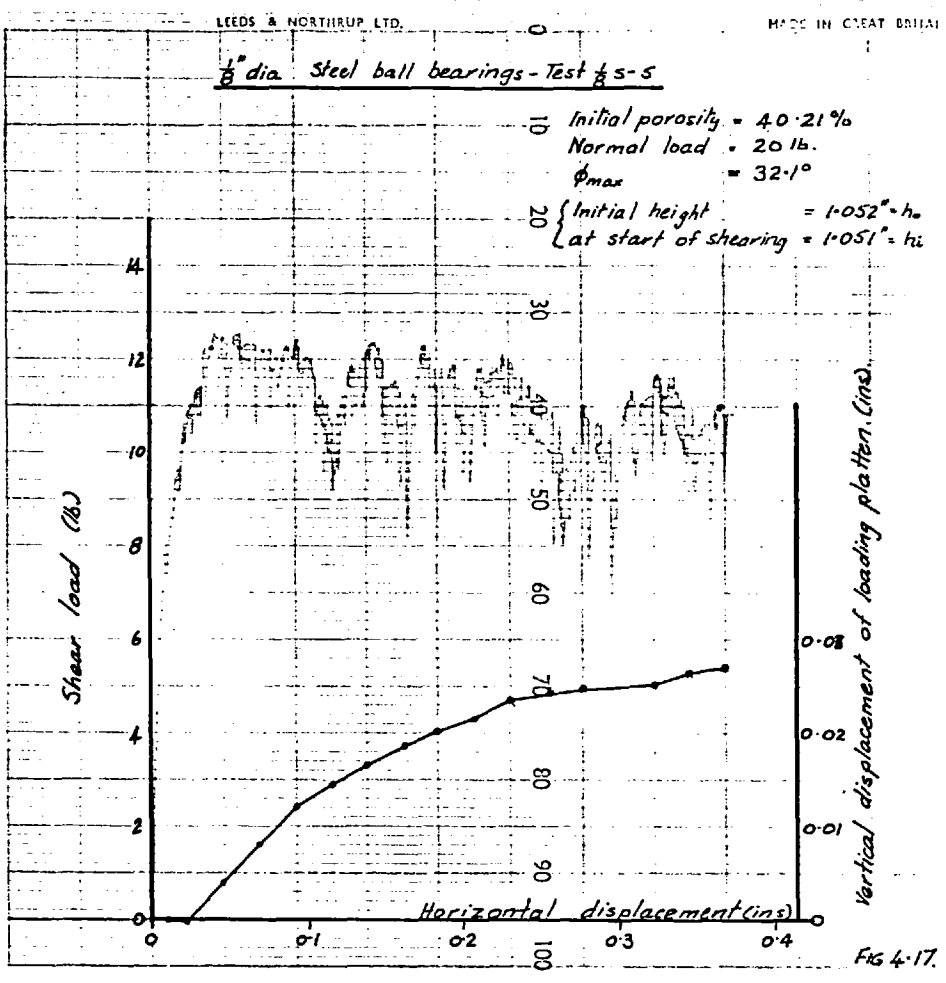


FIG 4·17.

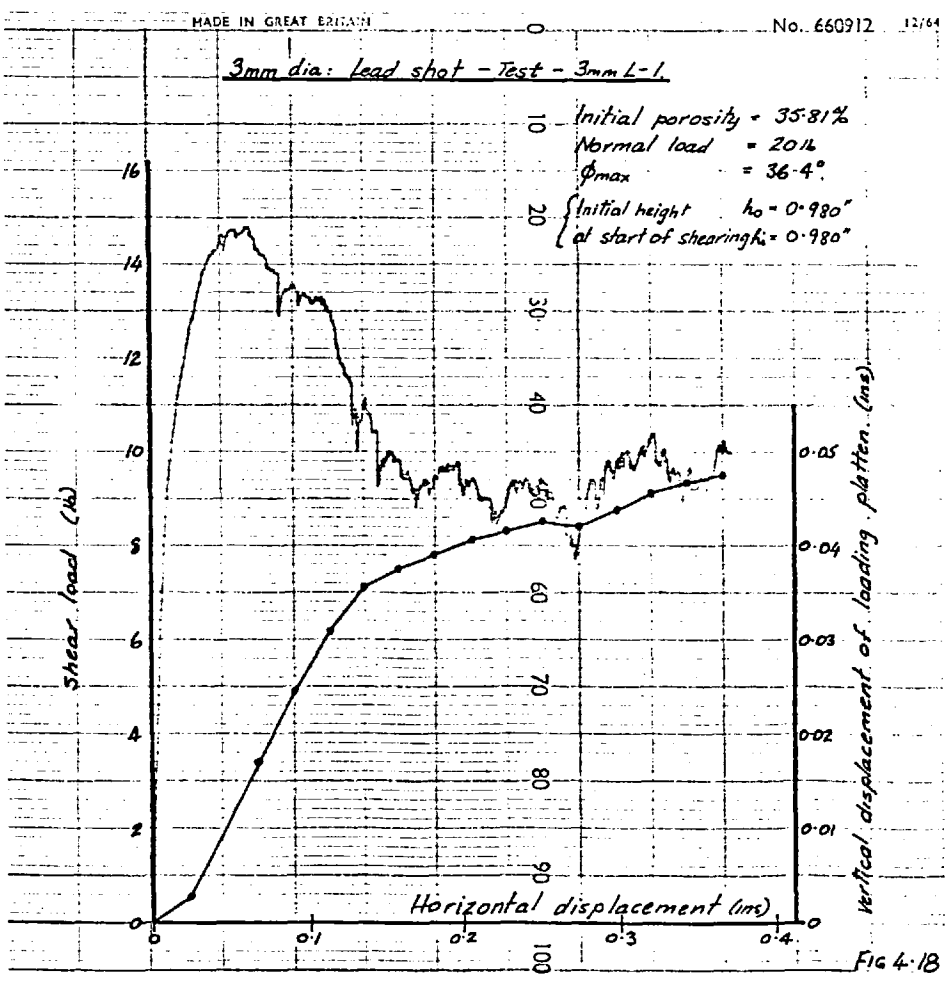


FIG 4·18

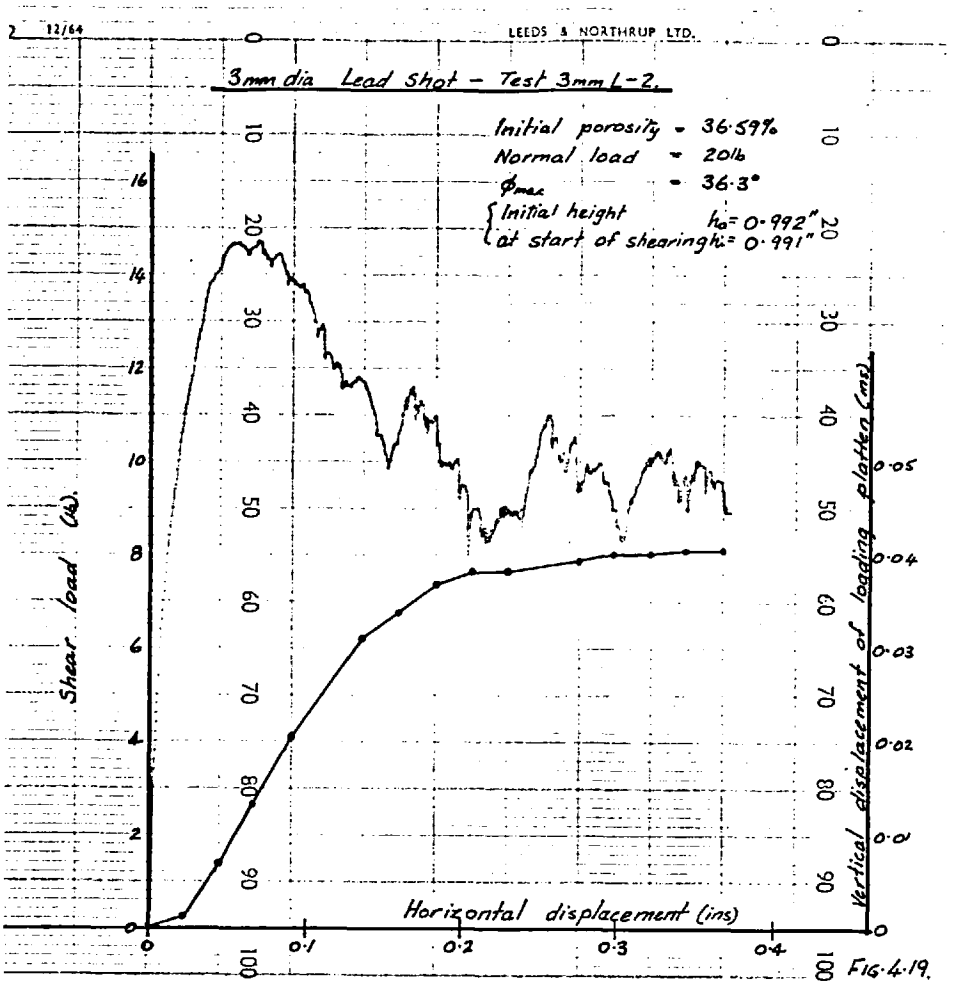


Fig 4·19.

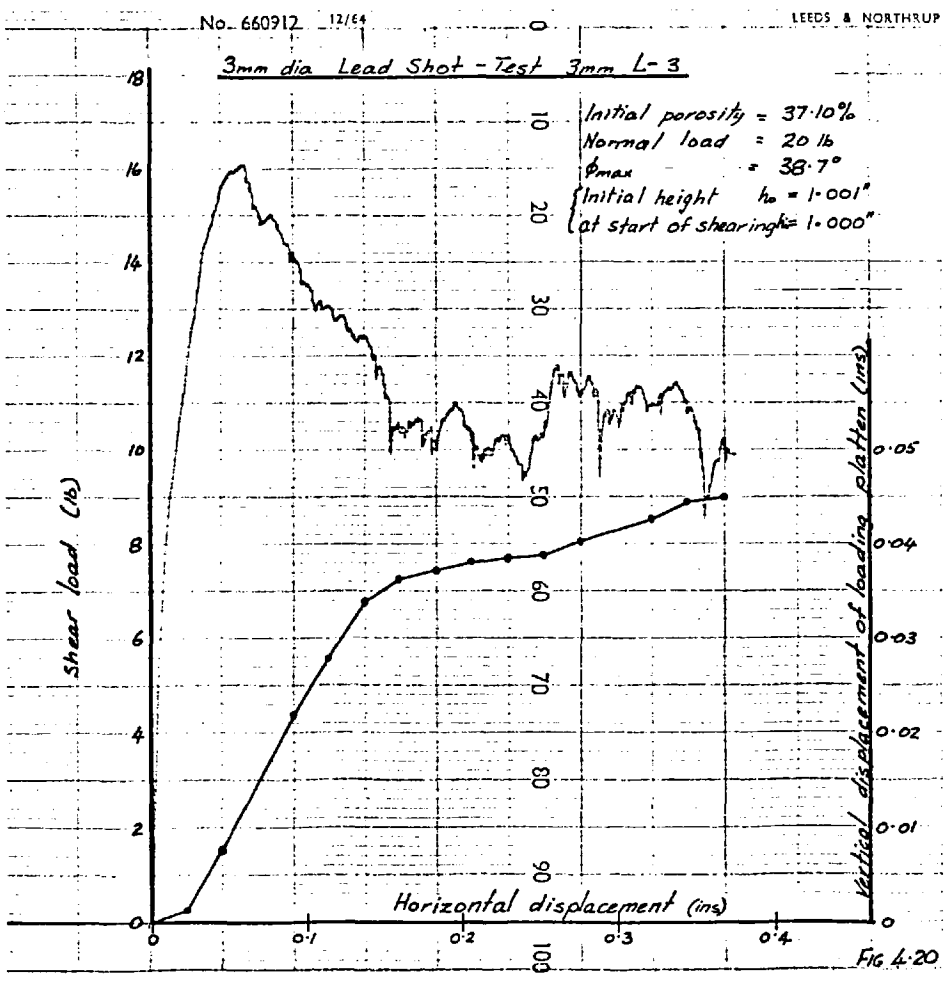


Fig 4·20

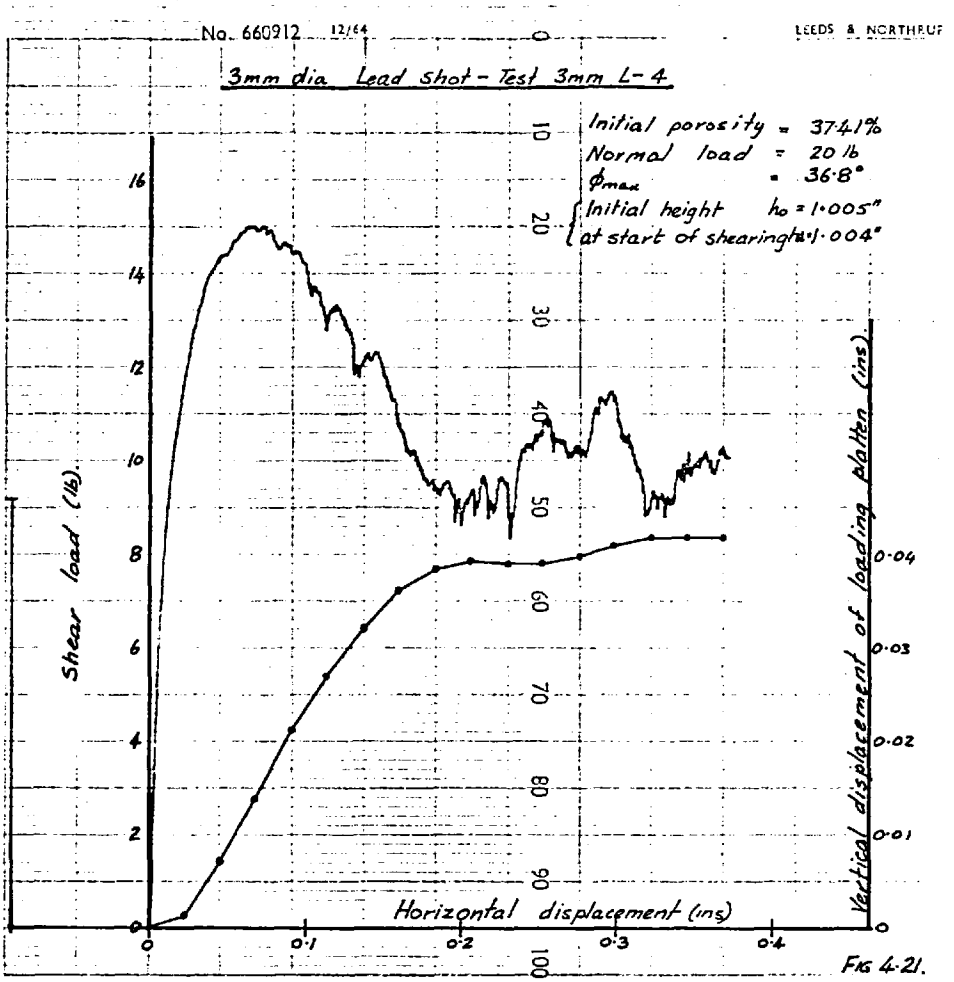


FIG 4.21.

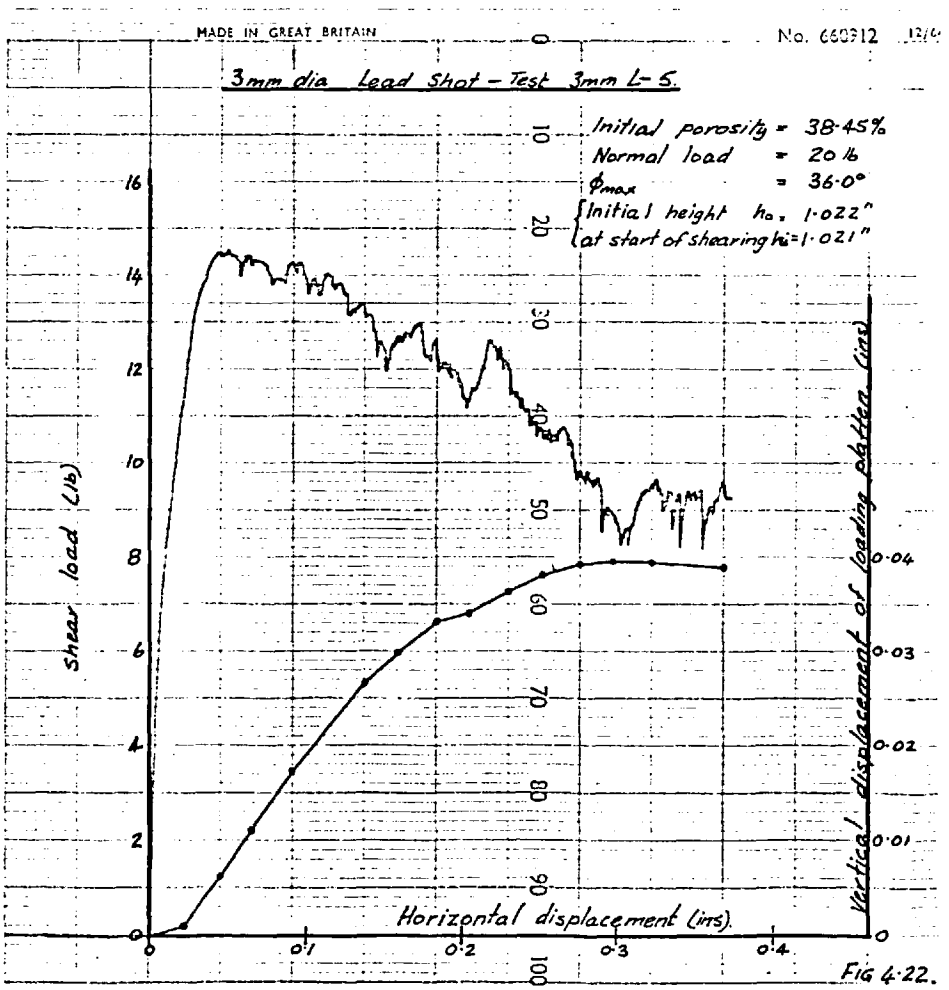


FIG 4.22.

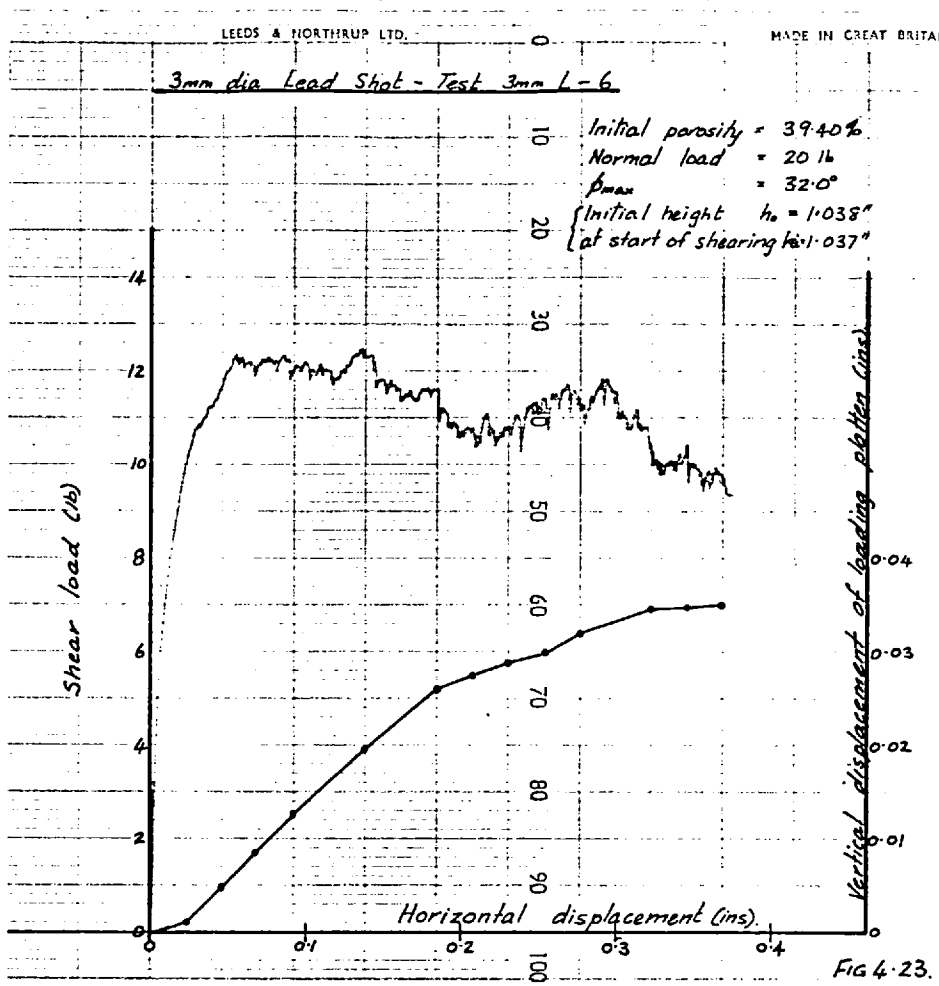


FIG 4·23.

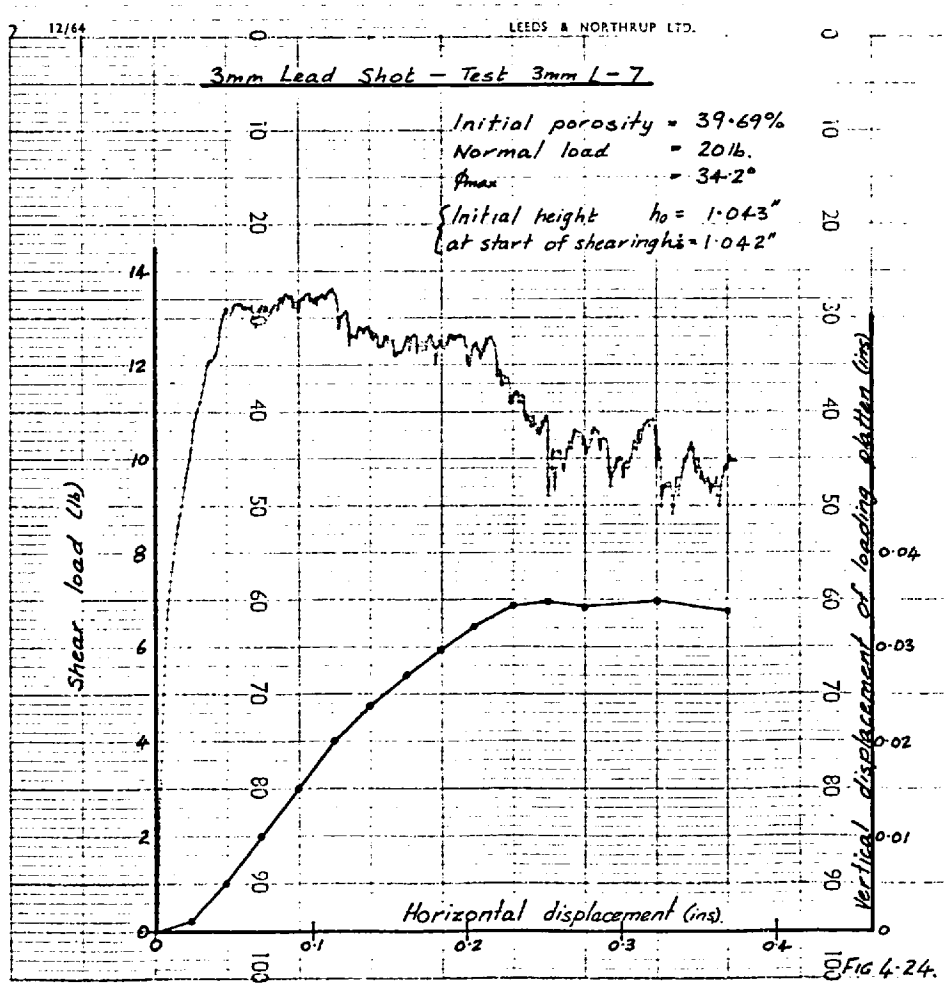


FIG 4·24.

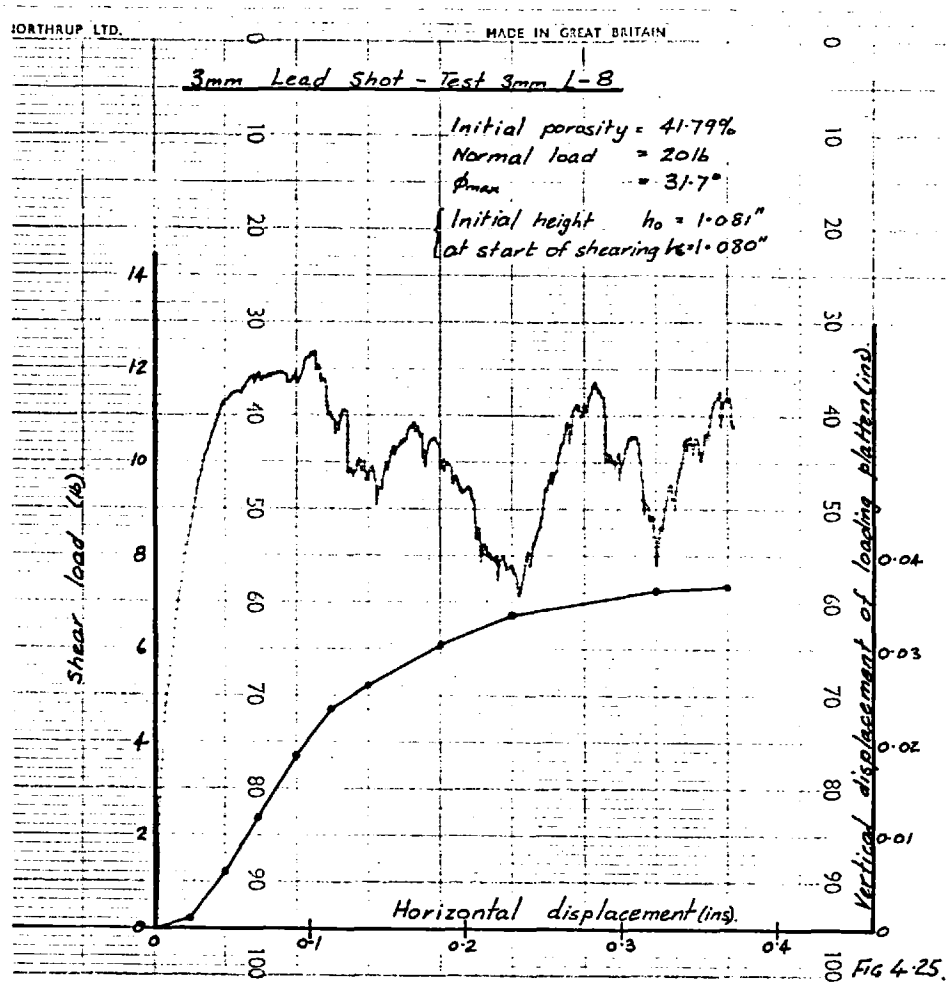


FIG 4·25.

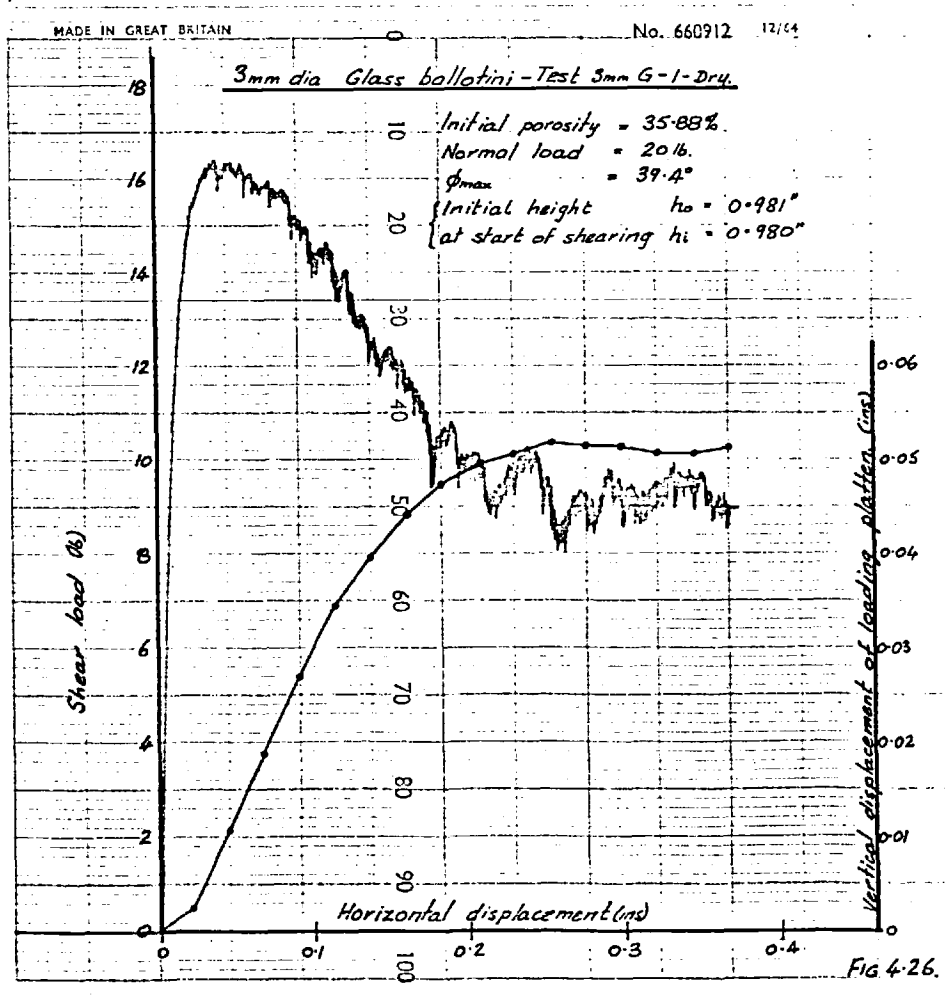


FIG 4·26.

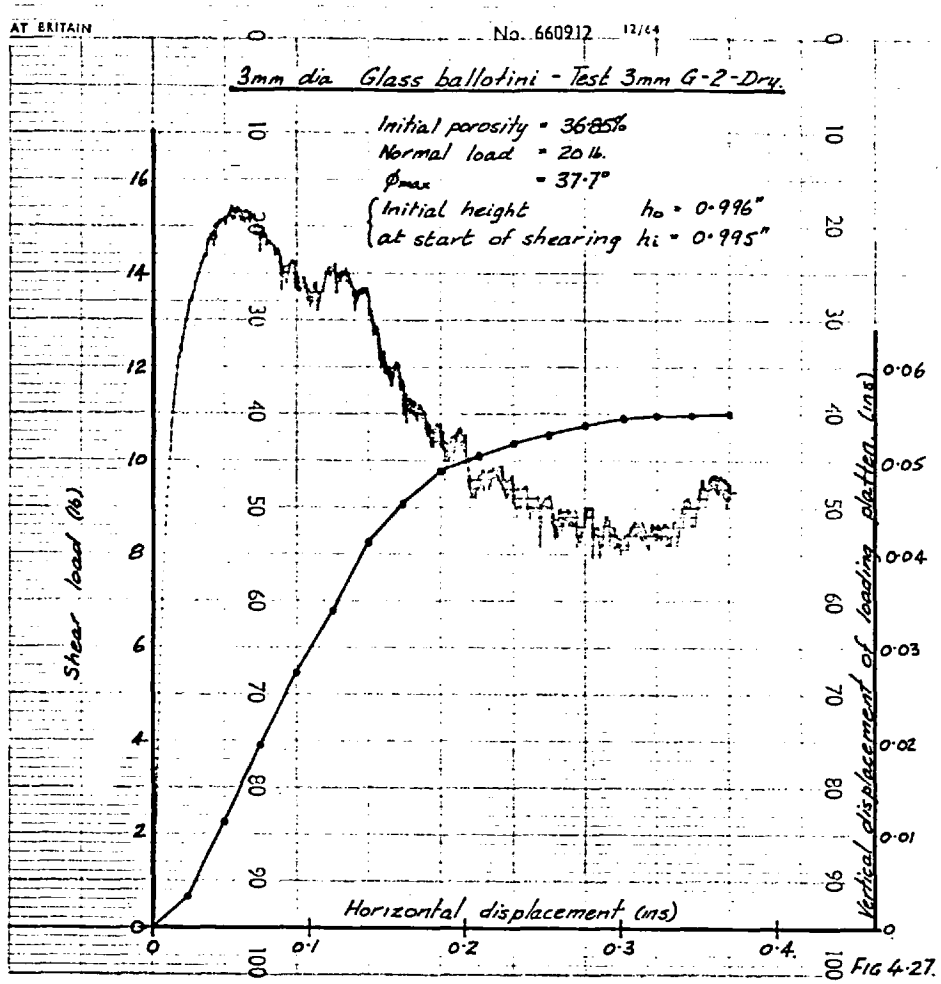


FIG 4·27.

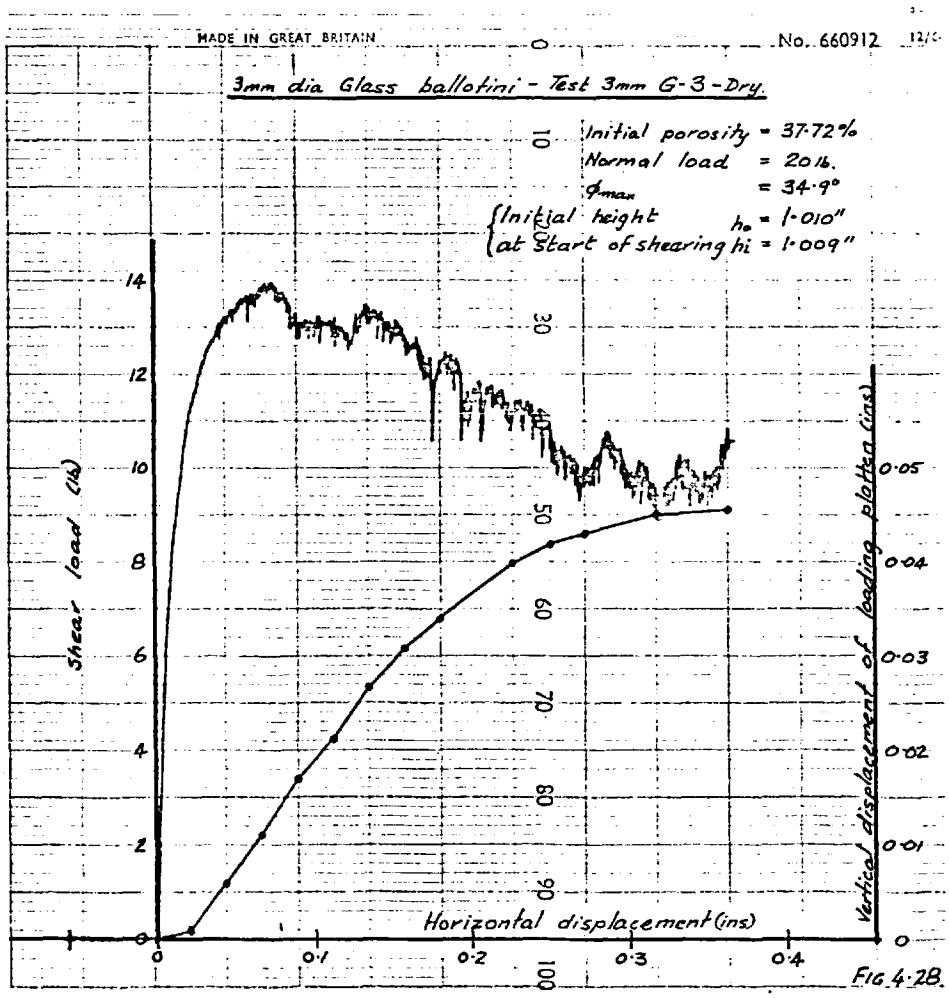


FIG 4·28.

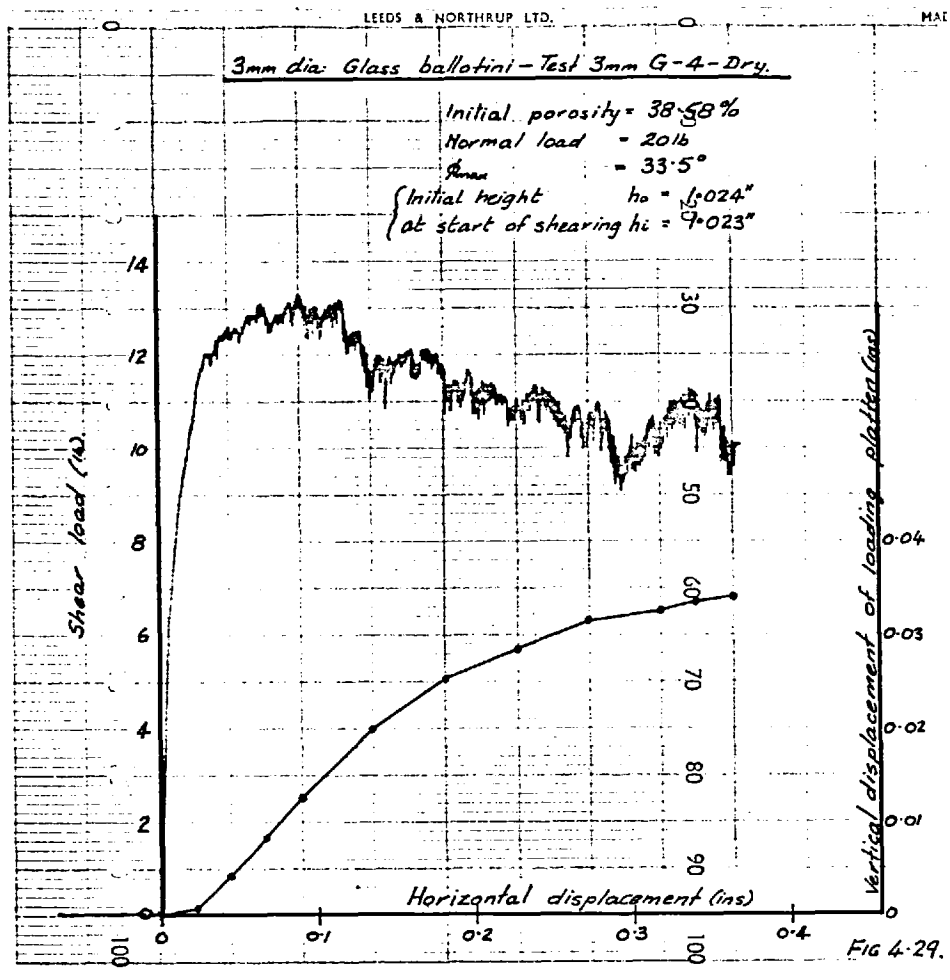


FIG 4·29.

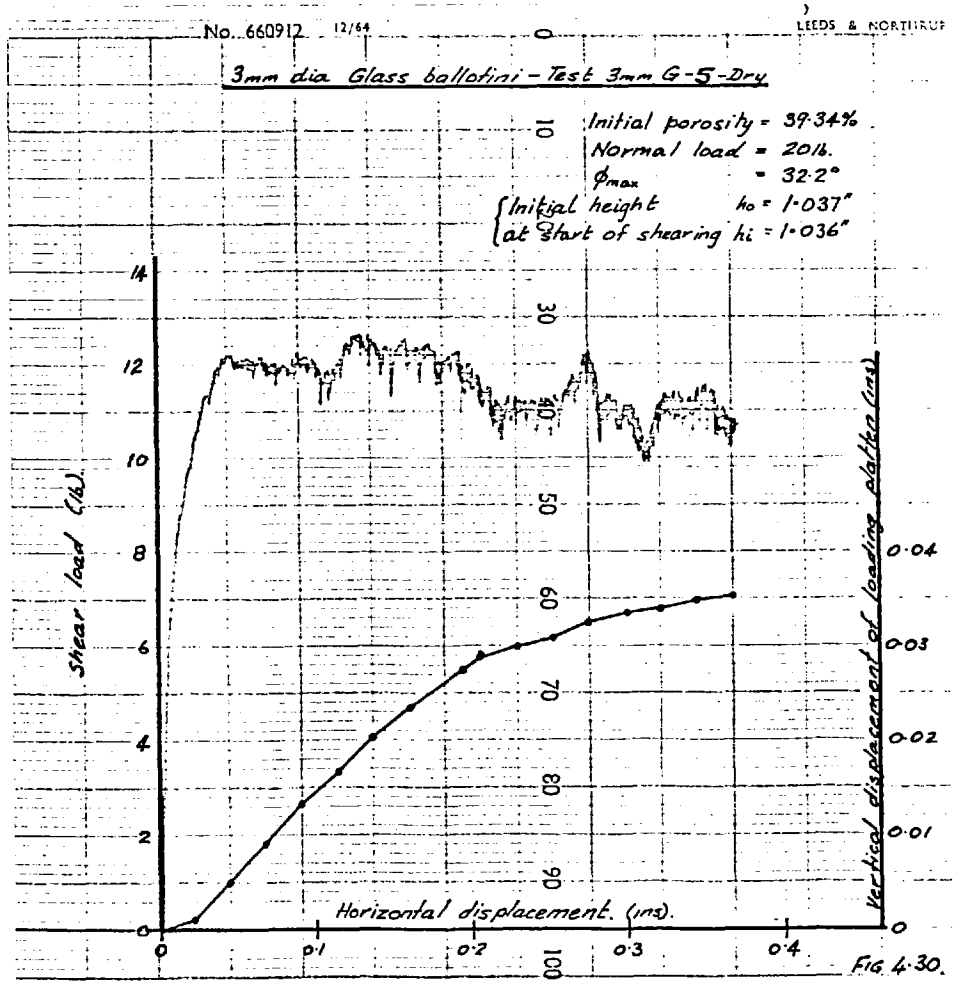


FIG 4·30.

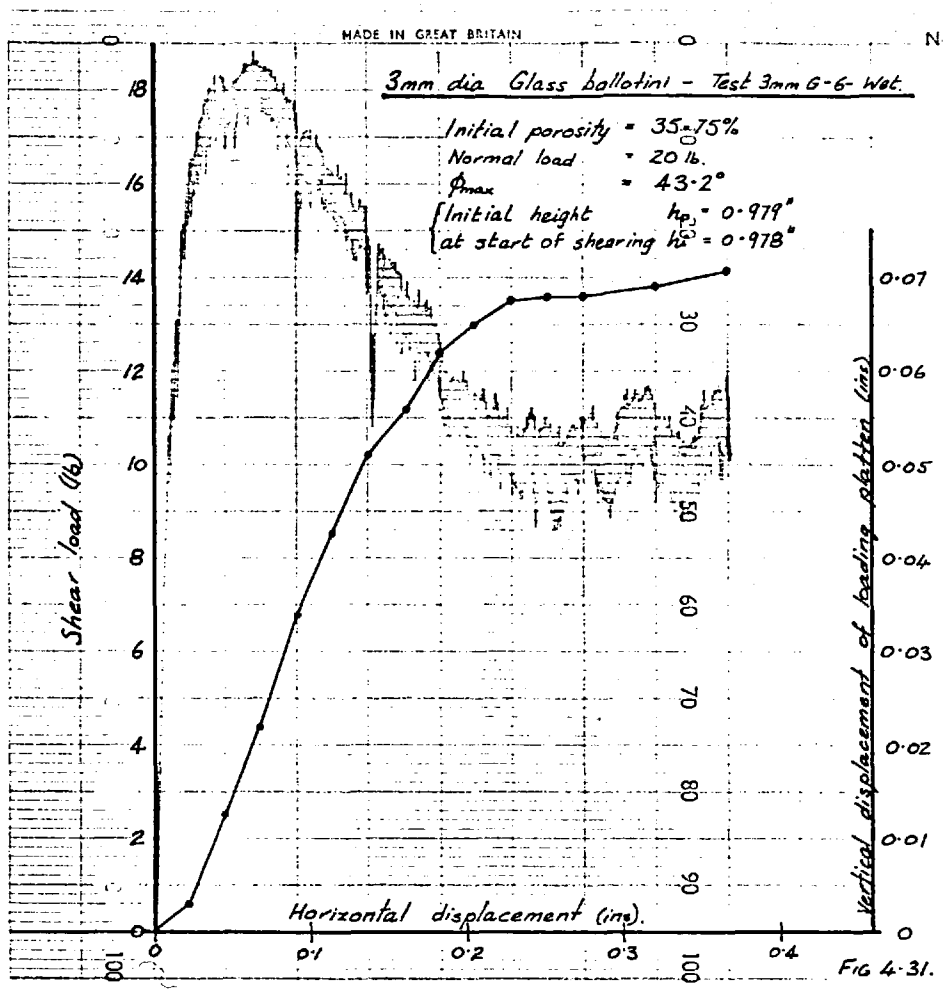


FIG 4·31.

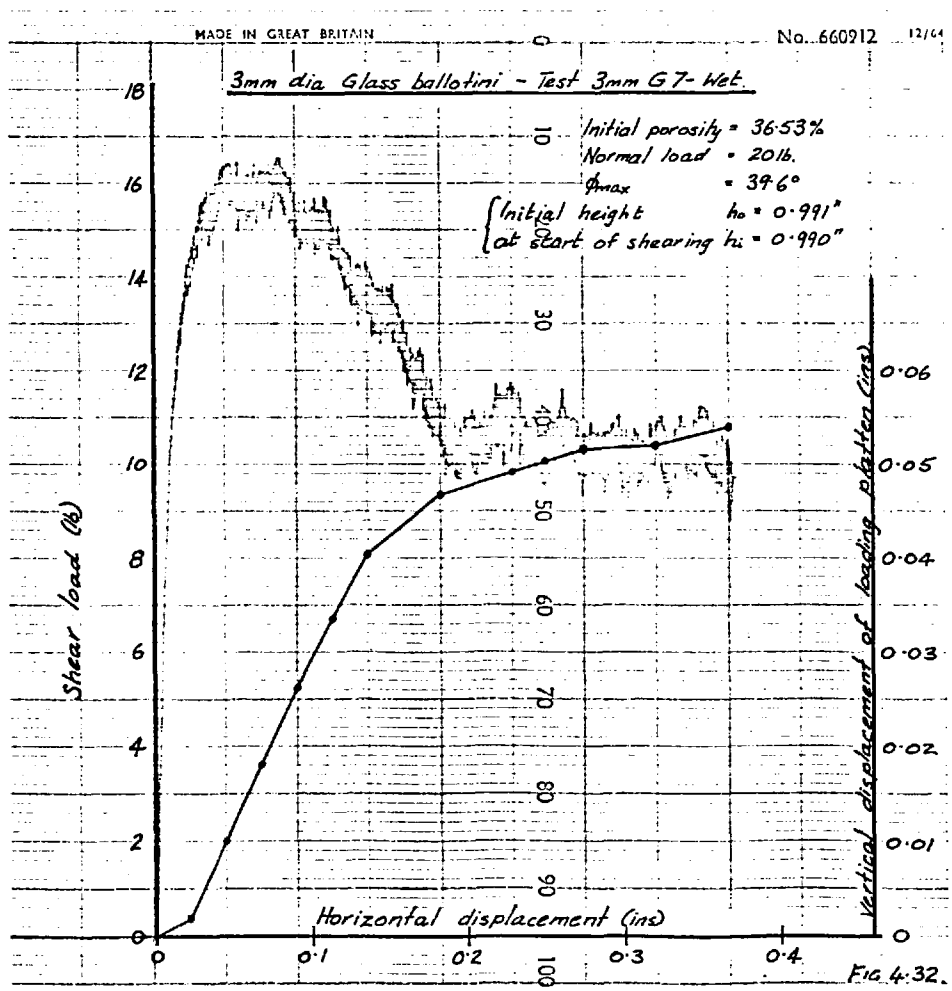


FIG 4·32.

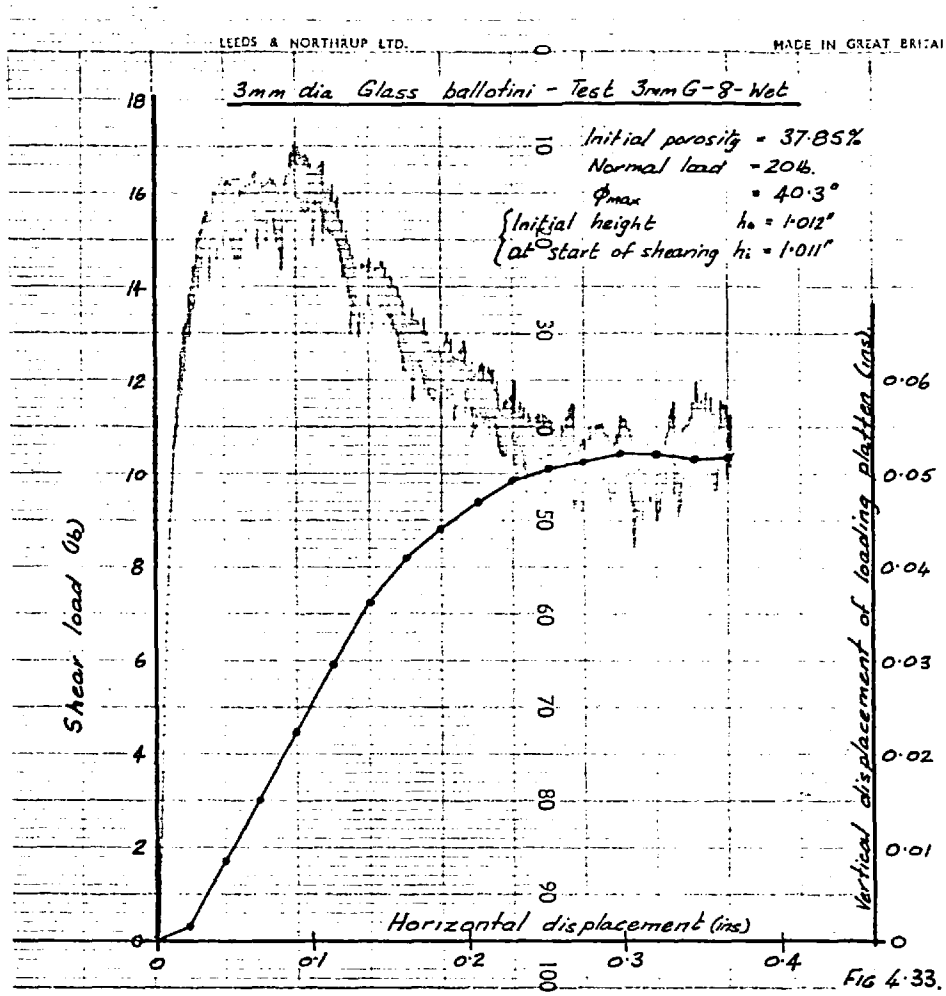


FIG 4·33.

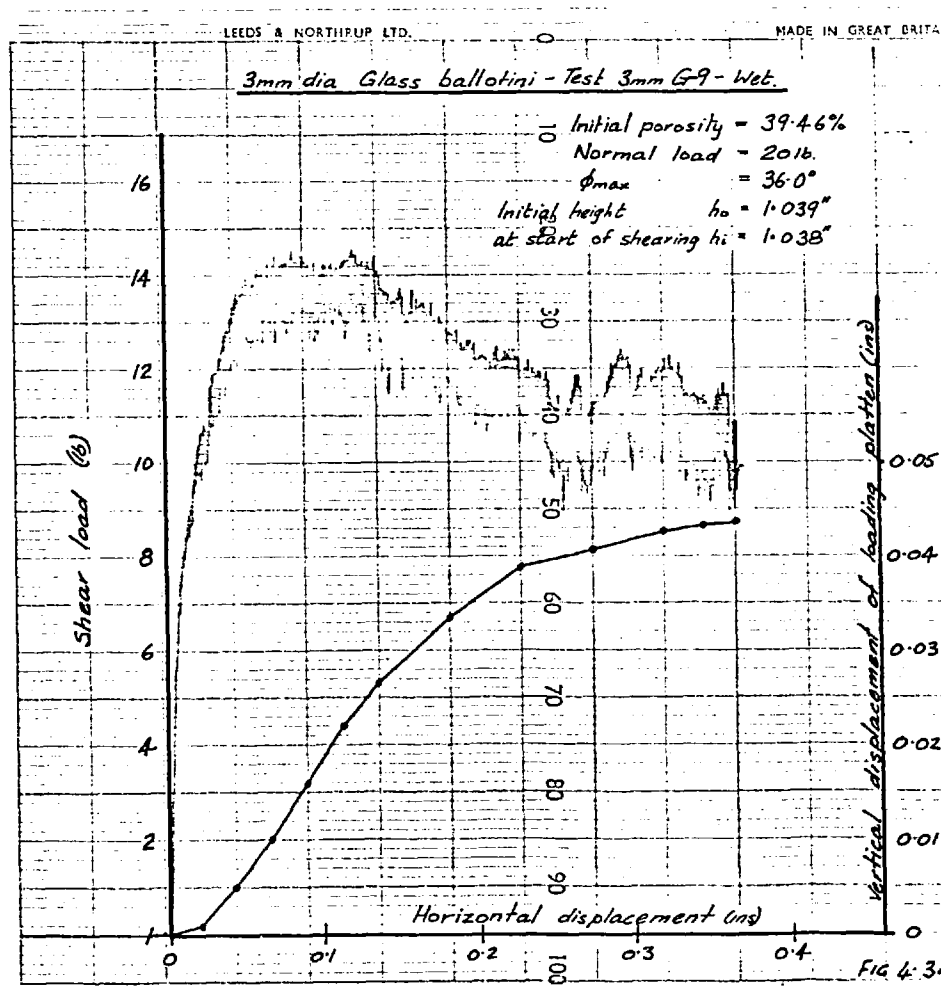


FIG 4·34.

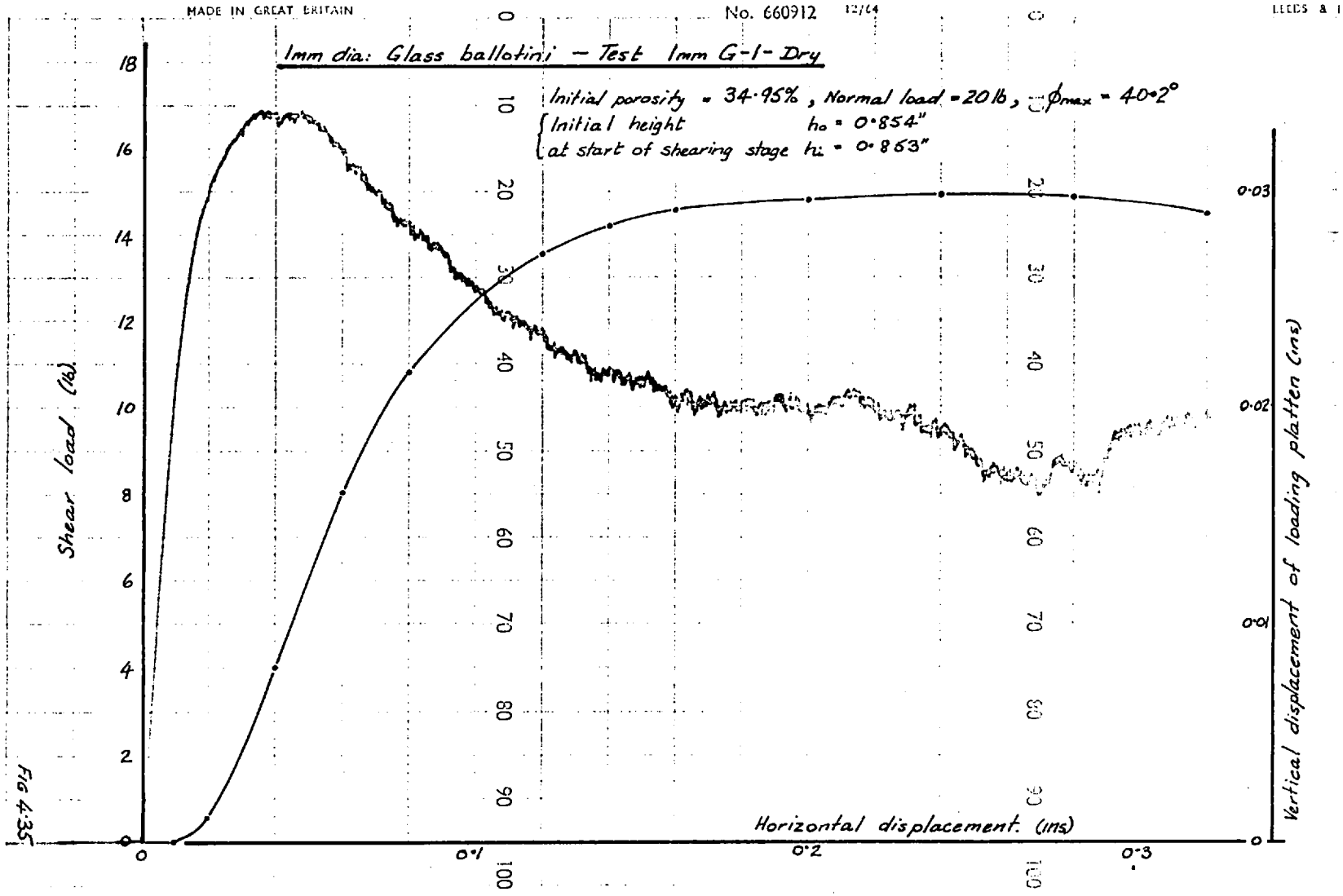
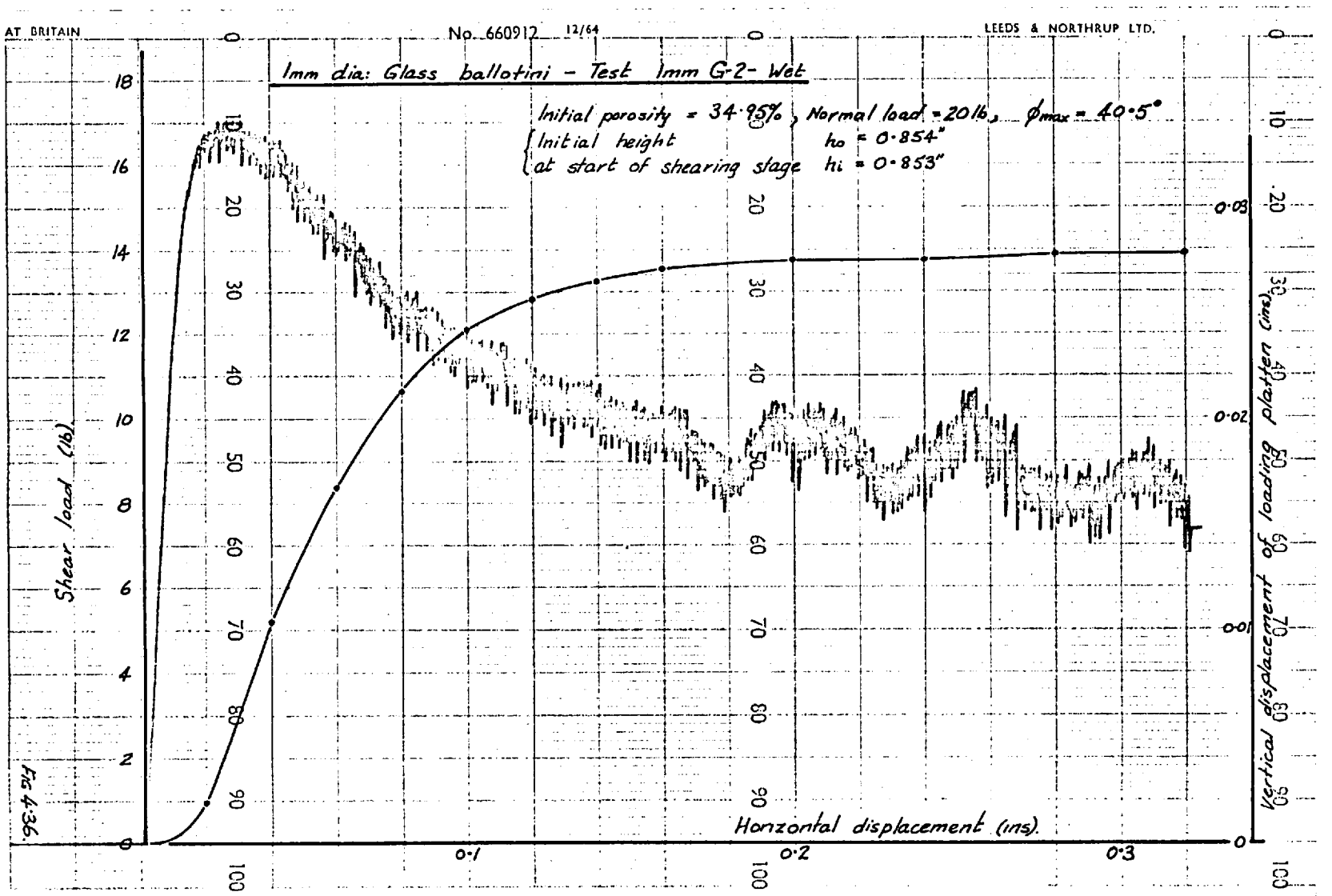

MADE IN GREAT BRITAIN
No. 660912
LEEDS & I
1mm dia: Glass ballotini – Test 1mm G-1- Dry
Initial porosity = 34·95%, Normal load = 20lb, ϕ_{max} = 40·2°
Initial height h_o = 0·854"
at start of shearing stage h_i = 0·863"
Shear load (lb)
Horizontal displacement (ins)
Vertical displacement of loading platten (ins)
0
2
4
6
8
10
12
14
16
18
0·1
0·2
0·3
0·01
0·02
0·03
10
20
30
40
50
60
70
80
90
100

FIG 4·35


AT BRITAIN
No. 660912 12/64
LEEDS & NORTHRUP LTD.
1mm dia: Glass ballotini - Test 1mm G-2- Wet
Initial porosity = 34·95%, Normal load = 20lb, ϕ_{max} = 40·5°
Initial height at start of shearing stage h_o = 0·854"
h_i = 0·853"
Shear load (lb)
Horizontal displacement (ins).
Vertical displacement of loading platten (ins)
Fig 4.36.

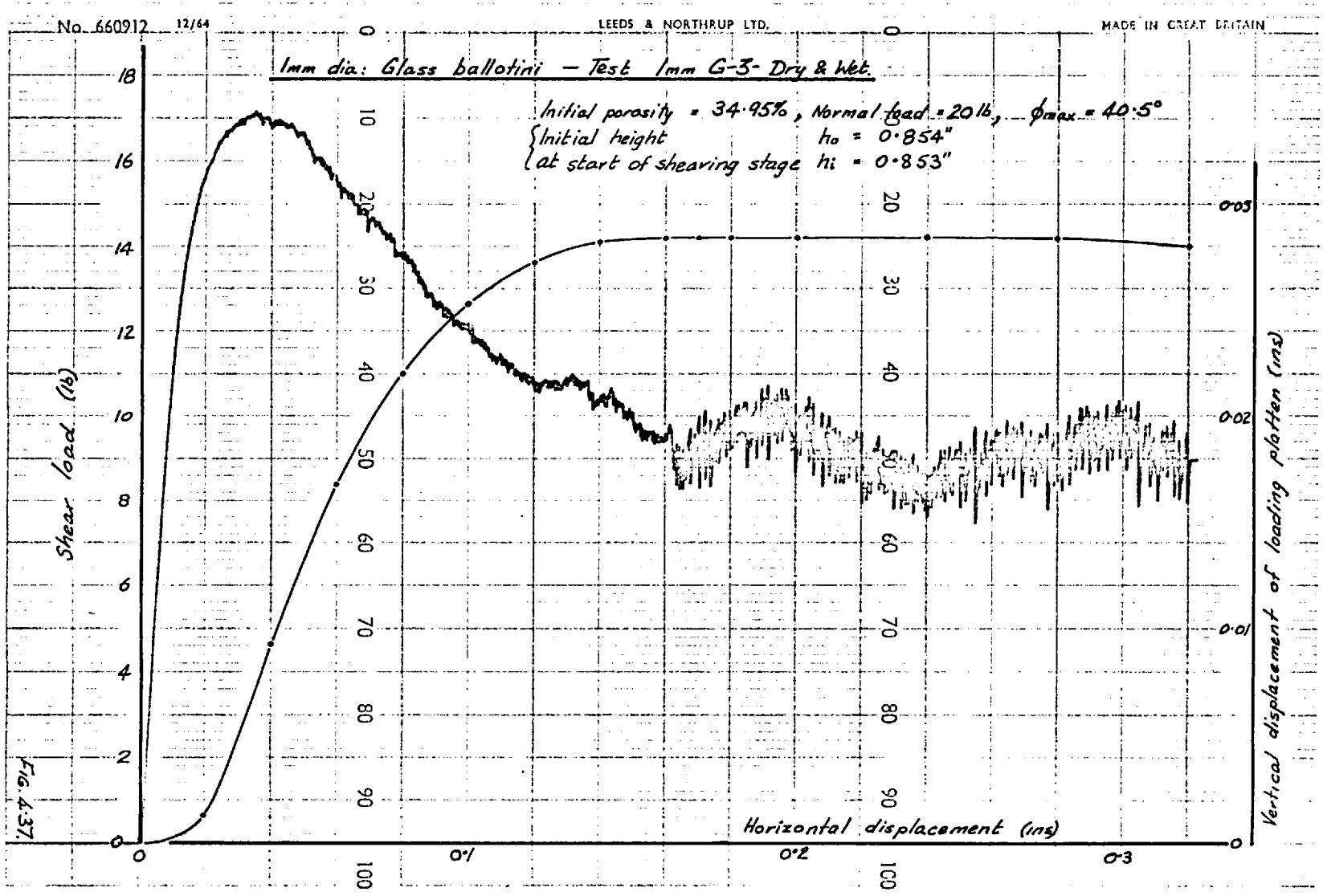

No. 660912 12/64
LEEDS & NORTHRUP LTD.
MADE IN GREAT BRITAIN
1mm dia: Glass ballotini — Test 1mm G-3- Dry & Wet.
Initial porosity = 34·95%, Normal load = 20 lb, φmax = 40·5°
Initial height ho = 0·854"
at start of shearing stage hi = 0·853"
Shear load (lb)
Horizontal displacement (ins)
Vertical displacement of loading platten (ins)
0
2
4
6
8
10
12
14
16
18
0·1
0·2
0·3
0·01
0·02
0·03
10
20
30
40
50
60
70
80
90
100

Fig. 4-37.

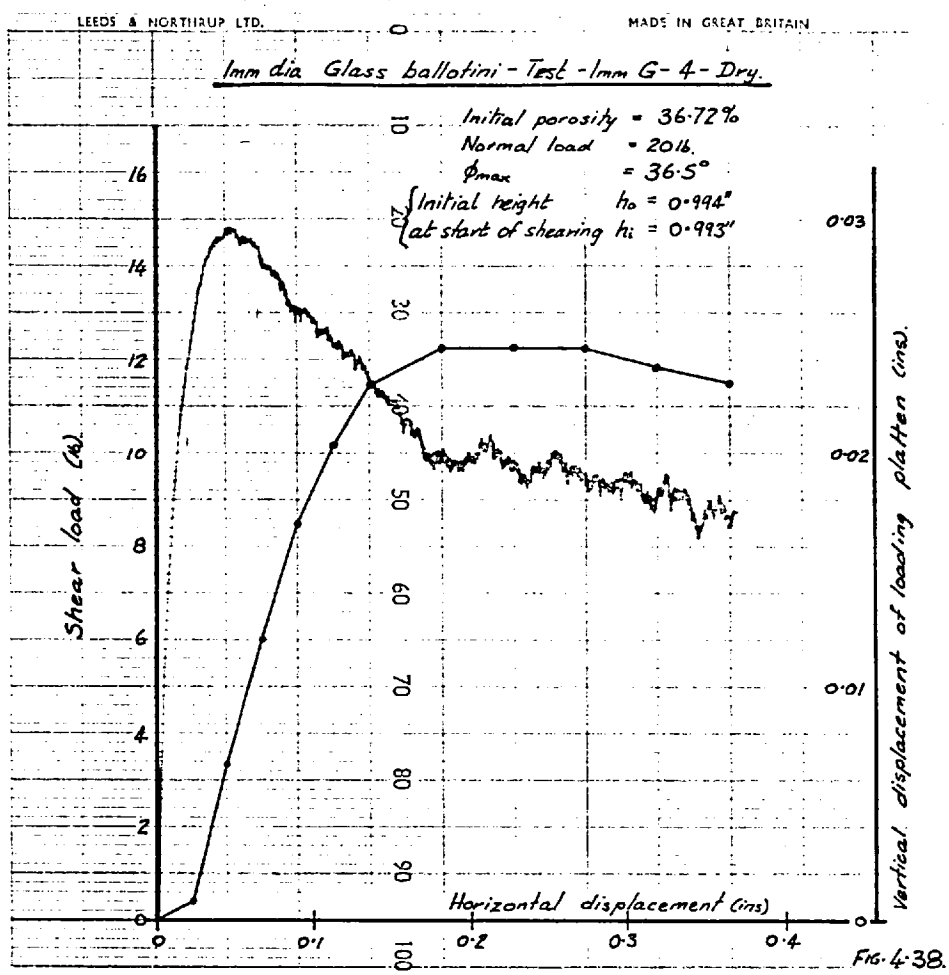


FIG. 4·38.

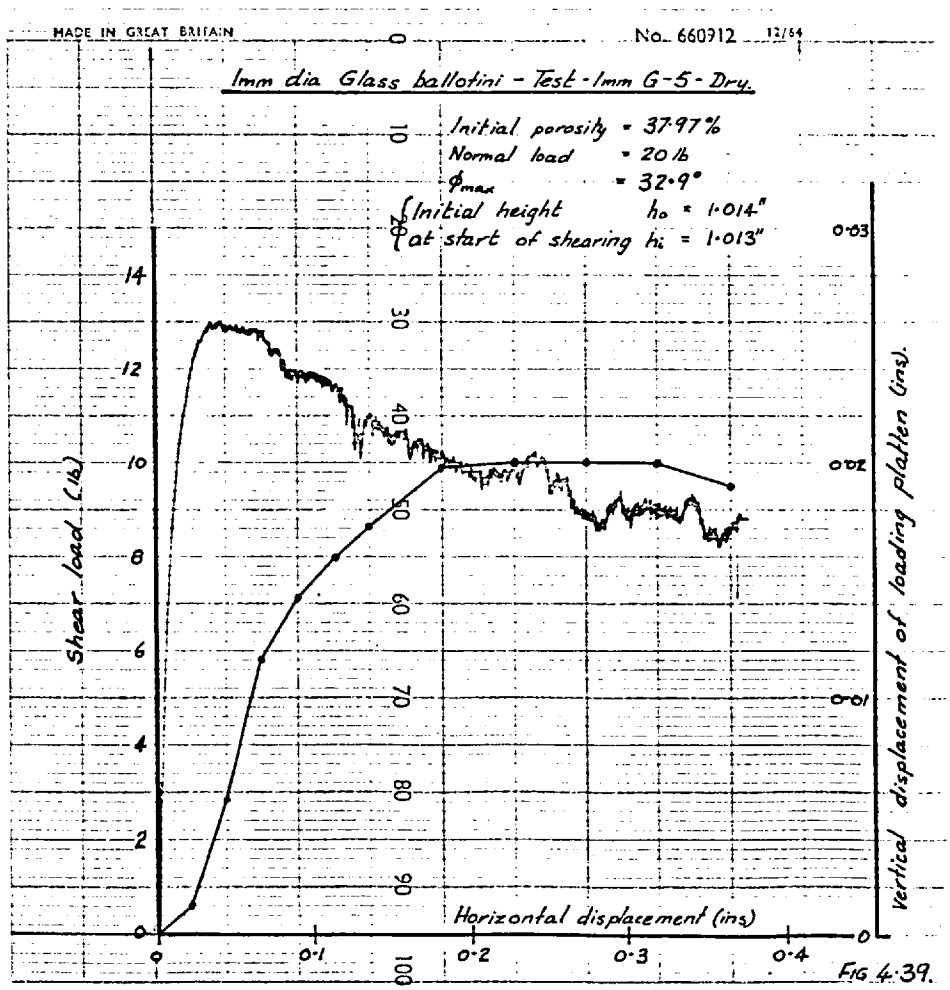


FIG. 4·39.

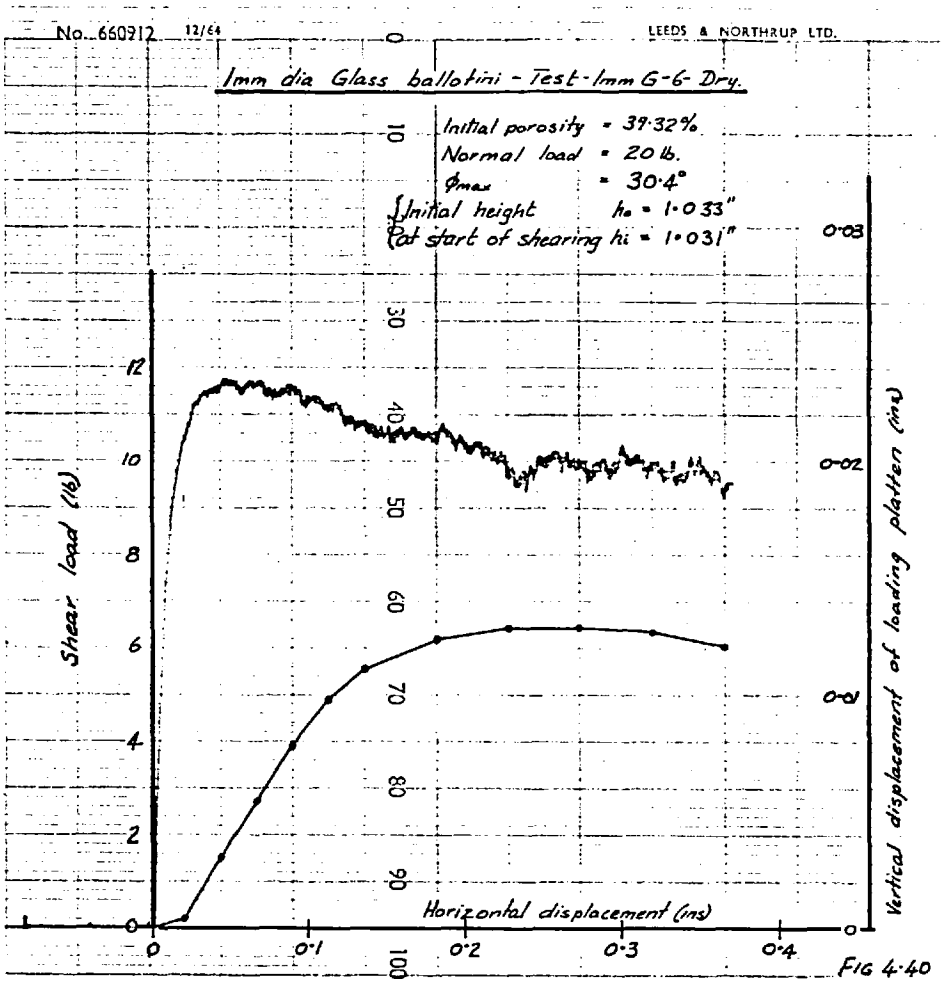


FIG 4·40

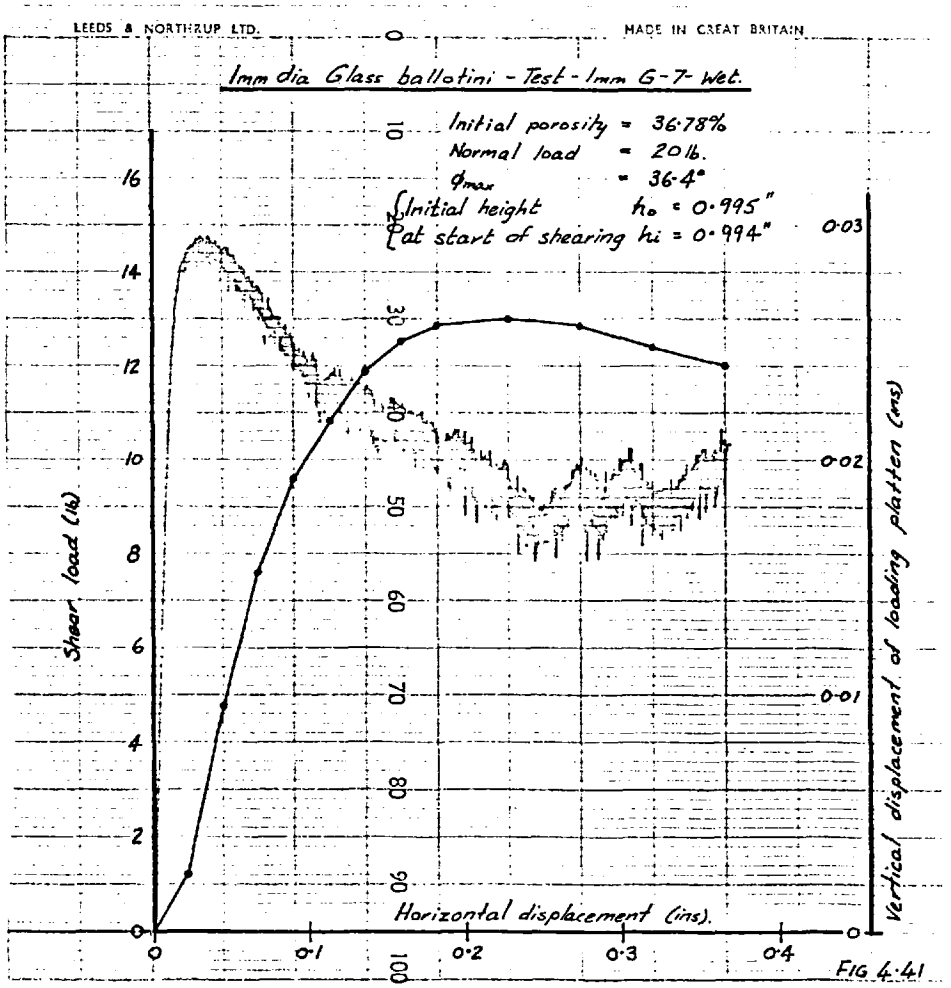


FIG 4·41

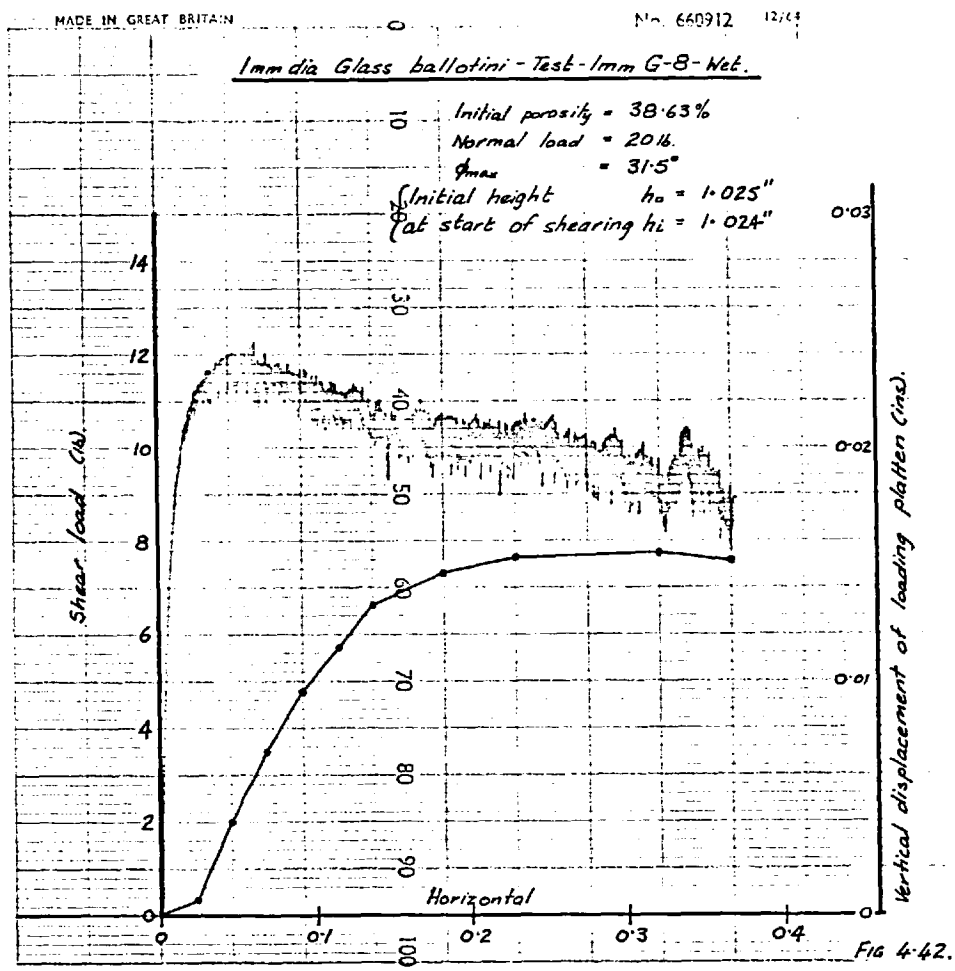

MADE IN GREAT BRITAIN
No. 660912
1mm dia Glass ballotini - Test - 1mm G-8-Wet.
Initial porosity = 38·63%
Normal load = 20lb.
φmax = 31·5°
Initial height h₀ = 1·025"
at start of shearing hi = 1·024"
Shear load (lb).
Horizontal
Vertical displacement of loading platten (ins).
0
2
4
6
8
10
12
14
0·1
0·2
0·3
0·4
0·01
0·02
0·03
10
20
30
40
50
60
70
80
90
100

FIG 4·42.

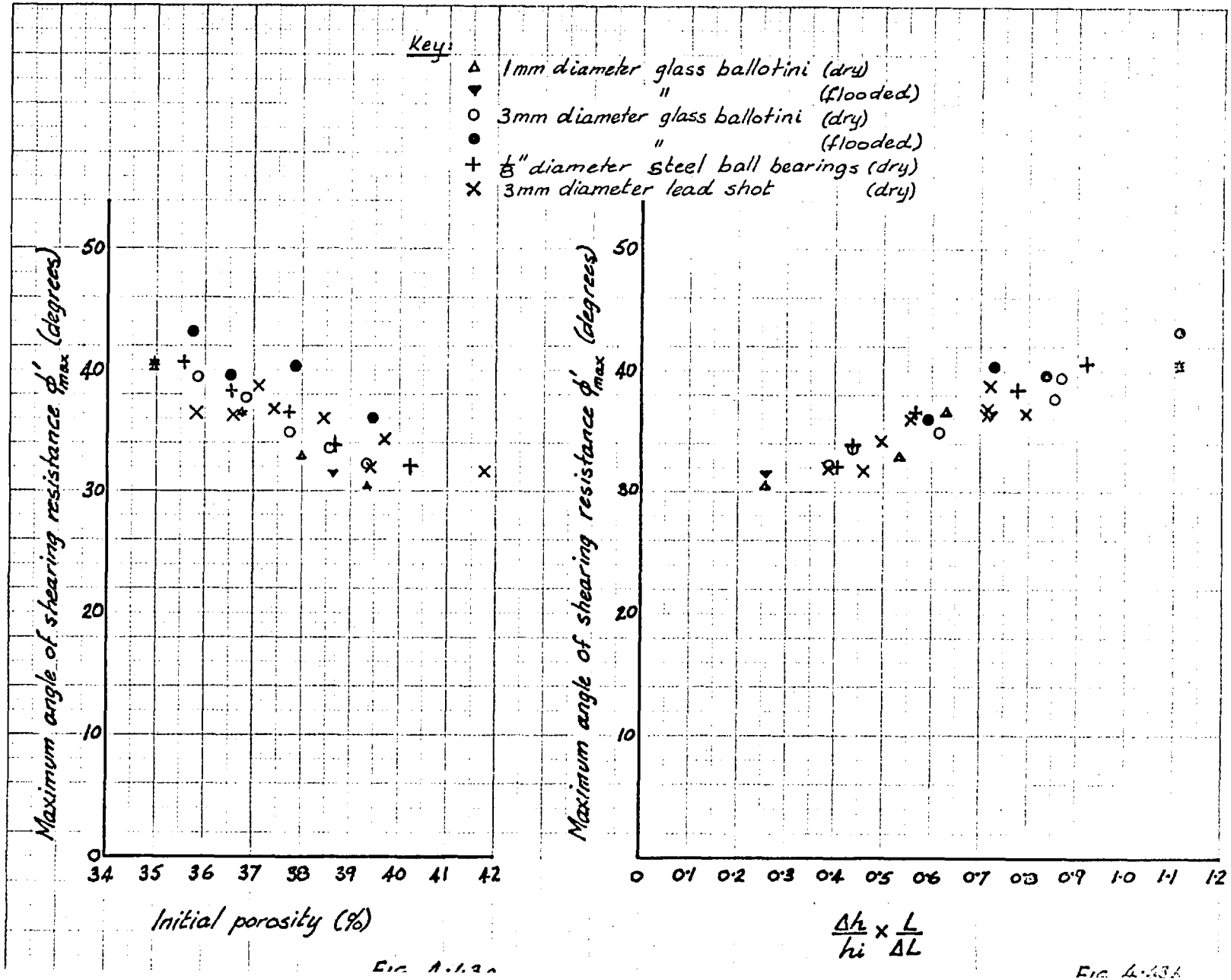


Fig. 4·43a

Fig. 4·43b

Key:
△ 1mm diameter glass ballotini (dry)
▼ 1mm diameter glass ballotini (flooded).
Maximum angle of shearing resistance ϕ'_{max} (degrees)
42°
40°
38°
36°
34°
32°
30°
34
35
36
37
38
39
40
Initial porosity (%)

FIG 4.44.

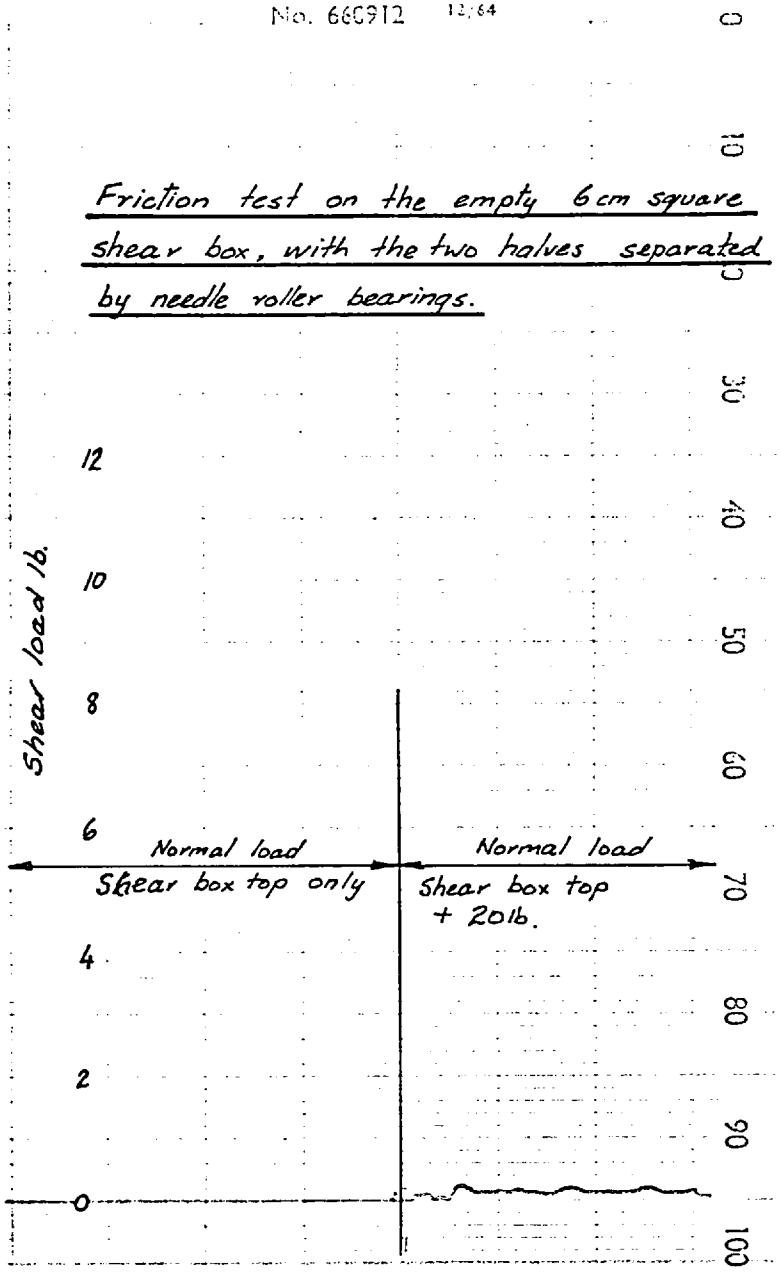

Friction test on the empty 6 cm square shear box, with the two halves separated by needle roller bearings.
Shear load lb.
12
10
8
6
4
2
0
Normal load
Shear box top only
Normal load
Shear box top + 20lb.
0
10
20
30
40
50
60
70
80
90
100

FIG. 4·45.

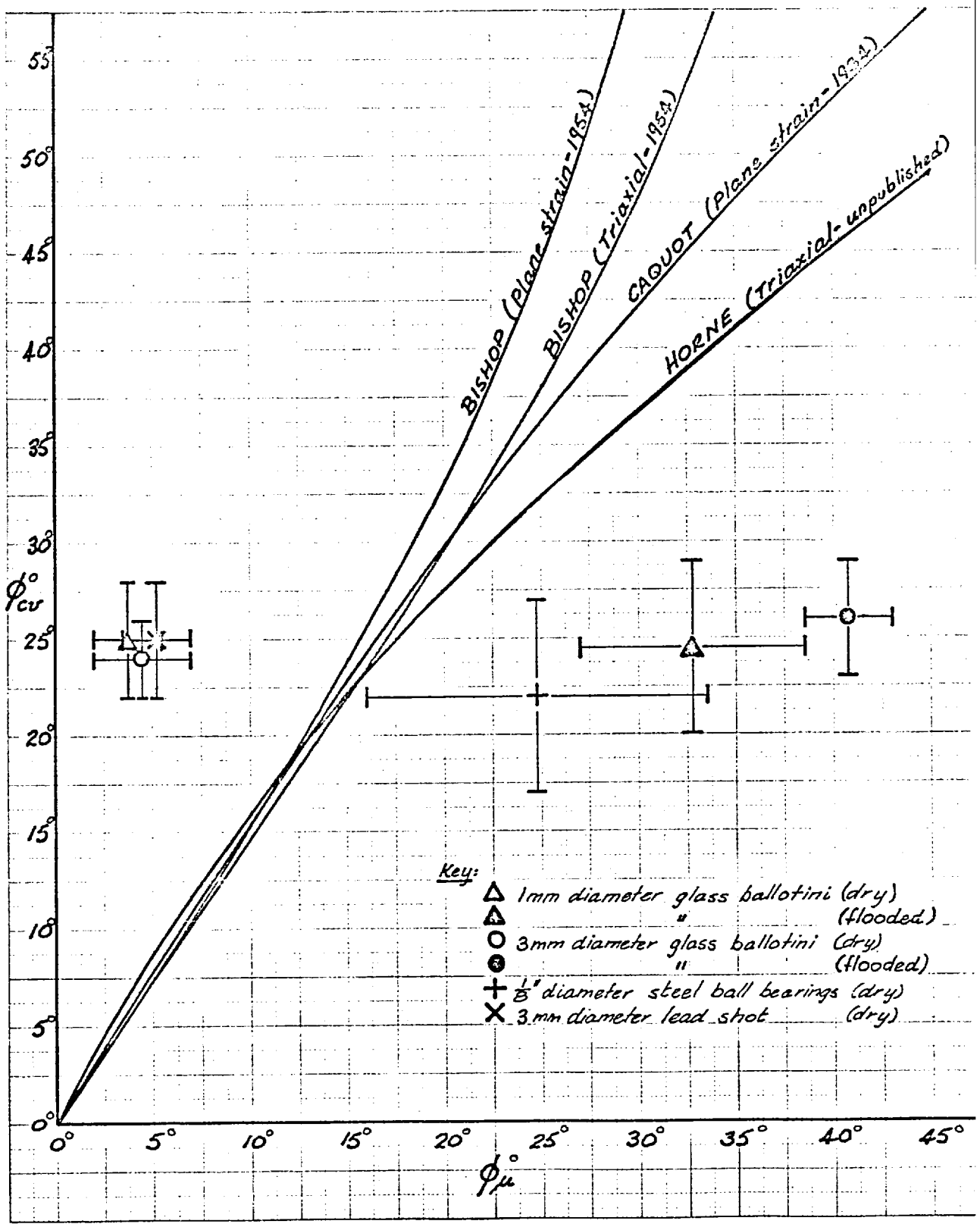

BISHOP (Plane strain - 1954)
BISHOP (Triaxial - 1954)
CAQUOT (Plane strain - 1934)
HORNE (Triaxial - unpublished)
ϕ_{cv}°
ϕ_μ°
0°
5°
10°
15°
20°
25°
30°
35°
40°
45°
50°
55°
Key:
1mm diameter glass ballotini (dry)
" (flooded)
3mm diameter glass ballotini (dry)
" (flooded)
1/8" diameter steel ball bearings (dry)
3mm diameter lead shot (dry)

FIG 4·46

CHAPTER 5

SHEAR CHARACTERISTICS OF PARTICULATE MATERIALS AND THE STRESSES THAT ARE 'EFFECTIVE' IN CONTROLLING THEM

5.1 Introduction:

The previous work (see Chapters 3 and 4) showed that there were many variables that influenced the frictional properties of mineral particles, and consequently we can expect these to play some part in the shear strength exhibited by a mass of particles. Some of these variables are properties of the mineral of which the particles are composed, others are to do with the physical nature of the particles, i.e. shape, surface texture and crystallographic orientation, and finally the nature of the pore fluid itself played an important role.

In this chapter the part played by these variables is considered in relation to the concept of effective stress, related to the strength of a granular material.

In the ensuing discussion 'effective stress' will be taken to mean that stress which controls changes in the strength of the material under consideration.

As will be seen later the concept of effective stress applied to granular soil is rather complex, and so the argument will

be built up step by step - and as the first step we shall consider the following:

5.2 Effective Stress as applied to a Single Solid Body:

We now have to define what is meant by 'strength'. We can say that it is the 'yield strength' or the 'peak strength' or the 'residual strength'. In fact it is best if we say that strength is characterized by the whole of the stress/strain behaviour under particular specified boundary conditions.

Now having defined 'effective stress' and strength, we can look at the elastic and plastic yielding of materials. First take the case of metals which have a stable plastic hardening characteristic such as mild steel and copper. H D Pugh (1964) reports that pressures up to 110,000 psi have no effect on the true stress/strain curves for tensile tests on mild steel, and for tensile tests under pressure up to 44,800 psi, no effect is observed in the stress/strain curve for copper. These results confirm earlier work by Bridgman, who concluded that to a first approximation the strain-hardening curve was independent of pressure. Thus these materials have unique stress/strain characteristics, and therefore the introduction of 'effective stress' is unnecessary.

Secondly, there are those materials whose stress/strain (and so strength) characteristics are significantly influenced

by the hydrostatic component of stress. This is the class into which most of the soil-forming minerals fall. Most of these materials behave in an elastic/brittle mode at low pressures, changing to an elastic/plastic mode at higher pressures. In the elastic range the stress/strain behaviour is generally only slightly influenced by confining pressure; for example in Chapter 3 the compressibility and Young's moduli for quartz were discussed.

However, the fracture or yield stress and plastic flow stress are markedly dependent on confining pressure, and Skempton (1960) has presented data for Calcite, Rock Salt and Quartz. Therefore for these materials it is evident that the 'effective stress' is the confining pressure σ_3 applied to the sample, but the form of the equation connecting the strength to 'effective stress' (i.e. the confining pressure σ_3) will vary from material to material, and could depend on other factors as well, typically temperature and straining rates. For example the temperature has a marked influence on the brittle to ductile transition pressure and also directly influences the flow stress. Straining rate is rather more difficult to deal with, and very little is known about its influence. Most of the data is summarized by M S Paterson (1970), who presents the work of Heard (1963) on Yule marble. Both of these factors are related to changes in the microstructure, and have a significant influence on the strength in the ductile range of behaviour and much smaller influence on the stress/strain characteristic when

the material is brittle.

But apart from noting that temperature and strain rate influence strength, we shall not actively consider them in the following work.

5.3 Effective Stress as applied to two Discrete Solid Bodies in Contact:

Here we are considering strength as 'frictional resistance' between the two bodies in contact under some constant external normal load, both bodies being submerged in a fluid in which the pressure can be varied. We will consider frictional resistance in the form of the coefficient of friction.

The friction of mineral surfaces was considered in detail in Chapter 3, where a theoretical analysis was put forward for the friction of mineral surfaces. The experimental results obtained for clean quartz surfaces were shown to be in satisfactory agreement with the theoretical predictions. The equation for the coefficient of friction is:

$$\mu = \tan \psi + \frac{k}{\sin \psi \left\{ H_v + \sigma_3 \frac{(1 + \sin \psi)}{(1 - \sin \psi)} \right\}} \qquad (3.19)$$

So we see that in this case the 'effective stress' is again the confining fluid pressure σ_3, for a particular value of load/asperity, i.e. H_v = constant.

To the knowledge of the writer no other analysis for the

friction between mineral surfaces has been published, but it is possible to modify the equations presented by Skempton (1960) to make them apply to this case. Skempton (1960) obtained the following equation for the strength of an assembly of particles:

$$\tau_f = c' + (\sigma - u)(\frac{m\beta}{M} + m \tan \psi_s) + a.u.m \tan \psi_s$$

where $c' = a_o.m.\beta.k$

and $a_o = A_{so}/A$

But in the case of solid body friction which we are considering, the factor $m = 1$, $\tau_f = \tau$, and for clean surfaces $\psi_s = \psi$. So we have:

$$\tau_f = \tau = c' + (\sigma - u)(\frac{\beta}{M} + \tan \psi) + a.u \tan \psi$$

But we want to find the coefficient of friction $\mu = \frac{T}{L}$ where the applied load is L, so we must insert the values of $\sigma = \frac{P}{A}$ and $\tau = \frac{T}{A}$. But in this case $P = L + uA$. Thus:

$$\frac{T}{A} = c' + (\frac{P}{A} - u)(\frac{\beta}{M} + \tan \psi) + a.u \tan \psi$$

$$T = c'.A + (P - u.A)(\frac{\beta}{M} + \tan \psi) + A.a.u \tan \psi$$

$$\mu = \frac{T}{L} = \frac{c'.A}{L} + \frac{\beta}{M} + \tan \psi + A.a \frac{u \tan \psi}{L}$$

But $A_s = A.a$, therefore:

$$\mu = (\frac{A_{so}}{A}.\frac{\beta k}{L}.A + \frac{\beta}{M} + \tan \psi) + A_s \frac{u \tan \psi}{L}$$

Again in the case which we are considering we have that

under zero external pressure and zero pore-water pressure the contact area ratio is zero, i.e. $a_o = 0$. Therefore:

$$\mu = \tan \psi + \left(\frac{\beta}{M} + \frac{A_s . u \tan \psi}{L}\right) \qquad (5.1)$$

If the strength of the material in the contact is the same as that of the body of the solid material $\beta = 1$.

However, equation 5.1 can not be used to predict the coefficient of friction of mineral surfaces because the coefficient M depends on the geometry of the asperities, and on the stress-strain characteristics, as does the value of the area of contact of the asperities A_s.

But equation (5.1) shows that the 'effective stress' is the confining pressure at the contacts, i.e. for constant load L on the contacts, u. (Note: u in equation (5.1) is equivalent to σ_3 in equation (3.19)).

Now we have two equations for friction coefficient; the terms in equation (3.19) can be isolated and determined, so that it can be used. It also explains the observed behaviour of materials for which $\psi \to 0$, i.e. clean metals, where gross seizure is observed and hence $\mu \to \infty$. As can be seen from equation (3.19), as $\psi \to 0$, $\sin \psi \to 0$, therefore $\mu \to \infty$. Considering equation (5.1) we see that as $\psi \to 0$, $\tan \psi \to 0$, and $\mu \to \frac{\beta}{M}$. Therefore, for $\mu \to \infty$, M must $\to 0$. But Skempton suggested that when $\psi = 0$, $M = N$, where

$$N = \alpha\sqrt{(1 - \beta^2)} \text{ and } \sigma_y^2 + \alpha^2 . \tau_f^2 = \alpha^2 . k^2$$

However, for clean surfaces $\beta \to 1$, and therefore $N \to 0$, and so again $\mu \to \infty$. So both predict the same type of behaviour.

Now, considering the implications of equation (3.19), we see that for $\psi > 0$ the 'effective stress' is σ_3, and for the special case $\psi = 0$, $\mu \to \infty$, irrespective of the value of σ_3. Therefore in this special case introducing 'effective stress' is again unnecessary. Now most crystal surfaces are not clean in nature, and therefore the above statements may not be correct. However, the analysis in Chapter 3 was extended to cover contaminated surfaces, and the coefficient of friction is given by equation (3.25).

$$\mu_c = \beta \tan \psi + \frac{\beta . k}{\left\{H_v + \sigma_3 \frac{(1 + \sin \psi)}{(1 - \sin \psi)}\right\} \sqrt{(1 - \beta^2 \cos^2 \psi)}}$$

and in this case for $\psi = 0$:

$$\mu_c = \frac{\beta . k}{(H_v + \sigma_3) \sqrt{(1 - \beta^2)}}$$

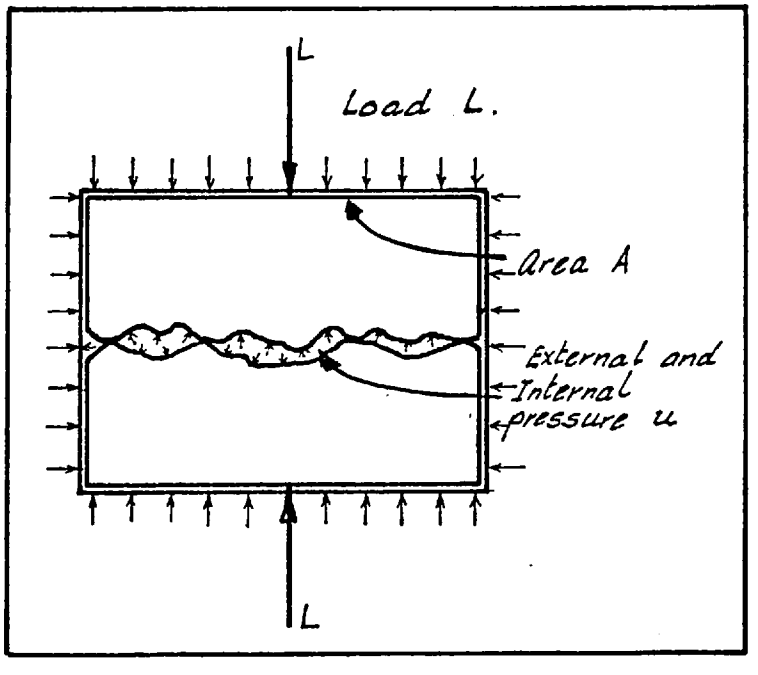
In this case σ_3 remains as the 'effective stress'.

One particular material, quartz, is of interest because much of the later work involves this material. The coefficient of friction for quartz is given in Figure 3.16. The variation to be expected by changing the confining pressure from atmospheric pressure (0 psi gauge) to 9000 psi gauge, depends on the load carried by an asperity, and lies between 0.1% to 1.0% for asperity loads of 2 gm to 1000 gm respectively. These

variations are only just within the discrimination of the experimental tests, and then only for the higher asperity loads. It can be seen, however, that the theoretical predictions were supported by the test results.

Therefore we can say that for the pressures used in these tests, which would in general be much larger than those encountered in engineering practice, strength, as represented by the coefficient of friction, for constant asperity loads, is almost independent of the confining pressure, which is the controlling or 'effective stress'.

As an addendum to the previous argument, we can consider the two blocks to be enclosed in a membrane as shown in the diagram. In this case the confining pressure at the contacts



is u (i.e. it is equivalent to σ_3 in equations (3.19) and (3.25) and to u in equation (5.1)). If now a pressure u

is also applied outside the membrane, there will be no load on the asperities. To make the loading conditions of the system equivalent to the cases discussed, we must apply an external load to the two blocks, say L, which must be kept constant. This load could then be considered as an external stress of magnitude $\frac{L}{A}$. Thus the total external stress σ on the upper and lower boundaries is $\sigma = \frac{L}{A} + u$.

Now, we noted that the coefficient of friction was a function of the load on the asperities (see Figure 3.16 for quartz surfaces). So, since we have shown that the magnitude of u (within the stress range considered) does not significantly change the coefficient of friction, as long as the load L is not altered, we can say that the stress generated by the load L is controlling the frictional behaviour and is therefore the 'effective stress', i.e. the 'effective stress' is $\frac{L}{A} = \sigma'$ $= \sigma - u$. This is the form of the equation which is familiar. So, for constant $(\sigma - u)$, variation of u from 0 psi to 9000 psi only changes the value of μ for quartz by 0.1% to 1.0% depending on asperity load.

We now consider the case where one of the mineral blocks is replaced by a random assembly of mineral particles:

5.4 Mineral Block in contact with a Random Assembly of Mineral Particles:

It will be assumed that the particles move relative to the

mineral block which remains stationary. If the particle geometry remains fixed and sliding takes place only at the contacts between the block and the particles adjacent to the block, then the conditions are the same as discussed in Section 5.3, and the same conclusions would be valid, i.e. the effective stress σ' can be represented by the equation:

$$\sigma' = \sigma - u$$

If, however, the arrangement of the particles in contact with the block is allowed to change, then the direction of movement of the particles need not coincide with the direction of application of the tractive force; this would mean that the magnitude of this tractive force would differ from that generated when the particles are fixed. In addition there would be a contribution (either addition or subtraction) to the energy applied across the boundaries of the sample due to the normal load moving towards or away from the fixed mineral block. Also, as discussed in Chapter 4, there is the possibility that some particles do not slide but rotate on their neighbours, and so the energy dissipated by these particles would be less than that dissipated if they had moved without rolling.

These various possibilities for the deformation mechanism, and hence strength response, makes the analysis for the force which is resisting deformation indeterminate. The only remaining possibility is to investigate experimentally

the stress controlling the strength for this particular arrangement.

In this experimental investigation we have to bear in mind some of the points made previously. This can be done if we consider a particular geometrical arrangement of particles, at a particular instant, during the shearing process. The particle mechanism will be controlled by the external constraints and by the coefficient of friction between the particles and between the particles and mineral block. This coefficient, as we saw previously, will be strongly influenced by the forces between the particles and fractionally so by the hydrostatic stress to which the contact asperities are subjected. Therefore, if the hydrostatic component of stress is increased, both in the pore space, and simultaneously on the external boundaries, the contact forces will not change and therefore there will only be the very small change due to the confining effect of the pore fluid. If this small change affects the particle mechanics and hence the strength of the sample, then the simple equation for effective stress $\sigma' = \sigma - u$ will not be valid. This point is investigated in the next section, where shearing within a mass of particles is considered. However, we must consider the influence of the pore fluid itself. As we saw in Chapters 3 and 4, substituting water for the pore fluid in place of air changed the coefficient of friction of both quartz and glass very significantly. In this case we make no changes to the boundary stresses, and so there is no change in the loads carried at the contact, for

a particular particle geometry; that is, there is no change in what was considered the 'effective stress' previously. However, because of the change in coefficient of friction, there is a change in the strength response for the particular configuration under consideration. The test arrangement described in Chapter 4 for the special tests on glass ballotini fits in with this argument, the test set up being shown in Figure 4.3, and typical results in Figures 4.4 and 4.5. The changes in friction for these materials are shown in Table 4-1 and Figures 4.8 and 4.10.

For the test shown in Figure 4.5 the range of values that could occur in the coefficient of friction between the glass surfaces in the dry and wet conditions was $0.02 < \mu < 0.13$ between the plate and the 3 mm ballotini with air as the pore fluid, and $0.61 < \mu < 0.91$ with water as the pore fluid. Between the ballotini particles the values are $0.03 < \mu < 0.12$ with air as the pore fluid and $0.79 < \mu < 0.93$ with water as the pore fluid. This change in pore fluid resulted in a change in the ratio of shear load T to normal load P from an average value of 0.20 with air as the pore fluid, to an average value of 0.36 with water as the pore fluid. This means that the shear load required nearly doubled for a tenfold increase in the average friction coefficient for the contacts at the plate surface, and the average increase was $11\frac{1}{2}$ times for the contacts between the ballotini themselves. This change in friction coefficient also induced a change in the shear behaviour, made evident

by the increased rate of dilation. Thus it is clear that the mechanics of the particles significantly influence the strength of the particulate mass, for had the particle mechanics not changed, then the shear strength would have changed in the same ratio as the change induced in the friction coefficient.

This test brings out two important points. First, when defining what we mean by 'effective stress' as the stress controlling 'strength', we should be careful to define the strength of the material as the *'resistance to deformation, at a particular instant of the shearing process, of a particular geometry of particles, whose mechanics for that particular instant are strictly specified'.*

And secondly, that factors such as the change of pore fluid, which lead to changes in strength, have to be considered separately, and can not be included in a theory which considers strength changes due only to changes in 'effective stress'.

There is another factor which would influence the strength, this being polymorphic transition of the mineral itself (see Skempton, 1960), and even though this change is controlled by the stresses (and temperature) it has to be excluded from consideration.

We have considered in the previous sections strength and

effective stress for formal configurations, and so we now go on to consider the more general case of shearing within a mass of mineral particles.

5.5. Effective Stress for a Mass of Mineral Particles Subjected to Shear:

Three theories have been advanced for the effective stress applied to soils and these are, taken in order:

a) Terzaghi (1925):

$$\tau_f = c' + (\sigma - u) \tan \phi' \qquad (5.2)$$

i.e. effective stress = $\sigma' = \sigma - u$ (5.3)

For the triaxial test (on non-cohesive materials such as the sand tested)

$$\sigma_1 - \sigma_3 = \frac{2(\sigma_3 - u) \sin \phi'}{1 - \sin \phi'} \qquad (5.4)$$

i.e. for constant $(\sigma_3 - u)$ the curve of $(\sigma_1 - \sigma_3)$ versus axial strain should be unchanged by varying σ_3 and u, this can be written as:

$$\Delta (\sigma_1 - \sigma_3) = 0 \cdot \Delta u \qquad (5.5)$$

b) Skempton (1960):

$$\tau_f = c' + (\sigma - u) \tan \phi' + a.u \tan \psi \qquad (5.6)$$

i.e. effective stress = $\sigma' = \sigma - \left(1 - \frac{a \tan \psi}{\tan \phi'}\right) . u$ (5.7)

Again, for non-cohesive soil, we have for the triaxial test:

$$(\sigma_1 - \sigma_3) = (\sigma_3 - u) \frac{2 \sin \phi'}{1 - \sin \phi'} + a.u \frac{\tan \psi}{\tan \phi'} \cdot \frac{2 \sin \phi'}{1 - \sin \phi'} \qquad (5.8)$$

Therefore for constant $(\sigma_3 - u)$, with u changed by Δu, the change in $(\sigma_1 - \sigma_3)$ is given by:

$$\Delta(\sigma_1 - \sigma_3) = a.\Delta u \frac{\tan \psi}{\tan \phi'} \cdot \frac{2 \sin \phi'}{1 - \sin \phi'} \qquad (5.9)$$

$$\text{or } \Delta(\sigma_1 - \sigma_3) = 2.a.\Delta u \tan \psi . \frac{\cos \phi'}{1 - \sin \phi'} \qquad (5.10)$$

c) Intergranular Stress Theory:

$$\tau_f = c' + (\sigma - u) \tan \phi' + a.u \tan \phi' \qquad (5.11)$$

i.e. effective stress $\sigma' = \sigma - (1 - a)u$ (5.12)

Again for the triaxial test for non-cohesive soil:

$$(\sigma_1 - \sigma_3) = (\sigma_3 - u)\frac{2 \sin \phi'}{1 - \sin \phi'} + a.u.\frac{2 \sin \phi'}{1 - \sin \phi'} \qquad (5.13)$$

and for constant $(\sigma_3 - u)$ and u changed by Δu we get:

$$\Delta(\sigma_1 - \sigma_3) = 2.a.\Delta u. \frac{\sin \phi'}{1 - \sin \phi'} \qquad (5.14)$$

Here again we are constrained to an experimental approach to discriminate between the three theories outlined above.

The experimental technique, as mentioned in the previous section, consists of increasing the hydrostatic component of the stress system on a cylindrical sample in a triaxial cell; the apparatus used for these tests is described in Chapter 2. The tests were consolidated drained triaxial tests, and during the shear stage of these tests both the confining pressure σ_3 and the pore water pressure u were simultaneously changed, so that $\sigma_3 - u$ = constant. For the tests with small differences

between confining pressure and pore water pressure, it was possible to do this automatically by subtracting the pressure due to a column of mercury of constant height from σ_3, thus ensuring the condition of $\sigma_3 - u$ = constant. But, for those tests with values of $\sigma_3 - u$ in excess of 60 psi, the change in σ_3 and u had to be done manually. It was very difficult to maintain exact rates of change for σ_3 and u, and this meant that the value of $(\sigma_3 - u)$ changed slightly, producing significantly large changes in the shear load and sample volume change. Therefore comparisons between strength for various different values of hydrostatic component of stress could not be made because the particle geometry and mechanics were different for the different conditions. This difficulty was not fully overcome, but two other techniques were tried; both of these were more successful but not completely satisfactory. The first of these was to temporarily stop the straining machine and to close the drainage line, thus isolating the sample. Then the cell pressure was changed to the new value required, the back pressure system adjusted to give the previous value of $\sigma_3 - u$, and then the drainage line re-opened. There are two drawbacks to this method; the first is that a small change in geometry occurs due to the differential compressibility of the pore water and soil grains, which could lead to a change in the strength of the sample, and secondly, the valves used were high pressure shut-off valves, which introduced a volume change in the back pressure line, which was not completely reproduceable. Thus it could not rigorously be said that the particular

strength response was not due to a change in sample volume during the process of changing the hydrostatic stress. Nevertheless, fairly good results were obtained using this method, the test shown in Figure 5.6 (test A7) being of this type.

The second method for large (σ_3 - u) values was to shear the sample partly, then unload it and at this stage to change the cell and pore water pressure simultaneously to their new values, and then to carry out a second shear stage under the new conditions. This technique gave more reproduceable results, but it still introduced some volume change during the unloading and reloading cycles. Tests using this technique are shown in Figures 5.7, 5.8, 5.9 and 5.10, test numbers A8 and A10.

Tests using the mercury column 'pressure subtracting' technique were also run on Ham River sand, Braehead silt, crushed marble and lead shot, and these tests are shown in Figures 5.1 to 5.5 and 5.11 to 5.15.

To compare the theoretical and experimental results, it is necessary to know what the contact area ratio 'a' is. Skempton (1960) defines this term thus: $a = \frac{A_s}{A}$ where A_s = area of solid contact and A = gross area parallel to contact; therefore the value of A_s has to be known. We can say that although it is not possible to find the exact value of A_s, the previous work on friction enables the range of possible

values of A_s to be determined, assuming that all the particles in contact carry equal loads ranging from 2 gm to 1000 gm, and that the only mechanism is particle slip, which is in accord with the theories to be compared.

In a triaxial sample, for the condition that $\frac{\tau}{\sigma'_n}$ is a maximum, the inclination of the shear surface to the horizontal is given by θ, where $\theta = 45^\circ + \frac{\phi'_m}{2}$ where ϕ'_m is the current ϕ mobilized, and the stress carried by the particles normal to this plane (following the argument given in the addendum to Section 5.3) is given by:

$$\sigma'_n = \frac{(\sigma'_1 - \sigma'_3)}{2} \left(\frac{1}{\sin \phi'_m} - \sin \phi'_m\right)$$

where $\sigma'_n = \sigma_n(\text{total}) - u$ (5.15)

But $$\sin \phi'_m = \frac{\sigma'_1 - \sigma'_3}{\sigma'_1 + \sigma'_3}$$

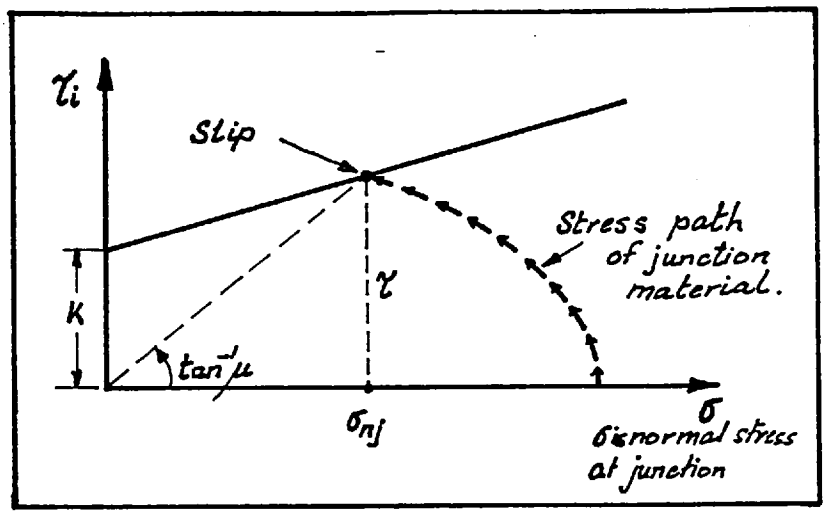
Therefore:

$$\sigma'_n = \frac{(\sigma'_1 - \sigma'_3)}{2} \left\{\frac{(\sigma'_1 + \sigma'_3)}{(\sigma'_1 - \sigma'_3)} - \frac{(\sigma'_1 - \sigma'_3)}{(\sigma'_1 + \sigma'_3)}\right\} \quad (5.16)$$

And from the friction coefficient for quartz under junction loads of a) 2 gm, and b) 1000 gm, i.e. $\mu = 0.4$ and $\mu = 0.8$ respectively, we get the normal stress across the junctions from the intrinsic strength envelope (see Figure on next page).

At slip $\mu = \frac{\tau}{\sigma_{nj}}$, and so $\sigma_{nj} = \frac{\tau}{\mu}$. But at slip we also have that:

$$\tau = k + \sigma_{nj} \tan \psi$$



Therefore $\mu\sigma_{nj} = k + \sigma_{nj} \tan \psi$

And so:

$$\sigma_{nj} = \frac{k}{(\mu - \tan \psi)} \qquad (5.17)$$

For quartz k = 9600 kg/cm^2, and $\psi = 16\frac{1}{4}^\circ$.

For the two limiting cases considered we get the normal stress σ_{nj} as:

$$1.26 \times 10^6 \text{ psi} > \sigma_{nj} > 2.69 \times 10^5 \text{ psi} \qquad (5.18)$$

Hence, from (5.16) and (5.17) we get the area ratio 'a' where $a = \frac{\sigma'_n}{\sigma_{nj}}$.

Substituting in the values of σ_{nj} from 5.18 we have:

$$\frac{\sigma'_n}{1.26 \times 10^6} < a < \frac{\sigma'_n}{2.69 \times 10^5} \text{ where } \sigma_n \text{ is in psi} \qquad (5.19)$$

We are now in a position where theoretical predictions and experimental results can be compared.

Ham River Sand:

1. *Test shown in Figure 5.2 (Test A3):*

$$\sigma_3 - u = 52.6 \text{ psi}$$

Consider the first increase of u from 97.4 to 3947.4 psi, i.e. $\Delta u = 3850$ psi at an axial strain of 9.403%.

$$\sigma_1 - \sigma_3 = 135.2$$

So $\sigma_1' + \sigma_3' = 135.2 + 105.2 = 240.4$

Therefore:

$$\sigma_n' = \frac{135.2}{2} \left(\frac{240.4}{135.2} - \frac{135.2}{240.4}\right) \text{ psi}$$

$$\sigma_n' = 67.6 \ (1.778 - 0.562) = 67.6 \times 1.216 = 82.2 \text{ psi}$$

Therefore:

$$6.52 \times 10^{-5} < a < 3.06 \times 10^{-4}$$

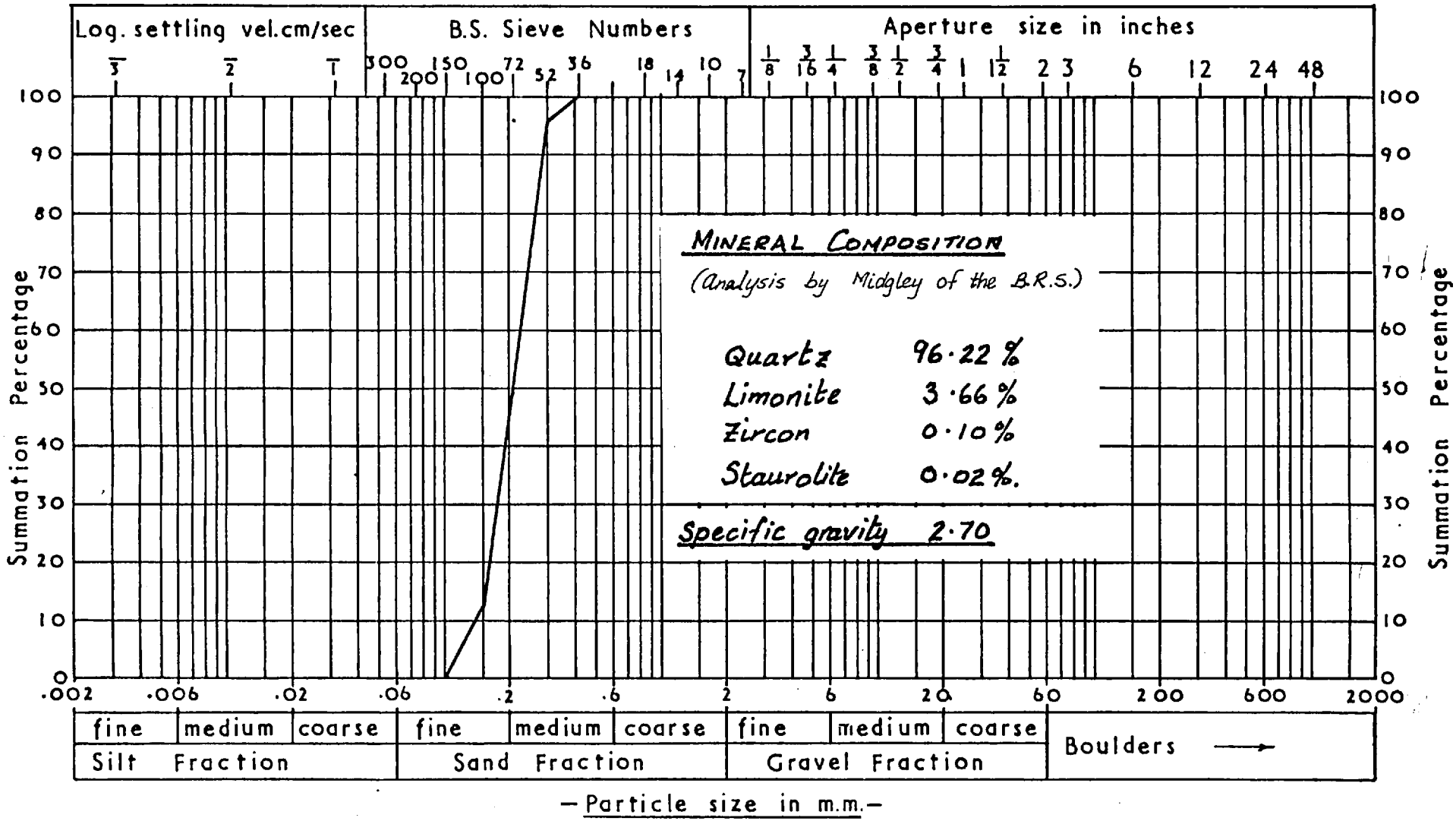
Now substituting into the equations for $\Delta(\sigma_1 - \sigma_3)$ for the three theories, and taking $\psi = 16\frac{1}{4}^{\circ}$ for quartz:

	a	b	c
$\Delta(\sigma_1 - \sigma_3)$ psi	0	Between 0.28 and 1.29	Between 0.64 and 3.02

From the test the value of $\Delta(\sigma_1 - \sigma_3)$ is, for all practical purposes, equal to zero.

Differences of about $\frac{1}{2}$% in the values of $(\sigma_1 - \sigma_3)$ would just give detectable jumps in the stress/strain curve for this test. This would correspond to values of $\Delta(\sigma_1 - \sigma_3)$ of approximately 0.7 psi, and since the

Description HAM RIVER SAND.



average particle size is approximately 0.2 mm diameter, it is probable that the load per particle is less than $\frac{82.2 \times 454}{(25.4 \div 0.2)^2} = 2.2$ gm.

This implies that theory c)would fall in the range where discrimination is just possible, and the test results do not support it - but one could not say that it is entirely disproved by these tests where $\sigma_3 - u$ is low.

As for the other two theories, Terzaghi's and Skempton's, the tests are not discriminating enough to verify one or the other.

2. *Test shown in Figure 5.6 (Test A7):*

For this test $(\sigma_3 - u) = 1002.6$ psi, and we shall consider the part of the test where $\Delta u = +6000$ psi, at an axial strain of 7.52%.

$$\sigma_1 - \sigma_3 = 1852 \text{ psi}$$

So $\sigma_1' + \sigma_3' = 1852 + 2005.2 = 3857.2$ psi

And $\sigma_n' = \frac{1852}{2} \cdot \left(\frac{3857.2}{1852} - \frac{1852}{3857.2}\right) = 926(2.083 - 0.480)$

$= 1484.4$ psi

Therefore $1.18 \times 10^{-3} < a < 5.52 \times 10^{-3}$.

Substituting into the equations for $\Delta(\sigma_1 - \sigma_3)$ we get:

	a (eq 5.5)	b (eq 5.10)	c (eq 5.14)
$\Delta(\sigma_1 - \sigma_3)$	0	Between 6.95 and 32.51	Between 13.07 and 61.15

Here again differences of about ½% would give detectable jumps in the curve, this corresponding to values of $\Delta(\sigma_1 - \sigma_3)$ equal to about 10 psi. The test data show that there is no jump in the curve, i.e. $\Delta(\sigma_1 - \sigma_3) \doteq 0$, indicated by the continuing shape of the curve, and the best fit is really given by the Terzaghi theory, i.e. $\sigma' = \sigma - u$. But here again one can not irrefutably discard theories b) and c) because in this test a substantial amount of particle breakage occurs, and thus again interparticle loads may be low.

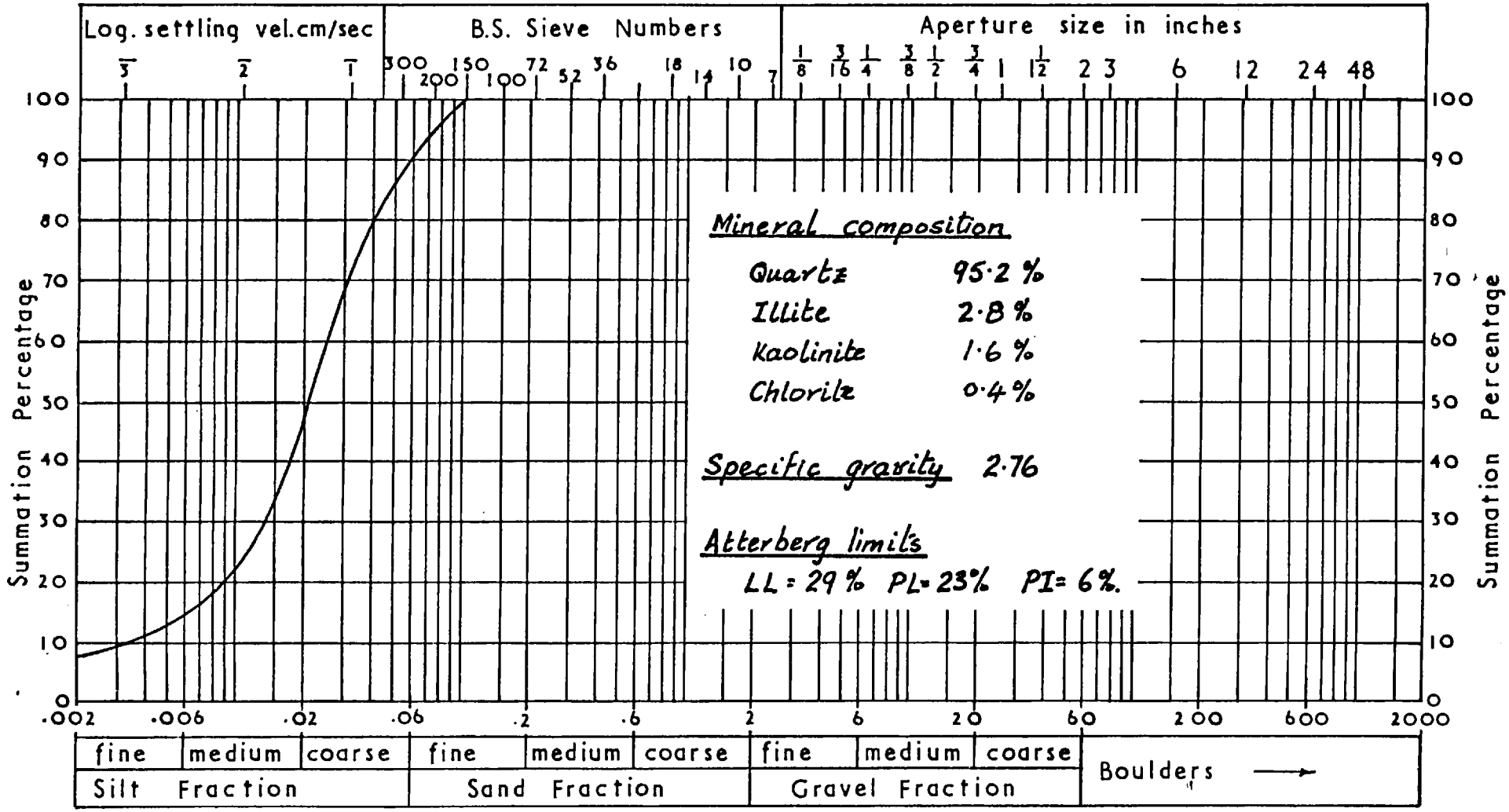
The tests for higher values of $(\sigma_3 - u)$ do not give as much discrimination as the test just analysed, because the value of Δu is restricted by the capabilities of the equipment. We can, however, note that the changes in $(\sigma_1 - \sigma_3)$ are clearly due to changes in the geometry of the particles during the unloading-pressure change-reloading cycle, as an increased strength is obtained for both increasing and decreasing hydrostatic component (see Figures 5.7 to 5.10, tests A8 and A10). The test data used for Figure 5.9 (test A10) are replotted in Figure 5.10, together with two consolidated drained tests run without change in the cell pressure. This figure shows clearly that the strength increases are caused by decreases in voids ratio during each of the unloading-pressure change-reloading stages.

We now pass on to consider the other materials tested.

Braehead Silt:

This material is composed mainly of quartz, as can be seen

Description BRAEHEAD SILT.



— Particle size in m.m. —

PARTICLE SIZE DISTRIBUTION

from the particle size curve, the median particle size is about ten times smaller than the sand tested.

So, if similar arguments are used for the tests on this material, we should expect to find the stress/strain curve unaltered by changing the hydrostatic component of stress. This conclusion is seen to be verified by the tests shown in Figures 5.11 and 5.12. Therefore for this material we can say that the effective stress σ' given by the equation $\sigma' = \sigma - u$ is valid for the stress range of the tests.

Crushed Marble:

No direct friction tests were done for this material. However, it is possible to calculate a value from the friction theory. Micro indentation hardness is 240 kg/mm^2, and from Skempton (1960) - for calcite - k = 1900 kg/cm^2 and $\psi = 8^\circ$. Using equation (3.19) with $\sigma_3 = 0$:

$$\mu = \tan \psi + \frac{k}{H_v \sin \psi}$$

Hence $\mu = 0.7$

This can be compared with the range of values obtained by Horn and Deere (1962) for saturated conditions; namely 0.6 to 0.68.

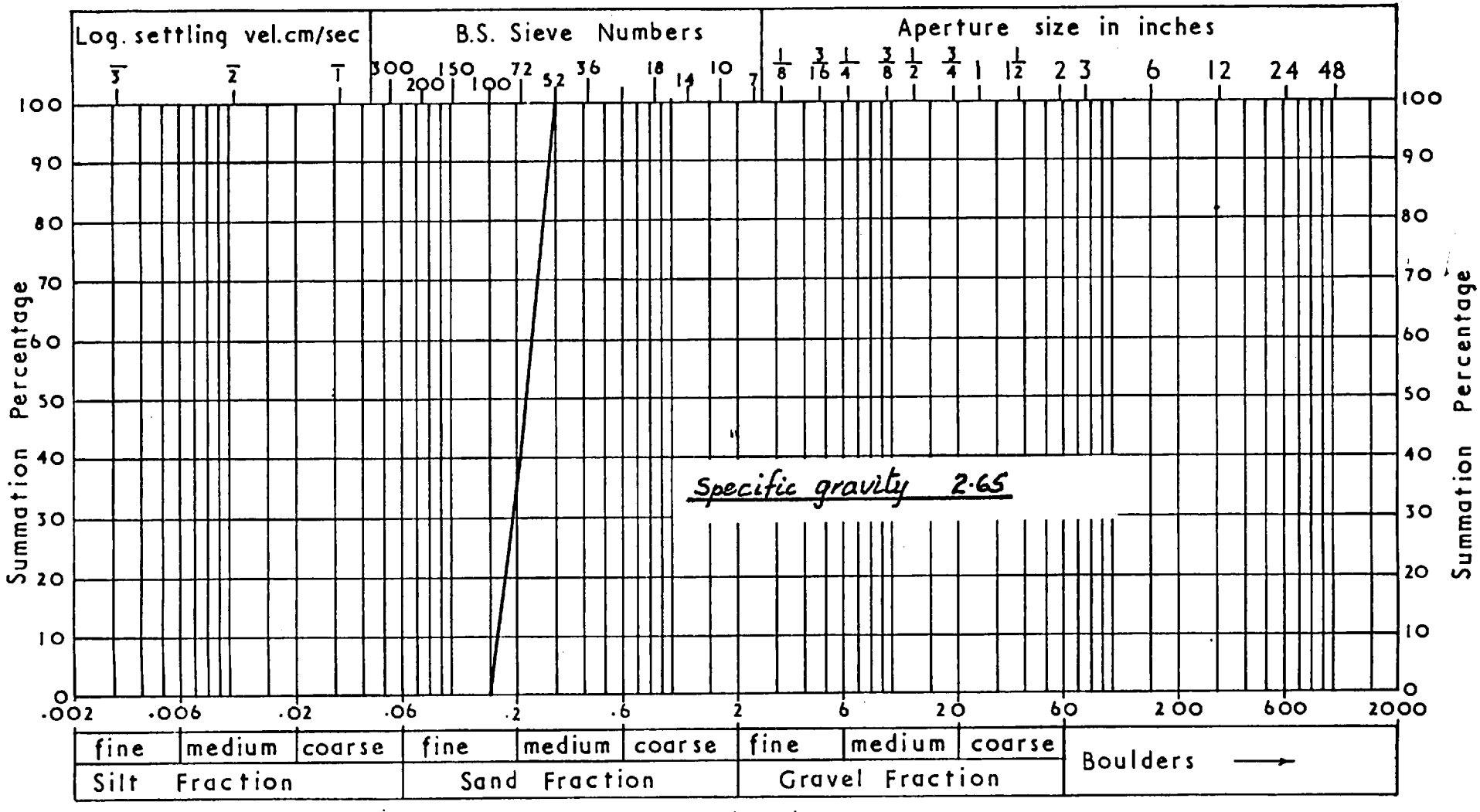
Test shown in Figures 5.13 and 5.14:

$$\sigma_3 - u = 10 \text{ psi}$$

Consider the first increase of u, i.e. $\Delta u = 950$ psi:

$$(\sigma_1 - \sigma_3) = 34.94 \text{ psi}, \quad (\sigma_1' + \sigma_3') = 54.94 \text{ psi}$$

Description CRUSHED MARBLE



PARTICLE SIZE DISTRIBUTION

So: $\sigma_n' = \frac{34.94}{2}\left(\frac{54.94}{34.94} - \frac{34.94}{54.94}\right) = 17.47\ (1.572 - 0.636)$

$\sigma_n' = 16.4$ psi

Now using equation 5.17:

$$\sigma_{nj} = \frac{1900 \times 14.22}{0.7 - 0.14} = \frac{27{,}018}{0.56} = 48{,}246 \text{ psi}$$

Therefore:

$$a = \frac{16.4}{48{,}246} = 3.40 \times 10^{-4}$$

and so $\Delta(\sigma_1 - \sigma_3)$ should be as shown in the table below:

	a (eq 5.5)	b (eq 5.10)	c (eq 5.14)
$\Delta(\sigma_1 - \sigma_3)$ psi	0	0.2	1.4

The experimental data clearly do not support theories b) or c). The stress/strain curve for this test is shown in Figure 5.14 to an expanded scale with a false origin, so that only the relevant data is shown. It is clear that even a change of the order of 0.2 psi could have easily been seen. The only theory to follow the experimental behaviour is Terzaghi's theory, i.e. effective stress $\sigma' = \sigma - u$.

Lead Shot:

Uniform particle size of 1 mm.

Specific gravity $G_s = 11.39$.

Coefficient of friction $\mu = 0.1$.

Indentation hardness $H_v = 950$ kg/cm^2, and taking lead to be a nearly perfect plastic material, we can say that the

value of k can be obtained from the relationship between the flow stress and indentation hardness, i.e.

$$H_v = 3Y \text{ and } 2k = Y$$

i.e. $$k = \frac{H_v}{6}$$

So: $$k = \frac{950}{6} = 158 \text{ kg/cm}^2$$

(Skempton (1960) gives values for lead as k = 100 kg/cm^2 and $\psi = \frac{3}{4}^\circ$.) We shall use the value of k = 158 kg/cm^2, but we shall adopt Skempton's value of $\psi = \frac{3}{4}^\circ$.

Test shown in Figure 5.15:

$$\sigma_3 - u = 52.6 \text{ psi}$$

Consider the first increase of u, i.e. Δu = 3850 psi at an axial strain of 9.24%, $\sigma_1 - \sigma_3$ = 179.2 psi. So:

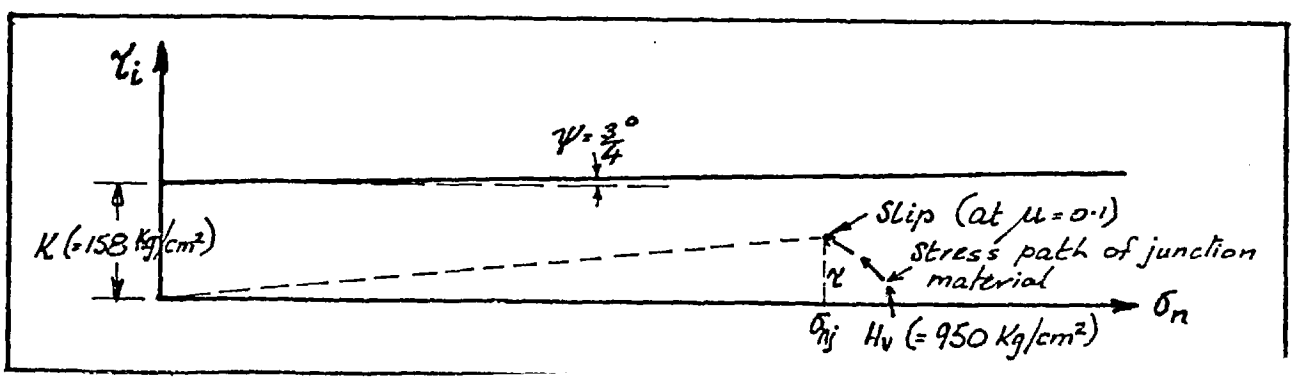
$$(\sigma_1' + \sigma_3') = 284.4 \text{ psi}$$

Therefore:

$$\sigma_n' = \frac{179.2}{2}\left(\frac{284.4}{179.2} - \frac{179.2}{284.4}\right) = 89.6\ (1.587 - 0.630)$$

So: $$\sigma_n' = 85.7 \text{ psi}$$

In this case we can not use the friction analysis as before, because it is evident that the friction is controlled by surface films on the lead.



If no junction growth takes place and the friction is controlled by the bulk properties of the lead, then we should have expected a friction coefficient of the order of 0.17, but we measured a value of 0.1; therefore we can expect only a little junction growth (see diagram). Therefore, in the analysis of this test we shall assume no junction growth, which gives the smallest area ratio. Therefore area ratio $a = \frac{85.7}{950 \times 14.22} = 0.0064$, and so $\Delta(\sigma_1 - \sigma_3)$ should be as shown in the table below:

	a (eq 5.5)	b (eq 5.10)	c (eq 5.14)
$\Delta(\sigma_1 - \sigma_3)$ psi	0	1.34	83

Again the experimental data do not support theories b) or c); in fact $\Delta(\sigma_1 - \sigma_3) = 0$. Thus we can say that the effective stress is given by $\sigma' = \sigma - u$.

These triaxial tests with systematic variation of σ_3 and u, keeping $(\sigma_3 - u)$ constant, have shown that the inter-granular stress concept for effective stress is not valid. Of the two remaining theories the experimental data agree with the simple expression due to Terzaghi, namely that the effective stress $\sigma' = \sigma - u$. However, the precision of the data is such that the discrimination between the theory due to Skempton (1960) and the Terzaghi theory is on the limit of the resolution of the data. This is not to imply that the data are in any way imprecise, but rather that the two theories yield solutions which are extremely close.

Any attempt to improve techniques would not be able to resolve

this problem. The only remaining way would be to substantially increase the pressure range of the equipment to enable much larger values of Δu to be obtained.

However, as has been repeatedly stressed, the comparisons between theory and experiment are only valid if the mechanism of deformation of the particles is restricted to frictional slip. Now, since the effect of increasing the hydrostatic component of stress is to decrease (marginally) the friction between the particles, this should therefore decrease the strength of the granular sample. But, as we have seen, it appears not to have this effect. This implies that the particle mechanism must change to allow the sample to have the same strength. To investigate this point tests were performed with glass ballotini, which enabled tests to be carried out with the same material but with radically different coefficients of friction, this change being associated with different pore fluid, namely air and water.

These tests are reported in Chapter 4. Making reference to the tests reported in Figure 4.44 and the corresponding interparticle friction values in Figure 4.9, it is seen that for small loads on the particles the average increase in the coefficient of friction is from $\mu = 0.04$ to $\mu = 0.54$ when changing from dry to wet conditions, and yet this large change produces no change in strength. The argument presented in Chapter 4 indicates that this result is due to a change in the mechanics of the particles caused by

the change of interparticle friction. It follows that the effective strength of this type of sample cannot be dissociated from the mechanics of the individual particles. Therefore, in this respect, the mechanism of pure sliding of the particles as used by Skempton (1960) for these materials and for the stress range used would not be correct.

One other factor that plays an important role in the shear behaviour of granular material is particle fracture. The influence of this factor, apart from absorbing additional energy, would be to alter the mechanics of the particles in contact with the grains being fractured, therefore invalidating the conditions imposed by only considering the changes in resistance of a particular particle geometry with a particular instantaneous deformation mechanism.

No study was made of the influence of fracture, but it is interesting to speculate that, for example, in a test on a material composed of grains of quartz and calcite, if the hydrostatic component was increased sufficiently, in the same way as in the tests reported previously, then because of the difference in compressibility of the two materials, internal shear stresses large enough to cause changes in structure could result and so modify the strength. So we could expect in this case that the stress equation $\sigma' = \sigma - u$ to be invalid.

However, apart from this interesting speculation, the results

presented support this very simple Terzaghi equation:

$\sigma' = \sigma - u$.

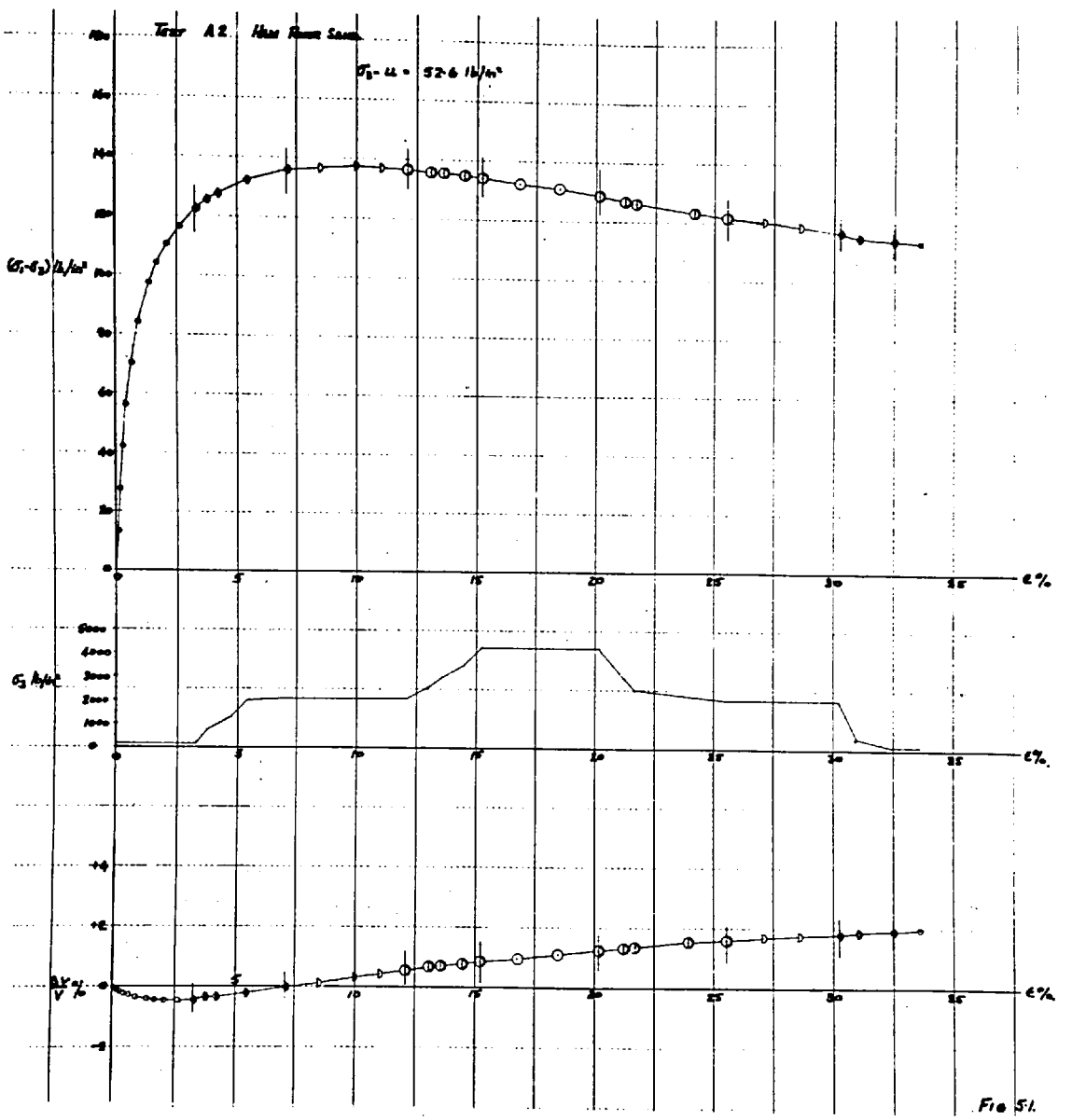


Fig 5·1.

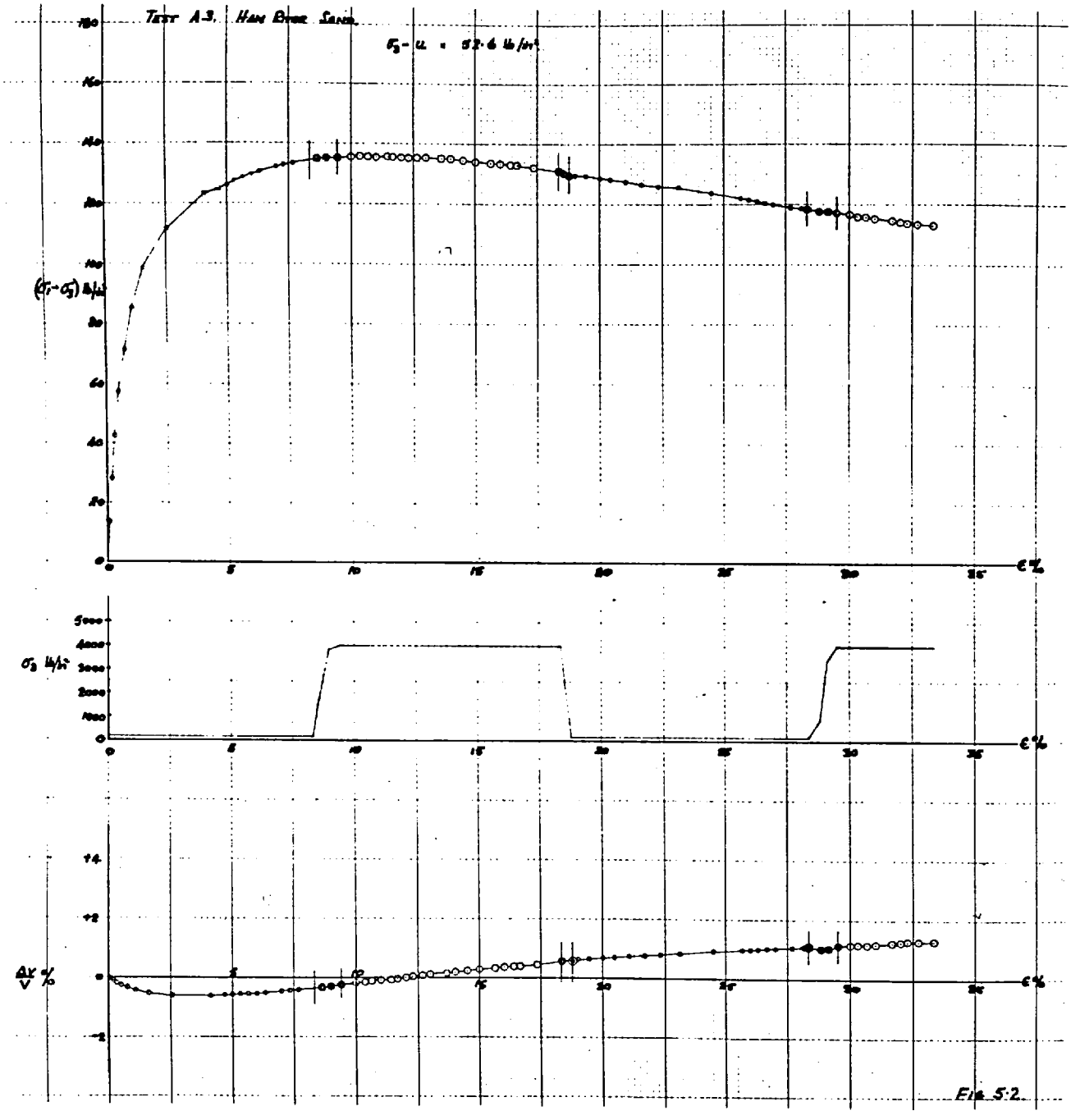

TEST A-3. HAM BONE SALEM.
σ_3 = 52.6 lb/in²
$(\sigma_1-\sigma_3)$ lb/in²
σ_3 lb/in²
$\frac{\Delta V}{V}$ %
ε %

FIG. 5.2.

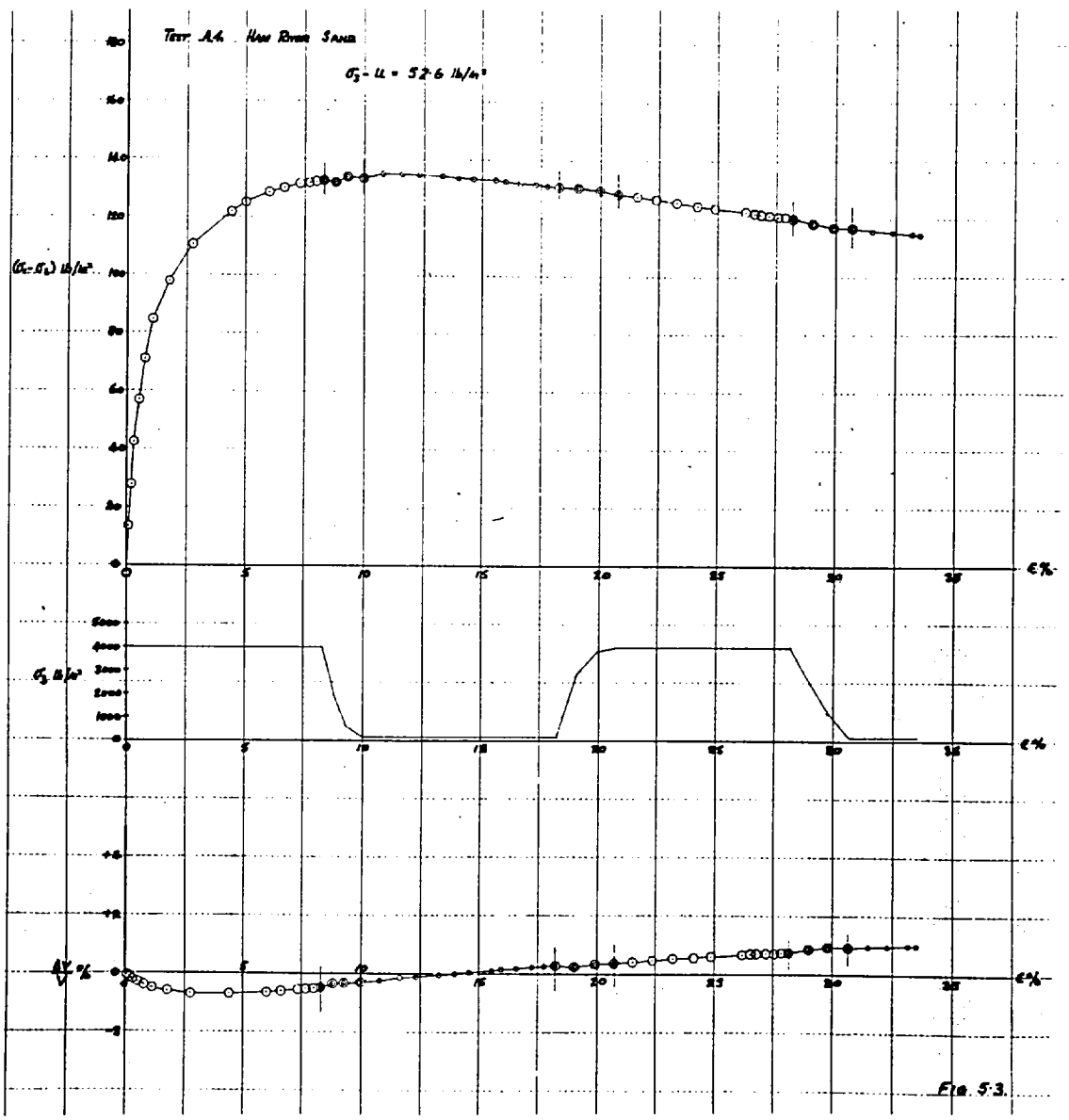

Test A.4. Ham River Sand
σ_3 - u = 52.6 lb/in²
$(\sigma_1 - \sigma_3)$ lb/in²
σ_3 lb/in²
ε%
ε%
ε%
Δv/v %

Fig. 5.3.

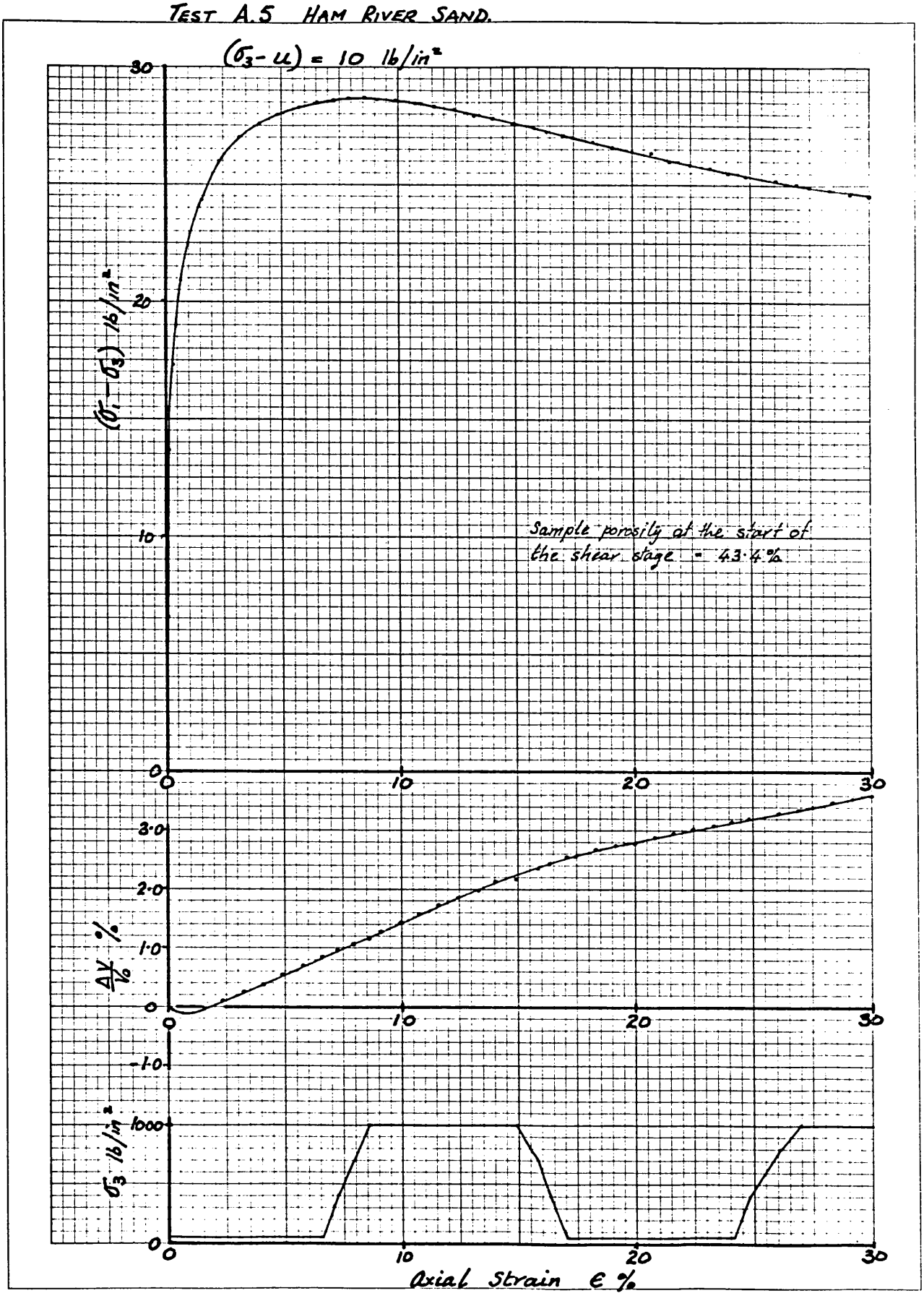

TEST A.5 HAM RIVER SAND.
$(\sigma_3 - u)$ = 10 lb/in²
$(\sigma_1 - \sigma_3)$ lb/in²
30
20
10
0
Sample porosity at the start of the shear stage - 43·4%
0
10
20
30
$\frac{\Delta V}{V}$ %
3·0
2·0
1·0
0
-1·0
σ_3 lb/in²
1000
0
Axial Strain ε %

FIG 5·4.

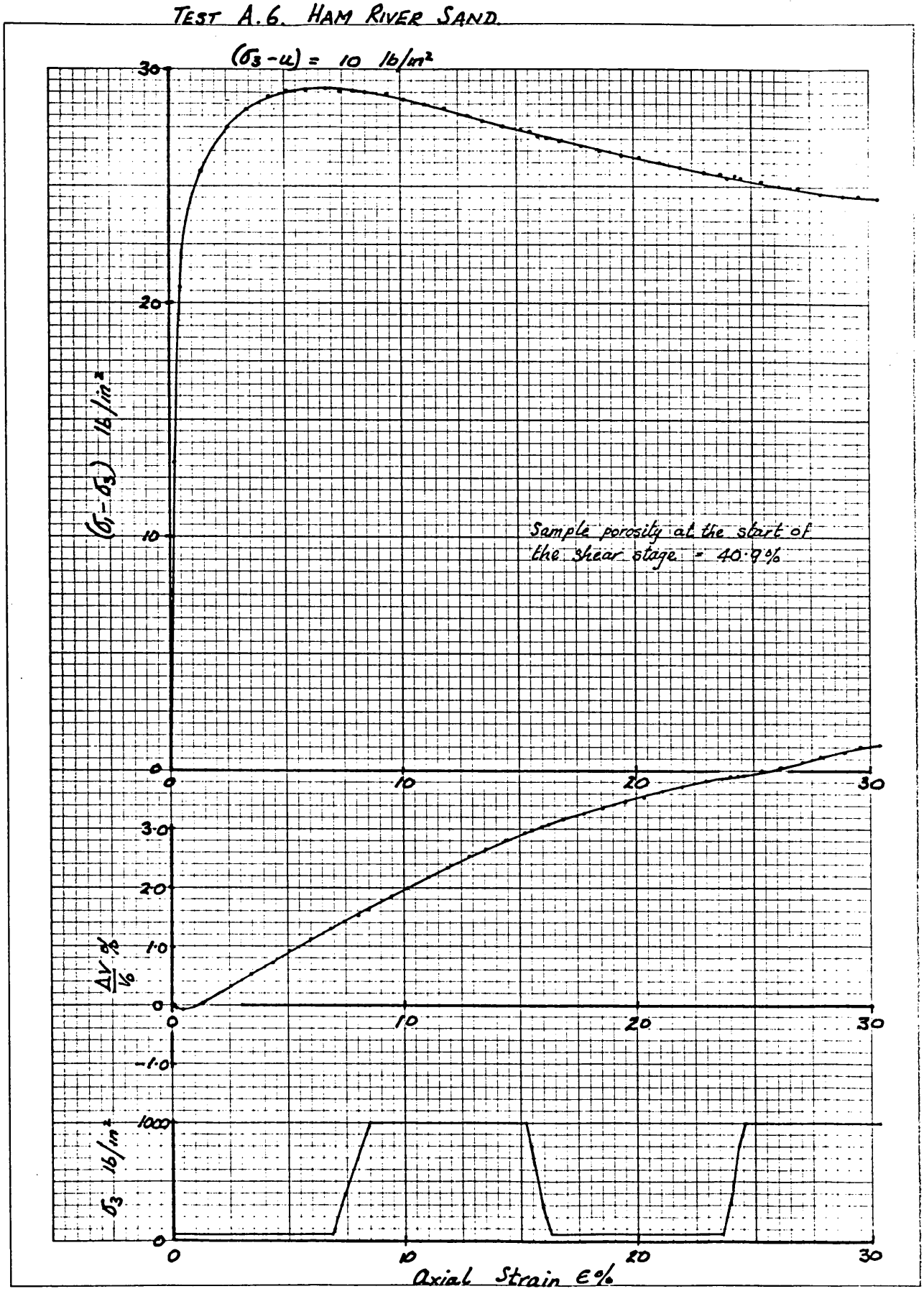

TEST A.6. HAM RIVER SAND.
$(\sigma_3 - u)$ = 10 lb/in²
$(\sigma_1 - \sigma_3)$ lb/in²
Sample porosity at the start of the shear stage = 40·9%
$\frac{\Delta V}{V_0}$ %
σ_3 lb/in²
Axial Strain ε%

FIG 5·5.

TEST A.7. HAM RIVER SAND

$(\sigma_3 - u) = 1002{\cdot}6$ lb/in²

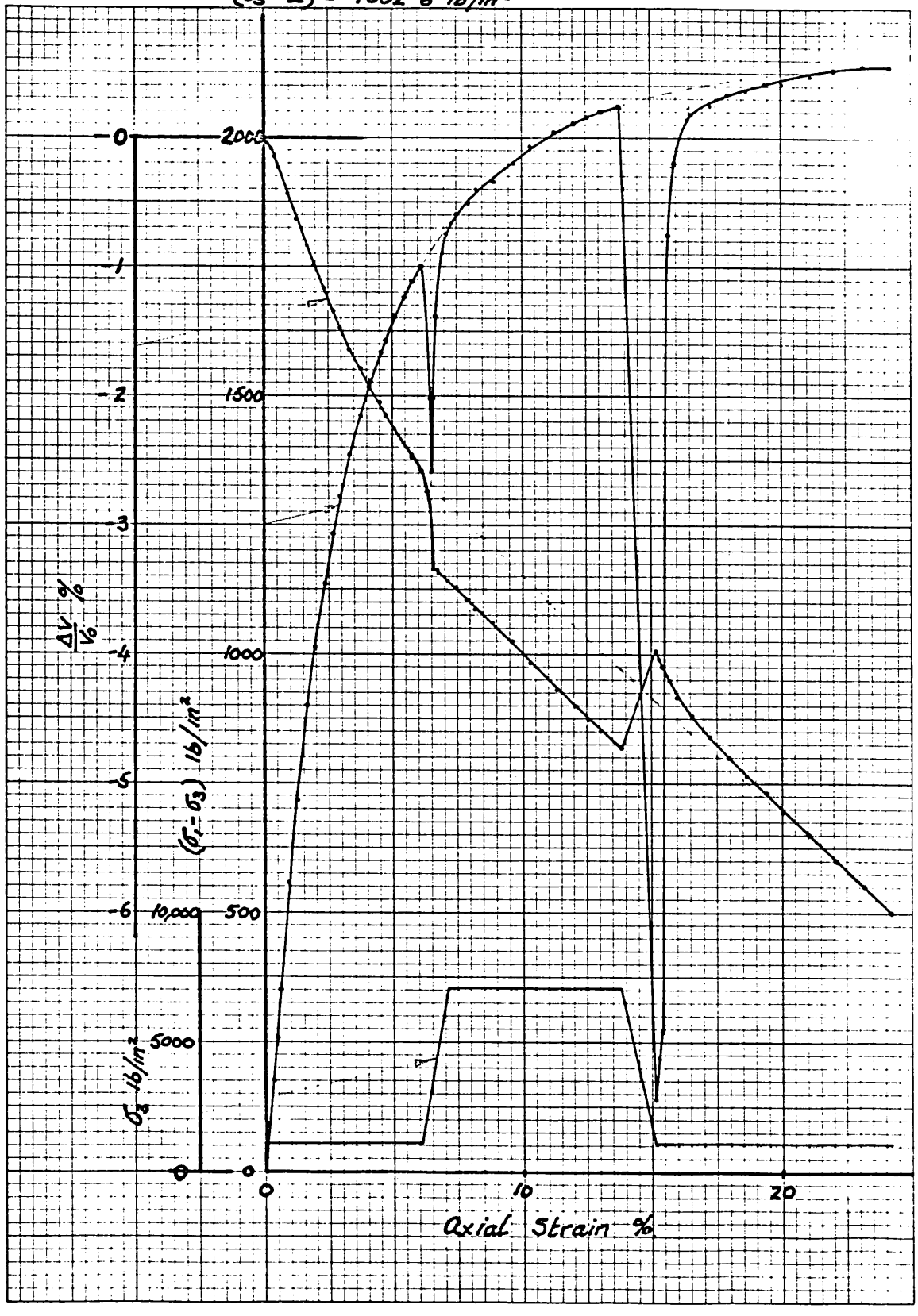


FIG 5·6

TEST A.8. HAM RIVER SAND

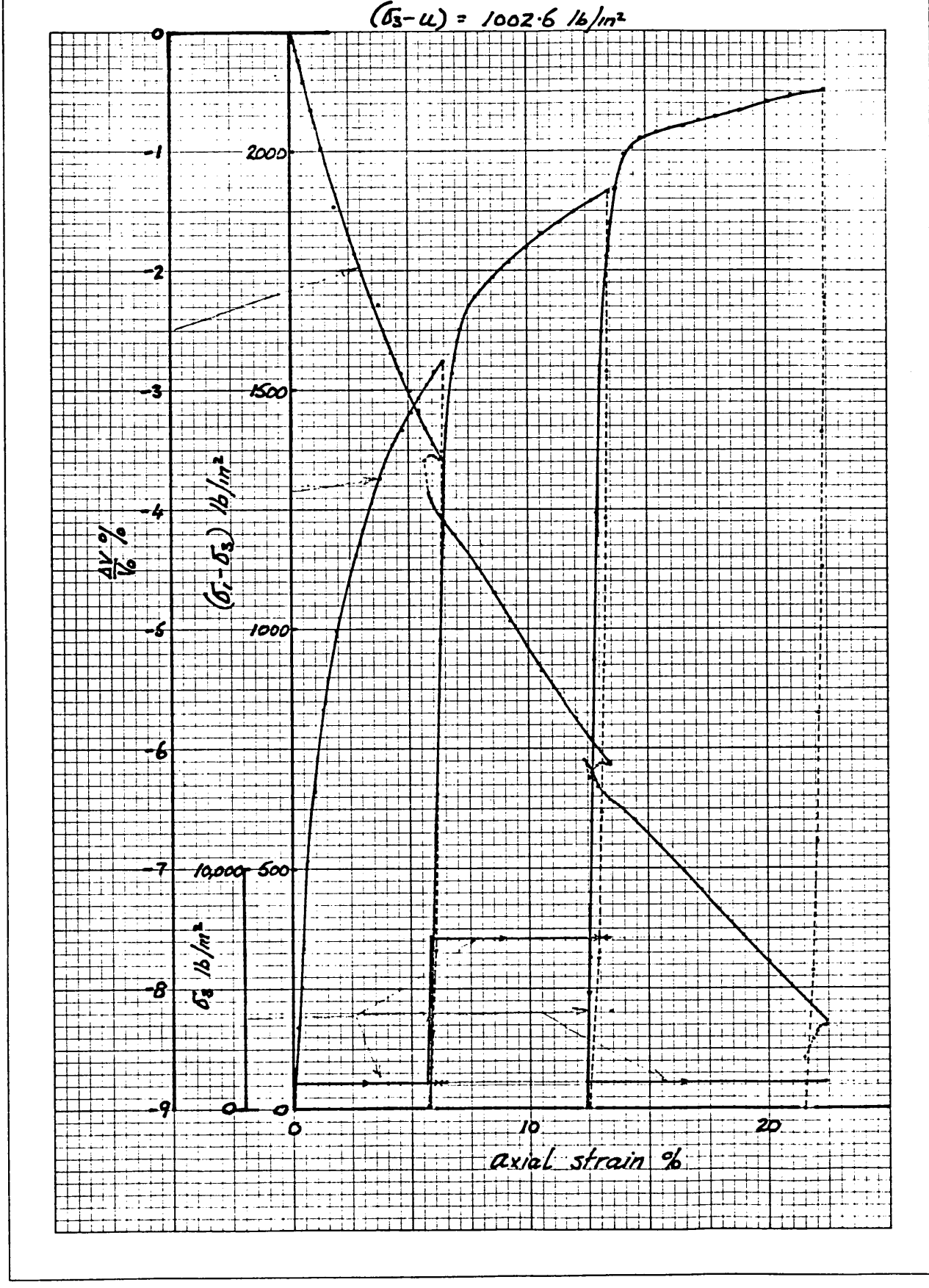


FIG 5·7.

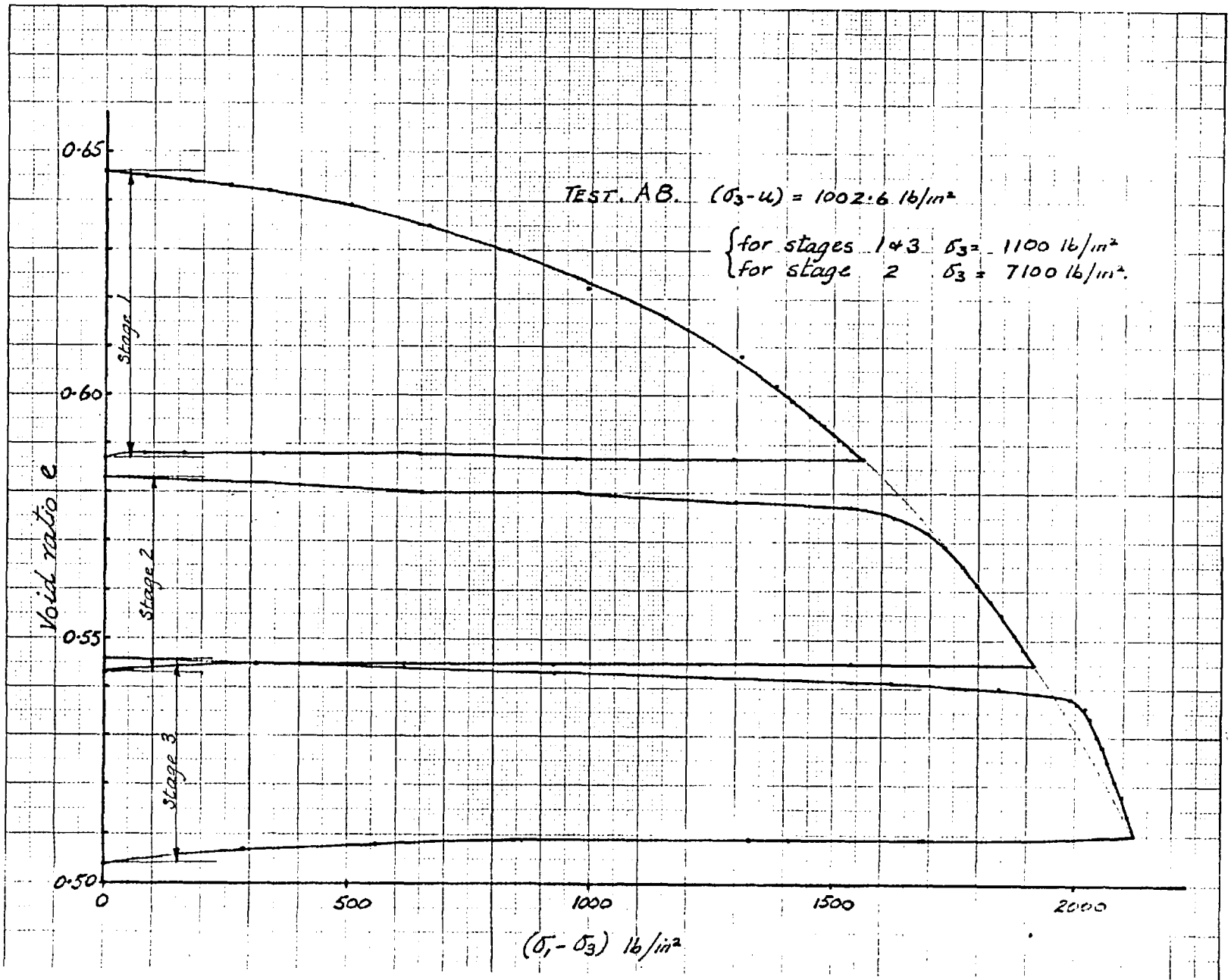

TEST. AB. (σ3-u) = 1002·6 lb/in²
for stages 1 & 3 σ3 = 1100 lb/in²
for stage 2 σ3 = 7100 lb/in².
Void ratio e
0·65
0·60
0·55
0·50
Stage 1
Stage 2
Stage 3
0
500
1000
1500
2000
(σ1 - σ3) lb/in²

FIG 5.8.

TEST A.10 HAM RIVER SAND

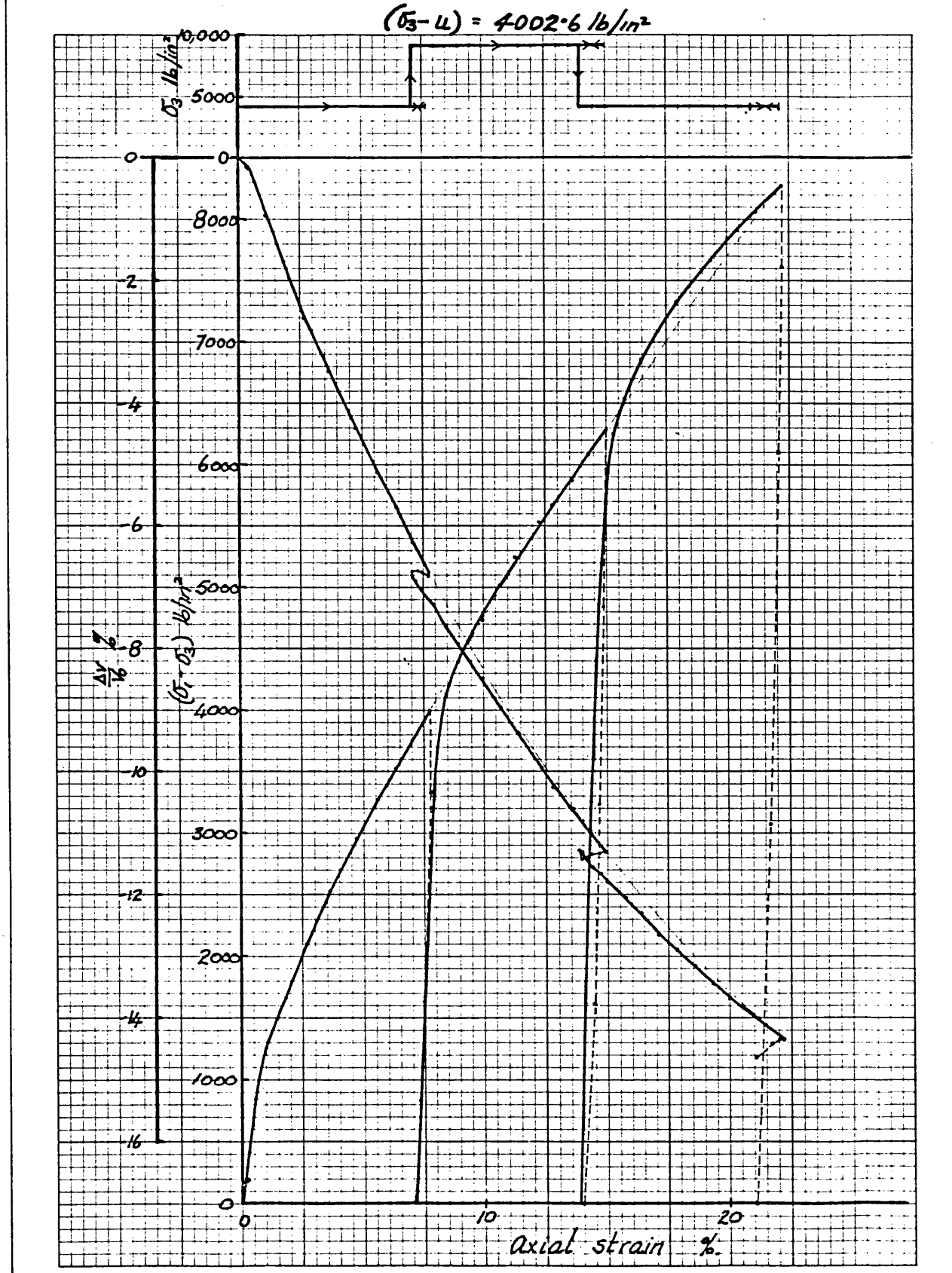


FIG 5·9

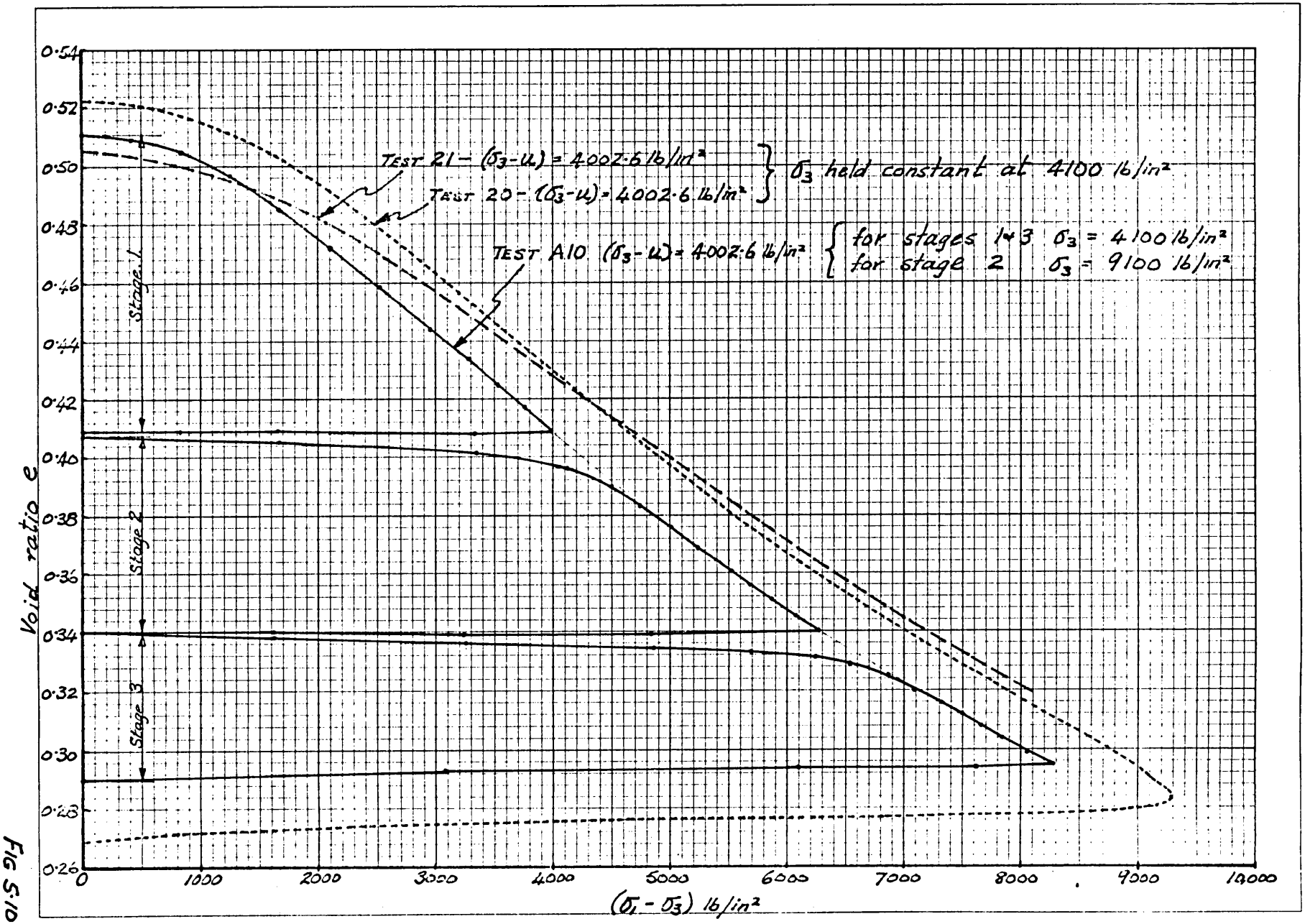

Void ratio e
0·54
0·52
0·50
0·48
0·46
0·44
0·42
0·40
0·38
0·36
0·34
0·32
0·30
0·28
0·26
0
1000
2000
3000
4000
5000
6000
7000
8000
9000
10000
(σ1 - σ3) lb/in²
Stage 1
Stage 2
Stage 3
TEST 21 – (σ3-u) = 4002·6 lb/in²
TEST 20 – (σ3-u) = 4002·6 lb/in²
σ3 held constant at 4100 lb/in²
TEST A10 (σ3-u) = 4002·6 lb/in²
for stages 1 & 3 σ3 = 4100 lb/in²
for stage 2 σ3 = 9100 lb/in²

Fig 5.10

TEST C.I. BRAEHEAD SILT.

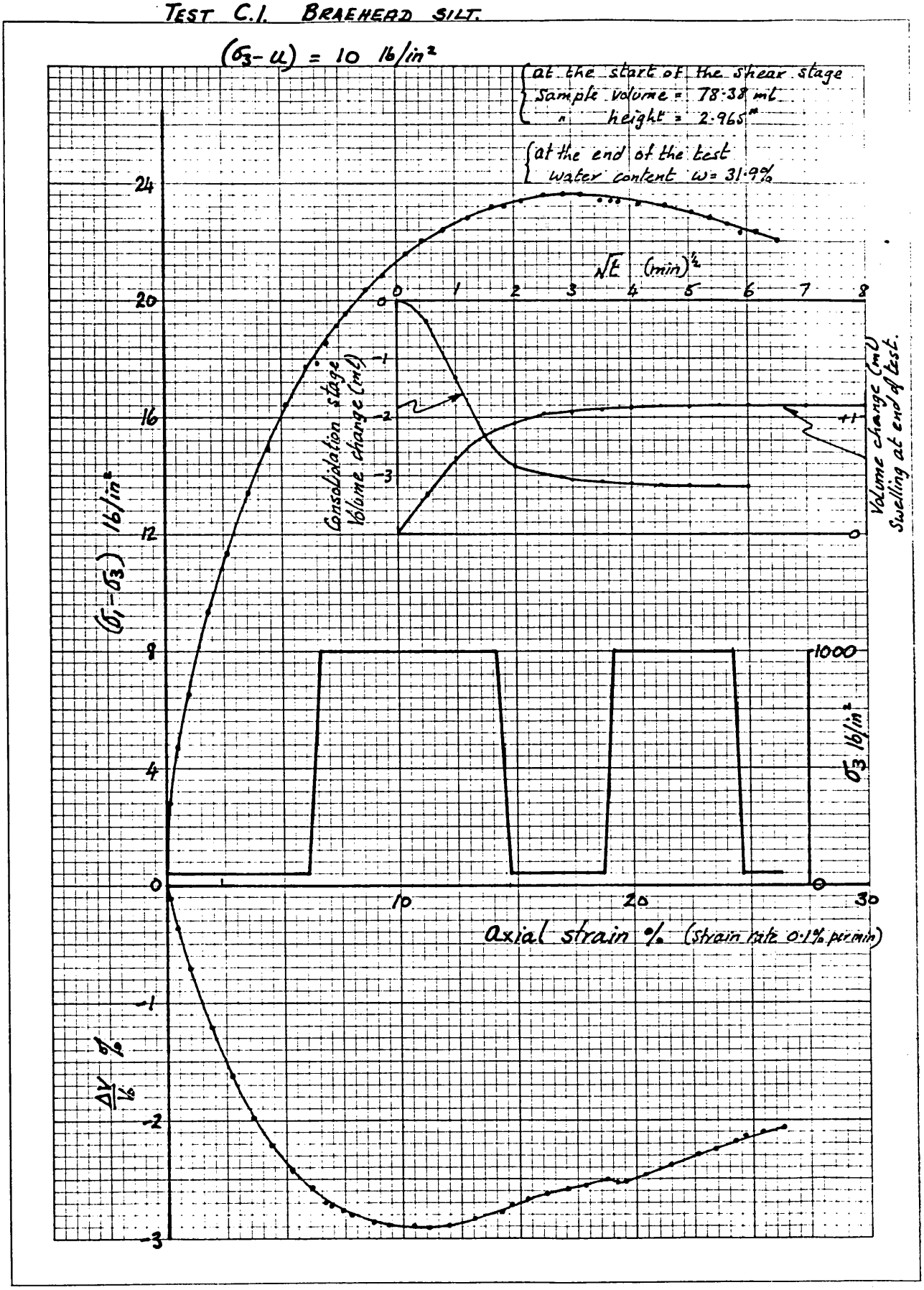


FIG 5·11

TEST C.2. BRAEHEAD SILT.

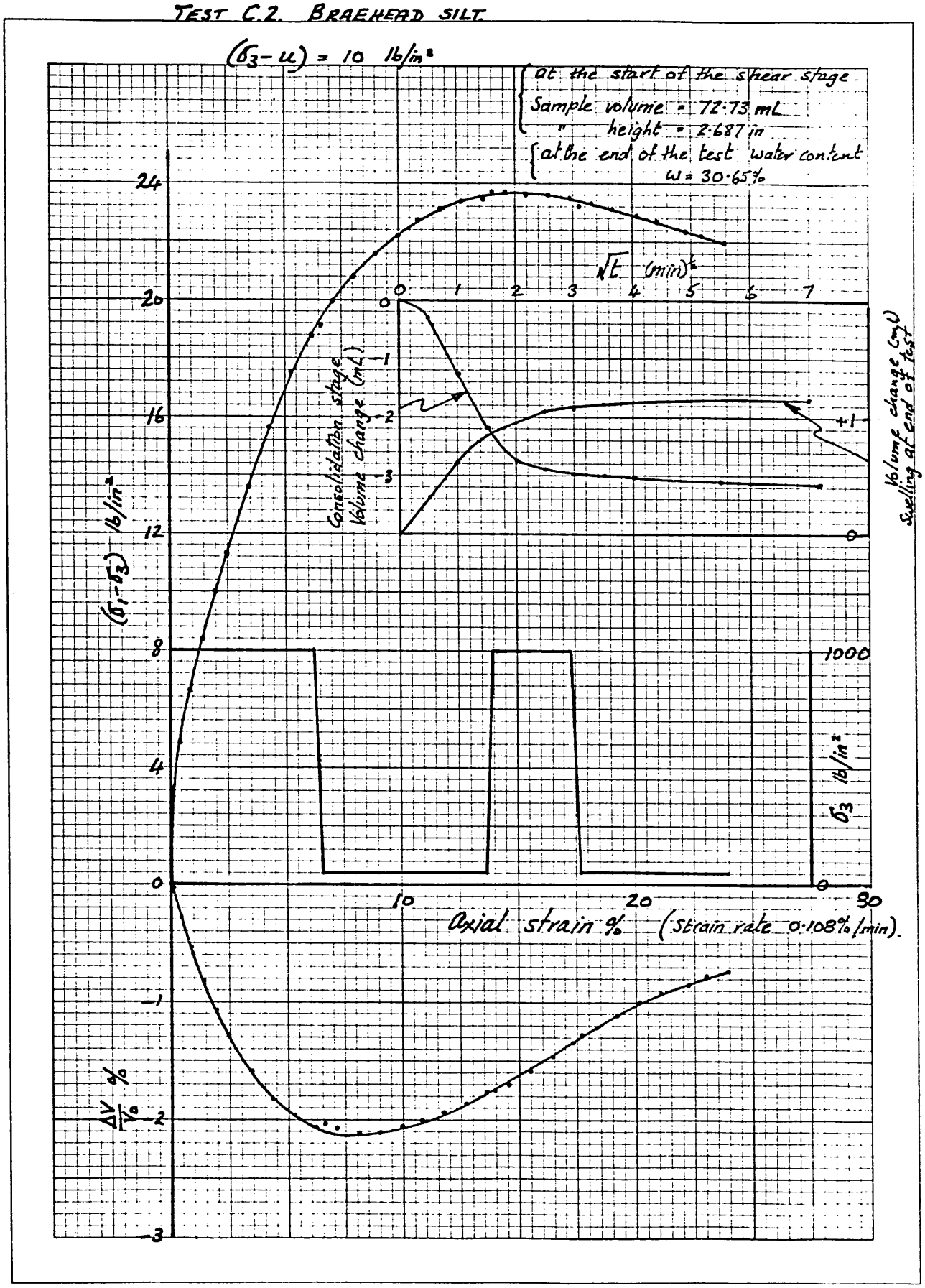


FIG 5·12

TEST D.I. CRUSHED MARBLE

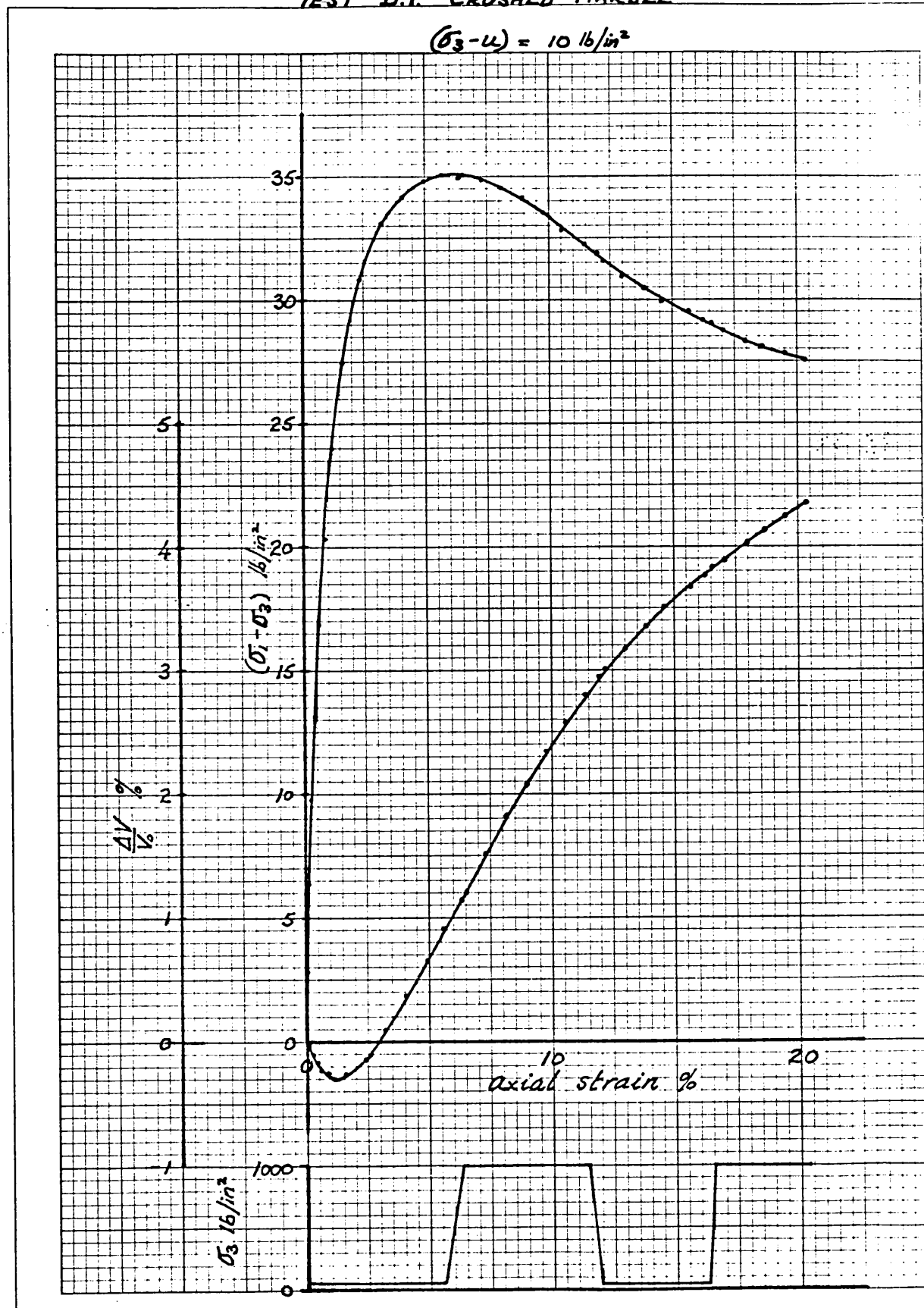


FIG 5·13

TEST D.I. CRUSHED MARBLE

$(\sigma_3 - u) = 10$ lb/in

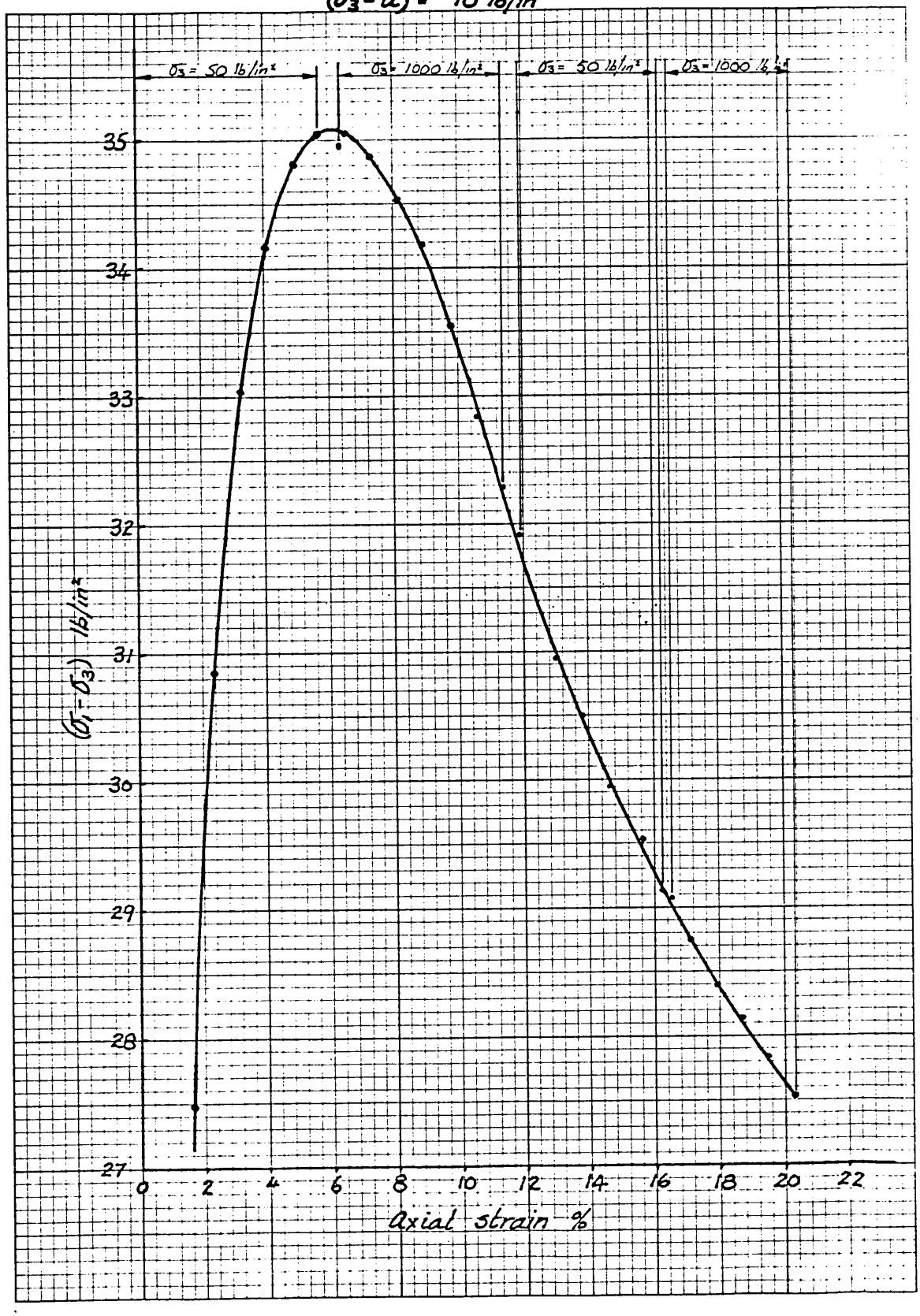


FIG 5·14.

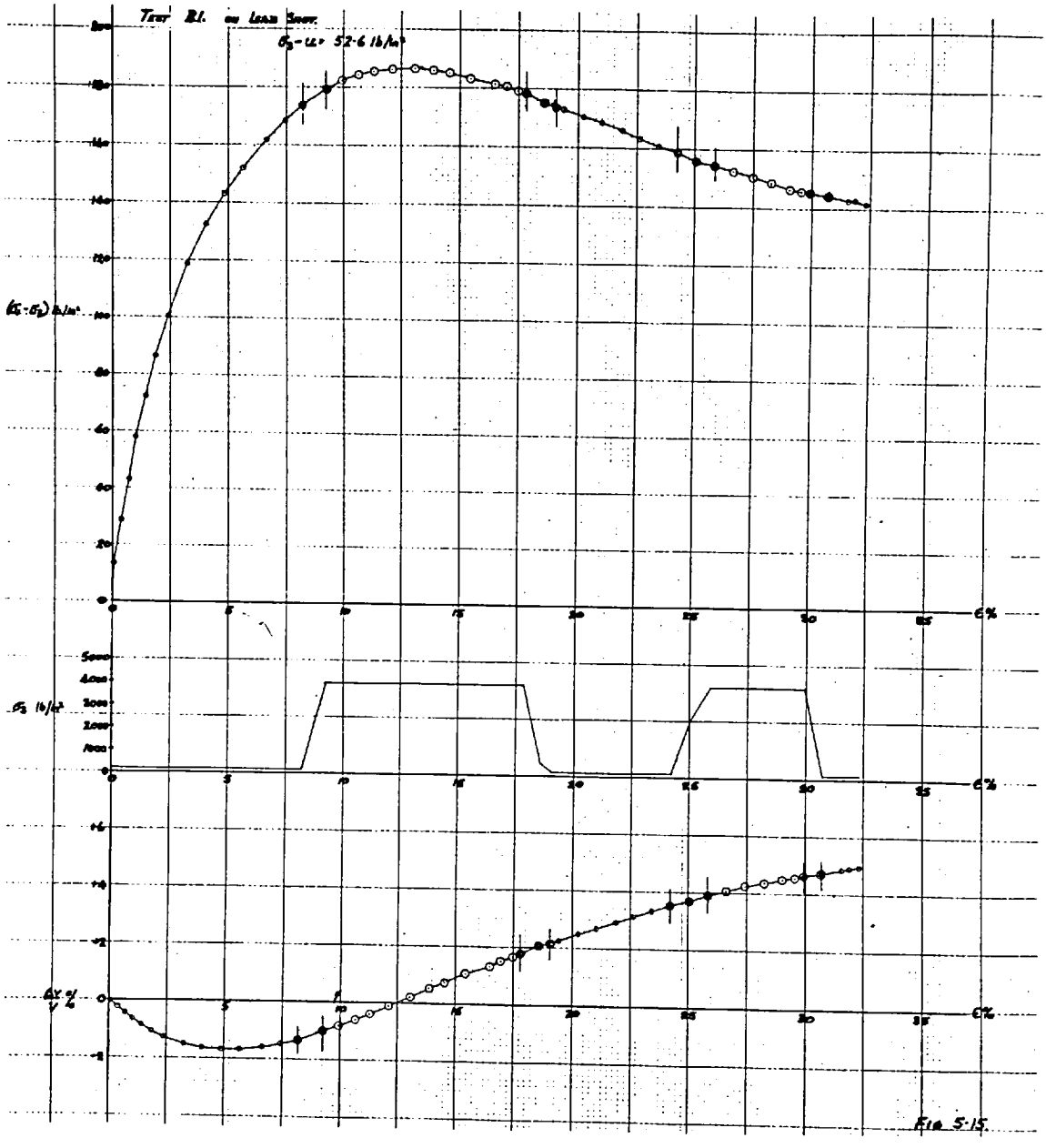

Test R1. on Lean Snow.
σ_3 = 52·6 lb/in²
$(\sigma_1-\sigma_3)$ lb/in²
σ_3 lb/in²
$\Delta V/V_0$ %
ε%

Fig 5·15.

CHAPTER 6

STRESSES CONTROLLING VOLUME CHANGES

6.1 Volume Changes due to Isotropic Stress Changes:

When effective stresses controlling shear strength were discussed, it was possible to define exactly what shear strength was. But in discussing changes in volume in a two (or more) phase material some difficulty arises, because any change in isotropic stress induces a volume change which is a function of two factors. The first is the compression of the soil skeleton associated with the compression of soil grains, and the second is associated with changes in geometry of the particles, and both these factors are not influenced in the same way by changes in the pore fluid pressure.

To describe these volume changes in more detail consider the three samples shown in Figure 6.1 below:

a) a simple solid cylinder made from some mineral crystal,

b) a cylinder of the same material, with the same external dimensions, but in this case with continuous pores, and finally,

c) a cylinder with the same external dimensions, composed of discrete particles of the same mineral.

Initially let these samples be subjected to an external stress of σ_3, and in the case of b) and c) a pore fluid pressure of σ_3 as well. σ_3 can have any value, and its significance is

discussed later.

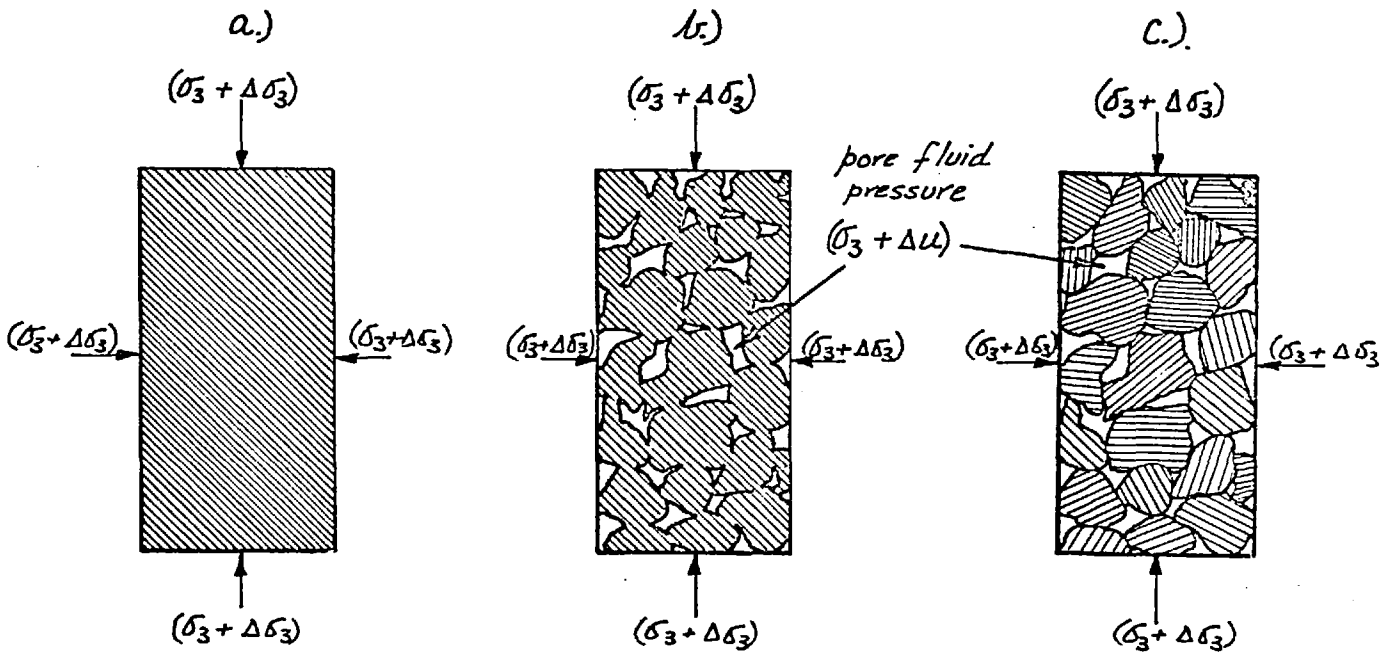


FIG 6.1

Now consider cylinder a). If the external stress is increased to $\sigma_3 + \Delta\sigma_3$, a change in external volume of ΔV will occur where

$$\Delta V = C_s . V . \Delta\sigma_3 \qquad (6.1)$$

where C_s is the compressibility of the solid material for the stress range of σ_3 to $\sigma_3 + \Delta\sigma_3$.

(Note: The sign convention that will be used in this case is that compressive stresses are positive, and they produce decreases in volume which are also considered positive.)

For sample b) suppose that the external stress is changed to $\sigma_3 + \Delta\sigma_3$ and the pore fluid pressure to $\sigma_3 + \Delta u$. Then the change in volume of the external boundary will be

$$V = C_s.V.\Delta\sigma_3 \text{ if } \Delta\sigma_3 = \Delta u \qquad (6.2)$$

That is the same as the first sample.

(Note: The external boundary in this case is considered to be the surface passing through the same points of the solid phase for both stress conditions. The points in the fluid phase which coincide with the boundary initially need not coincide with the boundary after the stresses have been changed. This point is discussed later.)

Now if $+\Delta\sigma_3 \neq +\Delta u$, then there will be a change in volume due to $(\Delta\sigma_3 - \Delta u)$. First because the geometry of the specimen will change, this being a function of the original shape of the specimen and also of the deformation characteristics of the solid material, and secondly, there will be a volume change due to the compressibility of the solid material itself. If this compressibility is dependent on the stress changes, this component of volume change will not be the same as in the first case, because each element of the solid material is not subjected to the stress change $+\Delta\sigma_3$ but to some stress change which is a function of the way in which the solid body is stressed. Also shear stresses will exist, the magnitude and distribution of which will be dictated by the geometry of the specimen. These shear stresses will not contribute to the volume change of the

solid material, if it is perfectly linear, elastic and isotropic, but they may cause some of the solid material to fail, and so add to the volume change by virtue of a further change in geometry. If that part of the volume change due to changes in geometry can be represented by a compressibility $\overline{C}$, then the total change in volume of the sample will be:

$$\Delta V = \overline{C}.V.(\Delta\sigma_3 - \Delta u) + \int C_s.\Delta\sigma_m.dV + \int C_s.\Delta u.dV \qquad (6.3)$$

where $\Delta\sigma_m$ is the mean stress change in the solid element dV, the first integral being taken over the volume of the solid material, and the second over the pore volume. If C_s can be taken to be the same for the stress changes $\Delta\sigma_m$ and Δu, then:

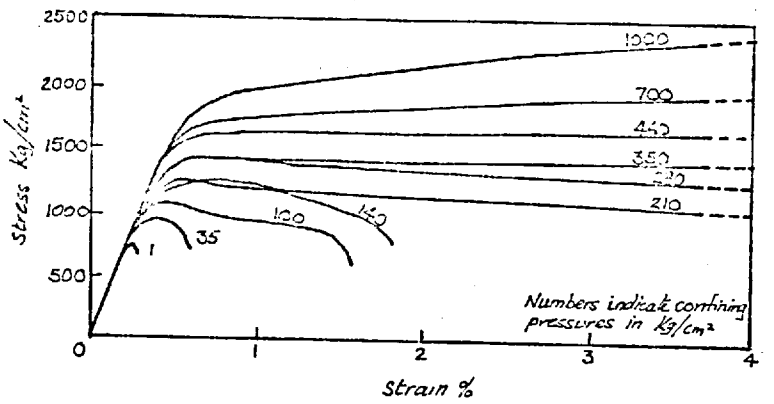
$$\Delta V = \overline{C}.V.(\Delta\sigma_3 - \Delta u) + C_s.V.\Delta u + C_s \int(\Delta\sigma_m - \Delta u).dV \qquad (6.4)$$

the last integral being taken over the volume of the solid material.

Although this expression for volume change contains only the changes in pressure from the original value of the ambient stress, namely σ_3, the influence of σ_3 is contained in the values of compressibility $\overline{C}$ and C_s, which have to be the correct values associated with changes in stress from the original value of σ_3 (see, for example, the variation in compressibility of quartz with ambient stress which is given in Figure 3.10.)

For the stress range used in the experimental work, where

confining stresses up to only 4000 psi were used, the variation in compressibility would only be significant in the small zones which 'bridge' between the larger blocks, and would only involve a small volume of material. Values of C_s as a function of the initial ambient stress σ_3 are available for most minerals, unlike the value of $\overline{C}$ which has to be determined for each sample. But for each sample it is only possible to determine the compressibility $\overline{C}$ for one value of σ_3, $\Delta\sigma_3$ and Δu for the reasons outlined previously. However, by considering data available on the the influence of confining pressure on the stress-strain characteristics of minerals, we can gain some insight into the effect that the pore fluid pressure could have on $\overline{C}$. Most minerals behave in an elastic brittle mode, and the main influence of increasing the pore pressure in this case is to increase the fracture stress. Therefore if fracture is a major mechanism contributing to the value of $\overline{C}$, it is to be expected that this compressibility would be influenced by the magnitude of the pore fluid pressure, but the magnitude of the influence will be unknown. In addition, for materials like calcite, in which the brittle-ductile transition occurs at a comparatively low ambient stress (about 300 bars)(see Figure 6.2), the mode of deformation contributing to the value of $\overline{C}$ could be significantly changed. However, no investigation was made into these effects and the points mentioned remain speculative. But the experimental variation of ΔV as a function of $(\Delta\sigma_3 - \Delta u)$ was carried out and this is discussed later in this Chapter.



Stress-strain curves for Wombeyan marble, after Paterson 1958.

FIG 6·2

Lastly we must consider cylinder c). For this sample all that was said for cylinder b) applies but in this case the change in geometry will be different because the 'bridges' between the particles will not be of the same form as before. Therefore the stress distribution throughout the solid phase will be different, and in addition a further volume change could occur through relative displacement of adjacent points across interparticle contacts, by either partial or gross slip at the contact.

Mindlin and Deresiewicz made a full study of elastic spheres in contact under varying oblique forces in 1953, and the following is an extract from their paper: *"Owing to the presence of slip, with its associated energy dissipation and permanent set, the changes in traction and displacements depend not only upon the initial state of loading, but upon the entire past history of loading and the instantaneous relative rates of change of the normal and tangential forces."*

However, all this can be summarized by incorporating in equation 6.4 an appropriate value for $\overline{C}$ which in this case will also depend on the sign of the stress increment and on the stress path taken to reach the ambient stress level σ_3.

Considering the terms in equation 6.4, it is evident that the value of $\Delta\sigma_m$ is indeterminate except for the simplest solid geometries, and its influence on the volume change could not normally be separated out from the $\overline{C}.V.(\Delta\sigma_3 - \Delta u)$ term experimentally, since it arises wholly as a consequence of $\Delta\sigma_3 \neq \Delta u$. Therefore it could be considered as a contribution to the $\overline{C}.V.(\Delta\sigma_3 - \Delta u)$ term, so equation 6.4 could be rewritten with a different value of compressibility C as:

$$\Delta V = C.V.(\Delta\sigma_3 - \Delta u) + C_s.V.\Delta u \qquad (6.5a)$$

$$\frac{\Delta V}{V} = C.\ \{(\Delta\sigma_3 - \Delta u) + \frac{C_s}{C}.\Delta u\} \qquad (6.5b)$$

Note: Skempton (1960) gives the equation below (where sign convention and symbols have been altered to agree with that used above.)

$$\Delta V = C.V.(\Delta\sigma_3 - \Delta u)(1 - \eta.\Delta u.\tan\psi) + C_s.V.\Delta u$$

where η is a function depending on the relative contributions

by particle re-arrangement and deformation to the total volume change, and involving the parameters a, $1/\tan \phi'$ and $1/K$ where a is the contact area ratio and K is the intrinsic cohesion of the solid material of the particles. This equation can be compared with equation 6.4 which is quite similar. Skempton goes on to say that it is sufficiently accurate to write:

$$\Delta V = C.V.\{\Delta\sigma_3 - (1 - \frac{C_s}{C})\Delta u\}$$

which is identical with equations 6.5, a and b, and is the same as the equation given by A W Bishop in a letter to A S Laughton (24th November, 1953). This gives the effective stress governing volume changes as:

$$\Delta\sigma_3' = (\Delta\sigma_3 - \Delta u) + \frac{C_s}{C}.\Delta u \qquad (6.6)$$

6.2 Measurement of Volume Changes when Pore Fluid Pressures are changed:

It is usual in soil mechanics to measure volume changes for saturated samples by monitoring the volume of water expelled or imbibed by the sample. This technique was used in the experimental work for this programme. Although this is a convenient method it provides some difficulty in those tests where the pore fluid pressure is changed during the test, as can be seen from equation 6.5b.

Many tests were run keeping the difference between the cell

pressure and pore water pressure constant, i.e. $\Delta\sigma_3 = \Delta u$. If we look at equation 6.5a we see that there will still be a change in the volume enclosed by the boundaries of the sample of magnitude $\Delta V = C_s.V.\Delta u$, but this will not be equal to the volume of pore fluid passing through the volume gauge, as the following analysis will show.

Initial conditions:

Sample (overall) volume	= V
Volume of solid particles	= V_s
Volume of pore water	= V_w
Compressibility of solid particles	= C_s per psi
Compressibility of pore water	= C_w per psi

Then for a simultaneous change in cell pressure and pore water pressure of P psi, we get (from equation 6.5a):

$$\text{Change in overall volume } \Delta V = C_s.V.P \tag{6.7}$$

But the change in the volume of voids will be:

$$\Delta V_v = C_s.V_v.P = C_s.n.V.P \tag{6.8}$$

and the change in the volume of water which occupies the original void volume is given by:

$$\Delta V_w = C_w.V_w.P = C_w.n.V.P \tag{6.9}$$

Because $C_w > C_s$ we have $\Delta V_w > \Delta V_v$, i.e. for a pressure increase of P psi there is an overall volume decrease in the sample

of $\Delta V = C_s.V.P$, and to maintain $\Delta\sigma_3 = \Delta u$ the sample must imbibe a small volume of water $(\Delta V_w - \Delta V_v) = n.V.P(C_w - C_s)$. So the volume gauge records an 'apparent' volume increase for a 'real' decrease in the volume of the sample. And the converse is true for a decrease in the pressure. In addition the volume gauge will record changes due to its own volume change, which is a function of pressure, and also the changes in volume of the tubing connecting it with the sample. In the test data plotted in the figures for Chapter 5, allowance for these 'apparent' volume changes was made to obtain the 'true' volume changes. The curves of volumetric strain versus axial strain show that this is apparently a sufficiently correct analysis of the data, which would justify the use of equation 6.6 for the effective stress controlling volume changes.

However the above statement must be qualified because of the very small sample boundary volume changes involved. Volume change apparatus with much greater accuracy than that which was used is required to provide firm justification.

For example, taking typical values of sample size used, the sample volume would be about 85 cc, and using for quartz a compressibility of $C_s = 2.6 \times 10^{-6}$ per Kg/cm^2 (or 0.183×10^{-6} per psi) from Bridgman (1925, 1928), the volume change associated with a pressure change of 4000 psi would be $\Delta V = 0.183 \times 10^{-6} \times 85 \times 4000 = 0.062$ cc, which represents a volume strain of $\frac{\Delta V}{V} = 0.00073$ or 0.073%. The water inflow into the sample for the conditions taken would have been

about 0.489 cc. (The value depends on the current porosity of the sample, and the volume change quoted would correspond to a porosity of 45%.)

The repeatability of the volume gauge in the tests reported in Chapter 5 was about $\pm$ 0.01 cc, although its resolution was much better (see Chapter 2). This lack of repeatability (or lack of accuracy) represents too large a percentage error of the true volume changes to be acceptable for checking the validity of equation 6.5b.

It is, however, perfectly acceptable for the measurement of pore water volume changes (inflow or outflow), the accuracy of the system would only induce errors of the order of $\pm$ 2%.

The other difficulty arising in these tests is that minute variations in the value of $(\sigma_3 - u)$ due to transient flow conditions are sufficient to cause significant 'apparent' errors in the context of these tests where boundary volume changes of only 0.06 cc should occur.

Another method of measuring volume changes is to use a length of fine bore transparent tubing containing a thread of mercury in the drainage line, and measure the travel of the thread of mercury caused by changes in volume. This method, although very accurate, is restricted to small changes in pressure. One test using this technique is described below.

The test equipment was set up as shown in Figure 2.2 except

that the volume gauge, consisting of a length of $\frac{1}{8}$" OD 'Saran' tubing, was connected between valves 15 and 16 (the null indicator being removed), and provision was made for driving the screw control ram so that the cell pressure could be slowly increased or decreased. (Also, at this time the 1000 psi volume gauge shown in Figure 2.3 had not been constructed. Thus the line from the top of mercury column 6 was connected to valve 15.)

A known weight of mercury was injected into the tube, which was laid horizontally along the bench, and the length occupied by the mercury enabled the internal volume per unit length of the tube to be determined. By keeping valve 16 closed and applying pressures to valve 13 the variation in internal volume as a function of pressure could be worked out, by measuring the change in length of the mercury thread, and taking the compressibility of mercury as 0.26×10^{-6} per psi. This calibration is shown in Figure 6.3. Different lengths of tubing, all cut from the same coil, showed virtually identical calibrations, which were nearly reversible, up to 400 psi; beyond this creep was observed. For example, the length/cc of tubing changed from 20.75" to 20.66" after two hours, and to 20.50" after $4\frac{1}{2}$ hours under a sustained pressure of 1000 psi.

However, an attempt was made to eliminate doubts about calibrations for that part of the test when σ_3 and u were varied simultaneously, by first performing the variation

several times, and then taking readings of travel of the leading edge of the mercury column for one pressure cycle; next, keeping valve 16 closed, a small quantity of water was allowed to drain out of the same tube, then sealing the tubing and re-opening valve 16, the test was repeated with a different length of Saran between the leading edge of the mercury column and the sample. Thus the volume changes due to the tubing and the water filling it could be eliminated from the results.

The raw data for this part of the test are reproduced below: sample volume, as measured at $\sigma_3 - u = 5.05$ psi, V = 80.63 ml; weight of Ham River sand used 126.53 gm, specific gravity = 2.7. Therefore V_s = 46.86 ml. During the erection of the cell and pressure cycling the sample decreased in volume by 1.307 and 0.064 ml respectively. Therefore sample volume at start of test = 80.63 - 1.371 = 79.259 ml. At this stage the cell pressure was 100 psi and $\sigma_3 - u = 5.05$ psi. The cell pressure was changed slowly from 100 psi to 350 psi, at a steady rate, in 40 minutes, then decreased steadily to 100 psi in 27 minutes. This difference in time is caused by the slow leak from the rotating bushes. The length of Saran tubing in circuit was 205.8 ins at 100 psi.

The next cycle was for 56.5 ins of tubing in circuit, and the time for the same pressure changes were 41 minutes for raising the pressure, and 28 minutes for decreasing the

pressure. The differences in rates between the two tests are probably due to a small temperature increase in the oil for the second test, which would increase the bleed rate through the bushes. The travel of the leading edge for the two tests is recorded in the table below. Negative values indicate travel towards the sample, i.e. a decrease in the length of water-filled tube.

Cell pressure	Change in length of water-filled tube for an initial length of	
	206.1 in	56.6 in
100	0	0
125	- 0.35	- 0.16
150	- 0.70	- 0.28
175	- 0.95	- 0.38
200	- 1.27	- 0.53
225	- 1.59	- 0.66
250	- 1.89	- 0.80
275	- 2.22	- 0.91
300	- 2.53	- 1.04
325	- 2.85	- 1.18
350	- 3.19	- 1.29
325	- 3.00	- 1.26
300	- 2.79	- 1.17
275	- 2.50	- 1.06
250	- 2.21	- 0.93
225	- 1.90	- 0.80
200	- 1.60	- 0.66
175	- 1.27	- 0.51
150	- 0.95	- 0.38
125	- 0.61	- 0.25
100	- 0.29	- 0.10

From these readings the changes in volume due to the sample,

porous disc at the base of the sample and the water in the drilled drainage ports in the pedestal and cell base can be found.

These volume changes have been plotted in Figure 6.4.

(Note: It has been assumed that the expansion of the drilled drainage ports can be neglected.)

A small hysteresis effect still persists in these results, the maximum difference being equivalent to about 0.1" of 'Saran' tube (0.005 cc). A small anomaly is apparent in these results when the behaviour during this part of the test is compared with the results of the shear stage (Figure 6.5), which shows a small decrease in shear strength for increasing pressures and an increase in strength for decreasing pressures. This was due to a pressure drop in the tubing supplying 'castor oil' to the cell. The viscosity of the oil used is large (aimed at preventing excessive leakage through the rotating bushes) and the oil flow required to pressurize the cell was sufficiently large to induce these pressure losses. This results in the value of $(\sigma_3 - u)$ being smaller when pressurizing the cell when compared with the pressure reduction cycle. Proof of this statement is demonstrated on Figures 6.6 and 6.7, which show results of tests with the small bore volume gauge tubes removed, to prevent pressure loss errors in the back pressure line, thus no volume change readings were taken for these two tests. Figure

6.6 shows a test when the cell pressure was varied between about 100 psi and 650 psi, increasing at about 24 psi per minute and decreasing at 34 psi per minute, i.e. about four times faster than the test reported in Figure 6.5. The change in strength is now very marked. Figure 6.7 shows a test with larger bore tubing in the cell supply lines ($\frac{1}{4}$" OD nylon tubes in place of the $\frac{3}{16}$" OD nylon tubes) and in this case the strain motor was stopped while the pressures were changed, and then re-started with the new pressure conditions established. In this case only a very small quantity of oil flows down the supply tubes, that required to replace the loss through the rotating bushes and to compensate for the volume changes in the sample. The result is a smooth stress-strain envelope to the six discrete straining periods.

These tests highlight the sensitivity of the strength response to small changes in test condition.

Now, referring back to Figure 6.4, the result shown enables a check to be made on equation 6.5a, bearing in mind the qualifications already discussed.

The calculation and the data required are given below. The object is to calculate the compressibility of quartz and check it against Bridgman's value of 0.183×10^{-6} per psi.

Volume of sample V_o	=	79.25 cc
Volume of sand used V_s	=	46.86 cc

Volume of pore water V_w	=	32.39 cc
Volume of porous stone	=	5.43 cc
Volume of pores in porous stone	=	2.17 cc
Volume of drillings in cell base	=	1.181 cc

These values were for σ_3 = 100 psi and $(\sigma_3 - u)$ = 5.05 psi.

If an average slope is taken in Figure 6.4, then the volume of water flowing into the sample for a change in ambient pressure of 250 psi is 0.0295 cc.

Change in water volume for 250 psi change (using C_w = 3.38 x 10^{-6} per psi) = 36.37 x 3.38 x 10^{-6} x 250 = 0.0307 cc (intake).

If we take $(\Delta\sigma_3 - \Delta u) = 0$, no change in the volume of the drillings, and assume that the compressibility of the porous stone material is the same as that of the solid material of the sample, then change in void volume $\Delta V_v = C_s$ x 34.56 x 250 = 8640.C_s. Therefore

$$C_s = \frac{0.0307 - 0.0295}{8640} = \frac{0.0012}{8640}$$

$$C_s = 0.139 \times 10^{-6} \text{ per psi (cf } 0.183 \times 10^{-6} \text{ per psi)}$$

This result is surprisingly good when one considers the comparatively poor resolution of the volume measuring device used, and all the qualifications listed in the previous discussion.

The data presented thus lend support to the expression given in equation 6.6 for the effective stress controlling volume changes, namely:

$$\Delta\sigma_3' = (\Delta\sigma_3 - \Delta u) + \frac{C_s}{C}.\Delta u$$

6.3 An Investigation into the Physical Nature of the Deformation Process of Isotropic Compression:

In applying equation 6.5, when trying to predict volume changes, the value of the compressibility C has to be specified for the particular stress range under consideration. It is therefore relevant to try to investigate the physical nature of the deformation process of isotropic compression.

In Chapter 3 the nature of the contact between mineral grains was discussed at length, and it was shown that the behaviour of grain contacts of quartz could be described by Marsh's equation, when no shear tractions are applied. These would be approximately the conditions induced by isotropic compression if the material was nearly homogeneous. Marsh's equation is based on 'plastic' radial compression of the material around the contact. The deformation conditions result in the formation of surfaces of equal displacement in the form of hemispheres, and is essentially the same for a wide range in indenter profiles, the maximum strain near the indenter for metals being approximately 8%. This being so it would be reasonable to say that, if the material had a fairly constant yield stress, the ratio of $\frac{P}{Y}$ would be the same for

all contacts. (In Chapter 3 it was shown that the relevant flow stresses for contact loads of 1000 gm and 50 gm were 38,000 Kg/cm^2 and 63,800 Kg/cm^2. This variation in contact load would be exceptional in practice. In the case of uniform sand used in this work the variation should be fairly small.)

Therefore if the mean contact stress P can be taken as a constant, then the value of $(\frac{\text{load on the contact}}{\text{area of contact}})$ would be constant. The area of the contact should/nearly proportional be to the square of the displacement or strain between the particles for pyramidal or conical contact points (see Chapter 3 for discussion of geometry of particle contacts).

Therefore $$\frac{\text{Load on contact (L)}}{(\text{Interparticle strain})^2} = \text{constant}$$

and since the change of load on the contact is directly dependent on the change in applied stress $(\Delta\sigma_3 - \Delta u)$, and the strains are assumed isotropic, we get:

$$(\Delta\sigma_3 - \Delta u)^{\frac{1}{2}} = \text{constant}.\frac{\Delta V}{V}$$

Assigning a value of $\frac{1}{C_o}$ for this constant we have:

$$\frac{\Delta V}{V} = C_o.(\Delta\sigma_3 - \Delta u)^{\frac{1}{2}} \qquad (6.10)$$

This relationship was hypothesized by Chaplin in 1961. In the volume change process there will also be a contribution due to elastic compression and particle fracture. However,

if when the particles fracture, the component parts do not grossly re-orient themselves, new contacts will be formed between the fragments, and the same mechanism should re-establish itself. But if the fractures are such that gross re-orientation is necessary, then departures from the above hypothesis will occur. There is some evidence to show that broken grains of sand tend to stay in their original orientations during isotropic stress increases (Maxwell, 1960 and Borg et al, 1960).

Now comparing equations 6.5b and 6.10 we can write, for the case when $\Delta u = 0$:

$$C(\Delta\sigma_3 - \cancel{\Delta u}) = C_o \, \Delta\sigma_3^{\frac{1}{2}}$$

However, it should be noted that the absolute value of the pore pressure can be any value as long as it does not change. There would be no significant difference to the argument if this pore pressure did change by a small amount. So for convenience we shall retain the original form of equation and write:

$$C = C_o(\Delta\sigma_3 - \Delta u)^{-\frac{1}{2}}$$

If it can be shown that C_o is constant for a particular sample it would be more convenient in the case of $\Delta u = 0$ to use equation 6.10, for deformation predictions rather than equation 6.5b.

It is possible to check this variation of C_o by plotting $\frac{\Delta V}{V}$

versus $(\Delta\sigma_3 - \Delta u)^{\frac{1}{2}}$ for isotropic consolidation tests. During the course of the experimental programme some tests were conducted to determine the uniformity of linear strains for isotropic stress changes. The results of one of these tests will be used to test the constancy of the coefficient C_o in the above expression.

The test arrangement is shown in Figure 6.8; the results were all very similar and one set is shown in Figure 6.9. This particular test was chosen because several unloading and reloading cycles were included. This data will allow a comparison to be made of the 'plastic' behaviour of the contacts, assumed in the above expression, with the elastic behaviour which must occur when unloading from a plastic state by decreasing the isotropic stress.

Figures 6.10 and 6.11 show these unloading and reloading cycles in more detail. The fact that there is a small amount of energy dissipated in each cycle of loading is to be expected, even though the assumption made is that the contacts are now behaving essentially in an elastic fashion. This is because the sample can not be expected to be perfectly homogeneous. In addition shear stresses will be induced at the top of the sample by the rigid top cap, and at the bottom by the guard ring and porous stone. If perfect homogeneity existed and perfect test conditions were attainable, then the linear strains measured by the transducer (see Figure 6.7) would be equal to the diametral strains, and therefore equal to a third of the volumetric strain (to the first order). Looking at Figure

6.9 we can see that the average ratio for the whole test is a quarter and not a third. A part of this discrepancy can be accounted for by membrane penetration. For example, if it is assumed that area and volume porosities are equal and that the maximum membrane penetration is to a depth of about half median particle size, which is about 0.1 mm, then the maximum volume change due to this cause would be 0.43%. Using this value the final ratio of linear to volumetric strain is 0.3 at $(\Delta\sigma_3 - \Delta u) = 700$ psi.

The hysteresis effect observed during the stress cycles implies that small shear forces must exist within the sand mass during the test, and the energy loss is associated with the influence of these shear forces at the interparticle contacts, which are assumed to be elastically loaded during this part of the test. Mindlin (1949), Mindlin et al (1952) and Mindlin and Deresiewicz (1953) obtained solutions for elastic spheres in frictional contact. Their results also show that this type of hysteresis loop occurs. This problem is also discussed in Bowden and Tabor, part 2 (1964). The small shift of successive cycles could be due to fretting at the contacts and perhaps fracture of a few particles which are unfavourably stressed. After a few cycles, however, only the energy loss due to microslip at the outside edge of contact areas should be apparent, and the strain load cycles should close. Figures 6.10 and 6.11 indicate that a larger number of cycles than those applied would be required to reach this condition.

Now, going back to the discussion on the value of C_o: In

Figure 6.12 the values of $(\Delta\sigma_3 - \Delta u)^{\frac{1}{2}}$ are plotted against volumetric strains caused by these stress changes for the whole test. It is clear that the experimental points for virgin stress conditions fall close to the line joining the origin to the last few points near the maximum stress state. This is encouraging, however it is possible that the index value of $\frac{1}{2}$ is slightly incorrect. To check this it is best to look at a graph of log $(\frac{\Delta V}{V_o})$ versus log $(\Delta\sigma_3 - \Delta u)$. This is shown in Figure 6.13. This shows a progressive change in slope of the virgin consolidation line from 0.87 initially to 0.45 between stresses of 50 psi to 750 psi. The large index for the low stress range may be due to membrane penetration and platten bedding effects. Figure 6.14 shows a similar plot, but in this case log $(\frac{\Delta H}{H_o})$ is plotted versus log $(\Delta\sigma_3 - \Delta u)$. This graph should be free from membrane penetration errors, but it will still have bedding errors. This graph also shows different slopes for the low stress range as compared with the high stress range, in this case 0.71 and 0.51 respectively. If the linear portion of the 0.51 slope is extrapolated back to intersect the $(\Delta\sigma_3 - \Delta u)$ value at 4 psi, we obtain a value of 0.0007 for $(\frac{\Delta H}{H_o})$ as compared with the initial value of 0.0004. This corresponds to a difference of 0.0003 x 1.754" = 0.0005", which would not be unreasonable to attribute to bedding of the two ends of the sample. From this it seems that the original assumption of pyramidal or conical forms of interparticle contact and that the contacts are plastically deformed, gives a very reasonable picture of the behaviour of the sample, for virgin loading conditions.

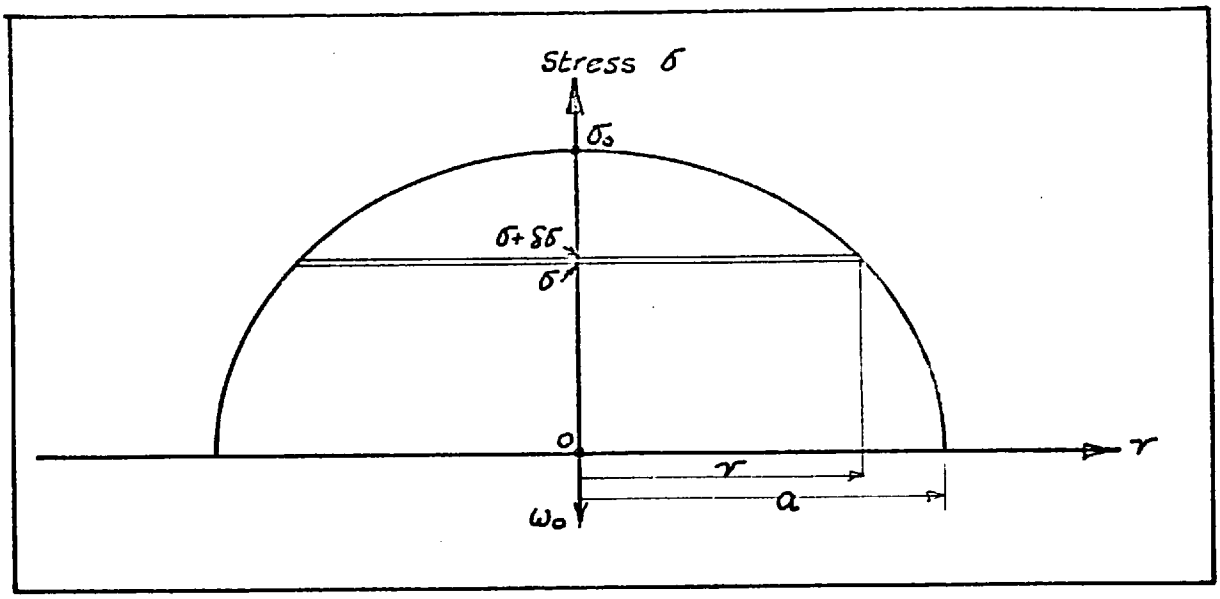
Now, consider the stress cycles where the interparticle contacts should be behaving elastically, because the contacts are being unloaded from a plastic state, if the hypothesis is correct. Figures 6.13 and 6.14 indicate that these unloading and reloading stages also give rise to approximately linear log $(\frac{\Delta V}{V_o})$ versus log $(\Delta\sigma_3 - \Delta u)$ and log $(\frac{\Delta H}{H_o})$ versus log $(\Delta\sigma_3 - \Delta u)$ graphs, with hysteresis loops, of course. So we might expect a power relationship even for these elastic conditions.

The shapes of the contacts will, for these conditions, be altered by plastic deformation, but some insight can be obtained by considering much simpler conditions.

For example the contact areas for quartz are extremely small because of the high stress at the contacts (of the order of 9.3×10^5 psi or 6.5×10^4 kg/cm^2), and it was shown in Chapter 3 that the asperities on the surface of grains would tend to be shallow conical or pyramidal projections.

If, as a first approximation, we assume that the contact stresses could be represented by a distributed stress (radially symmetric in this particular analysis) imposed on the surface of a semi-infinite homogeneous elastic domain, it is possible to determine the maximum displacement and the total load for various forms of stress distribution.

For example consider the distribution shown in the diagram below:



We can obtain the deflection at O, i.e. w_o, by summing the contributions to w_o from all such layers of uniform stress such as $\delta\sigma$. In this case $\delta\sigma$ acts over a circle of radius r, and if we can specify the function f in the relationship $\sigma = f(r)$, then the magnitude of w_o is easily obtained from:

$$w_o = \sum\left(\frac{2(1 - \nu^2)}{E}\right) r.\delta\sigma$$

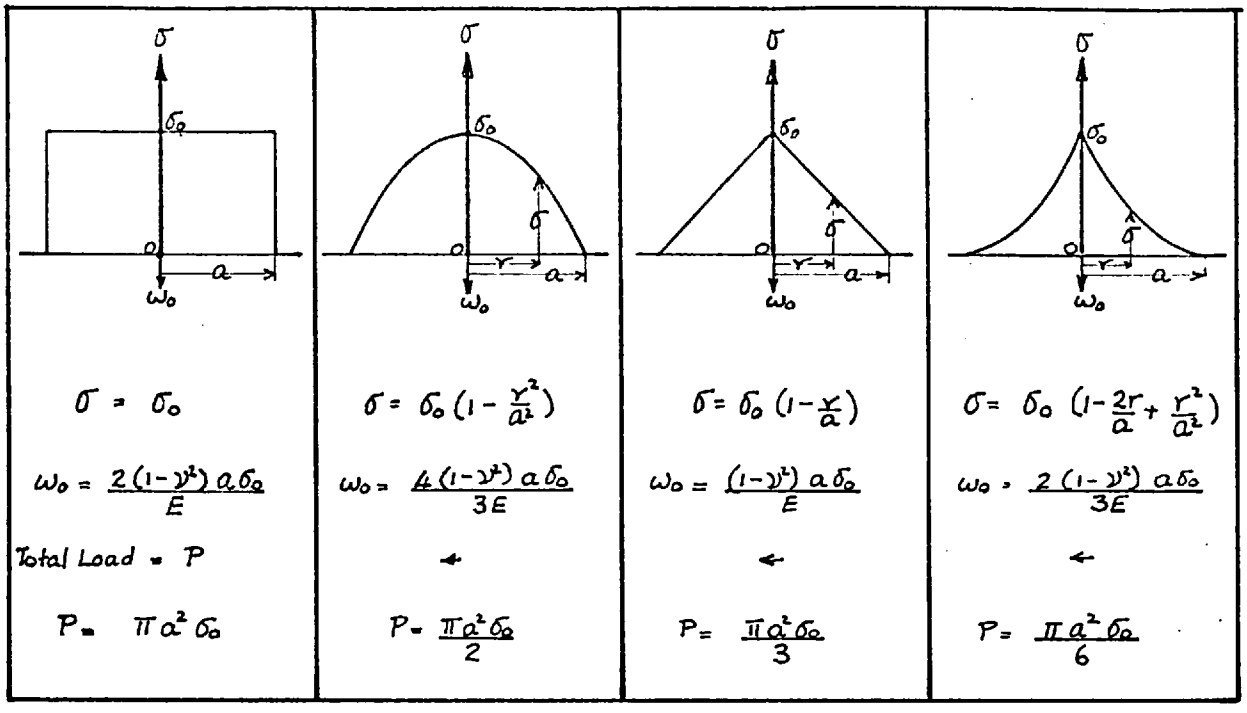
So $$w_o = \frac{2(1 - \nu^2)}{E} \int_o^{\sigma_o} r.d\sigma$$

and the total load $P = \int_o^a 2\pi r\sigma.dr$.

This has been done for four different distributions of stress and the results are shown in the table below.

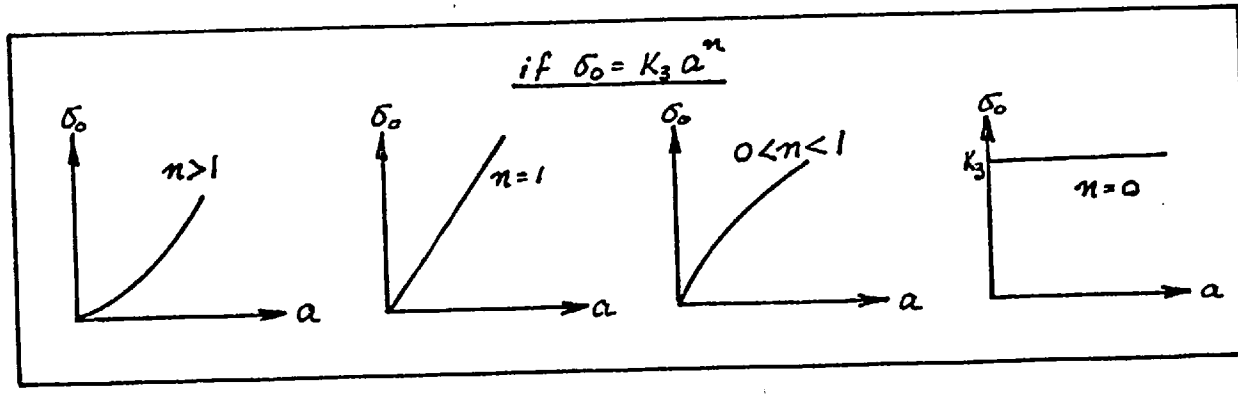
So in general $w_o = k_1\sigma_o a$

and load $P = k_2\sigma_o a^2$



Since volumetric strain $(\frac{\Delta V}{V_o})$ is proportional to w_o, it will also be proportional to $\sigma_o a$. Similarly change in load on the contact ΔP is proportional to effective stress change $(\Delta\sigma_3 - \Delta u)$, and so to $\Delta\sigma_o a^2$. Or if our datum is $P = 0$, $(\sigma_3 - u) = 0$, we can say that P is proportional to $(\Delta\sigma_3 - \Delta u)$ and so to $\sigma_o a^2$. If σ_o can be related to a, then the relationship between between $(\frac{\Delta V}{V_o})$ and $(\Delta\sigma_3 - \Delta u)$ could be established.

Let us speculate on the relationship $\sigma_o = k_3 a^n$:



We then have:

$$\frac{\Delta V}{V_o} = k_4(\Delta\sigma_3 - \Delta u)^x$$

Note: The values of V_o and $(\Delta\sigma_3 - \Delta u)$ must be taken from the datum of the start of elastic behaviour, and so will be different from the values used for the original datum taken for the virgin loading conditions. We have x defined such that:

$\frac{2}{3} < x < 1$ for $n > 1$

$x = \frac{2}{3}$ for $n = 1$

$\frac{1}{2} \leqslant x \leqslant \frac{2}{3}$ for $0 \leqslant n \leqslant 1$

This shows that the Hertzian type of contact stress is a special distribution of normal stress where $(\frac{\sigma_o}{a})$ is constant. In fact this is so because the normal stress distribution takes the form of a hemisphere on the surface of contact.

If σ_o is constant then $(\frac{\Delta V}{V_o})$ varies as a function of a, and the contact load or $(\sigma_3 - u)$ varies as a function of a^2, so $(\frac{\Delta V}{V_o})$ would be proportional to $(\sigma_3 - u)^{\frac{1}{2}}$. This relationship should be obeyed during unloading from the virgin compression condition, assuming that the contact had been plastically strained, so that the stress was nearly constant across the contact area.

We conclude from the above analysis that the index x in the expression:

$$\frac{\Delta V}{V_o} = C_o(\Delta\sigma_3 - \Delta u)^x$$

for elastic behaviour would lie between $\frac{1}{2}$ and 1, depending on the relationship between the maximum stress and contact size.

If the curves for the stress cycles shown on Figures 6.13 and 6.14 are replotted with appropriate datum values V* and H*, then we could see if the analysis is followed. This is done in Figures 6.15a and 6.15b, from which we can obtain values for the index x. In fact the variation is remarkably small, and lies close to the lower limit of the above analysis. These values are for:

$$\frac{\Delta V}{V^*} = C_o(\Delta\sigma_3 - \Delta u)^x \qquad 0.48 < x < 0.69$$

$$\frac{\Delta H}{H^*} = C_o(\Delta\sigma_3 - \Delta u)^x \qquad 0.54 < x < 0.88$$

The foregoing results are very encouraging. Also the Figures 6.13 and 6.14 show that there is a yield stress where transition from an elastic deformation regime to a strain hardening plastic one occurs, the plastic deformation conditions applying to the virgin loading path. Thus it is fair to say that for these conditions the constant C_o and the index x are useful soil constants.

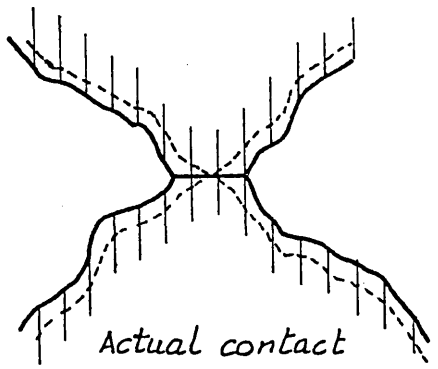
If the confining pressure were raised beyond those levels already investigated, then particle fracture could influence the deformation behaviour. In Figure 6.16 $(\frac{\Delta V}{V_o})$ values are plotted versus $(\Delta\sigma_3 - \Delta u)^{\frac{1}{2}}$ using the results of tests up to 1000 psi confining pressure.

The test on loose Ham River sand shows a very close agreement with the postulated behaviour, and yet this sample would be expected to show the influence of particle fracture first. The results for dense Ham River sand samples with fixed and free ends are also shown. The 'fixed' ends sample (test 25) shows some deviation from the linear relationship above 500 psi confining pressure, but it is suggested that this could be due to end platten effects as the test with the 'free' ends (test 16) shows good linearity. In this test rubber discs lubricated with silicone grease were used at both ends of the sample, the drainage being through one end only, through a $\frac{1}{4}$" diameter porous stone (sample size: 2.92" long, 1.46" diameter). The linear relationship is very good, even though the sample had a lower porosity than the 'fixed' end dense sample. Of course, in all the tests errors due to membrane penetration and to bedding would be present, but they do not appear to be significant.

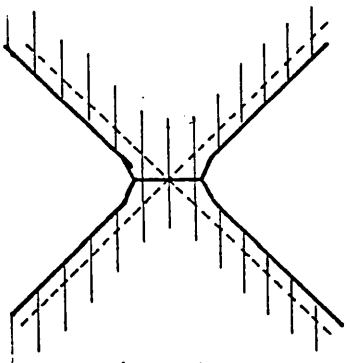
Also shown in Figure 6.16 are two tests on cast steel shot. These tests have linear $(\frac{\Delta V}{V_o})$ versus $(\Delta\sigma_3 - \Delta u)^{\frac{1}{2}}$ plots up to about 120 psi for test a, and up to 50 psi for test b; the results then curve away from the linear portion. This suggests that the steel shot behave as polyhedra in the low pressure range, the particle contacts being through small asperities. The tips of these asperities become plastic very easily at low pressures giving rise to the linear $(\frac{\Delta V}{V})$ versus $(\Delta\sigma_3 - \Delta u)^{\frac{1}{2}}$ plot, but at higher stresses the loads could be carried by means of elastic deformation

of the material. If the material under the asperities is assumed to be still of the same shape, then assuming the asperity is of conical shape, we can obtain an approximate elastic stress-strain behaviour.

Assume that the material forced down from the asperity tip displaces the material below to produce a larger effective area, and that we can neglect the change in volume of the material, then the situation is as shown below:



The idealized condition can be represented like this. The assumption that the displaced material goes into the same height of material below is arbitrary, but will not affect the argument, because we only want the general form of the behaviour assumed.



With these idealizations we have the following:

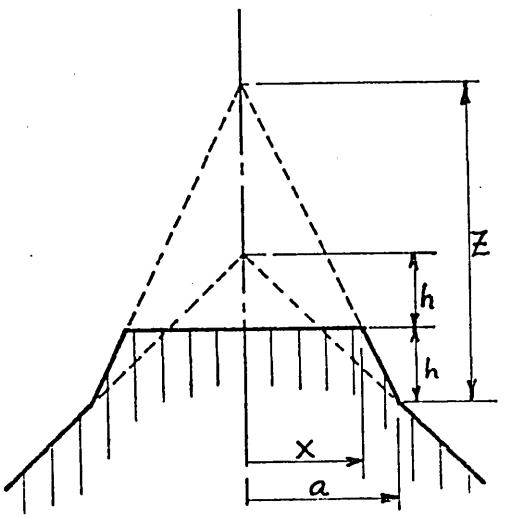
$$Z = 2.62\ h$$

$$X = \frac{Z - h}{Z}.a$$

So contact area =

$$\pi.X^2 = \pi.\{\frac{(Z - h)}{Z}\}^2.a^2$$

The stress distribution across the contact face will be nearly



Enlargement of idealized lower contact

conical in form, so taking maximum stress as σ_o we shall get for the load on the asperity $P \simeq 0.40\ a^2\sigma_o$.

But $a = 2h \tan \frac{\theta}{2}$ where $\frac{\theta}{2}$ is the half angle of the asperity tip and is a constant. So we can write $P \simeq K\ h^2\sigma_o$ where K is a constant depending on asperity angle.

In addition the change in P will be proportional to the change in confining stress $(\Delta\sigma_3 - \Delta u)$, and of course the displacement of the asperity tip is h, which will be proportional to the strain and the maximum stress σ_o.

Summarizing: $h \propto \sigma_o$

$P \propto h^2\sigma_o$

i.e. $P \propto h^3$

So, in terms of the symbols used previously:

$$\frac{\Delta V}{V_o} = C_o.(\Delta\sigma_3 - \Delta u)^{\frac{1}{3}}$$

So the index x should be $\frac{1}{3}$ for elastic behaviour of conical asperities. In fact the indices for both the tests on steel shot are close to this value; they are x = 0.4 and x = 0.3 as shown on Figure 6.17.

The behaviour reported may be due to the fact that the steel shot were initially rusted, and for these tests the shot were tumbled in a glass jar to remove any loose scale, and then washed in water until the waste water ran clear. This

process should have removed most of the loose rust scale, leaving behind a pitted surface which could have had the characteristic outlined above.

One test was also run on lead shot with a mean particle diameter of 1 mm. The maximum effective stress imposed was only 52.6 psi. The test data are shown in Figure 6.18. These indicate that lead shot contacts also appear to follow the plastic relationship for which the index $x = \frac{1}{2}$. This is not surprising as the lead has a very low yield stress.

If the shot deformed as true plastic spheres a linear relationship should exist between effective stress and volumetric strain, i.e. $x = 1$. No tests were conducted with a large enough effective stress to test this behaviour, but it is possible to use the data of Dr Laughton, published by Skempton (1960), to explore the validity of this statement.

Laughton's test was performed in an oedometer, therefore shear stresses at the particle contacts would also influence the volumetric strain behaviour. But the data should still indicate qualitatively the change in behaviour from 'pyramidal' to spherical type of behaviour. The e versus log P' relationship is drawn in Figure 6.19, and is replotted in Figure 6.2o as Log $\frac{\Delta V}{V_o}$ versus log P'. This figure clearly shows that the postulated change exists, the slope of the early portion of the consolidation plot being 0.52, changing to 0.96 for larger effective stresses, and finally curving

away when the particles no longer deform as spheres. This occurs when P' = 120 Kg/cm^2 when the contact area ratio was about 0.1 and the volumetric strain about 22%. The foregoing data for metals are seen to lend qualitative support for the concept of plastically deforming contacts for virgin loading conditions.

However, in the case of mineral grains fracture must sooner or later be a dominant factor, even though the parabolic relationship would seem to be valid up to very high confining stresses.

Figure 6.21 shows the results of a test on Ham River sand up to $(\Delta\sigma_3 - \Delta u)$ equal to 4002.6 psi. The parabolic relationship between effective stress and volumetric strain is seen to hold up to an effective stress of about 2000 psi, after which the volumetric strain becomes larger than predicted. This increase in strain could be accounted for by fracturing of those grains most severely stressed or those which already have inherent weaknesses.

The problem is to determine how the grains facture. At particle contacts the stresses are controlled by plastic deformation (sufficient data have been collected in the previous chapters and in this chapter to accept this statement), and as was shown in chapter 3, the stresses at the asperities include a very large hydrostatic component; therefore tensile fracture would be inhibited. If failure occurred at the

contacts the mode of failure would be by shear, but again the large hydrostatic stress raises the shear strength very considerably, and it is possible that before shear failure occurs at the contacts, the stresses within the bulk material could rise with increasing contact load until a point is reached where grain failure is permitted by the tensile fracture within the 'relatively' low stressed body of the grain. This is similar to the fracture mechanism encountered in the Brazilian tensile test for brittle materials.

Both types of failure probably occur in isotropic compression of sand, but the tensile fracture of the grains would probably cause more radical changes to the structure of the sample and it is probable that this mechanism is the cause of the behaviour shown in Figure 6.21. Fractures similar to fractures of Brazilian tensile test specimens are shown by Borg et al (1960) where the grains split across contact points.

If fracture of grains within the sand mass is controlled by this process, then we must look at the distribution of contacts per particle, because the load at each pair of diametrically opposed contact points may either relieve or add to the tensile stresses imposed by other contacts at various angles to them. Therefore we could not expect that the load per contact that would cause failure of the particle within the soil sample will be the same as the load to cause

failure of the same particle when loaded across a single pair of contacts.

To illustrate this point we could compare the load per contact (following Bishop (1965) in assuming a cubical pack) on an average particle assuming that this particle will fracture at 2000 psi confining stress, because it is loaded across only one diameter, due to misfit of the cubical pack, and compare the result with data published by Billam (1971) and Bergstrom (1963) for failure of sand particles loaded similarly.

Load per particle = $2000 \times d^2$.

For a tensile fracture stress of σ_t the fracture load is given approximately by $P_c = a.\sigma_t.d^2$, where the coefficient 'a' is approximately $\frac{1}{2}$ to $\frac{1}{3}$ for a spherical particle, and depends in general on Poisson's ratio, grain shape and size of loaded area. Jaeger (1967) gives reasons why 'a' may be smaller.

However, using

$$\tfrac{1}{3}\sigma_t.d^2 = 2000.d^2$$

gives $\sigma_t = 6000$ psi.

Extrapolation of Billam's data gives a mean value of about 12000 psi for particles with a mean diameter of 0.2 mm, which corresponds to the mean diameter of the Ham River sand. This

is twice the value obtained in the previous calculation. However, it seems reasonable that those particles with defects would be the first to fracture, which would imply that the value of σ_t = 6000 psi is reasonable for first fracture to be observed at a confining stress of 2000 psi. Further refinement in analysis would be unjustified at this stage in view of the little that is known about the way in which particles are stressed.

6.4 Settlement of Granular Fills:

We can now see if it is possible to use this general approach to calculate the settlement of granular materials, in particular for the conditions of one-dimensional settlement.

The suggestion is that if the influence of fracturing of the particles is small, then because the ratio of shear stress to normal stress remains appreciably constant, there will be tendency for particles to remain in contact with the same group of adjacent particles and the arguments used previously can be used again except that in this case the particle contact positions must adjust to the changing geometry of the sample and the contacts will be subjected to larger shear forces. But, as before, we could hypothesize that the relationship between changes in volumetric strain and changes in mean stress could be represented by an equation of the same form as used before, but in this case we could use the mean effective stress.

$$\frac{\Delta V}{V_o} = \text{constant} \cdot (\text{mean effective stress})^x$$

i.e. $$\frac{\Delta V}{V_o} = \text{constant} \cdot \left(\frac{\Delta\sigma_1'}{3}(1 + 2K_o)\right)^x \qquad (6.12)$$

(using the prime for effective stress)

The term $\left(\frac{(1 + 2K_o)}{3}\right)^x$ could be included with the constant and we would get:

$$\frac{\Delta V}{V} = D.(\Delta\sigma_1')^x \qquad (6.13)$$

In this case the index x will probably differ from 0.5 because the contact points would be subjected to fairly severe shear loads in addition to the normal loads. Nevertheless it would be of interest to observe if the form of the relationship is reasonable.

Figure 6.22 shows the result of a K_o test on Ham River sand conducted in the triaxial cell, plotted on a log-log basis. The readings lie on a remarkably straight line with a slope of 0.76, which gives the relationship for this test as:

$$\frac{\Delta V}{V_o} = 2.9 \times 10^{-4}.(\Delta\sigma_1')^{0.76}$$

(where $\Delta\sigma_1'$ is in psi and $D = 2.9 \times 10^{-4}\ (\text{psi})^{-0.76}$).

Chaplin's work in 1961 was referred to in connection with isotropic compression. He also indicated that a power law relationship should exist in the case of increasing stress

with a constant stress ratio, the index being $\frac{1}{2}$. The above result does not agree with this hypothesis although the power law is upheld.

So, for materials like Ham River sand, the relationship given in equation 6.13 holds true for one-dimensional strain.

We can use this relation in the analysis for the one-dimensional settlement of a layer which settles under its own weight, assuming that the placement density is always the same. (In rockfill dams this is usually the dry weight or weight of soaked material, the only water being present is held by capillary forces around the particle contacts. So it will be reasonable to assume that the effective stress is the same as the total stress.) As the dam is constructed, the lower layers are strained, and so increase in unit weight. This results in a thick layer of rockfill which has an increasing unit weight with depth. Since the settlement of any point within the layer is due to the compression of the material below the point stressed by the weight of the material above the point, it is obvious that the variation in unit weight of the material above the point should be taken into account.

We can do this fairly easily if the solution is approached in the following manner:

1. Assume that the layer is constructed under zero gravity conditions to some height H_o, with material of the same initial voids ratio. Also, there is a marker placed in

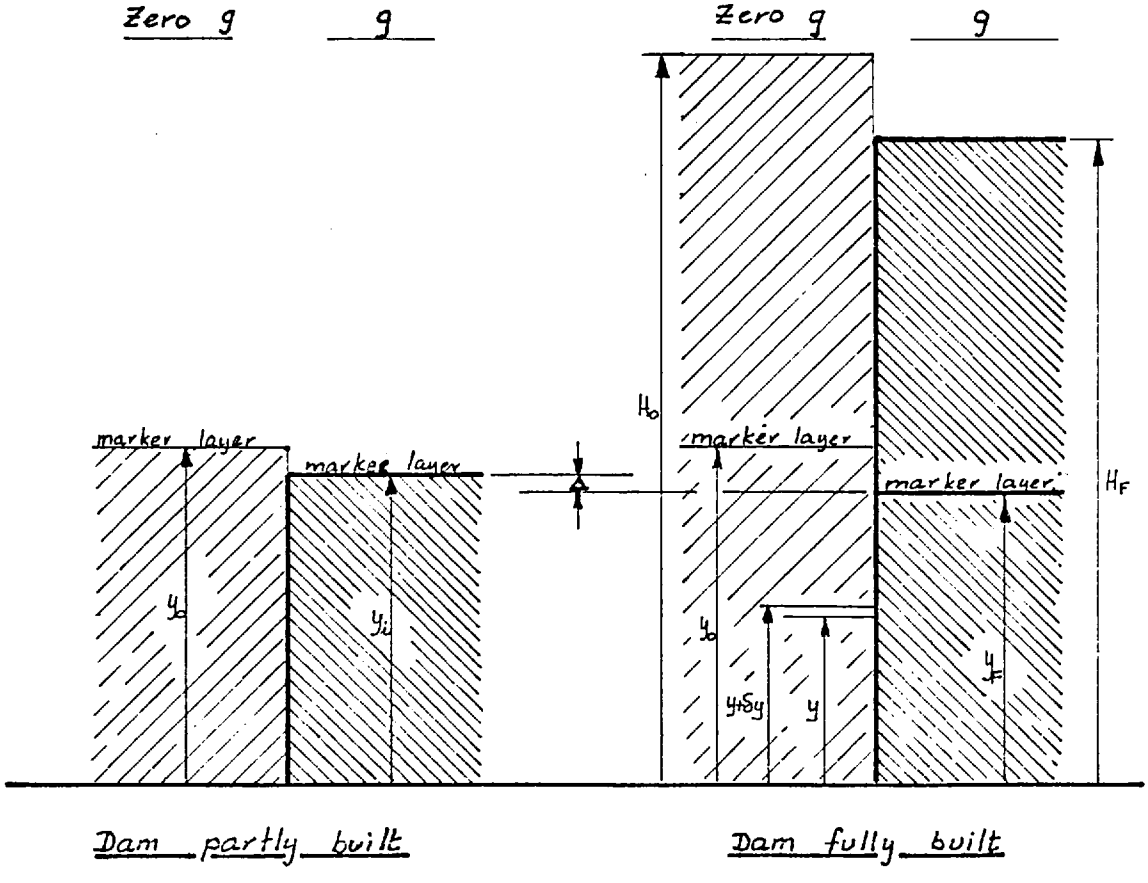
the material at some height y_o.

2. Allow the gravitational acceleration to be applied. Then the layer will settle to a final height of H_F and the marker will come to rest at some height y_F.

3. Now assume that an identical layer to the first is built under zero gravity to a height of y_o.

4. Allow this layer to settle under gravitational acceleration - the height of this layer will be some intermediate value, say y_i.

If the first layer had been constructed with the same quantity of rockfill under the influence of gravitational acceleration, then the thickness of the layer would have been H_F, and the measured settlement of the marker point would have been given by Δ where $\Delta = y_i - y_F$ as shown in the diagram.



Consider a small layer δy at a height of y (zero g). Then after applying g the layer would be subjected to a change in stress of $\gamma_o.(H_o - y)$, where γ_o is equivalent to the placement unit weight, and using equation 6.13 we would have:

$$\text{Change in thickness} = \delta y.D.\{\gamma_o(H_o - y)\}^x$$

So the marker layer displacement would be:

$$y_o - y_F = \Sigma_{y=o}^{y=y_o} D.\{\gamma_o(H_o - y)\}^x \delta y$$

$$\equiv D\gamma_o^x \int_o^{y_o} (H_o - y)^x \, dy$$

This gives

$$y_F = y_o - \frac{D\gamma_o^x}{x+1}\{H_o^{x+1} - (H_o - y_o)^{x+1}\} \qquad (6.14)$$

Similarly

$$H_F = H_o - \frac{D\gamma_o^x}{x+1}\{H_o^{x+1}\} \qquad (6.15)$$

and

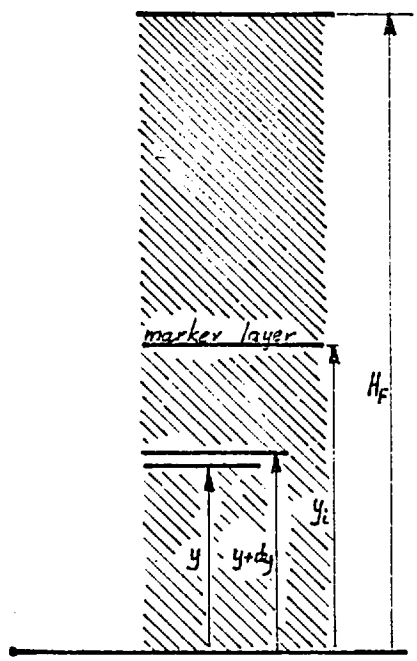
$$y_i = y_o - \frac{D\gamma_o^x}{x+1}\{y_o^{x+1}\} \qquad (6.16)$$

The measured settlement of the marker layer would have been:

$$\Delta = \frac{D\gamma_o^x}{x+1}\{H_o^{x+1} - (H_o - y_o)^{x+1} - y_o^{x+1}\} \qquad (6.17)$$

(Note: y_o and H_o are imaginary dimensions and so can not be measured in the field. The measured dimensions would be y_i, y_F and H_F. So, if equation 6.17 is to be used the values of y_o and H_o must be obtained from equations 6.15 and 6.16.)

If on the other hand it is assumed that the change in unit weight is not significant the relationship for settlement can be obtained in the following manner:



Initial stress on a small layer at y will be $(y_i - y)\gamma_o$.

Final stress on layer will be

$\gamma_o(y_i - y) + \gamma_o(H_F - y_i)$.

So initial strain in layer will be

ε_i where $\varepsilon_i = D.[\gamma_o(y_i - y)]^x$.

Final strain on the layer is ε_f where

$\varepsilon_f = D.\ [\gamma_o(y_i - y) + \gamma_o(H_F - y_i)]^x$.

So change in strain will be

$$\varepsilon_f - \varepsilon_i = D.\{[\gamma_o(y_i - y) + \gamma_o(H_F - y_i)]^x - [\gamma_o(y_i - y)]^x.\}$$

Therefore the measured settlement will be Δ where

$$\Delta = \int_o^{y_i}(\varepsilon_f - \varepsilon_i)dy = D.\gamma_o{}^x \int_o^{y_i}\{[(y_i - y) + (H_F - y_i)]^x - [(y_i - y)]^x\}dy$$

$$\text{So } \Delta = \frac{D.\gamma_o{}^x}{x + 1}\left[H_F{}^{x+1} - (H_F - y_i)^{x+1} - y_i{}^{x+1}\right] \qquad (6.18)$$

The solutions given by equations 6.17 and 6.18 can be compared using data published by Penman, Burland and Charles (1971) of measurements made during construction of Scammonden Dam. The dam is very wide so a large portion of the rockfill shoulders should be fairly close to a one-dimensional strain condition. Fortunately the stress-strain curve for the placement density conditions, obtained from laboratory oedometer tests, is also given in their paper. This data has been replotted on Figure 6.23, from which are obtained the values of the parameters D and x. They are:

$x = 0.52$ and $D = 1.07 \times 10^{-3}$ for true strain and for stress measured in kN/m^2.

Average placement bulk density was 21.2 kN/m^3.

The final height of the dam was $H_F = 70$ m. Taking one of the marker plates (B.10 in the paper), a reasonable value for y_i can be taken as $y_i = 18$ m. The measured settlement was 0.59 m.

Equation 6.15 gives $H_o = 72.31$ m and equation 6.16 gives $y_o = 18.29$ m. Substituting these values into equation 6.17 gives a settlement of 0.54 m. If on the other hand equation 6.18 had been used (assuming constant density) a calculated settlement of 0.52 m is obtained.

The settlement calculations have been repeated for other values

of H_F, and are shown on Figure 6.24a with the measured settlement values. The settlements predicted using constant bulk density (equation 6.18) are only very slightly smaller than those predicted using equation 6.17, which is more difficult to use. In practice, therefore, the use of equation 6.18 would suffice.

In the same paper Penman et al also reported the results of calculated settlements using an equivalent compressibility, which they found to be 0.257×10^{-4} m^2/kN. A comparison of results using this value of compressibility and results from equation 6.17 and 6.18 are shown on Figure 6.24b. It will be noticed that since the result obtained using equation 6.18 and the constant m_v curve were fitted to give the same final settlement at mid-height, there is little difference at other heights. In addition it was assumed that the bulk density was constant for both. However, using equation 6.17, which takes into account the increase in unit weight, results in larger final settlements throughout the layer. At mid-height for a y_i = 35 m the settlement is 0.7 m compared with 0.67 m, i.e. about 4.5% difference.

Papers giving settlement records for other dams are available, in the literature, but few give enough data to enable the values of the parameters x and D to be obtained. One dam, for which this is possible, is the Venemo Dam in Norway; it is a rockfill dam with an upstream asphalted concrete blanket. Settlement records are reported by Holestöl et al (1965)for two cross arm installations on the centre-line

of the dam, where near one-dimensional strain conditions can be expected. Average behaviour of the compression of the dam can be obtained if the compressions of layers between cross-arms are summed for each installation for the period during placing of rockfill. Compressions were recorded during the placing of the upstream asphaltic concrete apron, but these have not been taken into consideration.

The sum of the compressions for installation 1 is 2.44 ft, where 7 cross-arms were installed, and 3.02 ft at installation 2 where 8 cross-arms were installed. The average spacing between cross-arms is reported as 17.4 ft and Holeston et al used a field unit weight of 125 lb/cu ft (2 T/m^3) as a representative value in their paper. They also give results of field measurements of porosity; about 60% of the material excavated had a porosity of 35% and 40% had a porosity of 25%.

An analysis for the settlement is possible only because compressibility data for Venemo material are given by Pigeon (1969, unpublished PhD thesis). Results of three of his tests are shown in Figure 6.25. These results show that for the two tests at initial porosities of 30.3% and 35.9% the index x has the same value of 0.71. The test on the densest material shows a trend towards the same index value. (This index value is not very different from that obtained in the K_o test on Ham River sand shown in Figure 6.22, which was $x = 0.76$.)

Since the major portion of the test pit material had a porosity

of 35%, the following analysis is based on the results of test G-24-2 in Figure 6.25. This gives:

$$\frac{\Delta h}{h_o} = 42 \times 10^{-6} (\Delta\sigma')^{0.71} \quad \text{for } \Delta\sigma' \text{ in lb/ft}^2$$

The sum of the compressions between the cross-arms can be obtained by utilizing equation 6.18, and applying it to calculate the settlement of each cross-arm relative to the next cross-arm below for the final construction height of the dam, and summing the results, This was done and the results are shown below:

Sum of compressions measured at	Installation 1	2.44 ft
" " " " "	Installation 2	3.02 ft
Sum of compressions calculated for	Installation 1	2.22 ft
" " " " "	Installation 2	2.76 ft

The agreement is quite good, but it must be pointed out that it is assumed that the vertical effective stress is given by $\sigma_1' = \gamma h$, where γ is the field unit weight, and h is the height of fill above the point considered, that is assuming true one-dimensional conditions existed. This may not be true for the stress conditions in the dam. See, for example, the analysis by Bishop (1952) for a homogeneous elastic embankment; also Clough and Woodward (1967) for the state of stress in homogeneous embankments. If the Venemo Dam could be considered as homogeneous, it is likely that the ratio $(\sigma_1'/\gamma h)$ would vary from about 0.8 at the base to 1 at the top of the embankment. If this kind of variation was

inserted into the calculation then the agreement would not be as good.

Data published by Sowers et al (1965) also confirm the general behaviour of rockfill derived from hard rock, as is seen in Figure 6.26, but no porosities for their tests were given. It is interesting to note that the values of the index 'x' for all these materials lie in a very narrow band, the main variation being in the value of the coefficient D, which reflects the porosity and rock type. This varies from D = 3.8×10^{-6} for Greywacke (unknown porosity of maximum particle size $1\frac{1}{2}$", tested dry) to D = 86×10^{-6} for Granite (unknown porosity, maximum particle size $1\frac{1}{2}$", tested dry). The values of D are obtained for σ_1' measured in lb/sq ft.

It is of interest to note that the power law form of settlement relationship is also valid for other types of rockfill, examples of this being shown in Figures 6.27, 6.28 and 6.29, which are test results again taken from Pigeon's thesis, and are results of tests on a Silurian mudstone.

6.5 Creep of Rockfill:

The previous discussion indicates that the behaviour of both virgin isotropic and K_o compression of granular material can be considered as resulting from a plastic behaviour at particle contacts. One result of plastic behaviour in metals is that the material creeps in the plastic stress

range. So by analogy one would expect that granular material should also creep when stressed. There is a lot of evidence that rockfill creeps, and it is usually postulated that creep is due to 'cataclastic flow'. The primary deformation at higher stress levels would certainly be dominated by this mechanism, as has been previously argued, but in the lower stress range this mechanism could not be significant. For example it is necessary for a finite stress to be applied in order to build up the loads on particles to a sufficient level in order that fracture could take place. This implies a threshold stress level above which creep takes place. The writer has not been able to find a single reference where a threshold stress was found. In fact the opposite is the case. For example Pigeon (1969) states "There is no threshold value below which creep does not occur.".

Further evidence against fracture-induced creep is to be found in a paper by Sowers et al (1965). They report the results of tests using single rock pyramids or wedges forced against flat ground surfaces of the same rock; all tests indicated a sudden initial settlement, followed by slowly increasing settlement with time. (The load on the rock points was not quoted, but since the settlement recorded was large, the loads used must have been substantial.) The initial settlement was undoubtedly due to crushing; this took place very rapidly, which is understandable as fracture is a very fast process. On the other hand the time-dependent behaviour reported was a slow process, and so probably due

to an entirely different process. This conclusion is further strengthened because in their tests flooding of the loaded contacts resulted in additional rapid settlement.

These additional rapid settlements were observed to produce additional crushing, which would be consistent with a suddenly lowered strength*. This implies that the slow time-dependent behaviour was not associated with strength reduction, but (since the settlement rate decreased with time) it could be argued that the material was strain hardening, and this is consistent with the concept of straining of plastic junctions at particle contacts.

A few short-term creep tests were performed during the course of the research, the results of one of these are shown in

---

* The influence of moisture on the strength of rock has been related to a reduction in the molecular cohesion of the solid. Tests reporting this are given by Colback and Wiid (1965). The explanation is as follows - the molecular cohesion, which according to Orowan (1949) is given by:

$$\sigma_o = \sqrt{\frac{2\gamma E}{a}}$$

where E is Young's modulus and a is the interatomic spacing, both of which are unlikely to be moisture sensitive, implies that the change in strength must then be attributed to a change in surface energy γ when the fluid in contact with the solid has its surface tension changed or the fluid itself is changed.

Supporting evidence for this conclusion is shown in the Figure 6.30 which is from Colback and Wiid's paper.

This result explains the sudden increase in settlement on flooding, but is directly contradictory to the result of obtaining additional settlement by adding an agent (not named by them) which reduced the surface tension to half the normal value. It is of course possible that this agent caused a decrease in the molecular cohesion of the solid material, but this is pure speculation!

Figures 6.31 to 6.35. They show a test on saturated Ham River sand subjected first to an isotropic stress of 4000 psi, and allowed to creep for 60 minutes, after which the stress was reduced to 0.7 psi and the swelling creep observed. The swelling creep does not fit into the 'cataclastic flow' theory, as the stresses on the particles are being reduced, so they should not fracture.

One point that can be noticed is that at the high confining stress of 4000 psi, the volumetric strain is very nearly equal to 3 x axial strain, indicating that the membrane had probably penetrated as far as possible, and thus these results are probably free from this source of error. In contrast the volume changes in the swelling stage at low pressures are considerably larger than 3 x axial strain, which of course would be the result of the rubber disengaging from its deeply buried state. In this case it is better to rely on the axial strain measurements.

Concentrating on the axial strain measurements it is seen that a logarithmic creep relationship is a good fit to the swelling creep behaviour, but not so good for the consolidation behaviour. But if a power function is fitted as shown on Figure 6.34 and 6.35 the index for the power law is the same for both swelling and consolidating creep, and is in fact very close to the power law suggested by Andrade (1910, 1914):

$$\varepsilon_1 (t) = A\, t^{\frac{1}{3}}$$

The index in these tests on Ham River sand is in fact 0.39.

Further research into the effects of pore fluid with differing surface tensions and of varying temperatures on the creep behaviour of granular materials should throw some additional light on the physical basis of creep in these materials.

6.6 Summary:

It was shown that the effective stress controlling the volume changes in isotropic compression could be represented by the equation:

$$\Delta\sigma_3' = (\Delta\sigma_3 - \Delta u) + \frac{C_s}{C}.\Delta u$$

Also, the results reported again support the hypothesis of plastic junctions for granular material, for virgin loading conditions. Although the plastic strains and the elastic strains are of similar magnitude, they can be lumped together, as they both appear to be related to a power function of the effective stress.

Extending this lumped model to one-dimensional strain conditions has enabled a rather simple form of one-dimensional settlement calculation to be developed, which gave reasonable agreement with field measurements of rockfill dam settlements.

It was also shown that the creep behaviour of granular material supported the plastic junction hypothesis.

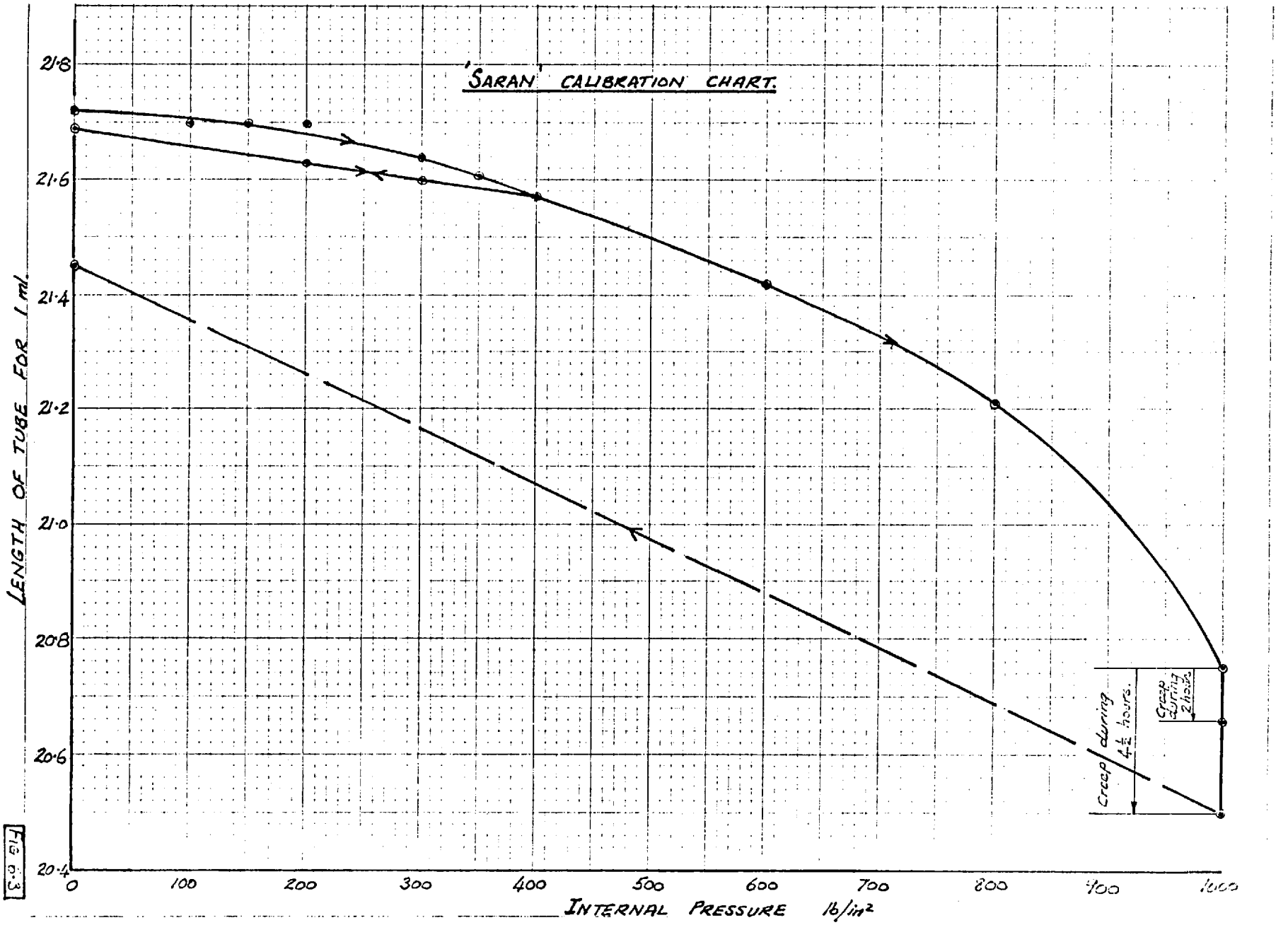

'SARAN' CALIBRATION CHART.
LENGTH OF TUBE FOR 1 ml.
21·8
21·6
21·4
21·2
21·0
20·8
20·6
20·4
0
100
200
300
400
500
600
700
800
900
1000
INTERNAL PRESSURE lb/in²
Creep during 4½ hours.
Creep during 2 hours.

Fig 6.3

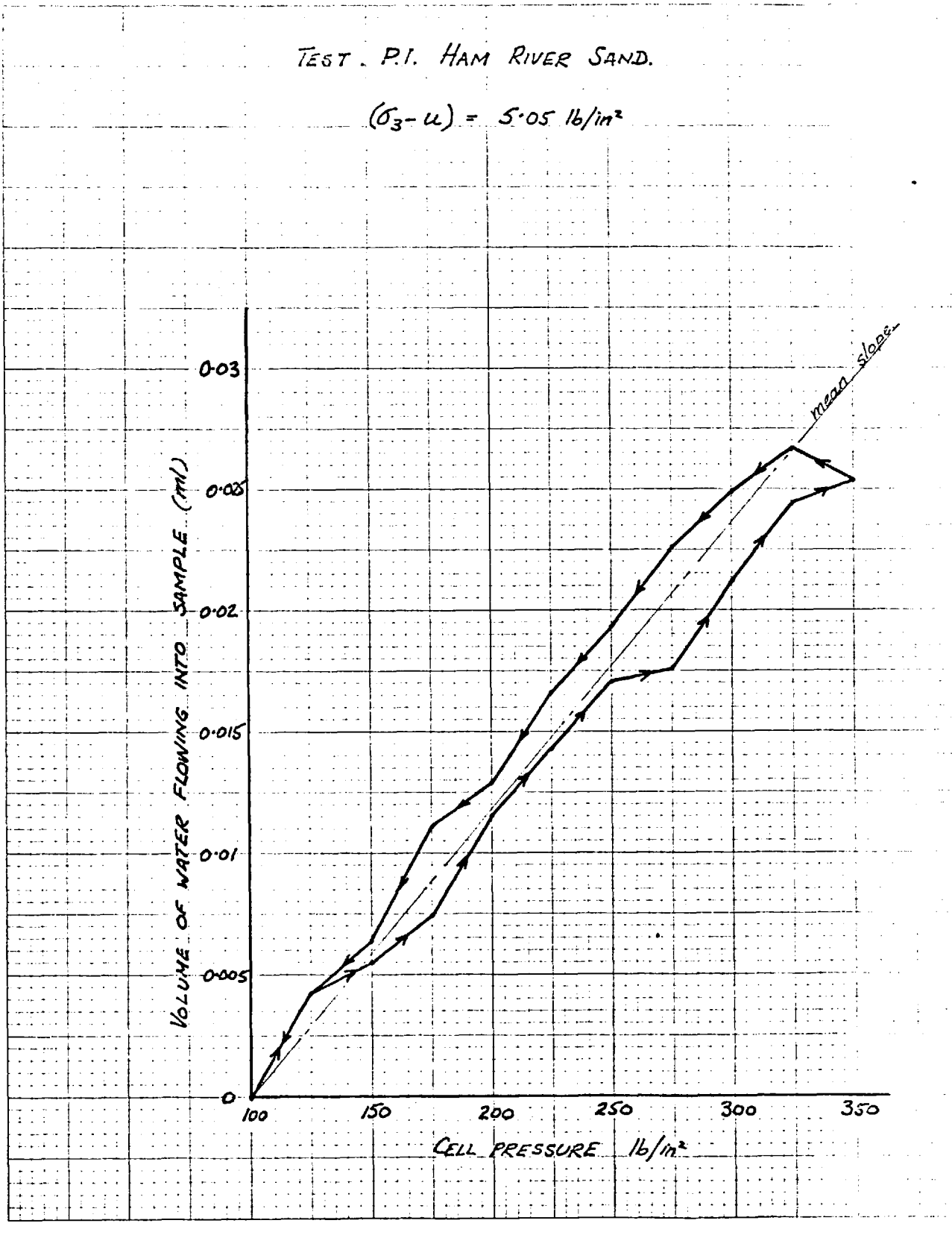

TEST. P.I. HAM RIVER SAND.
$(\sigma_3 - u) = 5.05$ lb/in²
mean slope
0·03
0·025
0·02
0·015
0·01
0·005
0
VOLUME OF WATER FLOWING INTO SAMPLE (ml)
100
150
200
250
300
350
CELL PRESSURE lb/in²

FIG 6·4

TEST P.1. HAM RIVER SAND.

$(\sigma_3 - u) = 5{\cdot}05$ lb/in²

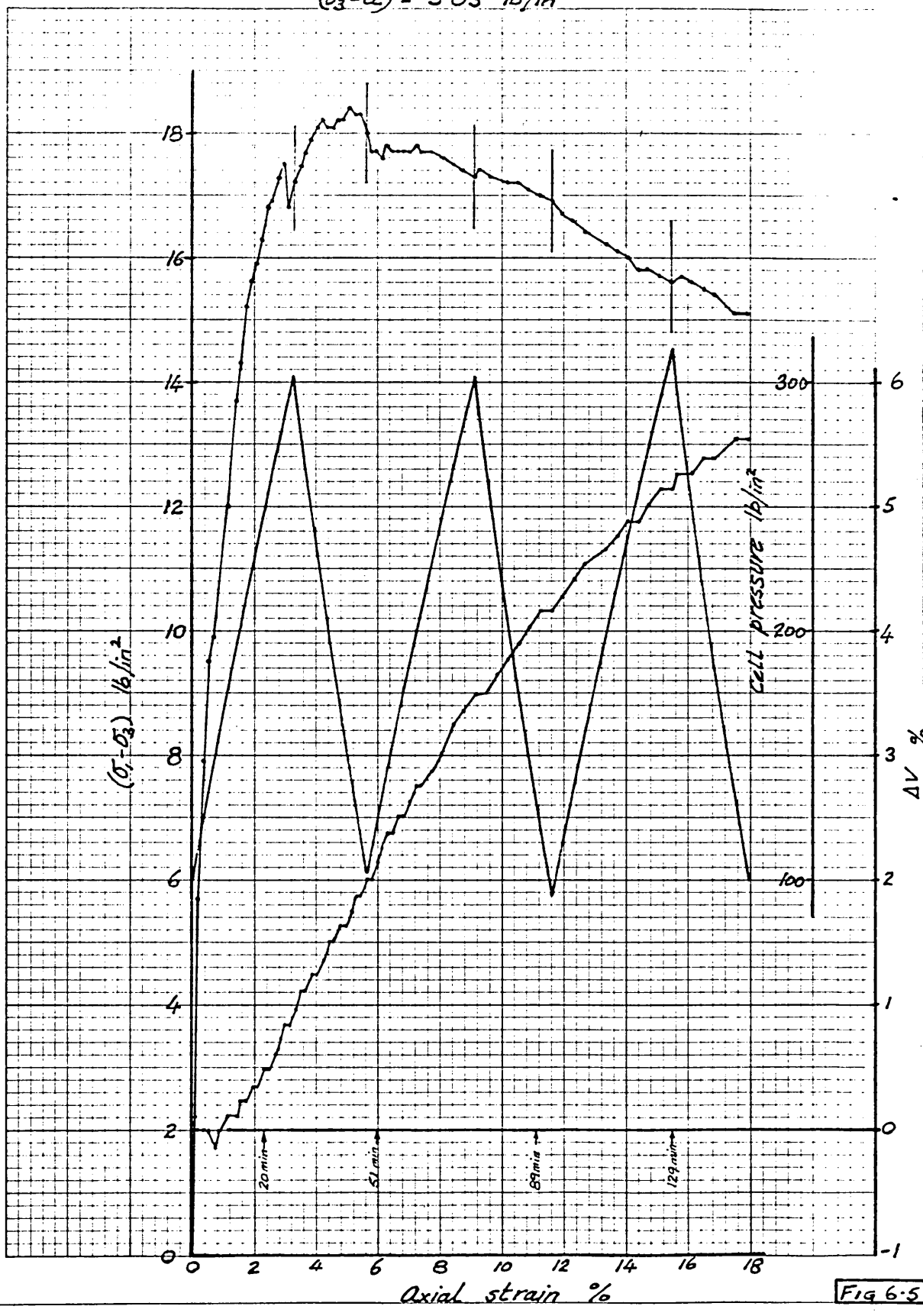


Fig 6·5

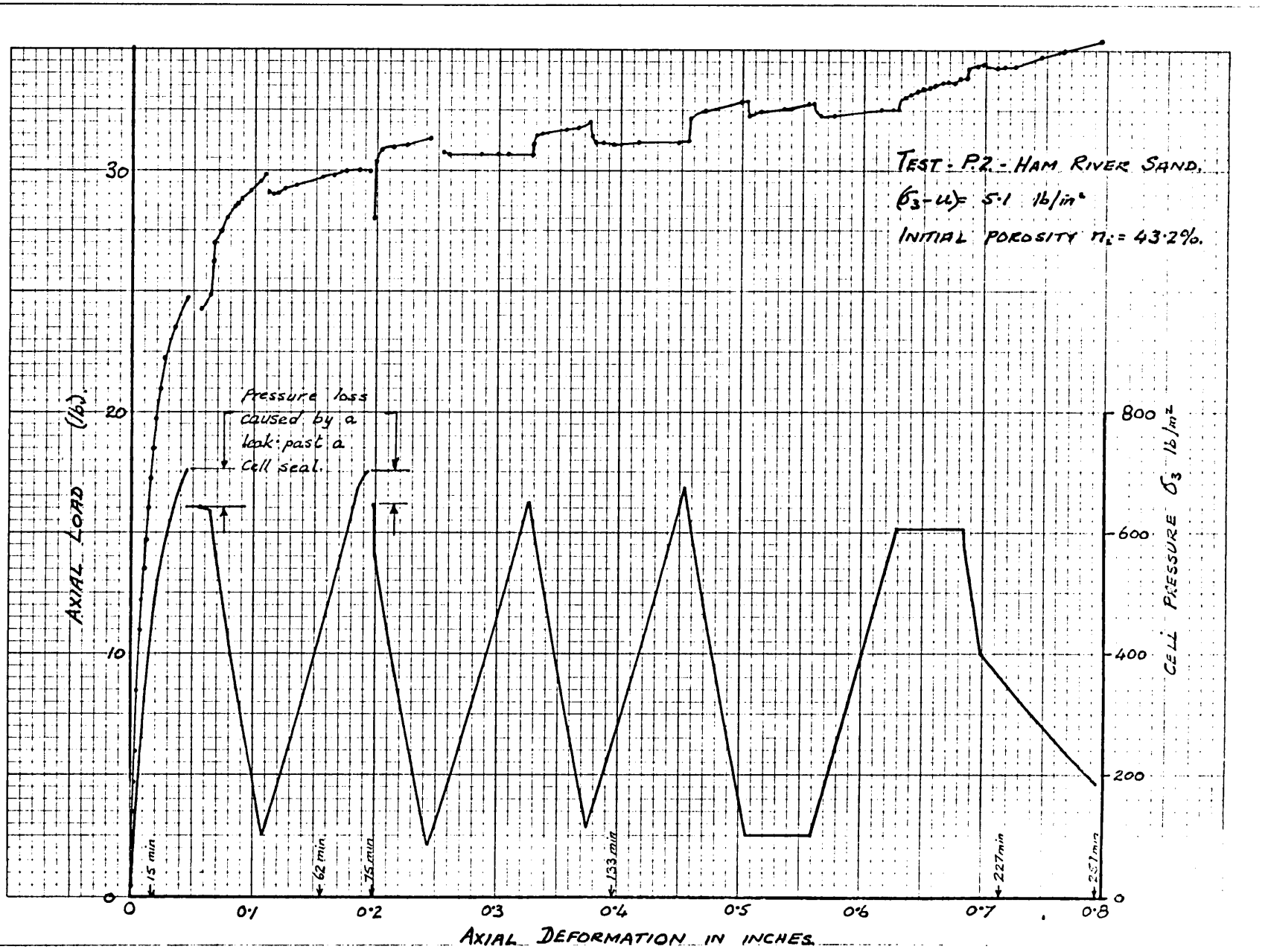

TEST - P.2 - HAM RIVER SAND.
$(\sigma_3 - u) = 5.1$ lb/in²
INITIAL POROSITY $n_i = 43.2\%$.
Pressure loss caused by a leak past a cell seal.
AXIAL LOAD (lb).
CELL PRESSURE σ_3 lb/in²
AXIAL DEFORMATION IN INCHES
0
10
20
30
0·1
0·2
0·3
0·4
0·5
0·6
0·7
0·8
200
400
600
800
15 min
62 min
75 min
133 min
227 min
281 min

Fig 6.9

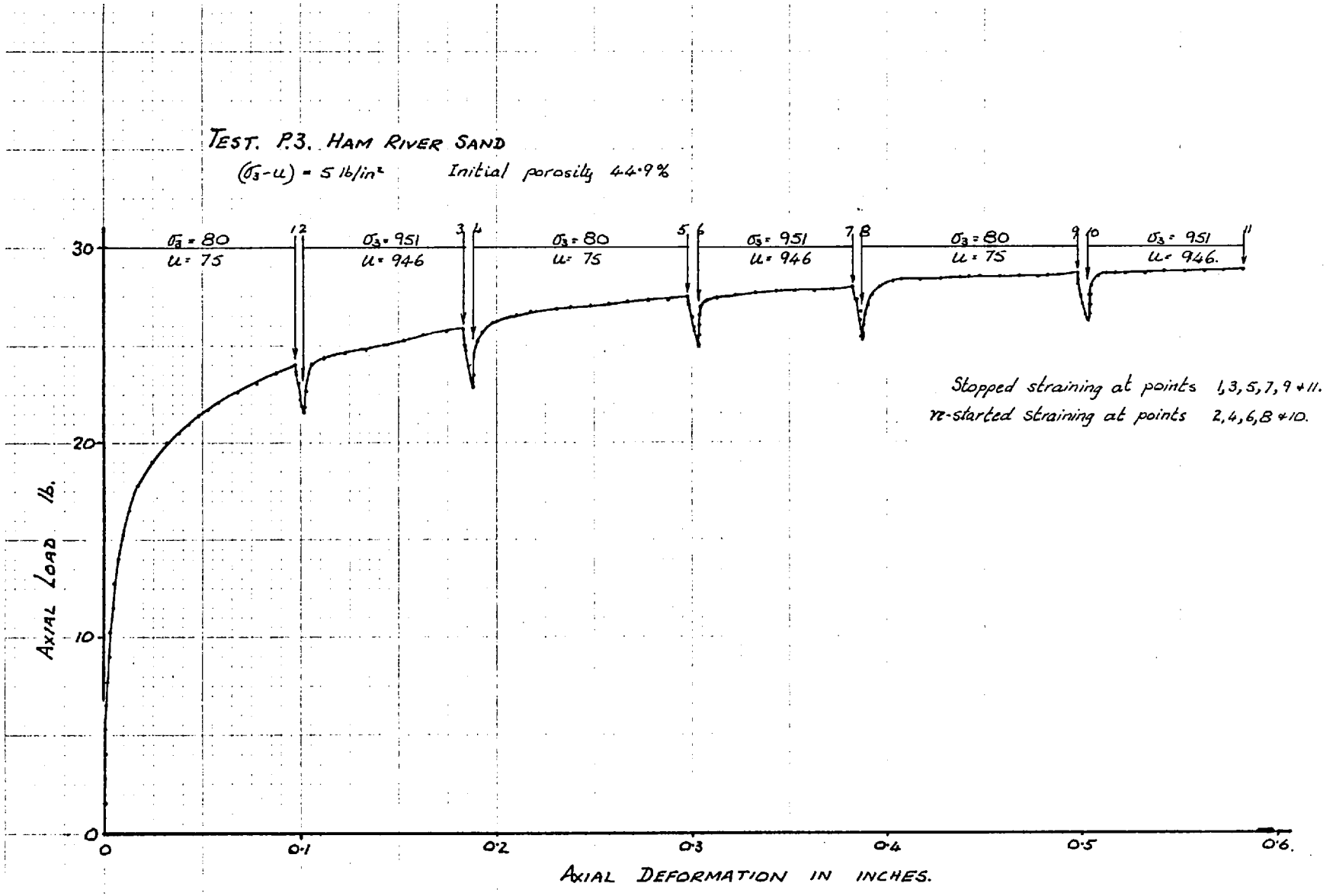
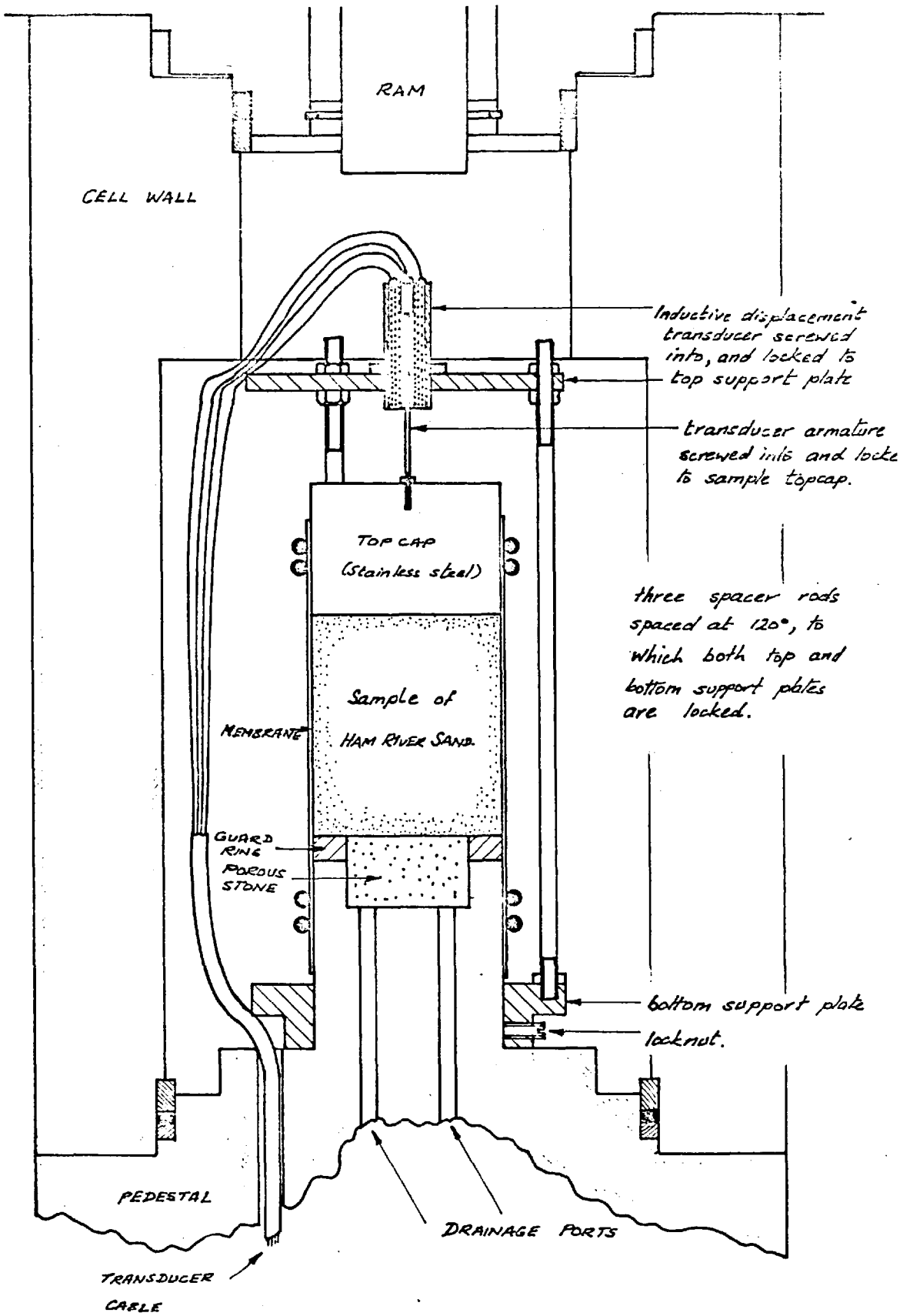

TEST. P.3. HAM RIVER SAND
(σ3-u) = 5 lb/in²
Initial porosity 44·9%
σ3 = 80
u = 75
σ3 = 951
u = 946
σ3 = 80
u = 75
σ3 = 951
u = 946
σ3 = 80
u = 75
σ3 = 951
u = 946.
1
2
3
4
5
6
7
8
9
10
11
Stopped straining at points 1, 3, 5, 7, 9 + 11.
re-started straining at points 2, 4, 6, 8 + 10.
AXIAL LOAD lb.
30
20
10
0
0
0·1
0·2
0·3
0·4
0·5
0·6.
AXIAL DEFORMATION IN INCHES.

Fig 6.7



TEST ARRANGEMENT FOR ISOTROPIC STRESS TESTS

FIG 6·8

TEST. IC.1. HAM RIVER SAND.

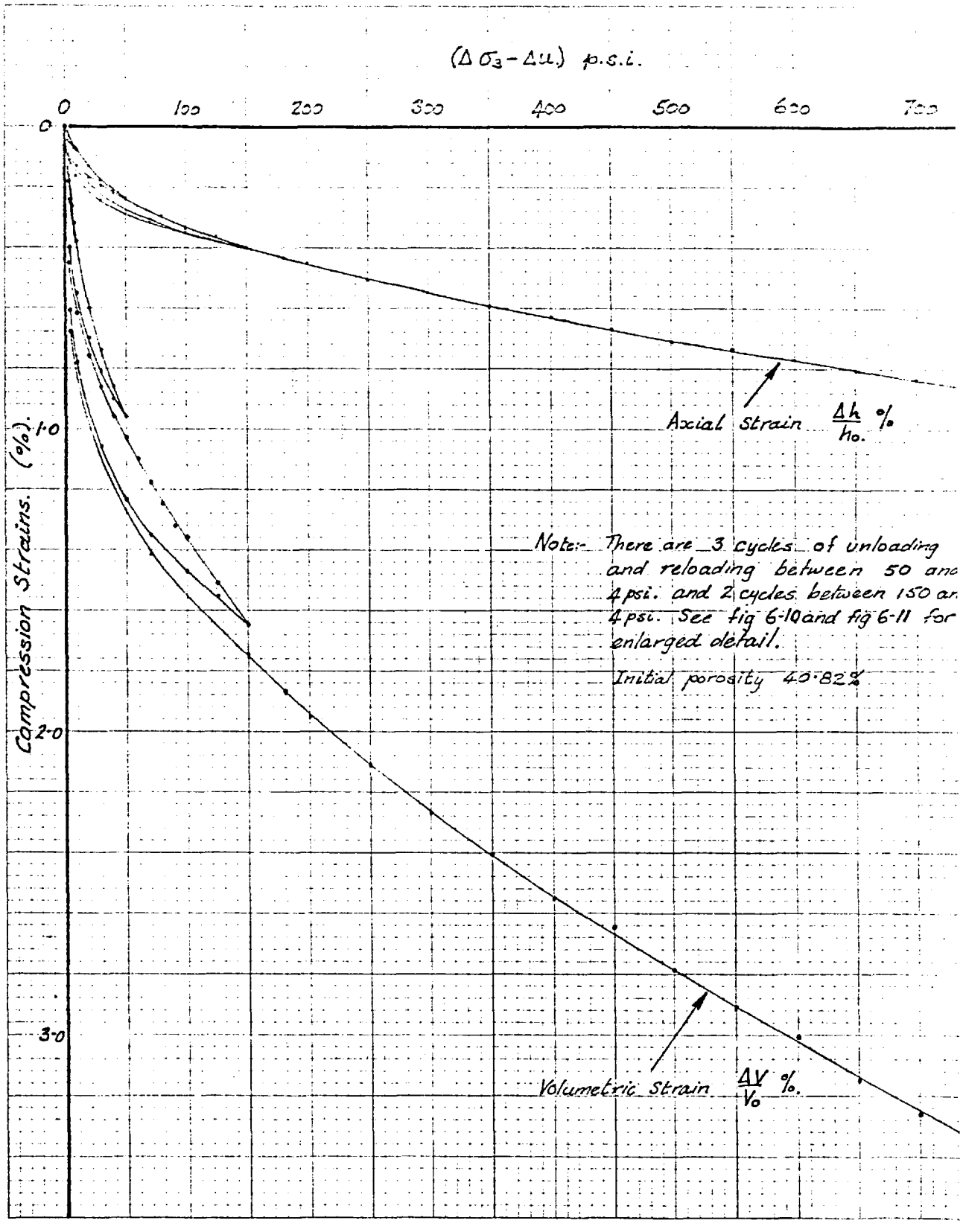


FIG 6·9

TEST. IC.1. HAM RIVER SAND.

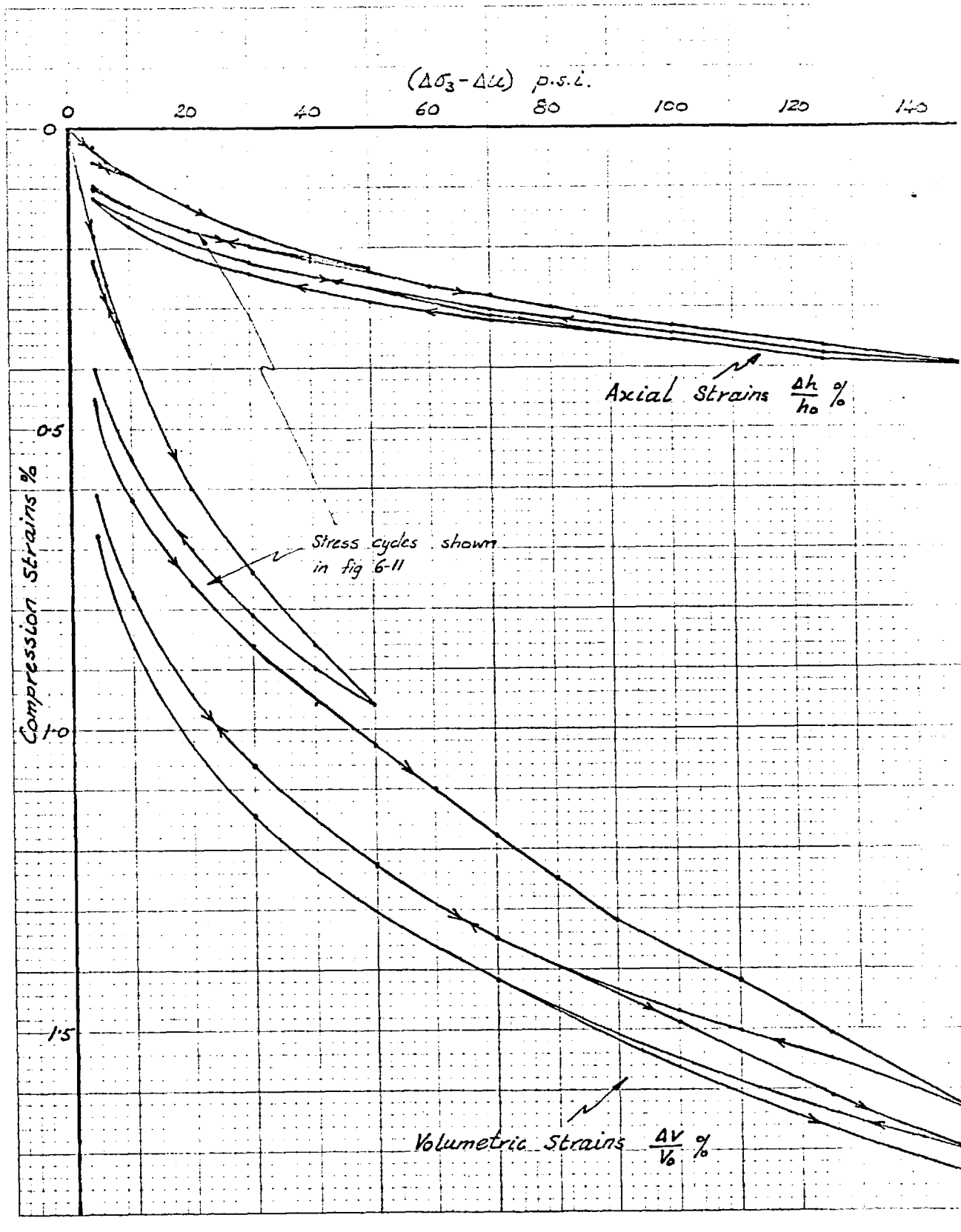


FIG 6·10

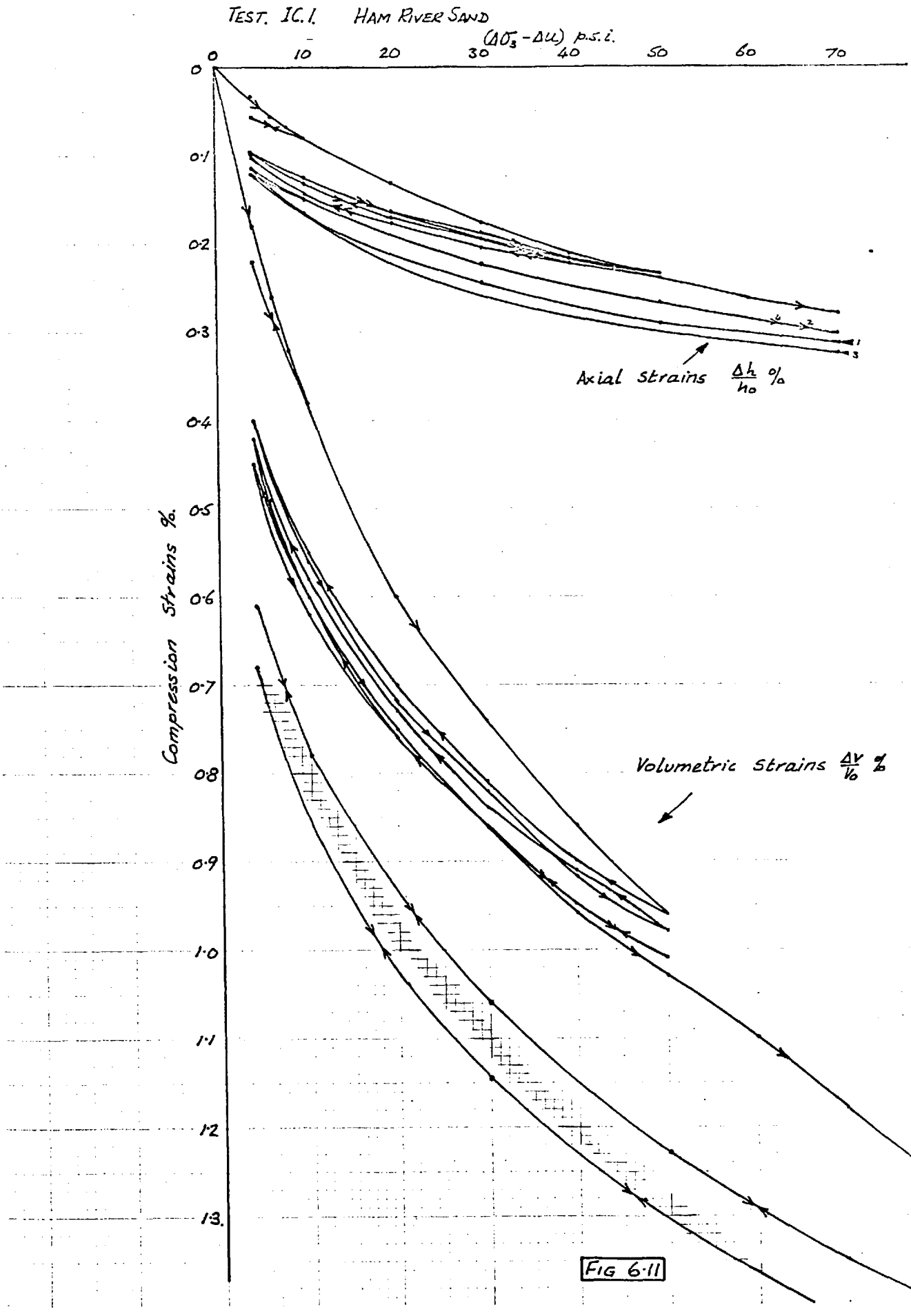

TEST. IC.1. HAM RIVER SAND
$(\Delta\bar{\sigma}_3 - \Delta u)$ p.s.i.
0
10
20
30
40
50
60
70
0
0·1
0·2
0·3
0·4
0·5
0·6
0·7
0·8
0·9
1·0
1·1
1·2
1·3
Compression Strains %.
Axial strains $\frac{\Delta h}{h_0}$ %
Volumetric strains $\frac{\Delta V}{V_0}$ %
1
2
3

FIG 6·11

TEST. IC.1. - HAM RIVER SAND.

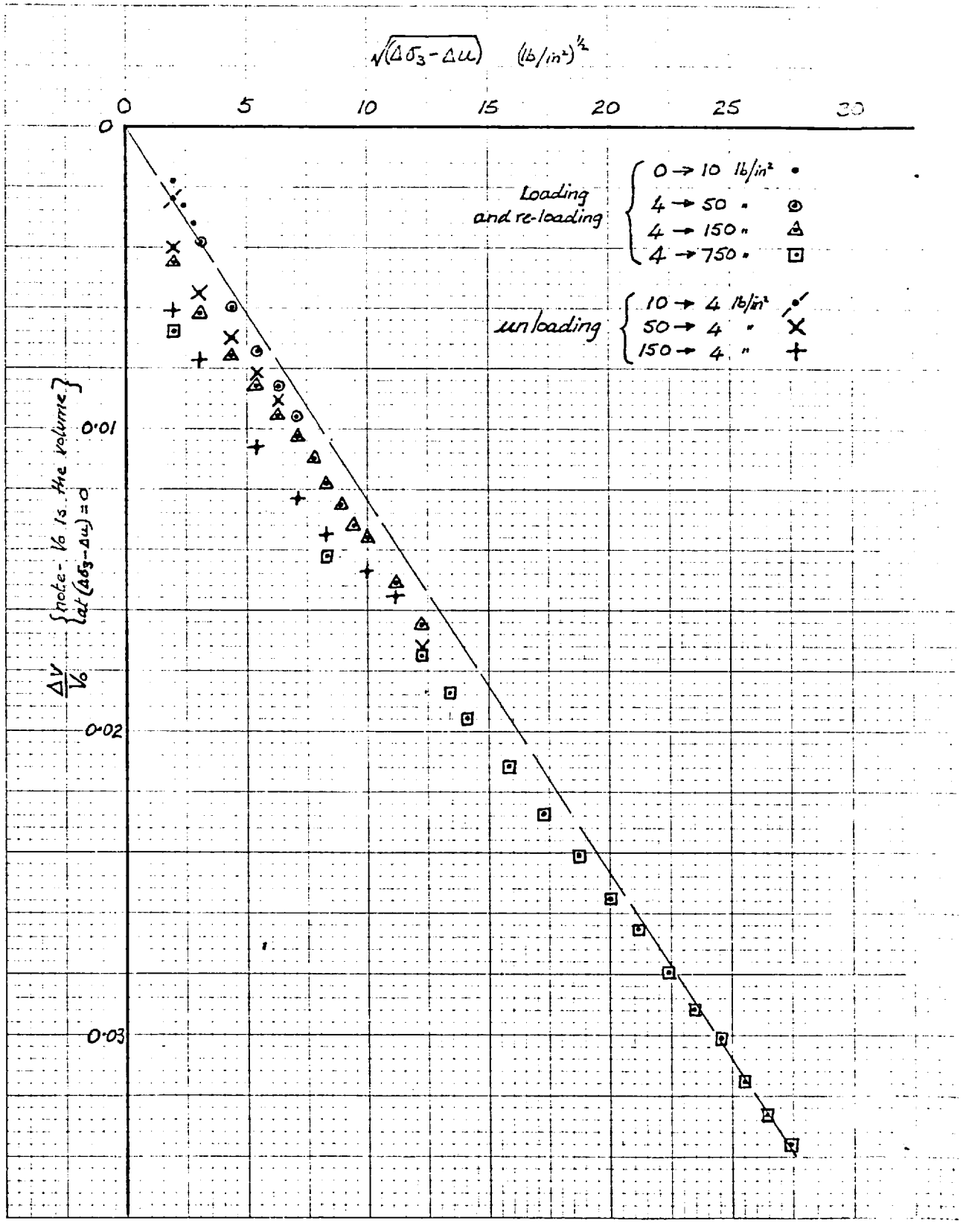


FIG 6·12

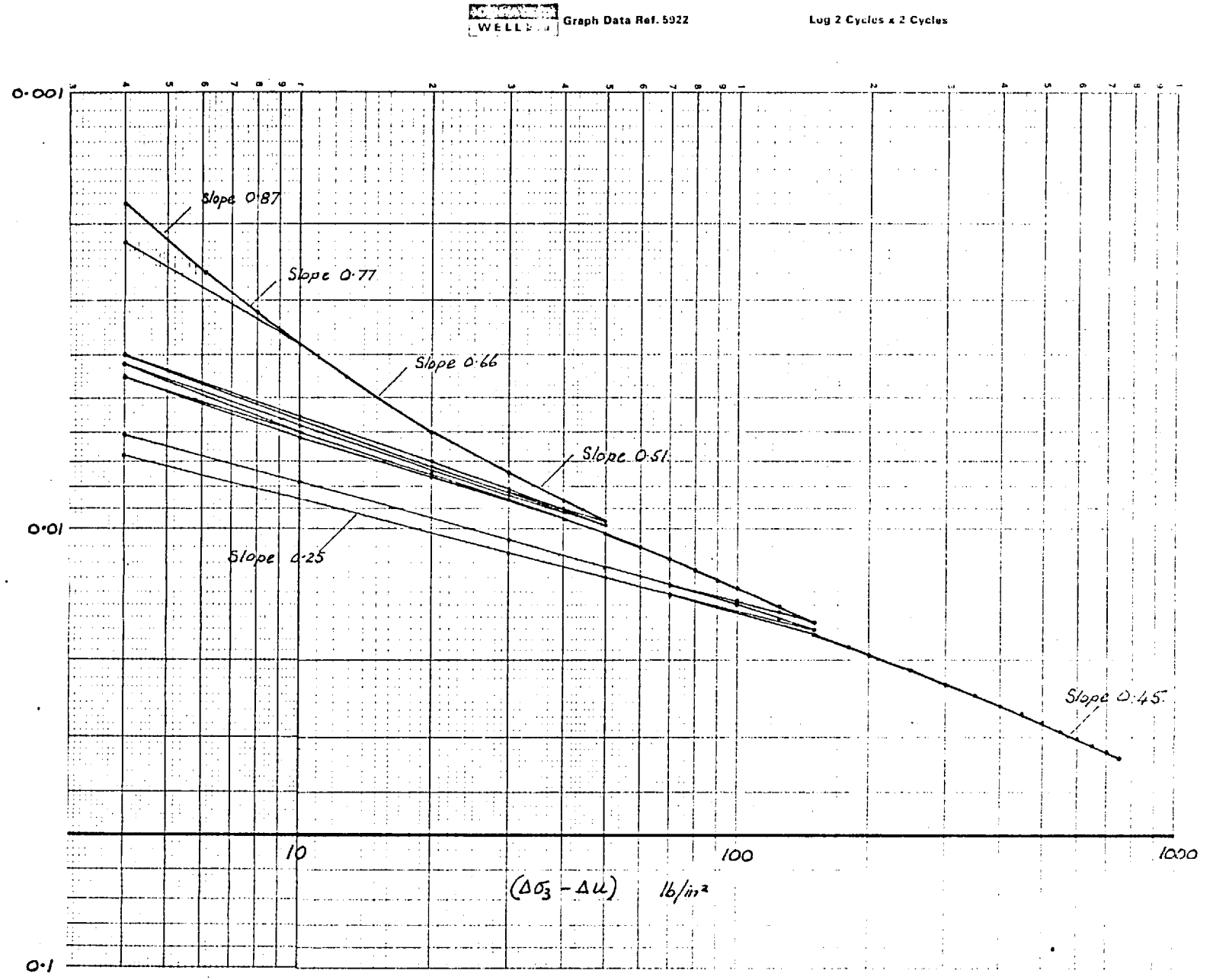

WELLS
Graph Data Ref. 5922
Log 2 Cycles x 2 Cycles
0·001
0·01
0·1
ΔV/V0
Slope 0·87
Slope 0·77
Slope 0·66
Slope 0·51
Slope 0·25
Slope 0·45
10
100
1000
(Δσ3 − Δu) lb/in²

FIG 6·13

Log 2 Cycles x 2 Cycles

SCHLUMBERGER WELL SERVICES Graph Data Ref. 5922

Log 2 Cycles x 2 Cycles

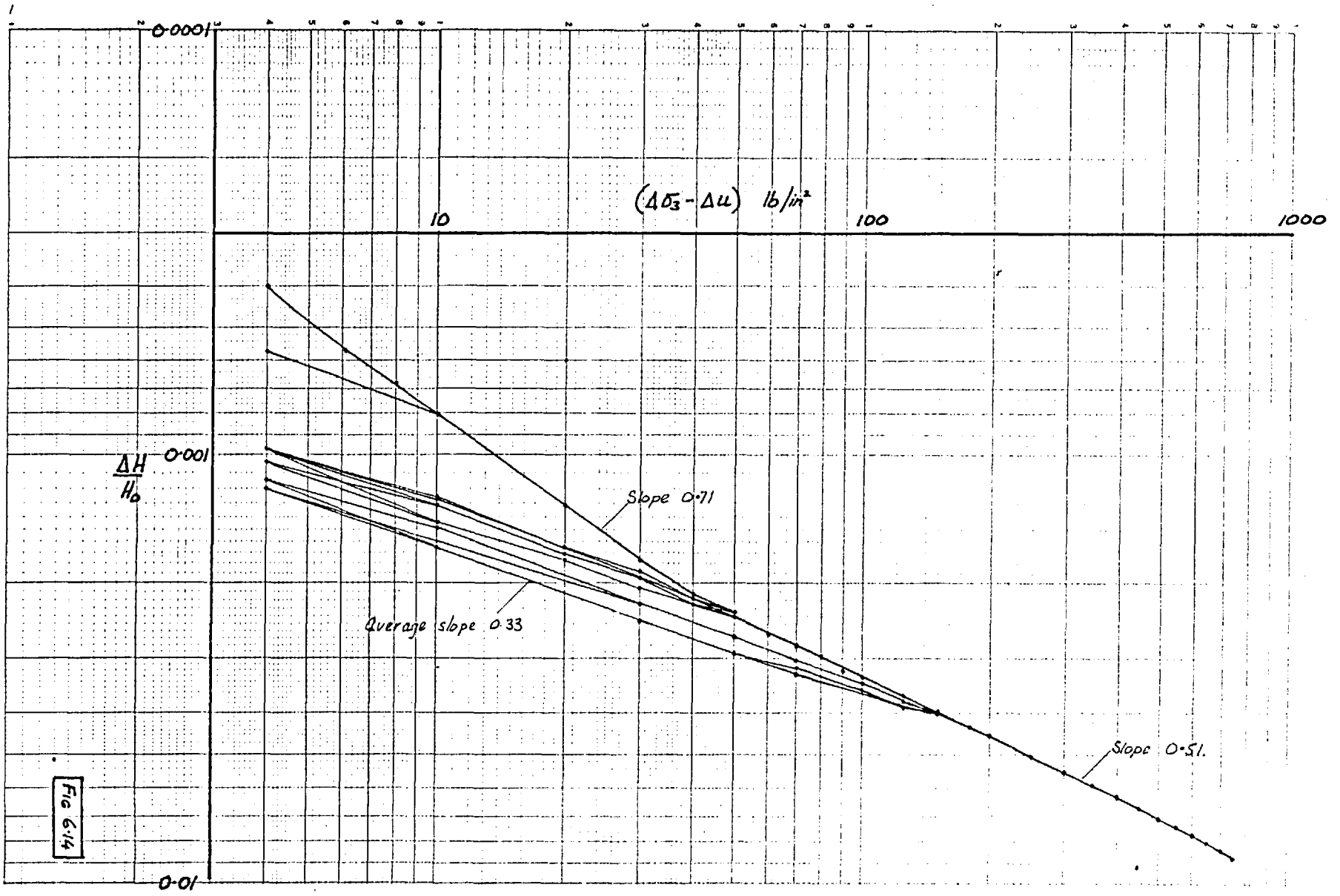
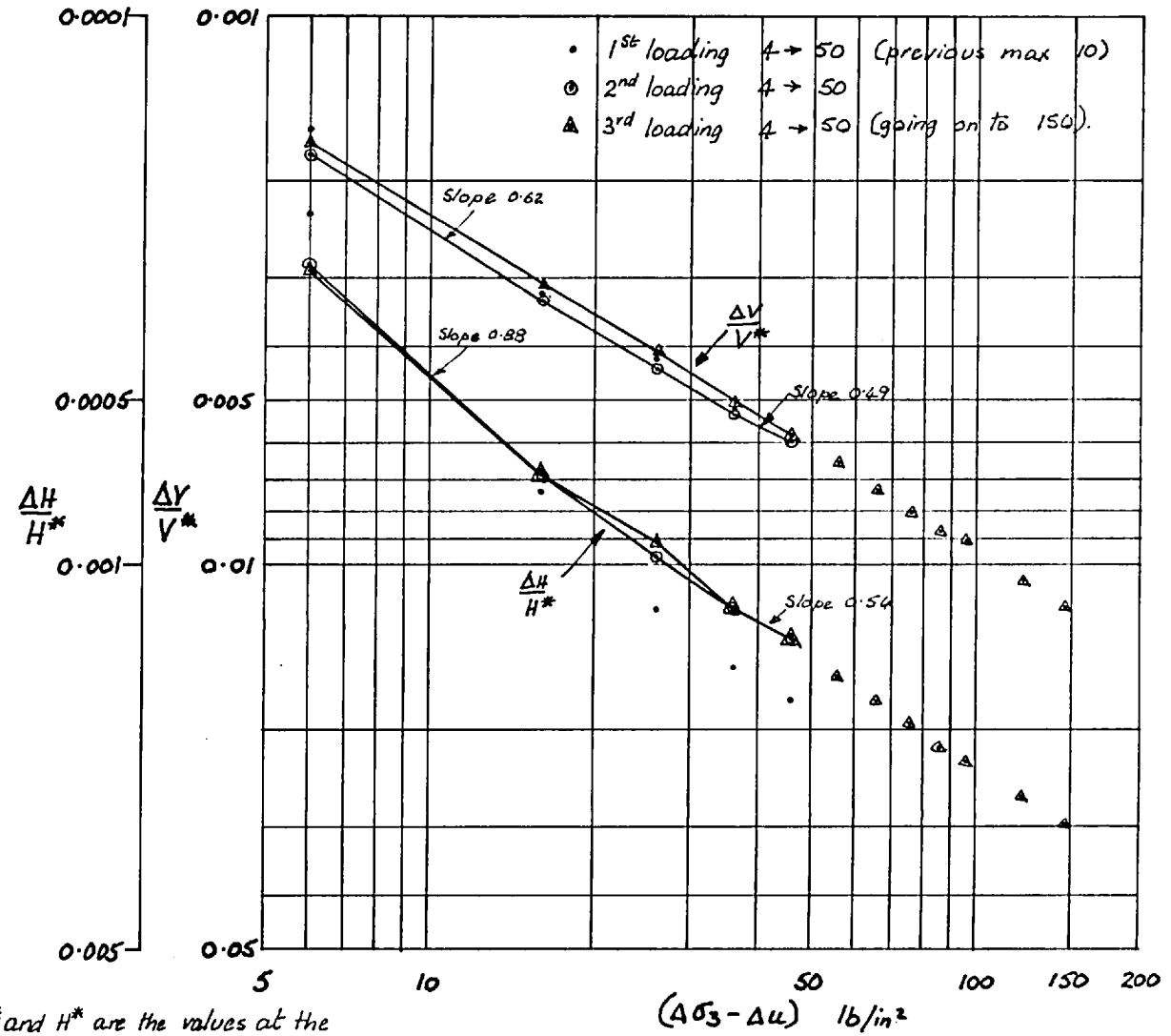
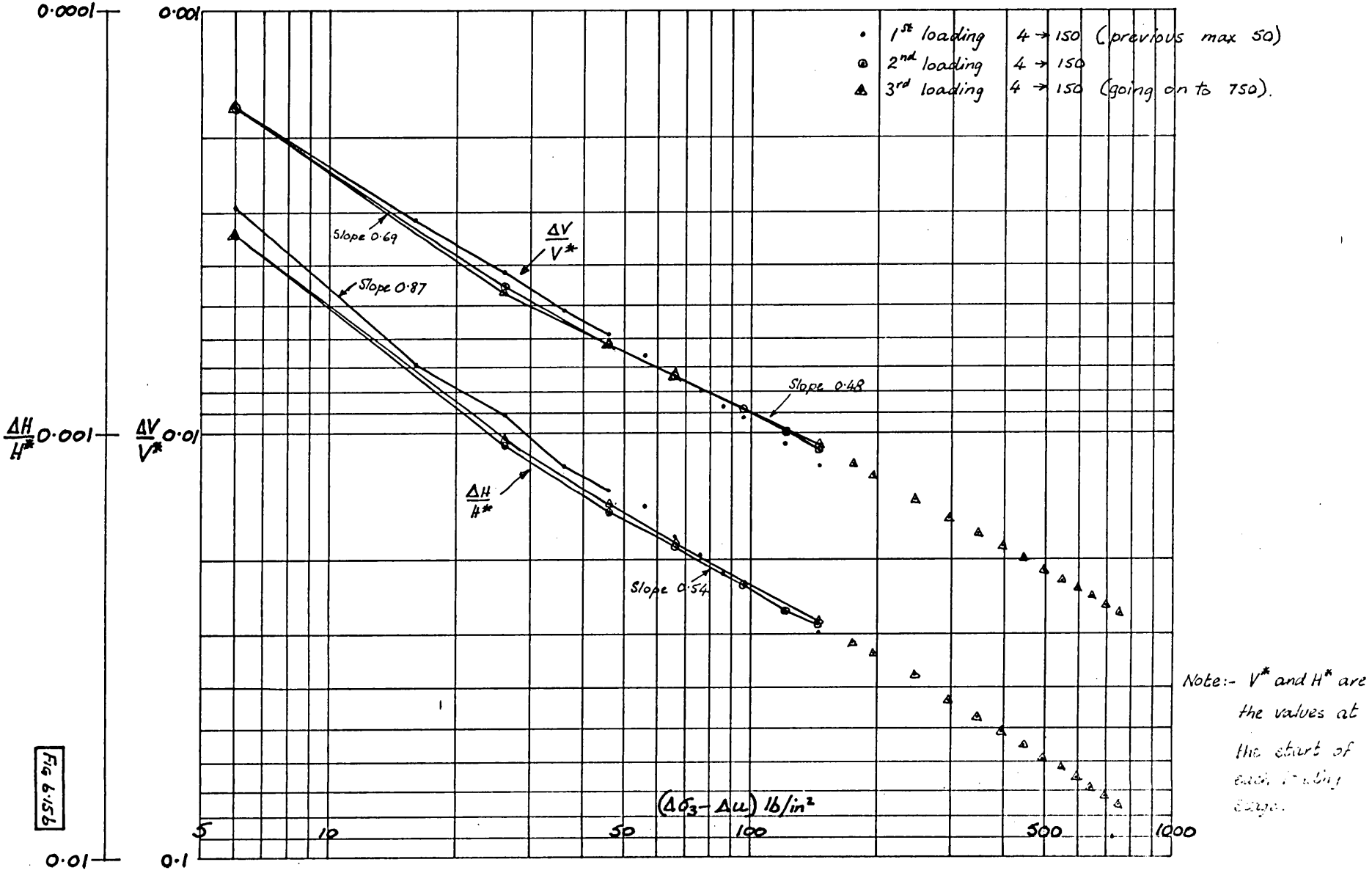


Fig 6·14



Note:- V^* and H^* are the values at the start of each loading stage.

Fig 6·15a



Note:- V* and H* are the values at the start of each loading stage.

Fig 6.15b

ISOTROPIC CONSOLIDATION TESTS ON HAM RIVER SAND AND CAST STEEL SHOT UP TO $(\Delta\sigma_3 - \Delta u) = 990$ lb/in²

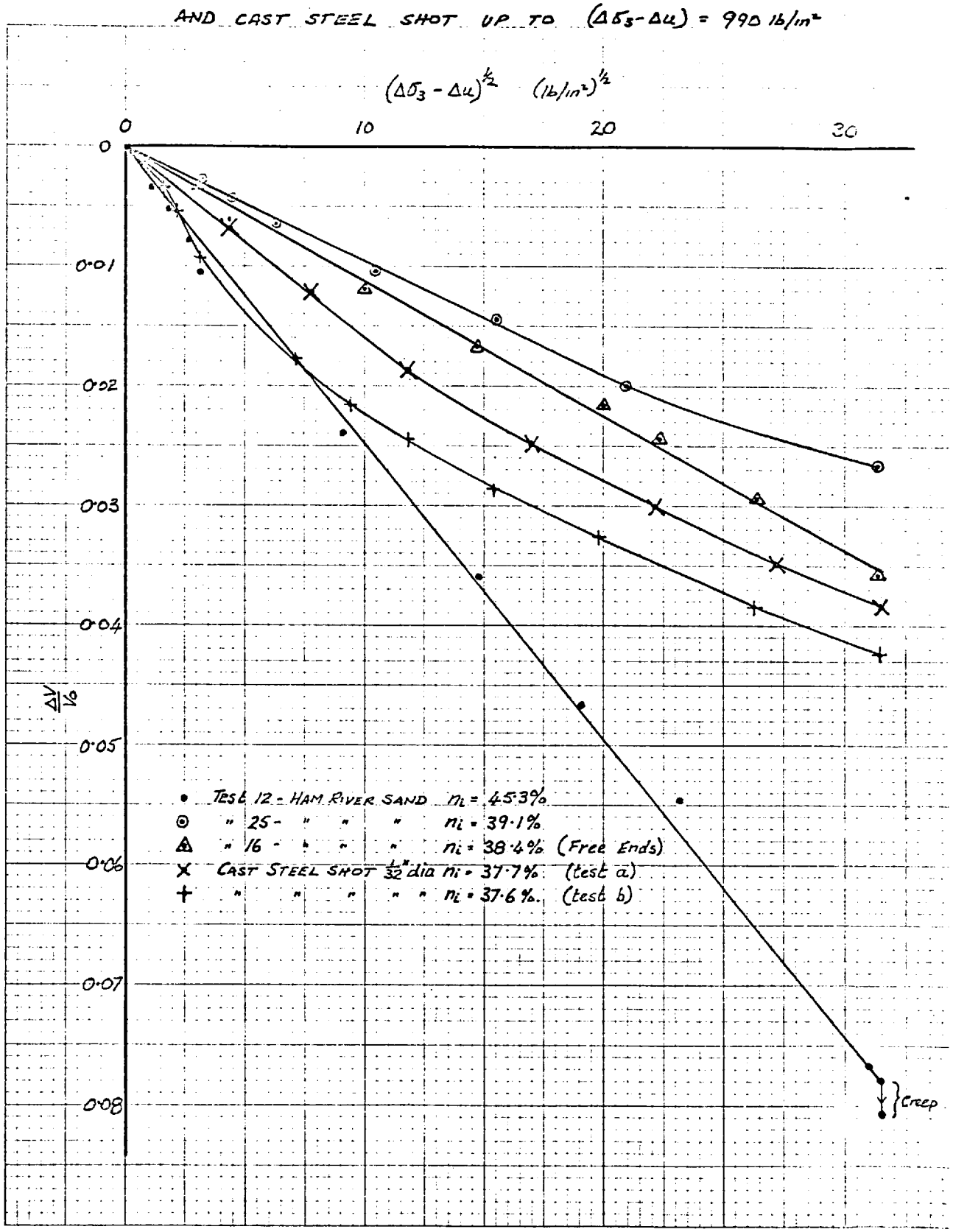


FIG 6·16

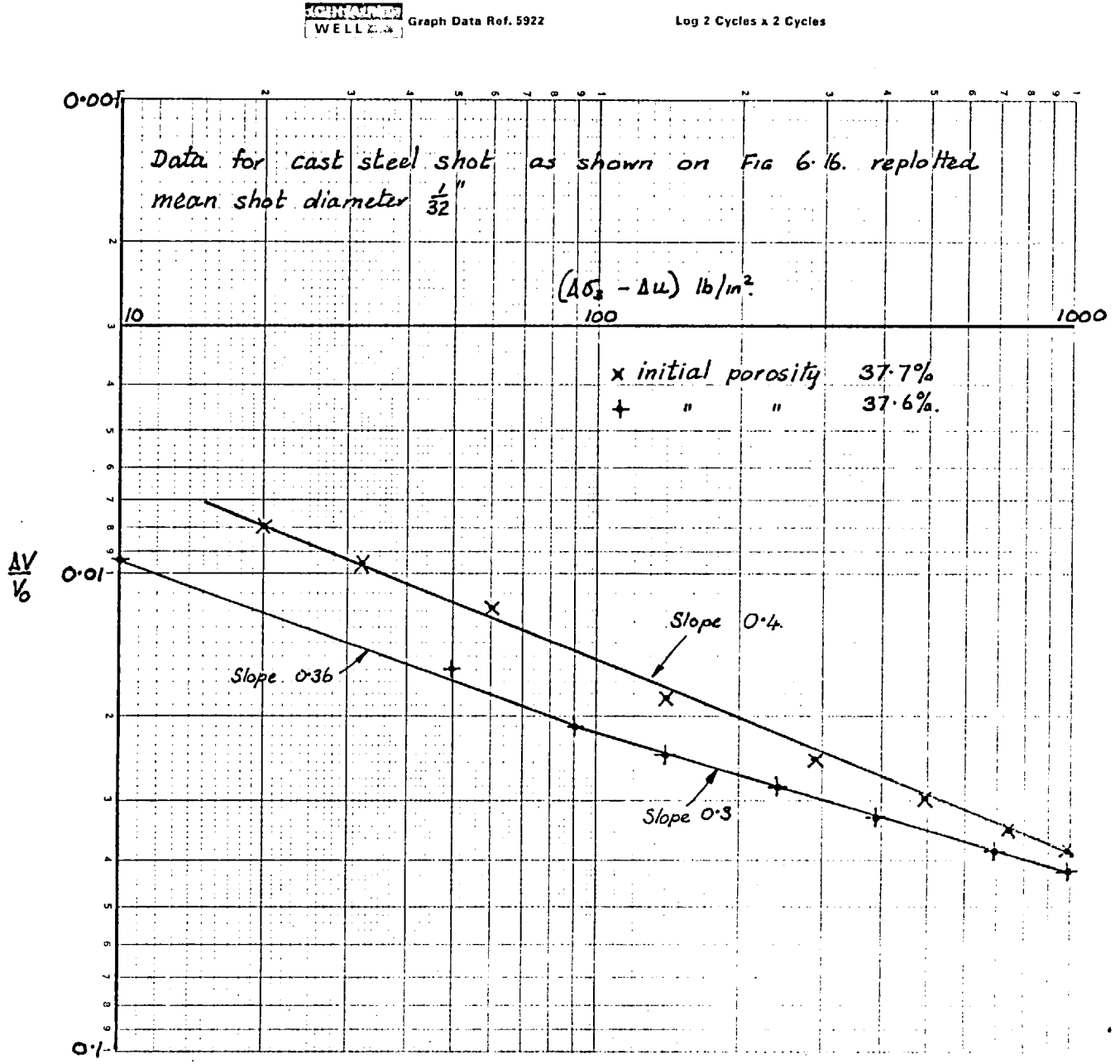

Graph Data Ref. 5922
Log 2 Cycles x 2 Cycles
Data for cast steel shot as shown on Fig 6·16. replotted
mean shot diameter 1/32"
(Δσ3 - Δu) lb/in²
10
100
1000
0·001
0·01
0·1
ΔV/V0
x initial porosity 37·7%
+ " " 37·6%.
Slope 0·4
Slope 0·36
Slope 0·3

Fig 6·17

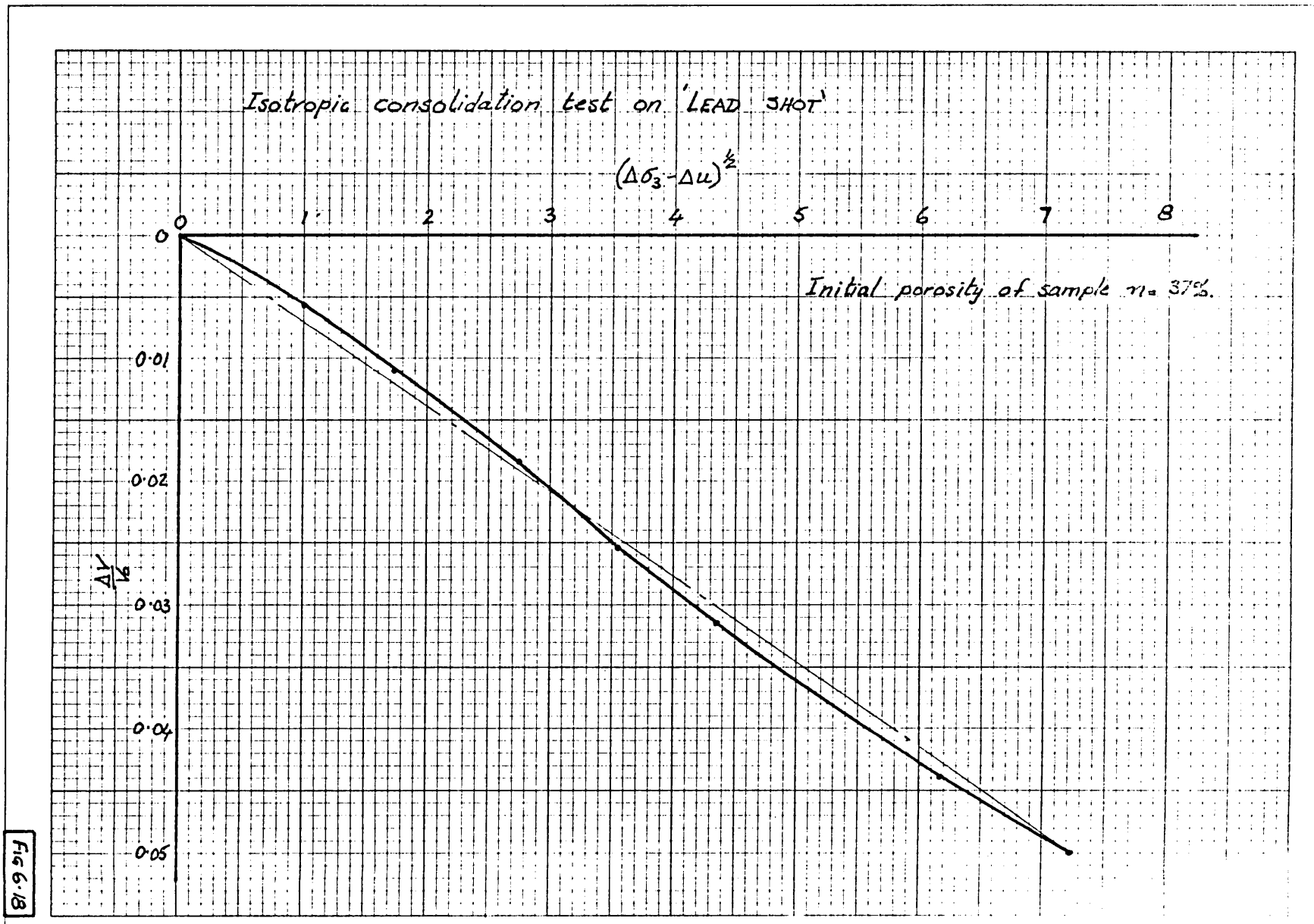

Isotropic consolidation test on 'LEAD SHOT'
$(\Delta\sigma_3 - \Delta u)^{1/2}$
0
1
2
3
4
5
6
7
8
Initial porosity of sample n = 37%.
0·01
0·02
$\frac{\Delta V}{V_0}$
0·03
0·04
0·05

Fig 6·18

CHART-EL GRAPH SHEET No. 5541 LOG 4 CYCLES X M/M A C/M

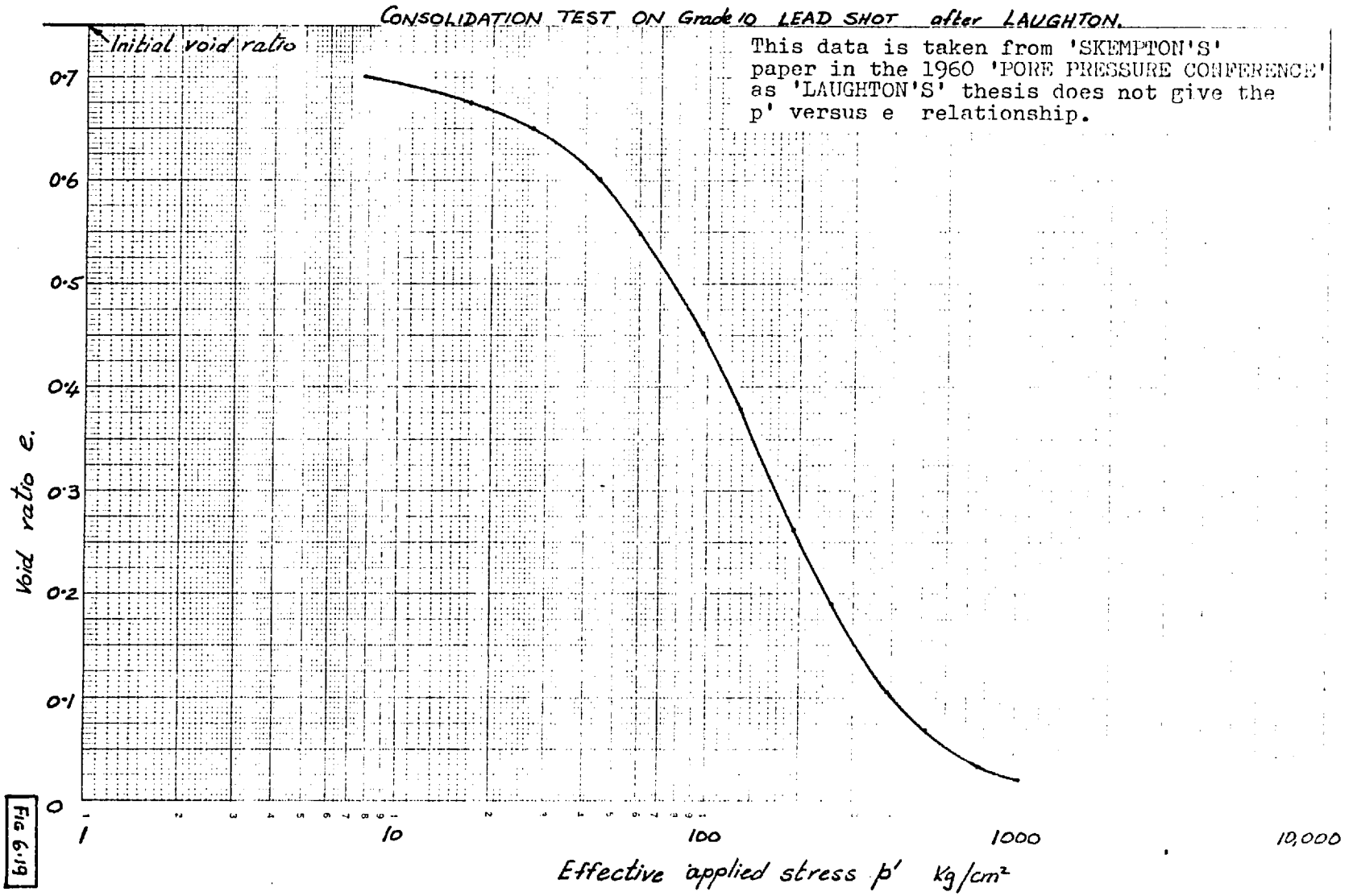


Fig. 6.19

WELL Graph Data Ref. 5922 Log 2 Cycles x 2 Cycles

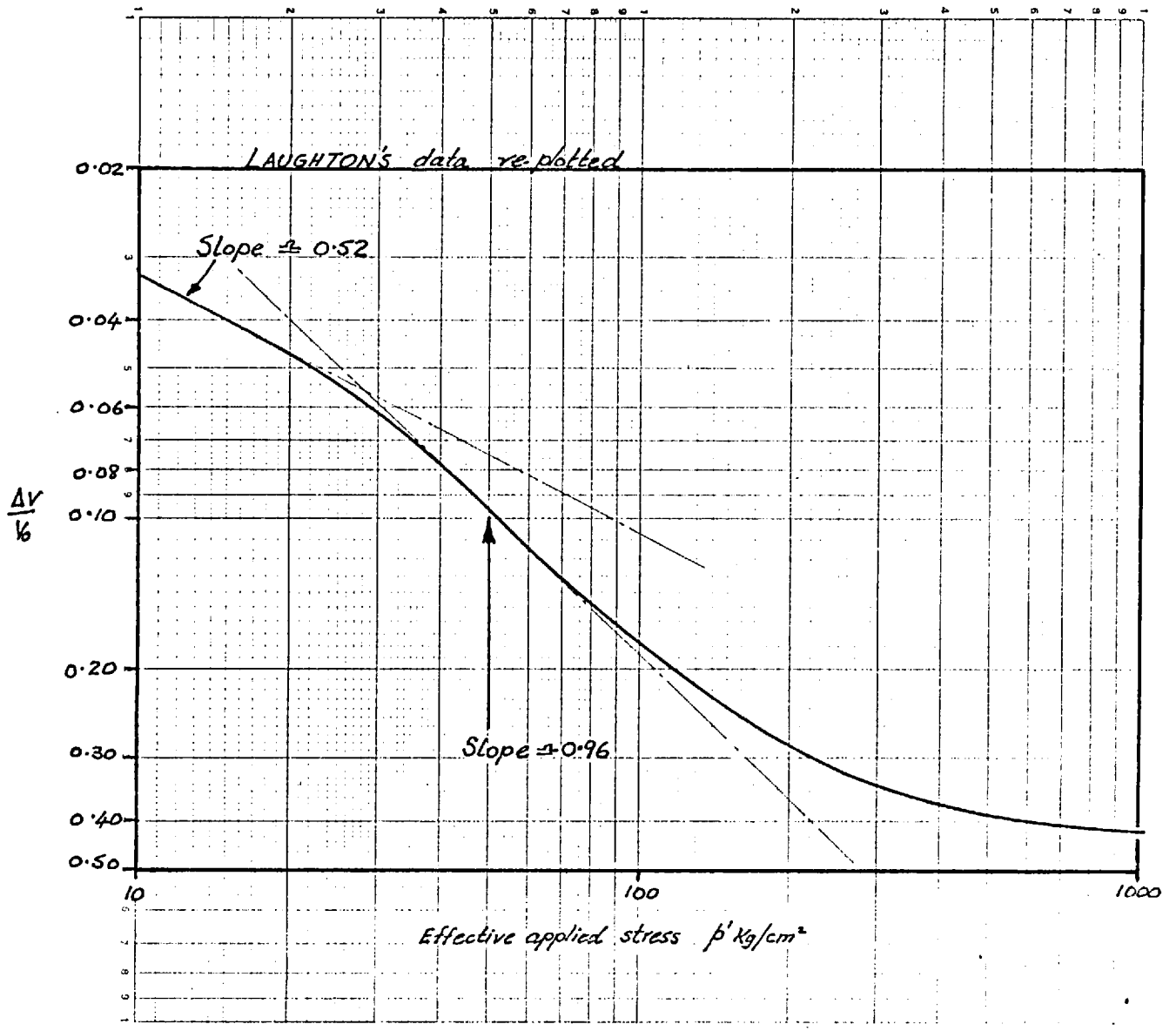


Fig 6.20

TEST 21 - HAM RIVER SAND

Isotropic consolidation Stage - $0 < (\Delta\sigma_3 - \Delta u) < 4000$ lb/in²

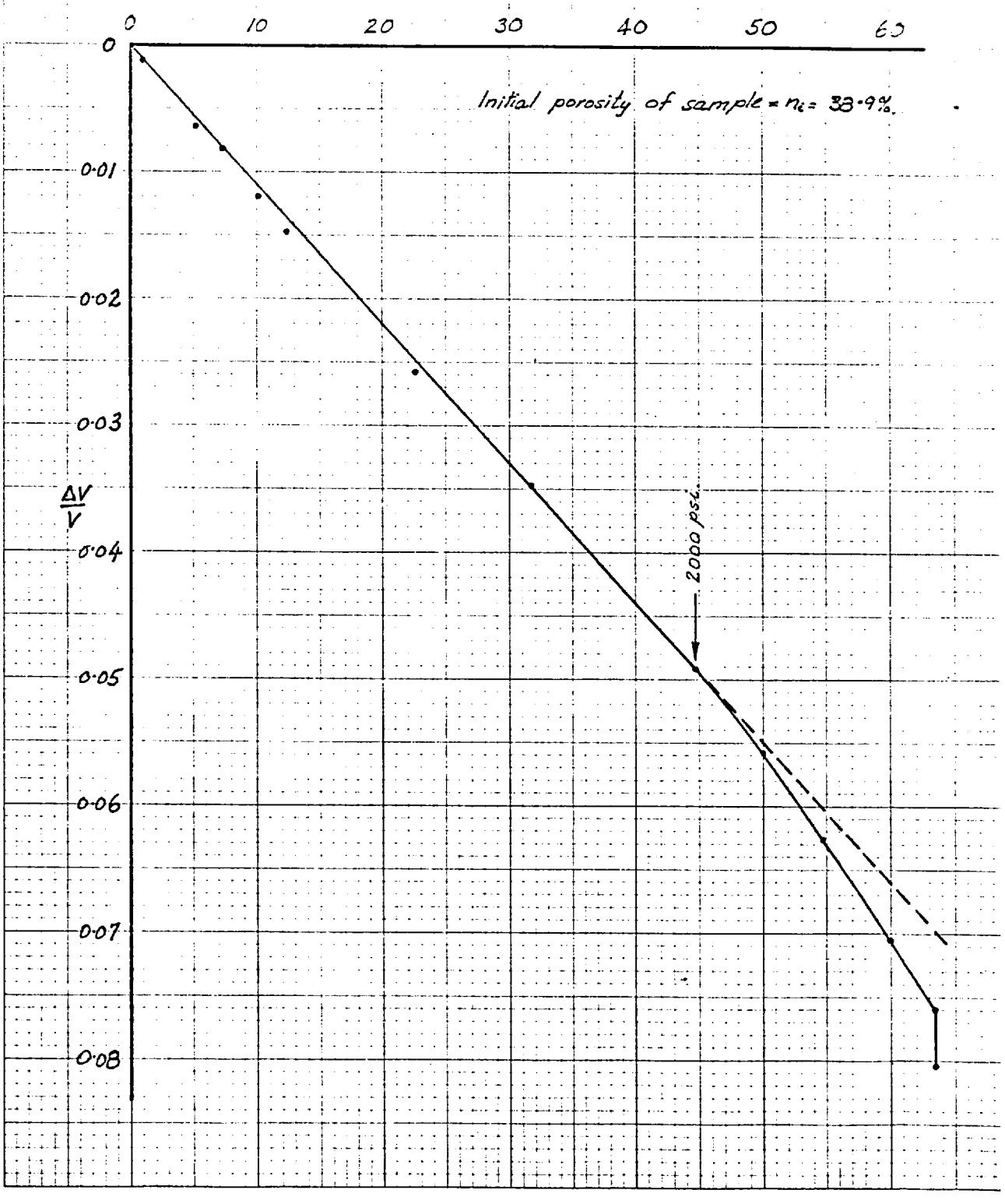
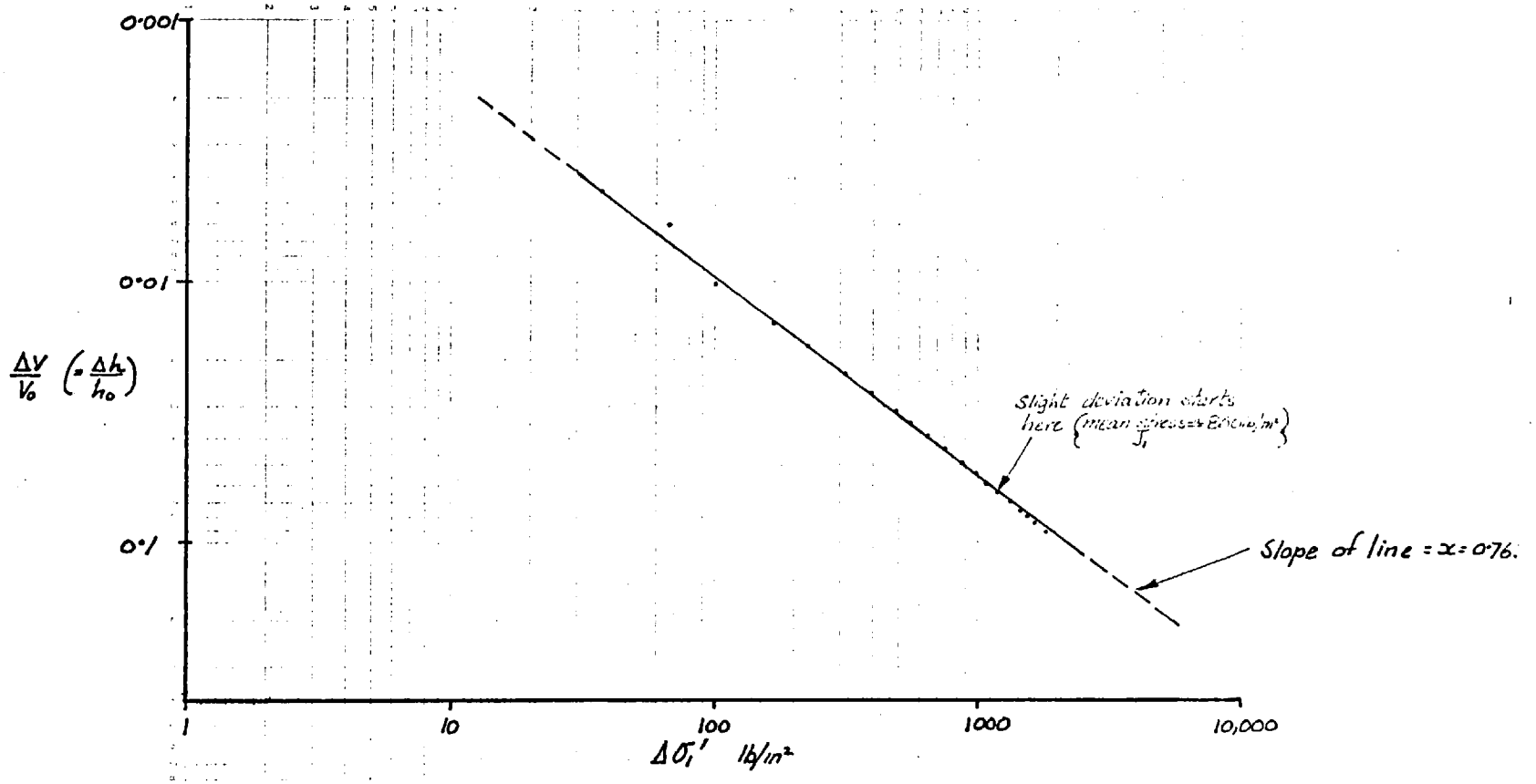


FIG 6·21



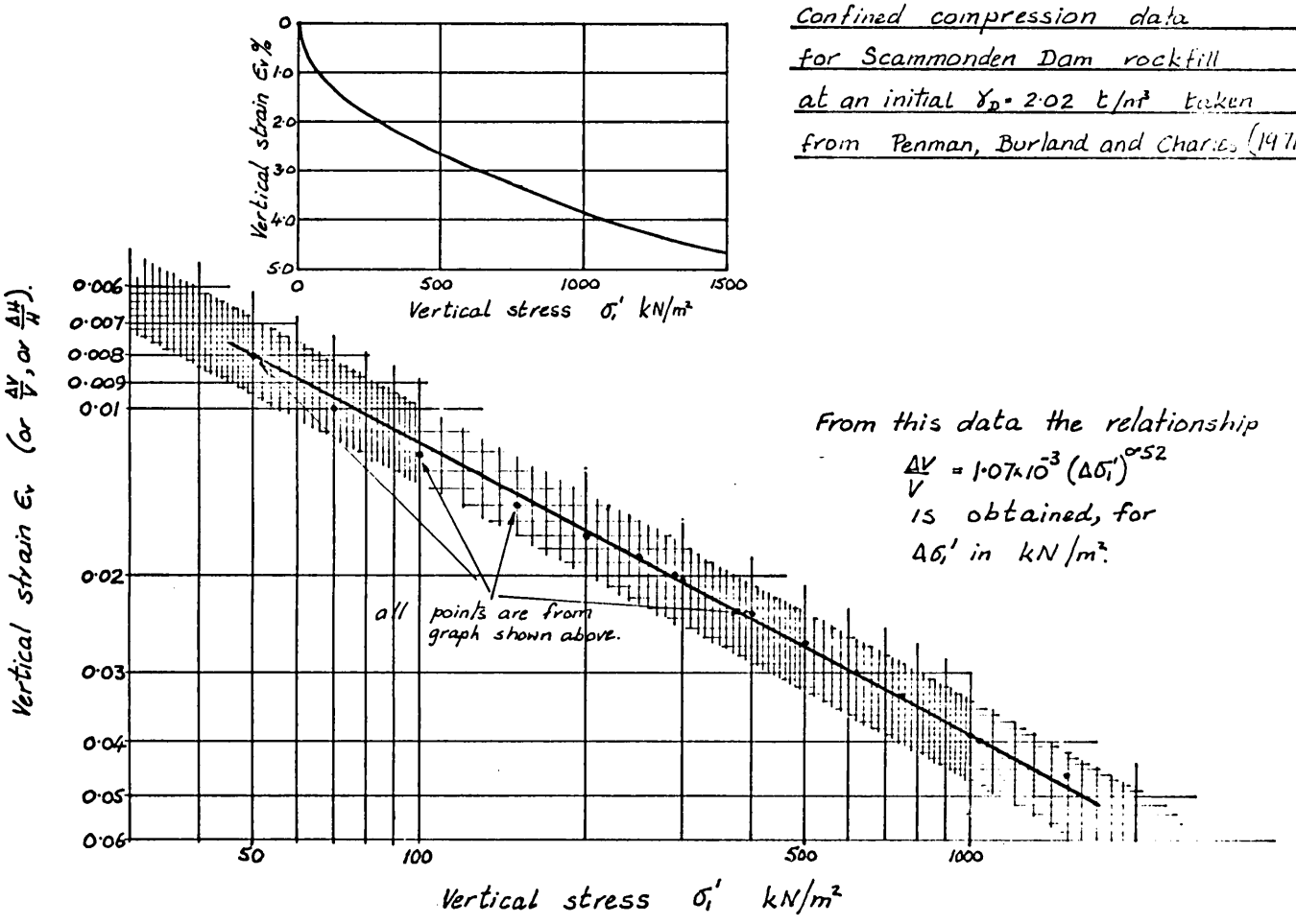
K_0 TEST ON HAM RIVER SAND.

from the straight line we get.

$$\frac{\Delta V}{V} = 2{\cdot}9\times10^{-4}(\Delta\sigma_1')^{0{\cdot}76} \quad \text{for } \Delta\sigma_1' \text{ in lb/in}^2.$$

$$\left[\text{or } \frac{\Delta V}{V} = 6{\cdot}63\times10^{-6}(\Delta\sigma_1')^{0{\cdot}76} \quad \text{for } \Delta\sigma_1' \text{ in lb/ft}^2\right]$$

FIG 6.22



Confined compression data for Scammonden Dam rockfill at an initial $\gamma_D = 2{\cdot}02$ t/m³ taken from Penman, Burland and Charles (1971)

From this data the relationship

$$\frac{\Delta V}{V} = 1{\cdot}07 \times 10^{-3} (\Delta\sigma_1')^{0{\cdot}52}$$

is obtained, for $\Delta\sigma_1'$ in kN/m².

FIG 6·23

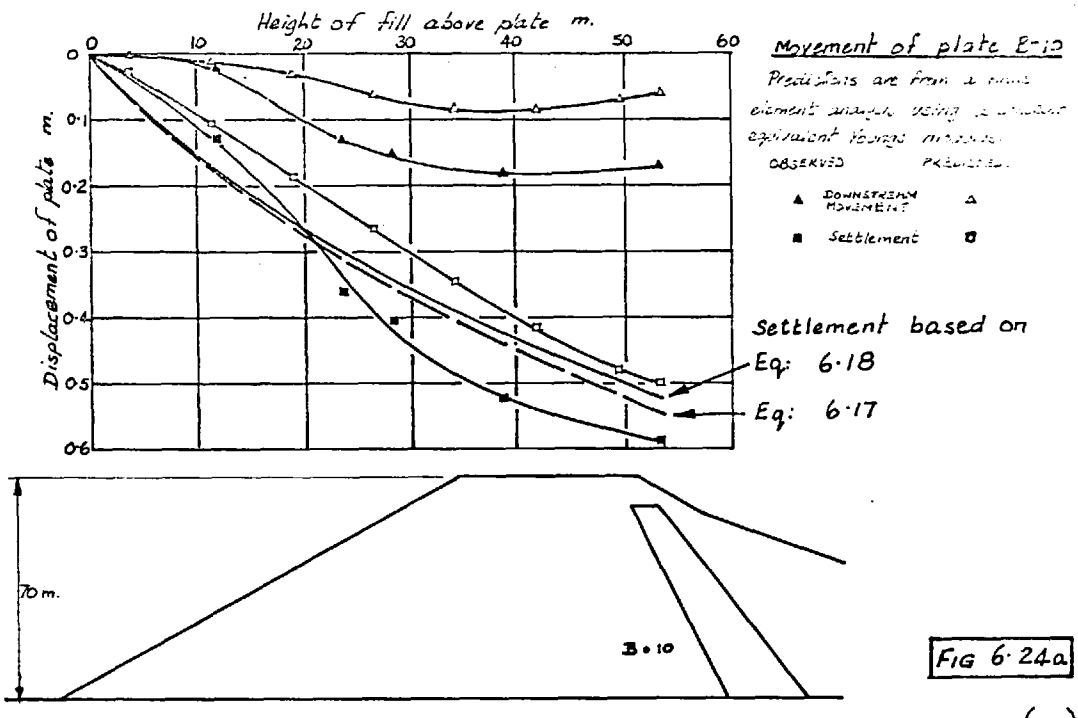


FIG 6·24a

Scammonden Dam :- Data from Penman Burland and Charles (1971)

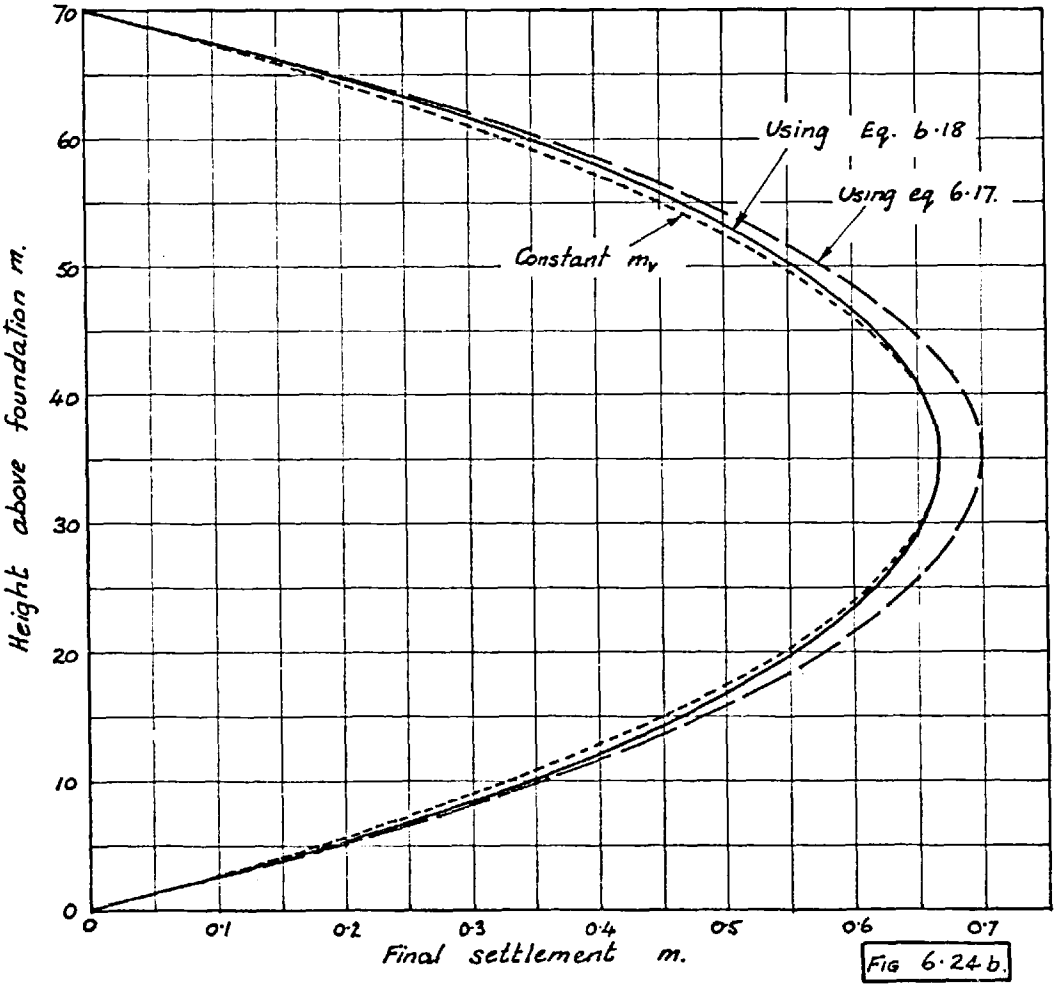
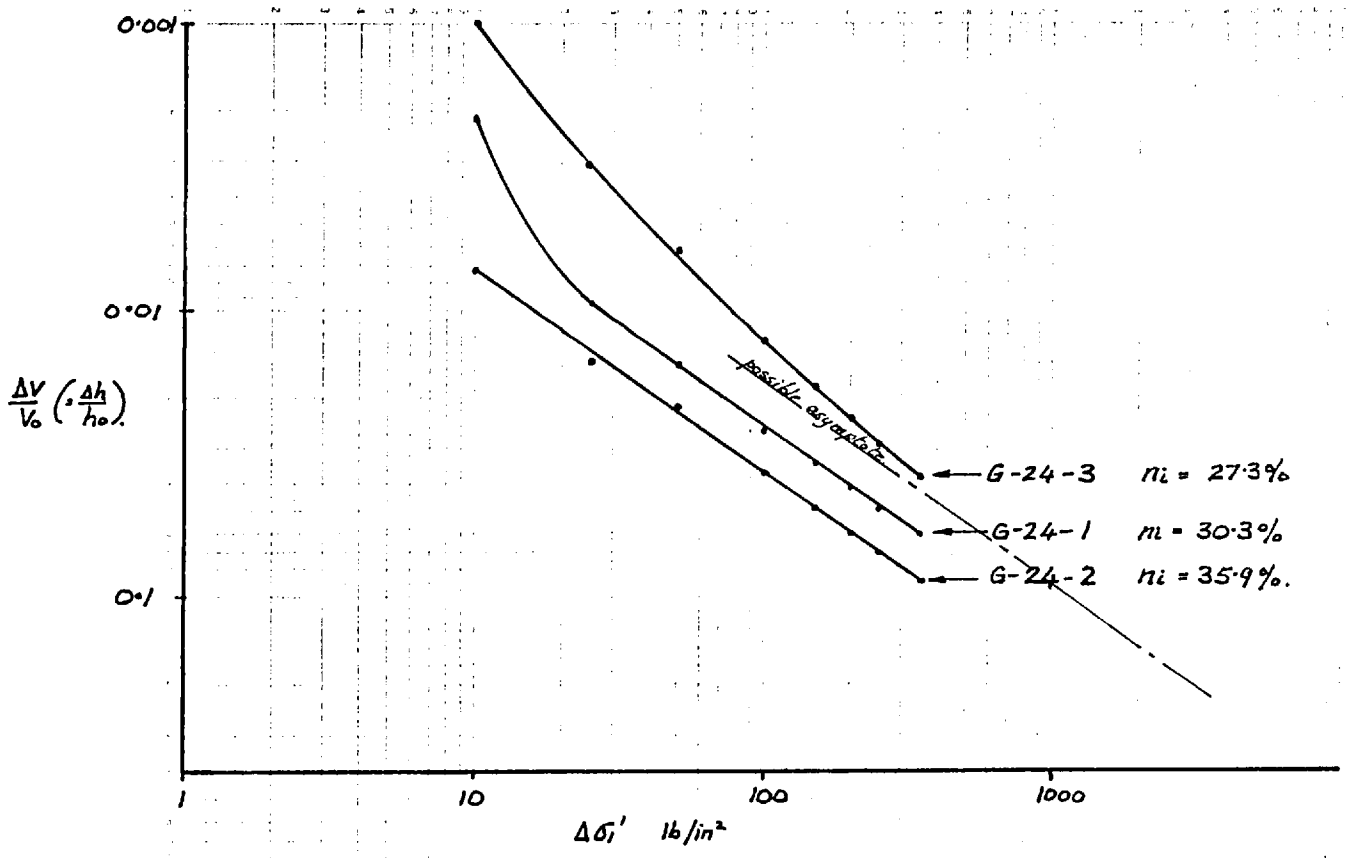


FIG 6·24b.



CONSOLIDATION TESTS ON SATURATED 'VENEMO' GRANITE (after PIGEON 1969).

results are for grading 'A' with 3" max particle size.

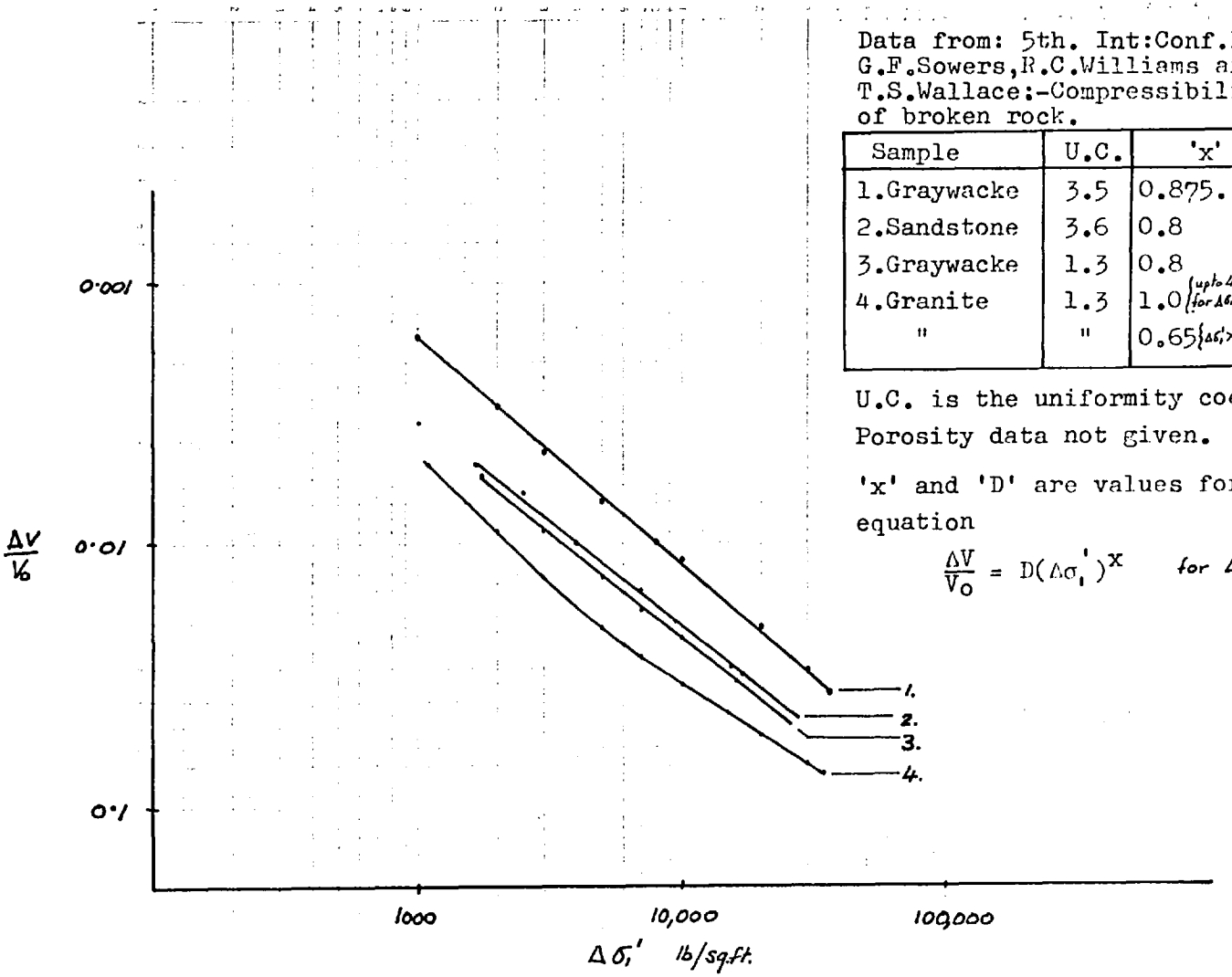
from linear relationship in this figure we get.

for sample G-24-1. (n_i = 30·3%) → $\frac{\Delta V}{V_0} = D(\Delta\sigma_1')^{0.71}$ where $D = 32\times10^{-6}$ for $\Delta\sigma_1'$ in lb/ft²

" " G-24-2. (n_i = 35·9%) → $\frac{\Delta V}{V_0} = D(\Delta\sigma_1')^{0.71}$ " $D = 42\times10^{-6}$ " " " "

FIG 6.25

Graph Data Ref 5943



Data from: 5th. Int:Conf.1965. G.F.Sowers,R.C.Williams and T.S.Wallace:-Compressibility of broken rock.

Sample	U.C.	'x'	'D'
1.Graywacke	3.5	0.875.	3.8×10^{-6}
2.Sandstone	3.6	0.8	13.2×10^{-6}
3.Graywacke	1.3	0.8	14.6×10^{-6}
4.Granite	1.3	1.0 (up to 4000 lb/ft² for Δσ₁')	4.5×10^{-6}
"	"	0.65 (Δσ₁' > 4000 lb/ft²)	86.0×10^{-6}

U.C. is the uniformity coefficient.

Porosity data not given.

'x' and 'D' are values for the equation

$$\frac{\Delta V}{V_0} = D(\Delta\sigma_1')^x \qquad \text{for } \Delta\sigma_1' \text{ in } lb/ft^2$$

FIG 6.26

W.E.L.I. Graph Data Ref. 5564

CONSOLIDATION TESTS ON A 'SATURATED' MUDSTONE (after PIGEON 1969)

In these tests the maximum particle size was 3".

Note:- $\frac{\Delta h}{h_0}$ corrected to zero for zero $\Delta\sigma_i'$

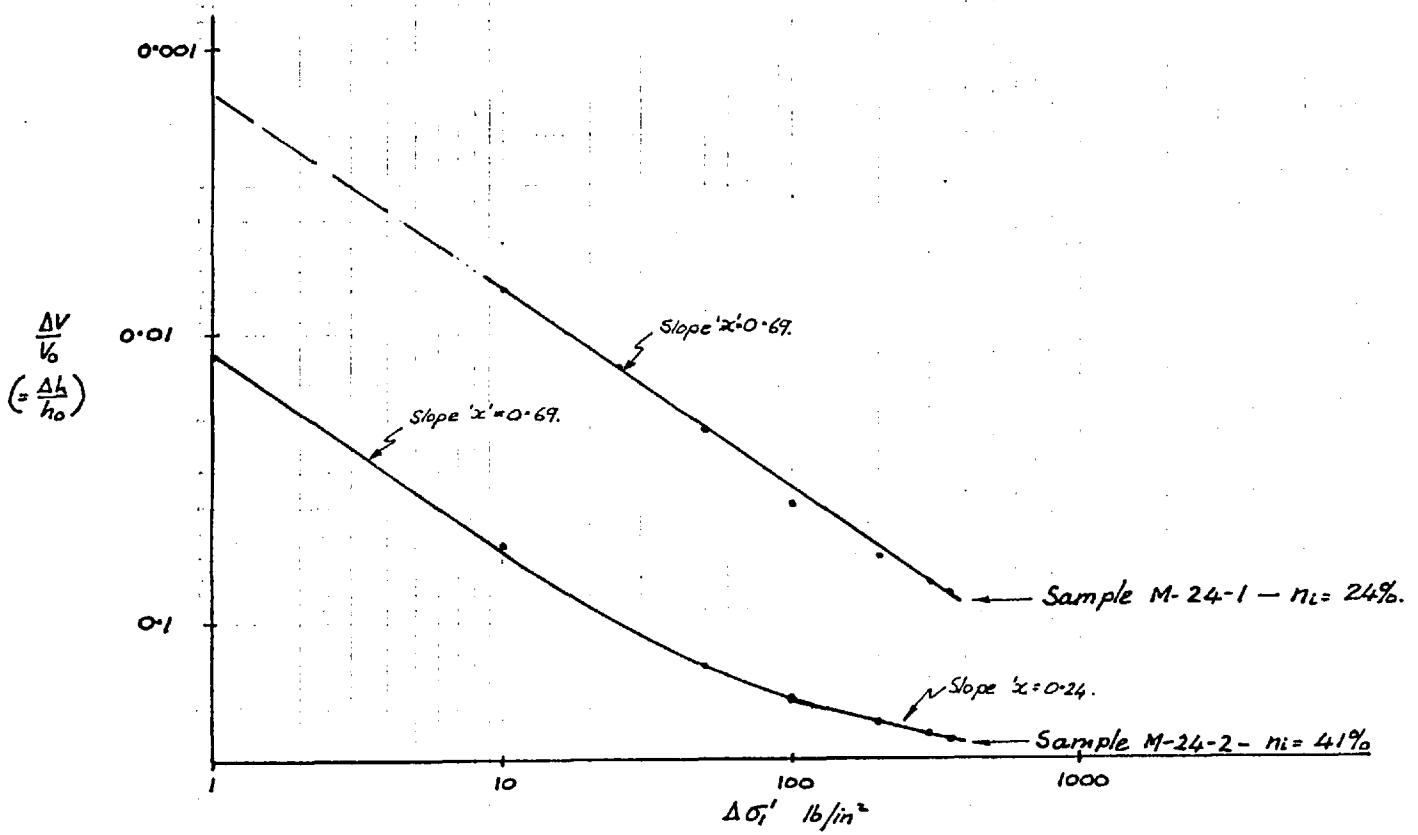


Fig 6.27

CONSOLIDATION TESTS ON A 'SATURATED' MUDSTONE (after PIGEON 1969).

In these tests the maximum particle size was 1"

Note $\frac{\Delta h}{h_0}$ corrected is zero for zero $\Delta\sigma_1'$

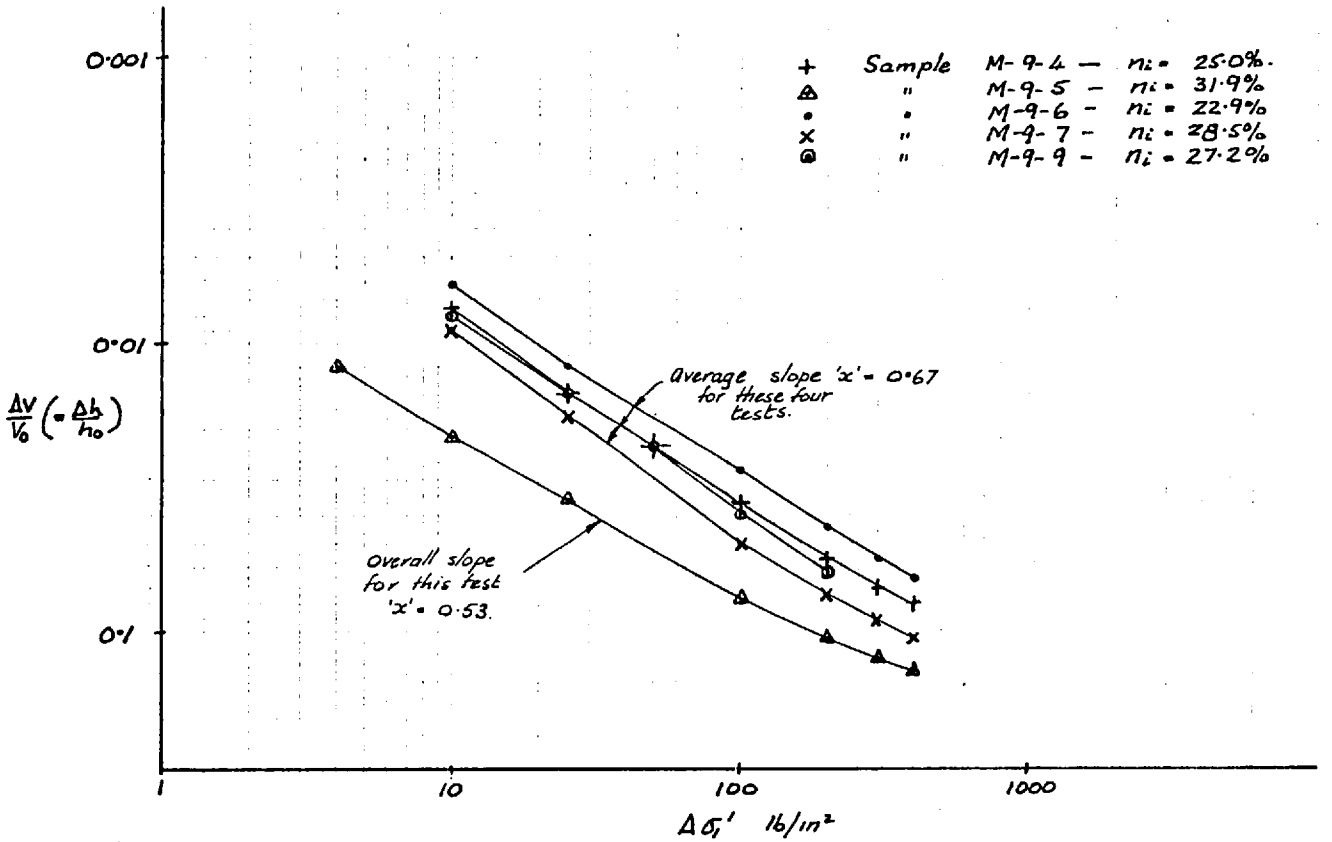


FIG 6·28

WELL Graph Data No. 5914

CONSOLIDATION TESTS ON A 'DRY' MUDSTONE (after PIGEON 1969).

In these tests the maximum particle size was 1"

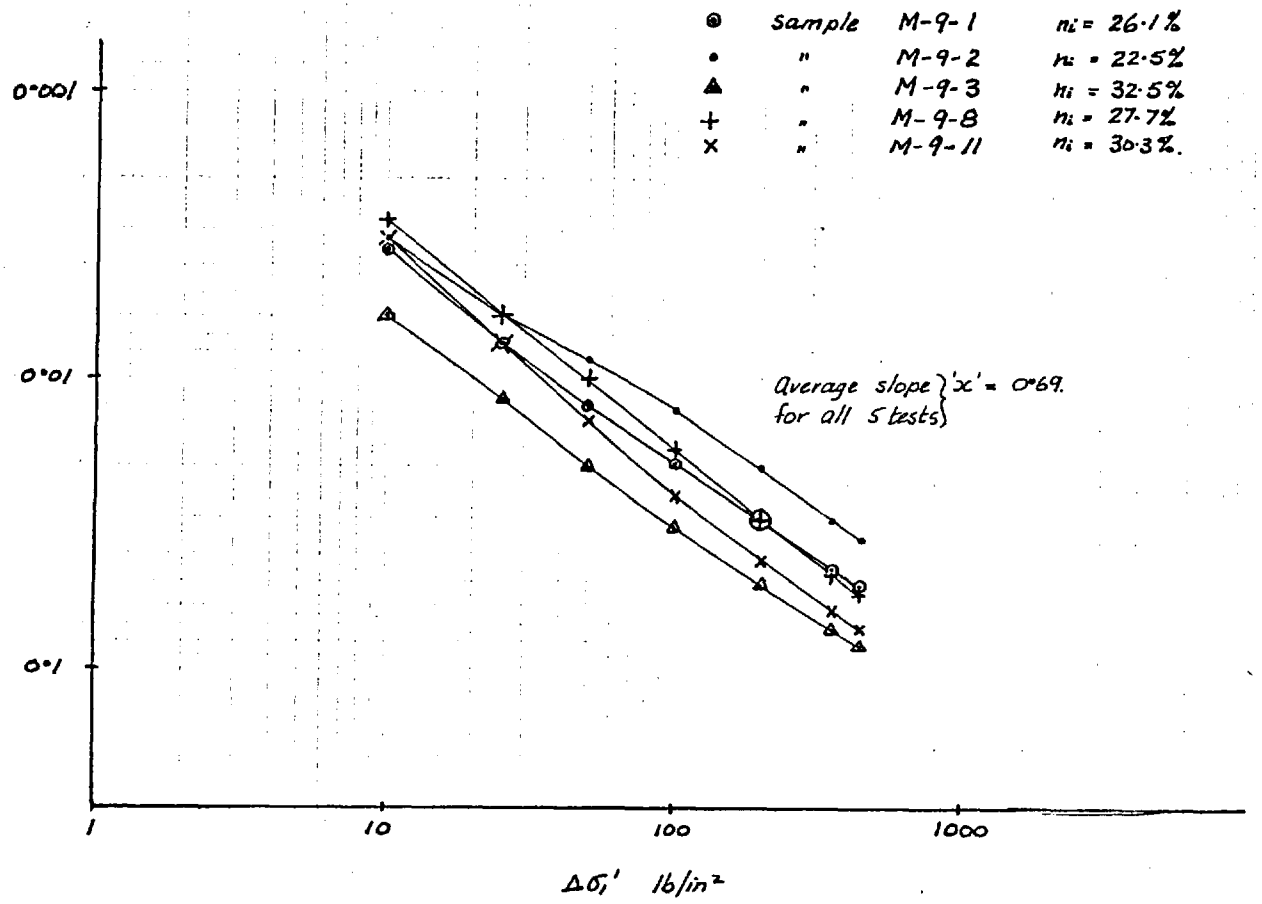
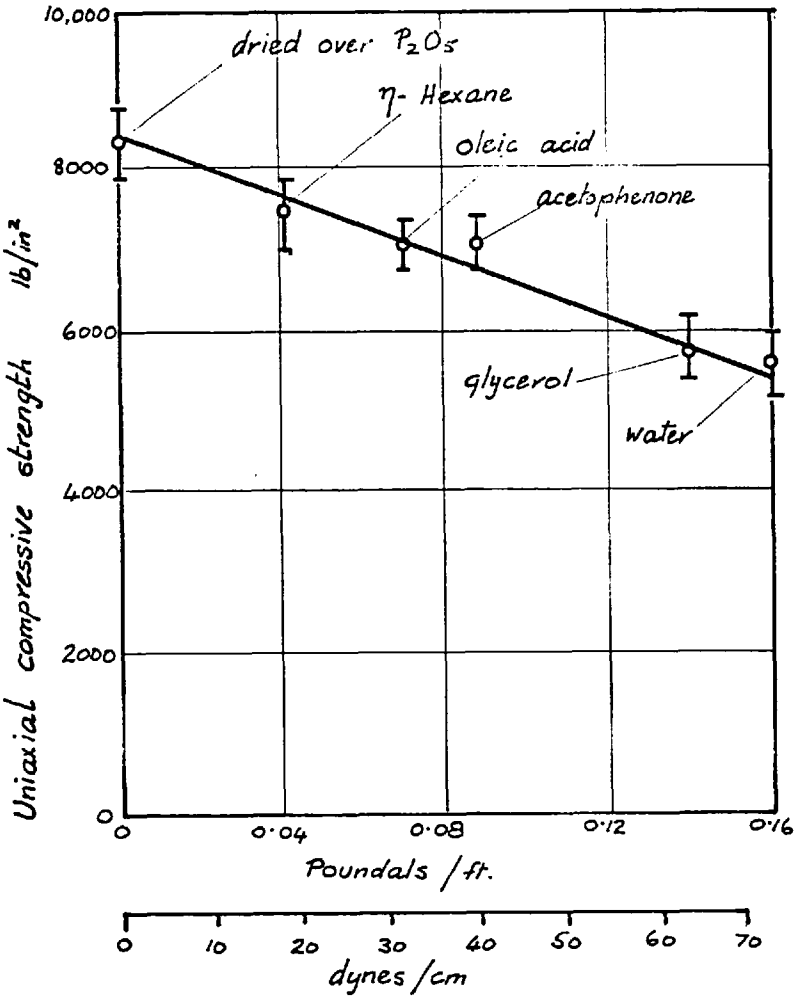


FIG 6.29



Surface tension γ of immersion liquids at 20°C.

The influence of the surface tension of immersion liquids upon the uniaxial compressive strength of quartzitic shale (from Colback and Wiid 1965).

FIG 6·30

TEST. IC.3. HAM RIVER SAND.

Creep under an isotropic stress of 4000·7 lb/in²

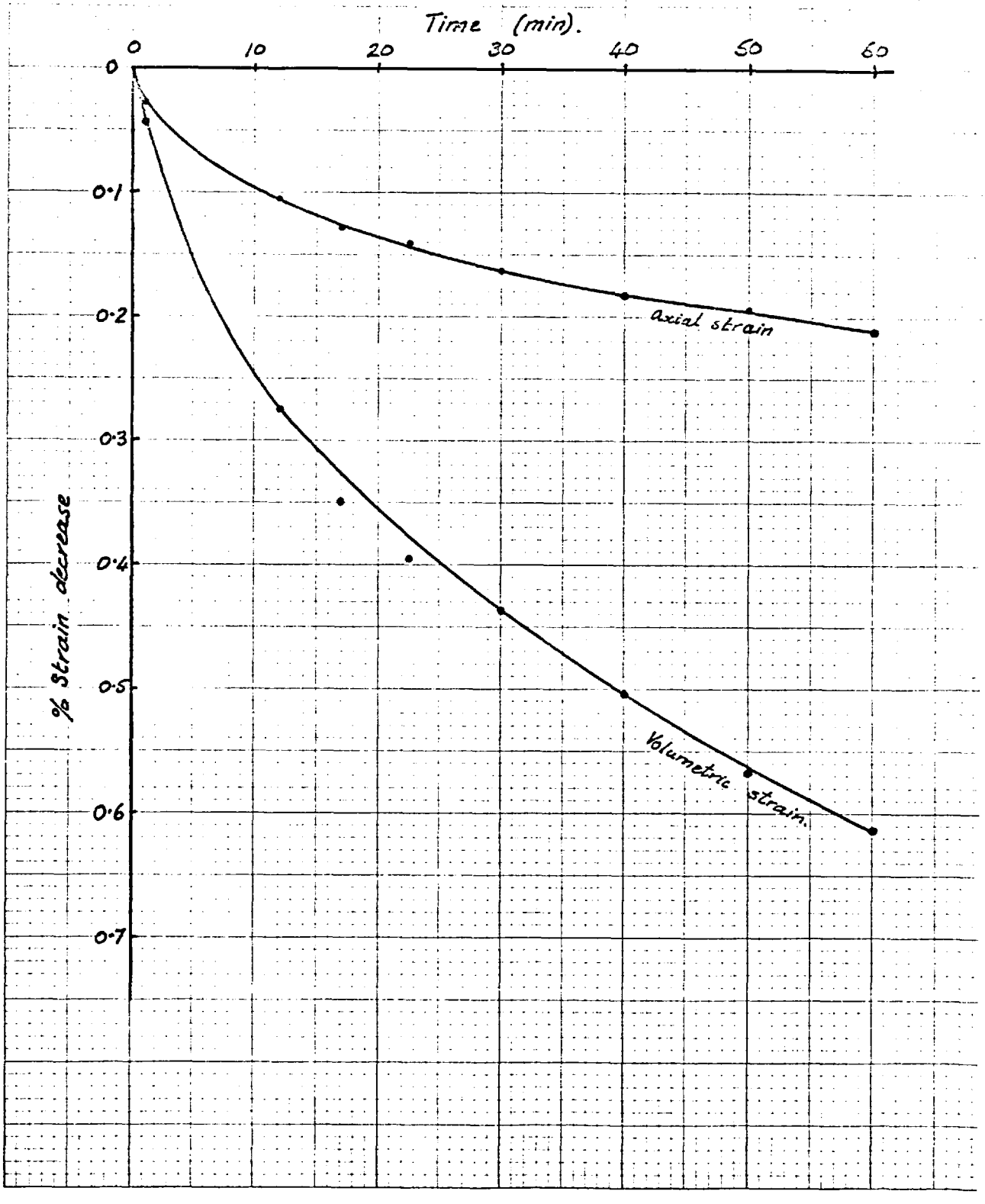


Fig 6·31

TEST IC.3. HAM RIVER SAND.

Swelling creep on release from an isotropic stress of 4000·7 lb/in² to an isotropic stress of 0·7 lb/in²

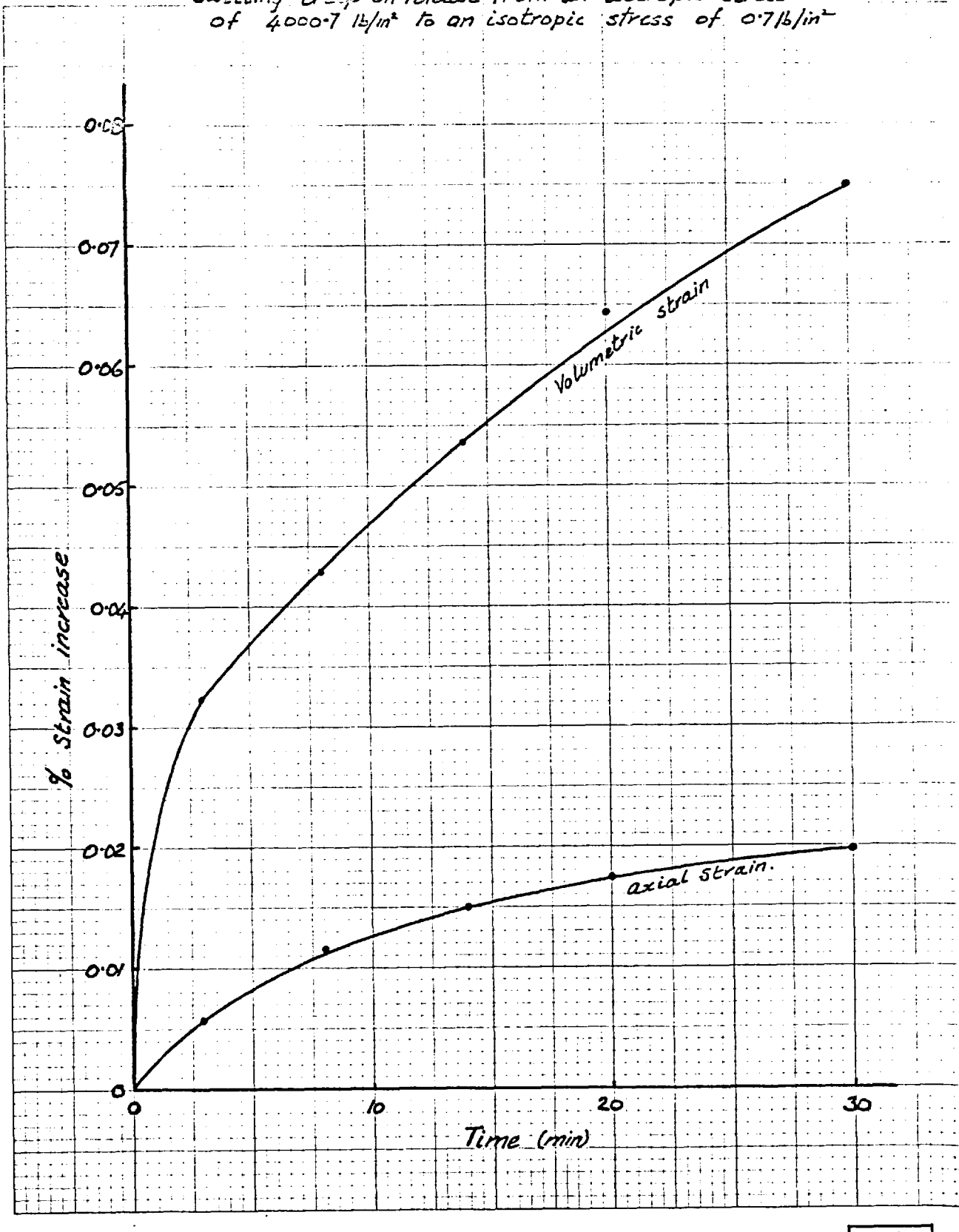


FIG 6·32

GRAPH SHEET Fig 5541 LOG 4 CYCLES X

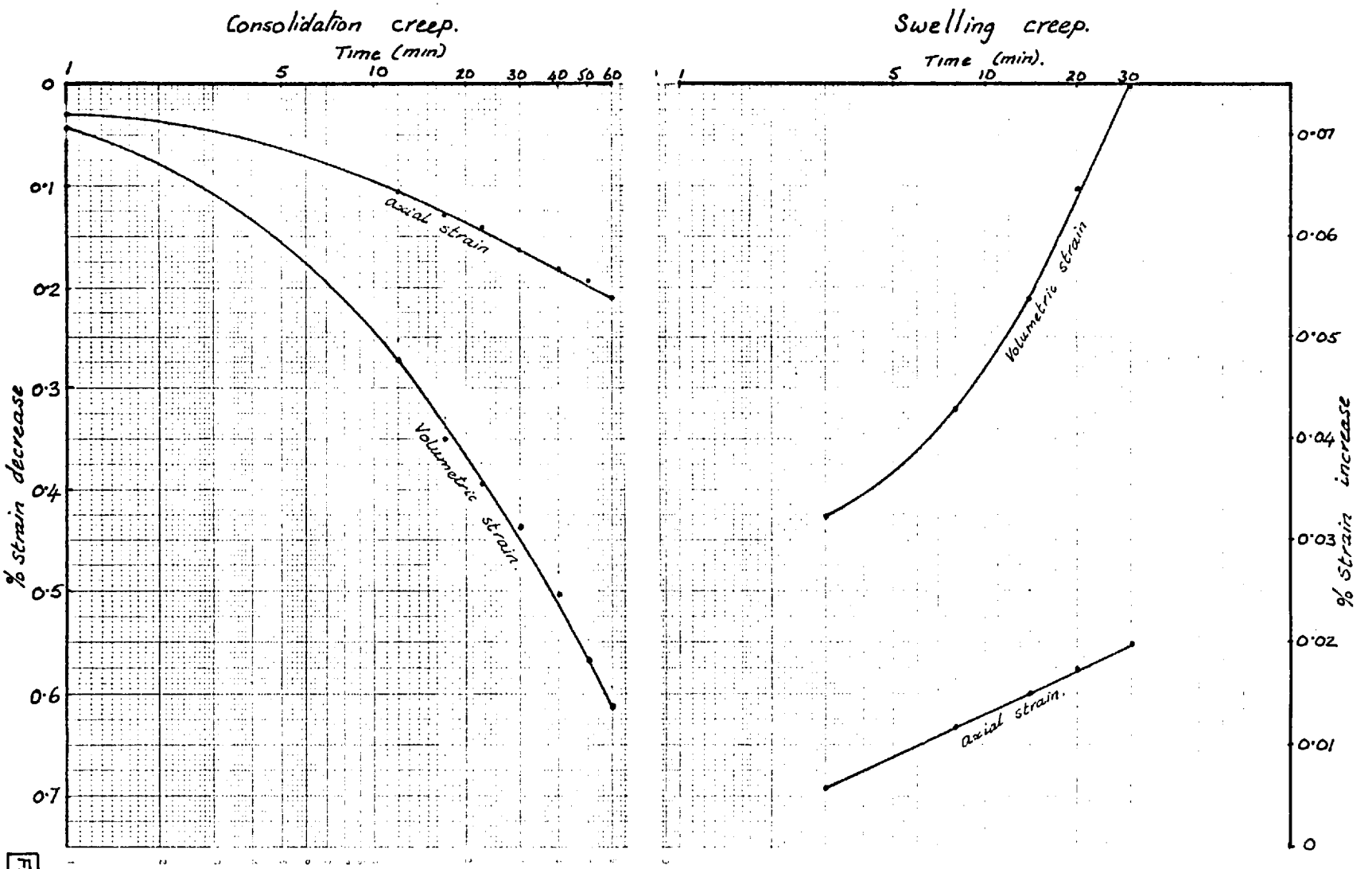
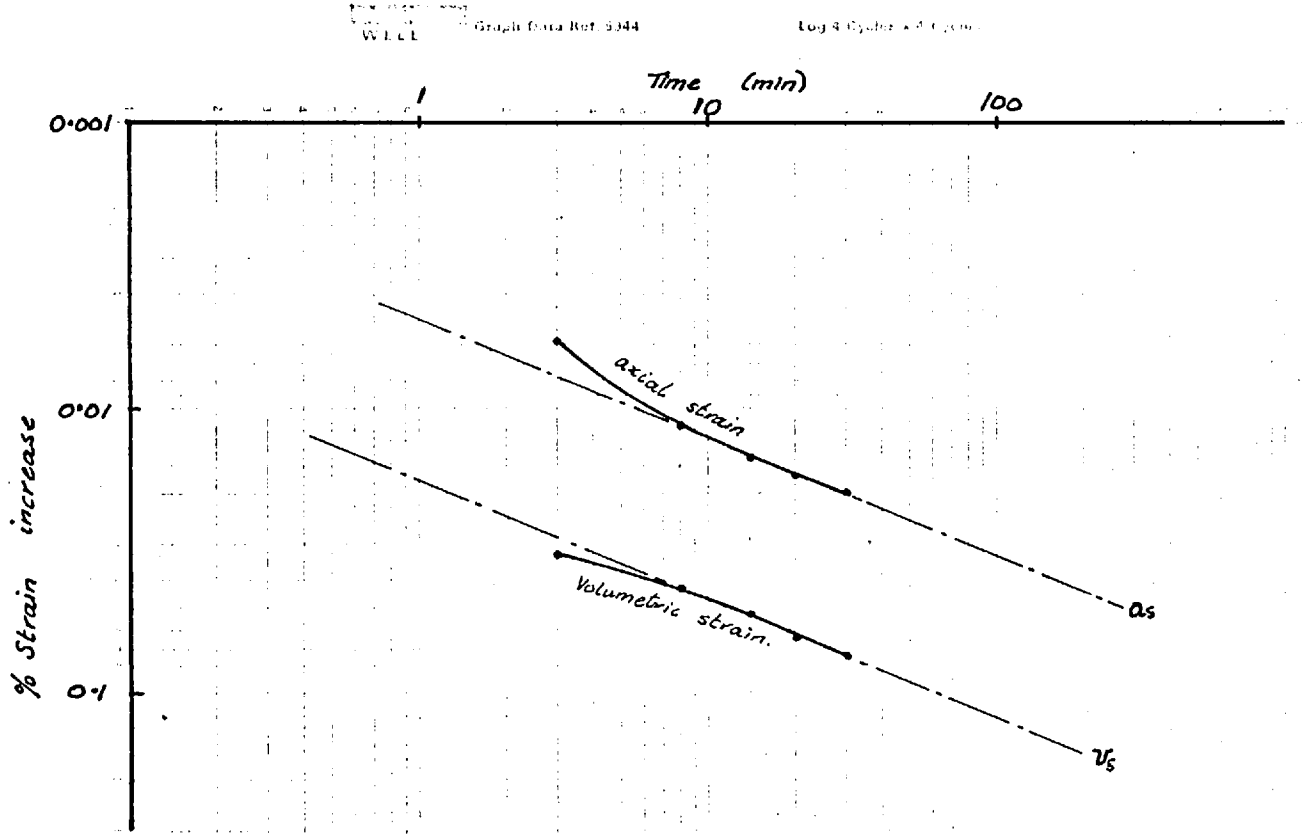


Fig 6·33

TEST. IC.3. HAM RIVER SAND.



TEST. IC.3. HAM RIVER SAND.

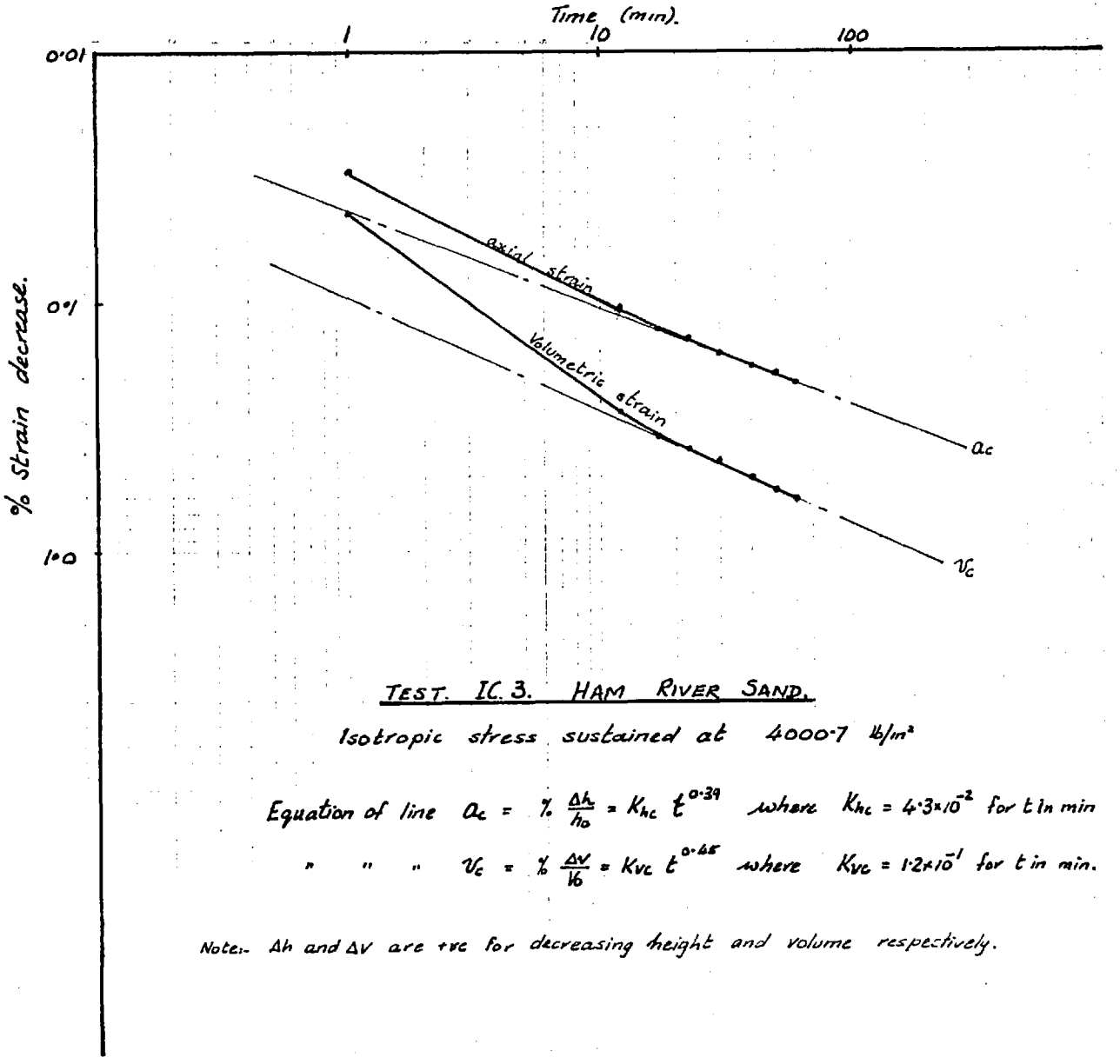
Stress relief from 4000·7 to 0·7 lb/in²

Equation of line a_s — $\% \frac{\Delta h}{h_0} = K_{hs}\, t^{0.29}$ where $K_{hs} = 5{\cdot}4\times10^{-3}$ for t in min.

" " " v_s $\% \frac{\Delta V}{V_0} = K_{vs}\, t^{0.39}$ " $K_{vs} = 1{\cdot}9\times10^{-2}$ " " " "

Note:- Δh and ΔV are +ve for increasing height and volume respectively.

FIG 6.34



TEST. IC.3. HAM RIVER SAND.

Isotropic stress sustained at 4000·7 lb/in²

Equation of line $a_c = \% \frac{\Delta h}{h_0} = K_{hc}\, t^{0.39}$ where $K_{hc} = 4{\cdot}3\times10^{-2}$ for t in min

" " " $v_c = \% \frac{\Delta V}{V_0} = K_{vc}\, t^{0.45}$ where $K_{vc} = 1{\cdot}2\times10^{-1}$ for t in min.

Note:- Δh and ΔV are +ve for decreasing height and volume respectively.

FIG 6.35

CHAPTER 7

FACTORS INFLUENCING THE STRESS-STRAIN BEHAVIOUR OF GRANULAR MATERIALS

7.1 Introduction:

In the previous chapters the physical nature of the contact between grains was discussed at length, and a lot of experimental evidence was presented to support the contention that the grain contacts could be considered as plastic junctions, and when shear was applied to the junctions a junction growth mechanism occurred allowing plastic deformations (compressions and shear) to take place before slip. (It must always be borne in mind that elastic strains would also be present.)

Secondly, it was pointed out that, under the influence of cyclic isotropic stresses, some energy was expended in overcoming micro slip (termed fretting slip) at the junctions when the junctions were unloaded and then reloaded essentially elastically. This energy loss can be expected to play an increasingly important role when the sample becomes more anisotropic. This anisotropy can be caused by shearing at large stress ratios.

One other mechanism was introduced when discussing volumetric strain behaviour, and that was particle fracture, which is

significant at high confining stresses.

So we have the following types of behaviour:

a) Elastic-plastic degenerating to frictional,

b) Elastic-(fretting) frictional during cyclic stressing,

c) Particle fracture.

All these mechanisms contribute to the stress-strain behaviour of the material, and it is hardly likely that a simple theory can be formulated to take account of all of them. However stress-strain theories have been developed and it will be interesting to see how well these interparticle mechanisms are modelled.

7.2 Particle Fracture due to Surface Contact Stresses:

It is not until fairly recently that fracture as a mechanism has been studied, so it is important to understand the mechanics of fracture and the conditions which best promote its occurrence.

In Chapter 3 the frictional properties of minerals were discussed in terms of a plastic junction growth mechanism, which terminated when the interfacial stresses coincided with the intrinsic strength envelope, or at some intermediate envelope which characterized the strength of the junction material. In the former case one could say that if the stresses at the junction interface were on the intrinsic strength envelope, then fracture would take place in the

junction material. Indications of this type of fracture should be observable if the surface friction conditions are not inhibited by weak junction material.

This mechanism has been observed in friction experiments by Bowden and Brooks (1966), and, in triaxial tests on Ham River sand at confining pressures of 40 psi, Bishop and Green (1965) report that in a microscopic examination at five times magnification of the sand grains before and after testing no discernable differences between the size and shape of the grains before and after a test were noted, but that a quantity of 'fines' was present after shearing. The size of these 'fines' ranged from 0.01 mm to 0.04 mm, and the sand grading of the original sample ranged from 0.1 to 0.4 mm. Fracture at interparticle contacts could explain the production of these 'fines'.

No analysis for a 3-dimensional elasto-plastic junction subjected to normal and shear forces is available, so it is difficult to be certain of the conclusions reached above. However, an analysis to determine the complete stress field for a contact carrying a hemispherical Hertzian normal pressure and proportional distributed shearing traction has been presented by Hamilton and Goodman (1966). Two important points are brought out in their analysis which are illustrated in Figure 7.1 and Figure 7.2. (These figures are reproductions from Hamilton and Goodman's paper.) Figure 7.1 shows that, as the friction coefficient

is increased, the zone of maximum octahedral shear stress becomes more intense and moves towards the surface from below. At the same time a secondary zone of high shear stress develops in the surface of contact, and this zone becomes dominant when the friction coefficient is larger than 0.27. Figure 7.2 shows that a very shallow system of large tensile stresses at the edge of the contact exists, which would indicate that if tensile fracture were to occur, small fragments of material could be broken out of the surface. This tends to support the findings of Bishop and Green (1965).

This elastic analysis would of course, be invalid if the contact was already plastically deformed under normal loading. However, it does give a good picture of the likely form of stresses near the surface, and it does indicate that it is necessary to look for other mechanisms which could produce the gross grain fracture observed during triaxial compression tests even at quite moderate confining pressures.

7.3 Particle Fracture due to Internal Stresses:

Hiramatsu and Oka (1966) presented an analytical analysis for the stresses in a sphere compressed diametrically. Also, by means of 3-dimensional photoelastic experiments using the stress freezing technique, they showed that the state of stress in an irregular test piece, subjected to concentrated loads, is much the same as for a sphere in the vicinity of the axis of loading. They went on to demonstrate for the

spherical test piece that the circumferential tensile stress along the compression axis is not strongly influenced by Poisson's ratio, and as long as the area over which the load is applied subtends an angle less than 5° at the centre of the sphere, this stress takes a value from:

$$\frac{1.21 \times W}{2\pi a^2} \quad \text{to} \quad \frac{1.36 \times W}{2\pi a^2}$$

where W is the applied load at a contact, and a is the radius of the sphere.

The variation of Poisson's ratio taken was $\frac{1}{7} \leqslant \nu \leqslant \frac{1}{3}$.

The tensile stress increases slightly with increasing distance from the centre to a maximum value of about 10% greater than the central value, and then decays becoming compressive at a radius equal to about 0.65a.

So the tensile strength of an irregular piece can be taken as:

$$S_t \simeq 0.22 \frac{W}{a^2} \qquad (7.1)$$

Their experimental results for irregular lumps of various rocks were in fairly good agreement with equation 7.1.

Thus if tensile fracture of the grains in a granular material is controlled by diametral compression and is a dominant feature of the shear process, then a scaling factor of $\frac{W}{a^2}$ could be used to compare the results of tests on

different materials. This was done very successfully by Billam (1967), who was able to unify test results on different materials for a series of consolidated drained triaxial tests on initially dense samples; the scaling factor he used was:

$$\left(\frac{P_c}{d^2_{50}}\right)$$

where P_c = mean crushing force for a single grain of d_{50} size.

However, work by Jaeger (1967) can be used to indicate where difficulties could arise, if this type of correlation was extended to a variety of loading conditions. For example, a particle in the granular sample is probably not loaded across a single diameter but sustains a number of loads distributed over its surface, each load contributing to the stress conditions within the particle. If the particle fractures under the influence of these loads, the tensile stress at fracture may not be the same as that for the simple diametral loading condition. Jaeger (1967) illustrates this point for cylinders compressed in two diametral planes. His analysis for the stresses within a cylinder for the case of a number of cylinders packed together in contact is shown in Figure 7.3. The maximum tensile stress and its position is also tabulated, as are the results of tests on specimens 2" in diameter x 1" long. It appears that as long as the included angle between the planes of loading is less than 45° the tensile stress at failure is very nearly the same as that obtained from a single diametral loading condition

(a Brazilian tensile strength test) but, when the included angle is greater, there are still substantial tensile stresses. However, they are much smaller than the Brazilian tensile strengths, and the contact loads required to produce fracture are much larger. Another point to notice is that the zone of material subjected to tensile stresses moves away from the centre of the cylinder, and the maximum tensile stress now occurs approximately on the line adjoining the loads.

Thus in general it is to be expected that if the loads on any particle are evenly distributed around its surface, tensile fracture will be inhibited. So for isotropic compression tests fracture should not play an important role, unless the confining stress is very large, leading to large contact forces.

In Chapter 6 it was shown that, for isotropic consolidation, fracture in the grains of Ham River sand probably started at about 2000 psi confining pressure, and for K_o consolidation, at a maximum principal effective stress of about 1200 psi, when the minor principal stress was at about 600 psi. These results lend support to Jaeger's analysis. The actual amount of particle fracture is rather difficult to quantify, and the best way would be to measure the amount of new solid surfaces produced so that the energy dissipated can be taken into account. In practice this turns out to be difficult although experimental techniques for doing this exist, but they appear to be limited in accuracy. For

example, Schellinger (1952) in his experiments to measure the surface energy of quartz by a calorimetric method used a gas absorption method to measure the surface area of the crushed material. The surface energy calculated from these measurements was 107,000 ergs/sq cm. If compared with values calculated by Brace and Walsh (1962) using an analysis by Gilman (1960), who obtained the relationship:

$$\gamma = \frac{E\ a^2}{d_o \pi^2}$$

where E = Young's modulus normal to the plane in question,

a = atomic radius of atoms lying in the cleavage plane,

d_o = spacing of cleavage planes ,

the values calculated by Brace and Walsh for different cleavage surfaces in quartz range between 480 ergs/sq cm and 760 ergs/sq cm. Schellinger's value is about two orders of magnitude larger - the most likely source of error in his results is the surface area measurement. The reason for the error may be because the gas is unable to penetrate the innumerable fissures produced in the crushed material.

In the case of the tests conducted in this research programme the influence of crushing was observed qualitatively. However, some samples were sieved before and after testing, typical results being shown in Figure 7.4 and Figure 7.5. Looking at Figure 7.4 it is apparent that the shift of the grading curve for the consolidated drained test at 500 psi is somewhat greater than that for the isotropic consolidation

test at 4000 psi. The apparently small shift of the grading curve is rather deceptive as can be seen from the two photomicrographs, plate 7.1, which show the material before and after a consolidated drained test at 500 psi confining pressure.

Other difficulties are encountered if diametral tensile strength is used as a scaling factor. One difficulty is that the same scaling factor has to be used when comparing the dilatancy of the same material at different voids ratios, and obviously different relationships are obtained because the dilatancy varies with initial voids ratio. Another difficulty is that if the grains of a material deform plastically, dilatancy at higher stresses is still suppressed, but in this case due to plastic deformation and not fracture.

Tests to illustrate this point are shown in Figure 7.6, which shows the results of consolidated drained triaxial tests using 1/32" steel shot at various confining pressures. For comparison Figure 7.7 shows the same relationship $(\frac{J_1'}{J_{1c}'}$, where J_{1c}' is the value of J_1' at the end of the consolidation stage plotted against void ratio e) for Ham River sand. For both materials the dilatancy is suppressed with increasing pressure. The dilatancy rates at failure for some consolidated drained tests are shown in Figure 7.8, which clearly illustrates this, but the suppression is caused by different mechanisms, fracture in the case of Ham River sand, and plastic deformation in the case of the steel shot.

In addition Figures 7.6 and 7.7 clearly indicate that the changes in void ratio are dependent on the initial void ratio for both materials, which could be anticipated, because it has been shown that the volumetric strain behaviour is controlled by the deformation at the interparticle contacts, which are a function of the particle packing and so of void ratio. It also follows that void ratio is not the correct parameter to use when discussing the stress-strain behaviour of particulate material, because it can not take into account the distribution of contacts in relation to the stress directions, and it is the contact distribution and loading with respect to the magnitude and direction of the applied stresses which control the behaviour.

Contact distribution is difficult to measure, but since it is linked to geometrical anisotropy, and work describing this aspect of soil structure is being actively studied (see, for example, Arthur (1972)), it is possible that progress in describing stress-strain behaviour with respect to contact distribution will become possible. However, in the following discussion void ratio will still be used.

Having discussed the underlying causes of straining in a soil structure it is now possible to see if some of the simple stress-strain models for soil behaviour provide reasonable predictions.

7.4 Factors Influencing the Stress-Dilatancy Theory:

This theory by Rowe (1962 and 1963) was based on the assumption

that the minimum amount of energy is absorbed in frictional slip within the deforming mass. Later Horne (1965) showed that the stress dilatancy equation could be obtained using the concept of virtual work. The relation for the triaxial compression test is:

$$\dot{E} = \frac{\frac{\sigma_1'}{\sigma_3'}}{1 - \frac{d\varepsilon_v}{d\varepsilon_1}} = \tan^2 (45^\circ + \frac{\phi_\mu}{2}) \qquad (7.2)$$

The volumetric strain increment $d\varepsilon_v = d\varepsilon_1 + d\varepsilon_2 + d\varepsilon_3$. Here $d\varepsilon_2 = d\varepsilon_3$ and $\dot{E}$, the ratio of energy supplied to energy transmitted per unit volume, is a minimum. Equation 7.2 is sometimes written as:

$$R = D.K \qquad (7.3)$$

where $$R = \frac{\sigma_1'}{\sigma_3'}$$

$$D = (1 - \frac{d\varepsilon_v}{d\varepsilon_1})$$

and $$K = \tan^2 (45^\circ + \frac{\phi_\mu}{2})$$

There have been criticisms of the derivation and of the assumed mechanism by Gibson and Morgenstern (1963), Roscoe and Schofield (1963), Scott (1964) and Trollope and Parkin (1963).

If this relationship is accepted we have to take into account the following limitations placed on its validity:

a) The particles must be rigid, rotund, cohesionless with a constant coefficient of solid friction.
b) Elastic and plastic deformations, crushing and cracking are all ignored (assumed not to occur).
c) Deformation occurs as a result of relative sliding motion between groups of particles.
d) Particles acting as rollers between groups are not present.

Rowe (1962) replaces ϕ_μ with ϕ_f to provide a better fit of experimental data. Horne (1964) explains the lack of fit in terms of rotation, which leads to lower $\dot{E}$ values in the early stages of the triaxial test, and at later stages. The lack of fit is due to variation of the sliding angle between particles leading to higher $\dot{E}$ values.

7.5 Stress Dilatancy Correlations for Variable Stress Ratio Paths:

Although in the derivation of equation 7.2 crushing and plastic deformations are specifically excluded, the strains produced by these mechanisms cannot be separated from the assumed rigid particle slips of the theory, and so verification of the theory is not possible when these mechanisms are present. Nevertheless let us examine the theory to see what the effect of these mechanisms is on the predictions.

Equation 7.2 expresses the result of a minimization process and so, if additional energy has to be provided to produce fracture or plastic distortion, the magnitude of the energy

ratio should be larger. This is simple to verify experimentally. From the results of a test on some material at low stresses during which little, if any, crushing or plastic work is done in comparison with the frictional work done, the R ~ D plot can be used to establish the magnitude of K (which is the slope of this plot) and hence the value of $\dot{E}$, which is equal to K for the purely frictional behaviour for this model. Then from the argument presented above, a test on the same material at a stress level which produces particle fracture or plastic distortion should provide a larger value of R for a particular value of D. The magnitude of the difference is a function of the additional energy required to provide for the current rate of production of new surface or the current rate of plastic work being done or both. This conclusion is verified for Ham River sand, as shown on Figure 7.9, which shows that $\dot{E}$ min = 3.04 for a consolidated drained test at a confining pressure of 10 psi. The results of two further tests at confining stresses of 990 psi and 4000 psi are also shown. (The voids ratio changes for these tests are shown on Figure 7.7). It is very clear that fracture in these two tests occurs, and that the effect of this is to increase the value of $\dot{E}$ quite markedly. In fact, in the early stages of both tests, D is negative, or in other words, no energy is transmitted; in fact energy is supplied both axially and radially. It is not until the very last stages of these tests that the magnitude of $\dot{E}$ falls to a value of 3.25, the same value obtained for the test at σ_3' = 10 psi. The results for the two high pressure tests when σ_3' = 990 psi and σ_3' = 4000 psi are rather deceptive, in that they appear to

be very close together on this plot. That this is not so is illustrated if a comparison is made, for example, between R values of 2 to 3. For the test at σ_3' = 990 psi, $\dot{E}$ = 4.7 falling to 3.95, whereas for σ_3' = 4000 psi the corresponding values are $\dot{E}$ = 7.9 falling to 4.2, showing that a much larger proportion of the energy supplied is being absorbed by crushing in the higher pressure test.

Similar results were obtained for tests on iron shot, and are shown in Figure 7.10. The values of $\dot{E}$ in the early stages of the high pressure test are certainly significantly larger than for the low pressure test, but, the values of $\dot{E}$ during the later stages of the low pressure test increase, whereas those for the later stages of the high pressure test remain almost constant.

The results for a test on lead shot are also shown on Figure 7.10. Here again the energy ratio for virtually the whole test is larger than the value at the end of the test, the shape of the $R \sim D$ plot being very similar to those for the high pressure tests on sand. Results presented by Billam (1971) also show that in general larger values of R are required than those predicted by the stress dilatancy theory for materials which crush easily.

Figure 7.9 and Figure 7.10 also show the $R \sim D$ plots for unloading at the end of the shear stage. In this type of stress path the axial stress is being reduced while the radial stress remains constant. So the form of the stress

dilatancy relation changes. Horne (1964) gives the analysis for this condition and obtains:

$$\dot{E} = \frac{R}{D} = \tan^2 (45^\circ - \frac{\phi_\mu}{2}) \qquad (7.4)$$

This relationship is shown in Figures 7.9 and 7.10.

The unloading stages of the tests at low pressure (shown inset in these Figures) do cross over very rapidly to these energy ratio lines, and then roughly follow them down as the stress ratio decreases. The fact that very large values of the dilatancy function D are obtained is a direct consequence of the severe anisotropy of the interparticle contacts induced in the sample during the drained compression stage, and does not imply that the sample is dilating strongly. In fact the sample is consolidating during this stress path. In the radial direction the strains are directed inwards and are large in comparison with the axial extension strains.

Now $$\dot{E} = - \frac{\sigma_1' d\varepsilon_1}{2\sigma_3' d\varepsilon_3} = \frac{\sigma_1'/\sigma_3'}{-2d\varepsilon_3/d\varepsilon_1} = \frac{\sigma_1'/\sigma_3'}{1-d\varepsilon_v/d\varepsilon_1}$$

$$= \tan^2 (45^\circ - \frac{\phi_\mu}{2})$$

where $d\varepsilon_v = d\varepsilon_1 + 2d\varepsilon_3$, and in this case $d\varepsilon_3$ is positive and $d\varepsilon_1$ is negative and $d\varepsilon_3$ is large compared with $d\varepsilon_1$.

Note: Different sign conventions are used in various papers; for example, Rowe (1962) uses compressive stresses as positive, and compressive strains as positive. Horne (1964) uses compressive stresses as positive and extension strains as positive. In the above equations compressive stresses and strains are considered positive.

So the sign of the denominator D (where $D = -2d\varepsilon_3/d\varepsilon_1$) is positive and large, although the sample is consolidating. This consolidation feature was observed in all the tests (see Figures 7.6 and 7.7) and shows how sensitive the strain response of an anisotropic granular material is to particular stress paths, as pointed out by Bishop (1971). It is possible that membrane penetration has some influence. However the cell pressure is maintained constant for these paths, so one would expect the membrane penetration effect to be small, and in any case the volume changes for the low pressure tests have the largest values. For example, for σ'_3 = 10 psi, 1.37 cc of water were expelled from the iron shot sample, and 0.84 cc from the Ham River sand sample; for the tests at σ'_3 = 990 psi the values are 0.43 cc for the iron shot and 0.44 cc 0.46 cc and 0.48 cc for the Ham River sand samples. These are comparatively large values, larger than would be expected for membrane penetration (see comments made on this in Chapter 6). But because this is a most important feature of the behaviour of granular material, apparatus must be developed to enable these strains to be monitored directly in future research programmes.

The magnitude of the consolidation behaviour during unloading increases with the magnitude of the stress ratio from which unloading takes place. It is, of course, the stress ratio attained during the drained compression stage of a test. This can be seen in Figure 7.11, which shows the volume changes during unloading stages from different stress ratios.

These volume changes are not recoverable and are therefore not elastic. This is clearly seen in Figure 7.12 which shows the volume changes during cyclic unloading and reloading at the end of the shear stage of a test with the confining pressure at 500 psi. A point to notice is that the stress ratio attained on reloading is slightly larger than the peak value obtained in the previous loading stage, indicating that the structure of the sample had been altered and strengthened.

The significance of these results with respect to the Cambridge models will be discussed later.

A model for this behaviour could be described as follows. During the compression stage of the test more contacts, many of them heavily loaded, are required in the axial direction to carry the larger axial stresses. These are formed by the sample becoming anisotropic with respect to its 'interparticle contact density' and should display an anisotropic (non-linear) elastic behaviour on unloading. During unloading particles whose axially loaded contacts which were strained least become unloaded first, so allowing the confining stress to push these particles radially inwards. If the sample is now reloaded it will exhibit an increased stiffness. If this mechanism is correct then it follows that slip strains occur, and the stress dilatancy model should be followed, if the elastic strains are small in comparison with the slip strains. In Figures 7.9 and 7.10 this is seen to be the case for the low pressure tests where the magnitude of the elastic strains should be

small, but the unloading stages for the high pressure tests only approach the $\dot{E}$ min line during the last stages of unloading. (Elastic strains were not separated out from these results. A suggested method of doing this is included in the discussion of the Cambridge Models.)

7.6 Stress Dilatancy Correlations for Constant R Paths:

It was pointed out that strains due to plastic deformation or crushing could not be separated from strains due to frictional slip. In any case the basic hypotheses of this theory exclude these mechanisms and elastic deformations as well, so it would be unreasonable to expect close correlations for stress paths where these mechanisms dominate, which should be for paths where $1 \leqslant R \leqslant 1/K_o$ during which the strains are compressive. (The following discussion would also be valid for the early stages of varying R tests when R is small and the sample contracts in volume.)

Note: Horne (1965) suggests that in the early stages of an ordinary triaxial test when the particle assembly is decreasing in volume, and there is a poor fit between the test data and the min $\dot{E}$ line, the groups of particles, instantaneously deforming as a unit, may be small, and that there exists the possibility of rotation. Rotation allows the transmission of energy without frictional loss so the energy ratio $\dot{E}$ might be expected to lie below that given by eqn 7.2. The results of experiments at low confining pressures give a reasonable fit with eqn 7.2 above stress ratios of R = 2 to R = 2.5; these ratios are slightly larger than the value of $1/K_o$ that could be expected for these materials (see Rowe, 1962, fig 21). This would suggest that the predictions of the stress dilatancy theory become better after the sample starts expanding radially. Frydman (1972) suggested that a yield point, defined as the point when the volume expansion starts, represents a point in the stress deformation process below which relatively little interparticle slippage occurs.

For first-time loading, when the stresses are low for these paths, fracture is not likely, so the mechanism to consider is an elasto-plastic one.

This elasto-plastic mechanism was shown to lead to a good description of the behaviour of granular material under isotropic stress conditions, and led to a relationship of the form:

$$\frac{\Delta V}{V} = D(\Delta \sigma'_3)^x \qquad (7.5)$$

It was also shown that by inferring a similar behaviour the one-dimensional compression behaviour of granular material could also be represented very well by a relationship of the same form, namely:

$$\frac{\Delta V}{V} = \text{constant} \times (\text{change in mean effective stress})^x \qquad (7.6)$$

Different values of the constant and the index x were obtained.

Figure 7.13 shows a K_o consolidation test and an isotropic consolidation test with the relationship shown in equation 7.6 fitted. It is seen that the agreement is very good. These tests were purposely chosen because the initial porosities of the sample were quite close, and the samples were prepared as loose as possible, because, as was shown previously, the strain behaviour is sensitive to the density of interparticle contacts, and it was felt that a more uniform behaviour could

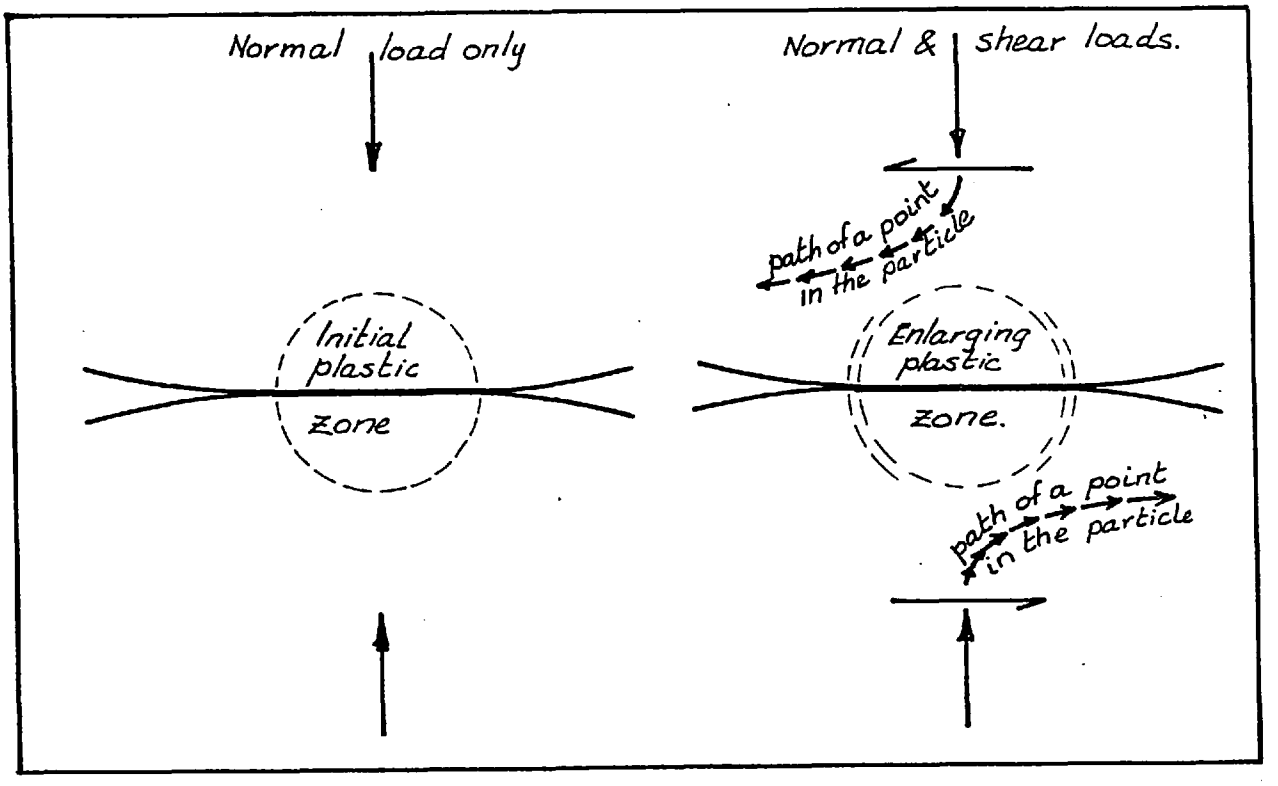
be obtained from the loose samples. (The measured porosities were 46.3% and 45.4% for the K_o and isotropic tests respectively.)

Membrane penetration again affects these results, but no allowance has been made for this in the results shown in Figure 7.13, which indicates that overall the K_o test has a larger void ratio change than the isotropic consolidation test, but for the early stages the reverse is indicated.

El-Sohby (1969) gives results for tests with constant R, for both dense and loose samples. His test results for loose samples show larger volumetric strains, for the stress ratios R = 1.5 and R = 2, $(1/K_o \simeq 2)$, than for R = 1, and for the dense samples the tests with R = 1 and R = 1.5 gave the same volumetric strains; only slightly smaller strains were obtained in the test for R = 2. Larger stress ratios for both loose and dense samples showed smaller volumetric strains, and in the case of dense samples, a stress ratio change from R = 4 to R = 4.5 changed the behaviour from consolidating to dilating. (Large stress ratios for the loose samples are not shown.)

We can now describe the mechanics of this behaviour. Consider a loose sample - the strains derived as a result of isotropic stress are simply due to plastic strains set up at each contact, accompanied by the elastic strains in the material below. If we suppose that at this stage the shear loads are applied at interparticle junctions, consider what could happen at

each junction. The junction is shown in the diagram with a purely normal load. The junction is in equilibrium in a plastic state.



The shear load is then applied progressively. First the junction must increase in area to lower the normal stress, so that it can accept the combined shear and reduced normal stress. Therefore the initial direction of motion will be directed towards the junction and this can be represented diagrammatically as shown.

The nett result is to produce additional consolidation of the granular sample. However, the lateral movements must also be accommodated; this is possible in a loose sample but as the packing becomes more compact, these lateral movements would

tend to produce dilation, and in the very dense samples appears to be a dominating factor. So the model can explain the observed behaviour.

Clearly for this type of mechanism the basic hypotheses of the stress dilatancy theory are invalid, and so it is only to be expected that the theory does not fit experimental data.

The same conclusion is obtained from an examination of the basic equation R = D.K. For R to be constant D must be constant.

So $$D = \frac{R}{K}$$

But $$D = \frac{-2d\varepsilon_3}{d\varepsilon_1}$$

and since both $d\varepsilon_3$ and $d\varepsilon_1$ for these stress paths ($1 \leqslant R \leqslant 1/K_o$) are positive, the resulting D is negative, which is impossible.

7.7 Stress Dilatancy Correlations for Elastic Paths (including Fretting Friction):

By definition elastic paths do not involve slip; therefore the stress dilatancy model is inapplicable.

7.8 Summary of the Conditions during which the Stress Dilatancy Theory can be used as a Soil Model:

The three mechanisms studied were listed at the start of the

Chapter. Of these it appears that this model can only apply to purely frictional behaviour when the sample is dilating under low to moderate stresses, and to the special case of unloading a highly anisotropic sample.

7.9 Factors influencing the Cambridge Soil Models - namely Granta Gravel and Cam Clay Models:

These models are considered together, because they are based on similar hypotheses.

The hypothesized behaviour of specimens following these models is illustrated in Figure 7.14a-f, taken from Schofield and Wroth (1968).

Data have already been presented to show that for a granular material the relationship between mean effective stress change and voids ratio is of a power form, so the mathematical equations developed for both these models based on a linear specific volume versus ln (mean effective pressure) relationship, will not be followed. Even so, it is instructive to see if the other assumptions for these modéls are valid.

When discussing the stress dilatancy model, unloading stress paths under drained triaxial test conditions were considered (see Figures 7.11 and 7.12). These paths result in non-recoverable volumetric strains, which violate the basic assumptions of the Cambridge models.

One further illustration that these models do not predict the

behaviour of granular material is indicated by the results from consolidated undrained tests on loose sand shown in Figures 7.15 and 7.16. Figure 7.16 indicates the false concept that undrained paths for tests with increasing consolidation pressures will be of identical shape. (This should be so even if Calladine's (1963) suggested modification to the yield curve is included.) Figure 7.16 also shows a test with K_o consolidation stage followed by an undrained shear stage. At the end of the shear stage all the samples were unloaded undrained. The pore water pressure changes induced were positive in all these cases and are shown in Figure 7.17. (Compare with the volume changes caused by unloading shown in Figures 7.11 and 7.12, see note.) The effective stress paths for these stages are also shown in Figure 7.16.

Clearly this response is not elastic and so the Cam Clay model is not valid for granular material.

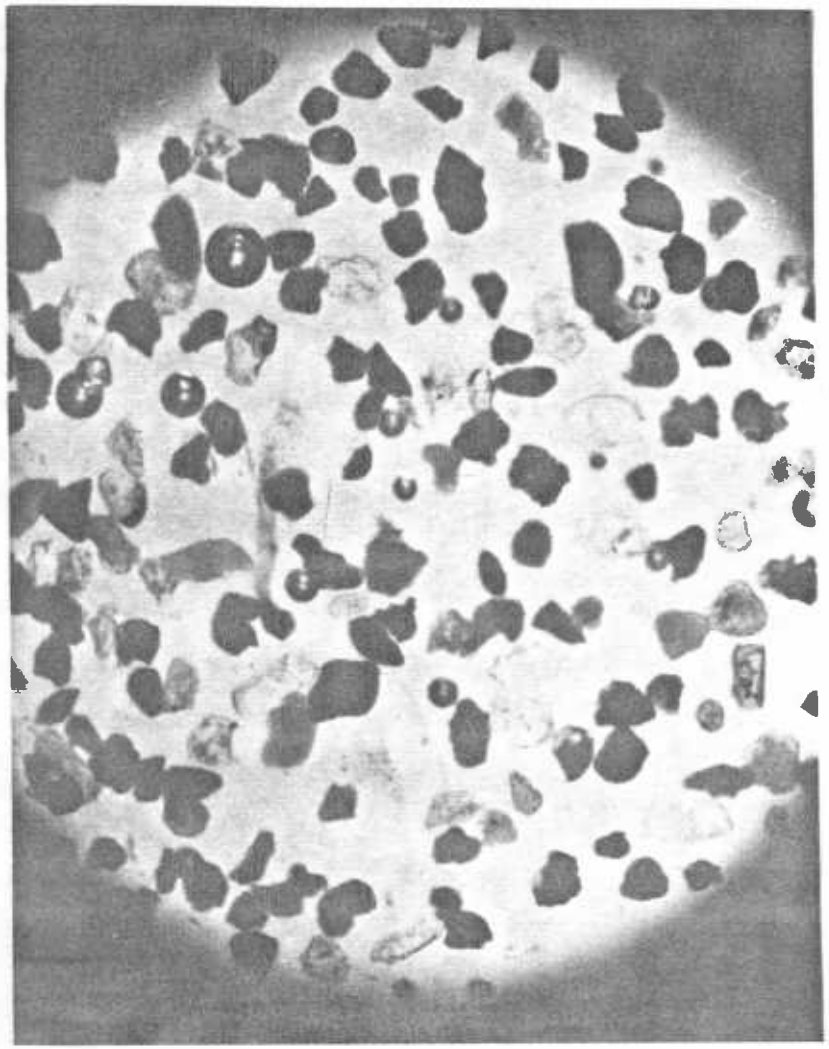
These arguments indicate that neither the Granta Gravel nor the Cam Clay models can be applied to granular material.

The data presented in this Chapter indicate that of the soil models discussed, the stress dilatancy model and the two Cambridge models, the former is to be preferred but has many shortcomings.

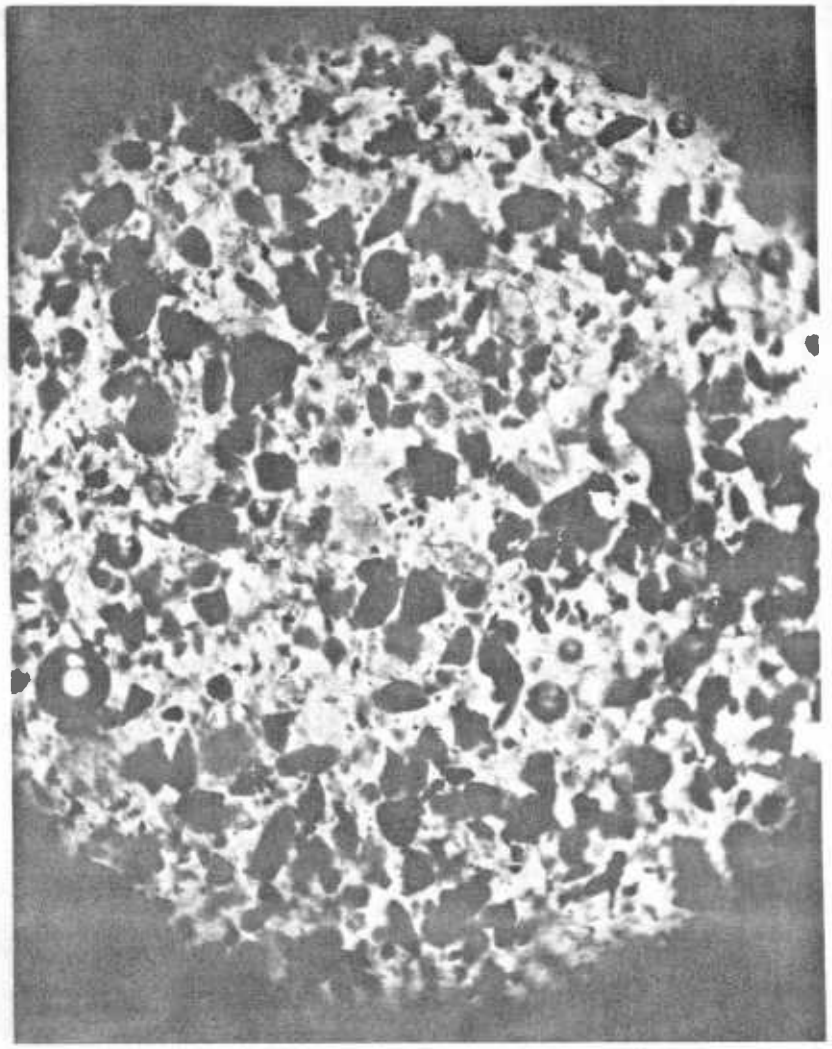
If the stress-strain behaviour of granular non-cohesive soil is to be adequately represented, a much more flexible predictive

model will have to be developed.

Note: Liquefaction due to undrained loading: It is obvious that this type of behaviour is a characteristic of anisotropic granular material, and forms part of a logical progression of the behaviour reported by Bishop (1971) (Figure 7.18). No undrained reloading cycles were done, but the results shown in Figure 7.12 can be used to argue that liquefaction can be associated with undrained unloading of anisotropic granular material as follows: If a saturated anisotropic granular material, initially in equilibrium, is unloaded undrained rapidly (eg. by an earthquake shock), then excess pore water pressures are built up. The vertical load will be reapplied and if the deposit is prevented from consolidating, as the data shown in Figure 7.12 indicate could happen, the pore water pressure must rise again. The strength would now be much lower than the previous equilibrium value, and the result would be a collapse of the structure; that is liquefaction occurs.

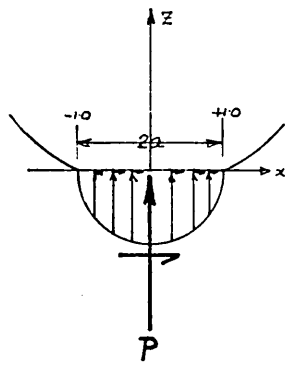


Before test



After test

Plate 7.1 Ham River sand grains before and after a consolidated drained test at 500 p.s.i. confining pressure.

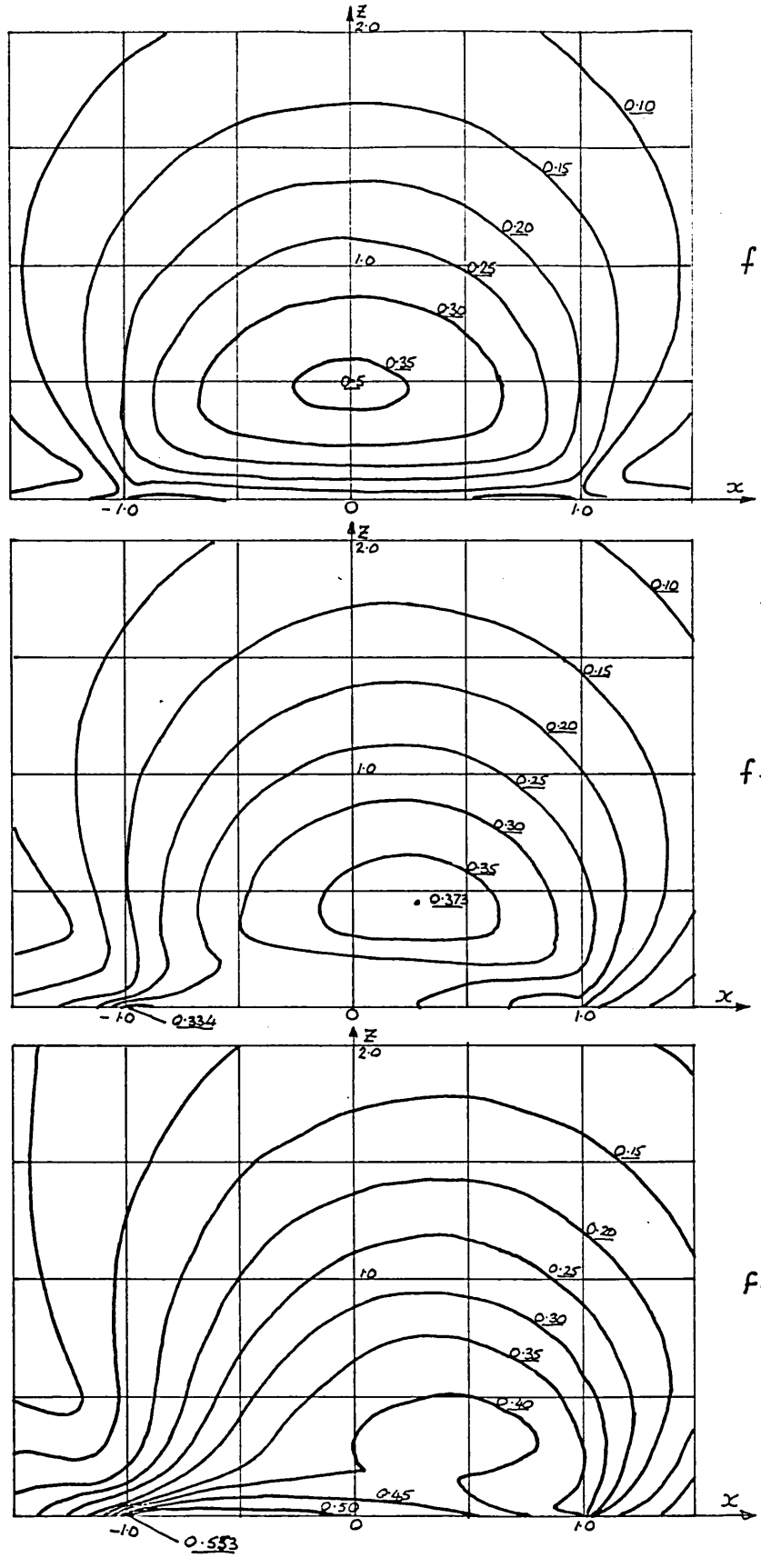


Horizontal traction proportionally distributed

$$p_0 = \frac{3P}{2\pi a^2}$$

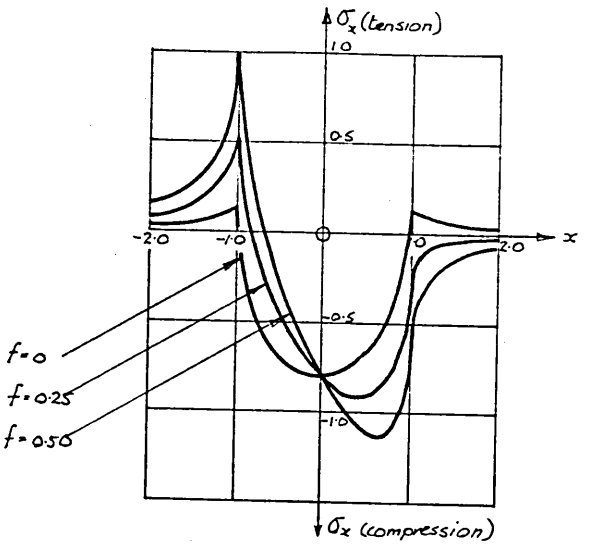
f = friction coefficient

$$J_2 = p_{xy}^2 + p_{xz}^2 + p_{zy}^2 + \frac{1}{6}\left[(p_{yy} - p_{zz})^2 + (p_{zz} - p_{xx})^2 + (p_{xx} - p_{yy})^2\right]$$

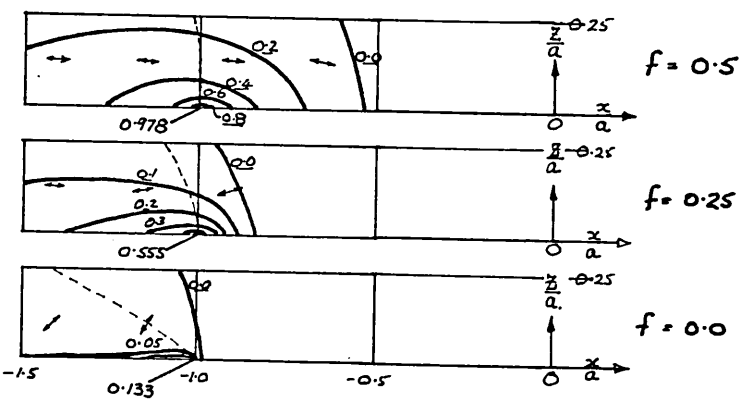


LINES OF CONSTANT $\frac{\sqrt{J_2}}{p_0}$ ON PLANE y=0 BENEATH CIRCULAR CONTACT after Hamilton and Goodman

Fig 7.1.



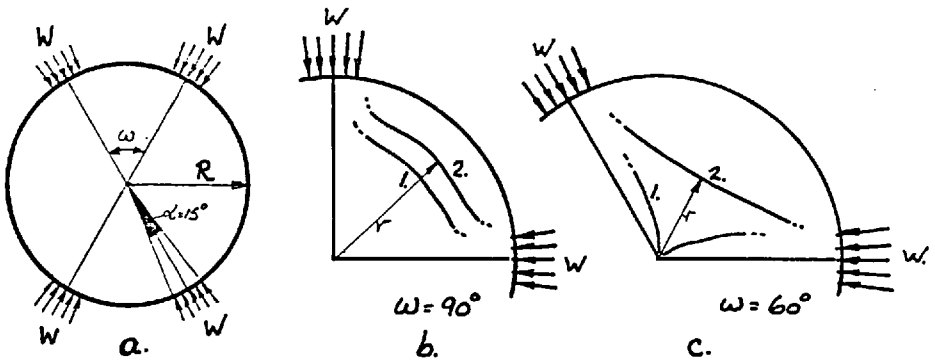
STRESS p_{xx} ALONG x AXIS OF CIRCULAR CONTACT FOR f= 0, 0.25 & 0.50.



PRINCIPAL STRESS ON PLANE Y=0 IN REGION WHERE IT IS IN TENSION, FOR f= 0, 0.25 & 0.5.

After Hamilton and Goodman. 1966

FIG 7.2.



a. Cylinder compressed in two diametral planes inclined at ω. (in b. & c. 1., limit of tensile field 2., locus of max: tensile stress.)

TABLE 1. Values and position of the maximum tensile stress attained in the system shown above.

ω	0°	30°	45°	60°	90°
$\frac{\pi R\sigma_t}{W}$	1·954	1·420	0·795	0·352	0·123
$\frac{r}{R}$	0	0	0	0·5	0·85

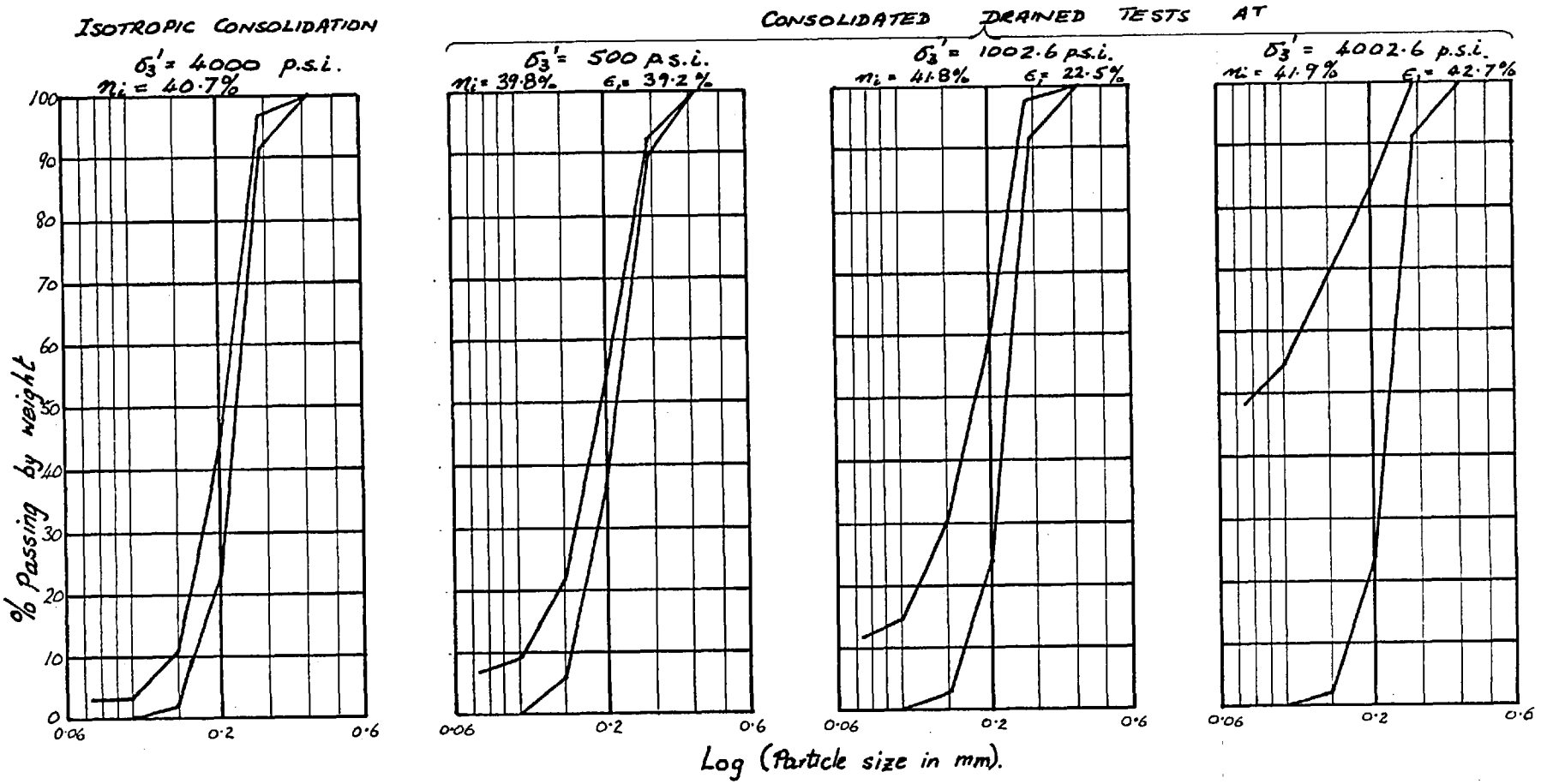
(In the Brazilian tensile test with loads 2W, $\frac{\pi R\sigma_t}{W} = 2$.)

TABLE 2. Normal loads W(lb) and maximum tensile stress σ_t (p.s.i.) at failure in the system shown above.

	ω = 0	45°	60°	90°
Carrara marble				
W	1600	4080	4130	5160
σ_t	1000	1030	460	200
Gosford sandstone				
W	850	2350	2900	3640
σ_t	530	590	330	140

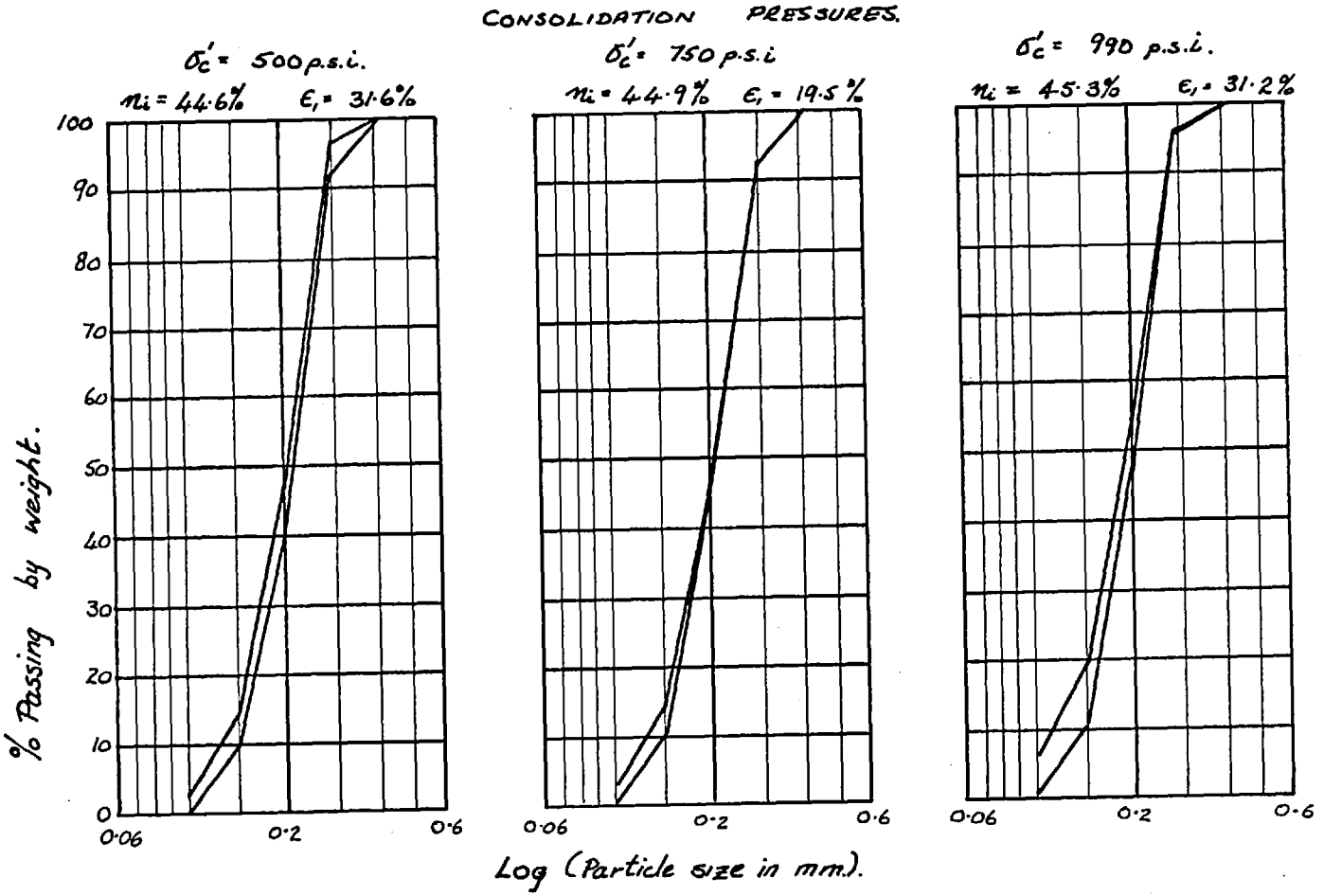
Data from Jaeger (1967).

FIG. 7·3.



CHANGES IN GRADING DURING DRAINED COMPRESSION

Fig 7.4.

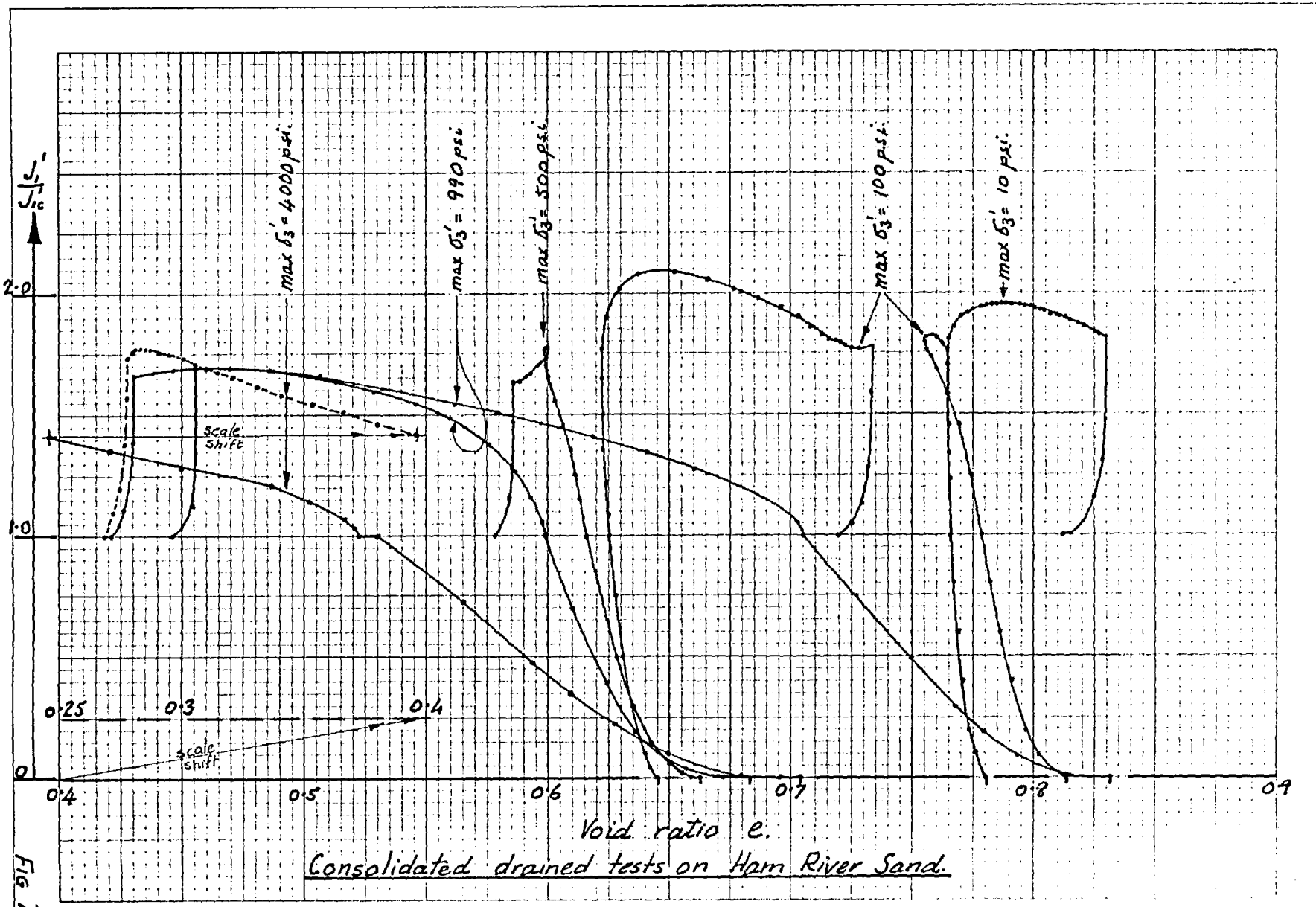


CHANGES IN GRADING DURING CONSOLIDATED UNDRAINED TESTS.

Fig 7.5

$J_1' = \sigma_1' + 2\sigma_3'$
$J_{1c}' = J_1'$ at end of consolidation stage.
2·0
1·0
0
$\frac{J_1'}{J_{1c}'}$
0·5
0·6
0·7
0·8
Void ratio e.
max σ_3' = 990 p.s.i.
max σ_3' = 500 p.s.i.
max σ_3' = 100 p.s.i.
max σ_3' = 40 p.s.i.
max σ_3' = 10 p.s.i.
Consolidated Drained tests on $\frac{1}{32}$" steel shot

Fig. 7.6.



Consolidated drained tests on Ham River Sand.

Fig 7.7

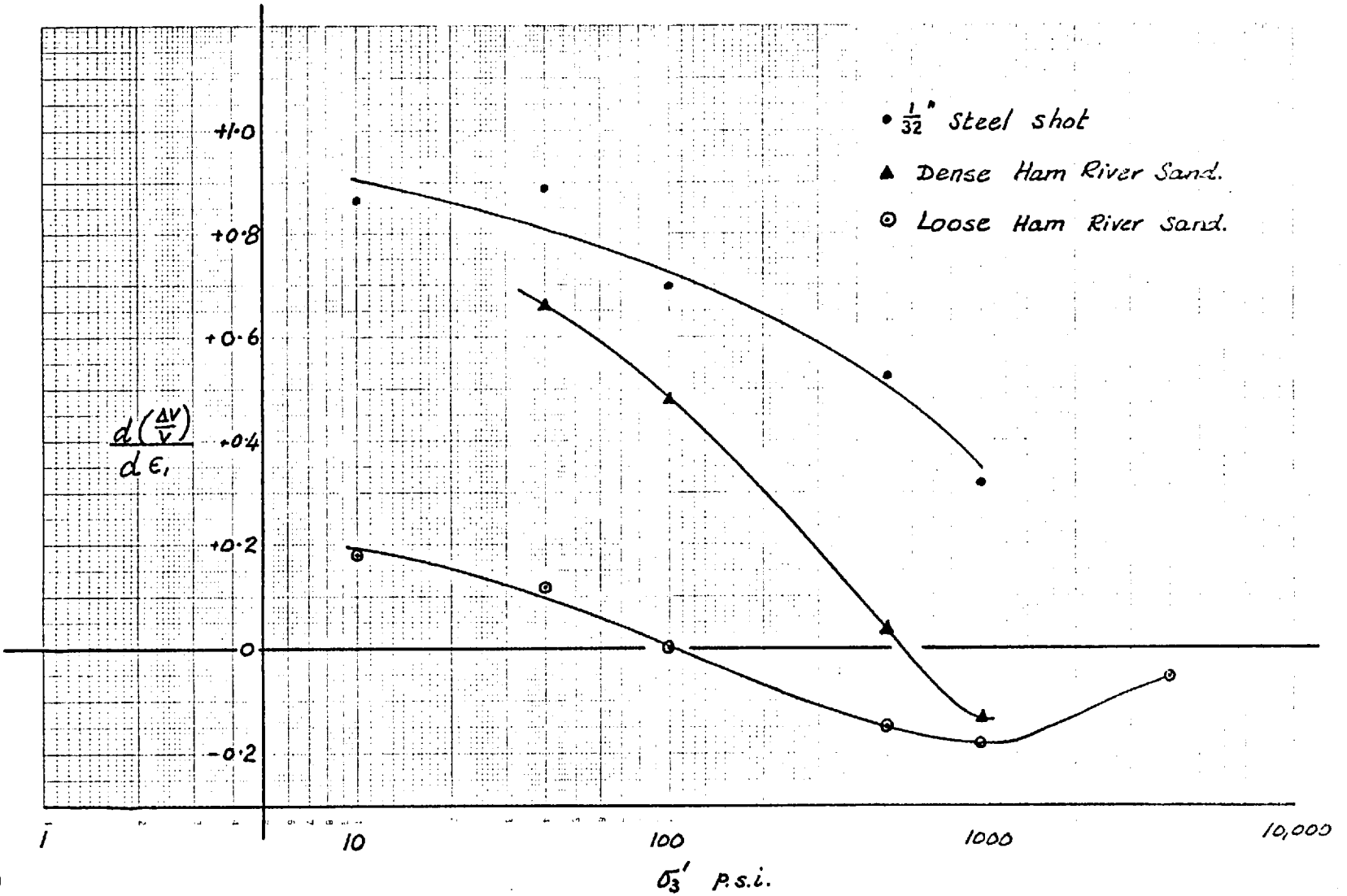

+1·0
+0·8
+0·6
+0·4
+0·2
0
-0·2
$\frac{d\left(\frac{\Delta V}{V}\right)}{d\epsilon_1}$
1
10
100
1000
10,000
σ_3' p.s.i.
• $\frac{1}{32}$" Steel shot
▲ Dense Ham River Sand.
⊙ Loose Ham River Sand.

FIG. 7.8.

CONSOLIDATED DRAINED TESTS ON HAM RIVER SAND.

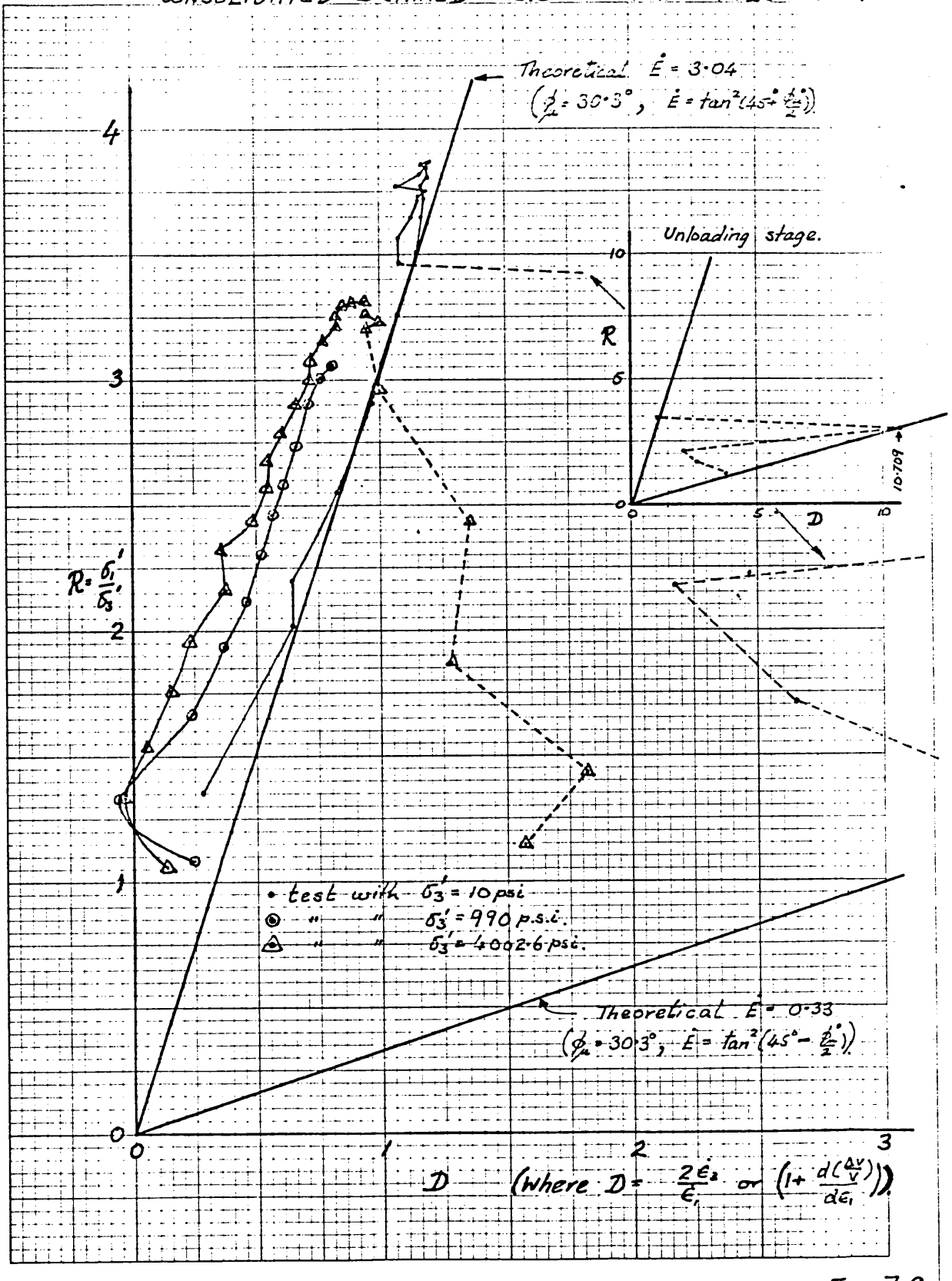


FIG 7·9

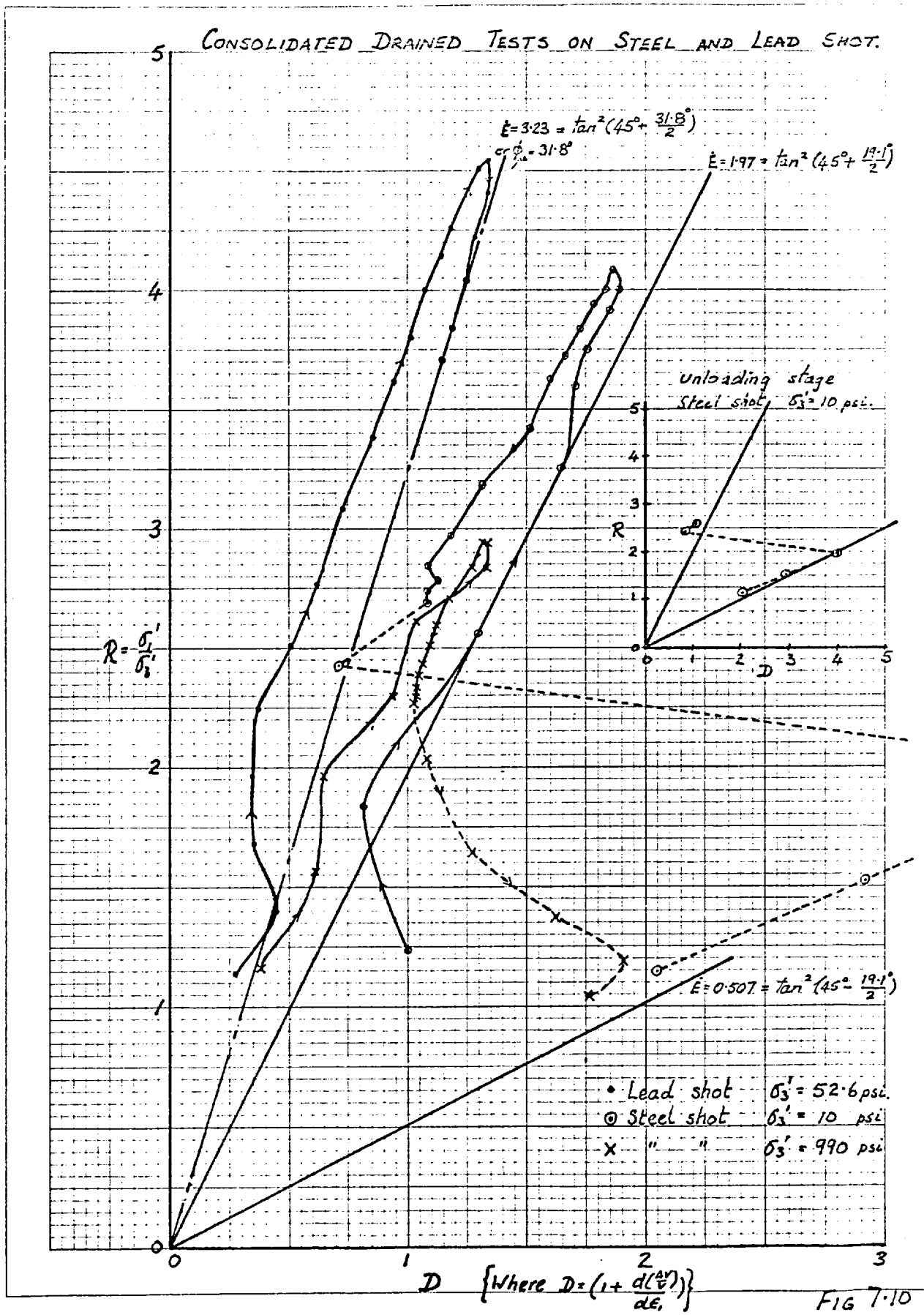

CONSOLIDATED DRAINED TESTS ON STEEL AND LEAD SHOT.
$\dot{E}=3.23=\tan^2(45°+\frac{31.8°}{2})$
or $\phi'_{max}=31.8°$
$\dot{E}=1.97=\tan^2(45°+\frac{19.1°}{2})$
unloading stage
Steel shot $\sigma_3'=10$ psi.
$R=\frac{\sigma_1'}{\sigma_3'}$
D
$\dot{E}=0.507=\tan^2(45°-\frac{19.1°}{2})$
• Lead shot $\sigma_3'=52.6$ psi.
⊙ Steel shot $\sigma_3'=10$ psi
× " " $\sigma_3'=990$ psi
D {Where $D=(1+\frac{d(\frac{\Delta V}{V})}{d\varepsilon_1})$}

FIG 7.10

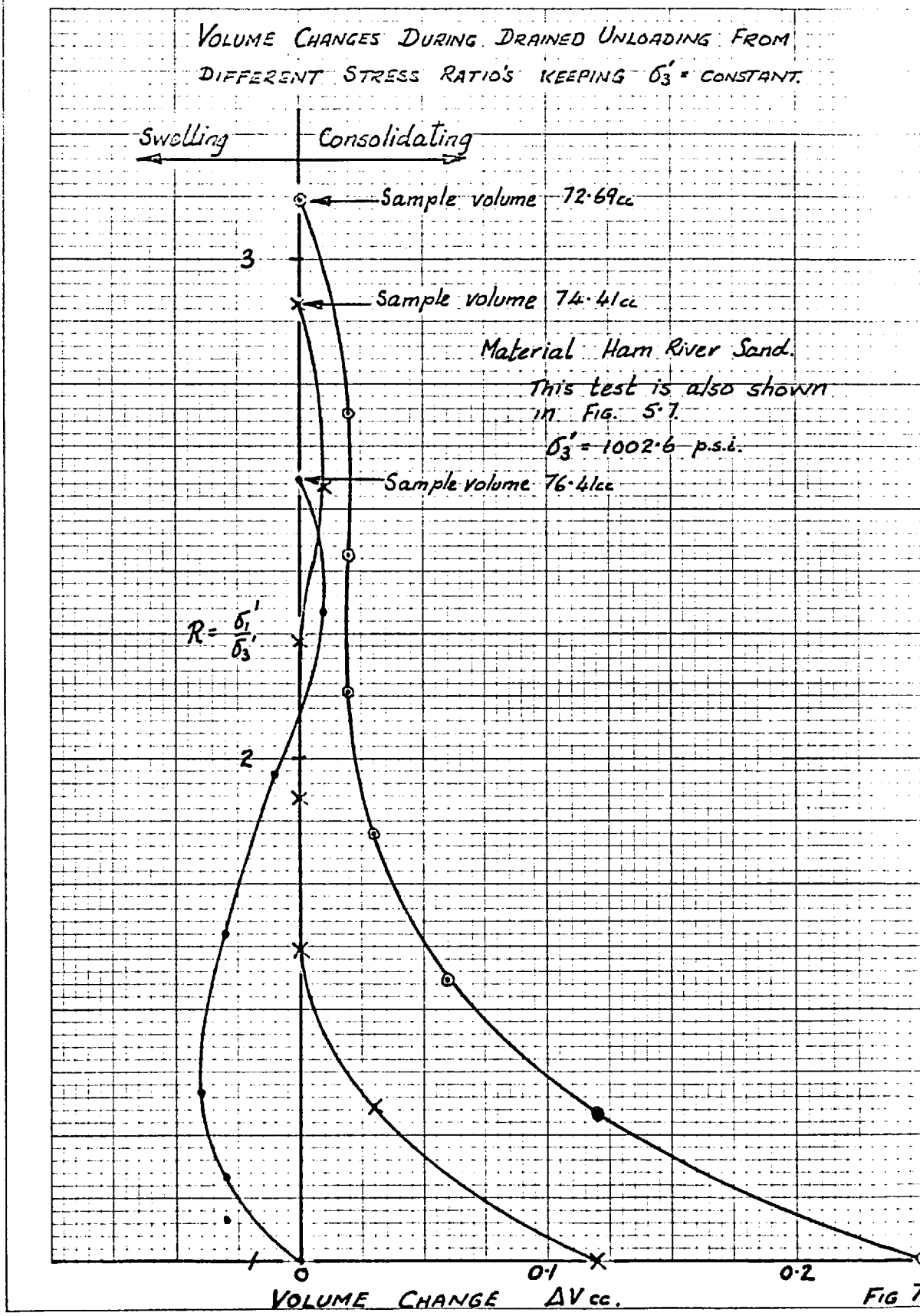

VOLUME CHANGES DURING DRAINED UNLOADING FROM DIFFERENT STRESS RATIO'S KEEPING σ_3' = CONSTANT.
Swelling
Consolidating
Sample volume 72·69cc
3
Sample volume 74·41cc
Material Ham River Sand.
This test is also shown in Fig. 5·7.
σ_3' = 1002·6 p.s.i.
Sample volume 76·41cc
$R = \frac{\sigma_1'}{\sigma_3'}$
2
1
0
0·1
0·2
VOLUME CHANGE ΔV cc.

FIG 7·11.

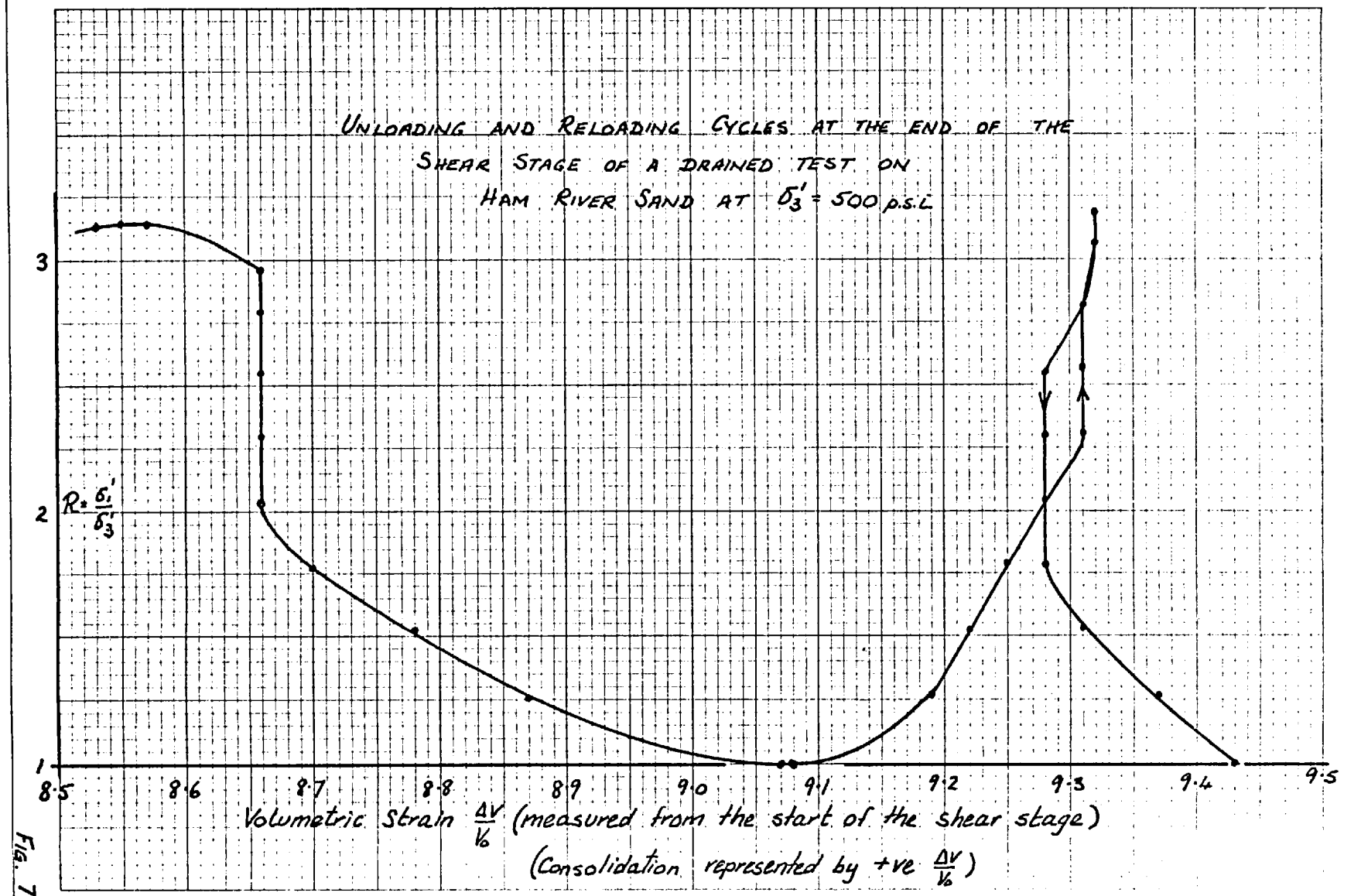

UNLOADING AND RELOADING CYCLES AT THE END OF THE SHEAR STAGE OF A DRAINED TEST ON HAM RIVER SAND AT $\sigma_3' = 500$ p.s.i.
$R = \frac{\sigma_1'}{\sigma_3'}$
3
2
1
8·5
8·6
8·7
8·8
8·9
9·0
9·1
9·2
9·3
9·4
9·5
Volumetric Strain $\frac{\Delta V}{V_0}$ (measured from the start of the shear stage)
(Consolidation represented by +ve $\frac{\Delta V}{V_0}$)

FIG. 7.12.

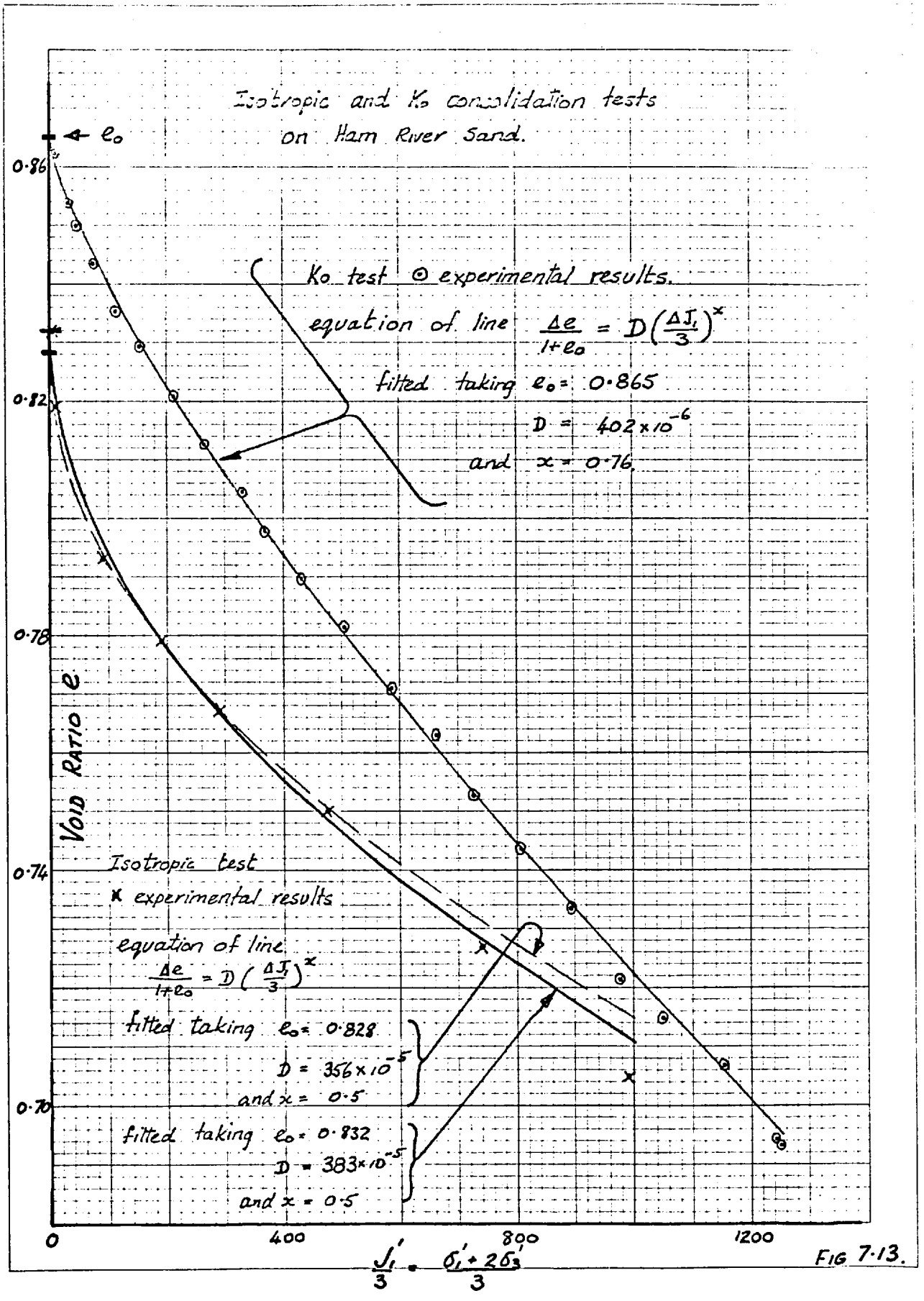
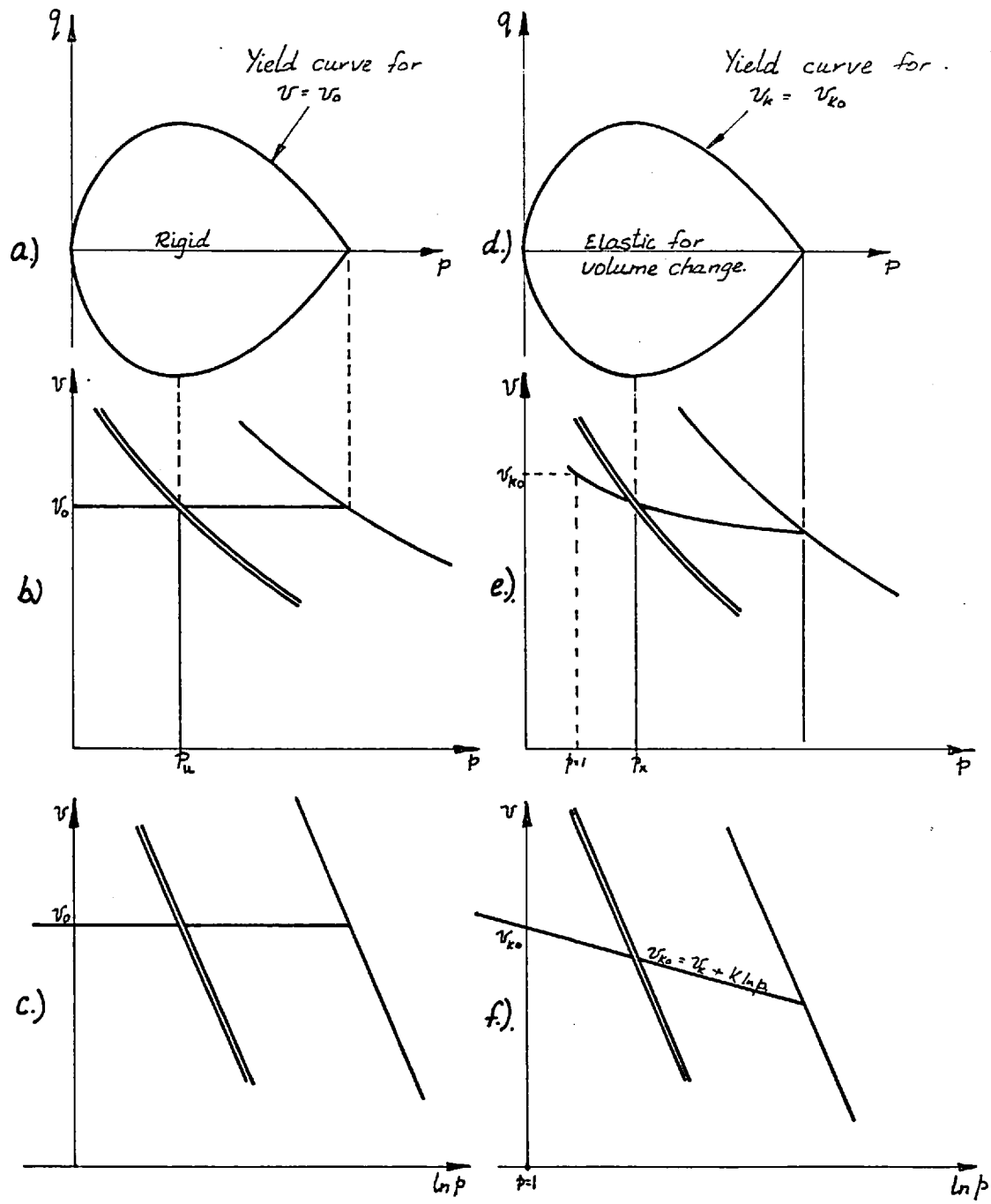

Isotropic and K_o consolidation tests on Ham River Sand.
e_o
0·86
0·82
0·78
0·74
0·70
VOID RATIO e
K_o test ⊙ experimental results.
equation of line $\frac{\Delta e}{1+e_o} = D\left(\frac{\Delta J_1}{3}\right)^x$
fitted taking $e_o = 0{\cdot}865$
$D = 402\times10^{-6}$
and $x = 0{\cdot}76$
Isotropic test
× experimental results
equation of line
$\frac{\Delta e}{1+e_o} = D\left(\frac{\Delta J_1}{3}\right)^x$
fitted taking $e_o = 0{\cdot}828$
$D = 356\times10^{-5}$
and $x = 0{\cdot}5$
fitted taking $e_o = 0{\cdot}832$
$D = 383\times10^{-5}$
and $x = 0{\cdot}5$
0
400
800
1200
$\frac{J_1'}{3} = \frac{\sigma_1' + 2\sigma_3'}{3}$

FIG 7·13.



Granta-gravel

Cam-clay

Yield Curves for Granta-gravel and Cam-clay

FIG. 7·14.

CONSOLIDATED UNDRAINED TESTS ON HAM RIVER SAND.

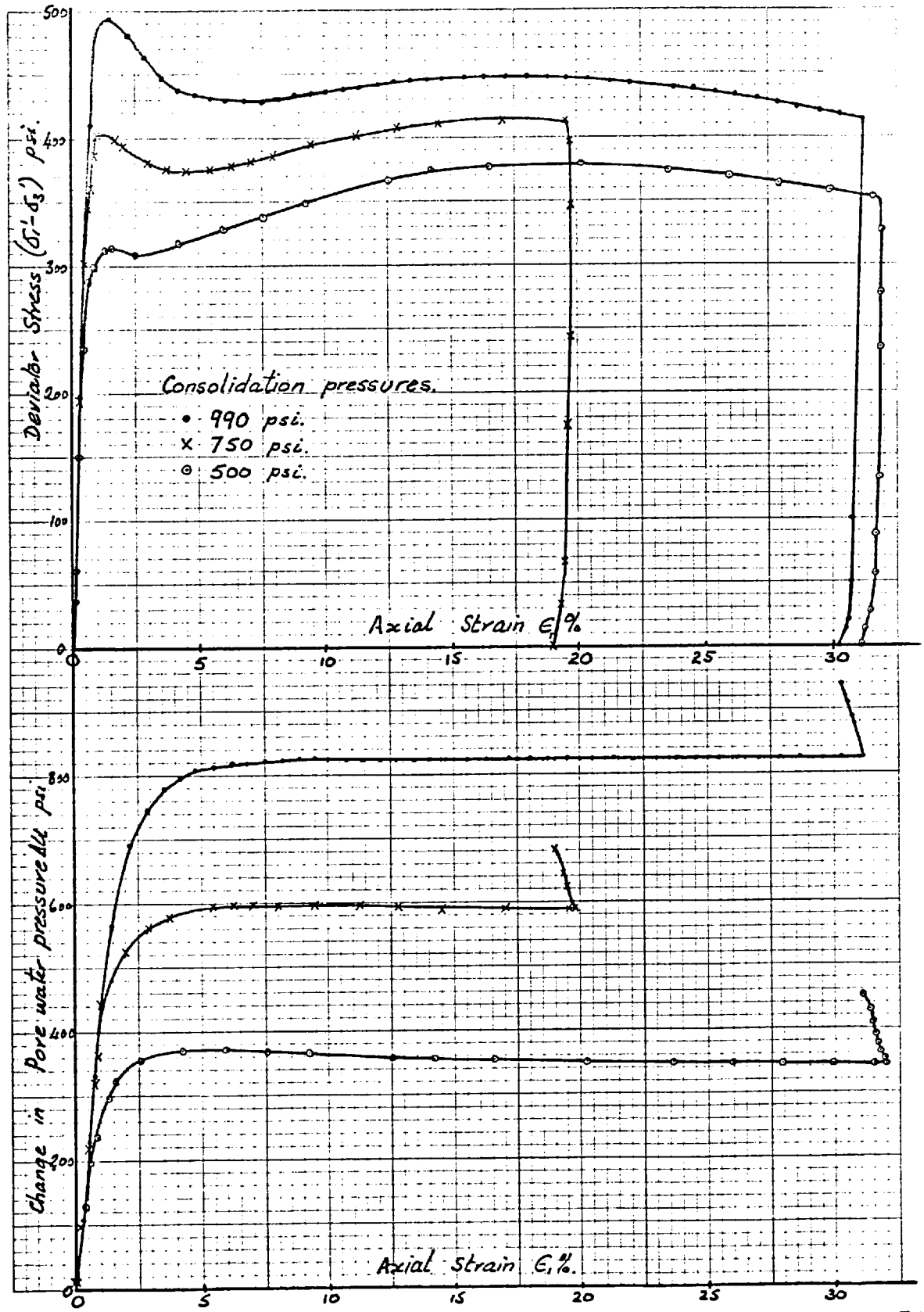


FIG 7.15

Stress paths for isotropically and K_o consolidated samples sheared and unloaded Undrained.

Material – Ham River Sand.

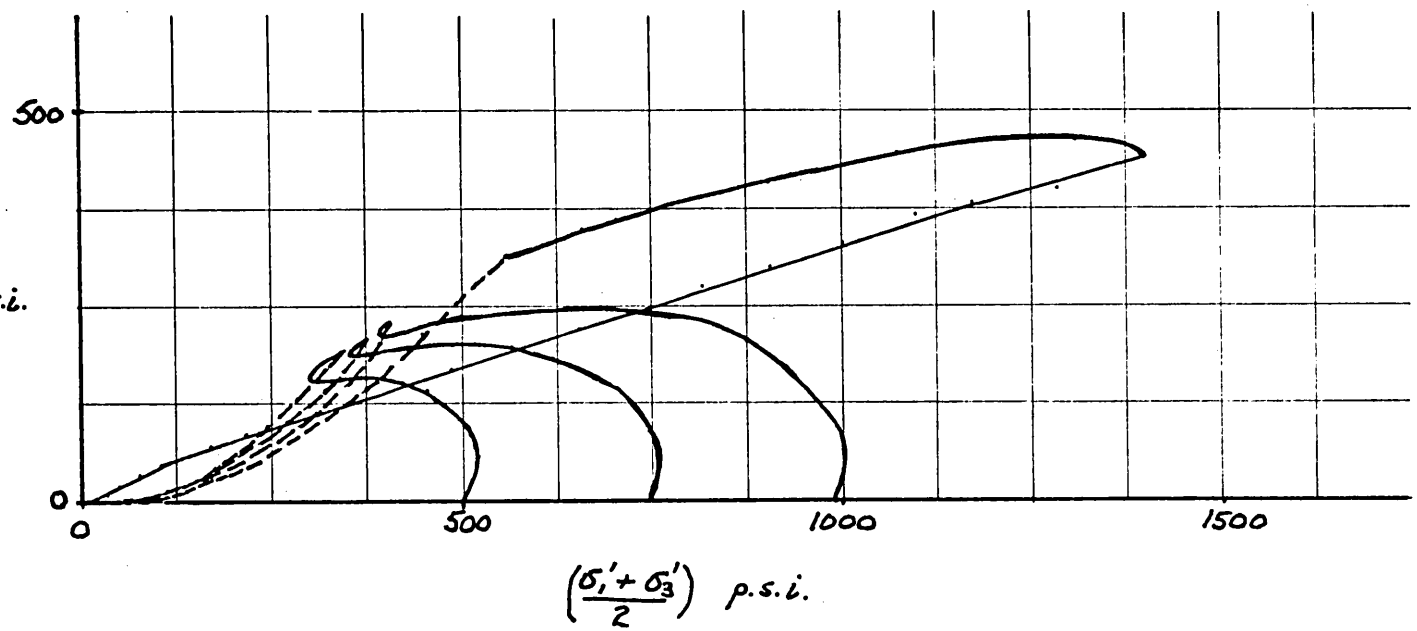


Fig. 7.16

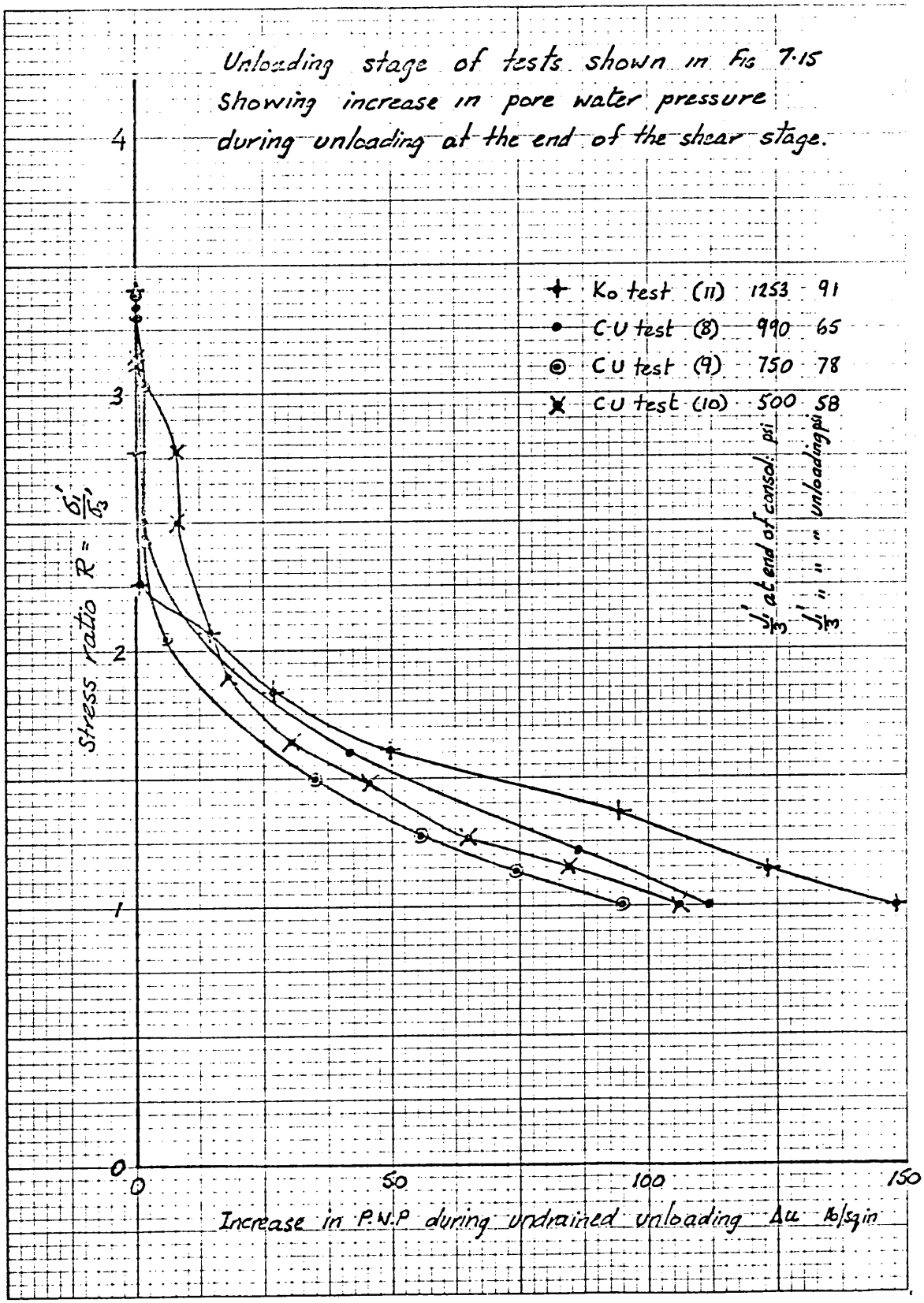
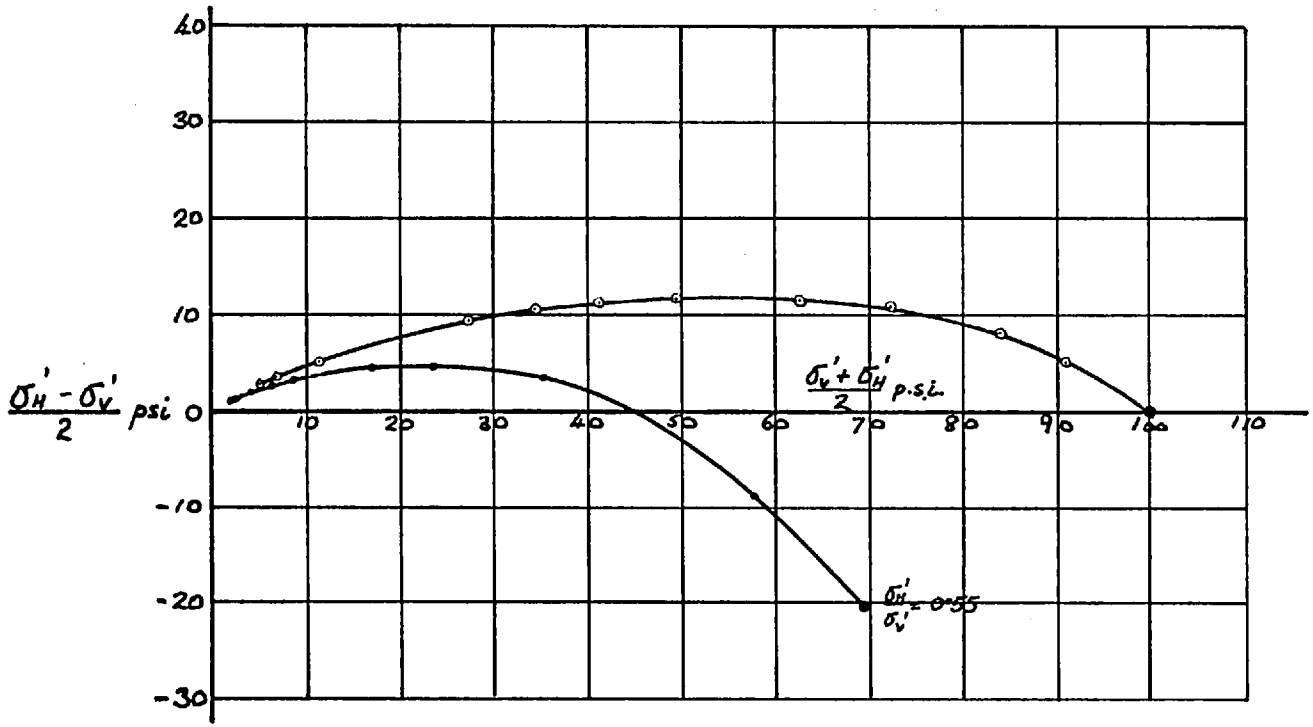

Unloading stage of tests shown in Fig 7.15
Showing increase in pore water pressure
during unloading at the end of the shear stage.
Ko test (11) 1253 91
C-U test (8) 990 65
C-U test (9) 750 78
C-U test (10) 500 58
σ'3 at end of consol. psi
σ'3 " " unloading psi
Stress ratio R = σ'1/σ'3
4
3
2
1
0
0
50
100
150
Increase in P.W.P during undrained unloading Δu lb/sq in

Fig 7.17.



Stress paths for consolidated undrained tests on samples having the same void ratio after consolidation (=0.789). Tests by Reades, 1971.

After Bishop 1971.

FIG. 7.18.

CHAPTER 8

BEHAVIOUR OF GRANULAR SOIL

8.1 A Conceptual Model for Granular Non-Cohesive Soil:

The model must incorporate the mechanisms which were shown to control the stress-strain behaviour. These were:

a) Elasto-plastic degenerating to frictional for certain stress paths, and fracture at higher stress levels.

b) Elastic-fretting frictional

c) Fracture.

A brief review of the previous findings in relation to the stress paths shown in Figure 8.1, for radially symmetric triaxial stress states is given below.

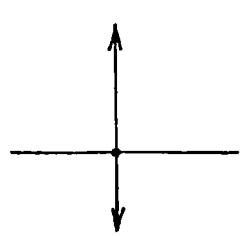
The material is assumed, initially, to be homogeneous (but not necessarily isotropic) and is subjected to isotropic stress, represented by point A in Figure 8.1. Particular stress probes directed away from A are shown as 1, 2, 3 and 4.

For 1: $\Delta\sigma_1' = \Delta\sigma_3' > 0$

For 2: $\Delta\sigma_3' = 0$

For 3: $\Delta\sigma_1' + 2\Delta\sigma_3' = 0$

For 4: $\Delta\sigma_1' = \Delta\sigma_3' < 0$



J_1' increasing

J_1' decreasing

A stress probe in the direction 4 results in a decrease in

interparticle contact load for an average contact within the soil, so that a material which had been plastically deformed would revert to elastic behaviour, but some frictional work is expended. A similar situation exists for probes between4 and 3 with progressively more frictional work being done as the probe becomes more inclined towards 3. At the same time there will be a tendency for the contacts to remain plastic for probes close to direction 3. The additional frictional work required could have been expected from the work of Mindlin and Deresiewicz (1953). At higher confining stresses fracture will influence the behaviour.

For probes between 3 and 1 both normal and shear loads will be increased at interparticle contacts, leading to additional plastic work requiring more expenditure of energy.

Thus no matter which way a stress probe is applied some work is done which cannot be recovered. Therefore the point A could be circumscribed by a primary yield surface.

Along path AO there should be no fretting slip for a perfectly homogeneous isotropic material, as no external shear stress is applied. But since granular material could never reach this ideal, some energy will be expended. This was what was observed for the tests reported in Chapter 6, where cyclic stresses produced hysteris loops, with a small permanent compression which could have been due to a small proportion of unfavourably stressed contacts which either fractured or

slipped. In general this path could be considered to be contained within an envelope of stress states, outside which either gross slip, re-orientation of the particles or fracture were the predominant mechanisms. Stress cycles within this envelope could be considered to lead to closed stress cycles with a very small amount of permanent compression or distortion. This second envelope could be called a secondary yield surface.

A stress probe fairly close to 3 is followed in the initial stages of an isotropically consolidated undrained compression test on a fully saturated specimen. If the elastic behaviour of the sample could be taken as approximately linear elastic for a small stress probe, then the value of

$$\frac{\Delta\sigma_1'}{\Delta\sigma_3'} = \Delta R' = -2$$

(if B = 1 and A = 1/3), or on the curves of Figure 7.16 the initial slopes should be:

$$\frac{\Delta\sigma_1' - \Delta\sigma_3'}{\Delta\sigma_1' + \Delta\sigma_3'} = \frac{\Delta R' - 1}{\Delta R' + 1} = 3$$

It is apparent, from the tests shown in this Figure, that the slope of 3:1 is only followed for a very small part of the stress path, the strain being considerably less than 1% at the breakaway point. This breakaway could be due either to particle crushing or slip or both.

Stress probe 2 is a conventional drained test, and the data for this type of test are shown in Figures 7.6 and 7.7. The continuity of these curves indicates that a hardening process, similar to that for isotropic compression, takes place for these tests, eventually giving way to slip and dilation for the lower pressure tests at a stress ratio of about R = 2. In the higher pressure tests strains due to particle fracture occur very early in the shear stage, so the secondary yield surface, in this direction, is adjacent to stress point A.

This enables the secondary yield surface to be drawn as shown in Figure 8.2, which is taken to apply to both sides of the $\sigma_1' = \sigma_3'$ line. This secondary yield surface is shown dotted as no overconsolidated tests were conducted.

Not very many shear tests on anisotropically consolidated sands have been reported so it will be hypothesized that primary and secondary yield should occur in much the same way as the isotropic case, but since the interparticle contacts always carry their shear components, after consolidating, in the same direction, the elastic domain will be unsymmetrical about the stress line along which the sample was consolidated.

The K_o consolidated undrained test shown in Figure 7.16 produced a very rapid increase in pore water pressure, which was larger than the small increase in axial load at the start of the undrained shear stage; this would indicate a

yield surface very close to the stress point at the start of the shear stage for this particular path.

It was also shown that at the end of the shear stages of undrained tests, the sample yielded during unloading. Similar behaviour was observed for the unloading stage of the consolidated drained tests. So it would appear that the secondary yield surface is very close to the line joining the stress point to the origin.

The writer is not aware of any published information on tests conducted on overconsolidated granular soils either isotropically or anisotropically overconsolidated. But tests of this type have been conducted on remoulded clays. A comprehensive series of tests were conducted by Namy (1970) on a silty clay, 68% of which was of silt or sand size. The results of his tests can be summarized by referring to Figure 8.3.

Path A0 is essentially elastic. For a stress path beyond A (i.e. for stress increment a)) a yield occurs just beyond A (i.e. A is on the yield locus). For stress paths b) and c) when unloading from comparatively large stress ratios, Namy states that yielding of second order was observed at the end of the unloading path of cyclic drained tests (which could be analogous to the behaviour noted for granular material in both drained and undrained tests).

For stress paths (d_1) and (d_2) yielding occurred when the

stress ratio was increased.

Using this information, the behaviour of granular material can be drawn up for various initial stress conditions. These are shown in Figures 8.4 to 8.7.

An idealization of this behaviour would be to consider the path AO as the elastic path, and the zone of progressive slip as that portion of the yielding process that can be associated with the voids ratio* at the particular stress ratio that the sample sustained at the start of the stress cycle being considered.

The material behaviour is thus never entirely elastic, and even when it approaches elastic behaviour is highly non-linear. In addition the elastic response is linked to the applied stress ratio. In other words a soil element adjusts its state of anisotropy to be compatible with the current state of stress. This means that an analysis using a linear elastic approach would be invalid for this material.

Work-hardening theories of plasticity would also be inappropriate

---

* Note: It has been pointed out previously that the mechanical response is controlled by interparticle contact behaviour which will be influenced by their distribution. This characteristic cannot be described by a scalar quantity such as the voids ratio. But there is no way, at present, to measure the number of contacts and their current load capacity, so voids ratio, which can be measured, will be used - but, always linked with the stress ratio and the magnitude of the mean effective stress currently sustained.

because the current stress point is entirely surrounded by a yield surface, or in the case where the stress path AO is taken as being elastic, the idealized primary yield surface reduces to the straight line AO. Since any movement of the stress point away from the line would produce a change in the elastic character, Drucker's stability postulate can not be applied and hence this approach to the normality criterion is blocked.

This point can be illustrated by referring back to Namy (1970), who stated that for Newfield clay, the permanent strain increment vectors depended on the loading history, and on the stress increment vectors, and that they were not normal to his experimentally determined yield locus. For example, see Figure 8.8.

So we are left with a model which can only be tested experimentally and used empirically, basing predictions on the observations of experiments. This is not too severe a restriction since the use of elastic or plastic theories requires at least that these models adequately predict the results of experiments, and if they do not, their use would be inappropriate.

8.2 Early Stress-Strain Behaviour Predictions from Anisotropic Consolidation Tests:

A series of anisotropic consolidation (R = constant) tests on fine sand were reported by El-Sohby in the Proceedings of the

7th International Conference. These data are replotted in Figure 8.9 and 8.10 for loose and dense samples respectively.

Two consolidated drained tests at a confining pressure of 100 psi, conducted on loose and dense samples of Ham River sand, are shown in Figures 8.11 and 8.12, and superimposed are paths, obtained from El-Sohby's data, assuming that the stress paths can be associated with the initial voids ratio used in the R = constant tests. The shear test path is then simply obtained by using the voids ratios at points corresponding to the intersection of the R = constant lines and the path for which $\Delta\sigma_3' = 0$, with the assumption that the voids ratio changes are independent of the stress path taken, providing that the magnitude of R' is always increasing towards the value being considered. These paths in Figures 8.11 and 8.12 are for J_1'/J_{1c}', where J_{1c}' is the value of J_1' at the end of the consolidation stage. Thus for these paths $J_1'/J_{1c}' = (R' + 2)/3$, so the value of e for any value of R' corresponding to the particular value of $J_1'/3$ being considered, can be obtained from the data in Figures 8.9 and 8.10. Both the materials are fine sand, but the material used by El-Sohby was finer (100/150 BSS), whereas the Ham River sand used was (36/150 BSS). However, the behaviour appears to be much the same.

Comparing the superimposed paths with the test paths, it is obvious that the assumed behaviour of no gross slip with R' increasing is a good approximation up to a value of R' = 2, in the case of the loose sample when the axial strain was

0.7%. Whereas the assumption appears to hold good to a stress ratio R' = 4 for the dense sample, which then had an axial strain of 2.1%. Beyond these values the assumed behaviour is not valid which is not surprising, because gross interparticle slip is occurring, and the slip directions are associated with a different stress path.

Using the same assumptions as before and employing El-Sohby's experimentally obtained relationship between volumetric and axial strains shown in Figure 8.13, comparisons between the stress ratio versus axial strain relationships for the loose and dense tests (previously used for the stress path correlation) can be made. These are shown in Figures 8.14 and 8.15. In the case of the loose sample it must be pointed out again that the two materials are not the same, and that the initial voids ratio of El-Sohby's tests was 0.859, while the Ham River sand sample started at a voids ratio of 0.813. Nevertheless the resulting strains compare very favourably. Unfortunately El-Sohby's data do not extend beyond a stress ratio of 2.5. The correlation is much better for the dense sample right up to a stress ratio of about R' = 4, when the test on Ham River sand starts showing appreciably larger strains.

No low pressure consolidated undrained tests were performed for this research programme, so comparison of the early strain behaviour can not be made.

Now, going on to the higher stress range it is only possible

to indicate the behavioural trend, as no experimental data are available for constant R' tests at higher stress levels. Looking back to Figure 7.13 and to Figure 7.7 it is seen that increasing stress ratios produce a marked increase in particle fracture, which leads to a rapid decrease in porosity. So in this case the tendency to dilate will be completely suppressed and the curves of e versus P' ($P' = J_1'/3$) for varying stress ratio will show smaller e values for increasing R' for particular values of P', even for those samples which started off dense and which initially showed positive dilatancy for high stress ratios in the low P' range.

One can qualitatively endorse this argument by considering the consolidated undrained tests shown in Figure 7.16. These tests show that for high confining pressures the undrained shear stage produces a reduction in the mean effective stress for increasing R', which is what the previous argument would have led us to expect.

8.3 Stress-Strain Behaviour during Shear Stages when Slip and/or Crushing Mechanisms Predominate:

These phases of the stress-strain behaviour need much more experimental work before stress-strain relationships can be established.

This does not imply a plasticity type of approach, as no recourse is made to the concept of yield nor the associated

normality concept.

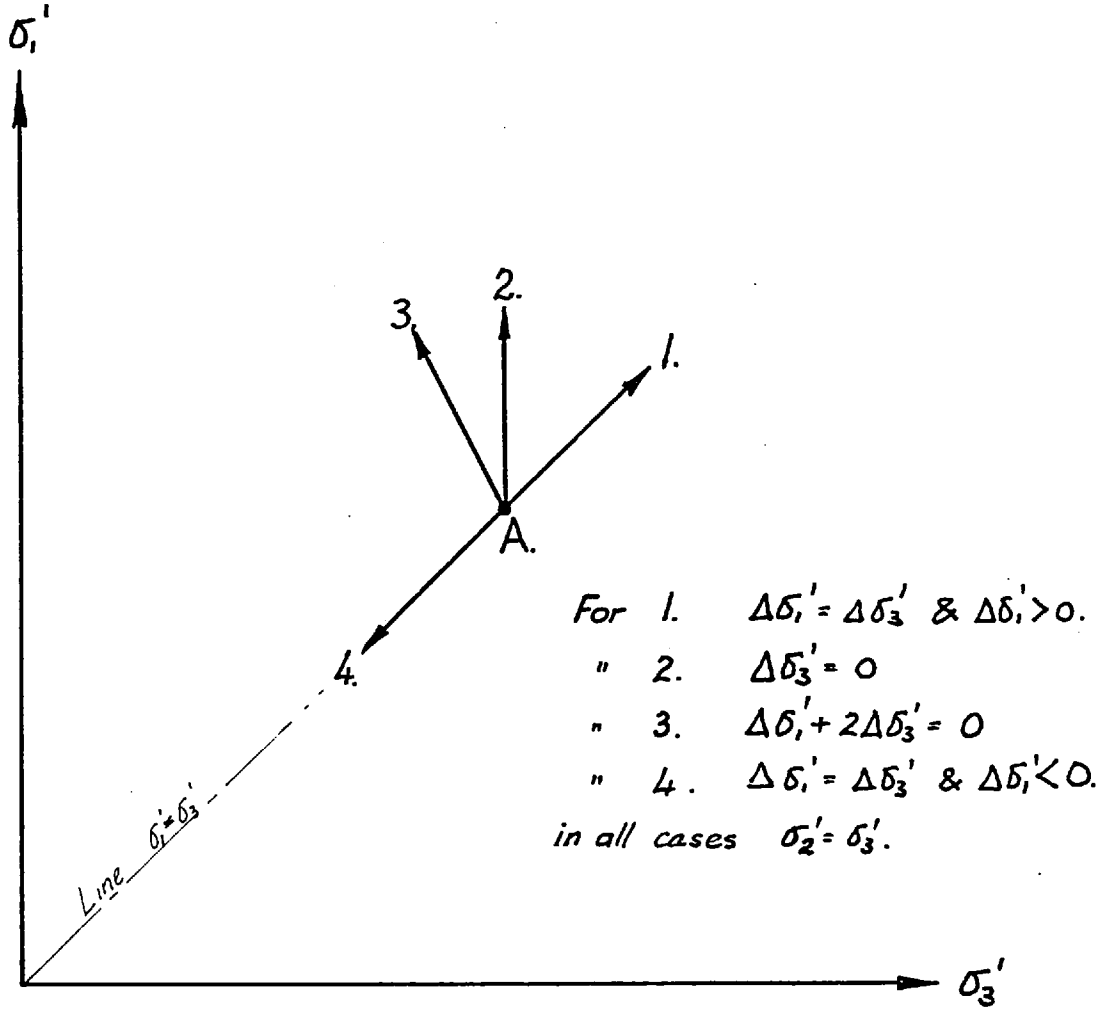
For the high stress region the stress dilatancy relationship was shown to be inadequate. At this stage it seems that a wholly empirical approach is the only course open.

In the lower stress ranges the stress-dilatancy relationship can be used as a flow-rule, with experimentally determined hardening and softening laws, for those cases where it was shown that a reasonable fit to the experimental data was obtained.

8.4 Summary:

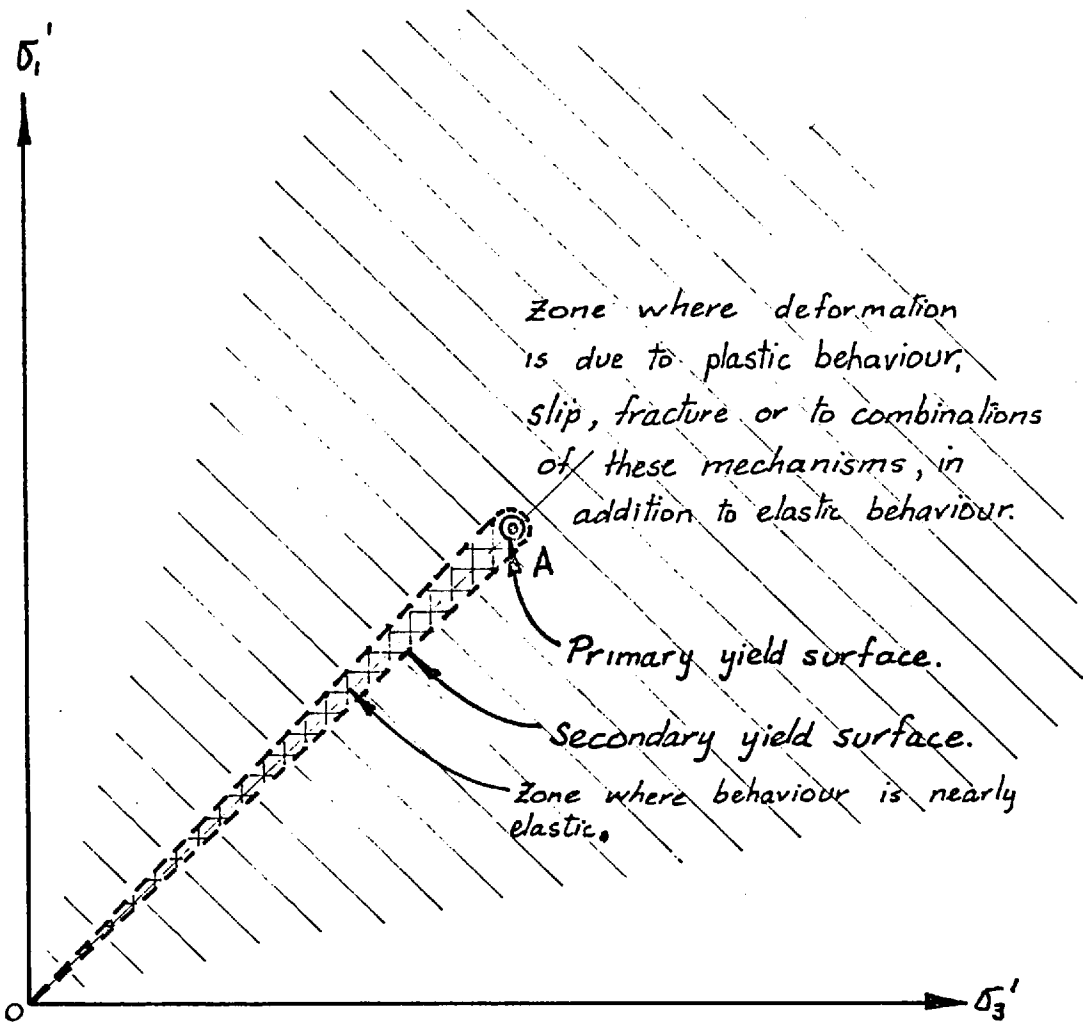
It has been shown that a classical pure plasticity approach to the stress-strain behaviour of granular non-cohesive material is inappropriate. In the low stress range an empirical assumption assuming that the voids ratio is a function of the stress ratio and mean effective stress and is independent of stress path, providing that the stress ratio is progressively increased, leads to reasonable predictions for moderate stress ratios.

Suggestions for future research work are that hardening and softening rules could be experimentally determined and used with suitable flow rules to provide a framework for the stress-strain behaviour for those stress ranges where crushing and/or slip are the dominant mechanisms.



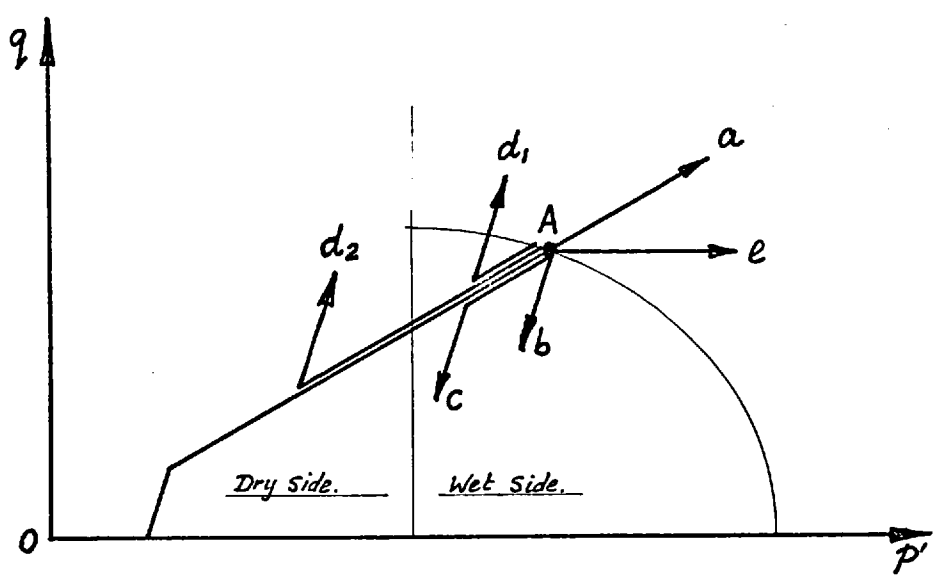
STRESS PROBES FROM AN ISOTROPIC STRESS STATE

FIG. 8·1.



Yield surfaces.

FIG. 8·2.



Different stress paths used for the investigation of the yield locus developed during Anisotropic-Consolidation to the stress point "A".

After Namy 1970.

Fig. 8·3.

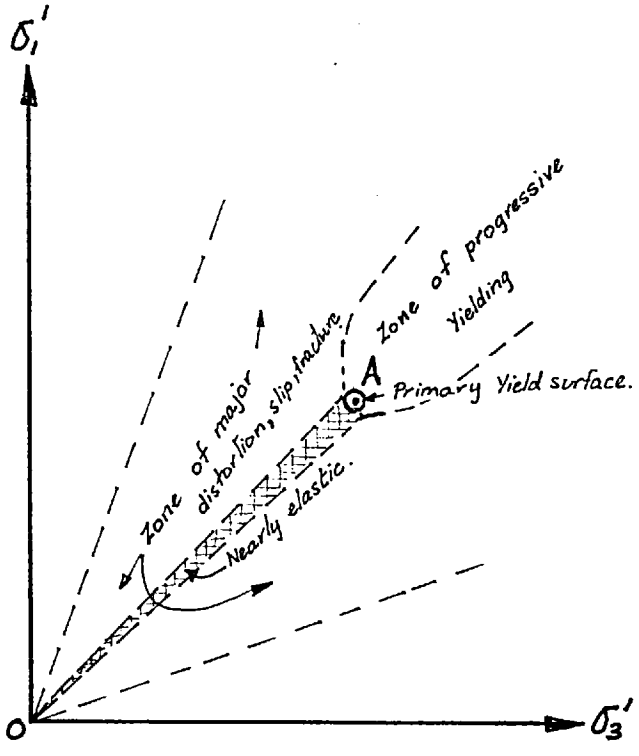


FIG 8·4

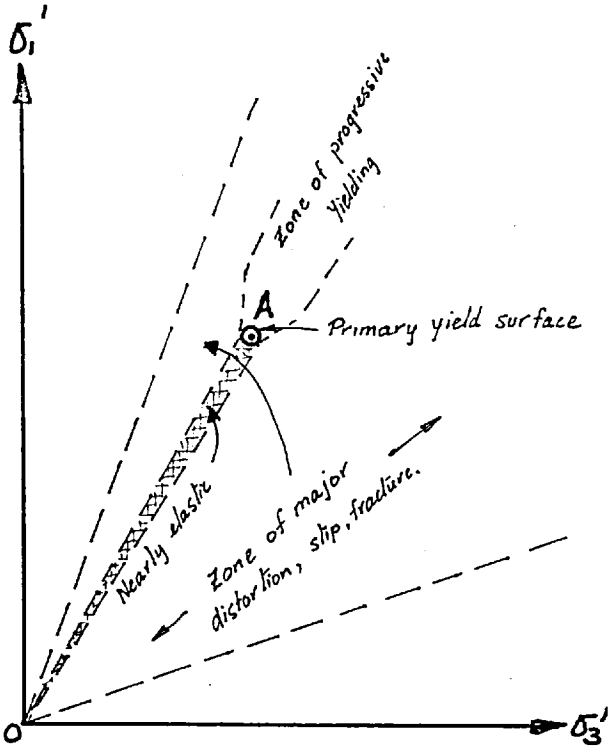


FIG 8·5

LOW PRESSURE

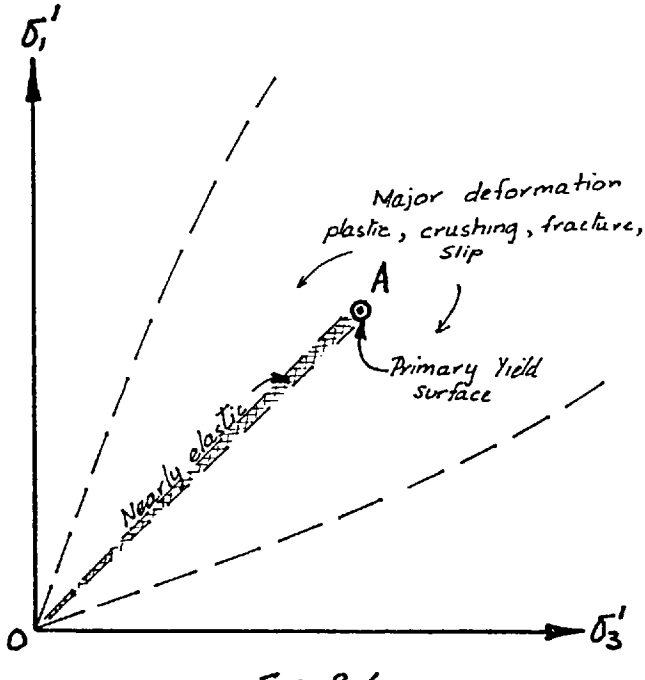


FIG 8·6

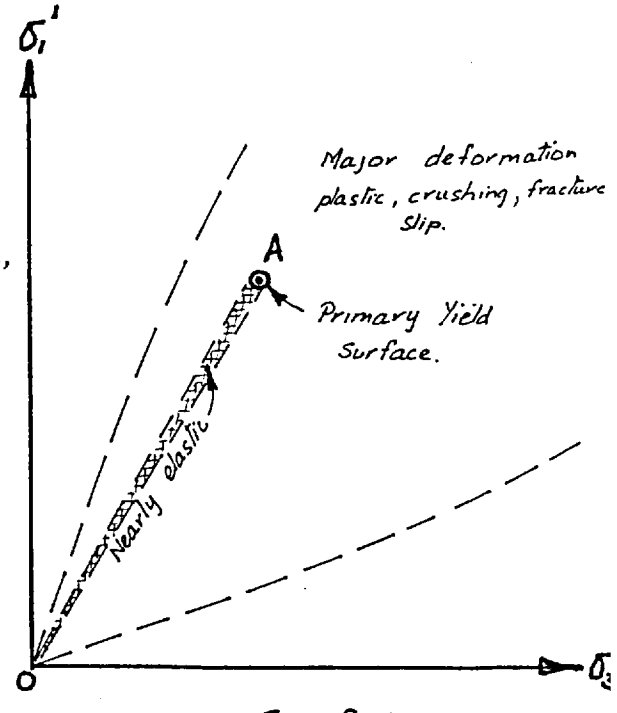
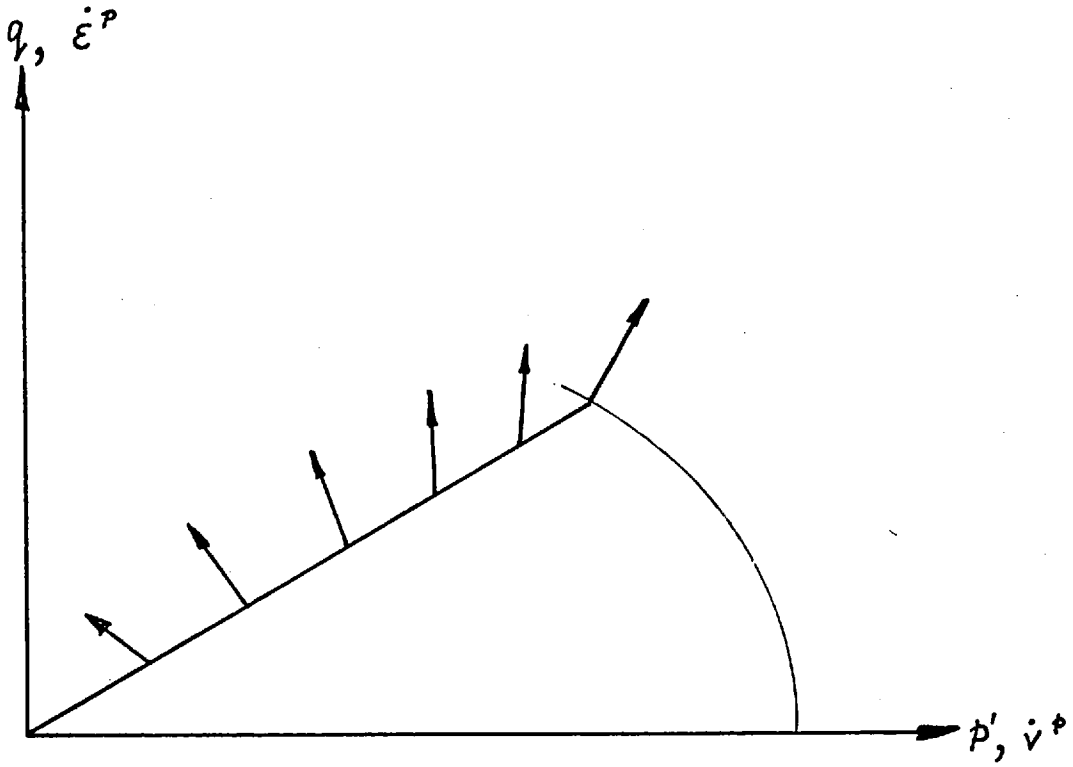


FIG 8·7

HIGH PRESSURE.



Rotation of the permanent strain increment-vector, along the η_{max} line, for the same type of stress path but different over-consolidation ratio.

After Namy 1970.

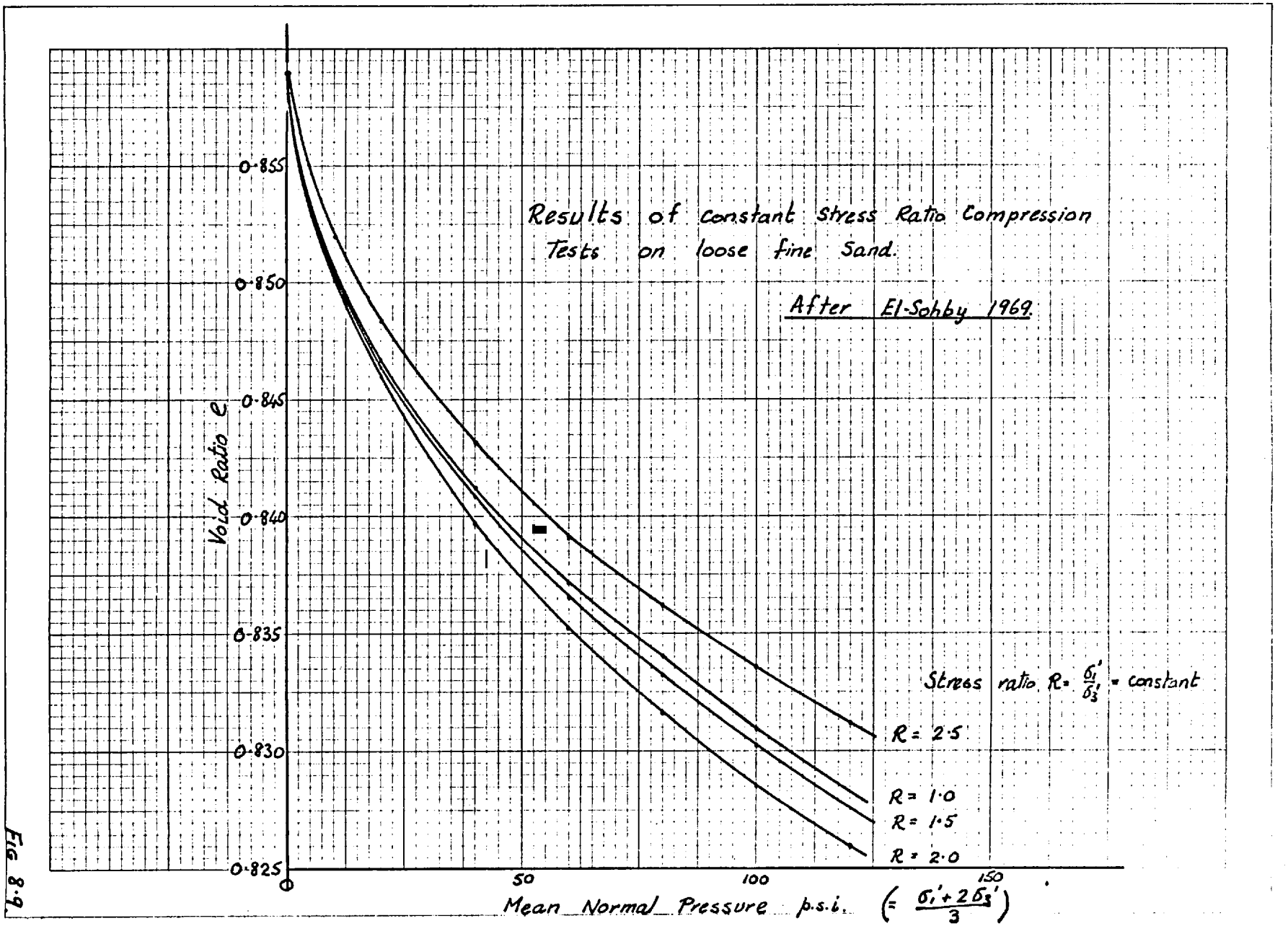

Results of constant Stress Ratio Compression Tests on loose fine Sand.
After El-Sohby 1969
Void Ratio e
0·855
0·850
0·845
0·840
0·835
0·830
0·825
0
50
100
150
Mean Normal Pressure p.s.i. (= σ1' + 2σ3' / 3)
Stress ratio R = σ1'/σ3' = constant
R = 2·5
R = 1·0
R = 1·5
R = 2·0

FIG 8·9.

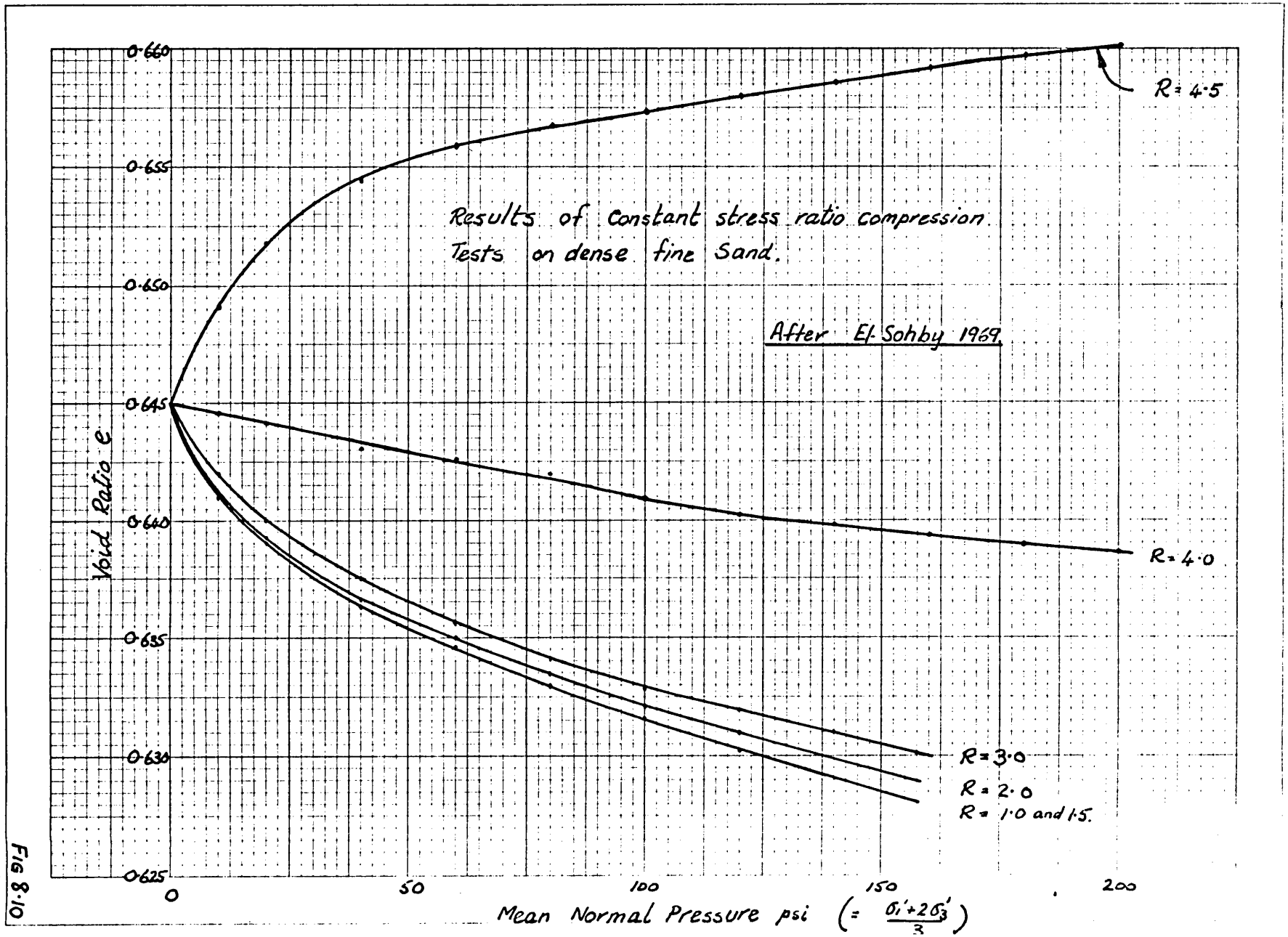

Results of Constant stress ratio compression Tests on dense fine Sand.
After El-Sohby 1969.
R = 4·5
R = 4·0
R = 3·0
R = 2·0
R = 1·0 and 1·5.
Void Ratio e
0·660
0·655
0·650
0·645
0·640
0·635
0·630
0·625
0
50
100
150
200
Mean Normal Pressure psi (= σ1'+2σ3'/3)

FIG 8·10

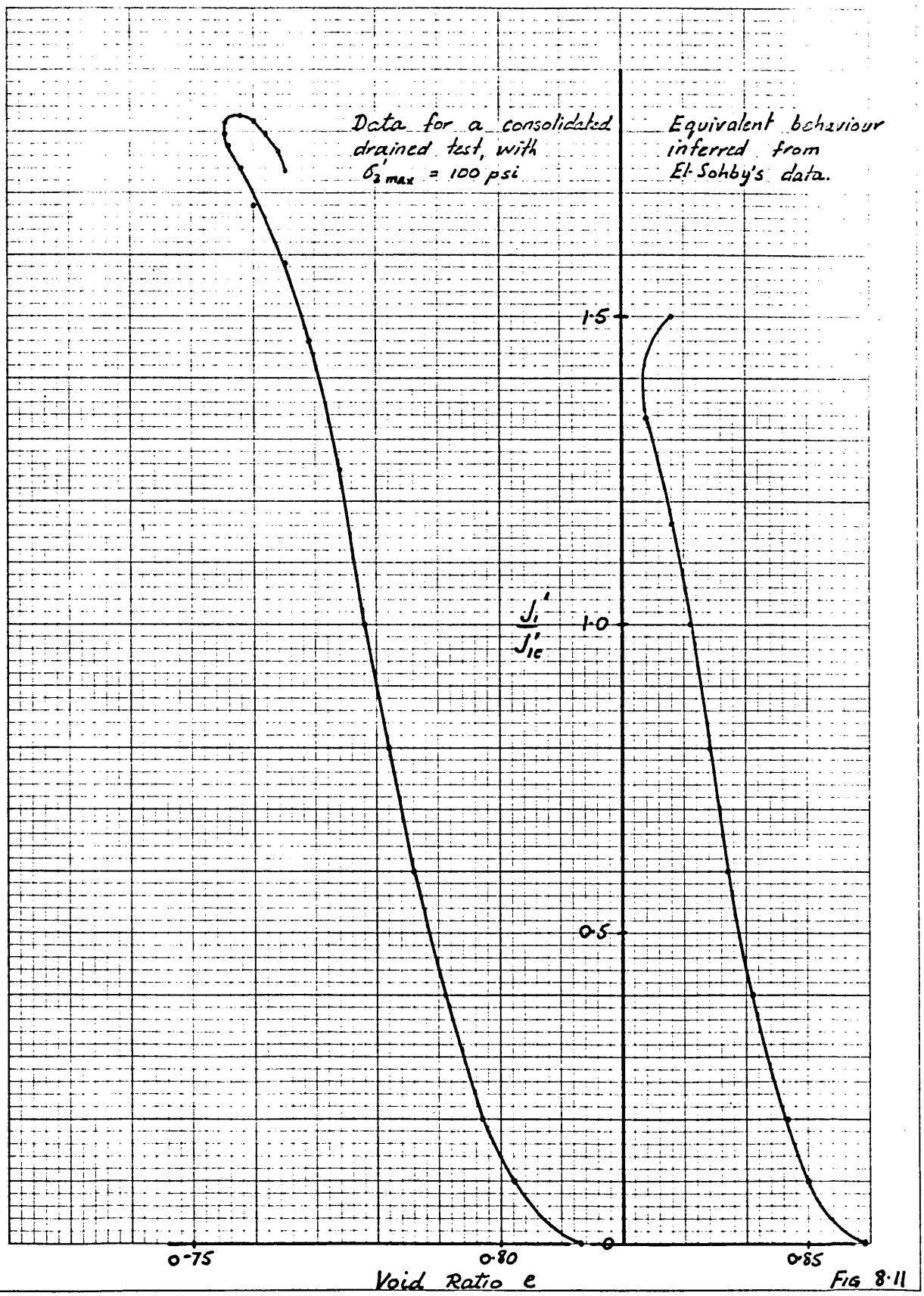

Data for a consolidated drained test, with $\sigma_{3\,max}' = 100$ psi
Equivalent behaviour inferred from El-Sohby's data.
1·5
1·0
0·5
$\frac{J_i'}{J_{ic}'}$
0·75
0·80
0·85
Void Ratio e

FIG 8·11

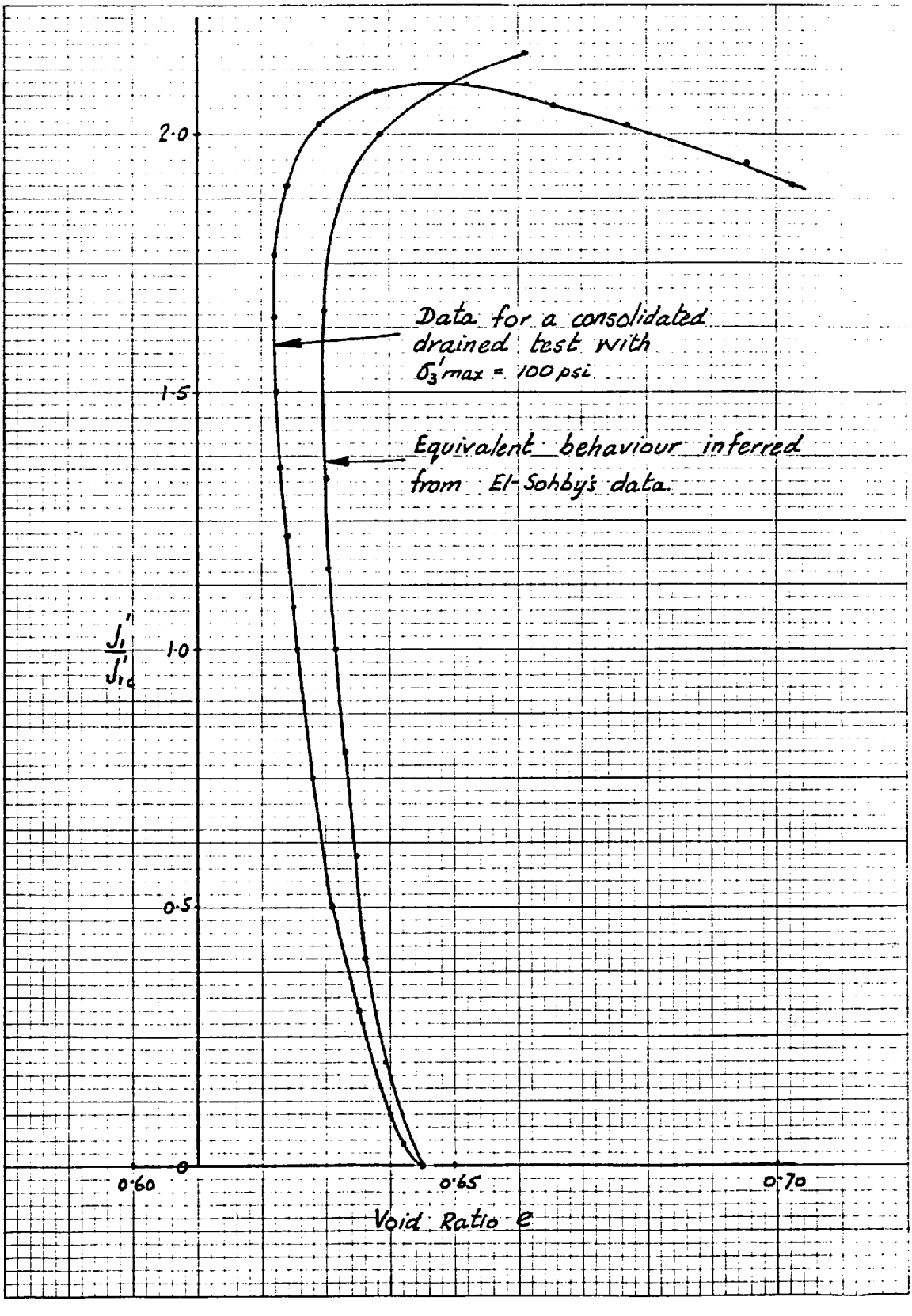
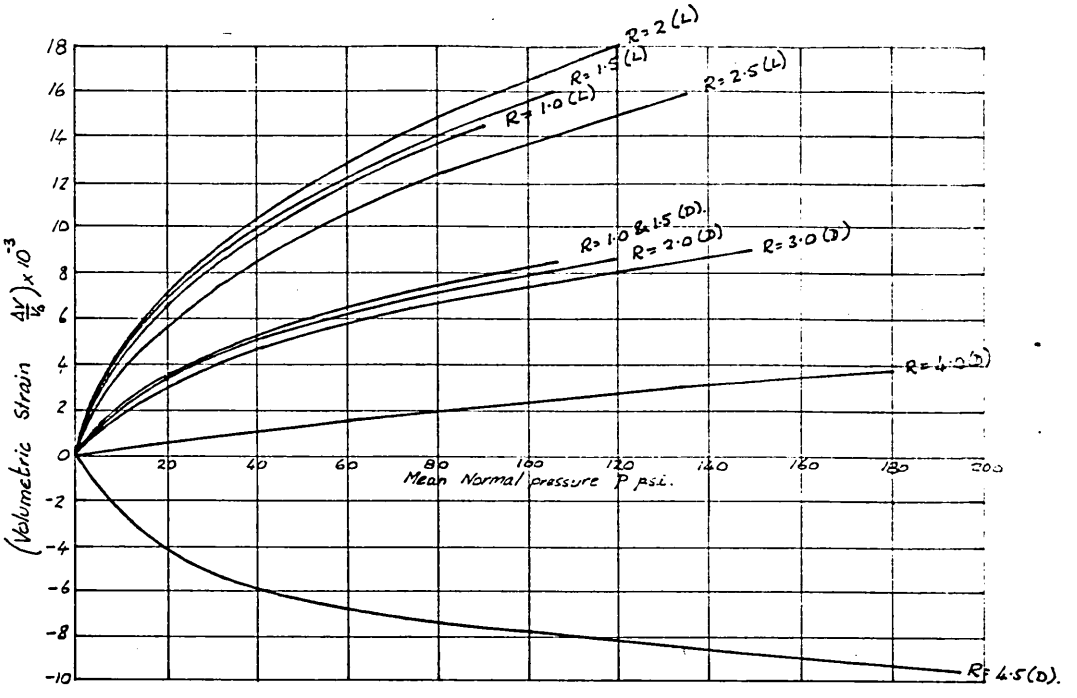
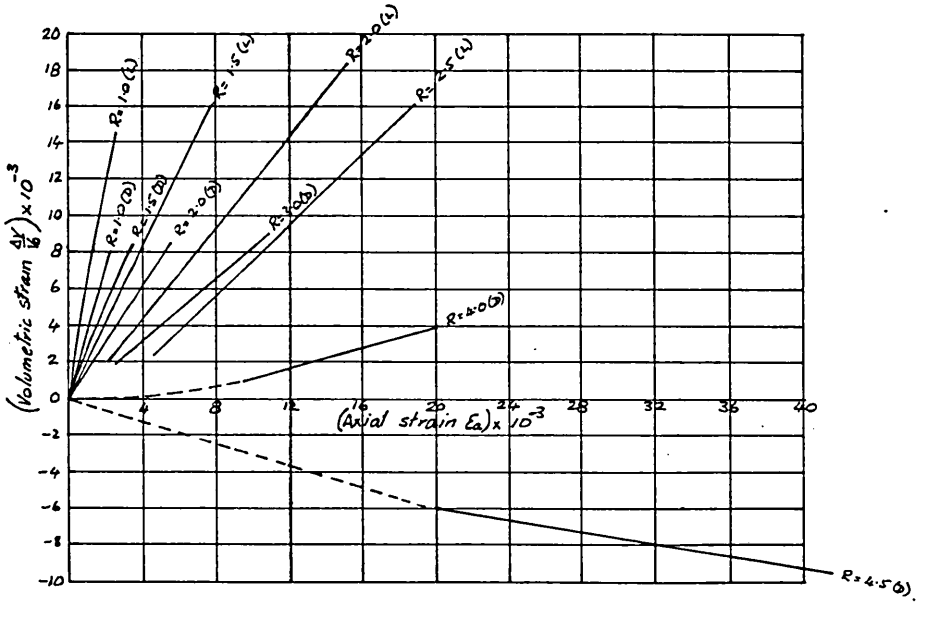

2·0
1·5
1·0
0·5
0
$\frac{J_1'}{J_{1c}'}$
0·60
0·65
0·70
Void Ratio e
Data for a consolidated drained test with $\sigma_3'_{max}$ = 100 psi
Equivalent behaviour inferred from El-Sohby's data.

FIG 8·12.



Compressibility of fine sand under constant stress ratios
Dense e_o=0.645, Loose e_o=0.859.



Relations between Volumetric and Axial strains under constant stress ratios.
Material -fine sand.
After El-Sohby 1969.

FIG. 8·13.

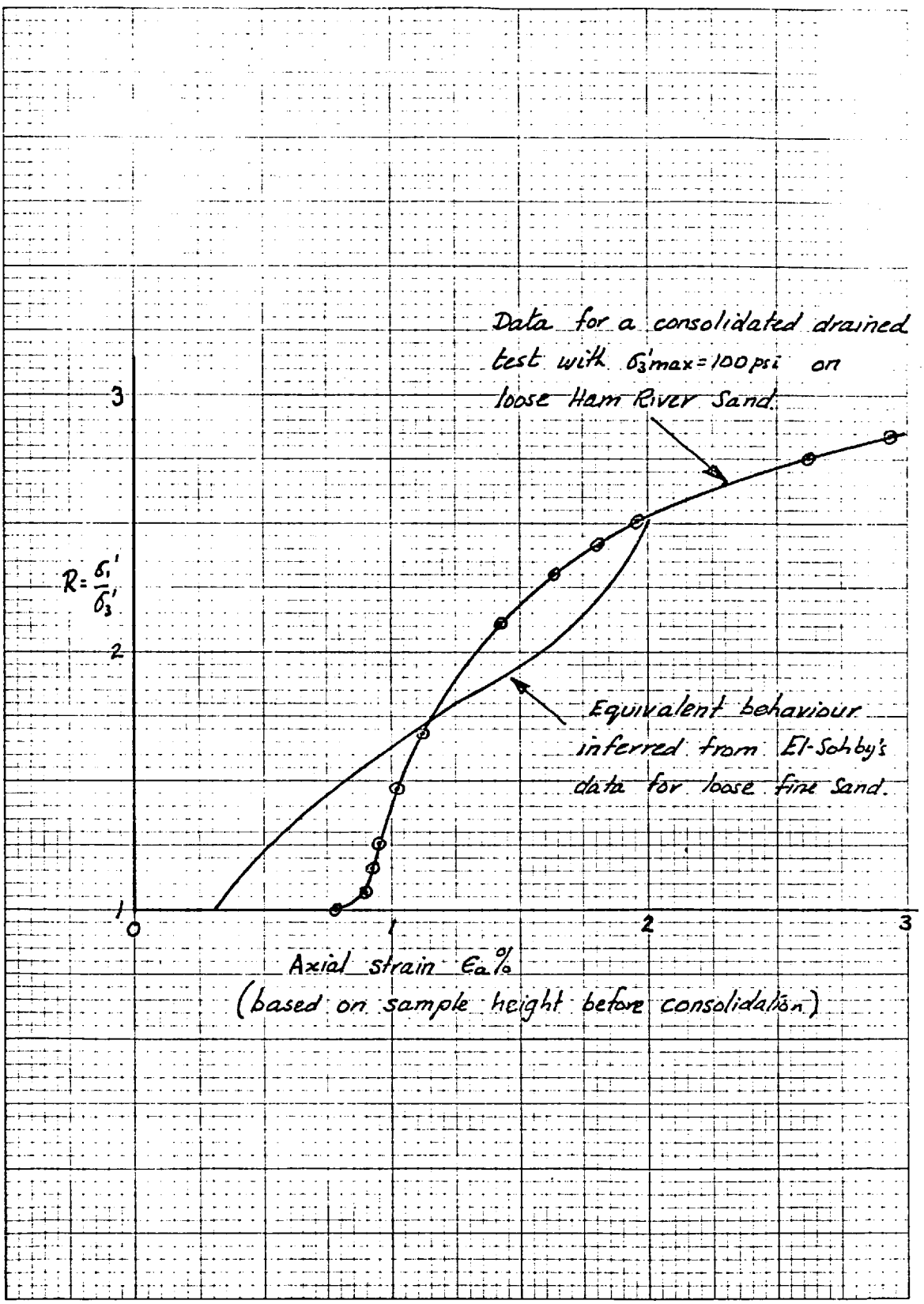

Data for a consolidated drained test with $\sigma_3'_{max}$ = 100 psi on loose Ham River Sand.
Equivalent behaviour inferred from El-Sohby's data for loose fine Sand.
$R = \frac{\sigma_1'}{\sigma_3'}$
3
2
1
0
1
2
3
Axial strain ϵ_a %
(based on sample height before consolidation)

FIG 8·14.

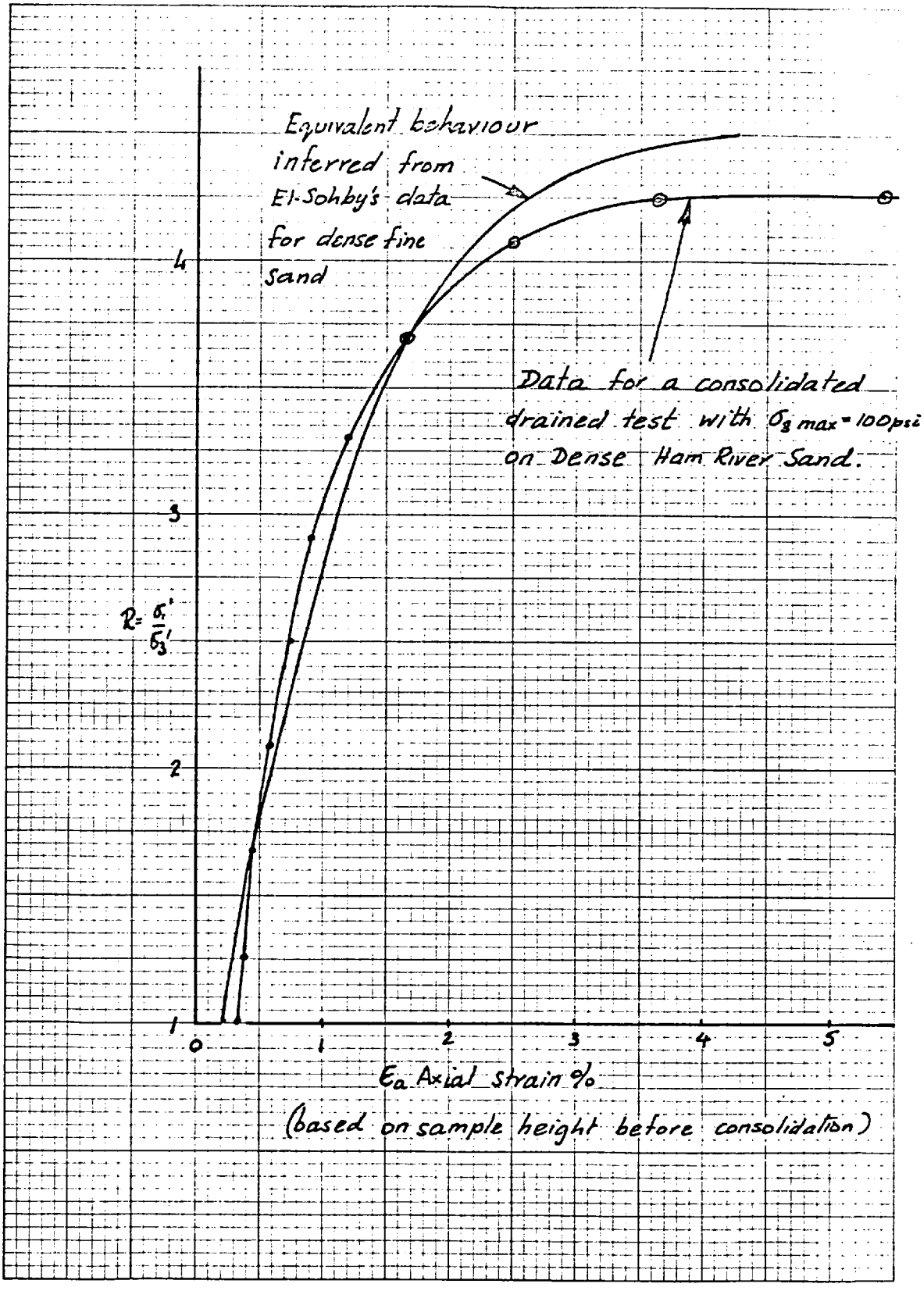

Equivalent behaviour inferred from El-Sohby's data for dense fine sand
Data for a consolidated drained test with $\sigma_{3\,max}$ = 100psi on Dense Ham River Sand.
$R = \frac{\sigma_1'}{\sigma_3'}$
4
3
2
1
0
1
2
3
4
5
ε_a Axial strain %
(based on sample height before consolidation)

FIG. 8·15.

BIBLIOGRAPHY

ADAMS, L.H. & WILLIAMSON, E.D. (1923). On the compressibility of minerals and rocks at high pressures. Jour. Franklin Inst., 195, 475-529.

ARTHUR, J.R.F. (1971). New techniques to measure new parameters. Proc. Roscoe Memorial Symp., Cambridge, 340-346.

BAILEY, A.L. & COURTNEY-PRATT, J.S. (1955). The area of a real contact and shear strength of monomolecular layers of a boundary lubricant. Proc. Roy. Soc., A227, 500-515.

BARDEN, L. & KHAYATT, A.J. (1966). Incremental strain rate ratios and strength of sand in the triaxial test. Geotechnique, 16, 338-357.

BERGSTROM, B.H. (1963). Crushing of single brittle particles. Proc. 1st Tewkesbury Symp., Faculty of Eng., University of Melbourne, 329-343.

BILLAM, J. (1967). The behaviour of granular materials at high pressures. PhD Thesis, University of Birmingham.

BILLAM, J. (1971). Some aspects of the behaviour of granular materials at high pressures. Proc. Roscoe Memorial Symp., Cambridge, 69-80.

BISHOP, A.W. (1952). The stability of earth dams. PhD Thesis, University of London.

BISHOP, A.W. (1953). Private communication to Dr A S Laughton.

BISHOP, A.W. (1954). Shear characteristics of a saturated silt, measured in triaxial compression. Correspondence, Geotechnique, 4, 43-45.

BISHOP, A.W. (1965). Shear strength behaviour of soils under high confining pressures. Discussion, Proc. 6th Int. Conf. Soil Mech., 3, 306-310.

BISHOP, A.W. (1971). Shear strength parameters for undisturbed and remoulded soil specimens. Proc. Roscoe Memorial Symp., Cambridge, 3-58.

BISHOP, A.W. & GREEN, G.E. (1965). The influence of end restraint on the compression strength of a cohesionless soil. Geotechnique, 15, 243-266.

BISHOP, A.W. & HENKEL, D.J. (1962). The measurement of soil properties in the triaxial test. Edward Arnold, London (2nd edition).

BISHOP, A.W., WEBB, D.L. & SKINNER, A.E. (1965). Triaxial tests on soil at elevated cell pressures. Proc. 6th Int. Conf. Soil Mech., 1, 170-174.

BORG, I., FRIEDMAN, M., HANDIN, J. & HIGGS, D.V. (1960). Experimental deformation of St Peter Sand: a study of cataclastic flow. Geol. Soc. America, Memoir 79, 133-191.

BOWDEN, F.P. & BROOKES, C.A. (1966). Frictional anisotropy in non-metallic crystals. Proc. Roy. Soc., A295, 244-258.

BOWDEN, F.P. & HANWELL, A.E. (1966). The friction of clean crystal surfaces. Proc. Roy. Soc., A295, 233-243.

BOWDEN, F.P. & TABOR, D. (1954). Friction and lubrication of solids. Part 1. Oxford Univ. Press.

BOWDEN, F.P. & TABOR, D. (1964). Friction and lubrication of solids. Part 2. Oxford Univ. Press.

BRACE, W.F. & WALSH, J.B. (1962). Some direct measurements of the surface energy of Quartz and Orthoclase. The American Mineralogist, 47, 1111-1122.

BRIDGMAN, P.W. (1925). The linear compressibility of fourteen natural crystals. Amer. J. Sci., 10, 483-498.

BRIDGMAN, P.W. (1928). The linear compressibility of thirteen natural crystals. Amer. J. Sci., 15, 287-296.

BURLAND, J.B. (1965). The yielding and dilation of clay. Correspondence, Geotechnique, 15, 211-214.

BYERLEE, J.D. (1967). Theory of friction based on brittle fracture. Jour. App. Physics, 38, 2928-2934.

CALLADINE, C.R. (1963). A theoretical and experimental study of strains in triaxial compression tests on normally consolidated clays. Correspondence, Geotechnique, 13, 250-255.

CAQUOT, A. (1934). Equilibre des Messifs à Frottement Interne, Pulvérulents et Cohérentes. Gauthier-Villars, Paris.

CHAPLIN, T.K. (1961). An experimental study of the settlement of footings in sand. PhD Thesis, University of Birmingham.

CHRISTIE, J.M., HEARD, H.C. & LaMORI, P.N. (1964). Experimental deformation of Quartz single crystals at 27 to 30 kilobars confining pressure and 24°C. Amer. Jour. Sci., 262, 26-55.

CLARK, S.P. (Ed.) (1966). Handbook of physical constants. (Revised edition). Geol. Soc. America, Memoir 97.

CLOUGH, R.W. & WOODWARD, R.J. (1967). Analysis of embankment stresses and deformations. Proc. Amer. Soc. civ. Engrs., 93, SM4, 529-549.

COLBACK, P.S.B. & WIID, B.L. (1965). The influence of moisture content on the compressive strength of rock. Proc. Rock Mech. Symp. at Univ. of Toronto. Pub. Mines Branch, Dept. of Mines & Tech. Surv., Ottawa.

DRUCKER, D.C., GIBSON, R.E. & HENKEL, D.J. (1955). Soil mechanics and work-hardening theories of plasticity. Proc. Amer. Soc. civ. Engrs., Eng. Mech. Div., 81, paper 798.

DRUCKER, D.C. & PRAGER, W. (1952). Soil mechanics and plastic analysis or limit design. Quart. Jour. App. Math., 10, 157-165.

FRYDMAN, S. (1972). An inquiry into the stress-strain behaviour of particulate media. PhD Thesis, Israel Institute of Technology - Haifa.

GIBSON, R.E. & MORGENSTERN, N. (1963). Stress-dilatancy, earth pressures, and slopes. Discussion, Proc. Amer. Soc. civ. Engrs., 89, SM6, 127-129.

GILMAN, J.J. (1960). Direct measurement of the surface energies of crystals. Jour. App. Physics., 31, 2208-2218.

HOLLUBEC, I. (1966). The yielding of cohesionless soils. PhD Thesis, University of Waterloo.

HAMILTON, G.M. & GOODMAN, L.E. (1966). The stress field created by a circular sliding contact. Jour. App. Mech., June, 371-376.

HEARD, H.C. (1963). Effect of large changes in strain rate in the experimental deformation of Yule Marble. Jour. Geol., 71, 162-195.

HILL, R. (1950). The mathematical theory of plasticity. Oxford Univ. Press.

HILLIG, W.B. (1961). Strength of bulk fused Quartz. Jour. App. Physics, 32, 741.

HIRAMATSU, Y. & OKA, Y. (1966). Determination of the tensile strength of rock by a compression test of an irregular test piece. Int. Jour. Rock Mech. & Mining Sci., 3, 89-99.

HOLESTÖL, K., KJAERNSLI, B. & TORBLAA, I. (1965). Compression of tunnel spoil at Venemo Dam. Proc. 6th Int. Conf. Soil Mech., 2, 490-494.

HORN, H.M. & DEERE, D.U. (1962). Frictional characteristics of minerals. Geotechnique, 12, 319-335.

HORNE, M.R. (1965). The behaviour of an assembly of rotund, rigid, cohesionless particles, I and II. Proc. Roy. Soc., A286, 62-97.

HORNE, M.R. (1969). The behaviour of an assembly of rotund rigid, cohesionless particles, III. Proc. Roy. Soc., A310, 21-34.

JAEGER, J.C. (1967). Failure of rocks under tensile conditions. Int. Jour. Rock Mech. and Mining Sci., 4, 219-227.

JOHNSON, K.L. (1955). Surface interaction between elastically loaded bodies under tangential forces. Proc. Roy. Soc., A230, 531-548.

JOHNSON, K.L. (1961). Energy dissipation at spherical surfaces in contact transmitting oscillating forces. Jour. Mech. Eng. Sci., 3, 362-368.

KING, R.F. & TABOR, D. (1954). The strength properties and frictional behaviour of brittle solids. Proc. Roy. Soc., A223, 225-238.

KJAERNSLI, B. (1962). Deformations of rockfill dams. NGI Pub. No 48.

LAUGHTON, A.S. (1955). The compaction of ocean sediments. PhD Thesis, University of Cambridge.

LAWTON, F.L. & LESTER, M.D. (1964). Settlement of rockfill dams. Proc. 8th Cong. Large Dams, 3, 599-613.

MARSH, D.M. (1964). Plastic flow in glass. Proc. Roy. Soc., A279, 420-435.

MAXWELL, J.C. (1960). Experiments on compaction and cementation of sand. Geol. Soc. Amer., Memoir 79, 105-132.

McCLINTOCK, F.A. & ARGON, A.S. (Ed.) (1966). Mechanical behaviour of materials. Addison-Wesley.

McFARLANE, J.S. & TABOR, D. (1950). Relation between friction and adhesion. Proc. Roy. Soc., A202, 244-253.

MINDLIN, R.D. (1949). Compliance of elastic bodies in contact. Jour. App. Mech. (Trans. ASME), 71A, 259-268.

MINDLIN, R.D. & DERESIEWICZ, H. (1953). Elastic spheres in contact under varying oblique forces. Jour. App. Mech., Sept, 327-344.

MINDLIN, R.D., MASON, W.P., OSMER, T.F. & DERESIEWICZ, H. (1951). Effects of an oscillating tangential force on the contact surfaces of elastic spheres. Proc. 1st. U.S. Nat. Cong. App. Mech., 203-208.

MOTT, B.W. (1956). Micro-indentation hardness testing. Butterworths.

MULHEARN, T.O. (1959). The deformation of metals by Vickers-type pyramidal indenters. Jour. Mech. Phys. Solids, 7, 85-96.

NAMY, D. (1970). An investigation of certain aspects of stress-strain relationships for clay soils. PhD Thesis, Cornell University.

OROWAN, E. (1949). Fracture and strength of solids. Rept. Prog. Phys., 12, 185-232.

PATERSON, M.S. (1970). Ch. 5: The mechanical behaviour of materials under pressure. (Pugh, H. Ll. D., ed.) Elsevier.

PIGEON, Y. (1969). The compressibility of rockfill. PhD Thesis, University of London.

PENMAN, A.D.M., BURLAND, J.B. & CHARLES, J.A. (1971). Observed and predicted deformations in a large embankment dam during construction. Proc. Inst. civ. Engrs., 49, 1-21.

ROSCOE, K.H. (1967). Discussion of Session 2. Proc. Geotech. Conf., Oslo, 2, 167-170.

ROSCOE, K.H. & SCHOFIELD, A.N. (1964). Stress-dilatancy, earth pressures and slopes. Discussion, Proc. Amer. Soc. civ. Engrs., 90, SM1, 136-150.

ROSCOE, K.H., SCHOFIELD, A.N. & WROTH, C.P. (1958). On the yielding of soils. Geotechnique, 8, 22-52.

ROSENQVIST, I.Th. (1959). Physico-chemical properties of soils: soil-water systems. Proc. Amer. Soc. civ. Engrs., 85, SM2, 31-53.

ROWE, P.W. (1962). The stress-dilatancy relation for static equilibrium of an assembly of particles in contact. Proc. Roy. Soc., A269, 500-527.

ROWE, P.W. (1963). Stress-dilatancy, earth pressure and slopes. Proc. Amer. Soc. civ. Engrs., 89, SM3, 37-61.

ROWE, P.W. (1964). Stress-dilatancy, earth pressure and slopes. Reply to discussion, Proc. Amer. Soc. civ. Engrs., 90, SM4, 145-180.

SAMUELS, L.E. & MULHEARN, T.O. (1957). An experimental investigation of the deformed zone associated with indentation hardness impressions. Jour. Mech. Phys. Solids, 5, 125-134.

SCHELLINGER, A.K. (1952). Solid surface energy and calorimetric determination of surface energy relationships for some common minerals. Min. Eng., 4, 369-374.

SCHOFIELD, A.N. & WROTH, C.P. (1968). Critical state soil mechanics. McGraw-Hill.

SCOTT, R.F. (1964). Stress-dilatancy, earth pressures and slopes. Discussion, Proc. Amer. Soc. civ. Engrs., 90, SM1, 133-135.

SKEMPTON, A.W. (1960). Effective stress in soils, concrete and rocks. Conf. on Pore Pressure and Suction in Soils. Butterworths.

SKEMPTON, A.W. (1964). Fourth Rankine Lecture - Long-term stability of clay slopes. Geotechnique, 14, 77-101.

SOWERS, G.F., WILLIAMS, R.C. & WALLACE, T.S. (1965). Compressibility of broken rock and the settlement of rockfills. Proc. 6th Int. Conf. Soil Mech., 2, 561-565.

SRIDHARAN, A. & VENKATAPPA RAO, G. (1973). Mechanisms controlling volume change of saturated clays and the role of the effective stress concept. Geotechnique, 23, 359-382.

TAYLOR, D.W. (1948). Fundamentals of soil mechanics. New York: John Wiley.

TCHALENKO, J.S. (1967). The influence of shear and consolidation on the microscopic structure of some clays. PhD Thesis, University of London.

TERZAGHI, K. (1920). Old earth-pressure theories and new test results. Eng. News-Record, 85, 632-637.

TERZAGHI, K. (1925). Erdbaumechanik auf bodenphysikalischer Grundlage. Leipzig, Deuticke.

TROLLOPE, D.H. & PARKIN, A.K. (1963). Stress-dilatancy, earth pressures and slopes. Discussion, Proc. Amer. Soc. civ. Engrs., 89, SM6, 129-133.

WACKERLE, J (1962) Shock-Wave compression of Quartz. Jour. App. Phys: 33, 922-937.

El-SOHBY, M.A. (1969) Deformation of Sands under constant stress ratios Proc. 7th Int. Conf. Soil Mech., 1, 111-119.